

Marinda Wu · Wei Gao · Lei Li ·
Yingchun Lu · Jingbo Louise Liu *Editors*

Advanced Materials for Multidisciplinary Applications



 Springer

Advanced Materials for Multidisciplinary Applications

Marinda Wu · Wei Gao · Lei Li · Yingchun Lu ·
Jingbo Louise Liu
Editors

Advanced Materials for Multidisciplinary Applications



 Springer

Editors

Marinda Wu
Chinese American Chemical Society
Castro Valley, CA, USA

Lei Li
Chemical and Petroleum Engineering
University of Pittsburgh
Pittsburgh, PA, USA

Jingbo Louise Liu
Department of Chemistry
Texas A&M University—Kingsville
Kingsville, TX, USA

Wei Gao
Corporate Research and Development
The Dow Chemical Company
Collegeville, PA, USA

Yingchun Lu
Chinese American Chemical Society
South Brunswick, NJ, USA

ISBN 978-3-031-39403-4 ISBN 978-3-031-39404-1 (eBook)
<https://doi.org/10.1007/978-3-031-39404-1>

© The Editor(s) (if applicable) and The Author(s), under exclusive license to Springer Nature Switzerland AG 2024

This work is subject to copyright. All rights are solely and exclusively licensed by the Publisher, whether the whole or part of the material is concerned, specifically the rights of translation, reprinting, reuse of illustrations, recitation, broadcasting, reproduction on microfilms or in any other physical way, and transmission or information storage and retrieval, electronic adaptation, computer software, or by similar or dissimilar methodology now known or hereafter developed.

The use of general descriptive names, registered names, trademarks, service marks, etc. in this publication does not imply, even in the absence of a specific statement, that such names are exempt from the relevant protective laws and regulations and therefore free for general use.

The publisher, the authors, and the editors are safe to assume that the advice and information in this book are believed to be true and accurate at the date of publication. Neither the publisher nor the authors or the editors give a warranty, expressed or implied, with respect to the material contained herein or for any errors or omissions that may have been made. The publisher remains neutral with regard to jurisdictional claims in published maps and institutional affiliations.

This Springer imprint is published by the registered company Springer Nature Switzerland AG
The registered company address is: Gewerbestrasse 11, 6330 Cham, Switzerland

Paper in this product is recyclable.

Preface

The book *Advanced Materials for Multidisciplinary Applications* is a compilation of contributions from many distinguished scientists, engineers, professors, and entrepreneurs who are members and allies of the Chinese American Chemical Society (CACS). This book celebrates the CACS's 40th anniversary and recognizes its members' outstanding achievements and contributions to society. The researchers behind this book overcame the obstacles posed by the COVID-19 pandemic, displaying resilience, determination, and adaptability to complete their missions. These professionals have also inspired and empowered the next generation with their empathy, diligence, and talent. This book comprises fourteen (14) chapters that showcase the latest research progress and reviews related to the advancement of materials with tunable structure and stoichiometry, surface area, pore sizes, and chemical functionality based on the diverse applications. Two standout chapters include "Chap. 1: *Leadership and Resiliency in the Global Chemistry Enterprise*" and "Chap. 14: *Achievements Made by Professionals with Diversified Backgrounds*". The book also covers three technical parts of advanced materials and their applications in biomedical, energy and fuels, and environmental and spectroscopic research fields. These topics address nanotechnological design, production, and application in diverse research fields. Overall, this book provides an excellent overview of the latest research in advanced materials, highlighting the contributions of the CACS's members and their allies. The book's research and insights will be a valuable reference tool for scientists, engineers, entrepreneurs, and students in materials science, engineering, chemistry, and chemical science.

Regarding the nanotechnological application in biomedical applications, this book includes four chapters. Chapter 2, *Recent Advancement of Nanotechnology in Bio Applications*, led by Dr. Ashraf Abedin, highlights the application of nanostructured materials and devices in various biological fields, such as diagnostics, drug administration, imaging, tissue engineering, and treatments. The authors have emphasized nanotechnology's recent developments and existing challenges in bio-applications. Their research has revealed the immense potential of nanotechnology in providing multiple diagnostic and therapeutic applications that can transform the healthcare industry. Studying these intricate nano-applications could encourage future research

and development in the biomedical sector. Ongoing efforts are being made to translate these scientific breakthroughs into clinical practice, which could revolutionize the field of biomedicine.

Chapter 3, *Functionalized Carbon Nanotubes as Gene Carriers*, led by Dr. Jih Ru Hwu, discusses the development and applications of carbon nanotubes (CNTs) as gene carriers. Modifying the surface of single- and multi-walled CNTs with various functional groups and ligands was discussed in detail. The types of bonds formed during the functionalization of pristine CNTs and the many different ligands used were emphasized. The interactions between functionalized CNTs (f-CNTs) and genes or oligonucleotides were also explored, highlighting the electrostatic interaction, hydrogen bonding, π - π stacking, and other intermolecular forces involved. The targets of f-CNTs and the creation of hybrids of genes @ f-CNTs were taken into account. The authors discovered that the success of these applications depended on the methods used for hybrid formation and dissociation. The article concluded by emphasizing that the practical techniques for the hybrid formation and dissociation were key to the success of CNTs as gene carriers for modern gene therapy.

Chapter 4, *Selected Recent Work on Endo-Functionalization of Cylindrical Macrocyclic Artificial Receptors for Mimicking Protein–Ligand Interactions*, led by Dr. Yahu A. Liu provided a medicinal process for modifying the way a small molecule interacts with a target receptor (typically a protein). As therapeutic techniques continue to evolve, scientists have been working to modify small molecules that interact with target receptors, such as proteins. By adjusting these interactions, researchers can achieve their desired therapeutic outcome. To better understand these interactions, scientists have begun using functionalized macrocyclic receptors as models for mimicking protein binding pockets. Recent advancements in functionalization have led to the creation of synthetic cylindrical- and vase-shaped cylindrical macrocyclic receptors. These new developments are thought-provoking and have caught the attention of medicinal chemists worldwide. In this chapter, the authors focused on the endo-functionalization of cylindrical and vase-shaped cylindrical macrocyclic receptors and their binding features in model protein-ligand interactions. By presenting selected examples from a medicinal chemist's perspective, we hope to provide insight into the potential applications of these tools in future medicinal processes.

Chapter 5, *Singlet Oxygen Photo-Generation by Light Irradiation Using Metal–Organic Frameworks as Photodynamic Therapy Agents*, led by Sajid Bashir Liu, presented the design and application of metal-organic-framework (MOFs). Dr. Bashir and his team created and tested a new MOF motif (abbreviated as Zr7Pr) and evaluated it in retinal pigmented epithelial cells in vitro for singlet oxygen inactivation of cell function. Cellular health was assessed through the measurement of stress biomarkers. The lactate dehydrogenase and mitochondrial membrane potential activity increases are consistent with singlet reactive oxygen species. The levels of nitric oxide and peroxynitrite as possible reactive nitrogen species were evaluated to identify the site of Zr7Pr's inhibitory function. The data indicated that singlet oxygen generates superoxide and nitric oxide. The reactivity of Zr7Pr is anticipated through the inactivation of mitochondrial pore transitions rather than complete membrane

peroxidation. The exposed cysteines or histidine in the molecular targets is modified, which affects the cell's ability to regulate apoptosis-inducing MPTs under oxidative stress. Cells tolerant to hydrogen peroxide poisoning are still susceptible to the actions of Zr7Pr. Its efficacy is most likely through the impairment of mitochondrial function and modification of the pore within the adenosine nucleotide translocase protein family domain of the MPT.

Part II of the book showcased the nanomaterials applied in energy and fuels to enhance CO₂ conversion and gas absorption. Chapter 6, *Chemical Looping for CO₂ Conversion and Utilization—Recent Advances and Perspective*, led by Dr. Liang-Shih Fan, provided solutions to the massive increase in the emissions of CO₂ that is contributing to global warming and negatively impacting Earth's ecosystems. To achieve CO₂ removal or carbon neutrality, authors carried out significant research on CO₂ conversion and utilization. Dr. Fan and his team invited clean energy technology in chemical looping with inherent CO₂ separation. This technology involves the reaction and regeneration of solid materials (the looping carriers). Recently, the team proposed and investigated novel chemical looping processes and looping carriers. They anticipated improving CO₂ utilization as a partial substitute for hydrocarbon feedstock or a soft oxidant for looping carrier regeneration. This chapter describes the advances in chemical looping technology, emphasizing the fundamentals of CO₂ conversion during reduction and oxidation (redox) reactions. Authors reported that these new advances would accelerate the large-scale deployment of CO₂ utilization technologies.

Chapter 7, *Diversity Oriented Synthesis of Metal-Organic Frameworks*, is led by Dr. Hong-Cai Zhou. The authors provided novel methods to produce metal-organic frameworks (MOFs), highly porous materials consisting of organic linkers and metal nodes, making them ideal for various applications such as gas storage/separation, catalysis, and biomedicine. A vast library of around 99,000 MOF structures has been established, largely due to the tireless efforts of MOF researchers who often use a Diversity-Oriented Synthesis (DOS) strategy. DOS is a well-established technique in organic chemistry that allows for creating a library of diverse molecules based on a starting compound. In the same vein, MOFs can be easily manipulated to produce a variety of structures thanks to their tunable skeleton, which can be readily modified or disintegrated into other materials. This chapter examines the various methodologies for DOS of MOFs, including linker functionalization and exchange, and evaluates their applicability and limitations. Advanced tools like automated synthesis and data mining can be incorporated into the DOS of MOFs. The authors also provided insight into how different post-synthetic methodologies can foster the discovery of diverse MOF structures, thereby inspiring future MOF design and synthesis.

Chapter 8, *The Promise and Reality of Sustainable Fuels*, led by Dr. Robert Luckett, provided a bigger vision emphasizing the challenges of the world's energy supply and fuel consumption. Energy consumption highly depends on using fossil fuels, coal, petroleum, and natural gases. The depletion of these resources is a major challenge as it leads to an increase in prices and a decrease in energy availability. Therefore, renewable energy sources, particularly sustainable fuels, become critically demanding. Renewable sources of energy and fuels are abundant and do not

emit greenhouse gases or contribute to climate change. Promoting efficient energy use techniques promises to reduce energy consumption and conserve fuel supplies. The diversity of sustainable fuel supplies is another driving force for the stakeholders to explore in this direction to foster development and commercialization. The exploration and production of more diverse energy sources like natural gas, nuclear power, and biofuels help to sustain a diverse and secure energy supply. This chapter summarized the background of energy development, different families of fuel supplies, geopolitical instability, and grand challenges of sustainable aviation fuels.

Chapter 9 was entitled *Thermal Analysis During Metallic Additive Manufacturing*, co-led by Gaoqiang Yang Feng-Yuan Zhang. These two teams collectively investigated the ability to produce 3D parts with anfractuous and complex structures, limited post-processing, and minimal wastage of raw materials. Additive manufacturing (AM) technology has revolutionized the manufacturing industry by enabling printing without tooling or machining limits. It is widely used in industrial and research sectors worldwide, with its prospects rapidly expanding. However, the temperature distribution and heat transfer during AM processes are critical factors that directly impact the structures and properties of metallic components. This chapter comprehensively summarizes the thermal analysis and heat transfer during metallic AM processes. Metallic AM methods are divided into several categories, including powder bed fusion, direct energy deposition, and other metallic AM processes. The challenges of heat transfer in each metallic AM process are fully discussed, and the energy insertion and material thermal properties are explained to aid fundamental understanding. Finally, the experimental and computational studies of thermal analysis in different metallic AM methods are summarized, and future research directions are provided. The chapter highlights the significance of thermal analysis in metallic AM for designing high-quality metallic components and improving the process capabilities of various metallic AM techniques.

Part III of this book highlights various environmental and spectroscopic applications of atomistic and nanostructured materials. Chapter 10, *Single Atom Catalysts for Environmental Remediation*, has been led by Dr. Xingmao Ma. Single atom catalysts (SACs) are highly advanced catalysts that incorporate well-dispersed metal atoms on a support material. Research studies have uncovered the enormous potential of SACs in environmental applications. For SACs to be fully effective, the supporting material used also plays a crucial role in determining their catalytic properties. Nitrogen-doped carbon is the most commonly used support material for SACs in environmental applications. SACs' reactivity is enhanced due to their active chemoelectrical property, adjustable surface functional groups, porous structure, and eco-friendliness. When used in environmental remediation, SACs often activate hydrogen peroxide, peroxy-monosulfate, and peroxydisulfate. This activation extends the reaction pH limitation from less than 4.0 to a wider range of 4.0–10.0, generating highly reactive radicals. This chapter showed the common characterization techniques for SACs and the role of supporting materials, followed by a discussion on the activation mechanisms of common oxidants by SACs. Additionally, research gaps and future needs are identified. Overall, SACs possess unique properties and exceptional catalytic performance

that offers great potential for addressing the persistent environmental challenges that threaten our planet.

Chapter 11, *Topological Interpenetrative Covalent Anchored Network (TIP CAN) for H₂S Detection, Storage, and Remediation Relevance to Shipboard Wastewater*, is led by Sajid Bashir. Hydrogen sulfide (H₂S) can be generated on ships from seawater with sulfates storage or oil-bilge tanks containing hydrocarbons with sulfur and sulfur-containing detergents or gray- and blackwater storage tanks. This workplace hazard requires carefully venting these tanks before inspection and maintenance. In this chapter, the authors reported the synthesis and evaluation of six formulations of detecting agents, demonstrating excellent removal of H₂S from an offline slurry reactor. These slurry reactor workflows have the advantages of speed of operation, simplicity of design, and ease of use. It would suit a ship with a general crew who would not require a specialist degree to operate the offline slurry reactor to remove H₂S. The kinetics of the reaction were modeled on a shrinking model, and the lowering of the effectiveness of H₂S was attributed to the formation of elemental sulfur and sulfate indirectly confirmed using X-ray photon electron spectroscopy which could block active hydroxyl sites that are avenues for attracting the H₂S molecule. The surface adsorption of H₂S by the exchange with oxygen is suggested as the main mechanism whereby H₂S is removed, followed by surface area and catalyst porosity. This study also offers guidelines for developing filter-based ceramics that could be deployed on ships to remove H₂S from tanks without venting or exposing the crew to possible exposure.

Chapter 12, *Matrix-Assisted Laser Desorption/Ionization Mass Spectrometry with Re-Engineered 2, a 5-Dihydroxypheny Acid Derivative*, was led by Sajid Bashir and dedicated to Dr. Peter Derrick. Authors presented that the matrix-assisted laser desorption ionization has been a mainstay in protein mass spectrometry, imaging, and proteomics. The common approach to matrix design and selection has been empirical. The most common matrices used are 2,5-dihydroxybenzoic (2,5-DHB) and alpha-cyano-4-hydroxycinnamic acid (aCCa). Using the known relationship between 2,5-phenyl carboxylic acid and tyrosine amino A 2,5-dihydroxyphenylcarboxylic acid molecule based on the hydroquinone core of 2,5-DHB was designed and synthesized (M10) by using the known relationship between 2,5-phenyl carboxylic acid and tyrosine amino acids. The two matrices (aCCa and M10) were compared and contrasted using neuronal peptide mixtures, tryptic digests from two-dimensional gel spots from culture *Escherichia coli*, and mature green tomato fruit. The peptide mixtures or mass fingerprints were analyzed similarly, except only a 30 s analysis time window per sample was allocated for M10, whereas 3 minutes per sample were allocated for aCCa.

Chapter 13, *Hydrophilic/Phobic Tailored Multi-laned/Layer Matrix-Assisted Laser Desorption/Ionization (HTML-MALDI)*, was led by Sajid Bashir and dedicated to Dr. Peter Derrick. Authors presented the enhancement of ion yield from a protein mixture using hydrophobic and hydrophilic structured surfaces to enhance analyte solubilization and the spatial separation of matrices to enable multi-matrix desorption and ionization of the peptide mixtures. The use of solid-stated anchored compounds can aid in sample cleanup and digestion, further improving the signal intensity of

digests. However, this research suggested that the results were partly dependent upon the protein's basicity. The more basic lysozyme was found to generate the highest sum of peptide intensities under the dried drop methods. On the other hand, the less basic myoglobin produced the highest sum intensities with anchor support. It was critical to use the matrix species in the middle lane for optimizing analyte peak intensities, although using matrices in peripheral lanes did lead to signal enhancements.

The editorial team is grateful beyond words to the illustrious authors who so meticulously crafted the diverse and fascinating chapters within this literary work, as well as to the invaluable multitudes of reviewers who selflessly scrutinized each manuscript with a keen eye, thereby ensuring that the utmost caliber of work was featured within this collection. The arduous task of planning, compiling, and editing such a comprehensive volume is a feat that could not have been achieved without the unwavering support and investment of Springer Nature Publishing, for which we are indescribably thankful. In particular, we would like to extend our heartfelt gratitude to the esteemed acquisition editor, Charlotte Hollingworth, and the tireless production editor, Cecil Joselin Simon, for their meticulous and indispensable contributions throughout the entire production process. Their assistance and unwavering dedication enabled us to deliver such a phenomenal publication, of which we are exceedingly proud. Looking ahead to the future, we are thrilled to have forged a fruitful and enduring relationship between Springer Nature and the Chinese American Chemical Society and hope to see our collaboration continue to flourish for many years to come. Once again, to all who assisted in bringing this masterful compendium to fruition, we extend our most profound appreciation and sincerest thanks.

Castro Valley, USA
Collegeville, USA
Pittsburgh, USA
South Brunswick, USA
Kingsville, USA

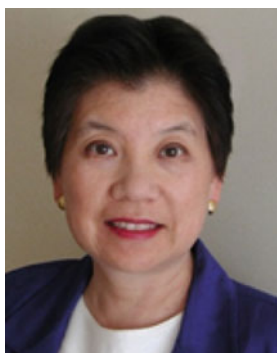
Marinda Wu
Wei Gao
Lei Li
Yingchun Lu
Jingbo Louise Liu

Contents

| | |
|--|-----|
| 1 Leadership and Resiliency in the Global Chemistry Enterprise | 1 |
| Marinda Li Wu, Wei Gao, Chu-An Chang, Lei Li, Yingchun Lu, and Jingbo Louise Liu | |
| Part I Biomedical Applications | |
| 2 Recent Advancement of Nanotechnology in Bio Applications | 59 |
| Ashraf Abedin, Jhonattan David Manosalvas Mora, Adiba Azad, Srikar Bhattar, S. M. Rezwanaul Islam, and Mohammad Hasibul Hasan | |
| 3 Functionalized Carbon Nanotubes as Gene Carriers | 105 |
| Jih Ru Hwu, Shwu-Chen Tsay, Uttam Patil, Animesh Roy, and Wen-Chieh Huang | |
| 4 Selected Recent Work on <i>Endo</i>-Functionalization of Cylindrical Macrocyclic Artificial Receptors for Mimicking Protein–Ligand Interactions | 131 |
| Yahu A. Liu, Zhuo Wang, Weibo Hu, Mingliang Ma, Hui Yang, and Ke Wen | |
| 5 Singlet Oxygen Photo-Generation by Light Irradiation Using Metal–Organic Frameworks as Photodynamic Therapy Agents | 155 |
| Sajid Bashir and Jingbo Louise Liu | |
| Part II Energy and Fuels Applications | |
| 6 Chemical Looping for CO₂ Conversion and Utilization—Recent Advances and Perspective | 173 |
| Zhuo Cheng, Pinak Mohapatra, Anuj Joshi, Rushikesh K. Joshi, and Liang-Shih Fan | |

| | | |
|---|--|-----|
| 7 | Diversity Oriented Synthesis of Metal-Organic Frameworks | 191 |
| | Yu-Chuan Hsu, Kun-Yu Wang, Kui Tan, Joshua A. Powell, and Hong-Cai Zhou | |
| 8 | The Promise and Reality of Sustainable Fuels | 213 |
| | Robert Luckett and Jingbo Louise Liu | |
| 9 | Thermal Analysis During Metallic Additive Manufacturing | 237 |
| | Gaoqiang Yang, Zheng Chen, Yaji Huang, Jingke Mo, Zhenye Kang, and Feng-Yuan Zhang | |
| Part III Environmental and Spectroscopic Application | | |
| 10 | Single Atom Catalysts for Environmental Remediation | 267 |
| | Jieming Yuan and Xingmao Ma | |
| 11 | Topological Interpenetrative Covalent Anchored Network (TIP CAN) for H₂S Detection, Storage, and Remediation Relevance to Shipboard Wastewater | 283 |
| | Sajid Bashir Liu and Jingbo Louise Liu | |
| 12 | Matrix-Assisted Laser Desorption/Ionization Mass Spectrometry with Re-Engineered 2, a 5-Dihydroxypheny Acid Derivative | 313 |
| | Sajid Bashir, M. Gomez, K. A. Beran, J. L. Liu, and P. J. Derrick | |
| 13 | Hydrophilic/Phobic Tailored Multi-laned/Layer Matrix-Assisted Laser Desorption/Ionization (HTML-MALDI) | 339 |
| | Sajid Bashir, Jingbo Liu, and Peter J. Derrick | |
| 14 | Achievements Made by Professionals with Diversified Backgrounds | 357 |
| | Marinda Li Wu, Wei Gao, Chu-An Chang, Lei Li, Yingchun Lu, and Jingbo Louise Liu | |

About the Editors



Dr. Marinda Wu has over 45 years of experience in the chemical industry. She worked many years in research for Dow Chemical R&D where she earned 7 U.S. patents and as a business leader for Dow Plastics. She subsequently held management roles at several smaller chemical companies. A strong advocate of STEM education, she founded “Science is Fun!” to interest young students in science and enhance public support for science education. She has served in many leadership roles for the American Chemical Society including the president (2013), Board of Directors (2006–2014), Councilor (1996–present), and the chair of CEPA, the Committee on Economic and Professional Affairs (2003–2005). She has also served on numerous other national ACS committees and ACS Board Committees. She has helped countless chemists as a certified ACS career consultant for almost 30 years. At her local ACS California Section, she was the 2001 centennial chair, the chair of the Women Chemists Committee (WCC) four times, the chair for the Government Affairs Committee (GAC), the chair or a member of over half a dozen other committees, and continues to serve on the CALACS Executive Committee. She served on the Council of Scientific Society Presidents (2012–2015) and the International Advisory Board for the 45th IUPAC World Chemistry Congress.

She was named an honorary member of the Romanian and Polish Chemical Societies. She is a longtime member of the University of Illinois Chemistry Alumni Advisory Board and the Chinese American Chemical

Society (CACS) Board of Directors (the chair, 2019–present). She also relaunched the CACS Northern California Chapter and serves as its President. She has authored over 70 journal articles, numerous Dow confidential research papers, and chapters, co-edited three ACS Symposium Books, and has been a frequent invited speaker at international and domestic conferences. She was an elected ACS fellow in 2015 and one of three 2023 Fellows for the Federation of Asian Chemical Societies. She has also been honored with the 2022 Shirley Radding ACS Award and named one of twelve 2023 IUPAC Distinguished Women in Chemistry and Chemical Engineering. She received her Ph.D. in inorganic chemistry from the University of Illinois in Urbana-Champaign and a B.S. cum laude with Distinction in Chemistry from The Ohio State University.



Dr. Wei Gao is a fellow in Analytical Science, Corporate Research and Development, at the Dow Chemical Company. She received her BS degree from Fudan University and Ph.D. in Polymer Chemistry and Physics from Peking University. She then worked as a postdoctoral fellow and an associate professor in the Institute of Chemistry, Chinese Academy of Sciences. Employment at the NSF-IUCRC center for Biocatalysis and Bioprocessing of Macromolecules at Polytechnic University (Now NYU Tandon School of Engineering) followed in 2000, and in 2005 she became a research assistant professor. In 2006, she joined Rohm and Haas/Dow. She intensively works on polymer and particle characterization, the synthesis–structure–property relationship of polymeric and colloidal systems, and sustainable polymers. As an active member and an alternate council for Polymer Division of American Chemical Society (ACS), she has organized ACS symposia in the areas of Separation and Characterization of Macromolecules and Particles, Polymer Sciences for Everyday Things, Polymer Colloids, Industrial Innovation of Polymer Science, and Natural Polymers.

She is a lifetime member of Chinese American Chemical Society (CACS). She also served on the steering board for international symposium on Field- and Flow-Based Separations (FFF2018 and FFF2022). She was the recipient of the NOVA Innovation Award from Rohm and Haas Company (2008), US EPA Presidential Green

Chemistry Challenge Awards (2003 and 2013), Vernon A. Strenger Scientists' Award from Dow (2019), a ACS Polymer Chemistry Division (POLY) fellow (2021), and ACS Philadelphia section Industrial Chemist Award (2021), Dow Consumer Solution Technical Achievement Awards (2021 and 2022). She has made impactful contribution to many Dow's sustainable product and process developments, and some of them has been recognized externally as Business Intelligence Groups (BIG) sustainability Awards (2020 and 2022) and Innovation award (2022), and R&D 100 award (2022). She is passionate about advancing polymer science for sustainable materials development while eliminating plastic pollution and fossil fuel dependence.



Dr. Lei Li is an associate professor of the Department of Chemical and Petroleum Engineering at the University of Pittsburgh. He obtained his Bachelor's degree in Chemical Engineering from Tsinghua University in 1994. Three years later, he received his Master's degree in polymer science from Tsinghua University. In 2001, he received his Ph.D. degree in Macromolecular Science and Engineering from the University of Michigan.

After spending nine years at Seagate Technology LLC as a postdoc, a research staff member, a research manager, and a Sr. research manager, He started his academic career at the University of Pittsburgh in 2010. His research focuses on surface, interface, 2D materials, and ultrathin films, ranging from polymer nanocoatings, graphene surface, ionic liquid nanofilms to 3D-printed membrane for water treatment. His work has been published in high-impact journals, including *Nature Materials*, *Accounts of Chemical Research*, and *ACS Nano* and *Chemical Science*. He also holds ten US patents. As the principal investigator, he has directed projects supported by NSF, Department of Energy, ACS Petroleum Research Funds, and Advanced Storage Research Consortium. Currently, he serves as the 2021 president for CACS.



Dr. Yingchun Lu is currently a general manager at Viwit Pharmaceuticals. Prior to joining Viwit in 2022, she was the director of Alliance Management at Atomwise, a preclinical pharma company revolutionizing how drugs are discovered with AI. In addition, she worked for the US Innovation Center of Shimadzu, a top-five global instrumentation company, and AcceleDev, a US-Sino CDMO company, as the director of Project Management. Her earlier careers include a senior medicinal chemist in Morphochem and Pharmacopeia Drug Discovery, focusing on drug discovery for oncology and immunosuppressants projects. She is a life member of the Chinese American Chemical Society (CACS). She has served on the Board of its East Chapter since 2012 and was the chair of 2019. She joined the American Chemical Society (ACS) in 1994 and has served as an alternate councilor in ACS North Jersey Chapter. She has also served on the Board of NJACS Mass Spectrometry Discussion Group and was the chair of 2017. She holds a Ph.D. in Organic Chemistry from Dartmouth College, an MS from Southern Methodist University, and a BS degree in Chemistry from Peking University.



Dr. Jingbo Louise Liu has >150 scholarly products and >180 talks about sustainable energy, catalysis, and environmental and biomedical applications of advanced nanostructured materials. She participated in > 42 funded projects to promote STEM education and energy materials and technology. For her contribution, she was named the Women of the Year by Texas Diversity Council (2023) and the Distinguished Women in Chemistry or Chemical Engineering by the International Union of Pure and Applied Chemistry (2021) due to her devotion and leadership. She was elected as a fellow by three professional societies, the American Chemical Society, the Linnean Society, and the Royal Society of Chemistry. She holds the chartered scientist and chartered chemist status due to her expertise in improving the core knowledge and research activities in chemical and materials sciences. She was appointed as the distinguished scientist by the Office of Naval Research to advance the high energy density battery and a DEBI faculty fellow at the Air Force Research Laboratory to develop functionalized materials to improve human health. She is an ACS-certified career consultant,

the ACS Energy and Fuels Division councilor, and the ACS Diversity Equity Inclusion and Respect Committee member.

She Liu is a full professor of Chemistry and served as the director of the Center for Teaching Effectiveness at Texas A&M University-Kingsville (2021–2023). She is affiliated with the Texas A&M Energy Institute due to her contributions to the field of engineered nanomaterials in alternative energy. She has taught more than 12,500 students, trained > 200 undergraduates and 45 graduate students, and hosted 15 visiting scholars/researchers in her research laboratory. During her tenure/post-tenure timeline, she further served as the NSF panelist reviewer, the journal guest editor, and the book editor.

Chapter 1

Leadership and Resiliency in the Global Chemistry Enterprise



Celebrating the 40th Anniversary of Chinese American Chemical Society

**Marinda Li Wu, Wei Gao, Chu-An Chang, Lei Li, Yingchun Lu,
and Jingbo Louise Liu**

About CACS

Chinese American Chemical Society (CACS) is a non-political and non-profit professional organization. The purpose of CACS is to encourage the advancement of chemistry and chemical engineering sciences and technologies in all branches, to improve career and professional opportunities of its members, to facilitate networking contacts, and to promote mutually beneficial interactions with other scientific communities. CACS is the only Chinese American professional organization that is

M. L. Wu · C.-A. Chang

Chinese American Chemical Society, 18427 Clifton Way, Castro Valley, CA 94546, USA

M. L. Wu

American Chemical Society, Olympia, Washington, D.C., USA

W. Gao

Corporate Research and Development, Dow Inc., Collegeville, PA 19034, USA

L. Li

Chem/Petroleum Engineering, University of Pittsburgh, 3700 O'Hara Street, Pittsburgh, PA 15261, USA

Y. Lu

Chinese American Chemical Society, South Brunswick, NJ 08824, USA

J. L. Liu (✉)

The Department of Chemistry, Texas A&M University-Kingsville, MSC 161, 700 University Blvd, Kingsville, TX 78363, USA

e-mail: jingbo.liu@tamuk.edu

The Texas A&M Energy Institute, Frederick E. Giesecke Engineering Research Building, 3372 TAMU, College Station, TX 77843-3372, USA

officially recognized by both the American Chemical Society (ACS) and the American Institute of Chemical Engineers (AIChE). CACS fulfills its mission through major events four times a year in conjunction with ACS and AIChE national meetings organized by the National CACS, and also through a wide range of activities that are organized by the local chapters.

ACS/CACS Collaboration

ACS and CACS signed a three-year Chemistry Enterprise Partnership (CEP) in August 2019. This ACS-CACS CEP started on Jan. 1, 2020 and includes joint collaborations to help celebrate the CACS 40th Anniversary in 2021. The alliance agreement recognizes the importance of cooperation between the ACS and the Chinese-American chemical communities in scientific, educational, and public outreach projects. The agreement is characterized by a shared commitment to cooperation in service to chemical scientists, engineers, students, educators and professionals. A great example of collaboration is the ACS-CACS Membership Drive in 2021.

Elements of the ACS-CACS CEP include:

A focus on the United Nations 2030 Sustainable Development Goals (SDGs) and specifically SDG Goal 4 on “Quality Education” and SDG Goal 17 on “Partnerships for the Goals” of the UN 2030 Sustainable Development Goals.

Technical programming and career development collaborations on symposia, workshops, webinars, and additional events.

Exploring ACS-CACS member benefits including short courses and discounted membership fees for students.

Chair and President’s Joint Message:

Dear Members and Friends of CACS, 2021 is a milestone year for CACS. Founded by Dr. Jesse Hwa forty years ago, our society is celebrating this anniversary with a number of special events and new membership benefits.

Two-Part 40th Anniversary Symposium

Although COVID-19 has understandably restricted our in-person CACS Keynote presentations and banquets, the CACS 40th Anniversary Planning Committee has continued to meet virtually throughout the pandemic to develop exciting plans to celebrate our big anniversary.

With uncertainty surrounding when it would be fully safe to resume in-person activities, CACS leaders decided earlier this year to host a virtual CACS 40th Anniversary Symposium: “*Leadership and Resiliency in the Global Chemistry Enterprise—Celebrating the 40th Anniversary of CACS.*” This two-part symposium will be held in conjunction with both the ACS and AIChE national meetings this fall. A virtual symposium will enable broad participation by global leaders and scientists who continue to face travel restrictions. Session times will accommodate a variety of time zones throughout the USA and Asia.

On August 23–25, 2021 in conjunction with the ACS Fall National Meeting, Part 1 of the symposium will include six sessions that feature both global leaders and

distinguished scientists. The first three sessions include remarks from the President of ACS, President of FACS (Federation of Asian Chemical Societies), President of SAPA (Sino-American Pharmaceutical Professionals Association) in addition to shared perspectives from the CEO of ACS, President of CAS (Chemical Abstracts Services), Editor in Chief of C&EN, and several distinguished scientists and other thought leaders from Asia. These global leadership sessions will be followed by technical sessions that feature exciting multidisciplinary research on Advances in Energy and Fuels, Advances in Nanomaterials and Biotechnology, and Advances in Energy Storage and Materials.

Part 1 of this CACS 40th Anniversary Symposium in conjunction with the Fall 2021 hybrid National ACS Meeting is sponsored by ENFL (ACS Energy and Fuels Division) and co-sponsored by POLY (ACS Polymer Chemistry Division). Since Dr. H. N. Cheng is the ACS President this year and also a Lifetime CACS Member, the CACS symposium will be designated as a PRES Symposium recommended by the 2021 ACS President.

Part 2 of our 40th Anniversary Symposium will consist of two sessions on November 15 in conjunction with the Fall 2021 National AIChE annual meeting. These sessions will feature distinguished researchers on advanced energy and materials including Prof. Zhenan Bao (Stanford Univ.), Prof. Jinguang Chen (Columbia Univ.), Prof. Liang-Shih Fan (Ohio State Univ.), Dr. Jun Lu (Argonne National Lab), Prof. Yushan Yan (Univ. of Delaware), and Prof. Peidong Yang (UC Berkeley).

Inaugural National CACS Awards

CACS is delighted to announce our first ever National CACS Awards Ceremony on August 26. It will be held as a virtual ACS Social Event starting at 7:00 pm EDT. Everyone is welcome and encouraged to attend for free, even if not registered for the ACS conference. This should be a great networking opportunity for students, famous professors, distinguished scientists, and friends of CACS. Past ACS President Ann Nalley will help celebrate our 40th Anniversary and deliver a few remarks at this inaugural National CACS Awards program.

CACS is pleased to announce the inaugural winners for the Outstanding Achievement Award to Professor Zhenan Bao from Stanford University and for the Rising Star Award to Dr. Dachao Li from Dow.

Since CACS is celebrating its 40th Anniversary this year, several long serving Lifetime Members will receive Extraordinary Service Awards. These include Dr. H. N. Cheng, ACS President, Dr. Norman Li (Past CACS Board Chair), Dr. Chu-An Chang (CACS Treasurer), and Dr. Marinda Li Wu (CACS Board Chair). Drs. Teng Xu (ExxonMobil Chemical), Longqin Hu (Rutgers University), and Sunny Wang (Genequantum Healthcare) will be also recognized for their extraordinary leadership, contributions and service to CACS on its 40th Anniversary.

Thanks to a generous donation from Dr. Anna Tai dedicated in memory of CACS Founder Dr. Jesse Hwa, beautiful personalized CACS embroideries will be presented to all awardees. In addition, her donation will enable CACS to send all existing and new CACS Lifetime Members for 2021 a personalized embroidery. So please consider upgrading your membership if you haven't already done so!

Relaunch of CACS Communications

CACS is thrilled to relaunch our CACS Communications as an e-issue. This first e-issue will be released this fall to celebrate our 40th Anniversary. It is our goal that CACS Communications will continue next year and beyond for years to come.

CACS Membership Drive

CACS is especially excited to launch a 40th Anniversary Membership Drive which will integrate membership in our three active local chapters with our national CACS. From now on, we will have only one unified CACS membership. Anyone who joins the CACS will have the benefits from both our national CACS and their local chapter. It is important to unite together for a stronger collective voice with more impact. See letter posted earlier this year on our *website* on “Solidarity for Asian Scientists.”

Discount for New ACS Membership

The ACS-CACS Chemistry Enterprise Partnership signed in 2019 includes cooperation between the two societies to celebrate our CACS 40th Anniversary. ACS has agreed to offer all CACS Members who are not currently ACS members a special one-time 50% discount on ACS Membership fees. This discount is valid for members joining ACS between July 1 and September 30, 2021.

Thanks to our CACS Board and Leadership Team

We would like to thank our CACS Board for its full support over many years. CACS has certainly evolved these past 40 years. It remains dedicated to its original mission of providing fellowship and career support for its professional community. It has partnered with like minded professional societies like ACS since 2016 and more recently with others like SAPA. Quarterly CACS Board meetings the past couple of years have taken care of many important CACS matters. These include revising and updating the original CACS Bylaws from 40 years ago.

We also want to extend our special thanks to our dedicated 2021 CACS Leadership Team and many active volunteers working together to ensure that our 40th Anniversary Symposium at both the Fall National ACS and AIChE meetings will be most successful. Indeed with ongoing support from all our volunteers, CACS can look forward to a bright future for decades to come.

Many thanks and best wishes to all!

Marinda Li Wu, CACS Board Chair

Lei Li, CACS President

See Table 1.1.

Table 1.1 Leadership team of Chinese American Chemical Society

| Name | Roles | Affiliation | Email |
|---|------------------------------|---|--|
| <i>Executive Committee Members</i> | | | |
| Marinda Li Wu* | Chair of the Board | Dow Inc. (retired) | marindawu@gmail.com |
| Lei Li* | 2021 President | University of Pittsburgh | lei55@pitt.edu |
| Yingchun Jasmine Lu* | 2021 the 1st Vice-President | Atomwise, Inc. | Jasmine@atomwise.com |
| Jingbo Louise Liu* | 2021 the 2nd Vice-President | Texas A&M University Energy Institute and TAMU-Kingsville | Jingbo.Liu@tamuk.edu |
| Chu-An Chang* | Treasurer | Thermo Fisher (retired) | chuan_chang@hotmail.com |
| Baoqing Ma | Secretary | FDA | mabqing@yahoo.com |
| Fanwen Zeng | Immediate Past President | Dow Inc. | zeng1999@yahoo.com |
| Wei Gao* | Co-editor of E-Communication | Dow Inc. | WeiGao@dow.com |
| <i>Directors of the Board (in alphabetical order)</i> | | | |
| Lin Li | Immediate Past Chair | Chevron | lin.li@chevron.com |
| L. S. Fan | Member | The Ohio State University | fan.1@osu.edu |
| W. S. Winston Ho | Member, Former Board Chair | The Ohio State University | ho.192@osu.edu |
| Shaw Huang | Member | Harvard University (retired) | shuang@gmail.com |
| Yinlun Huang | Member | Wayne State University | yhuang@wayne.edu |
| Ving C. Lee | Member | Adesis | VLee@adesisinc.com |
| Norman Li | Former Board Chair | NL Chemical Technology, Inc. | norman.li@nlchem.com |
| Marinda Li Wu | Board Chair, 2018–2023 | | marindawu@gmail.com |
| Qiong Yuan | Member | CAS | qyuan@cas.org |
| Fanwen Zeng | Immediate Past President | Dow Inc. | zeng1999@yahoo.com |
| Mark Zhen | Member | Valent BioSciences LLC | MarkYZhen@yahoo.com |
| Lubo Zhou | Member | Honeywell | Lubo.Zhou@honeywell.com |
| Frank Zhu | Member | Honeywell | Frank.Zhu@honeywell.com |
| <i>Local Chapter President</i> | | | |
| Wenmei Xue | 2021 Tri-State | BASF Corporation | wmxue@yahoo.com |
| Lixin You | 2021 CACS Southwest | Chevron | youlixin@yahoo.com |
| Ling Zhou | 2021 CACS Great Lake | Honeywell | ling.zhou@honeywell.com |

* Editorial Board Members of e-CACS Communications

W. Gao and J. Liu are the co-editors, and M. Wu, L. Li, C. Chang and Y. Lu are the board members of e-CACS Communications

Periodic Table of Leadership in Chinese American Chemical Society

Chair of Board ****
Dr. Mariela Li Wu

Directors of Board
 ♦ **Executive Committee**
 ♦ **Editorial Board**
 ♦ **Award Committee**
 ♦ **Award Winners**

40th Anniversary Planning Committee
 • **Local Chapter Leaders**
 1 CACS Tri-State
 2 CACS Southwest
 3 CACS Great Lake

2021 President:
Dr. Lei Li **

Vice-President
Dr. Y. Junjie Lu ***

Vice-President
Dr. J. Louie Liu **

Treasurer ****
Dr. Chu-An Chang

Secretary *
Dr. Baoqing Ma

Leaders of Local Chapters
 Dr. Wenmei Xue¹ Dr. Lixin You² Dr. Ling Zhou³ Dr. Yanfeng Zhang^{1*} Dr. Shuai Tan^{1*}

Directors of the Board
 Dr. W.S. Winston Ho Dr. Shao Huang Dr. Liang Shih Fan* Dr. Yuhua Huang Dr. Vag C. Lee Dr. Norman Li* Dr. Qiong Yuan** Dr. Mark Zhou Dr. Labo Zhou Dr. Frank Zhu Dr. Liu Li*

Directors of the Board
 Dr. W.S. Winston Ho Dr. Shao Huang Dr. Liang Shih Fan* Dr. Yuhua Huang Dr. Vag C. Lee Dr. Norman Li* Dr. Qiong Yuan** Dr. Mark Zhou Dr. Labo Zhou Dr. Frank Zhu Dr. Liu Li*

Interim Past Pres. **
Dr. Faoren Zeng

Co-Editor
Dr. Wei Guo

Award Winners
 Dr. Dehao Li Dr. Zhimin Bao Dr. H.N. Cheng Dr. Jing Xu Dr. Lougga Hu Dr. Sunny Wang

Award Committee
 Dr. Anna Tai¹ Dr. Helen Lou Dr. Mengqing Li

Thomas M. Connelly, Jr., Ph.D., is the Chief Executive Officer of the American Chemical Society. Prior to joining ACS, he served as Chief Science and Technology Officer, and then as Chief Innovation Officer, for the DuPont Company. In these roles, he was responsible for science and technology with special emphases on polymer science, chemical process development and, later, bioprocessing for chemical synthesis and production. At DuPont, Connelly led R&D organizations and businesses while based in the US, Europe and Asia. He graduated with highest honors from Princeton University with degrees in Chemical Engineering and Economics. As a Winston Churchill Scholar, he received his doctorate in chemical engineering from the University of Cambridge. Connelly was elected to the National Academy of Engineering, and recently chaired the National Academies Advisory Committee on Earth and Life Studies. He has served in advisory roles to the U.S. Government and the Republic of Singapore.



Title: Promoting ACS Core Values of DEIR (Diversity, Equity, Inclusion, and Respect, ID: 3597622 (A1))

Affiliation: American Chemical Society, Washington, District of Columbia, United States

Abstract: The American Chemical Society promotes basic Core Values of Diversity, Equity, Inclusion, and Respect (DEIR). ACS leaders believe in the “strength of diversity in all its forms, because inclusion of and respect for diverse people, experiences, ideas lead to superior solutions to world challenges and advances chemistry as a global, multidisciplinary science.” The ACS strategic plan has evolved over the years and continues to provide ACS a road map to achieve its vision of “improving all people’s lives through the transforming power of chemistry.” In 2019, ACS signed a Chemistry Enterprise Partnership with the Chinese American Chemical Society (CACS) and joins other global leaders of the chemistry enterprise in celebration of the CACS 40th Anniversary.

Marinda Li Wu received her Ph.D. in inorganic chemistry from the University of Illinois in Urbana-Champaign and a B.S. cum laude with Distinction in Chemistry from The Ohio State University. Dr. Wu has over forty years of experience in the chemical industry. She worked many years for Dow Chemical R&D, and Dow Plastics Marketing where she created partnerships between industry, education, government, and communities. She also has entrepreneurial experience, including founding “Science is Fun!” to engage young students in science and enhance support for science education.



Dr. Wu has served in many leadership roles for the American Chemical Society including Councilor (1996–present), Centennial Chair of the California Section (2001), Board of Directors (2006–2014), and President (2013). She was elected ACS Fellow (2015), and recently honored as a 50-year ACS member. She also served on the Council of Scientific Society Presidents (2012–2015), the International Advisory Board for 45th IUPAC World Chemistry Congress, and was named an honorary member of the Romanian and Polish Chemical Societies. She has served as a long-time member of the University of Illinois Chemistry Alumni Advisory Board and

the National Chinese American Chemical Society Board of Directors (elected Chair 2019–2022). She holds 7 U.S. patents, authored numerous journal articles and book chapters, and co-edited several ACS Symposium Books.

Lei Li is an Associate Professor of the Department of Chemical & Petroleum Engineering at the University of Pittsburgh. He obtained his Bachelor degree in Chemical Engineering from Tsinghua University in 1994. Three years later, he received his Master degree in polymer science from Tsinghua University. In 2001, he received his Ph.D. degree in Macromolecular Science and Engineering from the University of Michigan.



After spending nine years at Seagate Technology LLC as a postdoc, research staff member, research manager, and Sr. research manager, Dr. Li started his academic career at the University of Pittsburgh in 2010. Dr. Li's research focuses on surface, interface, 2D materials, and ultrathin films, ranging from polymer nanocoatings, graphene surface, ionic liquid nanofilms to 3D-printed membrane for water treatment. His work has been published in high-impact journals, including *Nature Materials*, *Accounts of Chemical Research*, *ACS Nano* and *Chemical Science*. Dr. Li also holds ten United States patents. As the principal investigator, Dr. Li has directed projects supported by NSF, Department of Energy, ACS Petroleum Research Funds, and Advanced Storage Research Consortium. Currently, Dr. Li serves as the 2021 President for CACS.

Title: Chinese American Chemical Society (CACS): Overview and 40th Anniversary (ID: 3585802 (A2))

Authors: Marinda Wu^{1,2}, Lei Li³

Affiliation: 1. Past President, American Chemical Society, Washington, District of Columbia, United States. 2. Chair of the Board, Chinese American Chemical Society, Orinda, California, United States. 3. Chemical Engineering, University of Pittsburgh Swanson School of Engineering, Pittsburgh, Pennsylvania, United States

Abstract: Founded in 1981, the Chinese American Chemical Society (CACS) is a non-profit professional society. We serve Chinese American students, practicing, and retired chemists, chemical engineers, as well as those working in related

fields. Our mission is broad, providing opportunities for fellowship and recognition, support for leadership and career development, and networking for job and research opportunities.

With neither a national nor regional political affiliation, CACS also collaborates with ACS, AIChE, SAPA (Sino-American Pharmaceutical Professionals Association) and other Asian and Asian American professional societies to provide a collective voice for impact and advocacy on issues of common interest.

To celebrate CACS' 40th anniversary, we have launched a series of exciting events in 2021 to supplement our distinguished keynote banquet series at national ACS and AIChE meetings. These include special symposia featuring leaders of the global chemistry enterprise and influential thought leaders. A global leader's session will kick off an ACS Presidential Symposium on "Chemistry Resilience: Advanced Materials and Multidisciplinary Applications—Celebrating the 40th anniversary of CACS." Three inaugural national CACS awards will also be presented. This talk will provide an overview of CACS, the National CACS leadership team, and highlights of activities from CACS local chapters as part of our exciting 40th Anniversary symposium at the ACS Fall National Meeting.

Norman Li is president of NL Chemical Technology, Inc. Mount Prospect, Illinois. He has a distinguished career of 50 years in American chemical and petroleum industries. He was at Exxon Research and Engineering Co. as a senior scientist and at UOP and Honeywell as Director of Research. In 1995, recognizing the critical needs of clean water in many parts of the world, he founded the NL Chemical Technology, Inc. to develop cost-effective advanced membrane technologies for worldwide operations of water purification and desalination of seawater.



Dr. Li has more than 100 technical publications, 44 U.S. patents, and more than 20 books edited, all in the field of separation science and technology. He has received many honors and awards. He was elected to the National Academy of Engineering of USA in 1990—the highest honor in the US in the engineering profession. He is also a member of the Chinese Academy of Sciences and a member of the Academia Sinica in Taiwan. Dr. Li has received the major awards in his field: The Founders

Award from the AIChE and the Award of Separation Science and Technology and the E. V. Murphree Award, both from ACS. In addition, he received the Perkin Medal from the Society of Chemical Industry—the highest honor in the chemical industry in the US. Dr. Li served the Chairman of the Chinese American Chemical Society (CACS) and has been serving as the board chair of the CACS Great Lakes Chapter in Chicago since its founding in 1997.

Title: CACS—Its Long History and Contributions to the Chemical Community (ID: 3,593,748 (A3))

Affiliation: NL Chemical Technology Inc., Mount Prospect, Illinois, United States

Abstract: Chinese American Chemical Society (CACS), a non-political and non-profit professional organization, was founded by the late Dr. Jesse Hua 40 years ago during the 181st ACS National Meeting in Atlanta. I was privileged to be invited by Jesse Hua to participate at its organization meeting and served as CACS Chair of the Board after Jesse Hua's term completed.

The purpose of CACS is to encourage the advancement of chemistry and chemical engineering, to improve the qualification and occupational opportunities of its members, to facilitate professional contacts, and to promote interactions with other scientific communities. CACS is the only Chinese professional organization that is officially recognized by ACS and AIChE. Under the leadership of the current Chair of the Board, Dr. Marinda Wu, a former president of ACS, CACS and ACS signed the Chemistry Enterprise Partnership (CEP). The agreement is characterized by the shared commitment to cooperation in service to chemists, chemical engineers, students, educators, and professionals.

CACS has made valuable contributions to the chemical community. It holds technical forum and banquet at each of the national meeting of ACS and AIChE and through the wide ranged activities that are organized by its three local chapters. Looking toward the future, CACS will expand its activities to include more technical conferences. It also plans to have more cooperative programs with the various divisions of ACS and AIChE. During this talk, I will share some of my personal experience in serving CACS and perspectives toward its future growth.

Manuel Guzman is president of CAS, responsible for driving innovative business and product strategy to create growth and novel solutions to business challenges. He joined CAS in 2013, bringing diverse global experience and a passion to help others succeed. Prior to joining CAS, Manuel held various executive positions within the information industry including EVP of Learning, Research Solutions & International for Cengage Learning; President of Thomson Learning's Career & Professional Group; and co-founder and CEO of Monument Information Resource/MIR Management Corporation. Manuel has a B.S. in accounting and an MBA in Finance from Seton Hall University.



Title: Everyday breakthroughs are the heart of scientific progress (ID: 3598314 (A4))

Affiliation: CAS, A Division of American Chemical Society, Columbus, Ohio, United States

Abstract: Published scientific information continues to grow at unprecedented rates, and the research paths required to accelerate breakthroughs are increasingly more sophisticated. At CAS, we connect breakthroughs, providing hindsight to build upon what others have done before; delivering insight that accelerates progress; and revealing unseen connections that inspire foresight that leads to a better future.

As a partner to the world's leading innovation organizations, CAS is continuously evolving to ensure we anticipate the needs of the research community and deliver the insights needed to accelerate discoveries. In this discussion, we'll explore the evolution of CAS, including expanding our coverage among interdisciplinary scientific domains, transforming our solutions portfolio to speed progress, extending custom services that solve unique problems for our growing customer base and leveraging our network of talented professionals to extend our global reach.

As we celebrate the 40th anniversary of the Chinese American Chemical Society together, we will also share insights on research collaborations in China and ways CAS is partnering with prestigious research organizations to inspire innovation.

H. N. Cheng (B.S., UCLA, Ph.D., Univ. of Illinois at Urbana-Champaign) is President of the American Chemical Society (ACS) in 2021. He has been active at ACS for a long time and has served in many leadership positions in a variety of Society committees and task forces at national levels, as well as being active at various capacities in local sections and technical divisions. He worked for many years in industry, and (since 2009) at USDA in New Orleans at its Southern Regional Research Center. His research over the years has included utilization of agro-based materials, green polymer chemistry, biocatalysis, pulp and paper chemistry, functional foods, polymer characterization, and NMR. His output has included 290 papers, 26 patent publications, and 23 edited books. He is a Fellow of the ACS (2009), a Fellow of the ACS Polymer Chemistry Division (2010), and a Fellow of the ACS Agricultural and Food Chemistry Division (2018), among other recognition and awards.



Title: Sustainability and the Chemistry Enterprise (ID: 3598326 (A5))

Affiliation: Southern Regional Research Center, US Department of Agriculture, New Orleans, Louisiana, United States

Abstract: With increasing public awareness of climate change, environmental pollution, and earth's declining resources, sustainability and green chemistry have become hot topics these days. In 2015, the United Nations adopted 17 sustainable development goals (SDGs) to be achieved in 2030. Chemistry can play a key role in meeting these goals, and the American Chemical Society (ACS) is committed to supporting its members and working with partners to address these SDG's. Several of the SDG's involve innovation, responsible consumption and production, and the food-water-energy nexus. One of the methods to achieve these goals is to use agro-based materials, not only for food and energy but also for product development, such as bioplastics, specialty chemicals, industrial products, and specific materials for different applications. In this talk, the speaker will provide an overview of the sustainability initiatives at ACS and his platform as ACS President in 2021. The speaker will also highlight selected research and development areas that are related to agro-based materials, as examples of the ongoing work in sustainability.

Bibiana Campos Seijo is the Editor in Chief of Chemical and Engineering News (C&EN) and vicepresident of the C&EN Media Group. C&EN is the news organization of the American Chemical Society, one of the largest scientific societies in the world. In her current role Dr Campos Seijo leads a large team of editors, reporters, designers and engineers based in the US, Europe and Asia. C&EN is the world's most comprehensive and authoritative news source about chemistry and related fields, providing coverage on a broad spectrum of topics, including research advances, business and policy trends, chemical safety practices, career guidance, and more.



Since Dr Campos Seijo took the helm of C&EN at the end of 2014, the Group has undergone a significant transformation, from a news organization centered around a lauded but niche print publication to a global, multichannel media brand. Under her leadership, C&EN has received a number of accolades and awards recognizing its editorial leadership, design, multimedia products, innovative culture and more. Prior to joining C&EN, Dr Campos Seijo was Editor in Chief of Chemistry World and Magazines Publisher at the UK's Royal Society of Chemistry. Earlier in her career, she worked as Editor of a portfolio of pharmaceutical titles at Advanstar Communications and as technical editor at the European Respiratory Society. Dr Campos Seijo holds a BSc in Chemistry from the University of Santiago de Compostela in Spain and a Ph.D. in Chemistry by the Manchester Metropolitan University in the UK.

Title: Helping Chemists Advance the Chemical Sciences (ID: 3584295 (B1))

Affiliation: American Chemical Society, Chemical and Engineering News, Washington, DC, United States

Abstract: C&EN is the official organ of the American Chemical Society. Our vision is to be the most trusted news source for ACS members and the global chemical sciences community. We are committed to: being a leading news organization that informs accurately, independently, and fairly; delighting audiences and fostering their trust in our news and information products; and including diverse voices and perspectives in our coverage. By providing essential news and evidence-based information that chemical scientists need we aim to help our audience advance our science. In this session, we'll examine if there is a place for modern science journalism in national societies and what role a news organization such as C&EN may play in advancing the chemical sciences.

Richard D. Connell obtained his Ph.D. in Organic Chemistry from the University of Notre Dame in 1989 and spent eighteen months as an NIH postdoctoral fellow at Harvard University rejection of Professor E. J. Corey: the 1990 Nobel Prize in Chemistry laureate.



In 1990, he began his industrial career at Bayer pharmaceuticals in West Haven CT and spent a two-year assignment in Wuppertal Germany prior to returning to the US to lead the Medicinal Chemistry group focused on diabetes and obesity research. In 1999, Rick joined Pfizer in Groton CT and Director of Cancer Chemistry department and led the team for four years including a 1-year secondment to Sandwich K to head up the Sex Health Chemistry department following the launch of Viagra®.

In 2004, Rick was asked to establish and implement a Chemistry Sourcing strategy for the seven Pfizer R&D sites. In 2008, he was named Vice President of Research Outsourcing and his responsibilities expanded to include all non-GMP sourcing for Pfizer research through 2018. This tenure included a 1-year secondment to China as part of an initiative to establish an R&D center in Shanghai. Rick joined WuXi AppTec in October of 2019, and presently serves as Sr. Vice President and Chief Operations Officer for the US, UK and EU sites. He is responsible for operations including Human Resources, IT, EHS, Legal, facilities and Supply chain as well as government relations.

A highlight of that period was the opportunity to chair the Early Clinical Management Team for CP-724,714: an Erb2 selective kinase inhibitor. In 2004, he moved into the newly created role of Executive Director of Discovery operations at Pfizer's Groton campus with responsibility for the antibacterial, immunology and cancer (AIC) therapeutic area zones. In that capacity, he chaired the 1st global committee that established the initial set of structural alerts and led the 1st cross-site affinity group associated with Chemistry outsourcing called the Discovery Chemistry Outsourcing Board (DCOB). In 2005, the DCOB became a line organization with the responsibility for outsourcing of Synthetic Chemistry, Parallel Chemistry, Monomers and templates and the externalization of the solid Sample collection at Sigma Aldrich. In 2008, he merged the DCOB, the Biology and PDM sourcing lines into the group now called External Research Solutions (ERS): a client-centric group that enables the external research relationships that underpin the R&D ecosystem of the future that underpins the ESI initiative.

He has worked in several foreign research settings including Stockholm in 1987 for six months as a graduate student; Sandwich, UK in 2002 for a twelve month

secondment as head of Sex Health Chemistry; and more recently in 2011 on secondment to Shanghai to establish the Anti-Infective research unit in China as part of the ESI initiative. He initiated and implemented some of the first income generations initiatives that monetized under-utilized assets from Pfizer research including the 2010 deal to make available non-GMP samples to the research community. He is listed as an inventor on over forty patent and patent applications and has authored or co-authored more than twenty science publications.

Title: WuXi AppTec's Contributions to the Global Chemistry Enterprise (ID: 3601857 (B2))

Affiliation: WuXi AppTec (13 facilities in seven US states including San Diego, CA; Austin, TX, Atlanta, GA; Cambridge, MA; Saint Paul, MN; Plainsboro and Cranbury, NJ, Philadelphia, PA)

Abstract: Today, we serve more than 4400 customers and partners across the globe—including biotechnology and pharmaceutical companies, research institutions, researchers, scientists and entrepreneurs. We support our customers through small molecule drug R&D and manufacturing; cell therapy and gene therapy R&D and manufacturing; drug R&D and medical device testing; and clinical development services that have life-saving and groundbreaking impacts globally.

With more than 27,000 employees globally, including 22,000 scientists worldwide, WuXi AppTec has an expansive global presence in China, Germany, Israel, Japan, South Korea, the United Kingdom and the United States—where we have over 1700 employees across facilities in California, Georgia, Massachusetts, Minnesota, New Jersey, Pennsylvania and Texas. Our localized yet globally-enabled platforms offer flexibility, reliability, and consistency to our customers.

Qiong Yuan received a B.S. degree from Wuhan University on Organic Chemistry and a Ph.D. from Shanghai Institute of Organic Chemistry (SIOC), Chinese Academic of Sciences. She actively promotes Asian culture and heritage and lead several organizations including Alliance of Chinese Alumni (ACA, Vice President), Chinese American Chemical Society (CACS, Board Director) and Columbus Asian Festival Corporation (AFC, Board Director). Currently, she serves as the director of CAS Innovation.



CAS is a division of American Chemical Society (ACS). Dr. Yuan currently works in its Innovation Division and focuses on developing transformative scientific information solutions to help customers accelerate breakthroughs. Since joined CAS in 1999, she served the organization through variety roles in Product Management, Sales, Research and SciFinder Product Development. She has been working collaboratively with ACS other Divisions (Publications, Membership, etc.) to promote ACS Core Values and execute ACS globalization initiative in Asia.

Title: Chemistry Resilience: A CAS REGISTRY View (ID: 3598316 (B3))

Affiliation: CAS, A Division of American Chemical Society, Columbus, Ohio, United States

Abstract: Covering advances in chemistry and related sciences over the last 150 years, CAS has built the world's largest collection of chemistry insights. This includes its authoritative substance collection, CAS REGISTRY, which reached 250 million unique substances in April 2021. CAS REGISTRY is the premier source relied upon by scientists, manufactures, regulators, and data scientists worldwide for accurate and complete information on chemical substances and biosequences disclosed in publications since the early 1800s. This overview of CAS REGISTRY development will also include insights from an analysis of new CAS Registry Numbers in the past 20 years that reflects chemistry resilience through interdisciplinary research and development worldwide.

Wansheng Jerry Liu Ph.D., J.D. is a Partner and the Chair of China Practice Group of Fox Rothschild LLP, a 950-lawyer U.S. law firm. Jerry practices in wide areas of intellectual property and corporate laws, including patent and trademark prosecution, litigation and opinions, contract review, formation of business entities, etc. He serves clients from individuals and start-up companies to Fortune 500 companies, including assisting a number of major Chinese pharmaceutical companies in IP protection and conducting business in the US, and has handled due diligence for investment, M&A and licensing deals valued from multi-million to multi-billion dollars. The China Practice Group he chairs is comprised of over 30 attorneys nationwide in many areas of laws.



Prior to law practice, Jerry worked as a Senior Research Investigator in process development at Bristol-Myers Squibb Company. He obtained Ph.D. in Organic Chemistry with Professor Sir Derek H. R. Barton (Nobel Prize, 1969) from Texas A&M University, J.D. from Rutgers University School of Law, and B.S./M.S. in Chemistry/Polymer Science from University of Science and Technology of China (USTC).

Jerry served as the Editor-in-Chief of Rutgers Law Record in law school and President (2019–2020) of Sino-American Pharmaceutical Professionals Association (SAPA), and is serving as Co-Chair of the CNIPA Committee of the New York Intellectual Property Law Association (NYIPLA) and General Counsel of the USTC Alumni Association of Greater New York (USTCAAGNY). A frequent speaker on IP laws and FDA regulations, Jerry has over 20 scientific and legal publications and four U.S. patents.

Title: Intellectual Property Right Protection in the Global Chemical and Pharmaceutical Industries and Recent IP Development and Trend (ID: 3598317 (B4))

Affiliation: Fox Rothschild LLP New York, New York, New York, United States

Abstract: During 2020, a year of unprecedented challenges, new patent applications filed at the United States Patent and Trademark Office (USPTO) dropped as expected, but the new patent lawsuit filings in the United States District Courts rose significantly, and so did the new inter partes review petitions filed with the Patent and Trademark Appeal Board (PTAB). What do these data mean? While we are getting closer to winning the war on the COVID-19 pandemic, thanks to the wide applications of the multiple vaccines available, it is also time to ponder on the impact of the pandemic on intellectual property protections in the corporate world. While providing an overview on the IP right protection mechanisms and sharing some recent development and current trend of IP, this presentation will also highlight various high-profile patent cases in the past decade that may have significant impact on IP right protections in general and on those in the global chemical and pharmaceutical industries in particular.

John Sun, Ph.D., MBA is an inspirational leader and a seasoned professional in the pharmaceutical industry and also a passionate practitioner and advocate for career development. Currently, he is the Global Program lead at Novartis, and has served as Global Analytics Project Manager and Global Program Team Director in different franchises and development unites. Before joining Novartis, John held positions with increased R&D responsibilities from Whiteball-Robins, Kos Pharmaceuticals, Schering-Plough and Sanofi-Aventis.



Over the years, John has actively volunteered in various professional organizations, served as Chair of Project Management Community in Drug Information Association (DIA), President and Career lead at Sino-American Pharmaceutical Professionals Association (SAPA), Chair of Chinese Culture Community, President of Novartis Toastmaster Club and Area Director of the Toastmasters International at District 83. John has presented in various domestic and international pharmaceuticals from Virginia Commonwealth University, MBS from Rutgers University and BMed from Beijing University of Traditional Chinese Medicine. John is a certified Project Management Professional (PMP), trained in black-belt for lean Six-Sigma, and a Distinguished Toastmaster (DTM).

Title: Elevate Leadership Capabilities (ID: 3595546 (B5))

Affiliation: Global Drug Development, Novartis Pharmaceuticals Corp, East Hanover, New Jersey, United States

Abstract: To different people, the word “leadership” has different meanings and connotations. What does it mean to you?

Today, “leadership” has a much deeper sense of calling and complexity. Both prevailing perception and research data show a disproportionate of leadership representation of Asian Americans, particularly Chinese Americans, in the corporate world. And the gap remains large and widens over the years. Despite ambition and diligent efforts, many are stuck beneath the seemingly impenetrable “bamboo ceiling.” Some are frustrated, but many are contented.

Both from the individual and group perspectives, we ought to examine these gaps holistically, with courage, determination, and multifaced approaches. Collectively, there is an urgent need for us to wake up and to step up.

Leadership skills are different from those hard skills we acquired from graduate school training. Many of them involve human skills. With openness and purpose, we all can rise up to elevate and expand our leadership capabilities. With mindful learning, we can incorporate many important elements into our own behaviors and become stronger leaders. For sure, it is a journey worth embarking on.

L.-S. Fan is Distinguished University Professor and C. John Easton Professor in Engineering in the Department of Chemical and Biomolecular Engineering at

The Ohio State University. His research fields are in particle technology and multiphase reaction engineering. He is an inventor of eight clean fossil energy conversion processes including OSCAR, CARBONOX, pH Swing, Calcium Looping, Hydrogen Looping, Syngas Looping, Coal-Direct Chemical Looping and SULGEN Processes for CO₂, SO₂, and NO_x emission control and electricity, syngas, hydrogen, chemicals or liquid fuels production. He has also invented the commercially used electrical capacitance volume tomography for three-dimensional multiphase flow imaging. Professor Fan is the Editor-in-Chief of Powder Technology and has authored or co-authored 460 journal papers, 60 patents, and six books including the most recent textbook (2021) “Dynamics of Multiphase Flows” by Cambridge University Press. He was named as one of the “One Hundred Engineers in the Modern Era” by the AIChE in its centennial celebration in 2008. Professor Fan is a member of the U. S. National Academy of Engineering, Academician of the Academia Sinica, National Academy of Inventors, and a Foreign Member of the Chinese Academy of Engineering, the Australia Academy of Technology and Engineering, the Indian National Academy of Engineering, and the Mexican Academy of Sciences.



Title: Metal Derivative Reaction Engineering: A Gateway to Novel Energy Conversion Technology (ID: 3597830 (C1))

Affiliation: Chemical Engineering, The Ohio State University, Columbus, Ohio, United States

Abstract: The science and engineering of metal derivative based technologies are characterized by the interplay among a broad spectrum of subjects in connection to metal derivative physics, chemistry and reaction engineering, and particle science and technology. These subjects encompass three main components—Materials: metal derivative material synthesis, reactivity, reaction-regeneration mechanism, recyclability, and physical strength; Reactors: flow pattern and stability, gas–solid contact mechanics, scaling rule; and Systems: process integration, intensification, and optimization. Such interplay is so complex that it has been over 100 years in which this technology has not been able to be commercially deployed.

However, with major advances made recently on the bottleneck areas in this technology development, the technology commercialization is now realistically possible and can be projected to take place in the near future. Using metal oxides as an example, these advances include the successful development of chemically, physically robust metal oxide oxygen carriers that are cost-effective and sustainable to long-term redox reactor environment, and the successful employment of CO₂ and H₂O as partial substitute of carbonaceous feedstock for combustion, gasification and reforming applications thereby yielding CO₂ negative chemical looping processes. These advances coupled with a novel reactor system design and operation give rise to a significant reduction in the capex compared to conventional approaches, when the chemical looping technology is used for carbonaceous feedstock conversions in the production of electricity, hydrogen, syngas, liquid fuels, and chemicals. The general concept of chemical looping can also have varied technology applications. For example, the SULGEN Process recently invented at Ohio State can be in one step capturing H₂S and another step separating it to hydrogen and sulfur. It can potentially be applied to petroleum fuel refining process, natural gas sweetening process, and other fossil fuel gasification and reforming processes. This presentation will describe these advances that are established over the OSU chemical looping system platform. The presentation will also illustrate the rationales of its commercialization readiness and timeline.

Chi-Huey Wong is the Scripps Family Chair Professor, Department of Chemistry, The Scripps Research Institute. He received his B.S. (1970) and M.S. (1977) degrees (with KT Wang) from National Taiwan University, and Ph.D. (1982) in Chemistry (with George M. Whitesides) from Massachusetts Institute of Technology. He then worked at Harvard University as a postdoctoral fellow (with George M. Whitesides) for another year, and became a faculty member at Texas A&M University (1983) where he was promoted to full professor in 1987. He then moved to the Scripps Research Institute in 1989 as Professor and Ernest W. Hahn Chair in Chemistry. From 2006 to 2016, he served as President of Academia Sinica in Taiwan. He is currently the Scripps Family Chair Professor in the Department of Chemistry at The Scripps Research Institute and holds a joint appointment as Distinguished Professor at the Genomics Research Center, Academia Sinica.



Professor Wong received numerous honors for recognition of his accomplishments, including, for example, the Searle Scholar Award in Biomedical Sciences (1985), the Presidential Young Investigator Award in Chemistry, USA (1986), the Roy Whistler Award of the International Carbohydrate Organization (1994), the ACS Harrison Howe Award in Chemistry (1998), the ACS Claude S. Hudson Award in Carbohydrate Chemistry (1999), the International Enzyme Engineering Award (1999), the US Presidential Green Chemistry Challenge Award (2000), The ACS Award for Creative Work in Synthetic Organic Chemistry (2005), Humboldt Research Award for Senior Scientists (2006), the FA Cotton Medal (2008), the Nikkei Asia Prize for Science, Technology and Innovation (2012), the ACS Arthur C. Cope Medal (2012), the Wolf Prize in Chemistry (2014), and the Robert Robinson Award of the Royal Society of Chemistry, UK (2015).

Dr. Wong is a member of Academia Sinica (1994), the American Academy of Arts and Sciences (1996), the US National Academy of Sciences (2002) and the US National Academy of Inventors (2014). He served as an Editorial Advisory Board member for the Journal of American Chemical Society and *Angewandte Chemie*, Chairman of the Executive Board of Editors of the *Tetrahedron Publications* (2006–2008), Head of the Frontier Research Program on Glycotechnology at RIKEN in Japan (1991–1999), and a board member of the US National Research Council on Chemical Sciences and Technology (2000–2003). In addition, he has received many honorary doctor degrees (including one from Technion), given numerous plenary and named lectures, and served as a science advisor to many organizations, including a scientific advisor to the Max-Planck Institute (2000–2008), a member of RIKEN Advisory Council (2010–16), and the Chief Science Advisor to the Taiwan Government (2006–2015).

His research interests are in the field of chemical biology and synthetic chemistry, with particular focus on the development of new methods and tools for the synthesis and study of complex carbohydrates and glycoproteins associated with disease progression related to aberrant biological glycosylation. He has published over 750 papers and more than 120 patents, and is a highly cited scientist with an h-index of 148.

Title: Universal vaccine development through glycoengineering (ID: 3590816 (C2))

Affiliation: Chemistry, The Scripps Research Institute, La Jolla, California, United States

Abstract: Carbohydrates are one of the three major classes of molecules that make up cells. They are often linked to proteins or lipids through glycosylation and expressed on cell surface, and they are capable of affecting protein folding and cellular functions, including microbial infection, cancer metastasis, neurodegenerative disorder, inflammatory reaction and immune response. Despite their importance, the roles of carbohydrates and the associated glycosylation reaction in biology have not been well understood, mainly due to the lack of tools and methods available for fundamental and translational research. This lecture will describe our recent development of chemical and biological methods for the study of glycosylation in disease progression and

application of new discoveries from this study to development of carbohydrate-based medicines, especially universal antibodies and vaccines against viral infection and cancer.

Reuben Jih-Ru Hwu received his bachelor degree from National Taiwan University, 1976; and Ph.D. from Stanford University in 1982. He serves in different positions, Associate Professor, The Johns Hopkins Univ. (1986–90); Director of Preparatory Office for College of Biomedical Science and Engineering (2010–12), Dean of College of Science (2007–10), Chair Professor (2008–2012), National Central University; Distinguished Chair Professor, National Tsing Hua University (2015–present); Founder, Well-being Biochemical Corp. (2000–); Curriculum Director (1996–99), International Foundation for Sciences; President of Chinese American Chemical Society, U.S.A. (1991–93); President of Asian Federation for Medicinal Chemistry (2012–13); President of the Federation of Asian Chemical Societies (2019–22).



Fellow of The Academy of Sciences for the Developing World (1999–); Fellow of IUPAC (2000–); Fellow of The Royal Society of Chemistry (2005–); Fellow of The Federation of Asian Medicinal Chemistry (2013–); Member of the European Academy of Sciences and Arts (2019–). Representative Awards: Excellent Senior Teacher with 30 Years of Service (2020); National Chair Professorship (2015–2018); National Academic Research Innovation Award (2017); Nano Industrial Technology Excellence Award (2013); Outstanding Scholar Award (2007–12); Award for an Outstanding Achievement (2008), Senior Distinguished Research Fellow (2005–07); The 1997 Third World Academy of Sciences Award (in Chemistry), The Third World Academy of Sciences; The Outstanding Young Persons of the World for 1994, Junior Chamber International; Federation of Asian Chemical Societies 1992 and 1993 Distinguished Young Chemist Award; Distinguished Research Award (3 times, 1992–2001); Alfred P. Sloan Research Fellow (twice 1988–1990), U.S.A.; Stuart Pharmaceuticals Achievement Award (1986), ICI Americas Inc.; Ming-Yu-Wen-Hwa Award (1976), Japan.

Research fields include nano-biomaterials, new drug development, organic synthesis, and organosilicon chemistry; published > 228 scientific articles and obtained 50 patents. Invented > 14 new biochemical products as merchandize being sold on the market.

Title: Interdisciplinary and International Cooperation to Enhance Chemical Materials for Solar Energy Conversion (ID: 3590495 (C3))

Affiliation: Chemistry, National Tsing Hua University, Hsinchu, TW, Taiwan

Abstract: In the 1970s, UNESCO understood the important role on the application of chemistry, which influenced the development of social, economic, and environmental well-being of nations. Accordingly, it helped the establishment of the Federation of Asian Chemical Societies (i.e., FACS). FACS was founded in 1979 and includes 32 chemical societies now. To the west part, we have Mendeleev Russian, Turkish, and Israel societies; to the east, there are Australian and New Zealand societies; in the middle, they are China, Indian, Japan, Korean, Taiwan, Thailand societies, etc. All of us advance chemistry in the region through networks, working groups, and collaboration, especially with ACS. Development of solar cells provides a possible solution to the current crisis of energy deficiency in the world. Methods provide cell efficiency often through crystalline silicon cells, emerging photovoltaics, multijunction cells, single-junction gallium arsenide cells, thin-film technologies, and others. Being a type of thin film, perovskite cells are built with layers and proven reaching efficiencies similar to crystalline silicon. Their efficiencies are improved faster than any other photovoltaic material during the past 13 years from 3% (2009) to 29% (2021). To be commercially viable, perovskite photovoltaic cells have to become stable to survive 20–30 years outdoors. Scientists, engineers, industrial experts, and entrepreneurs work on making them durable, developing large-scale, and manufacturing at low-cost. Many elites and enterprise of Asia and United States are devoted their efforts on this interdisciplinary technology. It requires collaboration among talents of ACS, CACS, and FACS to make the dream to come true.

Chunshan Song is currently the Wei Lun Professor of Chemistry and Dean of Faculty of Science at the Chinese University of Hong Kong in Shatin, Hong Kong. Until June 2020, he was a Distinguished Professor of Fuel Science and Director of EMS Energy Institute at the Pennsylvania State University at University Park and the Founding Director of the University Coalition for Fossil Energy Research consisting of 15 major research universities, funded by US Department of Energy, National Energy Technology Laboratory. His research interests focus on catalysis and chemistry of energy and fuels including adsorptive CO₂ capture and catalytic CO₂ conversion, nonthermal plasma catalysis for energy and fuels, adsorptive and catalytic hydrocarbon processing and synthesis and application of nano-porous catalytic materials. He has published over 380 refereed journal articles, 14 edited books, 8 patents granted, 34 book chapters, and delivered over 360 invited lectures worldwide including 60 plenary or keynote lectures at professional and international conferences. ACS has honored him with the George A. Olah Award, the Henry H. Storch Award, ACS Fellow and the ACS ENFL Distinguished Researcher Award. He served as elected chair for both ACS Fuel Division and ACS Petroleum Division prior

to their merger to form Energy and Fuels Division in 2011. Currently he is serving as the Chair of Selection Committee for ACS ENFL Distinguished Researcher Award.



Title: Advances in CO₂ Capture and Utilization for Carbon Neutrality (ID: 3598422 (C4))

Affiliation: Department of Chemistry, The Chinese University of Hong Kong, Hong Kong, Hong Kong. The Pennsylvania State University, University Park, Pennsylvania, United States

Abstract: Capturing CO₂ from flue gases and other gas streams and converting CO₂ using H₂ produced from H₂O with renewable energy into carbon-neutral chemicals, materials, and fuels, is an important path for reaching carbon neutrality for sustainable development. This presentation will discuss some new design approaches to CO₂ capture/separation and catalytic CO₂ conversion to chemicals and fuels. One of the new approaches for CO₂ capture is based on solid “Molecular Basket” sorbent (MBS) developed at the Pennsylvania State University. MBS consists of functional polymers and nano-porous materials which shows high selectivity to CO₂ at high capacity and has been successfully demonstrated at pilot plant scale. Various new bimetallic catalysts and multi-functional catalysts and integrated reaction processes have been shown to be effective for the more selective conversion of CO₂ to industrial chemicals and fuels including C₂–C₄ lower olefins, liquid hydrocarbon (gasoline, jet and diesel) fuels, methanol as well as aromatics. Methane and CO can also be readily produced with > 95% selectivity to either one of these products if desired. More background and recent results are available in reviews from our teams on CO₂ capture (*Catal. Tod.*, 2006; *Front. Energy Res.* 2020), CO₂ conversions to hydrocarbons (*Adv. Catal.* 2019) and methanol (*Chem. Rev.* 2021).

Song Gao, President of South China University of Technology, Academician of the Chinese Academy of Sciences, Professor of Chemistry, member of the Chinese Academy of Sciences, member of the World Academy of Sciences (TWAS). He received his B.Sc. in Chemistry (1985) and Ph.D. in Inorganic Chemistry (1991) at the Peking University (PKU), and then worked at PKU. He was a Humboldt Research Fellow in RWTH Aachen in 1995–1997 and served as dean in College of Chemistry

and Molecular Engineering at PKU in 2006–2010, and he served as executive Vice President and Provost of Peking University before becoming the President of South China University of Technology in 2018.



Dr. Gao is the Vice Chairman of the 9th and 10th Committee of China Association for Science and Technology since 2016. He also serves several Editorial Advisory Boards of international peer-reviewed journals, including *Chemical Society Reviews* (2007–2018), *Chemical Science* (2010–), *Accounts of Chemical Research* (2017–). He is also the Editor-in-Chief of *Inorganic Chemistry Frontiers* (2013–), and the Associate Editor of *National Science Review* (2013–). His research interests are molecular magnetism and its applications in chemistry, materials, biomedicine, and quantum technology. In 2006, 2011 and 2019, Professor GAO received the prestigious National Natural Science Award (the 2nd Grade) respectively. In 2013, he received Science and Technology Progress Award, Ho Leung Ho Lee Foundation.

Title: Several Changes in Chinese Chemistry Research-Observation from Personal Perspective (ID: 3585798 (C5))

Affiliation: South China University of Technology, South China University of Technology, Guangzhou, Guangdong, China. College of Chemistry and Molecular Engineering, Peking University, Beijing, China

Abstract: In recent years, the trend of interdisciplinary research has had a significant impact on the field and direction of chemical research in China. This includes the vigorous development of nanotechnology, chemical biology, and energy chemistry and materials etc., as well as the funding provided by the Department of Chemistry of the National Natural Science Foundation of China, the adjustment of the field direction and the establishment of a new interdisciplinary research department. From the perspective of regional development, the construction of scientific and technological innovation centers in the Beijing-Tianjin-Hebei, Yangtze River Delta, and Pearl River Delta includes the construction of large-scale scientific installations and new R&D institutions, which also brings new opportunities for chemistry and related research. From the perspective of the growth of young chemical talents, in recent years, a considerable number of outstanding young chemists have concentrated on

returning to work in China, including many synthetic organic chemists returning to work due to changes in the pharmaceutical industry structure, which will lay a solid foundation of chemical research for Chinese universities in the next few years. However, the new college entrance examination policy has also brought a negative impact on the cultivation of young talents in chemistry disciplines in colleges and universities because chemistry has become an elective exam. In the post-epidemic era, our university (SCUT) carried out a pilot project for local international education at the Guangzhou International Campus in the Guangdong-Hong Kong-Macao Greater Bay Area to explore new paths for international STEM education.

Yongdan Li received his Ph.D. degree in 1989 from Industrial Catalysis Program of Tianjin University, China, with Professor Liu Chang. He spent one year in the University of Twente as a visiting researcher and one and half a year in DCPR-ENSIC in INPL in Nancy as a post-doc. After that he got an associate professorship in Tianjin University and after another year, he was promoted to a full professor there. He served as the Chair of the Industrial Catalysis Program and the Chairman of the Department of Catalysis Science and Technology in Tianjin until 2017. In June 2017, he was appointed as the Tenured Full Chair Professor of Industrial Chemistry at the School of Chemical Engineering, Department of Chemical and Metallurgical Engineering of Aalto University, Finland. His track records include: Making up the fundamental framework for the characterization and optimization of mechanical strength of commercial porous catalyst which helped Chinese chemical industry in the 80–90's of last century to get rid of the plant shutdowns due to catalyst mechanical failure; Proposing the simultaneous production of CO-free hydrogen and nano-carbon from methane catalytic decomposition as a process; Achieving the complete decomposition of Kraft lignin to small molecules with catalytic ethanolysis. He has made contributions also to the development of non-aqueous redox flow battery, solid oxide fuel cell, catalytic combustion of hydrocarbons, and hydrogen production via hydrocarbon reforming, CO water–gas shift and solar driven water-splitting.



Title: Chemical and fuel commodities through catalytic solvolysis of lignin (ID: 3590872 (D1))

Affiliation: Chemical & Metallurgical Engineering, Aalto-yliopisto, Espoo, Finland

Abstract: Lignocellulosic biomass has been demonstrated as an abundant renewable resource for production of platform chemicals, fuels, and their respective value-added products. Kraft lignin (KL) and enzymatic hydrolysis lignin (EHL) are the major byproducts from the pulp and 2G bioethanol industries respectively. Both KL and EHL were completely converted into platform chemicals and fuels via catalytic solvolysis. For instance, C₆–C₁₀ contained branched alcohols, ethers, esters, substituted phenols, arenes and benzyl alcohols were obtained from KL on the Mo-based catalysts in ethanol without tar and char formation. However, EHL preserve its original lignin structure (due to mild catalytic enzyme reaction) and is much cleaner and more active than KL. The solvents, catalysts, reaction atmosphere and temperature have significant effects on EHL conversion and product distributions. For example, jet fuel ranged cycloalkanes (104.4 mg/g EHL) was obtained on γ -Al₂O₃ supported Ni-Mo alloy catalyst in presence of cyclohexane solvent at 320 °C and 3 MPa hydrogen pressure, whereas EHL with ethanol was converted into C₈–C₁₆ aliphatic and aromatic range compounds with a total maximum yield of 363.4 mg/g EHL at 320 °C over a WO₃/ γ -Al₂O₃. The conversion of EHL was also investigated over different Ni and Mo-based catalysts. As compared to KL, the exploitation of EHL for chemical and fuel commodities is still progressing in the research communities.

Yun Hang Hu is the Charles and Carroll McArthur Endowed Chair Professor at Department of Materials Science and Engineering, Michigan Technological University. He is an elected fellow of American Chemical Society (ACS), American Association for the Advancement of Science (AAAS), American Institute of Chemical Engineers (AIChE), American Society of Metals (ASM), and Royal Society of Chemistry (RSC). He was the chair of the ACS Energy and Fuels Division in 2015. He has been the president of the Hydrogen Storage Division of International Association of Hydrogen Energy since 2015. He is the editor-in-chief of “Energy Science & Engineering” (Wiley journal) and an editorial board member for 8 international journals published by Nature group, ACS, RSC, Elsevier, and Springer, such as ACS Energy Letters, Catalysis Today, Scientific Report, and International Journal of Energy. He has made pioneering contributions to various areas, such as nanomaterials, catalysis/ photocatalysis/electrocatalysis, clean fuels, solar energy, batteries, supercapacitors, fuel cells, hydrogen storage materials, and CO₂ conversion. He published more than 250 papers in prestigious journals and delivered more than 160 invited presentations, including 43 plenary/keynote talks to the national and international conferences, such as the very prestigious plenary talk for the opening session of the ACS National Meeting.



Title: New Alkali Metal Chemistry for Energy and Environments (Presentation ID: 3598340 (D2))

Affiliation: Materials Science and Engineering, Michigan Technological University, Houghton, Michigan, United States

Abstract: In this talk, I will summarize our efforts to explore new alkali metal chemistry for energy and environmental applications, including (1) Li_3N reaction with CO_2 to carbon nitride, (2) hydrogenation of Li_3N and Li_2NH for hydrogen storage, and (3) synthesis of novel carbon nanomaterials via alkali metals. Furthermore, the excellent performance of these synthesized materials for energy devices will be highlighted.

Kunyu Wang is a Ph.D. candidate at Texas A&M University. He received B.Sc. in Chemistry (Po-Ling class) from Nankai University in 2018, where he studied metal–organic frameworks under the guidance of Prof. Wei Shi. In 2017, he went to Northwestern University as an undergraduate researcher in Dr. T. David Harris’ group to study semiquinoid molecular magnets. In 2018, Kunyu joined Prof. Hong-Cai Zhou’s research group at Texas A&M University. His research interest now focuses on novel strategies to design multi-component and hierarchical metal–organic frameworks. During his study, Kunyu has published 29 peer-reviewed articles, including 7 first/co-first author papers on top-notch journals, such as *Angew. Chem. Int. Ed.*, *ACS Materials Lett.*, *ACS Cent. Sci.*, *Trends. Chem.*, *Chem. Soc. Rev.*, and *Matter*. Besides, he has presented his research in many conferences, including the RSC Faraday Discussion, Gordon Research Conference, and ACS National Meeting.



Hong-Cai “Joe” Zhou obtained his Ph.D. in 2000 from Texas A&M University under the supervision of F. A. Cotton. After a postdoctoral stint at Harvard University with R. H. Holm, he joined the faculty of Miami University, Oxford in 2002. He was promoted to a full professor within six years by working on the preparation and application of Metal–Organic Frameworks (MOFs), a field he had had no prior experience in as a graduate student or postdoctoral fellow.

Dr. Zhou moved to Texas A&M University in 2008, was promoted to a Davidson Professor of Science in 2014, and was appointed the Robert A. Welch Chair in Chemistry in 2015. In June 2013, he started to serve as an associate editor for *Inorganic Chemistry* (ACS). In 2014, he received a JSPS Invitation Fellowship. In 2014, 2015, and 2016, he was listed as a Highly Cited Researcher by Thomson Reuters, and in 2016 he was elected a fellow of the AAAS, ACS, and RSC. In 2017 he was given the Distinguished Achievement award in research by TAMU’s Association of Former Students.

Dr. Zhou published more than 375 peer-reviewed papers, including more than 150 in high impact journals such as *Nature Chemistry*, *Nature Communications*, *JACS*, and *Angewandte Chemie*, International He gave 285 invited talks, including 32 keynote or plenary talks. Published 16 book chapters. Awarded 8 patents and serves as an Associate Editor for *Inorganic Chemistry* since June of 2013. In addition, he served as a Guest Editor for the first MOF (metal–organic frameworks) *Chem. Rev.* thematic issue and a Guest Editor for the 2014 MOF *Chem. Soc. Rev.* themed issue. He spearheaded the ARISE (Advanced Research Initiative for Sustainable Energy, an organization of 48 principle investigators on campus) in Texas A&M, two DOE ARPA-E (Advanced Research Project Agency-Energy) projects (subcontractors: Texas A&M Chemical Engineering, GM, LBNL, and RTI), two EERE (subcontractor: Argonne National Lab), two NETL (subcontractor: framergy™) projects and participated in an EFRC (Energy Frontier Research Center), which was renewed in 2014.



He organized three ACS MOF Symposium and served in numerous international and national panels. He cofounded (with Jason Ornstein) a Texas A&M University based company, framergy™, which specializes in commercializing framework materials with applications in the clean-energy sector, especially for methane storage and carbon capture. He was appointed as the Director of the Center for Electrochemical Systems and Hydrogen Research. He served as the Chair of Inorganic Division from 2016 to 2018. He was elected as a fellow of AAAS, ACS, and RSC, respectively, in 2016.

He was awarded the Association of Former Students of Texas A&M University Distinguished Achievement Award in Research in 2017 and appointed as the Chair of Interdisciplinary Academic Council of Texas A&M University Energy Institute in 2018. He was the chemist in Texas A&M University System listed as a highly cited researcher (2014–2020) by Clarivate Analytics (formerly Thomson Reuters). Currently, he becomes the most cited chemist in Texas A&M System (13 Universities) with an annual citation beyond 8,674 in 2019 (58,476 in total) based on the data provided by 4 Web of Science. Since started independent research in 2002, amassed an h-index of 107 (Web of Science, accessed on June 22, 2021).

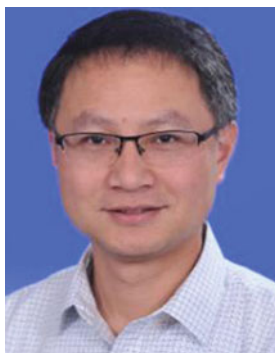
Title: A Laser Photolysis Approach to Generate Hierarchically Porous Metal–Organic Frameworks (ID: 3594934 (D3))

Affiliation: Departments of Chemistry and Materials Science & Engineering, Texas A&M University, College Station, Texas, United States

Abstract: Metal–organic frameworks (MOFs) are novel porous materials with great potential in the energy and fuel field. One main goal in this field is to create MOFs with hierarchical pores, which can not only improve mass transfer within frameworks, but also generate higher surface areas. Here we report a facile laser photolysis strategy to introduce mesopores into microporous MOFs by eliminating photolabile ligands in multivariate MOFs with laser treatment. As a proof-of-concept, we perform photolysis on a multivariate UiO-66 doped with photolabile ligand, which can be removed selectively under the laser, and the formation of mesopores are confirmed by N₂ isotherms. The crystallinity and structural integrity of the MOF can be preserved after laser exposure and the photolytic mechanism was further studied through IR, NMR, and TGA. This strategy features advantages such as accuracy, efficiency, and

feasibility in multiple MOFs, shedding a light on the programmable design of MOFs as gas storage materials.

Yunlong Zhang joined ExxonMobil Research Engineering Company as a staff scientist in 2014. He obtained his Ph.D. in Physical Organic Chemistry from The Ohio State University in 2010. He completed his postdoctoral fellowship at the Massachusetts Institute of Technology. His research in hydrocarbon science and petroleum chemistry focuses on upgrading heavy oils and asphaltenes, and synthesis of carbonaceous materials, with emphasis on theoretical understanding of reaction mechanisms and structures at the molecular level. He is currently applying molecular imaging non-contact Atomic Force Microscopy to study molecular structure and chemical reactivities of heavy petroleum molecules. His research has led to over 75 publications, conference presentations and invited keynote lectures, patents, a book chapter, and a book (as co-editor). He has served on the committees of ACS Energy and Fuels Division (ENFL) and Tri-state Chinese American Chemical Society (CACS) and organized many symposia. He is also currently serving as the chair of technical committee to organize the 21st International Conference of Petroleum Phase Behavior and Fouling (PetroPhase 2020) in Jersey City.



Title: Unlocking the Value of Petroleum Through Structure Characterization with nc-AFM Molecular Imaging (ID: 3598424 (D4))

Affiliation: Hydrocarbon Sciences, ExxonMobil Research and Engineering Company Annandale, Annandale, New Jersey, United States

Abstract: Most structures found in textbooks or publications are hypothetic or proposed (average) structures, derived from bulk chemical analysis, such as NMR, MS, FT-IR, UV-vis, EPR, elemental analysis, or scattering techniques, etc. However, advanced characterization techniques revealed that petroleum is an extremely complex molecular mixture, containing at least hundreds of thousands of species. Therefore, a huge uncertainty could be expected in our current understanding on petroleum molecules. Recently, the molecular imaging noncontact AFM technique has been applied to characterize individual molecules in petroleum in real space, and a summary of some recent findings will be presented in this talk.

Numerous novel polycyclic aromatic hydrocarbons (PAHs) have been discovered, with various degrees of condensation and substitutions by heteroatoms and aliphatic groups. Both alternant and nonalternant PAHs are present in the PAH structures, including benzenoids, and two types of five-membered ring structures. Few structures have been found to contain more than one PAHs so far. In order to address some long-standing questions regarding petroleum asphaltene structures, studied of model compounds have been conducted to shed light onto the structure of real petroleum molecules. In addition, recent applications to characterize petroleum pitch materials and decipher thermal reaction mechanism will be presented. Lastly, the advantages and challenges of applying nc-AFM will be discussed on characterizing petroleum mixtures, including representativeness of molecules, impact of sample preparation on structural integrity, and the identification of common features and reactive sites among diverse molecules. These new insights into petroleum molecules are poised to have a profound impact on the petroleum and energy industry by providing a foundation to study structure–reactivity relationships or other properties or behaviors.

Yun Liu (Ph.D. BPharm.) Dr. Yun Liu is currently working as a research scientist at Spark Therapeutics, a subsidiary of Roche. Yun Liu obtained a Bachelor of Pharmacy and was trained as a pharmacist in China in 2016. She then undertook doctoral studies at Eshelman School of Pharmacy at UNC-Chapel Hill, obtained a Ph.D. in Molecular Pharmaceutics and Pharmacoengineering in 2020. Yun Liu joined Spark Therapeutics after graduation and move to Philadelphia, the “Cellion Valley” and the birthplace of Gene and Cell Therapy. Spark Therapeutics is a clinical stage company committed to discovering, developing and delivering gene therapies for genetic diseases patient. In 2019, Spark launched first FDA-approved gene therapy product in the U.S.



Yun Liu’s research mainly focus on developing nanomaterial delivery of gene to targeted tissues. She has published 16 papers and book chapters in the field of gene and drug delivery and has been invited to give several talks at international conference. In addition, she took leadership roles in different professional communities, as an elected learning opportunity manager in American Association of Pharmaceutical

Science (AAPS) Student Community. She is dedicated to applying her scientific and clinical trainings to develop next-generation gene therapy for patients.

Title: Advances in Lipid Nanoparticles for mRNA Delivery: from Concept to Clinical Intervention (ID: 3597831 (E1))

Affiliation: Liver Research and Discovery, Spark Therapeutics Inc., Philadelphia, Pennsylvania, United States

Abstract: mRNA-based gene therapy has remarkable therapeutic potential in various disease area including infectious disease, cancer and rare disease. The success of mRNA-based gene therapies highly relies on the functional delivery of mRNA into the cytoplasm of targeted cells. However, due to the instability and inefficient in vivo delivery of mRNA, its application is heavily restricted. Recent advances in lipid nanoparticles (LNP) have profoundly driven the implementation of mRNA-based gene therapies in clinical settings, which attribute to the design and optimization of lipid component that enables safe and efficient delivery of mRNA. In this review, we first discuss and highlight the main factors impeding the successful target cell transfection and tropism of lipid nanoparticle-coated mRNA in vivo. In addition, the evolutionary design, characterization and optimization of lipid library for successful LNP development through the past decades will be summarized, with particular interest in recent progress in the development of LNP mediated mRNA-based gene therapies and their clinical utility in various disease treatment.

Dongling Ma, holder of the Canada Research Chair (Tier 1) in Advanced Functional Nanocomposites, has been a professor at Institut national de la recherche scientifique (INRS) since 2006. Her main research interest consists in the development of various nanomaterials (e.g., semiconductor quantum dots, transition metal catalytic nanoparticles, plasmonic nanostructures) and different types of nanohybrids for applications in energy, environment, catalysis and biomedical sectors.



Dr. Ma has co-authored > 150 journal articles in a broad range of areas, centered on materials science, in selective, high-impact journals such as *J. Am. Chem. Soc.*, *Nat. Commun.*, *Adv. Mater.*, *Adv. Energy Mater.*, *ACS Nano*, *Adv. Funct. Mater.*, *Energy Environ. Sci.*, *Chem. Mater.* and *Chem. Soc. Rev.* She has co-authored 6

patents (4 granted and 2 under review) and 4 book chapters. She has delivered > 120 invited speeches at international conferences and prestigious universities/government laboratories. She serves on multiple journal editorial advisory boards, including the prestigious *ACS Energy Lett.* (impact factor = 19.0), *Scientific Reports* (Springer-Nature), *Frontiers* (Energy), *ACS Applied Nano Materials*, *PhotonX* (Springer). She also acts as the section Editor-in-Chief for the section “Solar Energy and Solar Cells” of Nanomaterials. She serves as a panel / committee member for different funding agencies in Canada and other countries.

Title: Nanohybrids: perform better and be multifunctional (Presentation ID: 3585247 (E2))

Affiliation: Institut national de la recherche scientifique, Varennes, Quebec, Canada

Abstract: With unique physical and chemical properties, and high potential for many important applications, nanomaterials have attracted extensive attention in the past two decades. Further combining different nanomaterials into a single architecture can lead to improved properties/performance or, even better, multifunctional nanoplatforms. In this talk, I will present some of our recent work on the rational design and realization of nanohybrid materials as well as their applications in solar fuel, photocatalysis, biomedicine, etc. For instance, the stacking of 2-dimensional (2D) black phosphorous (BP) nanosheet and graphitic carbon nitride (g-C₃N₄) nanosheet led to a 2D-on-2D heterojunction photocatalyst, which demonstrated much enhanced activity (H₂ production rate) both under > 420 nm and > 475 nm light irradiation, as compared to BP and g-C₃N₄ nanosheets alone, and long-term stability as well. Another example is about the preparation of multifunctional nanoplatforms compose of multiple superparamagnetic nanoparticles and NIR quantum dots in single particles, which can serve as bimodal imaging probes and bimodal hyperthermia agents. Rational design in order to maximize benefits is highlighted for all these nanohybrids.

Bao Jian is CEO/co-founder of ZY Therapeutics Inc. Dr. Bao graduated from Peking University with a bachelor’s degree in organic chemistry in 1996, and received a doctorate degree in organic chemistry from University of Pittsburgh in 2001. In 2009, she was awarded Black belt in Six Sigma. In the last 20 years, Dr. Bao has participated in many programs for pharmaceutical and biologic therapeutic development. She worked for asymmetric catalysis in manufacturing of Lyrica in Pfizer. She then joined W. R. Grace, responsible for the synthesis of medicinal amino acids and short peptides. In Covidien she was awarded 10 patents in six years. In Novan, Inc. she led the effort in process development of both API and formulation for SB204, a topical drug treating acne. In 2015, Dr. Bao co-founded ZY Therapeutics Inc., focusing on therapeutic delivery innovation. In 2017, ZY’s first product ZY-010-PNP was selected as collaboration project by Nanotechnology Characterization Lab in a national effort to promote innovative cancer treatment delivery.



Dr. Bao has broad experience and overarching understanding of development, process optimization, and project management in pharmaceutical development. She has participated in and contributed to the development of a variety of drugs, including biological agents, analgesics, anti-infective products, and nano-formulation for anti-tumor drugs. She brought two drugs from the laboratory to the clinical trial approved by the US FDA (IND) and European Medicines Agency (IMP). She also received 19 patent grants and published about 10 papers.

Title: Biodegradable Nanoparticles for Drug Delivery (ID: 3585800 (E3))

Authors: Hui Zhang, Jian Bao, Aili Rong, Jun Li

Affiliation: ZY Therapeutics Inc., Research Triangle Park, North Carolina, United States

Abstract: Nanotechnology is an important tool by improving the delivery of cancer drugs; combining insoluble molecules with a biocompatible matrix to avoid dose-limiting-toxicity (DLT). Inclusion of targeting ligands can enhance accumulation and preferential uptake of drugs and improve the therapeutic index of both conventional chemotherapeutics and molecularly targeted therapeutics. Targeted biocompatible delivery of insoluble chemotherapeutics in a tunable manifold is ideal for cancer treatment.

ZY Therapeutics is developing a proprietary drug delivery platform based on biocompatible and biodegradable polysaccharide VMPC (Vitamin Modified Polymeric Carbohydrate) to generate nanoparticles (NPs) with encapsulated cytotoxic agents (taxanes) and other potential payload (immunotherapeutic agents). ZY-010-PNP was a VMPC nano-formulation of paclitaxel. It was specifically designed based on the hydrophobic characteristics of taxanes. The negatively charged modified-polysaccharide backbone ensures water solubility of the formulation and encapsulation chelator (Folate) ensures tunable encapsulation of the payload and the biocompatibility of the entire NPs in vivo with potential targeting effect to tumor cells. ZY-010-PNP is a unique solid nanoparticle that is designed to deliver cytotoxic agent paclitaxel selectively to cancer sites.

The VMPC platform is versatile in terms of formulation of active molecules with solubility issues. Drugs in different therapeutic areas can be encapsulated with VMPC polymers. We formulated molecules from metal complexes to peptide. The nanoformulations are sterilized stable lyophilized powder which can be reconstituted with saline to give mono-dispersed suspension with particles at 100 nm.

Our formulation advantages are: (1) ZY-010-PNP has completed Pre-IND meeting with the FDA and ready to translate to clinic. (2) All VMPC-Drug NPs were around 100–200 nm, a desired size takes advantage of EPR effect for increased accumulation at solid tumor site. (3) The polysaccharide carrier may have a time and concentration dependent release mechanism, as demonstrated in collaboration result from the NCL. (4) VMPC-Drug nanoformulation manufacturing process is scientific sound and reproducible. The process for this unique nanoparticle platform has overcome one of the biggest challenges of nanoformulation in therapeutics—manufacturing hurdle. Our next step is to work towards bringing the nano-formulation into clinic and address unmet medical need.

Yahu A. Liu received his Ph.D. degree from Case Western Reserve University in the laboratory of the late Prof. Lawrence M. Sayre (Chemistry/Pathology/Environmental Health). He earned a degree of Master of Engineering from Beijing Institute of Light Industry and obtained his early chemical education at Shanxi Teacher's College (China). He is Senior Outsourcing Manager at GNF/Novartis Institutes for BioMedical Research, and also serves as Chairman of the Board of Directors in Sino-American Biotechnology and Pharmaceutical Professional Association (SABPA). Yahu has 25 + years of experience in drug discovery and development. He previously worked in medicinal chemistry teams at ChemBridge, Vertex, and Pfizer. Prior to coming to the states, he had worked as an associate director in the Chinese Institute of Standards and Technology, CTO of Huarui Fine Chemical Co. Ltd. and a Certificate Engineer (Process Chemistry) at WH Chemical Co. (Beijing, China). In drug discovery research, Yahu has contributed to four drug/drug candidates. His main contribution to organic chemistry includes his discovery of three rearrangement reactions and syntheses of two natural products. He has been a co-editor of one book, a member of the editorial boards of two biochemistry journals, an issue editor of two journals, a co-organizer of ~ 50 conferences/symposiums, and a co-author of ~ 160 publications, patents and conference presentations. He received SABPA Distinguished Service Award in 2017, SABPA Outstanding Service and Leadership Award in 2016, SABPA Outstanding Leadership Award in 2011, SABPA Achievement Award in 2008 and SBTSC Scientific and Technical Achievement award twice.



Title: 6-Azaindole Derivative GNF2133 as DYRK1A Inhibitor for the Treatment of Type 1 Diabetes (ID: 3594348 (E4))

Authors: Yahu Liu, Qihui Jin, Yefen Zou, Qiang Ding, Shanshan Yan, Zhicheng Wang, Xueshi Hao, Bao Nguyen, Xiaoyue Zhang, Jianfeng Pan, Tingting Mo, Kate Jacobsen, Thanh Lam, Zhihong Huang, Tom Wu, H Michael Patrassi, Badry Bursulaya, Michael DiDonato, William Gordon, Bo Liu, Janine Baaten, Robert Hill, Van Nguyen-Tran, Minhua Qiu, You-Qing Zhang, Anwesh Kamireddy, Sheryll Espinola, Lisa Deaton, Sukwon Ha, George Harb, Yong Jia, Jing Li, Weijun Shen, Andrew Schumacher, Karyn Colman, Richard Glynn, Shifeng Pan, Peter McNamara, Bryan Laffitte, Shelly Meeusen, Valentina Molteni, Jon Loren

Affiliation: GNF/Novartis Institutes for BioMedical Research, San Diego, California, United States.

Abstract: Deficiency in β -cell mass or function can lead to insufficient levels of insulin, resulting in hyperglycemia and diabetes. Thus, promoting β -cell proliferation to increase β -cell mass could be one approach toward diabetes intervention. We identified 6-azaindole derivatives (including GNF2133) as potent and selective DYRK1A inhibitors which were able to proliferate both rodent and human β -cells. GNF2133 demonstrated significant dose-dependent glucose disposal capacity and insulin secretion in response to glucose potentiated arginine-induced insulin secretion challenge in RIP-DTA mice. The work showed that DYRK1A inhibition could be one of the new avenues to beta-cell regeneration and preservation for treatment of type 1 diabetes.

Mei Shen is an Assistant Professor of Chemistry, Neuroscience Program, and the Beckman Institute at the University of Illinois at Urbana-Champaign. Her research aims to push the limits of electroanalytical chemistry in bioanalysis, especially for the real-time interrogation of multiple groups of chemical transmitters with nanometer spatial resolution. She graduated with a B.S. and an M.S. with Prof. Yaoqiang Chen from Sichuan University, received her Ph.D. from The University of Texas at Austin with Prof. Allen J. Bard in 2011, and did her postdoctoral work with Prof. Shigeru Amemiya at the University of Pittsburgh.



Prof. Shen's group has pioneered the development of nano liquid/liquid interface electrodes for the real-time quantification of cholinergic neurotransmitters in single synapses and single cells. By expanding the electroanalytical toolbox to include both redox-active (e.g., dopamine, serotonin) and non-redox active (e.g., cholinergic and amino acid) neurotransmitters, her research has introduced exciting prospects to understand neuronal communication and decipher brain functions. Prof. Shen aspires to be a (female) role model to her students. Her distinctions include the NSF CAREER Award, the Award for Excellence in Guiding Undergraduate Research from the Office of Provost at the University of Illinois, and the Scialog Fellowship on Microbiome, Neurobiology and Disease.

Title: Super resolution study of neurotransmission in real time with scanning electrochemical microscopy and nanoelectrodes (ID: 3595706 (F4))

Affiliation: Chemistry, University of Illinois at Urbana-Champaign, Urbana, Illinois, United States

Abstract: Chemical sensing with electrodes offers chemical identity, quantification, fast response time, and high spatial resolution about biological processes in vivo. These advantages make electroanalytical chemistry one of the most widely used tools in studying signaling molecules in real-time, such as neurotransmitters. Acetylcholine, the first neurotransmitter identified in 1914, plays a key role in learning, memory, and human health. We recently developed Nanoscale ion-selective (liquid/liquid junction) electrodes for the detection and quantitation of several transmitters. We studied cholinergic neurotransmission of living neurons using Nano liquid/liquid junction electrodes and scanning electrochemical microscopy, around a single synapse and a single cell, where nanometer spatial resolution and millisecond temporal resolution were achieved. We are currently developing an integrated analytical platform to enable the multi-functional study of neurotransmission.

Qiang Zhen received his Ph.D. degree in the field of Metallurgical Physical Chemistry from the National Key Laboratory for Solid Electrolytes and Metallurgical Testing Techniques, University of Science and Technology Beijing in 2000. Currently, he is the executive member of the China instrument (functional) material society council and the member of China silicate society council. He serves as the Director of the Shanghai Advanced Ceramic Structure Design and Precision Manufacturing Professional Technology Service Platform; a distinguished Professor of Engineering Research Center of Material Composition and Advanced Dispersion Technology, Ministry of Education, China; and the Dean of the Division of Basic Research and International Cooperation of Shanghai University. In 2002, Dr. Zhen worked as visiting scholar in Department of Mechanical Engineering, Hong Kong University, and then visited the University of Science and Technology in Lille, France for six times in the period from 2005 to 2012.



Dr. Zhen's research interests focus on Solid electrolyte for fuel-cell or sensor application; Smart design, fabrication and characterization of micro/nano-ceramic composites. He has been directing more than 50 scientific research projects, supported by different funding agencies, such as the National Natural Science Foundation of China, and International Cooperation Plan. He published more than 100 peer-reviewed papers in the high impact journals and reviewed dozens of manuscripts. He has established a long-term collaboration with Dr. Liu and Dr. Bashir to facilitate the student and faculty exchange between universities in both countries of United States of American and the People's Republic of China. Through this collaboration, they published a book entitled *Nanostructured Materials for Next-Generation Energy Storage and Conversion: Advanced Battery and Supercapacitors*, by Springer Nature publishing in 2019. He also co-organized several symposia to provide platform for scientists, engineers and other professionals to disseminate their research discoveries in the National Meetings & Expositions, American Chemical Society.

Title: Design and Application of Functional Materials used in Energy Storage and Conversion (ID: 3585842 (F1))

Authors: Qiang Zhen, Rong Li, Sajid Bashir, Jingbo Liu

Affiliation: 1. Research Center of Nano Science and Technology, Shanghai University, Shanghai, Shanghai, China. 2. Chemistry, Texas A&M University Kingsville, Kingsville, Texas, United States. 3. Energy Institute, Texas A&M University System, College Station, Texas, United States

Abstract: The overarching goal of this research lies in the design, evaluation, and application of interactive nanomaterials to improve energy utilization and secure end-of-life safe disposal of the electrocatalyst and photocatalysts. The research activities include: (1) production of metal oxide-based bioinspired materials to control the oxygen reduction reaction and facilitate electron transfer mechanism; (2) Fabrication of porous metal-organic frameworks (MOFs, guest-host) used for onboard gas storage; and (3) study mechanism and interactivity between nanomaterials & reactants using spectroscopic and microscopic approaches. Series of synthesis methods will be discussed with optimized fabrication variables to produce materials with tunable structures. These approaches include chemical vapor deposition, high energy ball-milling, and wet chemistry methods (colloidal, hydrosolvo-thermal, and solid-state chemistries). Nanomaterial engineering plays critical roles to control and tune

the structure and functions of the products oriented by their end applications. This approach will enable nanomaterials to operate using biochemical redox-based principles to respond to the external environmental changes and to self-regulate via electron injection and/or O₂ detachment. Our research data indicated that material functionalization is one of the key factors to improve the catalytical reactivities of these interactive materials when used as electrocatalysts and photocatalysts. One example indicated the power density and current density of fuel cells were found to be increased by one fold magnitude while device durability was sustained at a 95% root mean square current modal value at 3,600 cyclic operations.

Wei Wang obtained his B.S degree in Chemistry from Shandong Normal University, China in 1983, and Ph.D. degree in Physical Chemistry from Changchun Institute of Applied Chemistry, Chinese Academy of Sciences (CAS) in 1993. He is a Research Science Specialist at Aramco Research Center-Boston, Aramco Americas. He joined in the Aramco Global Research Centers-North America as a founding member and the first research staff in 2012. Before joining the Aramco, he worked as a Staff Research Scientist at Environmental Sciences Division, Oak Ridge National Laboratory (ORNL) in 2001–2012, where he was the PI or co-PI for 17 research projects funded by DOE, NIH, BATTELLE and ORNL, etc., also supervised postdoctoral and junior researchers. Prior to that, he worked as a postdoctoral research associate at the University of Pittsburgh and as an associate professor at the Ocean University of China, in Qingdao. In the past 30 years, his research has centered on molecular spectroscopy, fabrication of nanomaterials and nanomaterial-based sensors and devices. In the Aramco Research Center, his research has been focused on the development of nanomaterials and nanotechnology for reservoir description and improving oil recovery. Wei has authored or co-authored more than 130 research papers, 4 book chapters and 15 US patents, and his publications have been cited for > 6300 time with a H-index 43. He has also reviewed manuscripts and proposals for 80 + scientific journals and 5 funding agents, given 30 + invited or keynote presentations at professional meetings and university seminars, organized or chaired > 10 scientific symposia at international conferences.



Title: Fabrication of Colloidal Photonic Crystal-Based Materials for Sensing and Coating Applications (Presentation ID: 3591833 (F2))

Affiliation: School of Materials Science and Engineering, Ocean University of China, Qingdao, Shandong, China. Aramco Research Center-Boston, Aramco Americas, Cambridge, Massachusetts, United States

Abstract: Colloidal photonic crystals have attracted extensive attentions for using as sensing and coating materials because of their unique optical properties. In this research, we have fabricated polymer hydrogel materials with embedded photonic crystal nanostructures which diffract light in visible wavelength region. By introducing molecular recognition functional groups into the hydrogels through covalent bonding, the functionalized smart hydrogels are highly responsive to metal ions such as mercury and beryllium ions selectively, enabling a rapid and real-time detection in seawater system for pollution monitoring in ocean. With a completion-based mechanism, a universal biosensor with sensitively responding to antibody-antigen interactions has been presented for point-of-care (POC) application. By taking advantage of the fadeless structural colors, we also fabricated powder materials with embedded three-dimensional ordered macropores (3DOM) structure by negatively replicating opal structures. The micron-sized ceramic inverse opal powders can diffract visible lights and exhibit vivid structural colors. As coating materials, the structural colors of the photonic crystal powders follow the Bragg diffraction of incident light on their stacked crystal planes while each of the powders is randomly oriented. As a collective effect in the aggregation of micron-sized powders, the structural colors are angle-independent and anti-reflective in a coating layer.

Wenhao Shao is a Ph.D. candidate from Dr. Jinsang Kim group in University of Michigan. His research focuses on organic semiconductors and light-emitting devices covering computation-driven molecular design, photophysical analysis, and device characterization.



Jinsang Kim received his Ph.D. (Materials Science and Engineering, Polymer) Massachusetts Institute of Technology, and completed his postdoctoral fellow at

the Division of Chemical Engineering and Chemistry), California Institute of Technology, 2001–2003 under supervision of Prof. David Tirrell. His research interests are molecular design, synthesis, modification, and self-assembly of smart polymers for biomedical and optoelectronic applications, including Plastic Electronics, Organic Light Emitting Molecules, Molecular Biosensors, Smart Gels, Optoelectronic Polymers, Conjugated Polymers, Block Copolymers, Organic–inorganic Hybrid Materials, Photovoltaic Cells, and Self-assembly.



Title: Crosslinking Chemistry for Solution Processable Multilayer Organic Light-Emitting Diodes (ID: 3597866 (F3))

Authors: Wenhao Shao, Jinsang Kim

Affiliation: University of Michigan, Ann Arbor, Michigan, United States

Abstract: One of the key advantages of OLEDs is that they can potentially be produced entirely by solution processes, more suitable for low cost and large area displays, compared to the conventional vacuum deposition. Here, we investigated an approach based on the thiolene click chemistry to overcome the solvent penetration issue in solution processed multilayer OLEDs. A generally applicable binder-type crosslinking strategy was designed. Compared to conventional crosslinking strategies, the devised bicomponent system renders synthetically simple and much faster crosslinking by means of thermal-assisted UV irradiation. While most thiolene systems in other applications operate on polymeric systems, our strategy has been optimized for the contemporary small-molecule-based OLED devices. Results have shown that our system could achieve a considerable crosslinking degree and > 85% solvent resistance within 10 min. Upon successful development, the devised strategy could be readily and universally applicable to widely used OLED materials to facilitate the development of solution-processable OLEDs.

Fanwen Zeng received his Ph.D. in organic chemistry at the University of Illinois at Urbana-Champaign, IL. He also held a post-doctoral position at the University of California Berkeley, CA. He is currently a Principal Research Scientist in Dow, Inc. He joined Dow/Rohm and Haas in 1999 as a R&D scientist. Since then, he has led to develop and commercialize a variety of products to serve markets including Personal

care, Plastics Additive, Coating, and Biocide. These products range from acrylic impact modifiers, rheology modifiers, hair styling polymers, hollow sphere polymers, opacifiers, water-proofing polymers, cosmetic active, to anti-microbial technology. His industrial expertise spans from emulsion and solution polymerization, small molecule organic synthesis, encapsulation, silicone-based technology, and recently to sustainable chemistry. He is an inventor of over 50 patent families, 25 granted US patents. He authored over 30 peer-reviewed scientific articles, which have been cited more than 3000 times. He has been the recipient of numerous awards, including for example an R&D 100 award for his contribution to the silver-based antimicrobial technology in 2014.



Dr. Zeng has been very involved in various external organizations such as the American Chemical Society, the Chinese American Chemical Society (CACS), and Controlled Release Society. He served as a board member and president of CACS-tristate chapter. He also served the president of CACS-headquarter in 2020. At Dow, he served the chair of the Asian Diversity Network-Delaware Valley Chapter in 2011–12.

Title: Novel acrylic emulsion polymers with high bio-carbon content for personal care applications (ID: 3593734 (E5))

Authors: Fanwen Zeng, Inna Shulman, David Lu, Ligeng Yin, Lu Bai, Tian Lan, Michaelen Pacholski, Jen Koenig, Meng Jing, Cathy Jackson, Peilin Yang, Matt Carter

Affiliation: Consumer Solutions, Dow Chemical Co, Collegeville, Pennsylvania, United States

Abstract: There is a growing trend to provide personal care products with better sustainability profiles. Among them, novel polymeric raw materials are highly sought after if they can either biodegrade or be made from bio-derived raw materials. For the latter case, there are a few existing standards, e.g. COSMOS (COSMetic Organic Standard) or NATRUE or ISO-16128 to define the natural content for personal care applications. Among them, ISO-16128 can be the best fit for bio-derived synthetic polymers. This standard comprises guidelines on definitions for natural and organic

cosmetic ingredients and offers a framework to determine the natural content of ingredients as well as formulations. The key to pass this standard is that the renewable bio-carbon content (BCC) needs to be > 50%. In this paper, we investigate the emulsion polymer syntheses from a selection of bio-derived monomers and their potential applications for the personal care industry while still meeting the ISO-16128 standard.

Chinese American Chemical Society Leaders and Award Winners

Zhenan Bao is Department Chair and K. K. Lee Professor of Chemical Engineering, and by courtesy, a Professor of Chemistry and a Professor of Material Science and Engineering at Stanford University. Bao founded the Stanford Wearable Electronics Initiative (eWEAR) in 2016 and serves as the faculty director. Prior to joining Stanford in 2004, she was a Distinguished Member of Technical Staff in Bell Labs, Lucent Technologies from 1995 to 2004. She received her Ph.D in Chemistry from the University of Chicago in 1995. She has over 500 refereed publications and over 65 US patents with a Google Scholar H-Index > 155.



Bao is a member of the National Academy of Engineering and the National Academy of Inventors. She is a Fellow of MRS, ACS, AAAS, SPIE, ACS PMSE and ACS POLY. Bao was selected as Nature's Ten people who mattered in 2015 as a "Master of Materials" for her work on artificial electronic skin. She was awarded the Gibbs Medal by the Chicago session of ACS in 2020, University of Chicago Alumni Award by the Department of Chemistry in 2020, the Wilhelm Exner Medal by Austrian Federal Minister of Science 2018, ACS Award on Applied Polymer Science 2017, the L'Oréal-UNESCO For Women in Science Award in the Physical Sciences 2017, the AIChE Andreas Acrivos Award for Professional Progress in Chemical Engineering in 2014, ACS Carl Marvel Creative Polymer Chemistry Award in 2013, ACS Cope Scholar Award in 2011, the Royal Society of Chemistry Beilby Medal and Prize in 2009, the IUPAC Creativity in Applied Polymer Science Prize in 2008.

Bao is a co-founder and on the Board of Directors for C3 Nano and PyrAmes, both are silicon-valley venture funded start-ups. She serves as an advising Partner for Fusion Venture Capital.

Dachao Li is currently a research scientist and segment leader in the Dow Chemical Company, who has significant contributions to the functional and formulated polymers industry in new technology development. Dachao recently expanded his role as segment leader in the Wire and Cable business, and is responsible for developing business winning strategy, identifying business opportunities, resource allocation, and decision making to take product development from initial concepts to commercialization. He is currently leading innovation portfolio with > \$90 MM dollars net present value (NPV).



Dachao has led a significant number of global innovation projects and commercialized multiple products with total financial impact > \$30 MM dollars, including the development of Submarine Fiber Optic Cable insulation and jacket materials in support of 5G telecommunication, electric track-resistant material for aerial cables in battle with wildfire issue, and a new insulation material with improved heat aging performance for Medium and Low Voltage power distribution. Dachao has been on the CACS board (Tri-State Chapter) for more than 5 years and served as the president of Tri-State CACS in 2020.

After receiving his B.S. and Ph.D. in Chemical Engineering from East China University of Science and Technology, Dachao joined Core R&D in Dow, Shanghai in 2011, and then left Dow in 2013 to join The Ohio State University as a post-doctoral researcher. In December 2014, Dachao rejoined Dow with Wire and Cable R&D based in Collegeville, PA. Dachao has authored 16 external publications, and over 20 patents (6 granted).

Lin Li is a Senior Staff Research Engineer at Chevron Technical Center, Richmond, CA. He received his BS, MS and Ph. D. degree in Chemical Engineering from Tianjin University (Tianjin, China) in 1983, 1986 and 1989, respectively, and then started his academic career at Tsinghua University (Beijing, China). During his tenure at Tsinghua, in addition to teaching and research, he served as the Director of

Laboratory of Membrane Technology and Vice Chairman of Department of Chemical Engineering.



Lin moved to the US in 1998 as a research scientist at Princeton University and UC Berkeley, and then started industrial career at UOP (Des Plaines, IL) in 2001. Lin published 2 books, 50 journal papers and many technical presentations, and is the author of 25 patents and patents applications. He is a certified 6-Sigma Black Belt. He is an AIChE Fellow, and his services to AIChE include serving as Meeting Program Co-Chair of 2016 AIChE Annual Meeting and Chair of AIChE Northern California local section (NorCal). He is currently an ABET program evaluator (PEV) for Chemical Engineering.

Frank Zhu is a Honeywell-UOP Senior Fellow, leading technology innovations and has made significant contributions to the fields of process efficiency, molecular modeling, process optimization and process development as well as industrial digitalization. More importantly, Franks' methods have been successfully applied to industries and generated significant benefits in economic margin, energy savings and emission reductions. He led process design of several grassroots refineries and petrochemical complexes which are ranked in the category of the highest energy efficiency worldwide.



Before joining UOP, Frank served as a Research Professor at the University of Manchester in England, where he supervised pioneering work in developing molecular based operation optimization and molecular based process synthesis. Frank's work aimed to exploit fundamental phenomenon for Process Development with the purpose of discovering breakthrough ideas in materials, catalysts, process and equipment.

Frank published more than 100 peer reviewed articles and 70 + patents, including four books: "Energy and Process Optimization for the Process Industries" in 2014, "Hydroprocessing for Clean Energy" in 2017, "Efficient Petrochemical Processes: Technology, Design and Operation" in 2019, "Digitalization and Analytics for Operation Excellence" in 2021 by Wiley/AIChE respectively. He was the recipient of US National Energy and Sustainability Award 2014 by AIChE, Patent of the Year Award and Technology Leadership Award by Honeywell. He is nominated for AIChE Funders Award in 2020.

W. S. Winston Ho is a Distinguished Professor of Engineering in the William G. Lowrie Department of Chemical and Biomolecular Engineering and the Department of Materials Science and Engineering at The Ohio State University. Before teaching for 21 years, he had 28 years of industrial R&D experience in membranes and separation processes, working for Allied Chemical, Xerox and Exxon, and serving as Senior Vice-President of Technology at Commodore Separation Technologies. He was elected to the National Academy of Engineering, USA in 2002 in recognition of his distinguished contributions to engineering. A New Jersey Inventor of the Year (1991), Dr. Ho holds more than 55 U.S. patents, generally with foreign counterparts, in membranes and separation processes. He received the 2006 Institute Award for Excellence in Industrial Gases Technology from the American Institute of Chemical Engineers (AIChE), and he was the 2007 recipient of Clarence G. Gerhold Award, from the AIChE Separations Division, one of the highest honors bestowed to those working on separations. He received the 2012 Lawrence B. Evans Award in Chemical Engineering Practice from AIChE. In 2014, he was elected to Academia Sinica, the highest form of academic recognition in the Republic of China in Taiwan. He obtained his B.S. degree from National Taiwan University and his M.S. and Ph.D. degrees from the University of Illinois at Urbana-Champaign, all in Chemical Engineering.



Dr. W. S. Winston Ho served as Chairman, Board of Directors, Chinese-American Chemical Society (CACS) from 2002 to 2008. After that till now, he has been a CACS' Board of Director.

Chu-An Chang received his Ph.D. in Organic Chemistry from the University of California, Berkeley, and his B.S. degree in Chemistry from the National Taiwan University. He worked in the biotech industry for over 30 years as a research scientist specializing in oligonucleotide synthesis and its chemical modifications. He retired in 2018 from ThermoFisher Scientific.



Dr. Chang is currently serving as a CACS Board member and the Treasurer of National Chapter. He joined CACS in 1984 through its Northern California Chapter (NCC) and became a Life Member in 1989. He assumed the role of the Treasurer in 1988 and had also served two years as the Chairperson of the CACS-NCC in 1990 and 1991. He was elected to the CACS Board in 2000.

Chu-An's Treasurer duty over the years has been responsible for keeping accurate books and maintaining financial viability of CACS. He participated in membership recruitment, renewal, database maintenance and assisted in the production and distribution of printed materials in the early days like CACS Membership Directory and

CACS Newsletter (became CACS Communications in 2007). For many years he has coordinated with local chapters and members to host CACS social events, including social hours, banquets, and keynote speeches, at the national meetings of both ACS and AIChE. Serving as an Election Committee member, Chu-An has also assisted in conducting elections of CACS officers and board members at the National Chapter.

Lixin You is the President of Southwest chapter of Chinese American Chemical Society. He is an Advisor Process Engineer at Chevron, where he is responsible for process design and consulting for LNG, GTL and other complex process facilities. He also conducted technology development work on fuel cells, fuel processors, hydrogen energy and biofuels at Chevron.



He has numerous publications in peer-reviewed journals and received numerous patents. He obtained a B.S. from Suzhou University, a M.S. from Shanghai Jiaotong University and his Ph.D. from the University of Miami.

Wenmei Xue is the president of Tri-State chapter of Chinese American Chemical Society. She holds a Ph.D. degree in Organometallic Chemistry from the University of Hong Kong. She is currently a senior chemist at BASF Corporation. A significant part of her research has focused on catalysts for environmental applications.



She was the recipient of the 2010 Thomas Alva Edison Patent Award from the R&D Council of New Jersey and the 2015 Excellence in Catalysis Award from the Catalysis Society of Metropolitan New York, in recognition of her contribution to the discovery and development of Cu-CHA catalysts for selective catalytic reduction (SCR) of NO_x from diesel vehicles.

“Mark” Yueqian Zhen received his Ph.D. in organometallic chemistry from the University at Buffalo. He came to the US for graduate school via then US-China CGP exchange program along with other top 50 chemistry graduates.



Mark is a life-time member of the Chinese American Chemical Society (CACS) and a member of American Chemical Society (ACS). Mark first participated in a CACS activity while postdoctoring at the University of Chicago. Mark was involved in Tri-State CACS organization as its 2014 President and as national CACS vice president and president from 2016 to 2018.

Mark is currently the Department Manager for Formulation Research at Valent BioSciences LLC, a global leader in the R&D and commercialization of biorational agricultural products, located in northern Chicago suburbs. Previously, Mark was a Lead R&D Manager at Dow Chemical Company and specialized in the formulation and delivery of a plant growth regulator for agricultural application. Mark started his professional career and received technical training as a Research Scientist in Procter and Gamble in its laundry division to formulate its next generation more sustainable liquid Tide™ detergent.

Baoqing Ma is a regulatory assessor working at Center of Drug Evaluation and Research, FDA, with primary focus on the drug product Chemistry, Manufacture and Control including pre-market and post-market products since 2016.



Before joining FDA, Baiqing has worked at Pharmaceutical company Sanofi and Bristol-Myers Squibb for more than 10 years with interest in preformulation, formulation and drug delivery. He had served as a president at Tri-State Chinese American Chemical Society. He earned his Ph. D. in chemistry from Peking University.

Yinlun Huang is Professor of Chemical Engineering and Materials Science at Wayne State University, where he directs the Laboratory for Multiscale Complex Systems Science and Engineering. Dr. Huang's research has been mainly focused on the fundamental study of multiscale complex systems science and sustainability science, with applied study on engineering sustainability, including sustainable nanomaterial development, integrated design of sustainable product and process systems, and manufacturing sustainability. He has published widely in these areas, and has given a large number of plenary/keynote speeches at national and international conferences. He has organized and chaired the National Science Foundation sponsored conference series—International Conference on Sustainable Chemical Product and Process Engineering and other conferences since 2007. Dr. Huang directs the NSF funded Sustainable Manufacturing Advances in Research and Technology Coordination Network.



Dr. Huang is currently the Co-Editor-In-Chief of ASTM Journal—Smart and Sustainable Manufacturing Systems, and Associate Editor of Springer Journal—Clean Technologies and Environmental Policy. He served as Chair of AIChE Sustainable Engineering Forum (2008–2009) and is Director of AIChE Environmental Division (2021–2023), and also served as Chair of AIChE International Committee (2015–2016). He is an elected AIChE Fellow.

Dr. Huang is a recipient of AIChE Sustainability Education Award and Research Excellence in Sustainable Engineering Award in 2016 and 2010, respectively, the NASF Scientific Achievement Award in 2013, the Michigan Green Chemistry Governor's Award in 2009, U.S. Department of State Fulbright Scholar in 2008, and Charles H. Gershenson Distinguished Faculty Fellow at Wayne State University in 2005.

Dr. Huang served as Vice President (1999–2000), President (2001–2002), Director (2008–present), and Chair of the Board of Directors (2010–2012) of Chinese American Chemical Society (CACS). Dr. Huang holds a B.S. degree from Zhejiang University, China, and an M.S. and a Ph.D. degree from Kansas State University, all in chemical engineering. He was a postdoctoral fellow at the University of Texas at Austin before joining Wayne State University in 1993.

Jasmine (Yingchun) Lu is currently a Senior Alliance Manager at Atomwise, a preclinical pharma company revolutionizing how drugs are discovered with AI. Prior to joining Atomwise in 2021, she worked for the US Innovation Center of Shimadzu, a top-five global instrumentation company, and AcceleDev, a US-Sino CDMO company, as the Director of Project Management. Her earlier careers included as a Senior Medicinal Chemist in Morphochem and Pharmacopeia Drug Discovery, focusing on drug discovery for oncology and immunosuppressants projects.



Jasmine is a life member of the Chinese American Chemical Society (CACS). She has served on the Board of its Tri-State Chapter since 2012 and was the Chair of 2019. She joined the American Chemical Society (ACS) in 1994 and has served as an Alternate-Councilor in ACS North Jersey Chapter. She has also served on the Board of NJACS Mass Spectrometry Discussion Group and was the Chair of

2017. Jasmine holds a BS degree in Chemistry from Peking University, an MS from Southern Methodist University, and a Ph.D. in Organic Chemistry from Dartmouth College.

Wei Gao is a Principal Research Scientist in Analytical Science, Corporate Research and Development, at Dow Inc. She received her BS degree from Fudan University and Ph.D. in Polymer Chemistry and Physics from Peking University. She then worked as a postdoctoral fellow and an Associate Professor in the Institute of Chemistry, Chinese Academy of Sciences. Employment at the NSF-IUCRC center for Biocatalysis and Bioprocessing of Macromolecules at Polytechnic University (Now NYU Tandon School of Engineering) followed in 2000, and in 2005 she became a Research Assistant Professor. In 2006, Wei joined Rohm and Haas/Dow. She intensively works on polymer and particle characterization, the synthesis–structure–property relationship of polymeric and colloidal systems, and sustainable polymers. She has published over 30 peer reviewed journal articles and book chapters, edited one book, and has more than 20 patents and patent applications. She has organized American Chemical Society (ACS) symposia in the areas of separation and characterization of macromolecules and particles, polymer sciences for everyday things, and polymer colloids. She a lifetime member of Chinese American Chemical Society (CACS) member. She also served on the scientific program committee for the GPC2015 conference and the Steering board member for international symposium on Field- and Flow-Based Separations (FFF2018 and FFF2022). She was the recipient of the NOVA Innovation Award from Rohm and Haas Company (2008), US EPA Presidential Green Chemistry Challenge Awards (2003 and 2013), Vernon A. Strenger Scientists' Award from Dow (2019), and ACS Polymer Chemistry Division (POLY) fellow (2021).



Dr. Jingbo Louise Liu was appointed Director of the Center of Teaching Effectiveness in 2021 and previously promoted to Full Professor in 2016 at Texas A&M University-Kingsville (TAMUK). She is also affiliated with the Texas A&M Energy Institute. Dr. Liu received her Ph.D. in Materials Science and Engineering from the University of Science and Technology Beijing in 2001. Her research expertise

focuses on nanostructured inorganic materials preparation, characterization, fundamental physical and chemical properties, and applications of engineered nanomaterials in alternative energy and biological science. She established the highest power density to advance the performance of proton exchange membrane fuel cells and directed a new paradigm to apply metal–organic frameworks in disinfection science. During her 16-year service at TAMUK, she taught about 12,000 students; trained more than 200 undergraduate students. She oversaw the completion of ca. 50 graduate (master and Ph.D.) students. She has hosted and co-hosted 15 visiting scholars to conduct leading-edge research on biomedicine, hydrogen fuel cells, photocatalysis, and nanotechnology. She served as an NSF panelist and chaired the proposal review panel. She also served as a journal editor and reviewer.



ACADEMIC HIGHLIGHTS: Dr. Liu has participated in nanotechnology research since 1987. She has authored and co-authored books (10), textbooks (4), book chapters (>20), and ca. 100 peer-reviewed journal articles. She chaired and organized conferences and presented > 150 talks in professional conferences. According to Google Scholar, the total number of citations to her work exceeds 21,000, and she has an h-index of 53 (with i10-index: 209).

Dr. Liu was a Woman of the Year Award winner of the Texas Diversity Council's 2023, named the Fellow of 2022 by the American Chemical Society, and awarded as the Distinguished Fellow at NSWC—Carderock Division ONR Summer Faculty Program in 2022. She was named Distinguished Women in Chemistry or Chemical Engineering by the International Union of Pure and Applied Chemistry in 2021. She serves as the ACS Certified Career Consultant, elected Councilor of the Energy and Fuels Division, Chair of the South Texas Chapter of the American Chemical Society, and Officer at the Sigma Xi, The Scientific Research Honor Society (TAMU Chapter). She has been elected as an Honorary member of the Golden Key International Society, a Fellow of the Linnean Society of London, a Fellow of the Royal Society of Chemistry, DEBI faculty fellow at the US Air Force Research Laboratory. She was awarded the Chartered Scientist and Chartered Chemist in March and May 2019, respectively. She was awarded Japan Society for the Promotion of Science

Invitation Fellow and worked at the Department of Materials Science, University of Tokyo (2010–2011). She has served as a “Faculty and Student Team” fellow, collectively funded by the National Science Foundation and US Dept. of Energy, Office of Science, and worked at the Argonne National Laboratory (2009). She also received Faculty Fellowship Summer Institute in Israel (2008) and outstanding research and teaching awards at the university level. She directed and participated in projects (> 40) supported by the NSF (USA, CHINA), NSERC (CANADA), ACS Petroleum Research Funds (PRF), R. Welch Foundation (departmental), Dept. of Education, industrial and TAMUK as PI, Co-PI, faculty participant, and senior personnel. She also received dozens of travel funds to attend dozens of workshops.

Part I
Biomedical Applications

Chapter 2

Recent Advancement of Nanotechnology in Bio Applications



Ashraf Abedin, Jhonattan David Manosalvas Mora, Adiba Azad, Srikar Bhattar, S. M. Rezwanul Islam, and Mohammad Hasibul Hasan

Abstract Nanotechnology is the production, design, and research of useful materials and devices with sizes ranging from 1 to 100 nm. Nanoparticles (NPs) have unique features with a wide range of applications due to their small size and large surface area. Nanoparticles are employed in a variety of biological applications, including treatments, diagnostics, imaging, and drug administration. Besides these, nanomaterials are also used in tissue engineering as scaffolds and as biomaterials in medicinal applications. In this chapter, we focused on these various applications of nanotechnology in bio-applications to update the readers on the most recent discoveries as well as the existing challenges. Nanotechnology has significant potential for providing different multimodal diagnostic platforms and therapeutic applications that will drastically alter the human health scenario. Thorough investigation of these complex nano-applications may encourage progressive research and development in future biomedical sectors. Attempts are currently underway to convert these scientific advances into clinical practice, which should usher in a new paradigm of biomedicine.

Keywords Tissue engineering · Drug delivery · Cancer treatment · Nanotechnology · Bio-imaging · Biosensors

A. Abedin (✉) · J. D. M. Mora · S. Bhattar · S. M. R. Islam
Cain Department of Chemical Engineering, Louisiana State University, Baton Rouge, LA 70820, USA
e-mail: mabedi1@lsu.edu

A. Azad
School of Public Health, West Virginia University, Morgantown, WV 26505, USA

M. H. Hasan
Department of Chemical Engineering, Clarkson University, Potsdam, NY 13699, USA

2.1 Introduction

Current developments in the field of nanotechnology research have inspired research activity in biomedical applications. In medicine, the application of these materials can be used to interact with cells and tissues at a receptor level with greater precision than ever before, allowing for a higher level of integration between technology and biological systems [84]. This integration of nanotechnology into biomedical applications is anticipated to be instrumental in tackling the current personal and global health care issues, as well as its economic strain on the billions of people around the world [59]. The increasing use of nanotechnology in biomedicine has driven the emergence of the hybrid science known as nanobiotechnology. Nanomaterials can be categorized as either organic or inorganic, with examples including nanofibers, nanotubes, liposomes, polymer nanoparticles, elementary substances, alloys, silica, and quantum dots [64]. Because of nanomaterials and bio-molecules having comparable size and structure, nanomaterials are valuable tools for biomedical research and applications, *in vitro* and *in vivo* conditions [19]. They are also biocompatible, biodegradable, and can gather inside human organs with minimal side effects [107]. Additionally, nanomaterials exhibit slow-release properties, which can mitigate toxic side effects on health and environment [68].

Carbon nanotubes, liposomes, inorganic and metal nanoparticles, and metallic surfaces are the materials most frequently employed in the development of biocompatible nanoparticles. Nanomaterials have interesting implementation in several bio-fields such as drug delivery, cancer therapy, diagnosis, tissue engineering and bioimaging. Tissue engineering is an integrative field combining engineering, materials science, medicine, and biology [63, 126]. It reproduces the materials which closely resembles to body's native tissue/tissues. In recent years, advances of nanotechnology and nanofabrication in tissue engineering have led to the development of implantable tissues, some of which are already in use in humans (e.g. skin and cartilage) or initiated clinical trials (e.g. bladder and blood vessels) [126]. Figure 2.1 represents the advantages of nanofabrication in tissue engineering.

A promising research area of healthcare is drug delivery systems (DDS), which is a constantly developing area of medical science. For more than 20 years, multidisciplinary research has improved the creation of DDS, which has successfully improved therapies for several illnesses [10]. Very simple but effective design methods for self-assembling drug nanostructures with unique benefits and tremendous promise for improving therapeutic targeting and lowering medication toxicity are provided by nanotechnology. When diseases and traumatic injuries rose, drug targeting with increased bioavailability, analgesic effects, controlled drug release, and human health is improved using nano scaled dimensions between 1.0 and 100.0 nm and by utilizing the unique properties of nano scaled particles, this is referred to as nanomedicine [120], which is one of the most useful creations of nanotechnology. Various stages of tumor, cancer, microbial infections, gene therapy, and chronic hyperglycemia can be treated by nanomedicines because they can improve medication delivery while minimizing its negative effects and those of the drug carrier [120]. The US-FDA

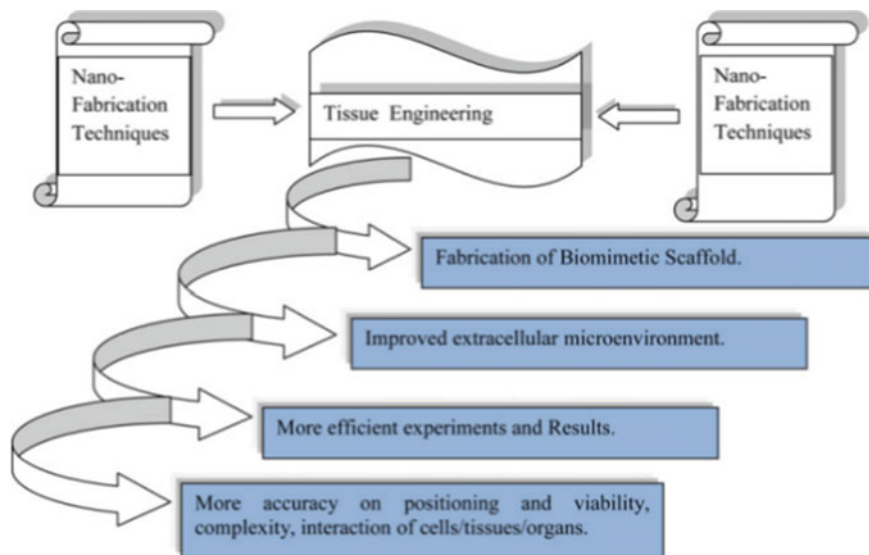


Fig. 2.1 Advantages of nanofabrication in tissue engineering [63]. Reproduced from Kingsley et al. Copyright © 2013 Elsevier. All rights reserved

has so far approved about 51 nanomedicines, afterwards when, 77 products are in pre-trial stage, with about 40% of them currently in the clinical trial stage. Polymeric liposomal and nanocrystal compositions make up most of these authorized nanomaterials, which will be developed and tested in clinical trials soon [116]. Due to their outstanding applications to distribute drugs to practically any organ or location of the body, Nanoparticles have become a crucial component of drug delivery research, resulting in focused, regulated, and long-lasting therapeutic effects [136].

Bioimaging and Diagnostics enabled the early detection of diseases during the pre-screening phase enhanced imaging of internal structures, and simplified diagnosis. It utilizes various advanced techniques including biosensors, nanobots, nano identification of single-celled structures, chips etc. to achieve these goals. These techniques are constantly being developed and refined in nano diagnostics [44]. By engineering nanomaterials to interact with targeted bio-components, they can be harnessed to leverage the benefits of personalized medicine techniques [159]. Also, Specific biological components can be targeted by engineering nanomaterials to interact with them [96]. Over the past years, a tremendous advancement of nanoparticles enhanced the capabilities of early detection and physiological understanding of a disease, which provides an opportunity for improved treatment. For example, early detection of breast cancer recurrences the mortality rate of patients with reduced significantly to 17–28% [80]. In comparison to single molecule-based contrast agents, nanoparticulate probes have demonstrated notable advantages. These benefits include establishing good contrast and integrating various features, such as a wide range of

materials that can generate contrast [149]. NPs integrated with diagnostic and therapeutic agents are highly desired for continuous monitoring of treatment effectiveness and side effects.

Cancer therapy is another major field of bioscience where nanotechnology research is making great progress. Cancer is the second leading cause of death after cardiovascular diseases worldwide [148]. It is caused due to abnormalities that occur during the cell cycle, which generate an uncontrolled proliferation of malignant cells. The most widely practiced cancer treatments are therapies including chemo, radio, and surgery, which are used individually or in combination depending on each patient [3, 13]. These treatments have some undesired side effects. Consequently, new strategies and/or therapies are required whose main objectives must be to detect, prevent and slow the progression of cancer while improving the patient's quality of life. Nanotechnology is presented as a viable alternative to reduce and overcome the major side effects of the current cancer treatments. Nanomaterials/nanocarriers, due to their different targeting strategies, play a significant and distinguished role in biomedical imaging, detection, and delivery of drugs.

Passive targeting: Passive targeting property of the nanoparticles is mainly due to the size and surface properties which aid in enhanced Permeability and Retention Effects (EPR) in tumors. The “Enhanced Permeability and Retention” effect (EPR) is the most studied approach mechanism (passive) [40, 111] in which chemotherapeutic agents bonded with nanocarriers [<500 nm [24]] reach and surround the tumor cells after penetrating flawed lymphatic vessels (endothelial cells) [65, 118] without losing their activity. Conventional small molecule medications have poor tissue selectivity, and most of them are dispersed in healthy tissues, which causes serious systemic toxicity. However, use of nanocarriers with high EPR improved the targeting of cancer cells, hence reducing the adverse effects. The EPR effect is described in Fig. 2.2. Nanoparticles should be designed in sizes larger than renal clearance levels and smaller enough to reduce accumulation in organs with mononuclear phagocyte system (MPS). NPs with sizes of 10–60 nm have shown enhanced cellular uptake [34].

Active targeting: Surface Labeling of NPs with specific ligands can improve binding of the NPs to the receptors in lesions. As a result, the imaging contrast and signals are significantly enhanced because of accumulation and localization. Also, usually, cancer cells exhibit overexpression of cell markers (folic acid and antigens) on their surface [40] which are identified and targeted by the affinity ligands from the nanocarriers for drug delivery and treatment. Antibodies and their fragments are one of the most important ligands used for active targeting strategy of NPs. As antibodies have high affinity towards antigens of receptors, they are highly effective in targeting and nanoparticle accumulation for high resolution imaging [34]. Aptamers and peptides also form a good ligand species due to their strong affinity and bonding towards cell surface receptors. For example, arginine-glycine-aspartic acid (RGD) peptide contains extreme affinity towards integrin $\alpha_v\beta_3$. Hence, fluorescent dyes conjugated with RGD can exhibit bifunctional role—both drug delivery and imaging. Thus, depending on the ligand and strategy adopted there are four

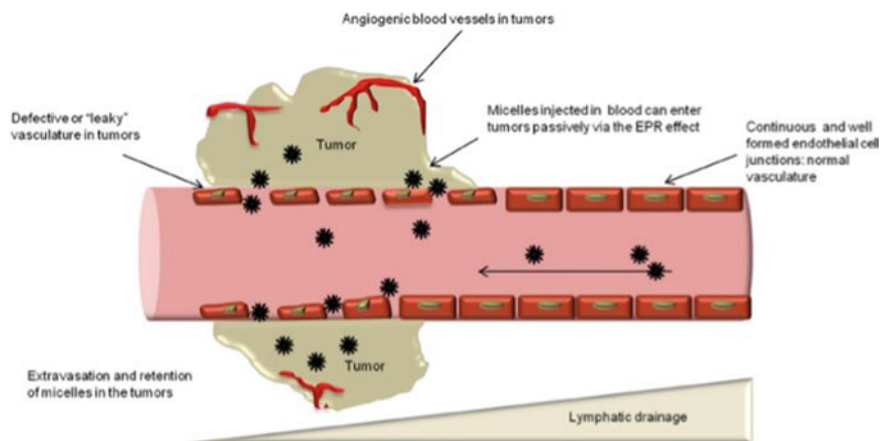


Fig. 2.2 Enhanced permeability and retention effect (EPR) [155]. Reproduced from Yoo et al. Licensed under CC BY 4.0

different active targeting strategies—receptor-mediated, peptide-mediated, antibody-mediated, aptamer-mediated. Nanocarriers using an active targeting mechanism are often compared with guided missiles [40, 142]. Ligand—receptor interaction is described in Fig. 2.3.

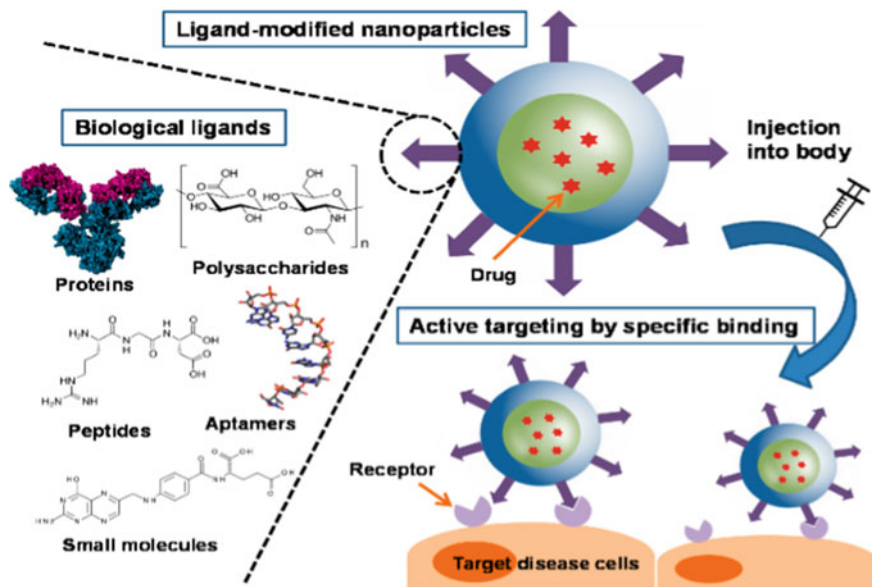


Fig. 2.3 Ligand—receptor interaction [155]. Reproduced from Yoo et al. Licensed under CC BY 4.0

Apart from the above two strategies, physical targeting which uses external stimuli like PH, light, magnetic field, temperature, enzyme activity and redox gradient is employed to target the nanoparticles to target sites discussed in later sections of the chapter. In this chapter, we put forward some of the major advances of nanotechnology in the field of biomedical applications. We also try to understand the current challenges and emerging technologies of nanoparticles in tissue engineering, drug delivery, cancer therapy, medical diagnostics and bioimaging. Efforts are also made to understand the physical, chemical, and biological properties of nanoparticles and nanocarriers which correlate to their successful application which can assist further developments in this field of study.

2.2 Tissue Engineering

Tissue engineering is an advancing bio-field which is applied to generate, replace, or restore cells, tissues, or organs by using combination of cells with bio-active molecules. It reproduces the constituents which closely resembles to body's native tissue/tissues. Professor Gasparo Tagliacozzi, who was a professor of surgery and anatomy at the University of Bologna in the sixteenth century, is credited with the first pioneering work in the field of tissue engineering. He successfully constructed a nose replacement from a forearm flap which was described in his work 'De Custorum Chirurgia per Insitonem' (The Surgery of Defects by Implantation), which was published in 1597. Another decisive contribution to the field of tissue engineering was made by Howard Green and his coworkers when they carried out the first mass production of typical human diploid cells (keratinocytes) in 1981. It was the first commercial product of tissue engineering using living autologous human skin epithelium. This enabled doctors to treat burn patients [84].

On the other hand, Nanotechnology is a branch of science that deals with the design, classification, and application of materials and devices on the molecular scale, with dimensions of less than 100 nm. Any material is classified as nanomaterial if it has at least one dimension in the nanometer size range. At this scale, these materials display unique properties compared to their bulk form, exhibiting different physical and chemical behavior. These materials can be used to interact with cells and tissues at a receptor level with greater precision than ever before, allowing for a higher level of integration between technology and biological systems [26, 84]. This integration of nanotechnology into biomedical applications are anticipated to be instrumental in tackling the current personal and global health care issues, as well as its economic strain on the billions of people around the world [59].

2.2.1 *Nanoscale Techniques for Tissue Engineering*

Tissue engineering has been greatly facilitated by the utilization of nanotechnologies, which are more efficient than traditional methods. In this section, various nanoscale techniques employed in various facets of tissue engineering will be discussed.

Bone cells tissue engineering through nanoscale techniques

- i. **Soft lithography** is employed to maintain cell orientation and behavior. For example, mesenchymal cells can be cultured on collagen which results into enhanced bone formation via appropriate surface topography [6, 63].
- ii. **Photolithography** is providing a superior groove topography for primary human osteoblasts, thus aiding in cellular adhesion [51].
- iii. **Microcontact printing** is an effective technique which can be used to guide selective osteoblast adhesion and alignment. Rat mesenchymal stem cell-derived osteoblasts are cultured on poly(3-hydroxybutyrate-co-3-hydroxyvalerate) to facilitate osseointegration [53].
- iv. **Electrospinning** in bone cells tissue engineering has an affirmative effect on osteogenic sarcoma cells culture [63, 139].

Vascular cells tissue engineering through nanoscale techniques

- i. **Soft lithography** using polydimethylsiloxane helps to induce global gene expression and alteration in cell signaling in mesenchymal stem cell cultures. Additionally, it helps to increase endothelial cells retention with poly-urethane, resulting into reduction of thrombogenicity during implantation [20, 66].
- ii. **Microcontact printing** technique is applied to observe a varied response to shear stress in a Bovine aortic endothelial cell culture when exposed to polydimethylsiloxane [73].
- iii. **Electrospinning** is an effective technique for attaching and migrating coronary muscle cells via the axis in poly(L-lactid-co ϵ -caprolactone) culture [63, 151].

Hepatic cells tissue engineering through nanoscale techniques

- i. **Electrospinning** enables the generation of spheroidnanofiber in rat primary hepatocytes culture with poly(ϵ -caprolactone-co ethyl ethylene phosphate) [151].
- ii. **Soft lithography** can supply adequate oxygen and nutrient mass transfer to maintain viability in both hepatoma cells cultures and primary rat hepatocytes cultures. This is achieved by using polydimethylsiloxane and polycarbonate [8].
- iii. **Photolithography** is used to maintain a three-dimensional structure in hepatocytes cultures, featuring poly(ethylene glycol). It is also capable of sustaining phenotypic functions for extended periods of time, when primary rat and human hepatocytes cultures are supplemented with polydimethylsiloxane [57, 138].

Stem cells tissue engineering through nanoscale techniques

- i. **Electrospinning** promotes the adhesion and proliferation of hematopoietic stem cells on a nanofiber mesh. This technique also acts as an efficient captor and carrier for hematopoietic stem cells [15, 82].
- ii. **Soft lithography** is a technique used to manipulate and regulate the distribution, alignment, proliferation, and morphology of human mesenchymal stem cells. It is also used to initiate differentiation of embryoid bodies more uniform in cell culture in vitro. In addition, it is a useful tool for studying the growth and differentiation of human embryonic stem cells under defined conditions as well as for homogeneous aggregation of human embryonic cells [50, 55, 56, 156].
- iii. **Photolithography** is used to keep the cells in the grooves rather than ridges, ensuring uniform shape. This affects the rate of lipid production, which in turn, affects the differentiation of cells into adipocytes [11].

2.2.2 Nanotechnology Application in Tissue Engineering

Nanotechnology has rapidly become an increasingly important field of application for tissue engineering. It involves the development of both soft and hard tissue replacements, such as artificial cartilage and even a heart, to regenerate damaged cells and improve patient's quality of life. Nanotechnology has made tissue engineering easier by using nanophase materials, as compared to conventional methods. Following are some applications of nanotechnology in tissue engineering in different fields.

2.2.3 Nanotechnology Application in Bone Cells Tissue Engineering

The complex and high vascularization nature of human bone restricts the applications of traditional bone tissue engineering, particularly in cases involving large bone defects. Recent advances in nanotechnology and 3D printing has offered new possibilities for bone tissue engineering [143]. Bone tissue engineering generally comprises three major components: bone scaffolds, bone cells, and bioactive molecules. Mechanical property and porosity of the scaffolds can be tailored to fit with the existing bone condition of the patients using 3D printing. This helps to prevent stress shielding and boost bone cell growth. Additionally, an ideal scaffold should have few other essential features such as biocompatibility, osteoinductivity, surface properties that facilitate cell adhesion, biodegradability, and radiolucency. In order to create more efficient scaffolds which can suit the needs of patients, scientists have applied unique features of nanoparticles. However, single-functional nanoparticles often fail to satisfy the requirements of scaffold applications. Multi-functional nanoparticles can improve the mechanical properties of scaffolds, making

them more suitable for various applications by boosting cell viability and increasing osteoinductivity [61, 83, 143].

Scaffold manufacturing techniques include solvent casting, particulate leaching, freeze-drying, gas forming, solution casting, and phase separation. Various techniques used for bone tissue engineering through micro and nanotechnology include soft lithography, photolithography, microcontact printing, and electrospinning [84].

2.2.4 Nanotechnology Application in Vascular Cells Tissue Engineering

Various methods have been employed to generate the structure and activity of blood vessels. Advancement of nanotechnology has enabled the optimization of the internal vascular graft surface, providing additional functionality to vascular conduits. Moreover, nanotechnology can direct the distinction of stem cells into the vascular phenotype. Additionally, nanotechnology provides the means to understand the surface characteristics of materials on valves and stents. This understanding enables scientists to improve biocompatibility of the devices by regulating cell adhesion ability and inhibiting thrombosis and formation of blood clots [42].

The advancement of nanotechnology-based strategies in the fabrication of vascular tissue is widely regarded as one of the most influential technological breakthroughs in the realm of vascular tissue engineering. Nano-structuralized scaffolding can replicate the arrangement of a natural extracellular matrix (ECM), which consequently results in optimization of cell adhesion. Differentiated endothelial cells (ECs) have been used as a method of seeding the biomaterials in order to promote vascular tissue repair after artificial graft implantation. Additionally, Nanotechnology approaches have been identified as playing a significant role in endothelialization processes, such as endothelial cell migration, adhesion, proliferation, and differentiation [42] (Fig. 2.4).

In one report, the use of magnetic nanoparticles-incorporated endothelial progenitor cells (EPCs) in a microfluidic channel with a syringe pump, has been shown to control the flow rate of cells. Magnetic cell delivery provides a new opportunity for targeted delivery of localized cell therapies. Magnetically tagged devices can be used at a site of artery injury to enhance EPC localization. This technology can provide a novel approach for systemic injection of cell therapies in vascular tissue engineering applications. Furthermore, labeling EPCs with monocrySTALLINE iron oxide nanoparticles (MIONs) does not negatively affect their viability and migration ability *in vitro*. This enables successful detection of even limited numbers of these cells in muscle [42].

Overall, there are strong evidence that nanotechnology holds great potential for the development of more effective vascular tissue-engineered products.

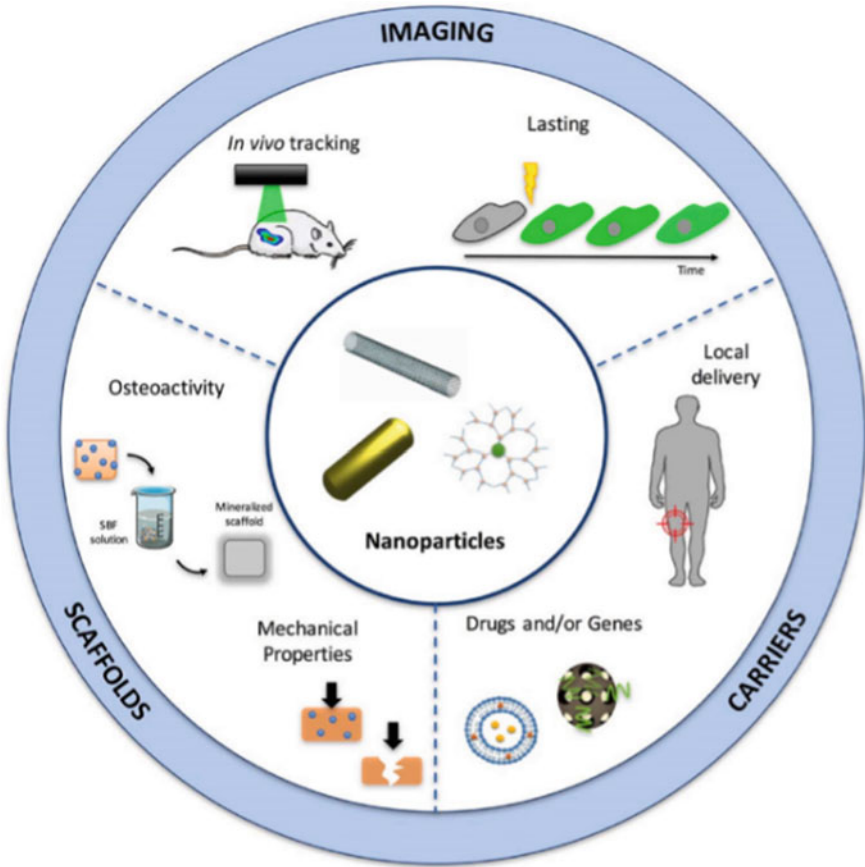


Fig. 2.4 Main applications of nanoparticles in bone tissue engineering. Reproduced from Vieira et al. Copyright © 2017 Wiley. All rights reserved

2.2.5 Nanotechnology Application in Hepatic Cells Tissue Engineering

The key objective of liver tissue engineering is to replicate the phenotype and functions of liver cells, especially primary hepatocytes, *ex vivo*. To achieve this, several strategies have been explored to culture the liver cells in the most suitable environment, including usage of biological scaffolds to support hepatocyte growth and differentiation. Due to the increased surface-to-volume ratio and porosity, as well as similarity to the native tissue extracellular matrix (ECM) environment, nanofibrous scaffolds are widely used in tissue engineering. Electrospinning is an important method for producing nanofiber scaffolds. It offers cell–matrix interactions that facilitate the adhesion and proliferation of cells, which are essential for optimal tissue functioning [140].

Nanopolymers are also being utilized for a wide range of tissue engineering applications. These applications include the fabrication of tissue implants for regenerative medicine, physiological tissue scaffolds for disease modeling, and drug screening. A number of techniques are employed to create nanofibers and nanopatterned structures, which includes electrospinning, particulate leaching, lithography, self-assembly, phase separation, and freeze drying [140].

Nanotechnology provides an effective method for reproducing and repairing cells, as it improves their properties. To achieve this, a 3D microenvironment is provided to the cells, using nanostructured collagen, matrix, elastin, and lamin. There is more evidence of interaction between the cell and the microenvironment at the nanoscale level, resulting in the differentiation of the cell. Additionally, the microenvironment provided by the nanotechnology inhibits hepatocytes from trans diffusing into fibroblasts, thus helping to retain their spheroidal morphology; this has been one of the key challenges in the cell-based culture of hepatocytes [84, 140].

2.2.6 Nanotechnology Application for Stem Cell Engineering

The use of nanomaterials and nanotechnology in stem cell research and development offers promising technological opportunities, giving new hope to resolve the current challenges faced by stem cell research and development. The application of nanotechnology in stem cell research and development has brought significant advances in this field. One example is the employment of magnetic nanoparticles (MNPs) to successfully isolate and sort stem cells. Quantum dots have been also utilized for molecular imaging and tracing of these cells. Additionally, nanomaterials such as carbon nanotubes (CNTs), fluorescent CNTs and fluorescent MNPs have been employed to supply genes or drugs into stem cells. Another application is designing of unique nanostructures to enable the controllable regulation of the proliferation and differentiation of stem cells, thus accelerating the development of stem cells for use in regenerative medicine [146].

Stem cell-based therapeutic strategies for human diseases have been developed through the combination of stem cells and tissue engineering principles. A particularly promising area of this research is the differentiation of stem cells and progenitor cells in conjunction with 3D materials, which is viewed as a potential breakthrough in tissue engineering. Several micro-/nanofabrication technologies have been applied to guide stem cells to develop into 3D biodegradable nanostructured scaffolds. These scaffolds are designed to trigger stem cells to become specific cell types that make up the body's tissues and organs. The cells deposit their own matrix as the scaffolds degrade, and form a 3D tissue structure that mirrors the body's natural tissues [146].

However, stem cell nanotechnology is still an emerging field and faces many challenges. It is still not well-understood how nanomaterials and nanostructures interact with stem cells and affect their function, as well as how nanomaterials inside stem cells are metabolized. These are significant challenges for further research [146].

2.2.7 Challenges and Future Prospects

Nanoparticles have shown promising potential in various tissue engineering applications, such as enhancing biological, mechanical, and electrical properties, providing antimicrobial effects, delivering genes, and constructing engineered tissues. However, there are still numerous challenges that need to be overcome before these nanoparticles can be used for clinical application on a wide scale. When nanomaterials are used in tissue engineering to replace damaged organs, several issues must be carefully considered. These include the sensitivity of the implanted materials, the potential immune response, toxicity, and the impact on reproduction and fetal development [25, 35, 161]. There are reports of toxicity of nanoparticles generated from the degradation of implanted nanomaterials. There are also reports regarding cellular uptake of nanoparticles in the lungs, immune system, and other organs, which have been published. This cellular uptake can occur in endothelial cells, alveolar macrophages, pulmonary or intestinal epithelium, nerve cells, etc. These issues are potential bottlenecks for this field if not thoroughly understood before being widely applied. Therefore, further in-depth investigations of nanomaterials and their effects on human health and the environment are required in order to decide whether they should be used in biomedical applications [157].

Nanomaterials have the potential to bring many benefits to human health. However, the application of these man-made nanomaterials also has potential health risks. To minimize these risks, precautionary principles must be applied during development, testing, and clinical applications of these materials [25].

2.3 Nanocarriers in Cancer Treatment

Cancer is the second leading cause of death after cardiovascular diseases worldwide [148]. Cancer can be due to abnormalities that occur during the cell cycle, which generate an uncontrolled proliferation of malignant cells. Metastatic cancer occurs when these malignant cells spread throughout the body via the lymphatic system and bloodstream. Later, the malignant cells invade tissues surrounding the blood vessels, where they multiply and form small tumors. As time goes by, new blood vessels are formed, feeding the tumor with blood, and allowing them to continue growing. Metastatic tumors commonly spread to the lungs, liver, and peritoneum. Cancer was among the four causes of death in people over 70 years in each country in 2019 [133]. In fact, according to data from the International Agency for Research on Cancer (IARC) GLOBOCAN (bureau of the World Health Organization), there were 19.3 million new cases and approximately 9.9 million deaths attributed to cancer in [28, 148]. A higher incidence of lung, prostate, and skin cancer (in that order) was found in men, meanwhile, in women the highest incidence were breast, lung, and cervical cancer respectively [28]. In a comparison between 2000 and 2016 the number of total deaths worldwide increased approximately 8.7% (from 52.307 million deaths

in 2000 to 56.874 million deaths in 2016), at the same time, the number of deaths related to cancer hiked 27.6% (from 7.029 million deaths in 2000 to 8.966 million deaths in 2016) [87]. In the same period, the world population rose from 6.144 billion people to 7.492 billion people [137] (an increment of 21.9%). As a result, although the total number of deaths worldwide has been lower than the population growth, the number of deaths related to cancer has expanded in a greater degree than the gain in population. It should be clarified that cancer incidence and mortality vary in each country. Specifically, there is a solid correlation between the HDI (Human Development Index) and cancer incidence. For example, high HDI countries represent 41% of the world's cancer cases, on the contrary, low HDI countries represent less than 6% [29]. To illustrate, just in the United States nearly 1700 people died from cancer every day. Of this number, approximately 21% was related to lung cancer in men and women (2022) [129]. In brief, these data only describe in a very general way the importance that governments should give to the fight against cancer and that the efforts in the development of new treatments have not provided us with definitive cures for this disease. Therefore, there is still a long way to go to achieve this goal. If the reader wishes to delve into different studies of world statistics regarding cancer, its types, mortality, and incidence by country, the following publications are recommended: [17, 28–30, 36, 45, 81, 87, 129, 133].

The most widely practiced cancer treatments are chemotherapy, radiotherapy, and surgery, which are used individually or in combination depending on each patient [3, 13]. These treatments have some undesired side effects. The most common after-effects in chemotherapy are related with hair loss, fatigue, inhibition of cell growth (cytostasis), cell damage (cytotoxicity), poor cancer cell targeting, gastrointestinal disorders, and so on [13, 32, 160]. Similarly, the side effects of radiotherapy are associated with cytostasis and cytotoxicity [92]. In the same way, cancer related surgeries are excellent options in early stages because the tumor can be completely removed, but they are hardly applicable in advanced stages of the disease [13]. Consequently, new strategies and/or therapies are required whose main objectives must be to detect, prevent and slow the progression of cancer while improving the patient's quality of life. Nanotechnology is presented as a viable alternative to reduce and overcome the major side effects of the current cancer treatments. For that reason, in this very brief section, the targeting mechanism, the nanocarriers types for cancer treatment, and the stimuli that nanocarriers must undergo to release anti-cancer therapeutic drugs in tumor tissues will be discussed.

2.3.1 Nanocarriers

Nanocarriers are nanoparticles which have been used as transport modules for different substances [40]. They should experience modifications to acquire some characteristics such as immunity against natural defenses (immune system), and the ability to accumulate and deliver (after external and internal stimulations) anticancer drugs at specific sites in the body [40, 65]. Additionally, nanocarriers must have

some important features such as pH, composition, size, surface area, shape, surface potential, surface adsorption, or chemical reactivity [110, 128] to be employed as a drug delivery system in cancer treatment. The diameter range of nanocarriers should lie between 5 and 200 nm [65, 163], but diameters below 100 nm are more employed [128]. For example, nanocarriers size is a crucial parameter for liver and kidney cancer treatment. The kidney leaks nanocarriers with a diameter smaller than 10 nm, and the liver traps nanocarriers bigger than 50 nm [65]. Nanocarriers must be large enough to avoid any infiltration into blood capillaries and small enough to leave the macrophages' reticuloendothelial system [110]. In addition, it has been shown that the ease of penetrating a tumor by a nanoparticle is inversely proportional to its size [110]. This means that for some drug delivery systems big enough nanoparticles will be needed to allow good distribution into the blood, but also nanoparticles must have the ability to leak from the blood vessels into cancerous tissues (fluid extravasation) [65, 110]. As a result, nanocarriers will need intrinsic or extrinsic stimuli to reduce their size [65]. Generally, nanocarriers need some transformational stages before their application in cancer treatment [40]. When nanocarriers start their journey inside the body to achieve the tumor tissues, nanocarriers will face biological drawbacks such the cleansing by the reticuloendothelial system (RES) which will send nanocarriers to the liver [40, 65]. However, to overcome this issue, nanocarriers must pass through a process called "PEGylation" which is a biochemical modification where Polyethylene glycol (PEG) is bonded (covalent and non-covalent) to the nanocarriers to activate them [33].

2.3.2 *Stimulus for Drug Release*

There are two types of stimuli, exogenous (extrinsic) and endogenous (intrinsic) [40].

Endogenous stimulus

- **pH—responsive**

pH level within the body is not constant and it is possible to say that pH varies between organs, tissues, or cell organelles [40, 75]. Additionally, cancer tissues' pH level (between 5.6 and 7.0 [75, 106]) is lower than normal tissues [153]. Cancer tissues are typically acidic because of disproportionate lactic acid accumulation and irregular elimination of metabolic waste, which induces a higher production of hydrogen ions [106]. Moreover, pH-sensitive nanocarriers can store and control drugs at specific pH levels, and then release or switch the arrangement of pH sensitive bonds at explicit values in cancer tissues [40, 153]. pH-sensitive nanocarriers are commonly anions, cations (ionizable groups such as phosphoric acid, carboxyl groups, or amine group), or acid-sensitive linkers [153]. Some common examples of pH-sensitive nanocarriers are acrylic acid (Paavo Perämäki) and methacrylic acid (PMAA) [106, 153].

- **Enzyme—responsive**

They are nanocarriers which are designed to have specific properties with the ability to respond to the biocatalytic actions of cancer tissue enzymes [40, 106]. Generally, these nanocarriers are employed in the extracellular environment of cancer cells (which are overexpressed of enzymes), but not in the intracellular environment because there is no distinction in the enzymatic levels between healthy and cancer cells [40]. The main advantage of enzyme-responsive nanocarriers lies in enzyme's excellent selectivity based on their substrate [106]. Proteases, phospholipases, and peptides are some examples of enzymes which can be used for this purpose [40, 106].

- **Redox sensitive**

Glutathione (GSH) is an antioxidant constituted by three amino acids which controls the cell redox environment [153]. A very useful characteristic of GSH (structure R-S-S-) is its potential to reduce the disulfide bond of nanocarriers to sulfhydryl [40, 106]. Also, there is a high level of GSH in cancer cells (at least four times higher than normal cells) which allows the modification of disulfide bonds in an intracellular environment [19, 30, 31]. Therefore, redox sensitive nanocarriers can bind drugs by disulfide bonds which will be modified in high GSH concentrations (intracellular cancer tissues), but not in extracellular environments [106].

Exogen stimulus

- **Thermo—responsive**

Thermo-responsive nanocarriers deliver drugs into the cancer tissues in reaction to temperature change [40]. Regularly, unhealthy tissues display higher temperatures (a phenomenon called hyperthermia and in temperatures between 40 and 42 °C) in relationship with the body's normal temperature (37 °C). For that reason, nanocarriers change their hydrophobicity-hydrophilicity state thanks to the "Lower critical solution temperature" (LCST) phenomena [40, 75]. LCST phenomena describes a temperature below which all the components of a mixture are completely miscible [4]. Therefore, these nanocarriers present a stable structure in healthy tissue temperatures, but they immediately release therapeutic drugs at unhealthy tissues (hyperthermia) [40]. Most of these nanocarriers are polymers such as Poly(N-isopropylacrylamide) (PNIPAM) [153].

- **Magnetic field—responsive**

Nanocarriers, which are composed of magnetic core structures such as magnetite (Fe_2O_4) or maghemite (Fe_2O_3) and are enclosed with polymer or silica, can be regulated remotely via magnetic field in situ [40, 106]. In addition, magnetic nanocarriers with an alternating magnetic field can generate heat which could damage tumor cells [106, 153]. Equally important, magnetic nanocarriers are used in magnetic resonance

imaging (MRI) an imaging technique to diagnose some types of cancer (breast) [90, 106, 153].

- **Photoresponsive**

These nanocarriers are made up of chromophores [106]. Chromophores are substances whose shape can change to a new conformation in response to external (environmental) modifications (UV, visible, or near-infrared light) [40, 106]. When these nanocarriers are exposed to light (of specific wavelengths), its conformational change allows the releasing of therapeutic cancer drugs in tumor cells [106, 153]. Furthermore, nanocarriers with metal particles can produce heat to damage cancer tissues due to light absorption [40]. To overcome the UV absorption from the skin, some polymeric materials (more sensitive to UV or NIR lights) are the main components of these nanocarriers [4].

- **Ultrasound—responsive**

Ultrasound-responsive drug delivery systems (also called URDDS) have three mechanisms of action in nanocarriers (thermally controlled, cavitation controlled, and radiation controlled) [40, 93]. Ultrasound nanocarriers drug delivery is controlled by waves at frequencies of 20 kHz, and their drug delivery capability is based on the energy absorption from an external ultrasound source [106]. Thermal sensitive liposomes are the most investigated nanocarriers from the thermally controlled ultrasound-responsive [93, 106]. This mechanism allows drug delivery at hyperthermia (39–41 °C) tissues [93]. Equally important, cavitation-controlled mechanism creates cavitation in cancer tissues which undermine nanocarriers' structure and allows them to enhance the delivery of therapeutic drugs. Also, ultrasound sources can adjust the permeability of cancer cells, helping in the distribution of drugs through unhealthy tissues [4, 93]. Finally, radiation controlled nanocarriers get their force due to the ultrasound transfer momentum waves (the higher the energy rate applied, the lower the speed of the ultrasound wave to the tissues) [93].

- **Electric field—responsive**

These nanocarriers are sensitive to electric fields [40]. Therapeutic drugs are released gradually thanks to an external low electric field source which produces an electrochemical redox reaction [109]. Electric conductive polymers such as polypyrrole (PPy) are generally used for this purpose [40].

2.3.3 Nanocarriers in Cancer Treatment

- **Liposomes**

They are self-assembly (colloids) vesicles with a spherical shape and structurally composed with a water nucleus, a hydrophilic core (diameter between 20 and

1 μm [65], and a hydrophobic phospholipid bilayer which made it possible to involve hydrophilic and hydrophobic anti-cancer drugs in one molecule [32, 47]. Liposomes were the first nanocarrier approved by the FDA in 1995, and currently they are the most widely studied nanocarrier with applications in clinical trials [141, 163]. The therapeutic drug release with liposomes mostly follows the EPR mechanism [141], also their drug delivery has been triggered via pH-responsive, enzyme-responsive, photo-responsive, thermo-response, and ultrasound-responsive [71, 124].

- **Carbon nanotubes (CNTs)**

They are a carbon allotrope (fullere) in a cylinder (tube rolled) from graphene layers [40, 65]. CNTs are assembled by rolling up graphene sheets into a hollow tube-like formation and have exterior diameters between 0.2 and 2 nm (single-walled carbon nanotubes) or 2–100 nm (single graphene sheet or multi-walled carbon nanotubes) and 1–100 nm in length [24, 154]. CNTs mode of action is based on their interaction with immune cells which help them to contain cancer cell growth [32]. CNTs have mostly been used with thermo-responsive and magnetic field-responsive [47]. The main disadvantage of CNTs is their toxicity due to their insolubility in water or any other biological fluid [124].

- **Dendrimers**

Dendrimers are hyperbranched polymeric macromolecules with spherical shapes or diameters in the range 1–15 nm [32]. This material shows distinctive physicochemical and biological characteristics such as size, cytotoxicity, biological distribution, water solubility, alkalinity, polarity, and hydrogen bond capacity which can be modified by changing radicals from its surface [47, 49]. In fact, anti-cancer therapeutic drugs are attached to the outer surface by electrostatic interactions and the drug delivery process is regulated by the chemical nature of these bonds [47, 163]. Moreover, dendrimers are very efficient in killing cancer cells because they can attach DNA to their outer surface [47].

- **Micelles**

Micelles are polymer molecules (<100 nm size [154]) which have hydrophilic and hydrophobic characteristics (amphiphilic molecules) and present self-assembly properties in different solvents [40]. These nanocarriers can catch hydrophobic anti-cancer drugs in their core (covalent bond) [47]. When the hydrophilic solvent concentration surpasses the critical micelle concentration (minimum concentration of surfactant in a bulk phase above which micelles start their formation [102], it is also known as CMC), hydrophobic sections are conducted away from the solvent, meanwhile, polar sections are oriented in direction of the solvent [40]. Furthermore, when micelles are exposed to hydrophobic solvents, micelles' structure undergoes a repositioning in which hydrophobic sections are the new core and hydrophobic sections are the halo [40]. After the crossing of CMC, micelles release water insoluble therapeutic anti-cancer drugs [40, 154]. The most used stimuli for drug release used with

this nanocarrier are thermos-responsive, pH-responsive, ultrasound-responsive, and redox responsive [40].

- **Quantum dots (QDs)**

They are nano scale semiconductors (sizes between 2 and 10 nm) mostly composed of graphene with high physical stability, and light sensibility (broad absorption and emission capabilities) [32, 47, 163]. The structural modifications of QDs allow their combination with biomolecules (peptides, folate, and antibodies) which later are delivered at cancer tissues via EPR effects [48, 163]. QDs are synthesized by a precipitation of metal solutions (Hg, Zn, Si, In, Ag, Pb) into metal hydroxides (Fe, Te, S, Se) [163]. The application of QDs is used to visualize cancer tumors while releasing anti-cancer drugs at this site [40, 125]. These nanoparticles are made up of two main sections, the core (a semiconductor, e.g., Fe_2O_3) which is surrounded by another semiconductor of different material (e.g., SiO_2 [40]). QDs release therapeutic anti-cancer drugs by the pH-responsive mechanism and photo-responsive mechanism [40, 154].

- **Super paramagnetic iron oxide nanoparticles (SPIONs)**

SPIONs (sizes between 10 and 100 nm) are composed of iron oxide (maghemite and magnetite) nanocarriers and in some cases their structure includes transition metals such as Cu, Co, or Ni [40, 154]. SPIONs have excellent magnetic sensitivity, and they are mainly used in MRI [40]. These nanoparticles have an effect called superparamagnetism (a magnetism pattern which appears in small ferromagnetic nanoparticles and can be modified by the influence of temperature) [85]. This effect helps the stable distribution of anti-cancer drugs in unhealthy tissues [154]. The most used stimulus for SPIONs nanocarriers is magnetic field response [40, 154].

- **Gold nanoparticles (AuNPs)**

AuNPs are colloidal nanoparticles (sizes between 3 and 50 nm) which have an Au core and a modifiable outer surface (anti-cancer drugs are attached into this surface) [40, 163]. These nanocarriers show EPR effect and ligand—receptor interaction to target cancer cells [48]. For active targeting, AuNPs couple with anti-cancer drugs which are released in cancer tissues. Meanwhile, in passive targeting, there is a gathering of AuNPs in the cancer tissue surroundings which helps in enhancing the EPR effect [48, 163]. Moreover, AuNPs presents an ultrasound-responsive stimulus in anti-cancer drug and gene delivery [48].

- **Mesoporous Silica Nanoparticles (MSNs)**

Silicon dioxide (silica, SiO_2) is an inorganic nanoparticle (sizes between 2 and 50 nm) with a honeycomb structure that allows the housing of large amounts of anti-cancer drugs within its pores [24, 40]. MSNs nanoparticles show high surface and pore volume, excellent chemical and thermal stability, and present hydrophilic and lipophilic characteristics which make them more versatile for hosting anticancer

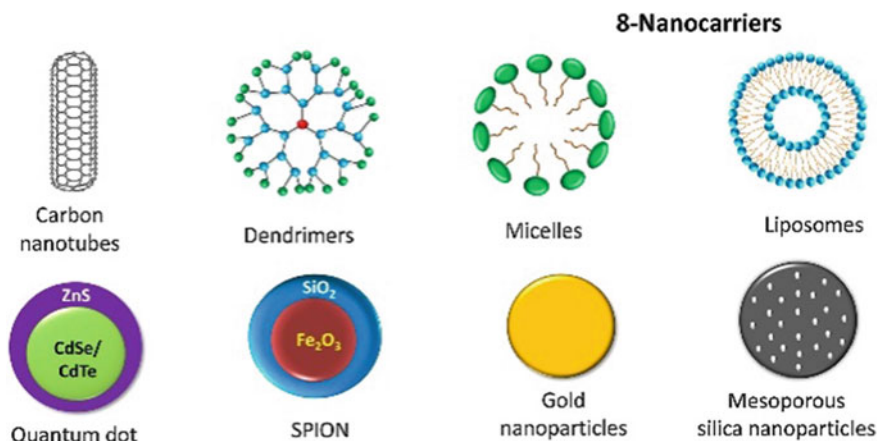


Fig. 2.5 Nanocarriers used as drug delivery system. Reproduced from Hossen S, Hossain MK, Basher MK, Mia MNH, Rahman MT, Uddin MJ. Smart nanocarrier-based drug delivery systems for cancer therapy and toxicity studies: A review. *J Adv Res* 2019; 15:1–18. Copyright © 2019 Elsevier. All rights reserved

drugs [24]. Passive targeting is the most common mechanism in drug delivering for MSNs [24], and responds to all drug delivery stimuli described in previous sections (the best results have been obtained with ultrasound-responsive stimuli) [40, 158].

Figure 2.5 shows the reviewed nanocarriers from this section.

2.3.4 Challenges

The use of nanocarriers for cancer treatment in patients began in the 1990s [106]. Since then, nanocarriers have offered an extra tool in the fight against this disease and showed dramatic improvements in preclinical stage because of their attribute to control location and timing of anti-cancer drugs delivery [75]. Additionally, nanocarriers have the capability to bond and deliver anti-cancer drugs, or antibacterial agents which can prevent tumor growth, repair not healthy tissues [158]. The main challenges that researchers must solve in the coming years are based on the degradation and assimilation of these nanocarriers inside the body, the insufficient biocompatibility that nanocarriers present with certain tumors, and the few numbers of studies about toxicity and/or secondary effects that nanocarriers can cause in the body [106]. Moreover, nanoparticle synthesis processes are required to balance the relationship between structure, biological activity, scaled to an industrial level, and therapeutic effectiveness [106].

2.4 Drug Delivery

Over the centuries, we have seen many discoveries happen in biomedical areas with the help of nanotechnology. Nanotechnology in biomedical applications, especially in drug delivery system (DDS) has immense attraction to the researchers and scientists for the new inventions. Researchers believe that these nanoparticles can be used for the betterment of the drug delivery system which can provide better efficacy with minimal side effects. Because simple but effective design methods for self-assembling nanostructures with unique benefits and tremendous promise for improving therapeutic targeting and lowering medication toxicity are provided by DNA nanotechnology.

One of the most promising areas of healthcare is drug delivery systems (DDS), which is a constantly developing area of medical science. Although there has been significant advancement in the field of DDS, formulation scientists still face a significant difficulty in creating a suitable carrier that is effective for drug delivery to the body with the best benefit to risk ratio possible [10]. Drugs that are chemical or biomolecular (such as iRNA or antibodies) have inherent problems with maximizing their therapeutic effects. The latter is subject to enzymatic breakdown and challenging to permeate the cell membrane, whilst the former frequently has low solubility and likely to generate undesirable side effects and toxicity issues, hence, development of active and targeted medication delivery devices is required to get over these barriers [41].

2.4.1 Drug Delivery Systems Employ Nanoparticles

The various biopolymeric polymers used in medication delivery systems are diverse, such as, Chitosan, Alginate, Cellulose, Xanthan gum, Liposomes, Polymeric micelles, Dendrimers, Inorganic nanoparticles, Nanocrystals, Metallic nanoparticles, Quantum dots, Protein and Polysaccharide nanoparticles are being utilized in drug delivery system [101]. However, natural substances have also been used to create nanoparticles, for instance, it has been reported that numerous microorganisms, including bacteria, fungi, algae, yeast, and so on, or plant extracts, can be used to create metallic, metal oxide, and sulfides nanoparticles [101].

2.4.2 Recent Utilization of Nanotechnology in DDS

Nanotechnology is being used for different types of DDS, to utilize the maximum efficacy of the drug and to shrink the overall side effects, so that the toxic materials of drug would not detriment the other vital organs in the body. Following that, some nanomedicines are being used for the targeted delivery in various diseases, such as, renal diseases, IVDD, Central Nervous System Disorders (CNS), COVID-19 and so on.

2.4.3 Developments in Renal Medication Delivery Systems Based on Nanotechnology

To successfully transport pharmaceuticals to the kidney, substantial research has been done on the properties of drug delivery systems and kidney structure [91]. Kidney is the vital organ of the body, which helps to filtrate all the toxic materials and metabolic waste product from the body. The primary route for drug elimination is renal filtration, emphasizing the significance of this organ for the developing field of nanomedicine [37]. Around 750 million people are affected with kidney disease globally, while the severity of the problem varies widely [91].

Acute kidney injury (AKI), a clinical disease that is frequently reversible, can result from acute renal damage to the kidneys caused by physical injury or nephrotoxic insults. Chronic kidney disease (CKD), which includes immune regulatory abnormalities, diabetes, hypertension, metabolic illness, and other disorders, is a progressive injury brought on by acquired or congenital diseases. Dialysis or kidney transplantation are needed to treat end-stage renal disease (ESRD), which can cause an irreversible loss of kidney function. In the US, the prevalence of CKD was 14.9% overall between 2015 and 2018 [37].

To repair kidney damage or postpone chronic harm and hence prevent end-stage renal disease, nanotechnology strives to increase the therapeutic choices available [37]. Just a few therapy alternatives exist currently to slow the development of CKD, therefore, Nano particles act as a kidney-targeted transport pathway for different medications and nucleic acids, nanomaterials are important [91]. The design of nanomedicines must consider the kidney, and NPs are promising tools for elucidating kidney functions and treating renal disorders. Nonetheless, despite being promising, those technologies still need to be developed for use in clinical settings [37].

2.4.4 Nanotechnology Used in DDS for Intervertebral Disk Disease (IVDD)

Low back pain (LBP) is mostly brought on by IVDD, a chronic degenerative disease that places a significant burden on both individuals and society [76]. LBP is currently estimated to impact 632 million people globally, is the largest cause of disability, according to recent research on public health called the Global Burden of Disease Study [117]. More than 80% of adults will experience LBP at some point, per pertinent study, therefore, 10% of LBP sufferers will experience long-term disability [76]. Even though there are numerous potential causes of low back pain, numerous studies have shown that intervertebral disc degeneration (IVDD) is the main underlying cause [117].

The IVD, which joins adjacent vertebrae and is situated between vertebrae to give flexibility and sustain pressure, is a fibrocartilage tissue [76]. The extracellular matrix (ECM), which is gradually being destroyed, changes in the IVD cell phenotype, the loss of active IVD cells, an increase in cell aging and death, and excessive inflammatory responses are all evidenced by existing research to be the main developmental factors of IVDD, aggravating the disorder and destroying normal IVD function [76].

Analgesics, non-steroidal anti-inflammatory medications (NSAIDs), and opioids make up most of the pharmacological therapy for OA or IVDD. The first effective treatment for managing minor pain is the administration of oral analgesics, such as paracetamol. The danger of adverse effects in the gastrointestinal (GI) tract and antiplatelet activity, however, prompts doctors to give NSAIDs (such as ibuprofen) at the lowest effective dose and for a short period of time while paracetamol is frequently ineffective. Furthermore, while many surgical techniques can reduce discomfort, their effectiveness is frequently insufficient in terms of stability and integration, failing to restore function [16]. Since Nano particles can combine various medications or therapeutic agents, have adjustable release and targeting capabilities, and may aid in enhancing the therapeutic effects of medications by concentrating and extending their presence in IVD tissues, nano-drug delivery systems (NDDSs) may play a significant role as part of new treatment strategies in this regard [76].

Nowadays, in situ IVD injections or systemic administration of medicines or bioactive molecules are the two most common ways to treat IVDD, although both have the drawback of having subpar treatment outcomes [76]. Drugs and materials' dimensions could be changed through nanotechnology, making it easier to manage their varied qualities. Meanwhile, numerous NDDSs have been created and introduced in the IVDD treatment sector because of the unique and spectacular advancements in nanotechnology (Fig. 2.6) [76].

2.4.5 Blood–Brain Barrier Penetration by Nanoparticles: A Path to Novel Therapeutic Strategies for Disorders of the Central Nervous System

Researchers must devote a lot of attention to studying central nervous system (CNS) illnesses, particularly neurodegenerative disorders, because they pose a serious threat to public health [24]. One of the two most prevalent neurodegenerative disorders is Alzheimer's disease, followed by Parkinson's disease [115]. The most prevalent kind of dementia among seniors is Alzheimer's disease (AD).

The blood–brain barrier (BBB) and blood-cerebrospinal fluid barrier (BSCFB), which protect the central nervous system (CNS) from harmful substances, present the biggest obstacles to getting drugs into the CNS for the treatment of CNS complications like Alzheimer's disease, Parkinson's disease, Huntington's disease, stroke,

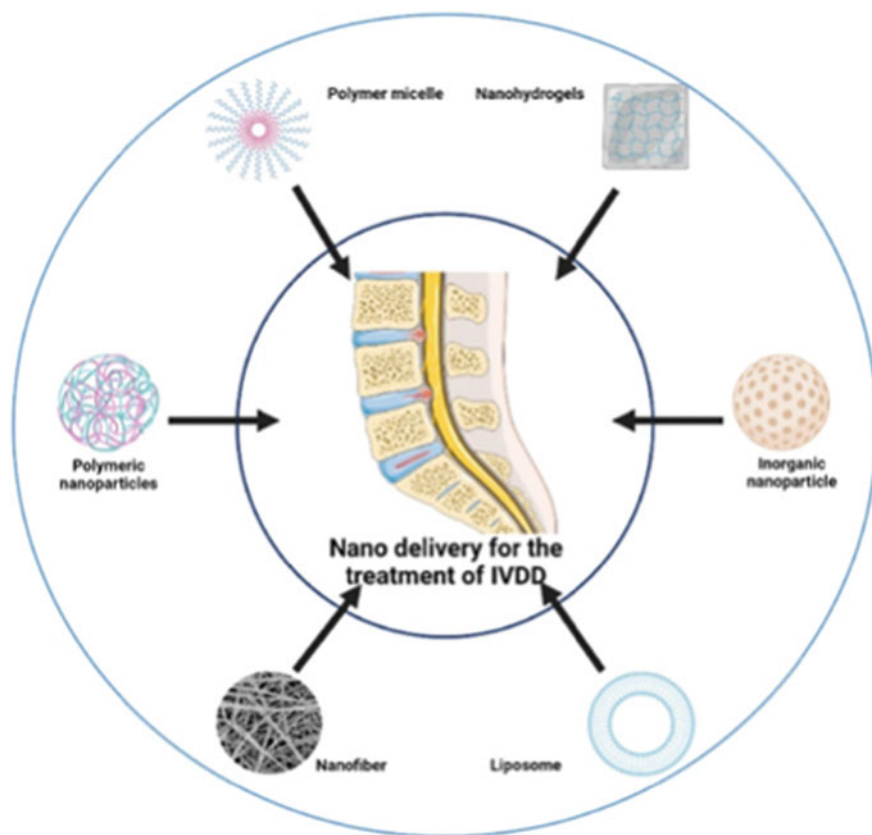


Fig. 2.6 Techniques frequently used for delivering nano-drugs to treat IVDD. Reprinted with permission of Liu et al. [76]

epilepsy, brain tumors, multiple sclerosis (MS), encephalitis, etc. [136]. The primary phase of treating neurological illnesses is drug diffusion through the blood–brain barrier (BBB) [115]. Consequently, the development of nanotechnology in targeted drug delivery is being aided by the demand for novel therapeutic strategies for CNS illnesses and the restrictions brought on by the BBB barrier [136].

The blood-brain-barrier (BBB) can be circumvented and drug distribution to the CNS made easier using nanoparticles (NPs) and polymer coatings [115]. Several promising nanocarriers are employed to target the brain in Alzheimer’s illness, such as, polymeric nanoparticles, liposomes, solid lipid nanoparticles, dendrimers, nano emulsions, cyclodextrins, silica nanoparticles, magnetic nanoparticles, gold nanoparticles, quantum dots [103], nanogels and carbon nanotubes etc. [115]. The surface of NPs can be easily modified to facilitate drug targeting, and they can encapsulate pharmaceuticals with a reasonably high drug loading. Also, because of its physiological qualities of reactivity, strength, surface area, sensitivity, solubility, and stability,

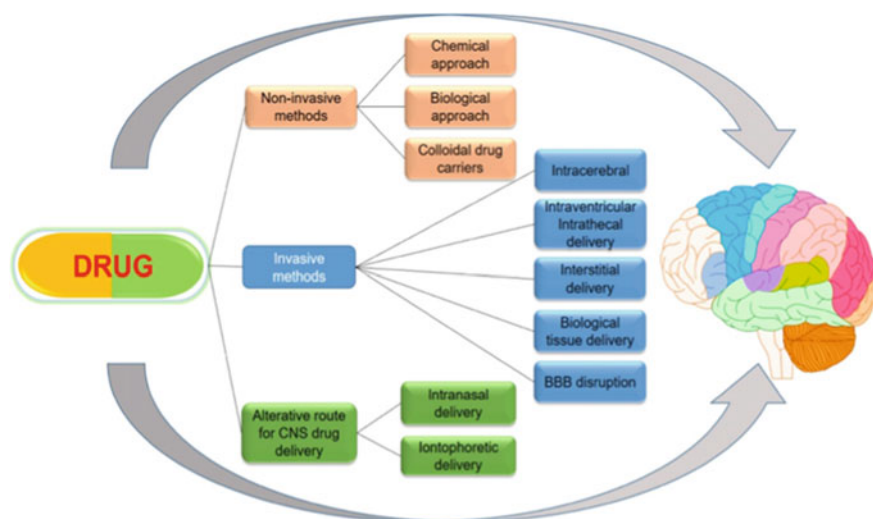


Fig. 2.7 Current approaches to CNS medication delivery are shown schematically. Reprinted with permission of Nguyen et al. [99]

nanomedicine may easily penetrate the blood–brain barrier (BBB), which is the main barrier to CNS therapy and the administration of therapeutic drugs into the CNS [99].

A nanomaterial-based BBB can be delivered to the brain in three different ways: non-invasively, invasively, or by using alternate drug delivery methods (Fig. 2.7); among them the non-invasive techniques are widely utilized and based on cellular mechanisms that help medications breach the blood–brain barrier through transcellular pathways [99].

The Food and Drug Administration (FDA) recently approved a number of nano-based medication delivery systems to prevent a variety of disorders [103]. Only five medications, tacrine, donepezil, rivastigmine, galantamine, and memantine, is officially approved by the FDA to treat Alzheimer’s disease (AD) and these medications work by modulating cholinergic levels, amyloid aggregates, and tau protein, which may help to prevent or delay the onset of Alzheimer’s disease or slow its progression [99].

The rational approach and continued design of nanomaterials based on in-depth and thorough knowledge of biological processes are essential for realizing the therapeutic potential of nanomedicine [114]. However, there have only been a few studies on these nanomaterials’ pharmacodynamics and pharmacokinetics, and additional research is needed to understand their potential negative effects.

2.4.6 Nanotechnology's Role in the Creation of Vaccines for COVID-19 Prevention

Since viruses and nanoparticles (NPs) operate at the same scale, developing vaccines and performing immunoengineering rely heavily on this strategy [152]. In comparison with conventional drug carriers, nanoparticles (NPs) have noteworthy distinct advantages, such as customized drug release profiles, increased surface areas, protection from degradation of the cargo, and altered drug pharmacokinetics [58]. Two mRNA-based vaccines created with lipid nanoparticles (LNPs) have received emergency use authorizations (EUAs) from the US FDA against the COVID-19 for the first time in history [58]. Due to their excellent efficacy and safety, lipid nanoparticles (LNPs) were discovered to be the most successful drug delivery technique [67]. Nanotech has accelerated the development of mRNA-based COVID-19 vaccines from Pfizer, Moderna and BioNTech [58]. The historical FDA clearance of the LNP encapsulated mRNA vaccines for COVID-19 has advanced the development of drug delivery technology, paving the way for the future creation of a wide range of mRNA-based therapeutics [67]. The present, when SARS-CoV-2 is a serious threat globally, is crucial from the standpoint of vaccine technology development, and nanotechnology and nanomedicine are offered as novel therapeutic technologies and approaches that can have a clinical impact.

2.5 Nanomaterials in Diagnosis

Nanomaterials are defined as particles with physical, chemical, or biological properties that fall within the nanoscale range of 1–100 nm [68]. They can be categorized as either organic or inorganic, with examples including nanofibers, nanotubes, liposomes, polymer nanoparticles, elementary substances, alloys, silica, and quantum dots [64]. Nanomaterials possess physical, chemical, optical, and electronic properties that are dependent on their size, shape, and composition. These properties can be engineered, making them a promising tool for disease diagnosis, treatment, monitoring, and management [94]. Due to the similarity in size between nanomaterials and biological molecules and structures, nanomaterials are valuable tools for biomedical research and applications, both *in vitro* and *in vivo* [19]. They are also biocompatible, biodegradable, and can accumulate in human organs with minimal side effects [107]. Additionally, nanomaterials exhibit slow-release properties, which can mitigate toxic side effects on health and environment [68].

2.5.1 Why Nanomaterials Are Important in Medical Diagnosis?

There are different ways to diagnose medical conditions, including bioassays, biosensors, and imaging. However, these methods often have limitations such as low sensitivity, specificity, and reproducibility. To improve patient outcomes, diagnostic techniques need to be more sensitive and able to detect diseases at an early stage. Conventional diagnostic methods may not be able to identify certain diseases, such as Alzheimer's and some cancers, early enough for effective treatment. Fortunately, nanotechnology has the potential to revolutionize medical diagnosis, just as it has transformed electronics and other fields.

Nanomaterials have unique properties that make them well-suited for use in medical diagnosis. The use of nanomaterials as therapeutic and diagnostic tools presents numerous advantages, including their design flexibility, small size, large surface-to-volume ratio, and ease of surface modification with multivalent ligands to enhance their affinity for target molecules. If nanomaterials can interact with specific biological components, they can be harnessed to leverage the benefits of personalized medicine techniques [159]. Also, Specific biological components can be targeted by engineering nanomaterials to interact with them [96].

2.5.2 Overview of Nanoparticle-Based Diagnostic Tools

The field of medical diagnosis has been transformed by emerging modalities like biochips, microarrays, nano barcodes, micro-electromechanical systems (MEMS), lab-on-chip, and nano biosensors. Nanoscale materials and techniques are utilized to diagnose a range of diseases including cancer, cardiovascular disease, diabetes, infectious disease, musculoskeletal disorders, and neurodegenerative diseases. Among these, enzyme nano biosensors, especially nano biosensors, are highly sensitive, reliable, robust, reproducible, and cost-effective diagnostic tools that can effectively meet the healthcare needs.

Silica and magnetic nanoparticles, quantum dots, microbubbles etc. are among the most popular types of nanomaterials. They have been utilized to identify and examine small molecules such as H_2O_2 , circulating tumor cells (CTCs), cancerous tissues etc., among other applications [94].

The design and function of point-of-care (PoC) diagnostics that incorporate nanomaterials depend heavily on their composition, size, and shape. Therefore, it is crucial to consider these factors when designing and utilizing nanomaterial based PoC diagnostics [108]. In nanoparticle-based assays, the binding of a nanoparticle label or probe to the target biomolecule is the primary event that produces a measurable signal characteristic of the target biomolecule. Various probes, such as nano shells, metal nanoparticles, and quantum dots (QDs), have been utilized for this purpose. QDs are the most used and promising nanostructures for diagnostic applications

due to their strong light absorbance and ability to serve as fluorescent labels for biomolecules. QDs, semiconductor nanocrystals with high photostability, single-wavelength excitation, and size-tunable emission, show great potential for use in diagnostics [2].

Lateral flow assays (LFAs) are simple tests that use antibodies labeled with nanoparticles, fluorescent dyes, or phosphor as signaling agents. Gold nanoparticles are used mostly in LFAs due to their characteristic red color. LFAs use paper-based porous membranes to allow samples and reagents to flow to the test line very fast, generating results in close to 15 min. They can be read easily and require no costly equipment. LFA devices are highly stable and can be kept at room temperature for close to 2 years, making them suitable for use in resource-limited and developing countries [130] (Fig. 2.8).

Overall, nanoparticle-based diagnostic tools offer a range of benefits over traditional diagnostic methods, including increased sensitivity, specificity, and early disease detection. As the technology continues to advance, it is likely that nanoparticle-based diagnostic tools will play a major role in the diagnosis and treatment of a variety of diseases.

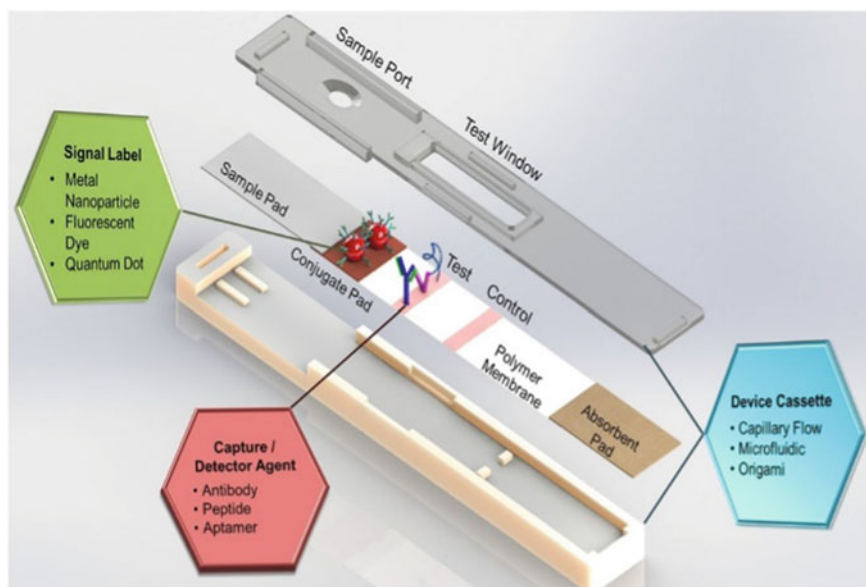


Fig. 2.8 Liquid Flow Assay working mechanism. Reproduced from Jun Hui S, Hsi-Min C, Jackie Y, Strategies for developing sensitive and specific nanoparticle-based lateral flow assays as point-of-care diagnostic device. *Nanotoday* 2020; 30:1–17. Copyright © 2020 Elsevier. All rights reserved

2.5.3 *Nanomaterials for Biosensing*

Based on the International Union of Pure and Applied Chemistry (IUPAC), a biosensor is a device that “utilizes isolated enzymes, immune systems, tissues, organelles, or whole cells to detect chemical compounds through specific biochemical reactions, often producing electrical, thermal, or optical signals [89]”. This definition highlights the key elements of a biosensor. Biosensors consist of three critical components [105]:

- i. A receptor that selectively binds to an analyte.
- ii. A transducer that produces a signal upon binding.
- iii. A detection system that measures and converts the signal into useful information.

These detection methods may be electrochemical, optical, or piezoelectric in nature. Nanoparticle-based biosensors are a rapidly growing field that offer a range of benefits in the detection and diagnosis of diseases. The development of nanotechnology has led to the creation of faster, cheaper, more sensitive, and accurate medical diagnostic assays and devices. Biosensors incorporating nanomaterials combine multiple fields, such as chemistry, molecular engineering, material science, and biotechnology [105]. In fact, some biosensors can detect as little as one parasite per microliter of blood [23]. The integration of nanotechnology with biosensing enables the identification of disease biomarkers at extremely low concentrations, allowing for the screening of diseases at very early stages. This can improve medical follow-up procedures and routine prognosis to monitor patient diagnosis. Figure 2.9 displays a diagram of inorganic nanoparticles working alongside various types of biomarkers and a linear process representing each stage of biosensing from analyte recognition through transduction, culminating in a measurable signal that is analyzed and displayed.

Additionally, the merging of nanotechnology with biosensing is crucial for point-of-care (POC) diagnosis in countries lacking advanced medical facilities [105].

Nanomaterials have proven to be a valuable tool in the field of medical diagnosis. They have the potential to revolutionize the way that diseases are detected and treated, allowing for earlier diagnosis and more effective treatments. As research in this field continues to advance, it is likely that we will see even more exciting developments in the use of nanomaterials in diagnosis in the future.

2.6 *Nanotechnology in Biomedical Imaging*

In 1896, Wilhelm Roentgen acquired the first X-Ray image of his wife’s hand which marked a new beginning in the history of bioimaging. Since then, several non-invasive imaging techniques were developed for biomedical applications which include, but are not limited to, clinical diagnosis and research in cellular biology and drug discovery. Thanks to the advancements in imaging technology, the structural and functional biological processes of biomolecules, cells, tissues, organs, and

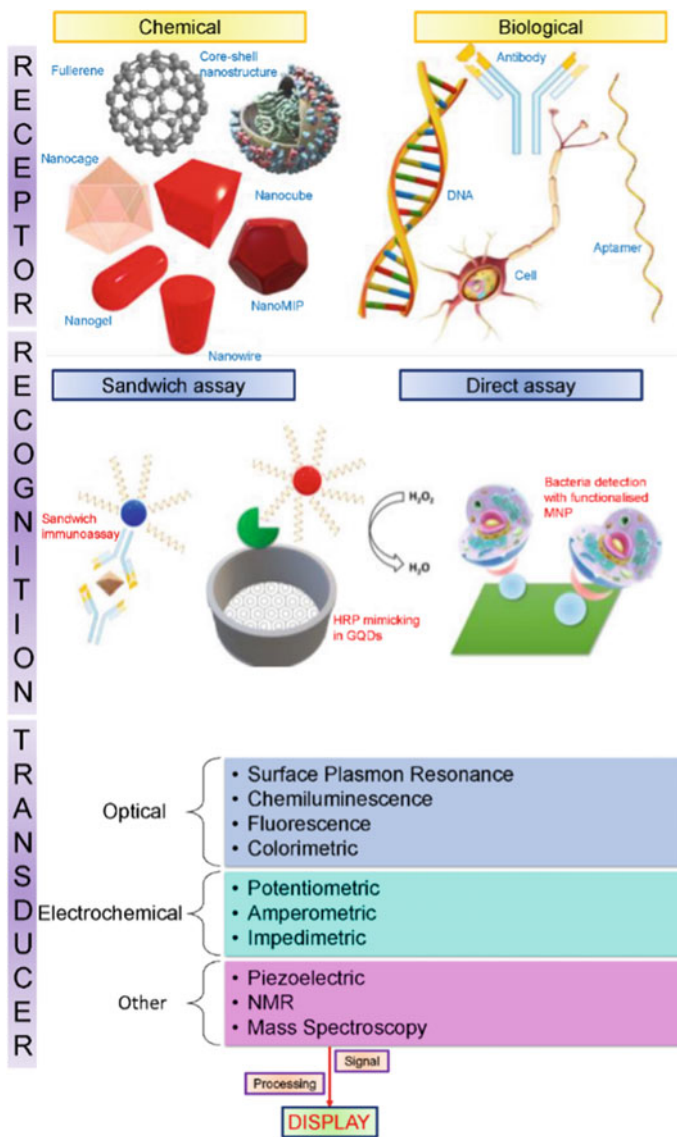


Fig. 2.9 Roles of different nanomaterials in biosensing. Reproduced from Muqsit P, Zeynep A. Nanomaterials for Healthcare Biosensing Applications. Sensors (Basel) 2019; 19(23):1–56. Licensed under CC BY

even complete live organisms are well understood [123]. Nanomaterials, due to their different targeting strategies, play a significant role in biomedical imaging and detection including passive and active targeting, which were discussed in the introduction section of this chapter. In this section, we will explore the most recent applications of nanotechnology in bio imaging.

2.6.1 *Imaging Modalities—Nanoparticle Applications*

In medical field, nanoparticles are currently used in several non-invasive modalities like Fluorescence Imaging, Magnetic Resonance Imaging (MRI), Computed Tomography (CT), Positron Emission Tomography (PET) and Single Photon Emission Computed Tomography (SPECT). Recent advancements of nanoparticle application in the above-mentioned imaging modalities are discussed below.

2.6.2 *Fluorescence Imaging*

Researchers tend to accept optical bioimaging, which mostly refers to a fluorescent bioimaging method, more readily than biochemical assessment techniques like western blotting, flow cytometry, and immunohistochemistry. This is vastly due to the fluorescence imaging results' simplicity, speed, and ease of interpretation. Fluorescence imaging utilizes visible light or Near Infrared sources to obtain high resolution images for disease diagnosis. Nonetheless, while being employed for a very long period in immunoassays, diagnostic imaging, and the analysis of biomarkers, fluorescence has several drawbacks, which include limited wavelength range, photobleaching, and self-quenching [22]. For this purpose, *fluorescent nanoparticles* are widely studied and applied, as their multiple fluorophore properties can overcome the above-mentioned limitations and provide increased photoluminescent emission. Fluorescence imaging using L1013 NPs successfully localized tumor pathology with a 'tumor to regular tissue ratio of 11.7 ± 1.3 '. These organic NPs were able to clearly visualize real time mouse vessels and hindlimbs with a 'high fluorescence quantum yield of 9.9%' [149]. A novel study on monosaccharides imprinted FITC doped Silica NPs, HepG2 cells displayed strong fluorescence revealing the shapes of the cells clearly. These imprinted NPs attach to the exposed terminal Mannose of Glycan conjugates in cancer cells [144]. NPs delivery makes it feasible to treat inflammatory illnesses with glucocorticoids, but their administration must be managed and monitored to reduce unfavorable side effects.

Poor stability of organic fluorescent dyes is a hindrance for long-term imaging. Lead Sulfide (PbS) Quantum dots used for in vivo NIR fluorescence imaging of cerebral venous thrombosis in septic mice revealed that the number of thrombi increased by administration of lipopolysaccharide (LPS) [43]. This shows the potential of quantum dots in studying the pathological state of cerebral blood vessels. Recently,

bifunctional graphene quantum dots doped with Nitrogen and Boron were shown to be excellent NIR-II imaging fluorescent agents. Additionally, these quantum dots were able to effectively convert absorbed NIR light into heat which was shown to successfully destroy tumor cells in glioma xenograft mouse model, demonstrating their photothermal therapeutic effect [77]. CuInSe₂/ZnS core/shell quantum dots, a novel and versatile imaging probe conjugated with CGKRRK (cys-Gly-Lys-Arg-Lys) tumor-targeting peptide showed minimal toxicity and successfully targeted the tumor boundaries [77]. Photosensitizer (chlorine e6, Ce6) modified carbon dots (CDs-Ce₆) and Cu²⁺ also act as excellent fluorescence imaging agents which can be adopted for trimodal synergistic cancer treatment by photothermal therapy (PTT) [131]. Excitation-dependent emission, high fluorescence quantum yields, photostability, and a lengthy photoluminescence decay lifespan are all characteristics of carbon quantum dots (CDs). Hence, they are perfect for use in imaging modalities.

Spherical nucleic acid Au NPs with densely packed oligonucleotides have high stability, high intracellular delivery efficiency and high signal-to-background ratio for mRNA detection using fluorescence imaging [127]. Also, self-assembled DNA nanostructures have shown considerable promise in recent years for producing nanoscale probes and labels for high-performance bioimaging. These nanoscale structures have highly programmable shape, nanometer addressability, and structural responsiveness [70].

2.6.3 *Magnetic Resonance Imaging*

Magnetic Resonance Imaging is a very strong imaging technique used currently in medical diagnosis which uses a human anatomy's natural magnetic properties to produce images in the presence of an external magnetic field excited by a radio frequency pulse. Contrast agents are used in MRI which are crucial in improving the image. A desired contrast agent is one which can be injected and removed from the body without causing any negative side effects. However, many of the contrast agents used today show adverse effects like physiologic responses, nephrotoxicity, allergic reactions, and gadolinium accumulation [38]. Recent developments in NPs (Nanoparticles) demonstrate their promise for use as an MRI contrast agent and reduce many of the negative effects.

One of the most common positive MRI contrasts is Gadolinium (Gd). Gadolinium chelates in the form of Gd (III) complexes are used because of the toxicity of free Gd ions. Atherosclerotic plaque can be localized in the artery wall by a nanoparticle synthesized from high density lipoprotein (HDL) coupled with Gd³⁺ chelates [112]. More recently, Paramagnetic MXene-Gd flakes with high thermal stability and cytostability were prepared which were demonstrated to be excellent T1 contrast agents. Gd³⁺ ions were entrapped in MXene-diethylenetriaminepentaacetic acid (DTPA) flakes to provide paramagnetic properties to the M-Xene flakes. Schematic representation of MXene flake functionalization with DTPA and subsequent chelation with Gd³⁺ ions is shown in Fig. 2.10. Surface modifications of MXene flakes

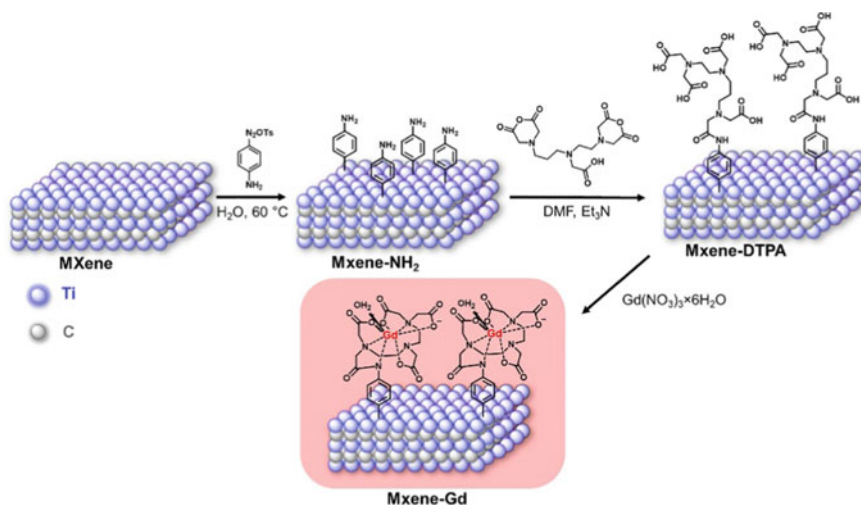


Fig. 2.10 Schematic representation of MXene flake functionalization with DTPA and subsequent chelation with Gd³⁺ ions. Neubertova V, Guselnikova O, Yamauchi Y, Olshtrem A, Rimpelova S, Čizmar E, Orendáč M, Duchon J, Volfova L, Lancok J et al. Covalent functionalization of Ti₃C₂T MXene flakes with GD-DTPA complex for stable and biocompatible MRI contrast agent. *Chemical Engineering Journal*. 2022; 446(2):136,939. Copyright © 2022 Elsevier Masson SAS. All rights reserved

with the help of DTPA-Gd complex inhibits the agglomeration of flakes and prevents surface oxidation while stored in blood plasma [98]. Polymeric nanoparticles prepared from mixing of poly (vinylphosphonic acid) based double-hydrophilic block copolymers with Gd ions measured high magnetic relaxivities for both in-vitro and in-vivo magnetic resonance imaging on rats. Moreover, these polymeric assemblies are highly stable to dilution and PH demonstrating their ability as potential MRI contrast agents [86].

In a study on FeraTrack Direct, a Super Paramagnetic Iron Oxide Nanoparticle (SPION), was used to label stem cells. From MRI observations it was very effective in tracking the stem cells of mice with glioma tumor [62]. Size of the SPION nanoparticles play a major role in MRI imaging and hyperthermia performance. Lactobionic acid (LA) and polyethylene glycol (PEG) modified SPION were prepared by Xia and team [150]. with a controlled particle size and dispersion. This enhanced the fluorescent labelling of HepG2 cells and can be suggested as a potential MRI contrast agents for in-vivo imaging. In a different study, GE11 peptide modified CSO-SPION showed no obvious micellar cytotoxicity with a high EGFR (Epidermal Growth Factor Receptor) expression. These modified SPION improved MRI imaging for Hepatic Carcinoma detection. Besides Gd and Fe based contrast agents, Carbon in the form of C¹³, nanodiamonds and nanotubes and graphene are promising for MRI imaging [79].

2.6.4 Computed Tomography

Computed Tomography uses an X-ray source and detector to form images with high spatial and temporal resolution. Despite the higher levels of ionizing radiation exposure, CT has quickly replaced plain-film radiography due to its quicker examination speed, lower cost, increased efficiency, and superior spatial resolution for clinical imaging [34]. A major drawback for CT imaging is its lack of sensitivity to contrast agents compared to other imaging modalities. Moreover, NP based contrast agents have to overcome potential issues like renal toxicity, non-specific blood pool distribution and anaphylaxis [34]. There are few promising NP contrast agents explored and reported in the literature.

Gold nanoparticles, attributing to their unique X-ray attenuation characteristics and simple surface modification, are one of the widely studied metal contrast agents for CT. Gold nanoparticles are functionalized using polymers to produce an effective contrast agent. A novel Polyethylene Glycol (PEG) functionalized Au particles with star shape (AuNS@PEG) based study demonstrated excellent in-vivo CT imaging behavior owing to their properties of ultrasmall sizes, effective metabolisability, high computed tomography value and biocompatibility [134]. Dendrimer-entrapped gold nanoparticles (DE-Au-NP) decorated with specific ligands for cancer cells can provide bifunctional properties. DE-Au-NP can serve as contrast agents for in-vivo CT imaging while the ligand attached could deliver plasmids for cancer therapy [54]. In another study, it was demonstrated that the PEG-MoS₂ nanosheets and Ce6 in the PEG-MoS₂-Au-Ce6 nanocomposites can be successfully used for dual-modal imaging of Computed Tomography and Near Infrared Fluorescence Imaging respectively. This assists greatly in cancer diagnosis and therapy [74]. Morphological properties of the NPs also show a significant effect on CT imaging contrast. Comparing porous Au NPs to solid Au NPs in computed tomography scans revealed substantially more contrast in a study conducted recently [5].

Iodinated contrast dangers have been reduced by using iodine-based liposomal nanotechnology. Long used in biomedical applications as a vector, liposomes use a lipid bilayer at the nanoscale scale. Iodine based polymer NP contrast agents have longer blood life (40 h) that provides better tumor intake and renal clearance in comparison to Au NPs. As they have organic structures, biodegradation becomes easier which further enhances the renal clearance abilities. Iodine containing diatrizoic acid (DTA) and perfluoropentane (PFP) conjugated with glycol chitosan (GC) nanoparticles (GC-DTA-PFP NPs) successfully accumulated on the tumor cells by enhanced permeation and retention (HER) effects and demonstrated strong X-ray CT imaging signals [14]. Apart from Iodine and Au, Bismuth in the form of Bi-diethylene triamine pentaacetate acid (DTPA) complex and hydrophobic Bi₂O₃ NPs were used for high performance CT imaging [72, 127] (Fig. 2.11).

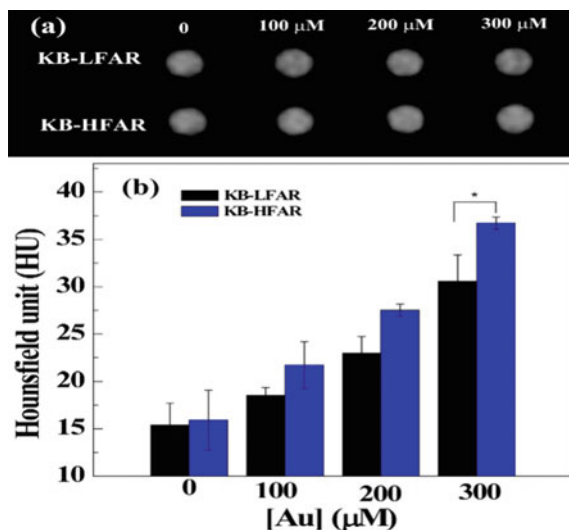


Fig. 2.11 In vitro CT images (a) and values (b) of KB-LFAR and KB-HFAR cells treated with the FA-Au PENPs at different Au concentrations (0–300 μM) for 3 h, respectively. Zhou B, Yang J, Peng C, Zhu J, Tang Y, Zhu X, Shen M, Zhang G, Shi X. Pegylated polyethylenimine-entrapped gold nanoparticles modified with folic acid for targeted tumor ct imaging. *Colloids and Surfaces B: Biointerfaces*. 2016; 140:489–496. Copyright © 2016 Elsevier Masson SAS. All rights reserved

2.6.5 Positron Emission Tomography (PET)/Single Photon Emission Computerized Tomography (SPECT)

PET is a dynamic nuclear medicine imaging technique that uses radiotracers to obtain images with high sensitivity and real time analysis. Using physiological substrates labeled with positron-emitting radionuclides, these tracers can offer information on a variety of biosynthetic systems non-invasively [119]. SPECT is another widely used nuclear imaging technique which uses gamma rays to evaluate biochemical anatomy changes [9]. For nanoparticle PET/SPECT imaging tracers, nuclides with a sufficiently long half-life are required. Fluorine-18, which has a half-life of 109.8 min and is frequently used in clinical practice for PET, is a radioisotope whose half-life is typically too short to be used in nanoparticles due to the time required for synthesis and cellular uptake [121]. Thus, other nanoparticle nuclides are widely studied.

In dendritic-based immunotherapy, monitoring dendritic cell (DC) movement is crucial. Gold NPs are one of the efficient PET nuclides which successfully aid visualization of dendritic cell mobility. Extremely low quantities of radioiodine-124-labeled tannic acid gold core-shell nanoparticles (124I-TA-Au@AuNPs) were used successfully to trace the dendritic cell migration in mice with the help of PET. These highly stable and sensitive NPs showed excellent DC labelling without affecting the cell biological functions [69]. Nuclide embedded nanoparticles aid in antitumor immunity property of the labelled DCs. Labelling DCs with radionuclide embedded

Au NPs enhanced the antitumor immunity of the DCs compared to their unlabeled counterparts. PET imaging revealed that the selective migration of labelled DCs to the draining lymph nodes was relatively fast (6 h) compared to the NIR fluorescent or MRI nanoparticles (12 h). A novel ¹²⁴I-labelled gold nanostar probe using PET demonstrated its superior behavior to other noninvasive imaging techniques by penetrating sub mm intracranial brain tumor detection levels [78].

Radioactive Cu NPs also form a good radiotracer imaging agent for PET due to their low toxicity and high half lifetime of 12.7 h. Radioactive [⁶⁴Cu]CuS NPs demonstrated excellent targeting ability and tumor uptake ($8.4 \pm 1.4\%$ injected dose/tissue) when combined with RGDfK peptide through PEG linkers showing its great potential in simultaneous clinical imaging, therapeutics and diagnostics [18]. Pharmacokinetically improved ⁶⁴Cu-labeled polyglucose NPs (Macrin) were prepared and tested for quantitative PET imaging macrophages in tumors [60]. A novel renal clearable Au NPs labelled with copper-64 (⁶⁴Cu) to form ⁶⁴Cu-NOTA-Au-GSH was reported by Feng Chen and co [12]. PET studies revealed the renal clearance information of both only labelled Au NPs (⁶⁴Cu-NOTA-Au-GSH) and labelled ⁶⁴Cu-NOTA-Au-GSH mixed with cold NOTA-Au-GSH. In vivo PET images at 4 h and 19 h were captured which shows that at 19 h the radioactivity reduced completely confirming the clearance of nanoparticles which is significantly fast.

Generally, SPECT requires nuclides with longer half-life time compared to PET. Thus Technetium—^{99m}Tc is the most used radionuclide for SPECT as its half lifetime is around 6 h. A combined SPECT/MRI study using ^{99m}Tc illustrated the presence of metastasis in cervical cancer patients without enlarged sentinel lymph nodes [39]. In penile cancer patients, accurate early detection by dynamic sentinel lymph node biopsy is highly important. Saad and team [113] investigated the role of SPECT/CT following 2-D planar lymphoscintigraphy (dynamic and static) and reported the improved rate of detection of true tracer-avid lymph nodes and described their precise (3-D) anatomic localization in drainage basins. In head-and-neck squamous cell carcinoma patients, ^{99m}Tc nanocolloid tracer enabled SPECT/CT can determine the risk level of contralateral nodal failure [21].

Other nanoparticles like carboxymethylcellulose-based NPs labeled with ⁶⁸Ga³⁺ [104], ¹⁸F-Macroflor modified polyglucose NPs [52], Cerium oxide NPs coated with ⁸⁹Zr [88] were also used for PET imaging. Macroflor increases PET signal simultaneously aiding enhanced macrophage monitoring for disease detection. ⁶⁸Ga³⁺ labeled carboxymethylcellulose based NPs enhances the spatial resolution for PET and SPECT.

2.6.6 Challenges

Advancements in nanotechnology explored various NPs based imaging contrast agents that can be used for a wide variety of imaging modalities. NPs conjugated with diagnosis or therapeutics can significantly improve the treatment processes like cancer therapy by continuous monitoring through in vivo images. Continuous

research in nanotechnology would have major in fields of medical imaging, however, significant efforts are required to study the limitations of NPs to reduce the side effects on humans. Cytotoxicity and biodegradability are still major obstacles for NPs clinical application. Even though *in vitro* and *in vivo* studies showed promising results for NP usage in bioimaging, there is still a huge scope for comprehensive study on NPs properties like composition, formulation, shape, surface charge, hydrodynamic diameter, solubility, stability, administration route, distribution, and metabolism to translate to commercial clinical practice [34]. Thus, future research should focus on solutions to above mentioned challenges along with the exploration of new NP based imaging contrast agents.

2.7 Conclusions

In this work, we discussed several sections of nanotechnology in biological applications including tissue engineering, biomedical imaging, drug delivery, cancer treatment, diagnosis. The application of nanotechnology in tissue engineering is growing rapidly. it can be used to create, repair, and replace cells, tissues, and organs. By combining nanoscale materials with tissue engineering, millions of patients may benefit from the resulting treatments and therapies. In this chapter, we have discussed the applications and advantages of using nanotechnology-based tissue engineering in different fields for different purposes. Although nanotechnology may bring undoubted benefits in biomedical applications, the application of manmade nanomaterials also has nonnegligible health risks. The development, testing and clinical applications of these materials must be conducted according to the precautionary principle to minimize the risk. This requires a large step forward in the biosafety, utilization, and stability of nanomaterials. We believe that the development of nanotechnologies that are rationally designed will help solve many of the current issues in tissue engineering.

The development of efficient bio-medical tools is a primary goal of the interdisciplinary field of nanotechnology, which merges biology, chemistry, engineering, and the fields of medicine and health care. Furthermore, nanotechnology is influencing many different stages of healthcare. Further research and utilization of nanoparticles in the field of health care, such as, drug delivery system (DDS) can minimize maximum chronic diseases and can provide an efficient treatment. Nanotechnology has proven to be a useful and pertinent option in the ongoing search for COVID-19 solutions which requires more attention and elucidation for future research.

Biomedical fields have seen a tremendous development in recent years due to the advancement of nanotechnology in various stages of healthcare. Understanding the properties of nanoparticles and the ability to tailor their design for specific applications has been beneficial and influential. NPs conjugated with diagnosis or therapeutics can significantly improve the treatment processes like cancer therapy by continuous monitoring through *in vivo* images. Although nanotechnology may bring

undoubted benefits in biomedical applications, the application of manmade nanomaterials also has nonnegligible health risks, thus, significant efforts are required to study the limitations of NPs to reduce the side effects on humans. Cytotoxicity and biodegradability are still major obstacles for NPs clinical application.

Nanocarriers have offered an extra tool in the fight against this disease and showed dramatic improvements in preclinical stage because of their attribute to control location and timing of anti-cancer drugs delivery. Additionally, nanocarriers have the capability to bond and deliver anti-cancer drugs, or antibacterial agents which can prevent tumor growth, repair not healthy tissues. The main challenges that researchers must solve in the coming years are based on the degradation and assimilation of these nanocarriers inside the body, the insufficient biocompatibility that nanocarriers present with certain tumors, and the few numbers of studies about toxicity and/or secondary effects that nanocarriers can cause in the body. Moreover, nanoparticle synthesis processes are required to balance the relationship between structure, biological activity, scaled to an industrial level, and therapeutic effectiveness [106].

Advancements in nanotechnology explored various NPs based imaging contrast agents that can be used for a wide variety of imaging modalities. Even though in vitro and in vivo studies showed promising results for NP usage in bioimaging, there is still a huge scope for comprehensive study on NPs properties like composition, formulation, shape, surface charge, hydrodynamic diameter, solubility, stability, administration route, distribution, and metabolism to translate to commercial clinical practice [34]. Thus, future research should focus on solutions to above mentioned challenges along with the exploration of new NP based imaging contrast agents.

Nanomaterials have also proven to be a valuable tool in the field of medicine. They have the potential to revolutionize the way that diseases are detected and treated, allowing for earlier diagnosis and more effective treatments. As research in this field continues to advance, it is likely that we will see even more exciting developments in the use of nanomaterials. Nanotechnology has proven to be a useful and pertinent option in the ongoing search for COVID-19 solutions as well [135], which requires more attention and elucidation for future research. We believe that the development of nanotechnologies that are rationally designed will help solve many of the current clinical approach limitations.

Acknowledgements The authors would like to thank Dr. Jingbo Liu and Dr. Sajid Bashir for the invitation to contribute this book chapter. The corresponding author would also like to acknowledge the contributions and revisions of all coauthors in successful completion of this chapter.

Author Contribution The contributions of the authors include the following (1) Ashraf Abedin: Writing, editing, proofreading, compilation and formatting of whole chapter; (2) Jhonattan D Manosalvas Mora: Rearranging the chapter, referencing and writing the section “Cancer therapy”; (3) Adiba Azad: Writing the section “Drug delivery” and chapter editing; (4) Srikar Bhattar: Writing the section “Imaging” and proofreading; (5) S M Rezwanul Islam: Writing the section “Tissue Engineering”; (6) Mohammad Hasibul Hasan: Writing the section “Diagnosis”. The authors further acknowledge that there is no financial relationship with the editors or publisher and have contributed original work in this chapter, other than what is acknowledged or appropriately cited with copyright permission.

References

1. Altintas Z (2017) Biosensors and nanotechnology-applications in health care diagnostics. ISBN: 978-1-119-06503-6. <https://www.wiley.com/en-us/Biosensors+and+Nanotechnology%3A+Applications+in+Health+Care+Diagnostics-p-9781119065036>
2. Alharbi KK, Al-sheikh YA (2014) Role and implications of nanodiagnosics in the changing trends of clinical diagnosis. *Saudi J Biol Sci* 21(2):109–117. <https://doi.org/10.1016/j.sjbs.2013.11.001>
3. Aslan B, Ozpolat B, Sood AK, Lopez-Berestein G (2013) Nanotechnology in cancer therapy. *J Drug Target* 21:904–913. <https://doi.org/10.3109/1061186X.2013.837469>
4. Atkins P, De Paula J, Keeler J (2018) Atkins' physical chemistry, 11th edn. Oxford University Press, Oxford
5. Aziz F, Ihsan A, Nazir A, Ahmad I, Bajwa SZ, Rehman A, Diallo A, Khan WS (2017) Novel route synthesis of porous and solid gold nanoparticles for investigating their comparative performance as contrast agent in computed tomography scan and effect on liver and kidney function. *Int J Nanomed* 12:1555–1563
6. Ber S, Torun Köse G, Hasırıcı V (2005) Bone tissue engineering on patterned collagen films: an in vitro study. *Biomaterials* 26:1977–1986. <https://doi.org/10.1016/j.biomaterials.2004.07.007>
7. Burdick JA, Khademhosseini A, Langer R (2004) Fabrication of gradient hydrogels using a microfluidics/topopolymerization process. *Langmuir* 20:5153–5156. <https://doi.org/10.1021/la049298n>
8. Carraro A, Hsu W-M, Kulig KM, Cheung WS, Miller ML, Weinberg EJ, Swart EF, Kaazempur-Mofrad M, Borenstein JT, Vacanti JP et al (2008) In vitro analysis of a hepatic device with intrinsic microvascular-based channels. *Biomed Microdevices* 10:795–805. <https://doi.org/10.1007/s10544-008-9194-3>
9. Chakravarty R, Hong H, Cai W (2015) Image-guided drug delivery with single-photon emission computed tomography: a review of literature. *Current Drug Targets* 16:592–609
10. Chandrakala V, Aruna V, Angajala G (2022) Review on metal nanoparticles as nanocarriers: current challenges and perspectives in drug delivery systems. *Emergent Mater* 5:1593–1615
11. Chaubey A, Ross KJ, Leadbetter RM, Burg KJL (2008) Surface patterning: tool to modulate stem cell differentiation in an adipose system. *J Biomed Mater Res Part B Appl Biomater* 84:70–78. <https://doi.org/10.1002/jbm.b.30846>
12. Chen F, Goel S, Hernandez R, Graves SA, Shi S, Nickles RJ, Cai W (2016) Dynamic positron emission tomography imaging of renal clearable gold nanoparticles. *Small* 12:2775–2782. <https://doi.org/10.1002/sml.201600194>
13. Cheng Z, Li M, Dey R, Chen Y (2021) Nanomaterials for cancer therapy: current progress and perspectives. *J Hematol Oncol* 14:1–27. <https://doi.org/10.1186/s13045-021-01096-0>
14. Choi D, Jeon S, You DG, Um W, Kim J-Y, Yoon HY, Chang H, Kim D-E, Park JH, Kim H et al (2018) Iodinated echogenic glycol chitosan nanoparticles for x-ray ct/us dual imaging of tumor. *Nanotheranostics* 2:117–127
15. Chua K-N, Chai C, Lee P-C, Tang Y-N, Ramakrishna S, Leong KW, Mao H-Q (2006) Surface-aminated electrospun nanofibers enhance adhesion and expansion of human umbilical cord blood hematopoietic stem/progenitor cells. *Biomaterials* 27:6043–6051. <https://doi.org/10.1016/j.biomaterials.2006.06.017>
16. Colella F et al (2020) Drug delivery in intervertebral disc degeneration and osteoarthritis: selecting the optimal platform for the delivery of disease-modifying agents. *J Control Rel* 328:985–999
17. Cormie P, Zopf EM, Zhang X, Schmitz KH (2017) The impact of exercise on cancer mortality, recurrence, and treatment-related adverse effects. *Epidemiol Rev* 39:71–92. <https://doi.org/10.1093/epirev/mxx007>
18. Cui L, Xiong C, Zhou M, Shi S, Chow DSL, Li C (2018) Integrin $\alpha\beta3$ -targeted [64cu]cus nanoparticles for pet/ct imaging and photothermal ablation therapy. *Bioconjugate Chem* 29:4062–4071. <https://doi.org/10.1021/acs.bioconjchem.8b00690>

19. Curtis A, Wilkinson C (2001) Nanotechniques and approaches in biotechnology. *Trends Biotechnol* 19(3):97–101. [https://doi.org/10.1016/S0167-7799\(00\)01536-5](https://doi.org/10.1016/S0167-7799(00)01536-5)
20. Daxini SC, Nichol JW, Sieminski AL, Smith G, Gooch KJ, Shastri VP (2006) Micropatterned polymer surfaces improve retention of endothelial cells exposed to flow-induced shear stress. *Biorheology* 43:45–55
21. de Veij Mestdagh PD, Schreuder WH, Vogel WV, Donswijk ML, van Werkhoven E, van der Wal JE, Dirven R, Karakullukcu B, Sonke J-J, van den Brekel MWM et al (2019) Mapping of sentinel lymph node drainage using spect/ct to tailor elective nodal irradiation in head and neck cancer patients (suspect-2): a single-center prospective trial. *BMC Cancer* 19:1110. <https://doi.org/10.1186/s12885-019-6331-8>
22. De-La-Cuesta J, González E, Pomposo JA (2017) Advances in fluorescent single-chain nanoparticles. *Molecules* 22(11). <https://doi.org/10.3390/molecules22111819>.
23. de la Escosura-Muñiz A, Baptista-Pires L, Serrano L, Altet L, Francino O, Sánchez A, Merkoçi A (2016) Magnetic bead/gold nanoparticle double-labeled primers for electrochemical detection of isothermal amplified Leishmania DNA. *Small* 12(2):205–213. <https://doi.org/10.1002/sml.201502350>
24. Din FU, Aman W, Ullah I, Qureshi OS, Mustapha O, Shafique S, Zeb A (2017) Effective use of nanocarriers as drug delivery systems for the treatment of selected tumors. *Int J Nanomedicine* 12:7291–7309. <https://doi.org/10.2147/IJN.S146315>
25. Dvir T, Timko BP, Kohane DS, Langer R (2011) Nanotechnological strategies for engineering complex tissues. *Nature Nanotechnol* 6:13–22. <https://doi.org/10.1038/nnano.2010.246>
26. Eftekhari A, Dizaj SM, Sharifi S, Salatin S, Saadat YR, Vahed SZ, Samiei M, Ardalan M, Rameshrad M, Ahmadian E et al (2020) The use of nanomaterials in tissue engineering for cartilage regeneration; current approaches and future perspectives. *Int J Molecular Sci* 21:1–24. <https://doi.org/10.3390/ijms21020536>
27. Feng-Dan Z et al (2021) Nanoparticles: a hope for the treatment of inflammation in CNS. *Front Pharmacol* 12
28. Ferlay J, Colombet M, Soerjomataram I, Parkin DM, Pineros M, Znaor A, Bray F (2021) Cancer statistics for the year 2020: an overview. *Int J Cancer*. <https://doi.org/10.1002/ijc.33588>
29. Fidler MM, Bray F, Soerjomataram I (2018) The global cancer burden and human development: a review. *Scand J Public Health* 46:27–36. <https://doi.org/10.1177/1403494817715400>
30. Fidler MM, Soerjomataram I, Bray F (2016) A global view on cancer incidence and national levels of the human development index. *Int J Cancer* 139:2436–2446. <https://doi.org/10.1002/ijc.30382>
31. Foucault-Collet A, Gogick KA, White KA, Villette S, Pallier A, Collet G, Kieda C, Li T, Geib SJ, Rosi NL et al (2013) Lanthanide near infrared imaging in living cells with Yb^{3+} nano metal organic frameworks. *Proc National Acad Sci United States of America* 110:17199–17204. <https://doi.org/10.1073/pnas.1305910110>
32. Gavas S, Quazi S, Karpinski TM (2021) Nanoparticles for cancer therapy: Current progress and challenges. *Nanoscale Res Lett* 16:1–21. <https://doi.org/10.1186/s11671-021-03628-6>
33. Gupta V, Bhavanasi S, Quadir M, Singh K, Ghosh G, Vasamreddy K, Ghosh A, Siahaan TJ, Banerjee S, Banerjee SK (2019) Protein pegylation for cancer therapy: Bench to bedside. *J Cell Commun Signal* 13:319–330. <https://doi.org/10.1007/s12079-018-0492-0>
34. Han X, Xu K, Taratula O, Farsad K (2019) Applications of nanoparticles in biomedical imaging. *Nanoscale* 11:799–819. <https://doi.org/10.1039/c8nr07769j>
35. Hasan A, Morshed M, Memic A, Hassan S, Webster TJ, Marei HE-S (2018) Nanoparticles in tissue engineering: Applications, challenges and prospects. *Int J Nanomed* 13:5637–5655. <https://doi.org/10.2147/IJN.S153758>
36. Hashim D, Boffetta P, La Vecchia C, Rota M, Bertuccio P, Malvezzi M, Negri E (2016) The global decrease in cancer mortality: trends and disparities. *Ann Oncol* 27:926–933. <https://doi.org/10.1093/annonc/mdw027>

37. Hauser PV, Chang HM, Yanagawa N, Hamon M (2021) Nanotechnology, nanomedicine, and the kidney. *Appl Sci* 11(16):7187
38. Heshmatzadeh Behzadi A, Farooq Z, Newhouse JH, Prince MR, Schaller B (2018) Mri and ct contrast media extravasation. *Medicine* 97:e0055–e0055. <https://doi.org/10.1097/MD.00000000000010055>
39. Hoogendam JP, Zweemer RP, Hobbelenk MGG, van den Bosch MAAJ, Verheijen RHM, Veldhuis WB (2016) ^{99m}Tc-nanocolloid spect/mri fusion for the selective assessment of nonenlarged sentinel lymph nodes in patients with early-stage cervical cancer. *J Nuclear Med* 57:551. <https://doi.org/10.2967/jnumed.115.164780>
40. Hossen S, Hossain MK, Basher MK, Mia MNH, Rahman MT, Uddin MJ (2019) Smart nanocarrier-based drug delivery systems for cancer therapy and toxicity studies: a review. *J Adv Res* 15:1–18. <https://doi.org/10.1016/j.jare.2018.06.005>
41. Hu Q, Li H, Wang L, Gu H, Fan C (2019) DNA Nanotechnology-enabled drug delivery systems. *Chem Rev* 119(10):6459–6506. <https://doi.org/10.1021/acs.chemrev.7b00663>
42. Hung H-S, Chen H-C, Tsai C-H, Lin S-Z (2011) Novel approach by nanobiomaterials in vascular tissue engineering. *Cell Transplant* 20:63–70. <https://doi.org/10.3727/096368910X532864>
43. Imamura Y, Yamada S, Tsuboi S, Nakane Y, Tsukasaki Y, Komatsuzaki A, Jin T (2016) Near-infrared emitting PBS quantum dots for in vivo fluorescence imaging of the thrombotic state in septic mouse brain. *Molecules* 21(8). <https://doi.org/10.3390/molecules21081080>
44. Jackson TC, Patani BO, Ekpa DE (2017) Nanotechnology in diagnosis: a review. *Adv Nanoparticles* 06(03):93–102. <https://doi.org/10.4236/anp.2017.63008>
45. Jemal A, Ward EM, Johnson CJ, Cronin KA, Ma J, Ryerson B, Mariotto A, Lake AJ, Wilson R, Sherman RL et al (2017) Annual report to the nation on the status of cancer, 1975-2014, featuring survival. *J Natl Cancer Inst* 109. <https://doi.org/10.1093/jnci/djx030>
46. Jhaveri AM, Torchilin VP (2014) Multifunctional polymeric micelles for delivery of drugs and siRNA. *Front Pharmacol* 5:1–26. <https://doi.org/10.3389/fphar.2014.00077>
47. Jin C, Wang K, Oppong-Gyebi A, Hu J (2020) Application of nanotechnology in cancer diagnosis and therapy—a mini-review. *Int J Med Sci* 17:2964–2973. <https://doi.org/10.7150/ijms.49801>
48. Jin JO, Kim G, Hwang J, Han KH, Kwak M, Lee PCW (2020) Nucleic acid nanotechnology for cancer treatment. *Biochim Biophys Acta Rev Cancer* 1874:188377. <https://doi.org/10.1016/j.bbcan.2020.188377>
49. Jurj A, Braicu C, Pop LA, Tomuleasa C, Gherman CD, Berindan-Neagoe I (2017) The new era of nanotechnology, an alternative to change cancer treatment. *Drug Des Devel Ther* 11:2871–2890. <https://doi.org/10.2147/DDDT.S142337>
50. Karp JM, Yeh J, Eng G, Fukuda J, Blumling J, Suh K-Y, Cheng J, Mahdavi A, Borenstein J, Langer R et al (2007) Controlling size, shape and homogeneity of embryoid bodies using poly(ethylene glycol) microwells. *Lab on a Chip* 7:786–794. <https://doi.org/10.1039/b705085m>
51. Karp JM, Yeo Y, Geng W, Cannizarro C, Yan K, Kohane DS, Vunjak-Novakovic G, Langer RS, Radisic M (2006) A photolithographic method to create cellular micropatterns. *Biomaterials* 27:4755–4764. <https://doi.org/10.1016/j.biomaterials.2006.04.028>
52. Keliher EJ, Ye Y-X, Wojtkiewicz GR, Aguirre AD, Tricot B, Senders ML, Groenen H, Fay F, Perez-Medina C, Calcagno C et al (2017) Polyglucose nanoparticles with renal elimination and macrophage avidity facilitate PET imaging in ischaemic heart disease. *Nat Comm* 8:14064. <https://doi.org/10.1038/ncomms14064>
53. Kenar H, Kocabas A, Aydinli A, Hasirci V (2008) Chemical and topographical modification of phbv surface to promote osteoblast alignment and confinement. *J Biomed Mat Res Part A* 85:1001–1010. <https://doi.org/10.1002/jbm.a.31638>
54. Kesharwani P, Choudhury H, Meher JG, Pandey M, Gorain B (2019) Dendrimer-entrapped gold nanoparticles as promising nanocarriers for anticancer therapeutics and imaging. *Prog Mat Sci* 103:484–508. <https://doi.org/10.1016/j.pmatsci.2019.03.003>

55. Khademhosseini A, Eng G, Yeh J, Kucharczyk PA, Langer R, Vunjak-Novakovic G, Radisic M (2007) Microfluidic patterning for fabrication of contractile cardiac organoids. *Biomed Microdev* 9:149–157. <https://doi.org/10.1007/s10544-006-9013-7>
56. Khademhosseini A, Ferreira L, Blumling J, Yeh J, Karp JM, Fukuda J, Langer R (2007) Co-culture of human embryonic stem cells with murine embryonic fibroblasts on microwell-patterned substrates. *Biomaterials* 27:5968–5977. <https://doi.org/10.1016/j.biomaterials.2006.06.035>
57. Khetani SR, Bhatia SN (2008) Microscale culture of human liver cells for drug development. *Nature Biotechnol* 26:120–126. <https://doi.org/10.1038/nbt1361>
58. Khurana A et al (2021) Role of nanotechnology behind the success of mRNA vaccines for COVID-19. *Nano Today* 38:101142
59. Kim E-S, Ahn EH, Dvir T, Kim D-H (2014) Emerging nanotechnology approaches in tissue engineering and regenerative medicine. *Int J Nanomed* 9:1–5. <https://doi.org/10.2147/IJN.S61212>
60. Kim H-Y, Li R, Ng TSC, Courties G, Rodell CB, Prytskach M, Kohler RH, Pittet MJ, Narendorf M, Weissleder R et al (2018) Quantitative imaging of tumor-associated macrophages and their response to therapy using 64cu-labeled macrin. *ACS Nano* 12:12015–12029. <https://doi.org/10.1021/acsnano.8b04338>
61. Kim K, Fisher JP (2007) Nanoparticle technology in bone tissue engineering. *J Drug Targeting* 15:241–252. <https://doi.org/10.1080/10611860701289818>
62. Kim SJ, Lewis B, Steiner M-S, Bissa UV, Dose C, Frank JA (2016) Superparamagnetic iron oxide nanoparticles for direct labeling of stem cells and in vivo mri tracking. *Contrast Media Molecular Imag* 11:55–64. <https://doi.org/10.1002/cmml.1658>
63. Kingsley JD, Ranjan S, Dasgupta N, Saha P (2013) Nanotechnology for tissue engineering: need, techniques and applications. *J Pharmacy Res* 7:200–204. <https://doi.org/10.1016/j.jopr.2013.02.021>
64. Kumar R, Aadil KR, Ranjan S, Kumar VB (2020) Advances in nanotechnology and nanomaterials based strategies for neural tissue engineering. *J Drug Deliv Sci Technol* 57:101617. <https://doi.org/10.1016/j.jddst.2020.101617>
65. Kumari P, Ghosh B, Biswas S (2016) Nanocarriers for cancer-targeted drug delivery. *J Drug Target* 24:179–191. <https://doi.org/10.3109/1061186X.2015.1051049>
66. Kurpinski K, Chu J, Hashi C, Li S (2006) Anisotropic mechanosensing by mesenchymal stem cells. *Proc Nation Acad Sci* 103:16095–16100. <https://doi.org/10.1073/pnas.0604182103>
67. Labouta HI, Langer R, Cullis PR et al (2022) Role of drug delivery technologies in the success of COVID-19 vaccines: a perspective. *Drug Deliv Transl* 12:2581–2588
68. Lan J (2022) Overview of application of nanomaterials in medical domain. *Contrast Med Mole Imag* 2022:1–5. <https://doi.org/10.1155/2022/3507383>
69. Lee SB, Lee S-W, Jeong SY, Yoon G, Cho SJ, Kim SK, Lee I-K, Ahn B-C, Lee J, Jeon YH (2017) Engineering of radioiodine-labeled gold core-shell nanoparticles as efficient nuclear medicine imaging agents for trafficking of dendritic cells. *ACS Appl Mater Interf* 9:8480–8489. <https://doi.org/10.1021/acsnami.6b14800>
70. Li F, Li J, Dong B, Wang F, Fan C, Zuo X (2021) DNA nanotechnology-empowered nanoscopic imaging of biomolecules. *Chem Soc Rev* 50:5650–5667. <https://doi.org/10.1039/D0CS01281E>
71. Li Z, Tan S, Li S, Shen Q, Wang K (2017) Cancer drug delivery in the nano era: an overview and perspectives (review). *Oncol Rep* 38:611–624. <https://doi.org/10.3892/or.2017.5718>
72. Liao W, Lei P, Pan J, Zhang C, Sun X, Zhang X, Yu C, Sun S-K (2019) Bi-dtpa as a high-performance ct contrast agent for in vivo imaging. *Biomaterials* 203:1–11. <https://doi.org/10.1016/j.biomaterials.2019.03.001>
73. Lin X, Helmke BP (2008) Micropatterned structural control suppresses mechanotaxis of endothelial cells. *Biophys J* 95:3066–3078. <https://doi.org/10.1529/biophysj.107.127761>
74. Liu L, Wang J, Tan X, Pang X, You Q, Sun Q, Tan F, Li N (2017) Photosensitizer loaded peg-mos2-au hybrids for ct/nirf imaging-guided stepwise photothermal and photodynamic therapy. *J Mater Chem B* 5:2286–2296. <https://doi.org/10.1039/C6TB03352K>

75. Liu M, Du H, Zhang W, Zhai G (2017) Internal stimuli-responsive nanocarriers for drug delivery: design strategies and applications. *Mater Sci Eng C Mater Biol Appl* 71:1267–1280. <https://doi.org/10.1016/j.msec.2016.11.030>
76. Liu W, Ma Z, Wang Y, Yang Z (2023) Multiple nano-drug delivery systems for intervertebral disc degeneration: current status and future perspectives. *Bioactive Mater* 23:274–299
77. Liu X, Braun GB, Zhong H, Hall DJ, Han W, Qin M, Zhao C, Wang M, She Z-G, Cao C et al (2016) Tumor-targeted multimodal optical imaging with versatile cadmium-free quantum dots. *Adv Func Mater* 26:267–276. <https://doi.org/10.1002/adfm.201503453>
78. Liu Y, Carpenter AB, Pirozzi CJ, Yuan H, Waitkus MS, Zhou Z, Hansen L, Seywald M, Odion R, Greer PK et al (2019) Non-invasive sensitive brain tumor detection using dual-modality bioimaging nanoprobe. *Nanotechnology* 30:275101. <https://doi.org/10.1088/1361-6528/ab0e9c>
79. Liu Z-Y, Yan G-H, Li X-Y, Zhang Z, Guo Y-Z, Xu K-X, Quan J-S, Jin G-Y (2021) Ge11 peptide modified cso-spon micelles for mri diagnosis of targeted hepatic carcinoma. *Biotechnol Biotechnol Equip* 35:1574–1586. <https://doi.org/10.1080/13102818.2021.1997154>
80. Lu WL, Jansen L, Post WJ, Bonnema J, Van de Velde JC, De Bock GH (2009) Impact on survival of early detection of isolated breast recurrences after the primary treatment for breast cancer: a meta-analysis. *Breast Cancer Res Treatment* 114:403–412. <https://doi.org/10.1007/s10549-008-0023-4>
81. Luo G, Zhang Y, Etxeberria J, Arnold M, Cai X, Hao Y, Zou H (2023) Projections of lung cancer incidence by 2035 in 40 countries worldwide: population-based study. *JMIR Public Health Surveill* 9:1–15. <https://doi.org/10.2196/43651>
82. Ma K, Chan CK, Liao S, Hwang WYK, Feng Q, Ramakrishna S (2008) Electrospun nanofiber scaffolds for rapid and rich capture of bone marrow-derived hematopoietic stem cells. *Biomaterials* 29:2096–2103. <https://doi.org/10.1016/j.biomaterials.2008.01.024>
83. Madrid APM, Vrech SM, Sanchez MA, Rodriguez AP (2019) Advances in additive manufacturing for bone tissue engineering scaffolds. *Mater Sci Eng C* 100:631–644. <https://doi.org/10.1016/j.msec.2019.03.037>
84. Maheshwari N, Tekade M, Chourasiya Y, Sharma MC, Deb PK, Tekade RK (2019) Nanotechnology in tissue engineering. In: Tekade RK (ed) *Biomaterials and bionanotechnology*, 1st edn. Elsevier Science, Amsterdam
85. Marghussian V (2015) *Nano-glass ceramics: processing, properties and applications*, 1st edn. Elsevier, Oxford
86. Markiewicz KH, Marmuse L, Mounsamy M, Billotey C, Destarac M, Mingotaud C, Marty J-D (2022) Assembly of poly(vinylphosphonic acid)-based double hydrophilic block copolymers by gadolinium ions for the formation of highly stable mri contrast agents. *ACS Macro Lett* 11:1319–1324. <https://doi.org/10.1021/acsmacrolett.2c00489>
87. Mattiuzzi C, Lippi G (2019) Current cancer epidemiology. *J Epidemiol Glob Health* 9:217–222. <https://doi.org/10.2991/jeqh.k.191008.001>
88. McDonagh PR, Sundaresan G, Yang L, Sun M, Mikkelsen R, Zweit J (2018) Biodistribution and pet imaging of 89-zirconium labeled cerium oxide nanoparticles synthesized with several surface coatings. *nanomedicine: nanotechnology. Biol Med* 14:1429–1440. <https://doi.org/10.1016/j.nano.2018.04.002>
89. McNaught AD (1997) *Compendium of chemical terminology*, vol 1669. Blackwell Science, Oxford
90. Meng Q, Zhong S, Xu L, Wang J, Zhang Z, Gao Y, Cui X (2022) Review on design strategies and considerations of polysaccharide-based smart drug delivery systems for cancer therapy. *Carbohydr Polym* 279:1–13. <https://doi.org/10.1016/j.carbpol.2021.119013>
91. Merlin JPJ, Li X (2022) Role of nanotechnology and their perspectives in the treatment of kidney diseases. *Front Genet* 12:817974
92. Mi Y, Shao Z, Vang J, Kaidar-Person O, Wang AZ (2016) Application of nanotechnology to cancer radiotherapy. *Cancer Nanotechnol* 7:1–16. <https://doi.org/10.1186/s12645-016-0024-7>
93. Mitra AK, Agrahari V, Mandal A, Cholkar K, Natarajan C, Shah S, Joseph M, Trinh HM, Vaishya R, Yang X et al (2015) Novel delivery approaches for cancer therapeutics. *J Control Release* 219:248–268. <https://doi.org/10.1016/j.jconrel.2015.09.067>

94. Mitragotri S, Anderson DG, Chen X, Chow EK, Ho D, Kabanov AV, Karp JM, Kataoka K, Mirkin CA, Petrosko SH, Shi J, Stevens MM, Sun S, Teoh S, Venkatraman SS, Xia Y, Wang S, Gu Z, Xu C (2015) Accelerating the translation of nanomaterials in biomedicine. *ACS Nano* 9(7):6644–6654. <https://doi.org/10.1021/acsnano.5b03569>
95. Moghimi H, Zohdiaghdam R, Riahi Alam N, Behrouzkhia Z (2019) The assessment of toxicity characteristics of cellular uptake of paramagnetic nanoparticles as a new magnetic resonance imaging contrast agent. *Iranian J Pharmaceutical Res* 18:2083–2092
96. Moghimi SM, Wibroe PP, Helvig SY, Farhangrazi ZS, Hunter AC (2012) Genomic perspectives in inter-individual adverse responses following nanomedicine administration: the way forward. *Adv Drug Deliv Rev* 64(13):1385–1393. <https://doi.org/10.1016/j.addr.2012.05.010>
97. Napp J, Markus MA, Heck JG, Dullin C, Moebius W, Gorpas D, Feldmann C, Alves F (2018) Therapeutic fluorescent hybrid nanoparticles for traceable delivery of glucocorticoids to inflammatory sites. *Theranostics* 8:6367–6383
98. Neubertova V, Guselnikova O, Yamauchi Y, Olshrem A, Rimpelova S, Čížmár E, Orendáč M, Duchon J, Volfova L, Lancok J et al (2022) Covalent functionalization of t₃c₂t mxene flakes with gd-dtpa complex for stable and biocompatible mri contrast agent. *Chem Eng J* 446:136939. <https://doi.org/10.1016/j.cej.2022.136939>
99. Nguyen TT et al (2021) Nanotechnology-based drug delivery for central nervous system disorders. *Biomed Pharmacotherapy* 143:112117
100. Paavo Perämäki LL (2004) Spectrochemical analysis by atomic absorption and emission, 2nd edn. The Royal Society of Chemistry, Cambridge
101. Patra JK et al (2019) Nano based drug delivery systems: recent developments and future prospects. *J Nanobiotechnol* 16(1):71
102. Perinelli DR, Cespi M, Lorusso N, Palmieri GF, Bonacucina G, Blasi P (2020) Surfactant self-assembling and critical micelle concentration: one approach fits all? *Langmuir* 36:5745–5753. <https://doi.org/10.1021/acs.langmuir.0c00420>
103. Pinheiro RGR, Coutinho AG, Pinheiro M, Neves AR (2021) Nanoparticles for targeted brain drug delivery: what do we know? *Int J Molecular Sci* 22(21):11654
104. Piras AM, Fabiano A, Sartini S, Zambito Y, Braccini S, Chiellini F, Cataldi AG, Bartoli F, de la Fuente A, Erba PA. 2019. Ph-responsive carboxymethylcellulose nanoparticles for 68ga-wbc labeling in pet imaging. *Polymers* 11(10). <https://doi.org/10.3390/polym11101615>
105. Pirzada M, Altintas Z (2019) Nanomaterials for healthcare biosensing applications. *Sensors* 19(23):5311. <https://doi.org/10.3390/s19235311>
106. Qiao Y, Wan J, Zhou L, Ma W, Yang Y, Luo W, Yu Z, Wang H (2019) Stimuli-responsive nanotherapeutics for precision drug delivery and cancer therapy. *Wiley Interdiscip Rev Nanomed Nanobiotechnol* 11:1–20. <https://doi.org/10.1002/wnan.1527>
107. Qiu M, Singh A, Wang D, Qu J, Swihart M, Zhang H, Prasad PN (2019) Biocompatible and biodegradable inorganic nanostructures for nanomedicine: Silicon and black phosphorus. *Nano Today* 25:135–155. <https://doi.org/10.1016/j.nantod.2019.02.012>
108. Quesada-González D, Merkoçi A (2018) Nanomaterial-based devices for point-of-care diagnostic applications. *Chem Soc Rev* 47(13):4697–4709. <https://doi.org/10.1039/C7CS00837F>
109. Rahim MA, Jan N, Khan S, Shah H, Madni A, Khan A, Jabar A, Khan S, Elhissi A, Hussain Z et al (2021) Recent advancements in stimuli responsive drug delivery platforms for active and passive cancer targeting. *Cancers (Basel)* 13:1–52. <https://doi.org/10.3390/cancers13040670>
110. Raj S, Khurana S, Choudhari R, Kesari KK, Kamal MA, Garg N, Ruokolainen J, Das BC, Kumar D (2021) Specific targeting cancer cells with nanoparticles and drug delivery in cancer therapy. *Semin Cancer Biol* 69:166–177. <https://doi.org/10.1016/j.semcancer.2019.11.002>
111. Rosenblum D, Joshi N, Tao W, Karp JM, Peer D (2018) Progress and challenges towards targeted delivery of cancer therapeutics. *Nat Commun* 9:1–12. <https://doi.org/10.1038/s41467-018-03705-y>
112. Ryan RO (2010) Nanobiotechnology applications of reconstituted high density lipoprotein. *J Nanobiotechnol* 8:28. <https://doi.org/10.1186/1477-3155-8-28>

113. Saad ZZ, Omorphos S, Michopoulou S, Gacinovic S, Malone P, Nigam R, Muneer A, Bomanji J (2017) Investigating the role of spect/ct in dynamic sentinel lymph node biopsy for penile cancers. *Europ J Nucl Med Molecular Imaging* 44:1176–1184. <https://doi.org/10.1007/s00259-017-3636-1>
114. Saba N, Archana P, Flora SJS (2020) Nanotechnology: a promising approach for delivery of neuroprotective drugs. *Front Neurosci* 14
115. Saeedi MK, Khezri K, Dizaj SK (2019) Applications of nanotechnology in drug delivery to the central nervous system. *Biomed Pharmacotherapy* 111:666–675
116. Sahu T, Ratre YK, Chauhan S, Bhaskar LVKS, Nair MP, Verma HK (2021) Nanotechnology based drug delivery system: current strategies and emerging therapeutic potential for medical science. *J Drug Deliv Sci Technol* 63(102487):1773–2247
117. Sakai D, Grad S (2015) Advancing the cellular and molecular therapy for intervertebral disc disease. *Adv Drug Deliv Rev* 84:159–171
118. Salazar N, Zabel BA (2019) Support of tumor endothelial cells by chemokine receptors. *Front Immunol* 10:1–9. <https://doi.org/10.3389/fimmu.2019.00147>
119. Santos BS, Ferreira MJ (2019) Positron emission tomography in ischemic heart disease. *Revista Portuguesa de Cardiologia* 38:599–608. <https://doi.org/10.1016/j.repc.2019.02.011>
120. Sarfaraz S, Bano T, Fatima W (2018) Nanotechnology and its therapeutic application—a review. *MOJ Bioequiv Availab*. 5(1):24–27
121. Schluep T, Hwang J, Hildebrandt IJ, Czernin J, Choi CHJ, Alabi CA, Mack BC, Davis ME (2009) Pharmacokinetics and tumor dynamics of the nanoparticle it-101 from pet imaging and tumor histological measurements. *Proc Nat Acad Sci* 106:11394–11399. <https://doi.org/10.1073/pnas.0905487106>
122. SH P (2014) Emerging trends in medical diagnosis: a thrust on nanotechnology. *Med Chem* 4(4). <https://doi.org/10.4172/2161-0444.1000172>
123. Sharma P, Brown N, Walter G, Santra S, Moudgil B (2006) Nanoparticles for bioimaging. *Adv Colloid Interf Sci* 123–126:471–485. <https://doi.org/10.1016/j.cis.2006.05.026>
124. Sharma P, Mehta M, Dhanjal DS, Kaur S, Gupta G, Singh H, Thangavelu L, Rajeshkumar S, Tambuwala M, Bakshi HA et al (2019) Emerging trends in the novel drug delivery approaches for the treatment of lung cancer. *Chem Biol Interact* 309:1–33. <https://doi.org/10.1016/j.cbi.2019.06.033>
125. Sharma S, Jain KK, Sharma A (2015) Solar cells: in research and applications—a review. *Mater Sci Appl* 06:1145–1155. <https://doi.org/10.4236/msa.2015.612113>
126. Shi J, Votruba AR, Farokhzad OC, Langer R (2010) Nanotechnology in drug delivery and tissue engineering: from discovery to applications. *Nano Lett* 10:3223–3230. <https://doi.org/10.1021/nl102184c>
127. Siddique S, Chow JCL (2020) Gold nanoparticles for drug delivery and cancer therapy. *Appl Sci* 10:1–21. <https://doi.org/10.3390/app10113824>
128. Siddique S, Chow JCL (2020) Application of nanomaterials in biomedical imaging and cancer therapy. *Nanomat* 10(9). <https://doi.org/10.3390/nano10091700>
129. Siegel RL, Miller KD, Fuchs HE, Jemal A (2022) Cancer statistics, 2022. *CA Cancer J Clin* 72:7–33. <https://doi.org/10.3322/caac.21708>
130. Soh JH, Chan H-M, Ying JY (2020) Strategies for developing sensitive and specific nanoparticle-based lateral flow assays as point-of-care diagnostic device. *Nano Today* 30:100831. <https://doi.org/10.1016/j.nantod.2019.100831>
131. Sun S, Chen Q, Tang Z, Liu C, Li Z, Wu A, Lin H (2020) Tumor microenvironment stimuli-responsive fluorescence imaging and synergistic cancer therapy by carbon-dot-cu₂+ nanoassemblies. *Angewandte Chemie International Edition* 59:21041–21048. <https://doi.org/10.1002/anie.202007786>
132. Sun Y, Ding M, Zeng X, Xiao Y, Wu H, Zhou H, Ding B, Qu C, Hou W, Er-bu AGA et al (2017) Novel bright-emission small-molecule nir-ii fluorophores for in vivo tumor imaging and image-guided surgery. *Chem Sci* 8:3489–3493. <https://doi.org/10.1039/C7SC00251C>

133. Sung H, Ferlay J, Siegel RL, Laversanne M, Soerjomataram I, Jemal A, Bray F (2021) Global cancer statistics 2020: Globocan estimates of incidence and mortality worldwide for 36 cancers in 185 countries. *CA Cancer J Clin* 71:209–249. <https://doi.org/10.3322/caac.21660>
134. Tang D, Gao W, Yuan Y, Guo L, Mei X (2017) Novel biocompatible au nanostars@peg nanoparticles for in vivo ct imaging and renal clearance properties. *Nanoscale Res Lett* 12:565. <https://doi.org/10.1186/s11671-017-2332-1>
135. Tavares JL, Cavalcanti IDL, Santos Magalhães NS et al (2022) Nanotechnology and COVID-19: quo vadis? *J Nanopart Res* 24:62
136. Teleanu DM, Negut I, Grumezescu V, Grumezescu AM, Teleanu RI (2019) Nanomaterials for drug delivery to the central nervous system. *Nanomaterials (Basel)* 9(3):37
137. The World Bank (2023) Databank world development indicators. The World Bank. <https://data.worldbank.org/indicator/SP.POP.TOTL>. Accessed 24 February 2023
138. Tsang VL, Chen AA, Cho LM, Jadin KD, Sah RL, DeLong S, West JL, Bhatia SN (2007) Fabrication of 3d hepatic tissues by additive photopatterning of cellular hydrogels. *FASEB J* 21:790–801. <https://doi.org/10.1096/fj.06-7117com>
139. Tuzlakoglu K, Bolgen N, Salgado AJ, Gomes ME, Piskin E, Reis RL (2005) Nano and microfiber combined scaffolds: A new architecture for bone tissue engineering. *J Mater Sci Mater Med* 16:1099–1104. <https://doi.org/10.1007/s10856-005-4713-8>
140. Vasudevan A, Tripathi DM, Sundarrajan S, Venugopal JR, Ramakrishna S, Kaur S (2022) Evolution of electrospinning in liver tissue engineering *Biomimetics (Basel)* 7. <https://doi.org/10.3390/biomimetics7040149>
141. Verma M, Sheoran P, Chaudhury A (2018) Application of nanotechnology for cancer treatment. In: Gahlawat SK, Duhan JS, Salar RK, Siwach P, Kumar S, Kaur P (ed) *Advances in animal biotechnology and its applications*, 1st edn. Springer, Singapore
142. Villiers C, Freitas H, Couderc R, Villiers MB, Marche P (2010) Analysis of the toxicity of gold nano particles on the immune system: effect on dendritic cell functions. *J Nanopart Res* 12:55–60. <https://doi.org/10.1007/s11051-009-9692-0>
143. Wang N, Dheen ST, Fuh JYH, Kadir AS (2021) A review of multi-functional ceramic nanoparticles in 3d printed bone tissue engineering *Bioprinting* 23:1–22. <https://doi.org/10.1016/j.bprint.2021.e00146>
144. Wang S, Yin D, Wang W, Shen X, Zhu J-J, Chen H-Y, Liu Z (2016) Targeting and imaging of cancer cells via monosaccharide-imprinted fluorescent nanoparticles. *Sci Rep* 6:22757. <https://doi.org/10.1038/srep22757>
145. Wang Y, Xu N, He Y, Wang J, Wang D, Gao Q, Xie S, Li Y, Zhang R, Cai Q (2019) Loading graphene quantum dots into optical-magneto nanoparticles for real-time tracking in vivo. *Materials* 12(13). <https://doi.org/10.3390/ma12132191>
146. Wang Z, Ruan J, Cui D (2009) Advances and prospect of nanotechnology in stem cells. *Nanoscale Res Lett* 4:593–605. <https://doi.org/10.1007/s11671-009-9292-z>
147. Wen MM, El-Salamouni NS, El-Refaie WM, Hazzah HA, Ali MM et al (2017) Nanotechnology-based drug delivery systems for Alzheimer’s disease management: technical, industrial, and clinical challenges. *J Controlled Release* 245:95–107
148. World Health Organization (2020) The top 10 causes of death. United Nations. <https://www.who.int/news-room/fact-sheets/detail/the-top-10-causes-of-death>. Accessed 20 February 2023
149. Wu W, Yang Y-Q, Yang Y, Yang Y-M, Wang H, Zhang K-Y, Guo L, Ge H-F, Liu J, Feng H (2019) An organic nir-ii nanofluorophore with aggregation-induced emission characteristics for in vivo fluorescence imaging. *Int J Nanomed* 14:3571–3582. <https://doi.org/10.2147/IJN.S198587>
150. Xia L, Song X, Yan G, Quan J, Jin G (2022) Preparation and evaluation of la-peg-spion, a targeted mri contrast agent for liver cancer. *17:952–959*. <https://doi.org/10.1515/biol-2022-0074>
151. Xu CY, Inai R, Kotaki M, Ramakrishna S (2004) Aligned biodegradable nanofibrous structure: a potential scaffold for blood vessel engineering. *Biomaterials* 25:877–886. [https://doi.org/10.1016/s0142-9612\(03\)00593-3](https://doi.org/10.1016/s0142-9612(03)00593-3)

152. Yang D (2021) Application of nanotechnology in the COVID-19 pandemic. *Int J Nanomedicine* 16:623–649
153. Yang K, Feng L, Liu Z (2016) Stimuli responsive drug delivery systems based on nanographene for cancer therapy. *Adv Drug Deliv Rev* 105:228–241. <https://doi.org/10.1016/j.addr.2016.05.015>
154. Yetisgin AA, Cetinel S, Zuvin M, Kosar A, Kutlu O (2020) Therapeutic nanoparticles and their targeted delivery applications. *Molecules* 25:1–31. <https://doi.org/10.3390/molecules25092193>
155. Yoo J, Park C, Yi G, Lee D, Koo H (2019) Active targeting strategies using biological ligands for nanoparticle drug delivery systems. *Cancers (Basel)* 11:1–13. <https://doi.org/10.3390/cancers11050640>
156. Yu B-Y, Chou P-H, Sun Y-M, Lee Y-T, Young T-H (2006) Topological micropatterned membranes and its effect on the morphology and growth of human mesenchymal stem cells (hmscs). *J Membrane Sci* 273:31–37. <https://doi.org/10.1016/j.memsci.2005.10.012>
157. Zhang L, Webster TJ (2009) Nanotechnology and nanomaterials: promises for improved tissue regeneration. *Nano Today* 4:66–80. <https://doi.org/10.1016/j.nantod.2008.10.014>
158. Zhang Y, Yu J, Bomba HN, Zhu Y, Gu Z (2016) Mechanical force-triggered drug delivery. *Chem Rev* 116:12536–12563. <https://doi.org/10.1021/acs.chemrev.6b00369>
159. Zhang X-Q, Xu X, Bertrand N, Pridgen E, Swami A, Farokhzad OC (2012) Interactions of nanomaterials and biological systems: implications to personalized nanomedicine. *Adv Drug Deliv Rev* 64(13):1363–1384. <https://doi.org/10.1016/j.addr.2012.08.005>
160. Zhao CY, Cheng R, Yang Z, Tian ZM (2018) Nanotechnology for cancer therapy based on chemotherapy. *Molecules* 23:1–29. <https://doi.org/10.3390/molecules23040826>
161. Zheng X, Zhang P, Fu Z, Meng S, Dai L, Yang H (2021) Applications of nanomaterials in tissue engineering. *RSC Adv* 11:19041–19058. <https://doi.org/10.1039/D1RA01849C>
162. Zhou B, Yang J, Peng C, Zhu J, Tang Y, Zhu X, Shen M, Zhang G, Shi X (2016) Pegylated polyethylenimine-entrapped gold nanoparticles modified with folic acid for targeted tumor ct imaging. *Colloids Surf B: Biointerf* 140:489–496. <https://doi.org/10.1016/j.colsurfb.2016.01.019>
163. Zhou Q, Zhang L, Wu H (2017) Nanomaterials for cancer therapies. *Nanotechnol Rev* 6:473–496. <https://doi.org/10.1515/ntrev-2016-0102>

Chapter 3

Functionalized Carbon Nanotubes as Gene Carriers



Jih Ru Hwu, Shwu-Chen Tsay, Uttam Patil, Animesh Roy,
and Wen-Chieh Huang

Abstract This chapter covers discussion of the history on the development of carbon nanotubes (CNTs) and the updates on their modifications and applications as gene carriers. In the first part, it concentrates on the illustration of methods for graft of various functional groups and ligands on the surface of single- and multi-walled carbon nanotubes (i.e., SWCNTs and MWCNTs, respectively). Emphasis is placed on the types of bond formation during the functionalization of pristine CNTs. Many established ligands are presented. The second part concentrates on the discussion of interactions between functionalized CNTs (*f*-CNTs) with genes or oligonucleotides. These include electrostatic interaction, hydrogen bonding, π - π stacking, etc. The third part outlines the gene targets of *f*-CNTs. Factors associated with the design on the formation of hybrids of genes@*f*-CNTs and deploy of the genes from the hybrids are depicted. The entire strategy and practical methods for the hybrid formation and dissociation are the keys to the success on their applications to modern gene therapy.

Keywords Carbon nanotubes · Graft · Bond formation · Gene carrier · Interaction · Delivery

3.1 Introduction

Recent advancement in nanoscience and nanotechnology makes nanomaterials become more effective therapies than a standard intervention. Applications of nanomaterials in drug delivery, gene therapy, targeted therapeutics, and translational medicine are under rapid development [1, 2]. The discovery of carbon nanotubes (CNTs) in 1991 by Iijima [3] has expanded the horizons of carbon-based nanomaterials like fullerene, graphene, etc. The outstanding characteristics associated with CNTs include their electronic, thermal, optical, mechanical, and biological properties. Some CNTs can be taken up by different types of cells. Moreover, their ultrahigh

J. R. Hwu (✉) · S.-C. Tsay · U. Patil · A. Roy · W.-C. Huang
Department of Chemistry and Frontier Research Center on Fundamental and Applied Sciences of Matters, National Tsing Hua University, Hsinchu 300044, Taiwan
e-mail: jrhwu@mx.nthu.edu.tw

surface area can even reach up to $1700 \text{ m}^2/\text{g}$ [4], which allows CNTs to be an efficient carrier of cargo molecules. After being functionalized with suitable ligands on the surface, CNTs can exhibit a high degree of specificity toward the target cells and tissues [5, 6]. These diverse and flexible traits allow CNTs to be developed as a novel nanocarrier for drugs and genes [5].

There are three common types of CNTs on the basis of the number of graphene layers: single-walled carbon nanotubes (SWCNTs) with one single layer of graphene (0.80–1.2 nm wide), double-walled carbon nanotubes (DWCNTs) with two layers (1.0–2.0 nm wide), and multi-walled carbon nanotubes (MWCNTs) with multiple layers (5.0–50 nm wide). The length of CNTs can be various depending on their source and manufacturing process (100–300 nm) or unprocess (2–5 μM) [6]. SWCNTs and MWCNTs are the most commonly used CNTs and have been studied extensively. MWCNTs once were preferred over SWCNTs because of their high surface area [7]. Pristine CNTs (*p*-CNTs) have several drawbacks during their bio-applications, such as the lack of solubility in aqueous medium, poor dispersibility in most solvents, and, in particular, the intrinsic toxicity toward organs. Different degrees of toxicity come from their purity and length of the tubes. *p*-CNTs often cause harm to DNA and rupture the cell membrane [8]. Moreover, their hydrophobicity makes *p*-CNTs with limited applicability in terms of biocompatibility.

Solubility is the crucial aspect for the CNT-based gene-delivery system. Accordingly, surface modifications of *p*-CNTs are required and can be performed with deliberation. For example, modification with hydrophilic ligands can improve the water solubility and biocompatibility of functionalized CNTs (*f*-CNTs). Furthermore, a homogenous dispersion can be obtained and even well-dispersed in different solvents relying on the types of the introduced functional groups and the extent of functionalization on the *f*-CNTs [9]. The guideline is to maintain the ratio of hydrophobicity to hydrophilicity in the ligands and make the system well-dispersed in polar and/or non-polar solvents.

Size of *f*-CNTs is another important aspect for the development of efficient gene-delivery system. As the size, especially the length, of *f*-CNTs increases, the functional and available surface area exponentially decreases and thus becomes less reactive toward the surrounding biological components. Moreover, suitable modification on length and functional groups can reduce toxicity of *f*-CNTs.

In this review article, we first demonstrate a number of examples of functionalized SWCNTs (*f*-SWCNT) and MWCNTs (*f*-MWCNTs). Through modifications with covalently or non-covalently (e.g., π - π stacking) functional groups as illustrated in Fig. 3.1, *p*-CNTs possess anchoring sites on their surface.

Often these anchoring sites possess positive charge species to interact with negative charges of the genes or the neutral species, which can interact with the genes. The gene@*f*-CNT hybrids thus formed have the ability to cross the cell barrier and enter the cell membrane as shown in Fig. 3.2. Afterwards, these hybrids release the gene and the *f*-CNTs, which are excreted by exocytosis. The usage of *f*-CNTs as a carrier vehicle requires efficient delivery system to transport the gene or DNA to their action within the cell. At the same time, the effective liberation of the gene is also crucial.

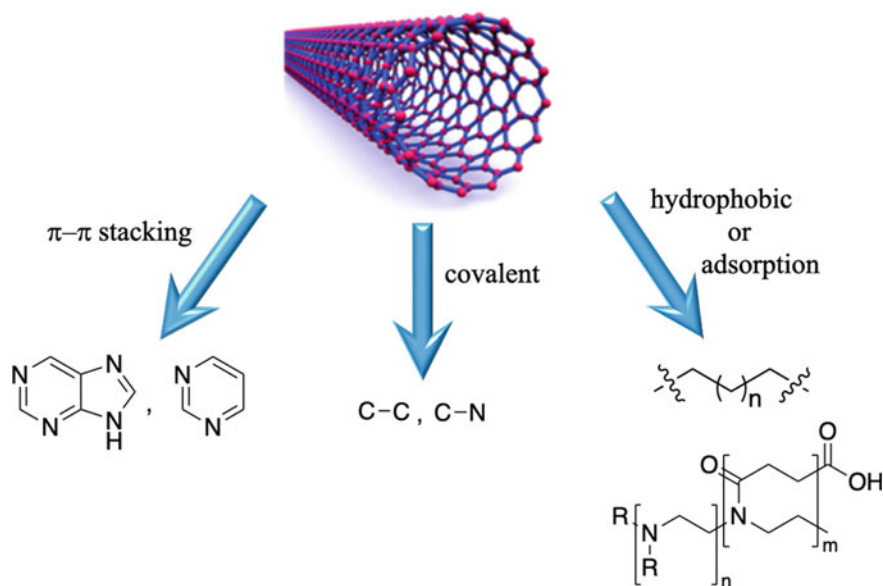


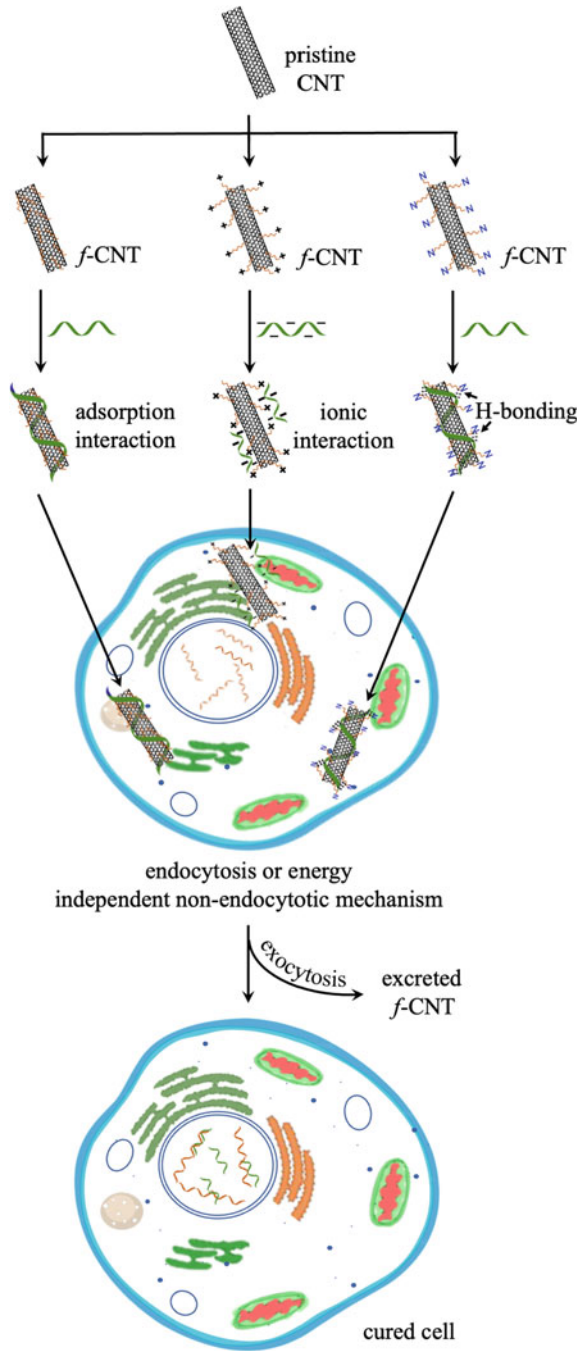
Fig. 3.1 Interface between the nanotubes and ligands

Various types of interaction between the *f*-CNTs and the gene are discussed in the second part of this review article. They include electrostatic interaction, ionic interaction, hydrogen bonding, covalent bond, π - π stacking, etc. Finally, the delivered gene inside the cell membrane interacts with the complimentary gene in the nucleus of the cell, which leads to the cure of the cell. Several therapeutic applications of *f*-CNTs to anti-cancer, gene therapy, and other applications are included in the third part.

3.2 Functionalization of CNTs

Functionalized carbon nanotubes (*f*-CNTs) are valuable nanomaterials for biomedical applications. Pristine CNTs exist in the form of bundles through π - π stacking [10]. The high lateral interaction among the *p*-CNTs is responsible for their low solubility and dispersibility. One of the major concerns of *p*-CNTs to be applied in biomedical systems is their toxicity toward organs by incurring harmful effects, such as inflammatory and fibrotic reactions, and even leading to cell death [5, 7]. Modification of the surface of *p*-CNTs not only provides a solution to this enigma but also advances these materials as gene carriers. Some bio-functionalized CNT composites [5] can reach the nuclei without being cytotoxic, cross cell membranes, and accumulate in the cytoplasm [5, 11, 12]. Thus new functionalization methods have been developed continuously in order to improve solubility and biocompatibility of CNTs.

Fig. 3.2 A representative diagram for the *f*-CNTs as delivery vehicles for therapeutic applications



Covalent and non-covalent functionalization are the major approaches to introduce different functional groups. The covalent method is based on the chemical modification on CNTs sidewalls or ends or both to create a new anchoring site. Chemical transformation generates a new reactive moiety; the resultant *f*-CNTs can be used for further modifications. The non-covalent functionalization occurs on the basis of π - π and other physical interactions.

3.2.1 Covalent Functionalization

A direct method of modification on the surface of sp^2 -hybridized carbons of CNTs is covalent functionalization. It generates strong covalent bonding between CNTs and coupling agents. As it alters the state of bond connectivity, the degree of functionalization can be easily assessed by Raman spectroscopy due to the formation of sp^3 -hybridized carbons [13, 14].

In general, the choices of chemical bonds formation are quite limited to the formation of C-C and C-N bonds [15]. Nevertheless, the properties can be improved by modifications of the ligands attached further with biomolecules, such as aptamer, siRNA, ssDNA, and dsDNA, for efficient gene-delivery vehicle application [16, 17]. One method is introduction of multiple $-NH_2$ groups [16, 18–20], which can be easily protonated to give positively charged groups over the CNT surface. The cationic species aids their water solubility. MWCNTs can be covalently functionalized with ligands containing terminal $-OH$ groups for increment of their dispersion properties [17, 21]. Another covalent functionalization strategy is plant of hydrophobic and hydrophilic functional moieties on the surface of the CNTs. Such bi-functional approach brings the benefits by the suspension of CNTs in various solvents [22, 23]. Recently, Song et al. [24] reported their results on functionalization of SWCNT with hydroxyl, amino, and carboxyl groups as well as polyethylene glycol. These functionalized nanotubes enhance the dispersive properties of poorly soluble curcumin in water. Singh, Mamtamin, Bianco, and their co-workers [25–27] used purines and pyrimidines as molecular frameworks to incorporate with SWCNT for biocompatibility.

3.2.2 Non-Covalent Functionalization

Non-covalent functionalization occurs mainly due to hydrophobic adsorption, van der Waals force, or π - π stacking interactions between the CNT surface and the functionalization species [23]. It is on the basis of the attachment or wrapping of hydrophobic surfactants onto the hydrophobic surface. Polyethylenimine (PEI) or its modified derivatives [28], 1,2-dioleoyl-3-trimethylammonium-propane [29], PEGylated phospholipids [30, 31], and polyamidoamine dendrimer [32] have been

used to functionalize the CNTs. Other related advanced methods include the utilization of complex proteins, enzymes, antigens, and antibodies to interact with the SWCNT [32] as shown in Tables 3.1 and 3.2. Suitably modified SWCNTs exhibit biocompatibility, non-immunogenic, and photo luminescent caliber [22, 33, 34]. The resultant *f*-SWCNTs become more dispersible [35] or highly biocompatible [36] in aqueous media and organic solvents. These properties display their potential as clinical nano-carriers for drug delivery and imaging.

3.3 Interaction of *p*-CNTs and *f*-CNTs with Genes or Aptamers

The CNTs have a length from hundreds of nanometers to several micrometers. Homma et al. [56] studied the adsorption of DNA directly on the surface of SWCNT and investigated the intrinsic effects of DNA on the transition of SWCNT. Wang et al. [35] reported the cellular uptake of SWCNT–DNA conjugates, which are localized in the nuclei of microvascular ECs. The DNA-coated *p*-CNTs show permeability through the cell membrane [57]. These hybrids become a suitable material to be fabricated as a delivery vehicle for gene therapy [58]. Munk and co-workers [59] used bovine embryo to study the possibility for pristine MWCNTs to pass through the pellucid zone barrier. This animal model shows its similarity with a human embryo.

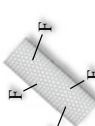
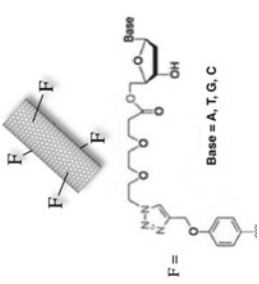
In advanced approaches, some gene@*f*-CNT hybrids are stable to sustain the enzymic environment so that the hybrids can transport the gene to the target area. Besides the successful delivery, detachment of the gene from the surface of *f*-CNT is equally important as its attachment. The release of a gene could be get triggered under physiological conditions. The pH of the medium and temperature are the two main parameters that define the physiological conditions. Being an ideal carrier, the *f*-CNT can be attached by a gene under certain conditions.

Moreover, once the conditions change, the gene is released. The hybrid formation is thus reversible. Interaction between the gene and the carrier must be strong enough to carry the gene; meanwhile, the gene can be deployed from the hybrid under different conditions. These are essential aspects for the development of efficient gene-delivery vehicles. For application of this strategy in a biological system, understanding of the interaction between the *f*-CNT and the gene is crucial.

3.3.1 *Electrostatic Interaction*

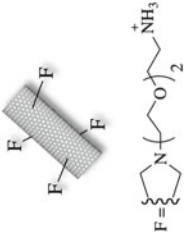
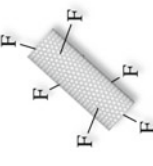
Electrostatic repulsion between the positive charges on the functional groups of *f*-CNTs prevents the nanotubes from aggregation. It makes *f*-CNTs available to interact with the negatively charged genes due to ionic interactions. Accordingly,

Table 3.1 Functionalized SWCNTs as a gene carrier and their applications: a summary of representative types of functionalization carried out on SWCNTs by various interactions between the surface and the functionalization species along with the genes aimed to a particular target

| Grafted nanotubes | Mode of attachment | Gene or aptamer | Interaction between tube and aptamer | Application |
|--|--------------------|--|--------------------------------------|----------------------------------|
|  <p>F = -CONH-PEI + SFU</p> | Covalent bond | aptamer-siRNA chimeras: 5'-GGTGGTGGTGGTTGTGGTGGTGGAA-GCTGTTGACTGGAAGAACAUU-3' | Electrostatic interaction | Treatment of gastric cancer [37] |
|  <p>F =</p> | Covalent bond | ssDNA: 5'-TCGAGTACGTCCCGTCCAGCTCGA-3' | H-bonding | Potential for gene therapy [22] |

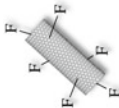
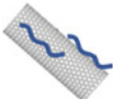
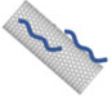
(continued)

Table 3.1 (continued)

| Grafted nanotubes | Mode of attachment | Gene or aptamer | Interaction between tube and aptamer | Application |
|--|----------------------|--|---|--------------------------------------|
|  <p style="text-align: center;">F = -CONH-PEI-NHCO-piperazine</p> | <p>Covalent bond</p> | <p>DNA oligonucleotide sequences:</p> <p>5'-Cy3-TAGTGTGACGAAAGGGAC-(CH₂)₃-S-(CH₂)₂-CH₃-3'</p> <p>5'-TAGTGTGACGAAAGGGAC-(O)-(CH₂)₆-NH₂-3'</p> <p>5'-TAGTGTGACGAAAGGGAC-(O)-(CH₂)₆-VT680-3'</p> <p>5'-GTCCTTCGTCAACACTA-(O)-(CH₂)₆-NH₂-3'</p> <p>5'-GTCCCTTCGTCAACACTA-(O)-(CH₂)₆-VT750-3'</p> <p>RNA oligonucleotide sequences:</p> <p>5'-GUCCCUUCGUCAACACUA-(CH₂)₆-NH₂-3'</p> <p>5'-UAGUGUUGACGAAAGGGAC-(CH₂)₆-NH₂-3'</p> <p>5'-UAGUGUUGACGAAAGGGAC-(CH₂)₆-VT680-3'</p> <p>5'-Cy3-AAAAAAAAAAAAAAAAA-3'</p> <p>5'-UUUUUUUUUUUUUUUUU-(CH₂)₆-NH₂-3'</p> | <p>Electrostatic interaction, H-bonding, and π-π stacking</p> | <p>Vectors for gene therapy [16]</p> |
|  <p style="text-align: center;">F = -CONH-PEI-NHCO-piperazine</p> | <p>Covalent bond</p> | <p>BCL9] siRNA: 5'-GGAUGUUCAGAAGUCCCAUGGAGCTC-3'</p> | <p>Electrostatic interaction</p> | <p>Targeting breast cancer [38]</p> |

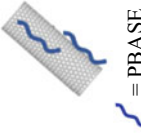
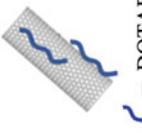
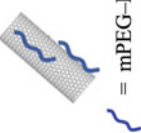
(continued)

Table 3.1 (continued)

| Grafted nanotubes | Mode of attachment | Gene or aptamer | Interaction between tube and aptamer | Application |
|--|---|--|--------------------------------------|---|
|  $F = -CONH-PEG-CONH-PEI_n-CONH-CONH-CONH-CONH-$ | Covalent bond | Bcl-xI shRNA: 5'-CTCACTCTTCAGTCGGAAATGACCAGACA-3' | Electrostatic interaction | Targeting breast cancer [39] |
|  $= CH_3(CH_2)_n-PEI$ $n = 9 \text{ or } 17$ | Hydrophobic interaction | plasmid DNA: <i>Renilla</i> sp. luciferase gene | Electrostatic interaction | In vivo gene delivery [28] |
|  $= \text{peptide lipid (PL)} + \text{sucrose laurate (SL)}$ | Hydrophobic interaction and van der Waals | anti-survivin siRNA: 5'-CACCCGAUCUCUACAUCATT-3' | Electrostatic interaction | Suppression of survivin expression in cancer cells [40] |

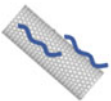

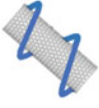


(continued)

Table 3.1 (continued)

| Grafted nanotubes | Mode of attachment | Gene or aptamer | Interaction between tube and aptamer | Application |
|--|--------------------------|---|--------------------------------------|--|
|  = PBASE | Hydrophobic interaction | adenosine aptamers: 5'-NH ₂ -ACCTGGGGGAGTATT- GCGGAGGAAGGT-3' (27-mer) 5'-NH ₂ -AAAAAAAAAACCTGGG- GGACTATTGCGGAGGAAGG-3' (35-mer) | Covalent | targeting adenosine in cancer immunotherapy [41] |
|  = DOTAP | Hydrophobic interaction | hTERT siRNA: 5'-CAGUGCGGUCACCCGUGTT-3' | Electrostatic interaction | Cancer therapy [42] |
|  = mPEG-DSPE + PAH | Hydrophobic interactions | K-Ras siRNA-FAM: 5'-FAM-CUACGCCAUCAGCUCCAACUU-3' | Electrostatic interaction | Pancreatic cancer [30] |

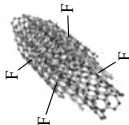
(continued)

Table 3.1 (continued)

| Grafted nanotubes | Mode of attachment | Gene or aptamer | Interaction between tube and aptamer | Application |
|--|--|--|--------------------------------------|--|
|   | Hydrophobic interactions | Braf siRNA: 5'-GCUUACUGGAGAGGAGUUACA-3' | Electrostatic interaction | Melanoma [43] |
|   | π - π stacking | ssDNA: 5'-(GCG) ₅ -GAAGTGCTCGAATCCAC-CACGAACAATTC-3' 5'-(TAT) ₅ -GAAGTGCTCGAATCCAC-CACGAACAATTC-3' 5'-CAGTGACGGCAATTT-GAAGTGCT-CGAATCCACCACGAACAATTC-3' | π - π stacking | Renal interstitial fibrosis [36] |
|  | Direct attachment without modification | ssDNA-FITC: 5'-FITC-CCTGAGCCATGATCAACCTGTGCAGT-3' | π - π stacking | Uptake by microvascular endothelial cells [35] |

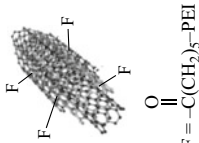
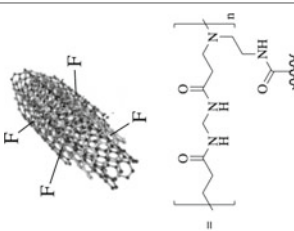
Abbreviations: PEI (polyethylenimine); 5-FU (5-fluorouracil); PBASE (1-pyrenebutanoic acid succinimide ester); PEG [poly(ethylene glycol)]; DOTAP (1,2-dioleoyl-3-trimethylammonium propane); DSPE (1,2-distearoyl-sn-glycero-3-phosphorylethanolamine); PAH [poly(allylamine hydrochloride)]; FAM (fluorescein amidite)

Table 3.2 Various grafted MWCNTs as a gene carrier and their applications

| Grafted nanotubes | Diameter | Length | Mode of attachment | Gene or aptamer | Interaction between tube and aptamer | Application |
|--|----------|--------|--------------------|---|--------------------------------------|---------------------------------|
|  <p>F = -COOH</p> | N. A. | N. A. | Covalent | 5'-NH ₂ -TCGTATGGCACGGGGTTGGTGTGGGTGG-3' | Covalent | Aneurysm detection [44] |
|  <p>F = -COOH</p> | 10–40 nm | 600 nm | Covalent | Apt3: 5'-TCGCGCGAGTCTGCTGGGGAACC ATCGAGTTACACCGACCTTCTATG TGGGGCC CCCCCGATCGTCTCC-3' | π - π stacking | Tumor cells targeting [45] |
|  <p>F = -pyridine</p> | < 100 nm | N. A. | Covalent | iC9: 5'-ATTCTCGAGACCATGGGAGTGCAGGTG-3' | π - π stacking | Treatment of breast cancer [46] |

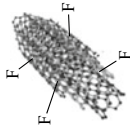
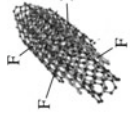
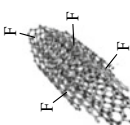
(continued)

Table 3.2 (continued)

| Grafted nanotubes | Diameter | Length | Mode of attachment | Gene or aptamer | Interaction between tube and aptamer | Application |
|--|----------|---------------------------|--------------------|-----------------|--------------------------------------|--|
|  <p style="text-align: center;">$F = -C(CH_2)_5-PEI$</p> | N. A. | 78 nm, 115 nm, and 211 nm | Covalent | Plasmid DNA | Electrostatic interaction | Vector for gene delivery [10] |
|  | 30–40 nm | 300 nm | Covalent | Plasmid DNA | Electrostatic interaction | Gene delivery into HeLa and COS-7 cells [47] |


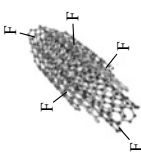
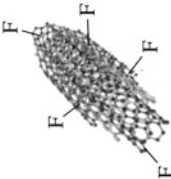
(continued)

Table 3.2 (continued)

| Grafted nanotubes | Diameter | Length | Mode of attachment | Gene or aptamer | Interaction between tube and aptamer | Application |
|--|----------|------------|--------------------|---|--------------------------------------|---|
|  F = -CONH-PEG-COOH | 15 nm | 400 nm | Covalent | 5'-NH ₂ -GGGAGGACGAUGCGGAGCAGCCAUUUUACGUCACUCCU-3' | Covalent | Diagnosis of prostate cancer [48] |
|  F = -O(C=O)-polymer-ammonium cationic | 20–30 nm | 0.5–2.0 μm | Covalent | siRNA (siNEG): 5'-CAUCGUGGAUCGUAGGGCAA-3' | Electrostatic interaction | Cancer immunotherapy [49] |
|  F = -COOH | 25 nm | 200 nm | Covalent | AmCyan I DNA: 5'-AGGTGTGGAACTGGCATCTGTA-3' | Electrostatic interaction | Gene delivery (in vitro) to Nile tilapia spermatogonial stem cells [50] |

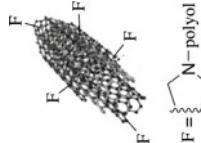
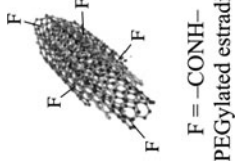
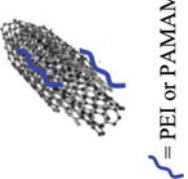
(continued)

Table 3.2 (continued)

| Grafted nanotubes | Diameter | Length | Mode of attachment | Gene or aptamer | Interaction between tube and aptamer | Application |
|--|----------|-----------------------|--|-----------------|--------------------------------------|--|
|  | 40 nm | < 0.6 μm | Direct attachment without modification | Plasmid DNA | π - π stacking | Gene delivery into <i>E. coli</i> cells [51] |
|  F = -CONH-PEI | N. A. | N. A. | Covalent | Plasmid DNA | Electrostatic interaction | Mesenchymal stem cells [52] |
|  F = -CONH-PEI | 20-40 nm | 0.5-2.0 μm | Covalent | Plasmid DNA | Electrostatic interaction | Human lung carcinoma [12] |

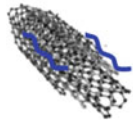
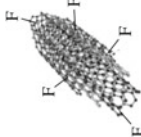
(continued)

Table 3.2 (continued)

| Grafted nanotubes | Diameter | Length | Mode of attachment | Gene or aptamer | Interaction between tube and aptamer | Application |
|--|----------|-------------|-------------------------|--|--------------------------------------|--|
|  <p>F = N-polyol</p> | 11 nm | 980 nm | Covalent | CS-ODN: 5'-ACGCTGCCGCCACACACCA-3' AS-ODN: 5'-TGGTGTGGTGGCCGACGCCGT-3' | Electrostatic interaction | Bladder carcinoma [17] |
|  <p>F = -CONH-PEGylated estradiol</p> | 20–30 nm | 1–5 μ m | Covalent | Plasmid DNA | π - π stacking and wrapping | Gene-delivery vector for MCF-7 and HeLa cells [53] |
|  <p>= PEI or PAMAM</p> | 20–40 nm | 200–1200 nm | Hydrophobic interaction | Pre-miR-503: 5'-TACCCTGGCAGCGGAAACAA-3' | Electrostatic interaction | Gene delivery into HUVEC cells [54] |

(continued)

Table 3.2 (continued)

| Grafted nanotubes | Diameter | Length | Mode of attachment | Gene or aptamer | Interaction between tube and aptamer | Application |
|--|----------|-----------------------|-------------------------|---|---|---|
|  <p>= peptide lipid (PL) + sucrose laurate (SL)</p> | 10 nm | 0.5–2.0 μm | Hydrophobic interaction | Anti-survivin siRNA: 5'-CACCGCAUCCUACAUCATT-3' | Electrostatic interaction | suppression of survivin expression in cancer cells [40] |
|  <p>F = -COOH + sorafenib</p> | N. A. | N. A. | Covalent | siRNA targeted to EFGR gene: 5'-GUGUGUAACGGAAUAGGUATT-3' | H-bonding and electrostatic interaction | Gene therapy for liver cancer [55] |

Abbreviation: PEG (polyethyleneglycol); PEI (polyethylenimine); PAMAM (polyamidoamine dendrimer)

the electrostatic interaction induces the formation of a hybrid [16, 30, 42]. Variation in parameters, such as pH and temperature, can release the gene from the hybrid by neutralizing the ionic interaction. Surface area and the charge density on the nanotubes are also critical parameters that determine the interaction between *f*-CNTs and genes. Nonetheless, larger surface area and higher charge density leading to efficient ionic interaction are not necessary for effective gene delivery. It is due to the factor that the detachment of the genes should also be taken into consideration. McDevitt et al. [16] used ammonium-*f*-CNTs as DNA and RNA delivery vehicles. The assembly of ammonium-*f*-CNTs and oligonucleotide species involves primarily electrostatic and hydrogen bonding interactions as well as to a less extent of π - π stacking forces.

3.3.2 Hydrogen Bonding

Hwu and co-workers [22] used H-bonding interaction as an efficient way to form the DNA@*f*-SWCNT complex to facilitate gene delivery. Nucleobase-functionalized SWCNT interacts with the nucleobases of DNA through H-bonding to form a pseudo duplex hybrid. The H-bonds being susceptible to variation in pH and temperature offers the possibility for the DNA to be released to the target site.

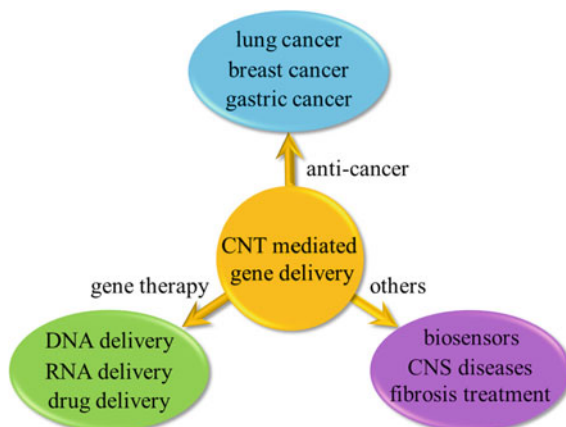
3.3.3 π - π Stacking

The *p*-CNT are used as a gene carrier. The π electrons of the aromatic purine and pyrimidine nucleobases in DNA interact with the π electrons of the CNT surface to form π - π stacking. These gene@*p*-CNT conjugates are stable enough under physiological conditions for gene delivery [36]. Wang et al. [35] observed that pristine SWCNT-DNA conjugate labelled with FITC fluorophore enters the nuclei of microvascular endothelial cells of rat skeletal muscles. Xing and Qiu et al. [36] proved that the conjugates formed by different secondary structures of ssDNA with SWCNTs have different binding affinities and show different permeability through cell barriers. Nevertheless, difficulty in release of the gene is the main drawback due to the strong π - π stacking interactions.

3.4 Gene Targets of *f*-CNTs

Mutation of a gene or a set of genes is the main cause of most diseases known to mankind [60]. A unique technique to correct these mutations gains much attention from the research community worldwide. Ever since the article by Friedmann and Roblin [61] stated “*that exogenous good DNA be used to replace the defective DNA*

Fig. 3.3 Applications of CNT mediated gene delivery



in those who suffer from genetic defects ...” gives birth to a unique technique called “gene therapy.” This technique involves treatment of acquired as well as inherited diseases. Either through transplant of the absent genes or through substitution of the mutated genes by healthy ones [62], a transport system or vector is required. The transporter or vector has to be efficient enough to carry and deliver the gene to the target cell nucleus without being affected under the physiological conditions. Viral and non-viral vectors are used to fulfil the requirement of the transportation.

Viral vectors are more effective compared with the non-viral vectors, but also possess a high risk to the patients’ life due to their immunogenicity and cytotoxicity. On the other hand, non-viral vectors are less immunogenic and have simple and versatile methods for their preparation [63]. Variable ratios of length-to-diameter and the large surface area of CNTs act as a template for chemical functionalization. These factors also increase their biocompatibility to make them as suitable non-viral vectors [33]. Nowadays, CNTs has been widely studied for applications to nanomedicine, including anti-cancer, gene therapy, biosensors, central nervous system (CNS) diseases, fibrosis treatment, etc. (see Fig. 3.3).

3.4.1 Anti-Cancer

Applications of CNTs for anti-cancer are explored extensively. The CNTs are grafted by diverse anti-cancer drugs, nucleobases, or polymers, which are attached covalently or non-covalently to the *p*-CNT surface. SWCNT–PEI–siRNA vector is used for efficient siRNA delivery to breast cancer cells [38, 39, 46]. For inhibition of the growth of nucleolin-abundant gastric cancer cells, CNT-based nanoplatform with high cell selectivity and exceptional anti-tumour activity is developed [37]. Yong et al. [30] used an SWCNT-based nanocarrier for gene delivery into pancreatic cancer cells. Among the macromolecules, oligonucleotides are the potential candidates for CNT

functionalization as these oligonucleotides can sense specifically the target of interest [15, 44]. Kaufmann and co-workers [17] identified MWCNT-*f*-OH as a promising carrier, which is able to transport and release antisense oligodeoxynucleotide inside bladder cells. They used a carrier strand oligodeoxynucleotide adsorbed to MWCNT-*f*-OH followed by hybridization with a therapeutic antisense oligodeoxynucleotide. Nevertheless, it is impractically applied to *p*-MWCNTs due to their poor dispersion properties.

3.4.2 Gene Delivery

The ability to deliver nucleic acids by plasmid DNA, antisense oligonucleotides, siRNA, etc. is under vigorous studies [64]. It offers potential to develop potent vaccines and novel therapeutics to cure diseases that cannot be remedied by traditional therapies. Gene delivery becomes a favourable approach for the treatment of irredeemable diseases, either assimilated or genetic. Nonetheless, there are many challenges to overcome. The requirements of being an effective gene carrier involve the capability to have reduced side effects, to enter the cell membrane, and to deliver the gene selectively at their target sites. The key to success is to increase the local density of a drug inside the target cell. Moreover, an efficient gene-delivery vehicle can protect and carry the transgene to the target cells.

The *f*-CNTs possess great potential towards gene delivery for animal and plant cells. Ramezani et al. [28] developed vectors by using a condensation method to functionalize MWCNTs. Resende et al. [50] provided evidence of in vitro gene delivery into the Nile tilapia spermatogonial stem cells. Wang et al. [65] applied the DNA–MWCNT delivery vehicle for controlling infectious disease in the aquaculture industry. Kostarelos et al. [66] used dendron–MWCNT to silence genes efficiently. They provide evidence of delivering siRNA in the cytoplasm [66].

3.4.3 Other Applications

The assorted characteristics associated with the surface of *f*-CNT broaden the applications in tissue engineering, bio-sensing, bio-imaging, and drug delivery [6, 41]. Advances in CNTs-based nano devices lead to a significant breakthrough in detection of macromolecules like DNA and proteins. McDevitt et al. [16], Ramezani et al. [28], and our group [22] independently developed gene-delivery vehicles that can be used for diverse DNAs to form hybrids. They can be used as vectors for targeted gene therapy. Furthermore, Wang, Harvey, and their co-workers [35] discovered gene-delivery vehicles, which can be applied to renal interstitial fibrosis treatment. Uptake by microvascular endothelial cells is also possible. Porterfield et al. [67] reported the application of SWCNT hybrids with ssDNA. The outcomes are beneficial to the development of new micro biosensors.

3.5 Summary

This review article aims to highlight the unique properties of various types of CNTs as gene-delivery vehicles. Solubility of the *p*-CNT can be enhanced through grafting with proper functional groups that can interact with various solvents and help the CNTs to be soluble and dispersible. Furthermore, biocompatibility can be improved by optimization of surface modifications. Some *f*-CNT-gene hybrids are stable towards the enzymic environment and carry the genes into the specific targets with success. Variations in pH and temperature are controllable in order to offload the gene from the hybrid. High loading of genetic cargos, stability outside the target tissues or cells, ability to protect the gene against enzymic degradation, intracellular release of the gene, controllable gene expression, and minimization of cytotoxicity are hot topics to the research. The results will enrich the role of CNTs in nanomedicine. This review article shows high potential of grafted CNTs as gene carriers.

3.6 Further Reading

For a nice and comprehensive review of carbon nanotubes as drug- and gene-delivery carriers published in 2021 [33]. This paper concentrates on the discussion of CNT's cellular uptakes through different mechanisms, phototherapy, toxicology, environmental effects, in vivo and in vitro applications on infectious diseases. There are 50 references cited in the Tables 1–6 therein. None of those references are listed in the two tables of this review article, which concentrates on discussions of design and functionalization of CNTs by various chemical methods and the interaction of resultant *f*-CNTs with genes or aptamers.

Acknowledgements This research was funded by Ministry of Education, Taiwan, R.O.C. grant number 111QR00115 and 110QR00115, National Science and Technology Council (NSTC), Taiwan, R.O.C. grant number 111-2634-F-007-023 and 111-2113-M-007-027. We extend our gratitude to the NSTC in Taiwan for its support of The Featured Areas Research Centre Program within the framework of the Higher Education Sprout Project through the Frontier Research Centre on Fundamental and Applied Sciences of Matters.

References

1. Ibraheem D, Elaissari A, Fessi H (2014) Gene therapy and DNA delivery systems. *Int J Pharm* 459:70–83
2. McDevitt MR, Scheinberg DA (2014) Fibrillous carbon nanotube: an unexpected journey. *Crit Rev Oncog* 19:261–268
3. Iijima S (1991) Helical microtubules of graphitic carbon. *Nature* 354:56–58
4. Merum S, Veluru JB, Seeram R (2017) Functionalized carbon nanotubes in bio-world: applications, limitations and future directions. *Mater Sci Eng B* 223:43–63

5. Karimi M, Solati N, Ghasemi A, Estiar MA, Hashemkhani M, Kiani P, Mohamed E, Saeidi A, Taheri M, Avci P, Aref AR, Amiri M, Baniyasi F, Hamblin MR (2015) Carbon nanotubes part II: a remarkable carrier for drug and gene delivery. *Expert Opin Drug Deliv* 12:1089–1105
6. Kotagiri N, Kim JW (2014) Stealth nanotubes: strategies of shielding carbon nanotubes to evade opsonization and improve biodistribution. *Int J Nanomedicine* 9:85–105
7. Madani SY, Mandel A, Seifalian AMA (2013) Concise review of carbon nanotube's toxicology. *Nano Rev* 4:21521 and references cited therein
8. Höfingler S, Melle-Franco M, Gallo T, Cantelli A, Calvaresi M, Gomes JANF, Zerbetto F (2011) A computational analysis of the insertion of carbon nanotubes into cellular membranes. *Biomaterials* 32:7079–7085
9. Benko A, Duch J, Gajewska M, Marzec M, Bernasik A, Nocuń M, Piskorz W, Kotarba A (2021) Covalently bonded surface functional groups on carbon nanotubes: from molecular modeling to practical applications. *Nanoscale* 13:10152–10166
10. Nia AH, Amini A, Taghavi S, Eshghi H, Abnous K, Ramezani M (2016) A facile Friedel-Crafts acylation for the synthesis of polyethylenimine-grafted multi-walled carbon nanotubes as efficient gene delivery vectors. *Int J Pharm* 502:125–137
11. Eivazi Zadeh Z, Solouk A, Shafieian M, Haghbin Nazarpak M (2021) Electrospun polyurethane/carbon nanotube composites with different amounts of carbon nanotubes and almost the same fiber diameter for biomedical applications. *Mater Sci Eng C* 118:111403
12. Nunes A, Amsharov N, Guo C, Van den Bossche J, Santhosh P, Karachalios TK, Nitodas SF, Burghard M, Kostarelos K, Al-Jamal KT (2010) Hybrid polymer-grafted multiwalled carbon nanotubes for in vitro gene delivery. *Small* 6:2281–2291
13. Rebelo SL, Guedes A, Szcfczyk ME, Pereira AM, Araújo JP, Freire C (2016) Progress in the Raman spectra analysis of covalently functionalized multiwalled carbon nanotubes: unraveling disorder in graphitic materials. *Phys Chem Chem Phys* 18:12784–12796
14. Graupner R (2007) Raman spectroscopy of covalently functionalized single-wall carbon nanotubes. *J Raman Spectrosc* 38:673–683
15. Hirsch A, Vostrowsky O (2005) Functionalization of carbon nanotubes. In: Schlüter AD (ed) *Functional molecular nanostructures*. Springer Berlin, Heidelberg, p 193–237
16. Alidori S, Asqiriba K, Londero P, Bergkvist M, Leona M, Scheinberg DA, McDevitt MR (2013) Deploying RNA and DNA with functionalized carbon nanotubes. *J Phys Chem C* 117:5982–5992
17. Kaufmann A, Kunhardt D, Cirillo G, Hampel S, Schwenzer B (2014) Functionalized carbon nanotubes as transporters for antisense oligodeoxynucleotides. *J Mater Chem B* 2:7000–7008
18. Ramanathan T, Fisher FT, Ruoff RS, Brinson LC (2005) Amino-functionalized carbon nanotubes for binding to polymers and biological systems. *Chem Mater* 17:1290–1295
19. Shen J, Huang W, Wu L, Hu Y, Ye, M (2007) Study on amino-functionalized multiwalled carbon nanotubes. *Mater Sci Eng A* 464:151–156
20. Wang Y, Iqbal Z, Malhotra SV (2005) Functionalization of carbon nanotubes with amines and enzymes. *Chem Phys Lett* 402:96–101
21. Redondo-Gómez C, Orozco F, Michael Noeske P-L, Soto-Tellini V, Corrales-Ureña YR, Vega-Baudrit J (2017) Cholic acid covalently bound to multi-walled carbon nanotubes: Improvements on dispersion stability. *Mater Chem Phys* 200:331–341
22. Hwu JR, Kapoor M, Li R-Y, Lin Y-C, Horng J-C, Tsay S-C (2014) Synthesis of nucleobase-functionalized carbon nanotubes and their hybridization with single-stranded DNA. *Chem Asian J* 9:3408–3412
23. Premkumar T, Mezzenga R, Geckeler KE (2012) Carbon nanotubes in the liquid phase: addressing the issue of dispersion. *Small* 8:1299–1313
24. Yuan S, Zeng L, Zhuang Y, Hou Q, Song M (2016) Functionalized single-walled carbon nanotubes for the improved solubilization and delivery of curcumin. *Fuller Nanotub Carbon Nanostructures* 24:13–19
25. Singh P, Ménard-Moyon C, Battigelli A, Toma FM, Raya J, Kumar J, Nidamanuri N, Verma S, Bianco A (2013) Double functionalization of carbon nanotubes with purine and pyrimidine derivatives. *Chem Asian J* 8:1472–1481

26. Sidik S, Mamtimin X (2014) Supramolecular functionalization of single-walled carbon nanotubes with poly(2,5-dihexyl-1,4-phenylene-alt-2-amino-4,6-pyrimidine) and their electrochemical performance. *J Mater Sci Res* 29:2634–2643
27. Sureshbabu AR, Kurapati R, Russier J, Ménard-Moyon C, Bartolini I, Meneghetti M, Kostarelos K, Bianco A (2015) Degradation-by-design: surface modification with functional substrates that enhance the enzymatic degradation of carbon nanotubes. *Biomaterials* 72:20–28
28. Behnam B, Shier WT, Nia AH, Abnous K, Ramezani M (2013) Non-covalent functionalization of single-walled carbon nanotubes with modified polyethyleneimines for efficient gene delivery. *Int J Pharm* 454:204–215
29. Pereira S, Lee J, Rubio N, Hassan HA, Suffian IB, Wang JT, Klippstein R, Ballesteros B, Al-Jamal WT, Al-Jamal KT (2015) Cationic liposome-multi-walled carbon nanotubes hybrids for dual siPLK1 and doxorubicin delivery in vitro. *Pharm Res* 32:3293–3308
30. Anderson T, Hu R, Yang C, Yoon HS, Yong KT (2014) Pancreatic cancer gene therapy using an siRNA-functionalized single walled carbon nanotubes (SWNTs) nanoplex. *Biomater Sci* 2:1244–1253
31. Hadidi N, Kobarfard F, Nafissi-Varcheh N, Aboofazeli R (2013) PEGylated single-walled carbon nanotubes as nanocarriers for cyclosporin A delivery. *AAPS PharmSciTech* 14:593–600
32. Yang K, Qin W, Tang H, Tan L, Xie Q, Ma M, Zhang Y, Yao S (2011) Polyamidoamine dendrimer-functionalized carbon nanotubes-mediated GFP gene transfection for HeLa cells: effects of different types of carbon nanotubes. *J Biomed Mater Res A* 2011 99:231–239
33. Zare H, Ahmadi S, Ghasemi A, Ghanbari M, Rabiee N, Bagherzadeh M, Karimi M, Webster TJ, Hamblin MR, Mostafavi E (2021) Carbon nanotubes: smart drug/gene delivery carriers. *Int J Nanomedicine* 16:1681–1706
34. Jena PV, Shamay Y, Shah J, Roxbury D, Paknejad N, Heller DA (2016) Photoluminescent carbon nanotubes interrogate the permeability of multicellular tumor spheroids. *Carbon* 97:99–109
35. Harvey J, Dong L, Kim K, Hayden J, Wang J (2012) Uptake of single-walled carbon nanotubes conjugated with DNA by microvascular endothelial cells. *J Nanotechnol* 2012:196189
36. Wang G, Zhao T, Wang L, Hu B, Darabi A, Lin J, Xing MM, Qiu X (2015) Studying different binding and intracellular delivery efficiency of ssDNA single-walled carbon nanotubes and their effects on LC3-related autophagy in renal mesangial cells via miRNA-382. *ACS Appl Mater Interfaces* 7:25733–25740
37. Chen W, Yang S, Wei X, Yang Z, Liu D, Pu X, He S, Zhang, Y (2020) Construction of aptamer-siRNA chimera/pei/5-fu/carbon nanotube/collagen membranes for the treatment of peritoneal dissemination of drug-resistant gastric cancer. *Adv Healthc Mater* 9:2001153
38. Mohammadia M, Salmasi Z, Hashemi M, Mosaffa F, Abnous K, Ramezani M (2015) Single-walled carbon nanotubes functionalized with aptamer and piperazine–polyethylenimine derivative for targeted siRNA delivery into breast cancer cells. *Int J Pharm* 485:50–60
39. Taghavia S, Nia AH, Mosaffa F, Askarian S, Abnous K, Ramezani M (2016) Preparation and evaluation of polyethylenimine-functionalized carbon nanotubes tagged with 5TR1 aptamer for targeted delivery of bcl-xl shRNA into breast cancer cells. *Colloids Surf B Biointerfaces* 140:28–39
40. Zhao Y, Zhao T, Cao Y, Sun J, Zhou Q, Chen H, Guo S, Wang Y, Zhen Y, Liang XJ, Zhang S (2021) Temperature-sensitive lipid-coated carbon nanotubes for synergistic photothermal therapy and gene therapy. *ACS Nano* 15:6517–6529
41. Nguyen HPT, Murugathas T, Plank NOV (2021) Comparison of duplex and quadruplex folding structure adenosine aptamers for carbon nanotube field effect transistor aptasensors. *Nanomaterials* 11:2280
42. Li H, Hao Y, Wang N, Wang L, Jia S, Wang Y, Yang L, Zhang Y, Zhang Z (2016) DOTAP functionalizing single-walled carbon nanotubes as non-viral vectors for efficient intracellular siRNA delivery. *Drug Deliv* 23:840–848
43. Siu KS, Chen D, Zheng X, Zhang X, Johnston N, Liu Y, Yuan K, Koropatnick J, Gillies ER, Min WP (2014) Non-covalently functionalized single-walled carbon nanotube for topical siRNA delivery into melanoma. *Biomaterials* 35:3435–3442

44. Guo J, Tan J, Dou N, LakshmiPriya T, Gopinath SCB (2021) Multiwalled carbon-aptamer conjugates for dielectric detection of matrix metalloproteinase-9. *Appl Phys A* 127:95
45. Barbosa MB, Martins EMDN, Teixeira TF, Carvalho RDE, Coelho JP, Resende RR, Oliveira EF, Santos AP, Andrade ASR, Furtado CA (2019) A carefully designed nanoplatfrom based on multi walled carbon nanotube wrapped with aptamers. *Colloids Surf B Biointerfaces* 175:175–183
46. Mohseni-Dargah M, Akbari-Birgani S, Madadi Z, Saghatchi F, Kaboudin B (2019) Carbon nanotube-delivered iC9 suicide gene therapy for killing breast cancer cells in vitro. *Nanomedicine* 14:1033–1047
47. Liu M, Chen B, Xue Y, Huang J, Zhang L, Huang S, Li Q, Zhang Z (2011) Polyamidoamine-grafted multiwalled carbon nanotubes for gene delivery: synthesis, transfection and intracellular trafficking. *Bioconjug Chem* 22:2237–2243
48. Gu F, Hu C, Xia Q, Gong C, Gao S, Chen Z (2018) Aptamer-conjugated multi-walled carbon nanotubes as a new targeted ultrasound contrast agent for the diagnosis of prostate cancer. *J Nanopart Res* 20:303
49. Li D, Ahmed M, Khan A, Xu L, Walters AA, Ballesteros B, Al-Jamal KT (2021) Tailoring the architecture of cationic polymer brush-modified carbon nanotubes for efficient siRNA delivery in cancer immunotherapy. *ACS Appl Mater Interfaces* 13:30284–30294
50. Tonelli FMP, Lacerda SMSN, Silva MA, Ávila ES, Ladeira LO, França LR, Resende RR (2014) Gene delivery to Nile tilapia spermatogonial stem cells using carboxi-functionalized multiwall carbon nanotubes. *RSC Adv* 4:37985–37987
51. Rojas-Chapana J, Troszczyńska J, Firkowska I, Morszczyk C, Giersig M (2005) Multi-walled carbon nanotubes for plasmid delivery into *Escherichia coli* cells. *Lab Chip* 5:536–539
52. Moradian H, Fasehee H, Keshvari H, Faghihi S (2014) Poly(ethyleneimine) functionalized carbon nanotubes as efficient nano-vector for transfecting mesenchymal stem cells. *Colloids Surf B Biointerfaces* 122:115–125
53. Jain S, Thanki K, Pandi NK, Kushwah V (2016) Estradiol functionalized multi-walled carbon nanotubes as renovated strategy for efficient gene delivery. *RSC Adv* 6:10792–10801
54. Masotti A, Miller MR, Celluzzi A, Rose L, Micciulla F, Hadoke PW, Bellucci S, Caporali A (2016) Regulation of angiogenesis through the efficient delivery of microRNAs into endothelial cells using polyamine-coated carbon nanotubes. *Nanomedicine* 12:1511–1522
55. Wen Z, Feng Y, Hu Y, Lian L, Huang H, Guo L, Chen S, Yang Q, Zhang M, Wan L, Xu K, Degejirifu, Yan X (2021) Multiwalled carbon nanotubes co-delivering sorafenib and epidermal growth factor receptor siRNA enhanced tumor-suppressing effect on liver cancer. *Aging* 13:1872–1882
56. Ito M, Kobayashi T, Ito Y, Hayashida T, Nii D, Umemura K, Homma Y (2014) Intense photoluminescence from dried double-stranded DNA and single-walled carbon nanotube hybrid. *Appl Phys Lett* 104:043102
57. Cai D, Blair D, Dufort FJ, Gumina MR, Huang Z, Hong G, Wagner D, Canahan D, Kempa K, Ren ZF, Chiles TC (2008) Interaction between carbon nanotubes and mammalian cells: characterization by flow cytometry and application. *Nanotechnology* 19:345102
58. Bates K, Kostarelos K (2013) Carbon nanotubes as vectors for gene therapy: past achievements, present challenges and future goals. *Adv Drug Deliv Rev* 65:2023–2033
59. Munk M, Ladeira LO, Carvalho BC, Camargo LSA, Raposo NRB, Serapião RV, Quintão CCR, Silva SR, Soares JS, Jorio A, Brandão HM (2016) Efficient delivery of DNA into bovine preimplantation embryos by multiwall carbon nanotubes. *Sci Rep* 6:33588
60. Clancy S (2008) Genetic mutation. *Nat Educ* 1:187
61. Friedmann T, Roblin R (1972) Gene therapy for human genetic disease? *Science* 175:949–955
62. Bak RO, Gomez-Ospina N, Porteus, MH (2018) Gene editing on center stage. *Trends Genet* 34:600–611
63. Patil S, Gao YG, Lin X, Li Y, Dang K, Tian Y, Zhang WJ, Jiang SF, Qadir A, Qian AR (2019) The development of functional non-viral vectors for gene delivery. *Int J Mol Sci* 20:5491
64. Mastrobattista E, Hennink WE, Schiffelers RM (2007) Delivery of nucleic acids. *Pharm Res* 24:1561–1563

65. Liu G, Wang Y, Hu Y, Yu X, Zhu B, Wang G (2016) Functionalized multi-wall carbon nanotubes enhance transfection and expression efficiency of plasmid DNA in fish cells. *Int J Mol Sci* 17:335
66. Al-Jamal KT, Toma FM, Yilmazer A, Ali-Boucetta H, Nunes A, Herrero MA, Tian B, Eddaoudi A, Al-Jamal WT, Bianco A, Prato M, Kostarelos K (2010) Enhanced cellular internalization and gene silencing with a series of cationic dendron-multiwalled carbon nanotube:siRNA complexes. *FASEB J* 24:4354–4365
67. Shi J, Cha T-G, Claussen JC, Diggs AR, Choi JH, Porterfield DM (2011) Microbiosensors based on DNA modified single-walled carbon nanotube and Pt Black nanocomposites. *Analyst* 136:4916–4924

Chapter 4

Selected Recent Work on *Endo-Functionalization of Cylindrical Macrocyclic Artificial Receptors for Mimicking Protein–Ligand Interactions*



Yahu A. Liu, Zhuo Wang, Weibo Hu, Mingliang Ma, Hui Yang, and Ke Wen

Abstract In medicinal chemistry, a significant part of the process involves modifying the way a small molecule interacts with a target receptor, which is typically a protein. The objective is usually to enhance or dampen these interactions to achieve the desired therapeutic outcome. To gain a better understanding of these interactions, researchers have utilized functionalized macrocyclic receptors as models for mimicking protein binding pockets. Recent advancements in the functionalization of synthetic cylindrical and vase-shaped cylindrical macrocyclic receptors, including cavitands, calixpyrroles, naphthotubes, and pillar [1] arene-derivatives, among others, have been noteworthy and thought-provoking. In this short review, we present selected examples from a medicinal chemist's perspective, with an emphasis

Dedicated to the memory of Professor Lawrence M. Sayre (1951–2009).

Y. A. Liu (✉)

Novartis Institutes for BioMedical Research (NIBR), San Diego, CA 92121, USA

e-mail: yahu.liu@novartis.com

Z. Wang · W. Hu · H. Yang · K. Wen

Shanghai Advanced Research Institute, Chinese Academy of Sciences, Shanghai 201210, China

e-mail: yangh@sari.ac.cn

K. Wen

e-mail: wenk@sari.ac.cn

Z. Wang

University of Chinese Academy of Sciences, Beijing 100049, China

Z. Wang · H. Yang · K. Wen

School of Physical Science and Technology, ShanghaiTech University, Shanghai 201210, China

M. Ma

Shanghai Engineering Research Center of Molecular Therapeutics and New Drug Development, School of Chemistry and Molecular Engineering and Key Laboratory of Brain Functional Genomics, Ministry of Education, East China Normal University, Shanghai 200062, China

on the *endo*-functionalization of cylindrical and vase-shaped cylindrical macrocyclic receptors and their binding features in model protein–ligand interactions.

4.1 Introduction

Proteins are large, complex molecules that perform a variety of important functions in biological systems. One of the key roles of proteins is to interact with small molecules, or ligands, in order to carry out specific tasks within the cell or organism [2, 3]. For example, enzymes are proteins that catalyze chemical reactions in the body, and they often require a specific ligand to function properly. Hormones, neurotransmitters, and other signaling molecules are also small molecules that interact with specific protein receptors in order to transmit information within the body [2, 3]. Understanding the mechanisms of these interactions between proteins and ligands is crucial for the advancement of basic science and drug discovery. By studying how proteins and ligands interact, scientists can gain insights into the underlying mechanisms of biological processes and develop new drugs that can selectively target specific proteins in order to treat diseases [2, 3]. Towards this direction, biochemists and biologists frequently study specific proteins and aim to identify the endogenous metabolites that bind to them. Conversely, chemists may employ bioactive small molecules, drugs, or tool compounds as probes to identify therapeutically relevant protein targets. Proteins that recognize ligands include a diverse range of molecules such as antibodies, enzymes, lectins, signaling partners, transcription factors, and membrane transport proteins [1, 4]. Among others, antibodies and related binding proteins are highly desirable in recognition studies due to their broad binding affinities and target selectivities. While natural protein receptors can be highly effective, they are often costly to produce, have limited storage capacity, and may not be compatible with certain chemical transformations [1, 4]. As a result, synthetic biomimetic receptors, which are artificial macrocyclic hosts that mimic the structure and function of protein binding pockets, are essential alternatives for studying and testing. These model studies can provide valuable complementary methods to those using proteins.

In general terms, numerous instances of host–guest arrangements might be viewed as imitating interactions between pockets and ligands. Synthetic macrocyclic receptors, such as crown ethers, cryptands, cyclodextrins, cucurbiturils, cavitands, calixarenes, naphthotubes, and pillararenes have been extensively used as hosts in molecular recognition [5]. By exploiting the principles of supramolecular chemistry, such as molecular recognition and self-assembly, these synthetic receptors can be designed to selectively bind to specific targets, making them ideal candidates for drug discovery and other biomedical applications. However, the artificial macrocyclic receptors that interest medicinal chemists the most are pocket-like structures, for example, cylindrical macrocyclic artificial receptors. Despite their widespread use, most of the synthetic macrocyclic receptors that are currently well-established do not possess the same binding affinity and selectivity as bioreceptors. This discrepancy can be attributed to the lack of functional groups inside the binding cavities.

Most of the known synthetic receptors contain either a hydrophobic cavity or polar binding pockets only, and those with polar functional groups inside a hydrophobic cavity are rare [5]. Therefore, the functionalization of now-established synthetic receptors through the introduction of functional groups into a hydrophobic cavity could be an effective means to create useful artificial molecular pockets that can mimic protein–ligand interactions. This review focuses primarily on the most recent work (since year 2019) on the functionalization of the synthetic cylindrical and vase-shaped cylindrical macrocyclic receptors and their application in model studies of protein–ligand interaction. As this short review is focused on cylindrical and vase-shaped cylindrical structures that have been purposely functionalized, other types of hosts, such as helical foldamers [6], crown ethers [7], cryptands [8], will not be discussed.

4.2 Functionalization of Cylindrical and Vase-Shaped Cylindrical Macrocyclic Receptors

4.2.1 *Cavitands*

A cavitand is a type of cylindrical (or vase-shaped cylindrical) macrocycle consisting of an enforced concave cavity surrounded by four aromatic rings. It is synthesized by covalently linking neighbouring phenolic hydroxyl groups in a resorcinarene (Fig. 4.1) [9–12]. Cavitands can be utilized as a means for examining protein structure, as they can function as inflexible frameworks onto which novel proteins can be attached through chemical means [9]. Additionally, cavitands have the capability to mimic certain properties of natural proteins and are proficient in acting as artificial hosts [9]. Since cavitands have an open top end and a closed bottom end, functionalizing the bottom rim of cavitands can change their overall properties, but not the binding properties inside the cavity [13, 14]. For example, functionalizing the bottom rims with alkyl or aryl groups improves their solubility in organic solvents, while adding water-soluble groups increases their aqueous solubility [14]. On the other hand, functionalizing the upper rim is often used to modify the binding properties of the vase-like cavity, endowing these open-ended molecules to resemble protein binding pockets. For instance, Rebek, Yu and co-workers investigated the effects of metal complexation on the molecular recognition behaviour of cavitands with quinoxaline walls (Fig. 4.2) [15]. They found that complexing Pd(II) with nitrogen atoms of the quinoxalines close to the upper rim of the vase-like shape cavitands could afford 2:1 Pd(II):cavitand derivative which demonstrated enhanced the binding of hydrophobic and even water-soluble guests [15].

Protein pockets interact with ligands in various ways, including hydrophobic effect, hydrogen bonding, π -stacking, weak hydrogen bonding, salt bridge, amide stacking, and cation- π interaction. To explore the roles of cation- π interaction and the hydrophobic effect in controlling recognition in biological systems, Hunter,

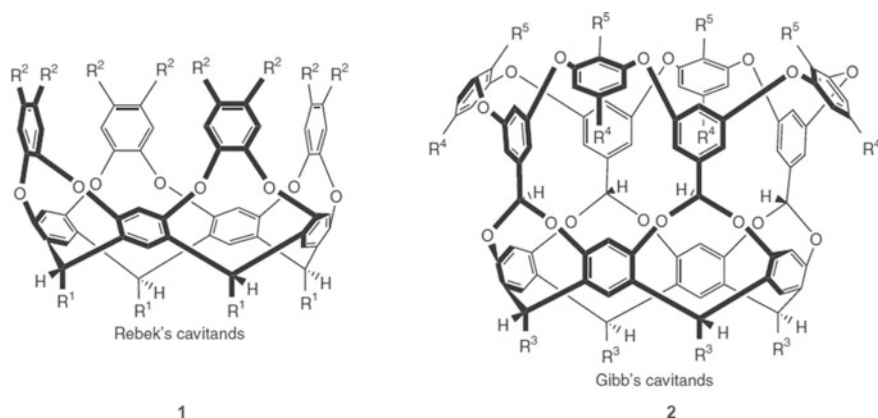


Fig. 4.1 The upper (R^2 or R^5) and lower rim (R^1 or R^3) functionalization of Rebek's and Gibb's cavitands (**1** and **2**). Reproduced with permission from Ref. [11]. Copyright © 2016 Nature Publishing

Yu and co-workers studied intramolecular competition between trimethylammonium head group $-N^+(\text{CH}_3)_3$ and *tert*-butyl head group $-C(\text{CH}_3)_3$ of molecular “dumbbell” guests in cavitand hosts [16, 17]. They found that the host molecules consistently prefer binding to the uncharged $-C(\text{CH}_3)_3$ groups, regardless of the presence of anionic, cationic, or zwitterionic groups, because the solvation of the polar $-N^+(\text{CH}_3)_3$ group in water outcompeted the cation- π interaction, the attraction between the positive charge in $-N^+(\text{CH}_3)_3$ and the π -surfaces in the container. However, when the “dumbbell” guests had short linkers, the functional groups on the rim of the cavitand hosts affected the binding modes of the guests in the hosts (Fig. 4.3a). The cationic $-N^+(\text{CH}_3)_3$ head group tended to interact with the polar urea groups (red) in cavitand **6** (Fig. 4.3b), but the cation- π interaction between the positive charge and the π -surfaces in the cylinder became a predominating interactive attraction in the complex **11** where the host has hydrophobic methyl groups (green) on the upper rim (Fig. 4.3c) [16].

The discriminatory recognition of neutral hydrophilic molecules in water is common in nature, where hydrophilic biomolecules like sugars can be selectively recognized by receptors through the cooperative action of hydrophobic effects and other non-covalent interactions. However, creating a biomimetic receptor that can mimic such recognition has proven to be a challenge. Recently, Yu's group has developed two deep cylindrical water-soluble cavitands, and the molecular recognition of neutral hydrophilic molecules such as THF and dioxane is enhanced by water-mediated hydrogen bonds (Fig. 4.4) [18]. In a non-covalent interaction analysis to determine the nature of the interaction between the guest (THF) and cavitand, the interactions between the guest and the cavitand were identified as weak dispersion interactions. Still, THF molecules can form additional favorable hydrogen bonds with the water molecules inside the cavitand in the presence of water molecules. These interactions may be attributed to the presence of imidazole N or NH on the inner

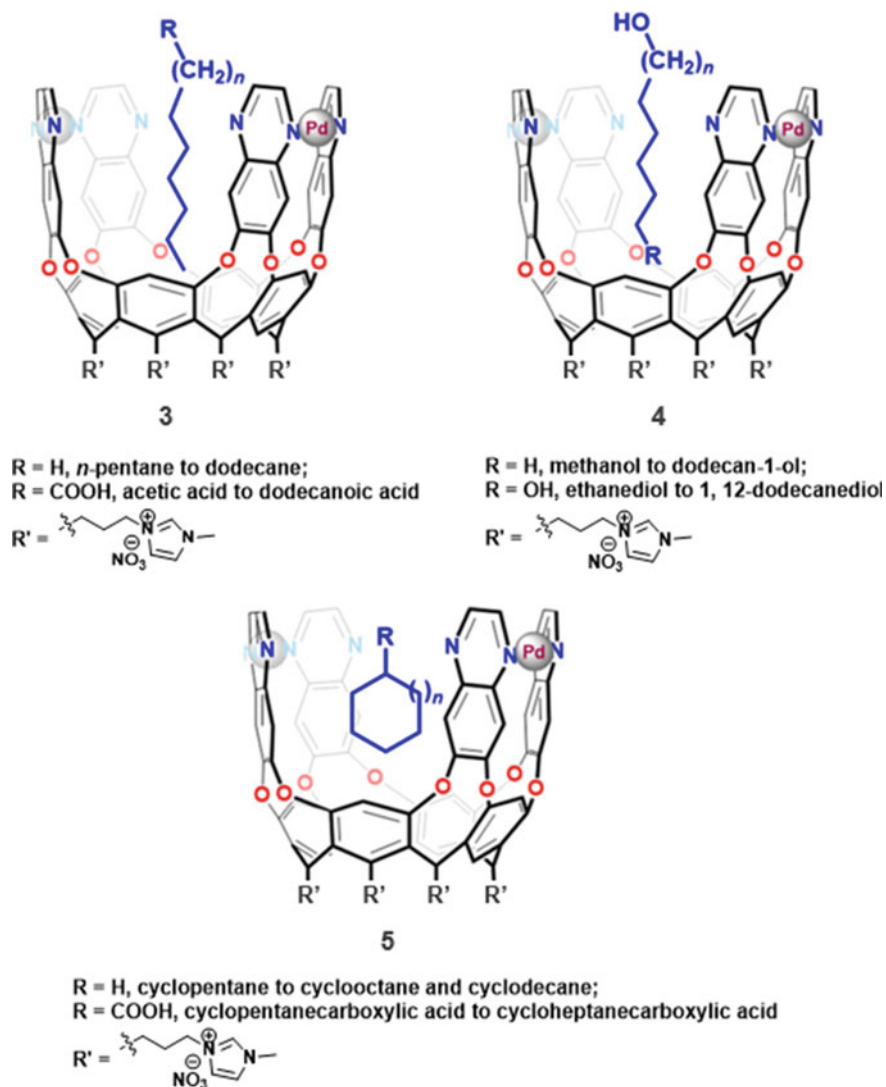


Fig. 4.2 Cartoon illustration of the interactions of the Pd-complexed cavitand with *n*-alkanes, *n*-alkanoic acids, *n*-alcohols, α,ω -*n*-alkanediols, cycloalkanes, or cyclic alkanic acids. The chain alkyl compounds were inserted into the pocket linearly and cycloalkanes tumbled rapidly, while cyclic acids were fixed with the carboxyl groups exposed to aqueous environment. Reproduced with permission from Ref. [15]

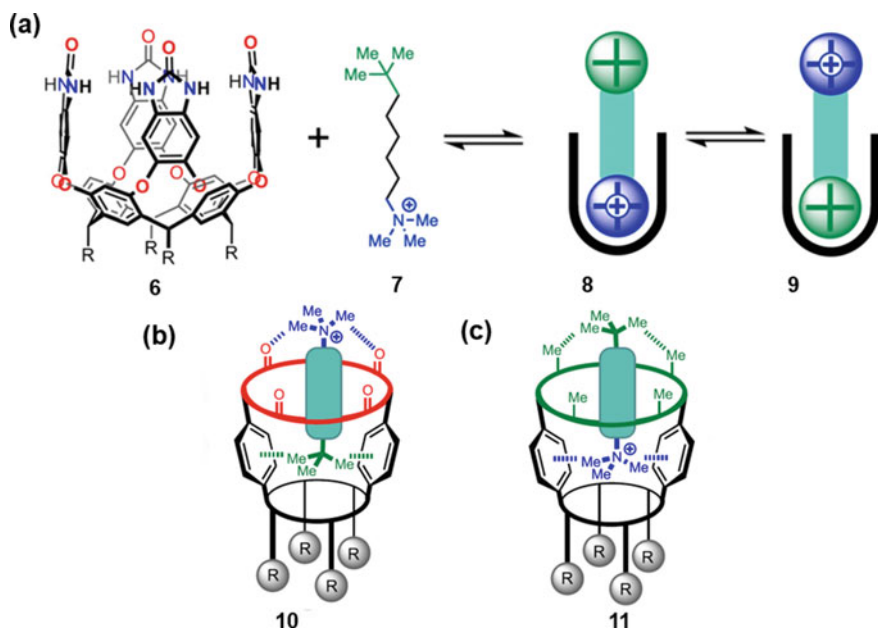


Fig. 4.3 a Cartoon representation of the two isomeric complexes **8** and **9** formed between cavitaand host **6** and dumbbell guest **7**. b The polar urea groups (red) in **6** attractively interact with **7**'s cationic head group, forming complex **10**. c In complex **11**, the hydrophobic methyl groups (green) make attractive interactions with **7**'s t-butyl head group. Reproduced from Ref. [16] which is available online at pubs.acs.org/doi/10.1021/jacs.1c06510

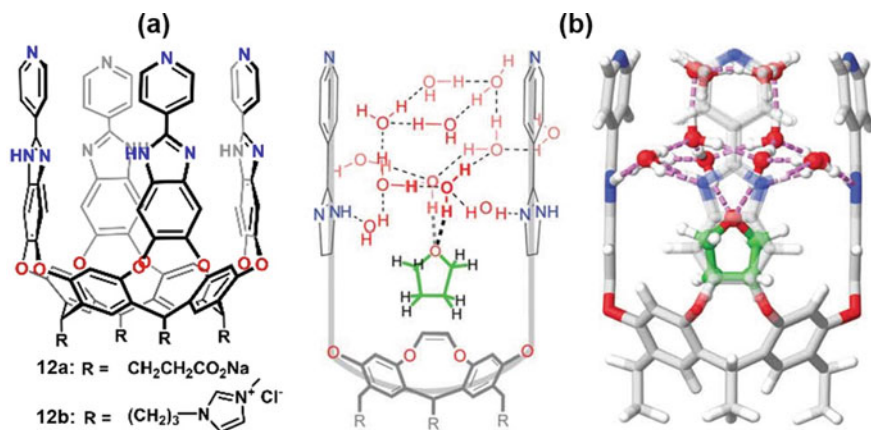


Fig. 4.4 a Chemical structures of cavitaands **12a** and **12b**. b Geometry of the complex of cavitaand **12** with THF optimized by density functional theory (DFT) calculations. Reproduced with permission from Ref. [18]. Copyright © 2021 Royal Society of Chemistry. The figures have been published in Ref. [18] which is available online at pubs.rsc.org/en/content/articlelanding/2021/cc/d1cc02505h

surface of the cylindrical tube and the introduction of pyridine functional groups to the upper rim [18].

4.2.2 *Calix[4]pyrroles*

Calixpyrroles are macrocycles made by condensing acetone and pyrrole to form tetrapyrrolic structures. They are relatively easy to modify, and the ditopic nature of calix[4]pyrrole derivatives endows them to be good receptors and extractants for both anions and cations, given the right conditions [19–21]. For example, when four hydrogen bonds are formed between an anion and a calix[4]pyrrole molecule, the molecule converts from the 1,3-alternate conformation to a bowl-like shape which can selectively recognize a variety of analytes, including Lewis basic anions, neutral aromatic molecules, and fullerenes. Penuelas-Haro and Ballester recently reported the functionalization of both upper and lower rims of the aryl-extended calix[4]pyrrole derivatives [21]. Functionalization of the bottom rim of the calix[4]pyrroles impacted their solubility in organic solvents and aqueous medium. For instance, calix[4]pyrroles **13–16**, which had pyridinium groups located at their bottom rims, were water-soluble, while calix[4]pyrroles **17–20**, featuring non-polar functional groups (such as 4-chloro-*n*-butyl) at the bottom rims, were soluble in chloroform (Fig. 4.5) [21]. However, it was the modifications made to the upper rim that altered the binding selectivity of the pockets. This was shown by differences in the binding properties among four different calix[4]pyrrole derivatives: the bis-phosphonate calix[4]pyrrole cavitand **13**, its in–out stereoisomer **14**, the methylene bridged analogue **15**, and the calix[4]pyrrole counterpart **16**.

4.2.3 *Naphthalene-Based Molecular Tubes*

Naphthalene-based molecular tubes, initially discovered by Glass and co-workers, consist of a pair of configurational isomers bearing amide protons in the well-defined deep cavity (Fig. 4.6) [22, 23]. In order to generate diverse biomimetic receptors for molecular recognition, Jiang and his team replaced the amide moiety with various hydrogen-bond acceptors (such as ether, ester, and imine) and hydrogen-bond donors (such as amine, urea, and thiourea). As a result, the corresponding naphthalene-based molecular tubes, referred to as “naphthotubes” by Jiang, exhibit unique recognition capabilities [23]. The unique recognition capabilities of naphthotubes have opened up infinite potential for their use in a variety of fields, and their properties continue to be explored for further applications.

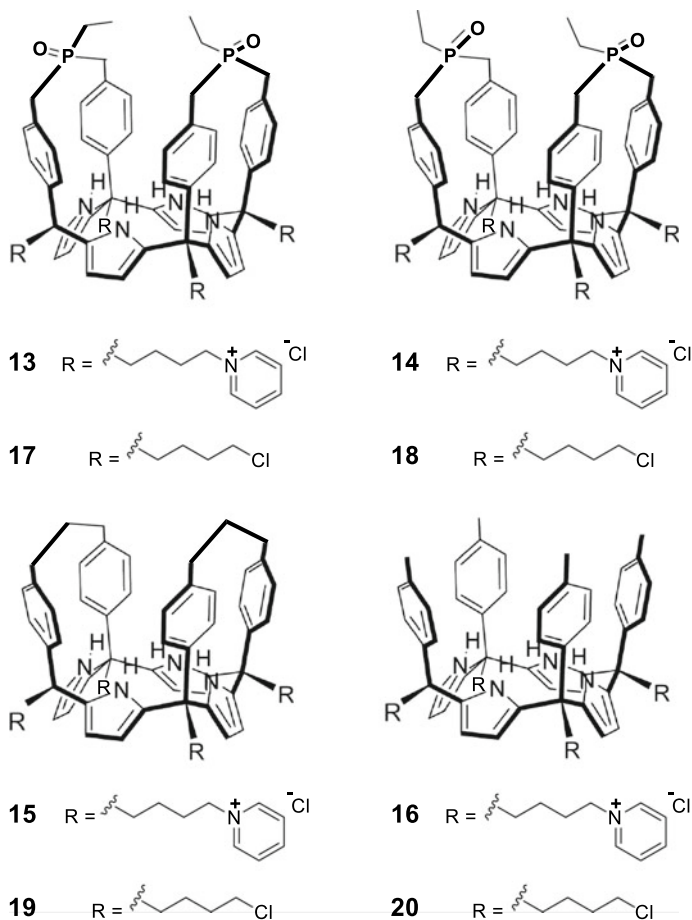


Fig. 4.5 Chemical structures of aryloxtended calix[4]pyrrole derivatives **13–20**. Partially reproduced from Ref. [21] which is available online at <https://pubs.rsc.org/en/content/articlelanding/2019/sc/c8sc05034a>

Jiang's research group investigated the host–guest interactions of two naphthalene-based molecular tubes, NT-*syn* (**21a**) and NT-*anti* (**21b**), with 18 neutral molecular fragments and 13 drug molecules in water [24]. In the 17 neutral molecular fragments **23–39** (Fig. 4.7a), attached to the phenyl ring **22** were various functional groups including methyl, methoxyl, methylthio, cyano, methylamino, dimethylamino, nitro, ester, amide, ketone, oxazole, thiazole, and pyrimidine, many of which were polar groups. In addition, drug molecules **40–52** (Fig. 4.7b) included in the study contained one or two of the above-mentioned 18 molecular fragments in their structural backbones. The cavities of **21a** and **21b** (Fig. 4.6) were deep enough to encapsulate both polar and nonpolar groups, and hydrogen bonds formed between the polar groups of guests and the amide protons of the hosts. Density functional

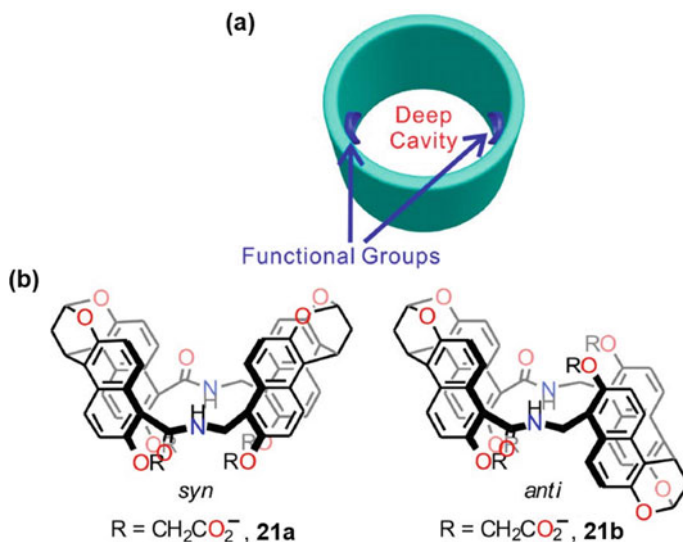


Fig. 4.6 A cartoon model of naphthotubes **a** and chemical structures **b** of amide naphthotubes NT-syn (**21a**) and NT-anti (**21b**). Reproduced with permission from Ref. [23]. Copyright © 2020 American Chemical Society

theory (DFT) calculations revealed that the energy gained through interacting with the polar groups of guests compensated for the desolvation penalty. In addition, it was found that the two amide naphthotubes exhibit an even stronger binding affinity towards organic drug molecules with multiple polar groups, comparable to those of the corresponding bioreceptors [24]. In particular, **21b** was found to be capable of improving the aqueous solubility of two poorly soluble drug molecules, which was understandable as solubility of the pocket-ligand complexes was enhanced owing to the water-soluble carboxylate groups at the rims of the cylindrical receptor. As such solubility-enhancing effect was shown to be more effective than that of β -cyclodextrin, which has been commonly used to deliver poorly water-soluble drugs [25, 26], **21b** was expected to have potential for applications in drug formulation and delivery. Therefore, the amide naphthotubes not only serve as biomimetic receptors to facilitate our understanding of biomolecular recognition, but also offer potential applications in the field of drug delivery. Overall, the findings demonstrated the potential of amide naphthotubes as versatile biomimetic receptors for both fundamental research and practical applications in the pharmaceutical sciences.

The modulation of luminescence properties in organic dye molecules has the potential to enhance their usage in a variety of fields, such as optical devices, biological imaging, drug delivery, and sensors. Recently, researchers have been exploring the use of macrocyclic hosts to encapsulate fluorescent dyes through supramolecular interactions. By binding a luminescent ligand within the host cavity, these interactions can significantly modify the spectral properties, fluorescence lifetime, and photostability of the dye. In an effort to further tune these properties, Jiang's group

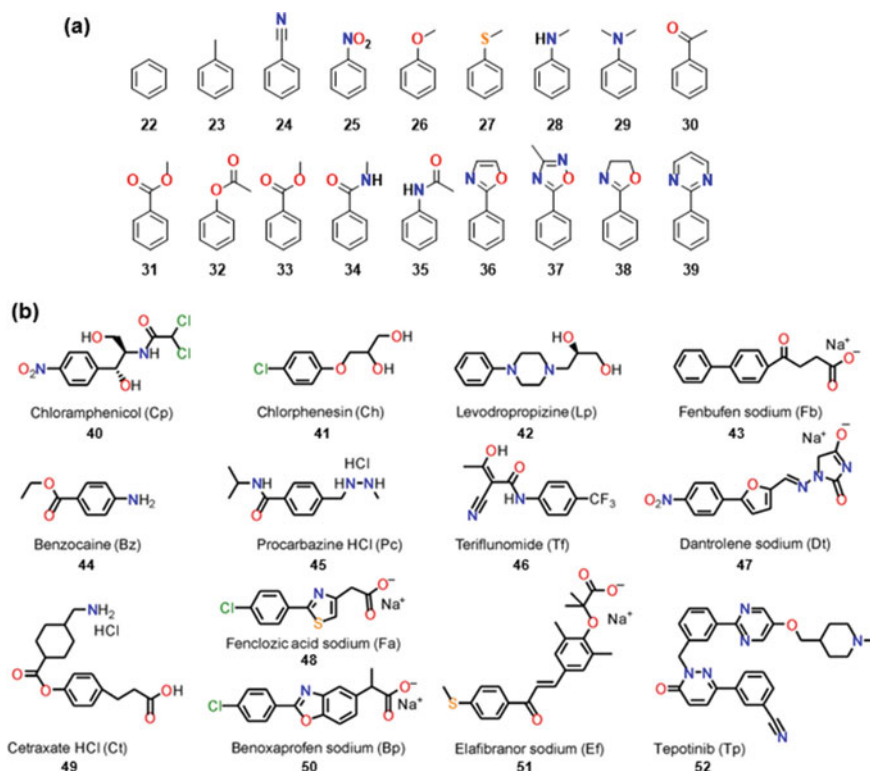


Fig. 4.7 The structures of 18 molecular fragments **a** and 13 drug molecules **b** used in the study. The figures have been published in Ref. [24] which is available online at <https://doi.org/10.31635/ccschem.020.202000288>

investigated the use of amide naphthotubes (**21a** and **21b**) to bind a diverse range of fluorescent dyes. The study focused on organic dyes **53–65** (Fig. 4.8), which varied in both charge and shape, in order to fully understand the range of binding behavior and fluorescent tuning effects of naphthotubes **21a** and **21b**. Results indicated that the amide naphthotubes were highly effective at binding fluorescent dyes in water, exhibiting higher binding constants than those observed with cucurbit[7]uril and β -cyclodextrin. Additionally, the inward-pointed hydrogen bonding sites in the amide naphthotubes played a critical role in determining the absorption and fluorescence spectra of the dye-host complexes [27]. This study demonstrated the potential of amide naphthotubes as a versatile tool for modulating the luminescence properties of fluorescent dyes, further expanding their potential applications.

Salt bridge bonds are crucial in protein structures as they form through the attraction of opposite charges between residues that are in close proximity. These bonds are also significant in determining the specificity of protein interactions with other biomolecules. To imitate the binding pockets found in bioreceptors, Jiang

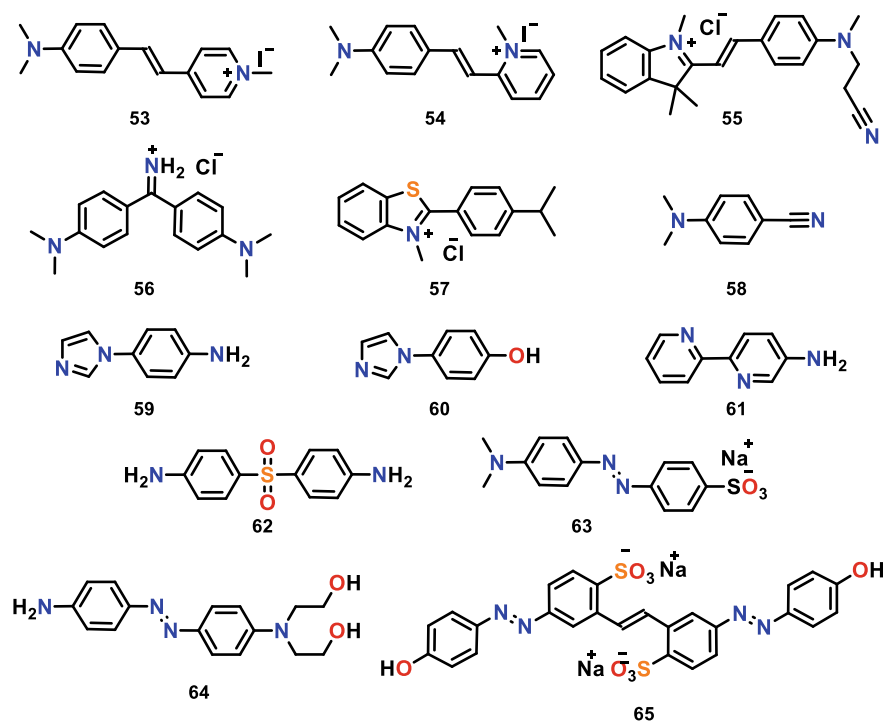


Fig. 4.8 The structures of the water-soluble organic fluorescent dyes **53–65** involved in the study

and colleagues designed and synthesized a pair of naphthotubes that are *endo*-functionalized with secondary ammonium groups in their hydrophobic cavities (Fig. 4.9) [28]. These *endo*-functionalized macrocyclic hosts could utilize the buried salt bridges and the hydrophobic effect to achieve efficient and selective recognition of functional carboxylic acids in water. Furthermore, the naphthotube receptors could be employed for circular-dichroism-based optical chirality sensing of chiral carboxylic acids and fluorescent sensing of phenylpyruvic acid, as demonstrated by Jiang's group. As optical chirality sensing is a powerful tool for studying the role of chirality in various fields and has numerous practical applications, naphthotube chirality sensors could become increasingly important.

The use of targeted covalent inhibitors has been acknowledged as a crucial aspect in drug discovery and therapy for overcoming acquired resistance in oncology [29, 30]. Cancer is a complex disease that can develop resistance to many different types of drugs, making treatment difficult. One potential approach to address this challenge is the use of targeted covalent inhibitors, which are designed to irreversibly bind to a specific protein target in cancer cells. By forming a covalent bond with the target protein, these inhibitors can inhibit its activity, leading to cell death and ultimately shrinking or eliminating the tumor [29, 30]. Cysteine residues have been a common target for irreversible inhibition due to their nucleophilic properties. However, it

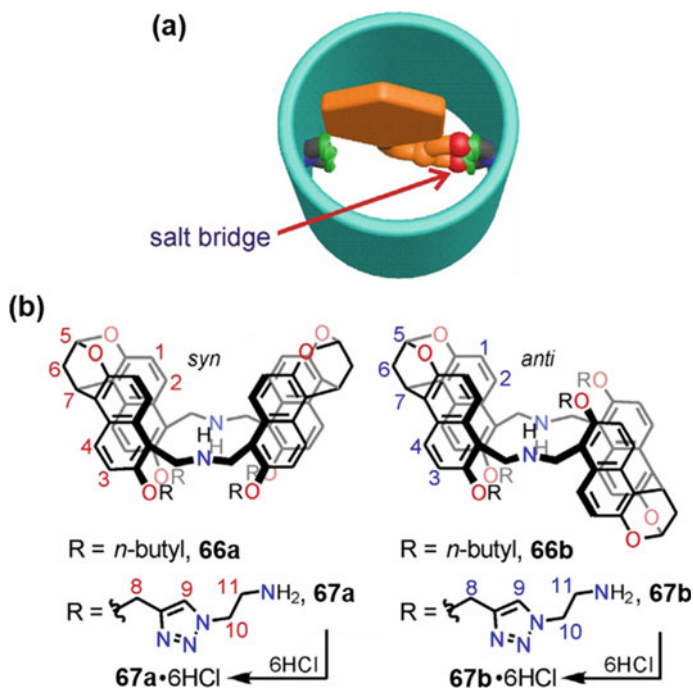


Fig. 4.9 **a** Cartoon illustration of an endo-functionalized cavity for binding carboxylic acids in water through a buried salt bridge and the hydrophobic effect. **b** Chemical structures of amine naphthotubes **66** and **67**. Reproduced with permission from Ref. [28]. Copyright © 2022 Wiley-VCH GmbH

has been increasingly recognized that lysine residues, another type of nucleophilic amino acid, can also serve as viable targets for irreversible inhibition. By reacting with lysine residues, inhibitors can form covalent adducts, leading to irreversible inhibition of the target protein [31, 32]. Lysine is nearly three times more abundant than cysteine in the human body, but its basicity presents challenges for this strategy as the ϵ -amino group of in lysine may become protonated at acidic pH or even at pH 7.4 [31, 32]. Recently, scientists have been investigating compounds that can form reversible covalent bonds with proteins. For instance, Taunton's group showed that covalent inhibitors based on aldehydes are capable of binding to target proteins in a reversible manner (Fig. 4.10) [32, 33]. Selectivity of irreversible electrophiles relies only on the attachment rate to the right lysine site, while reversible electrophiles depend on both attachment and detachment rates. Due to the basicity of the ϵ -amino group in lysine, protonation of the lysine amino groups can make them unavailable for covalent bond formation, especially in acidic or slightly basic environments. As such, In drug discovery, lysines that are situated within the inner folds of a protein are often targeted because they are less likely to become protonated. To mimic aldehyde-amino interaction in these protein inner pockets, Jiang's group synthesizes naphthotube **68** whose the amine side chain is folded into the cavity

when in water (Fig. 4.11a) [34]. The cavity of **68** had hydrogen bonding sites and a primary amine group, making it to some extent analogous to the active site pocket of aldolase I. The hydrogen bonding site of **68** was protected by its hydrophobic cavity, creating a suitable environment for stabilizing alkyl imine in aqueous conditions. Aldehydes containing longer alkyl chains have the ability to form an imine bond with **68** (Fig. 4.11b). Longer aldehydes required less saturation than shorter ones, consistent with their binding affinities. Longer aldehydes were also able to quickly displace shorter ones to form new imines, which demonstrated reversibility of the imine formation. The inner space of naphthotubes is not entirely separated from the surrounding aqueous environment, unlike container molecules with completely isolated cavities. This means guest molecules can enter and exit the cavity through the portals of **68**. Furthermore, the cylindrical pocket's inner surface contains hydrogen bonding sites that point inwards, contributing to the stabilization of labile imine and hemiaminal molecules. These cylindrical biomimetic receptors were analogous to enzyme binding pockets, and their guest exchange kinetics and stabilization mechanisms share similarities. The model studies using **68** and aldehydes are useful not only in understanding of binding of lysines by aldehyde-based covalent inhibitors, but also inspiring designing new compounds that can selectively target specific lysine residues in proteins, potentially leading to more effective cancer therapies.

Another impressive work on naphthotubes recently disclosed by Jiang's group was the enantioselective recognition which was achieved by using chiral naphthotubes

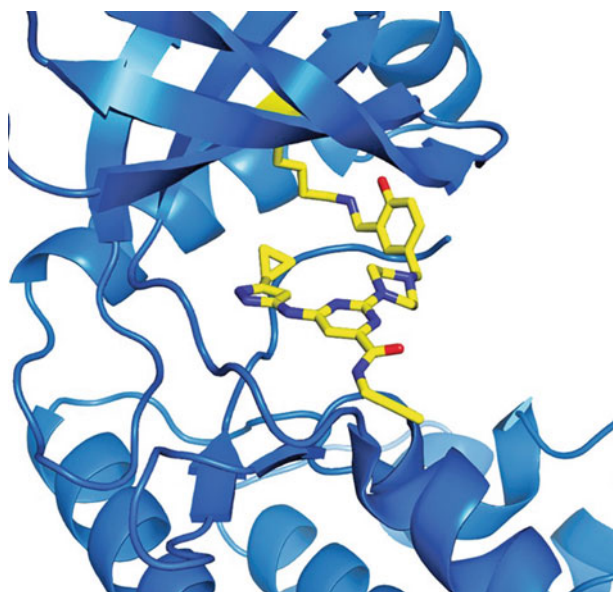


Fig. 4.10 The covalent binding between a small molecule that contains an aldehyde group and a lysine residue (yellow segment on the blue ribbon) on a kinase protein. Reproduced from Ref. [32] with permission from Professor Jack Taunton (University of California, San Francisco)

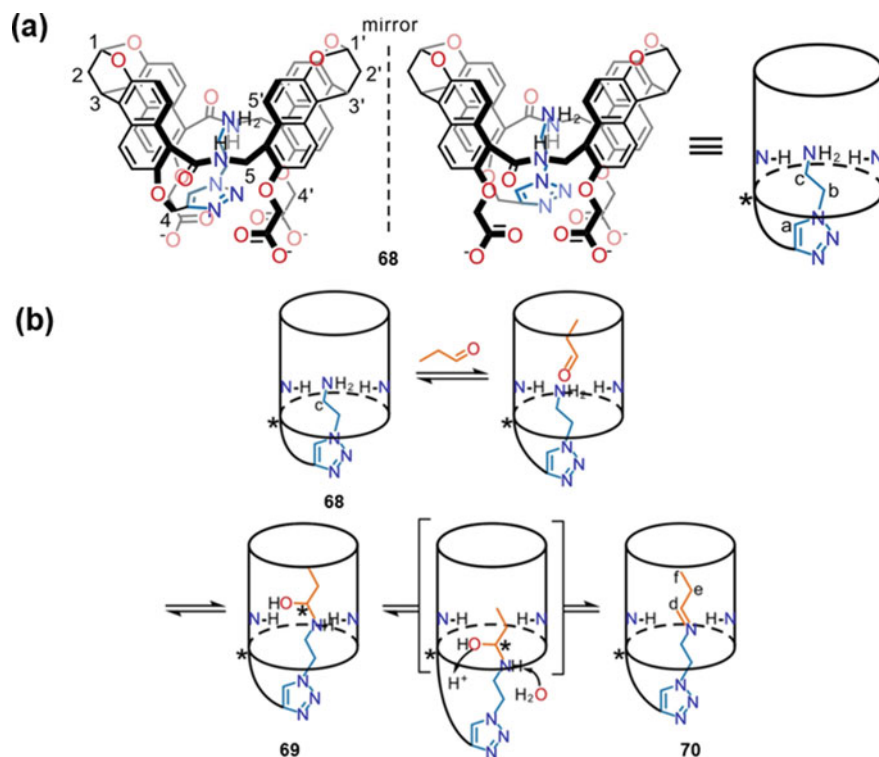


Fig. 4.11 a Structure of naphthotube **68**. b Schematic representations of energy-minimized major structures involved during the reaction of **68** with propanal in water. (Produced with permission from Ref. [34]. Copyright © 2022 Wiley-VCH GmbH)

synthesized through a chirality-directed macrocyclization strategy (Fig. 4.12) [35]. Enantioselective recognition is a crucial process that occurs in biological systems, where specific molecules must be recognized and differentiated based on their chiral properties. Nature has developed several mechanisms for enantioselective recognition, such as enzymes and chiral receptors. These systems can recognize and bind to specific enantiomers, promoting reactions with high stereoselectivity. The chiral naphthotubes, R^2 , S^2 -**71** and S^2 , R^2 -**71**, showed the ability to differentiate between enantiomers of neutral chiral molecules in an aqueous environment. This phenomenon can be explained by the “three-point contact” model developed through DFT calculations. The model suggests that the enantioselectivity towards racemic guests **72–78** is the result of the varying contributions of hydrogen bonding and weak C–H π interactions, which are shielded within the hydrophobic cavity of the naphthotubes. Unlike their achiral analogue, R^2 , S^2 -**71** and S^2 , R^2 -**71** are both CD-active and fluorescent. The chiral naphthotubes exhibited distinctive circular dichroism responses towards both chiral and achiral molecules, and had the potential to function as fluorescent sensors for determining the enantiomeric excess (ee) values of chiral

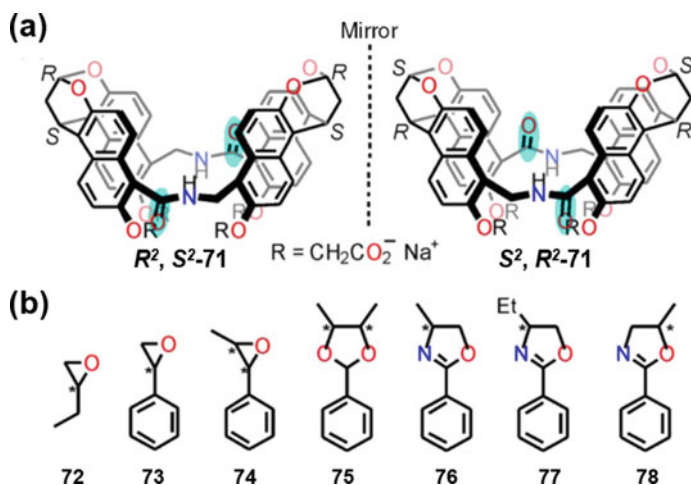


Fig. 4.12 **a** Chemical structures of amide naphthotubes chiral naphthotubes R^2, S^2-71 and S^2, R^2-71 . **b** The Chemical structures of the chiral guests **72**–**78** involved in the study. This figure has been published in Ref. [35] which is available online at <https://doi.org/10.31635/ccschem.020.202000160>

guests. Enantioselective recognition in aqueous environment is extremely important in protein–ligand interaction as many biological processes and chemical reactions occur in water-based environments. Thus, the chiral naphthotubes R^2, S^2-71 and S^2, R^2-71 could serve as model binding pockets to explore mechanisms of enantioselective recognition in nature, which is crucial in the development of new drugs, as many pharmaceuticals must target specific enantiomers to be effective and safe for use.

Stimuli-responsive hosts are molecules or materials that are capable of changing their properties in response to external stimuli such as light, temperature, pH, or electric fields. These materials have a range of potential applications in areas such as drug delivery, sensors, and nanotechnology [36]. Stimuli-responsive hosts can be designed with specific binding sites that can selectively capture and release target molecules based on the specific stimuli applied. This selectivity can be achieved through changes in the shape, charge, or hydrophobicity of the host molecule or material, which can alter the strength of interactions between the host and guest molecules [36]. Jiang’s team has published research on water-soluble naphthotubes **79** and **80** that feature a pH-responsive *endo*-functionalized cavity (Fig. 4.13) [37]. These two naphthotubes differ from the most naphthotubes reported before as they include an amide group and a secondary amine group in the framework, both of which function as inward-directing groups. The naphthotubes remained soluble over a broader pH range due to the four carboxylate groups installed at the bottom rim, preventing precipitation of the host upon protonation (at pH 7.4) and deprotonation (at pH 12) of the secondary amine group. As the inward-directing amine group’s protonation and deprotonation depend on the environment’s pH value, the naphthotubes exhibited different binding preferences and selectivity in water under the

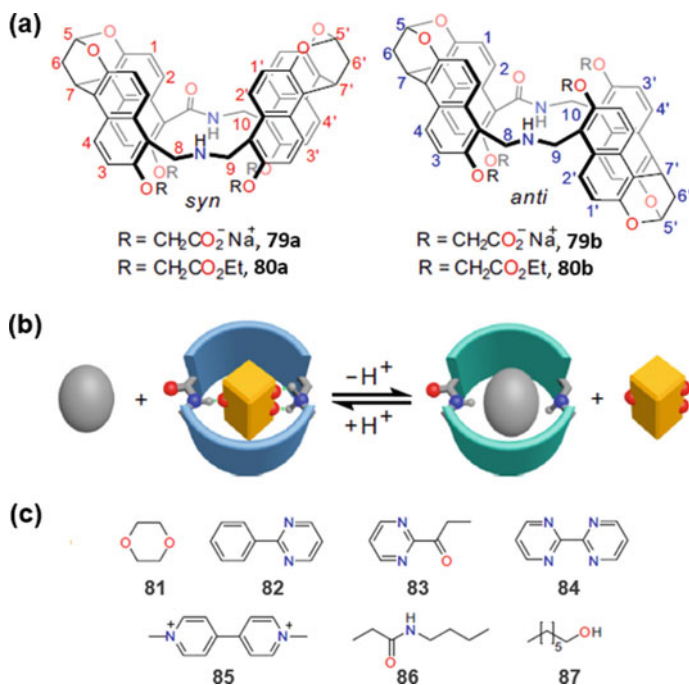


Fig. 4.13 **a** Chemical structures of the naphthotubes (**79** and **80**) with the amide and secondary amine groups in the cavities. **b** Cartoon representation of switchable bifunctional molecular recognition in water using the pH-responsive naphthotubes. The sidewalls of protonated naphthotubes are colored as blue. **c** Chemical structures of the guests involved in the study. Reproduced from Ref. [37]. The figures have been published in Ref. [32] which is available online at <https://www.nature.com/articles/s41467-022-30012-4>

protonated and deprotonated states. The differences in charge repulsion, hydrogen bonding, and hydrophobic effects were thought to cause the guest-binding disparities. Hence, manipulating the environmental pH value allowed for the guest-binding to be switched between two guest molecules in a ternary mixture [37].

4.2.4 Pillar[5]arene-Derived Receptor

Pillararenes are a distinctive category of macrocyclic hosts used in host–guest chemistry, renowned for their superior properties in host–guest recognition. Firstly, their symmetrical and inflexible structures provide them with the ability to selectively bind with guests. Secondly, by introducing various substituents on some or all of the benzene rings, their guest-binding behaviors can be adjusted. Thirdly, pillar[*n*]arenes are readily soluble in most organic solvents, making them useful complements to water-soluble macrocycles with comparable cavity sizes [38–42].

While pillar[*n*]arene homologues with *n* values between 5 and 15 have been synthesized, pillar[5]arene with five repeating units is the most extensively researched, owing to its simplicity of synthesis and thermodynamic stability. The internal pentagonal diameter of the cavity of pillar[5]arene is calculated to be 4.7 Å (based on van der Waals radii of the atoms), and it has a strong binding affinity for various electron-poor or neutral molecules that complement its shape [38–42].

Various functional substituents, such as hydroxylimine and amino groups, can be linked to the rims of pillar[5]arene derivatives. However, in all previously reported cases, the polar functional substituents embedded in the rim of the pillar[5]arene pointed outward [38–42]. Recently, a new tubular molecular pocket derived from pillar[5]arene, *endo*-[P4-(OH)BPO] (**88**), was created with an inward-pointing hydroxyl group (Fig. 4.14) [43]. X-ray crystallography data revealed that **88** orients its phenyl group towards the exterior of the tubular frame, and the hydroxyl group towards the core of the cavity, encapsulating an acetone molecule inside the cavity through the formation of a hydrogen bond between the C=O group of acetone and the O–H group of **88**. H-bonds play a vital role in fragment-pocket complexes, making **88** an ideal artificial protein binding pocket. The inwardly pointing hydrogen bond donor (–OH) at the bottom of the deep cavity and a robust hydrogen bond acceptor (C=O) on the tubular inner wall of a primarily hydrophobic surface allow unidirectional interaction with various shape-complementary molecular guests within the tubular cavity through a combination of hydrophobic and hydrogen bonding interactions. This mimics a protein–ligand or fragment-pocket interaction event in a protein binding pocket [43].

Tubular pocket **88** was utilized in a model study of fragment-pocket interaction in fragment-based drug design (FBDD) due to its ability to interact with various small shape-complementary polar molecular guests through synergistic hydrophobic and

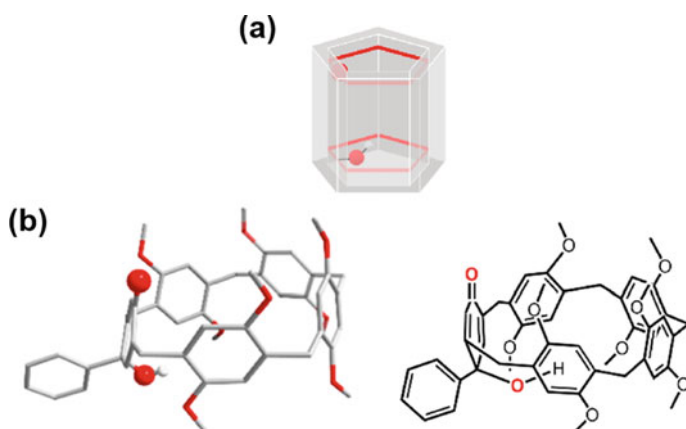


Fig. 4.14 a Cartoon representation of **88**. b Crystal structure (lef) and chemical structure (right) of **88**. Partially reproduced with permission from Ref. [43]. Copyright © 2021 American Chemical Society

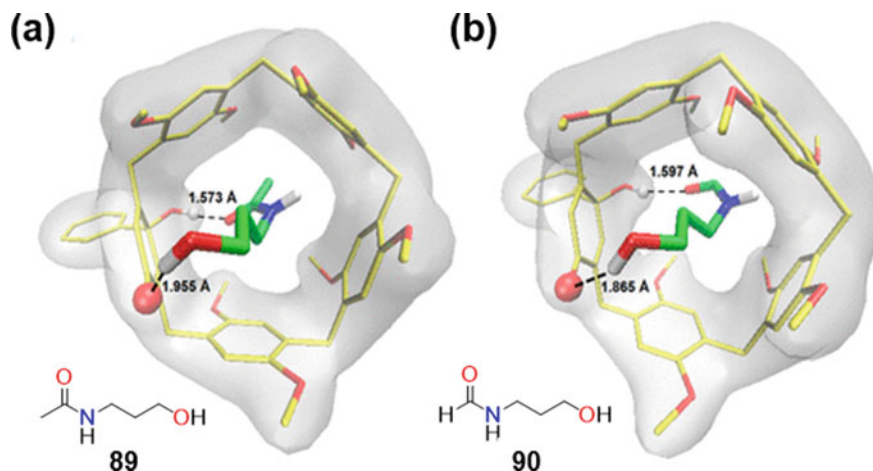


Fig. 4.15 Molecular docking models of **89** and **90** in **88**. **a** **89** was docked into the pocket **88** with AutoDock Vina. **b** **90** was docked into the pocket **88** with AutoDock Vina. Reproduced with permission from Ref. [43]. Copyright © 2021 American Chemical Society Society

hydrogen bonding interactions within its tubular cavity [43]. A library of structurally diverse “fragment ligands” that were shape-complementary to the “target pocket” **88** were screened, and weak to moderate binding affinities were observed between the model pocket and the fragment ligands. To investigate the correlation between binding strength (K_a) and properties of the guest fragments, molecular descriptors were collected, including the logarithm of the n-octanol/water partition coefficient ($\log P$), dipole moment (μ), molecular volume (V), surface area (S), and asphericity (Ω_a). Using information about how various fragment ligands bind inside the pocket of **88**, Wen and co-workers designed two “lead molecules”, **89** and **90**, which were intended to make use of both the hydrogen-bond donating (OH) and accepting (C=O) features of the pocket (Fig. 4.15). Both “lead molecules” had much stronger binding affinities than the “hit molecules” generated during the initial screening process. The model pocket demonstrated its usefulness in understanding FBDD because it allows researchers to study the binding behavior of fragments in a simplified system. By analyzing the interactions of the fragment **89** or **90** with the model pocket **88**, researchers can gain insights into how to optimize the fragments’ binding affinity and selectivity in FBDD.

4.2.5 Anthracene-Derived Receptor

Jiang's research group, which has experience in mimicking ligand-pocket interactions during the fabrication of naphthotubes [23, 24, 27, 28, 34, 35, 37], recently disclosed new cylindrical pockets that go beyond naphthotubes. Their latest development is a novel anthracene-derived host (**91**), which was constructed by stitching two pieces of bent anthracene dimers through a simultaneous construction (Fig. 4.16) [44]. With a deep hydrophobic pocket defined by the four anthracene sidewalls with the inwardpointing hydrogen bonding sites, host **91** effectively binds p-benzoquinone (**92**) as well as other quinones **93–104** with high selectivity through the cooperative effect of shielded noncovalent interactions and the hydrophobic effect. Control experiments, X-ray single crystal structures, and DFT calculations were used to verify these findings. Because they were located in a hydrophobic microenvironment, hydrogen bonding, C@H...p, and charge transfer interactions were able to persist and contribute to the strong binding affinity and high selectivity observed in the system. As a result, found that the p-benzoquinone had the highest association constant among all the known synthetic receptors, and it was even comparable in affinity to bioreceptors [44].

4.3 Conclusions

The development of macromolecules that mimic protein binding pockets has enabled the study of protein–ligand interactions in simplified model systems. However, most synthetic receptors currently known possess either hydrophobic cavities or polar binding sites only, which do not fully resemble the binding pockets found in proteins that typically feature both polar and hydrophobic groups. To address this limitation, functional groups can be introduced into hydrophobic cavities via the functionalization of synthetic receptors, resulting in artificial binding pockets that more closely resemble those found in real protein environments. By endowing synthetic pockets with both hydrogen bond donors and receptors at the inner surface, these biomimetic receptors can mimic the native-like features of protein binding pockets, providing a useful tool for studying host–guest interactions in a way that more closely resembles nature.

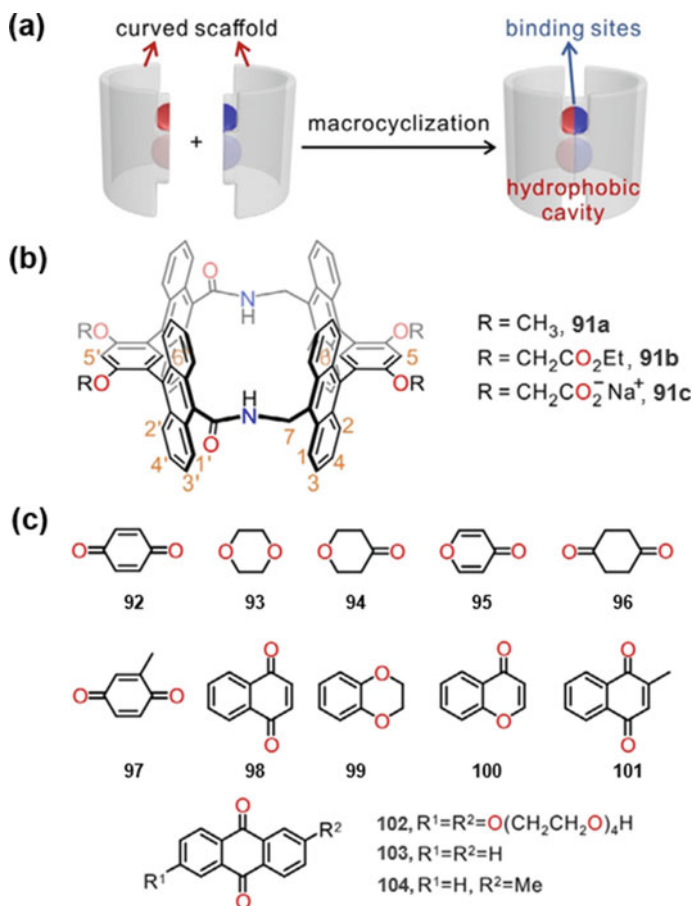


Fig. 4.16 **a** Cartoon representation and chemical structure of the simultaneous construction of anthracene-derived receptor with an endo-functionalized cavity. **b** Chemical structures of **91**. **c** Chemical structures of the guests **92–104** involved in the study. Reproduced with permission from Ref. [44]. Copyright © 2021 Wiley–VCH GmbH

Acknowledgements Z. W., W. H., M. M., H. Y., and K. W. thank the financial support from National Key Research and Development Program of China (2017YFA0206500), National Natural Science Foundation of China (21871281 and 21902176), Shanghai Sailing Program (19YF1452900).

References

1. Peck EM, Smith BD (2013) Applications of synthetic receptors for biomolecules. In: Smith BD (ed) *Synthetic receptors for biomolecules: design principles and applications*. Royal Society of Chemistry, Cambridge, UK, pp 1–38. <https://doi.org/10.1039/9781782622062-00001>
2. Babine RE, Bender SL (1997) Molecular recognition of protein–ligand complexes: applications to drug design. *Chem Rev* 97:1359–1472. <https://doi.org/10.1021/cr960370z>
3. McFedries A, Schwaib A, Saghatelian A (2013) Methods for the elucidation of protein–small molecule interactions. *Chem Bio* 20:667–673. <https://doi.org/10.1016/j.chembiol.2013.04.008>
4. Gellman SH (1997) Introduction: molecular recognition. *Chem Rev* 97:1231–1232. <https://doi.org/10.1021/cr970328j>
5. Yu G, Jie K, Huang F (2015) Supramolecular amphiphiles based on host–guest molecular recognition motifs. *Chem Rev* 115:7240–7303. <https://doi.org/10.1021/cr5005315>
6. Huc I, Kwon S, Lee H-S (2021) Synthetic foldamers: rational design of advance structures with diverse applications. *ChemPlusChem* 86:1042–1043. <https://doi.org/10.1002/cplu.202100288>
7. Nicolì F, Baroncini M, Silvi S, Groppi J, Credi A (2021) Direct synthetic routes to functionalised crown ethers. *Org Chem Front* 8:5531–5549. <https://doi.org/10.1039/d1qo00699a>
8. Kang SO, Llinares JM, Day VW, Bowman-James K (2010) Cryptand-like anion receptors. *Chem Soc Rev* 39:3980–4003. <https://doi.org/10.1039/C0CS00083C>
9. Butterfield SM, Rebek J (2006) A synthetic mimic of protein inner space: buried polar interactions in a deep water-soluble host. *J Am Chem Soc* 128:15366–15367. <https://doi.org/10.1021/ja0663374>
10. Purse BW, Rebek J (2015) Functional cavitands: chemical reactivity in structured environments. *PNAS* 102:10777–10782. <https://doi.org/10.1073/pnas.0501731102>
11. Mosca S, Yu Y, Rebek J (2016) Preparative scale and convenient synthesis of a water-soluble, deep cavitand. *Nat Protocols* 11:1371–1387. <https://doi.org/10.1038/nprot.2016.078>
12. Yang J-M, Chen Y-Q, Yu Y, Ballester P, Rebek J (2021) Rigidified cavitand hosts in water: bent guests, shape selectivity, and encapsulation. *J Am Chem Soc* 143:19517–19524. <https://doi.org/10.1021/jacs.1c09226>
13. Ashbaugh HS, Gibb BC, Suating P (2021) Cavitand complexes in aqueous solution: collaborative experimental and computational studies of the wetting, assembly, and function of nanoscopic bowls in water. *J Phys Chem B* 125:3253–3268. <https://doi.org/10.1021/acs.jpcc.0c11017>
14. Yu Y, Yang J-M, Rebek J (2020) Molecules in confined spaces: reactivities and possibilities in cavitands. *Chem* 6:1265–1274. <https://doi.org/10.1016/j.chempr.2020.04.014>
15. Rahmana F-U, Li Y-S, Petsalakis ID, Theodorakopoulos PG, Rebek J, Yu Y (2019) Recognition with metallo cavitands. *PNAS* 116:17648–17653. <https://doi.org/10.1073/pnas.1909154116>
16. Zhu Y, Tang M, Zhang H, Rahman F, Ballester P, Rebek J, Hunter CA, Yu Y (2021) Water and the cation– π interaction. *J Am Chem Soc* 143:12397–12403. <https://doi.org/10.1021/jacs.1c06510>
17. Zhu Y-J, Zhao M-K, Rebek J, Yu Y (2022) Recent advances in the applications of water-soluble resorcinarene-based deep cavitands. *Chem Open* 11:e202200026. <https://doi.org/10.1002/open.202200026>
18. Guan H-W, Zhu Y-J, Peters J, Brea O, Himo F, Rebek J, Yu Y (2021) Recognition of hydrophilic molecules in deep cavitand hosts with water-mediated hydrogen bonds. *Chem Commun* 57:8147–8150. <https://doi.org/10.1039/D1CC02505H>
19. Guo CC, Wang H, Lynch VM, Ji X, Page ZA, Sessler JL (2020) Molecular recognition of pyrazine *N,N'*-dioxide using aryl extended calix[4]pyrroles. *Chem Sci* 11:5650–5657. <https://doi.org/10.1039/D0SC01496F>
20. Kim DS, Sessler JL (2015) Calix[4]pyrroles: versatile molecular containers with ion transport, recognition, and molecular switching functions. *Chem Soc Rev* 44:532–546. <https://doi.org/10.1039/C4CS00157E>

21. Penuelas-Haro G, Ballester P (2019) Efficient hydrogen bonding recognition in water using aryl-extended calix[4]pyrrole receptors. *Chem Sci* 10:2413–2423. <https://doi.org/10.1039/C8SC05034A>
22. Shorthill BJ, Avetta CT, Glass TE (2004) Shape-selective sensing of lipids in aqueous solution by a designed fluorescent molecular tube. *J Am Chem Soc* 126:12732–12733. <https://doi.org/10.1021/ja047639d>
23. Yang L-P, Wang X, Yao H, Jiang W (2020) Naphthotubes: macrocyclic hosts with a biomimetic cavity feature. *Acc Chem Res* 53:198–208. <https://doi.org/10.1021/acs.accounts.9b00415>
24. Ma Y-L, Quan M, Lin X-L, Cheng Q, Yao H, Yang X-R, Li M-S, Liu W-E, Bai L-M, Wang R, Jiang W (2020) Biomimetic recognition of organic drug molecules in water by amide naphthotubes. *CCS Chem* 2:1078–1092. <https://doi.org/10.31635/ccschem.021.202101178>
25. Stella VJ, Rajewski RA (1997) Cyclodextrins: their future in drug formulation and delivery. *Pharm Res* 14:556–567. <https://doi.org/10.1023/A:1012136608249>
26. Muankaew C, Loftsson T (2018) Cyclodextrin-based formulations: a non-invasive platform for targeted drug delivery. *Basic Clin Pharmacol Toxicol* 122:46–55. <https://doi.org/10.1111/bcpt.12917>
27. Chen Z, Quan M, Dong YW, Li MS, Wang SM, Zhao LM, Yang LP, Wu J, Jiang W (2022) Molecular recognition and spectral tuning of organic dyes in water by amide naphthotubes. *Chem Commun* 58:9413–9416. <https://doi.org/10.1039/d2cc03270h>
28. Huang X, Wang X, Quan M, Yao H, Ke H, Jiang W (2021) Biomimetic recognition and optical sensing of carboxylic acids in water by using a buried salt bridge and the hydrophobic effect. *Angew Chem Int Ed* 60:1929–1935. <https://doi.org/10.1002/anie.202012467>
29. Sutanto F, Konstantinidou M, Dömling A (2020) Covalent inhibitors: a rational approach to drug discovery. *RSC Med Chem* 11:876–884. <https://doi.org/10.1039/D0MD00154F>
30. Boike L, Henning NJ, Nomura DK (2022) Advances in covalent drug discovery. *Nat Rev Drug Discov* 21:881–898. <https://doi.org/10.1038/s41573-022-00542-z>
31. Abbasov ME, Kavanagh ME, Ichu TA, Lazear MR, Tao Y, Crowley VM, am Ende CW, Hacker SM, Ho J, Dix MM, Suci R, Hayward MM, Kiessling LL, Cravatt BF (2021) A proteome-wide atlas of lysine-reactive chemistry. *Nat Chem* 13:1081–1092. <https://doi.org/10.1038/s41557-021-00765-4>
32. Kim SE (2022) Drug developers look to lysine on disease-linked proteins. *C&EN* 100:15–17. <https://cen.acs.org/pharmaceuticals/drug-development/Drug-developers-look-lysine-disease/100/i30>
33. Yang T, Cuesta A, Wan X, Craven GB, Hirakawa B, Khamphavong P, May JR, Kath JC, Lapek JD, Niessen S, Burlingame AL, Carelli JD, Taunton J (2022) Reversible Lysine-targeted probes reveal residence time-based kinase selectivity. *Nat Chem Biol* 18:934–941. <https://doi.org/10.1038/s41589-022-01019-1>
34. Li M-S, Dong Y-W, Quan M, Jiang W (2022) Stabilization of Imines and hemiaminals in water by an Endo-functionalized container molecule. *Angew Chem Int Ed* 61:e202208508. <https://doi.org/10.1002/anie.202208508>
35. Chai H, Chen Z, Wang S-H, Quan M, Yang L-P, Ke H, Jiang W (2020) Enantioselective recognition of neutral molecules in water by a pair of chiral biomimetic macrocyclic receptors. *CCS Chem* 2:440–452. <https://doi.org/10.31635/ccschem.020.202000160>
36. Chen T, Xiao G, Wang Z, Zou J, Wang J, Hu W, Liu YA, Yang Y, Wen K (2022) s-Tetrazine-bridged photochromic aromatic framework material. *ACS Omega* 7:11276–11284. <https://doi.org/10.1021/acsomega.2c00278>
37. Wang X, Quan M, Yao H, Pang X-Y, Ke H, Jiang W (2022) Switchable bifunctional molecular recognition in water using a pH-responsive *Endo*-functionalized cavity. *Nat Commun* 13:2291. <https://doi.org/10.1038/s41467-022-30012-4>
38. Ogoshi T, Yamagishi T-A, Nakamoto Y (2016) Pillar-shaped macrocyclic hosts Pillar[n]arenes: new key players for supramolecular chemistry. *Chem Rev* 116:7937–8002. <https://doi.org/10.1021/acs.chemrev.5b00765>
39. Cao D, Kou Y, Liang J, Chen Z, Wang L, Meier H (2009) A Facile and efficient preparation of pillararenes and a Pillarquinone. *Angew Chem Int Ed* 48:9721–9723. <https://doi.org/10.1002/anie.200904765>

40. Li Z, Yang Y-W (2021) Functional materials with pillarene struts. *Acc Mater Res* 2:292–305. <https://doi.org/10.1021/accountsmr.1c00042>
41. Li Q, Zhu H, Huang F (2020) Pillararene-based supramolecular functional materials. *Trend Chem* 2:850–864. <https://doi.org/10.1016/j.trechm.2020.07.004>
42. Hu W-B, Hu W-J, Liu YA, Li J-S, Jiang B, Wen K (2016) Multicavity macrocyclic hosts. *Chem Commun* 52:12130–12142. <https://doi.org/10.1039/C6CC03651A>
43. Wang Z, Chen T, Liu H, Zhao X, Hu W-B, Yang H, Liu YA, Wen K (2021) Pillar[5]arene-derived *endo*-functionalized molecular tube for mimicking protein-ligand interactions. *J Org Chem* 86:6467–6477. <https://doi.org/10.1021/acs.joc.1c00314>
44. Zhou H, Pang X-Y, Wang X, Yao H, Yang L-P, Jiang W (2021) Biomimetic recognition of Quinones in water by an *endo*-functionalized cavity with anthracene sidewalls. *Angew Chem Int Ed* 60:25981–25987. <https://doi.org/10.1002/anie.202112267>

Chapter 5

Singlet Oxygen Photo-Generation by Light Irradiation Using Metal–Organic Frameworks as Photodynamic Therapy Agents



Sajid Bashir and Jingbo Louise Liu

Abstract A metal–organic-framework zirconium (pyrene-1,3,6,8-tetrayl) tetrabenzoic acid (Zr7Pr) was fabricated and evaluated in retinal pigmented epithelial cells *in vitro* for singlet oxygen inactivation of cell function. Cellular health was evaluated through the measurement of stress biomarkers. It was shown that increases in lactate dehydrogenase (LDH) and mitochondrial membrane potential (MMP) activity are consistent with singlet reactive oxygen species (ROS). The levels of nitric oxide (NO) and peroxyxynitrite (ONOO⁻) as possible reactive nitrogen species (RNS) were evaluated to identify the site of Zr7Pr's inhibitory function. The analysis indicates that singlet oxygen generates superoxide and nitric oxide, which generates peroxyxynitrite. The most likely site of action of Zr7Pr is through the inactivation of mitochondrial pore transitions (MPTs) rather than complete membrane peroxidation. The exposed cysteines or histidine in the molecular targets of MPTs are modified, which affects the cell's ability to regulate apoptosis-inducing MPTs under oxidative stress. Cells tolerant to hydrogen peroxide poisoning are still susceptible to the actions of Zr7Pr, whose efficacy is most likely through impairment of mitochondrial function and modification of the pore within the adenosine nucleotide translocase protein family (ANT) domain of the MPT.

Keywords Mitochondria · ROS · MOF · Singlet oxygen · RNS · MPT · Stress

S. Bashir (✉) · J. L. Liu
The Department of Chemistry, Texas A&M University, Kingsville, 700 University Blvd.,
Kingsville, TX 78363-8202, US
e-mail: br9@tamuk.edu

J. L. Liu
Texas A&M Energy Institute, 1617 Research Pkwy, College Station, TX 77845, US

5.1 Introduction

The inactivation of damaged cells and recycling of cellular material occurs through programmed cascade signals, known as apoptosis [1]. Apoptosis occurs in normal and pathological conditions and can be induced through photodynamic therapy to stimulate cell death in cancerous cells [2]. A specific manifestation of apoptosis includes cytochrome c release [3] and changes in nitric oxide production [4], which distinguishes it from oxidative stress caused by reactive oxygen species [5].

Reactive oxygen species (ROS) induce death through lipid peroxidation, DNA fragmentation, and covalent modification of critical proteins [6]. Cancer therapy utilizes this process by (a) increasing intracellular ROS levels through the addition of agonists to induce tumor necrosis factor (TNF), resulting in cell death [7]; (b) generating ROS with photosensitizers [8], or (c) directly adding oxidizing agents to induce cell death [9]. ROS-induced cell death is implicated. In cells incubated with anti-oxidants and oxidants, cell death is retarded or stopped [10]. Similarly, cells with over-expression of enzymes responsible for reducing oxidative stress exhibit similar tolerance [11].

Reactive oxygen species include oxygen-containing free radicals, hydrogen peroxide, and singlet oxygen and often also include peroxynitrite (ONOO^-). High intracellular concentrations of these chemicals are usually accompanied by high caspase-3 activity induced by nitric oxide [12]. It was previously shown that methylene blue (MB) and visible light-induced singlet oxygen-induced apoptosis in *Salmonella typhimurium* [13]. What has not been demonstrated is whether singlet oxygen can induce nitric oxide or peroxynitrite as the lethal agents in inducing cell death or slowing cellular proliferation. This aspect is the focus of the current study.

5.2 Materials and Methods

Materials All chemicals were procured from VWR International (Atlanta, GA) or Sigma-Aldrich (St. Louis, MO). The buffers used in cell cultures were prepared using doubly distilled and sterilized water. CM-H2DCFDA (ROS), a reagent for measuring reactive oxygen species [14], DAF-FM Diacetate for NO quantification [15], and Singlet Oxygen Sensor dye (SOS) for singlet oxygen determination [16], were purchased from Invitrogen/Molecular Probes (Eugene, OR). Tetramethyl rhodamine methyl ester (MMP) was acquired to measure mitochondrial membrane potential [17]. CytoTox-ONE™ Homogeneous Membrane Integrity Assay (LDH) was used to determine cell viability.

Cell Culture Human telomerase reverse transcriptase retinal pigment epithelium (hTERT-RPE) cell cultures [18] were maintained in an essential medium with Earle's salts supplemented with 10% heat-inactivated fetal bovine serum, 100 units/mL penicillin, 100 $\mu\text{g}/\text{mL}$ streptomycin, and 1.4 mM L-glutamine. The cells were maintained at 35 °C with 95% air/5% CO_2 at 75% humidity. The utilized cells were in the

log-phase growth stage. A membrane integrity assay for lactate dehydrogenase was conducted after examining the cells by microscopy.

Monitoring of Protein Content, NO Activity, ROS, SOS, LDH, and MMP Activity The protein content, NO activity, ROS, SOS, LDH, and MMP activity was estimated using appropriate kits by strictly following the manufacturer's protocols. The cell pellets obtained were re-suspended in phosphate-buffered saline (PBS, pH 7.4), and the cell placements were kept between 100,000–150,000 cells/well or measured [19]. Fluorescence ($\lambda_{Ex}/\lambda_{Em}$) or absorbance (A) was evaluated at different wavelengths to determine various cellular activities. The following experimental settings were used: NO (Excitation λ_{495} /Emission λ_{515} nm), ROS (Ex $_{492}$ /Em $_{517}$ nm), LDH (A $_{\lambda_{490}-\lambda_{680}}$ nm), SOS (Ex $_{504}$ /Em $_{525}$ nm), or MMP (Ex $_{549}$ /Em $_{575}$ nm), Zr7Py NO (Excitation λ_{432} /Emission λ_{612} nm), and peroxynitrite (A $_{\lambda_{302}}$ nm). The samples were incubated in the dark for 45 min, following which fluorescence was measured. For inhibitor comparison, the whole cells were suspended in phosphate-buffered saline supplemented with 8 mM pyruvate [20] and various concentrations, ranging from 1 μ M to 900 mM, of specific inhibitors or additives. The actual concentration of the inhibitors was explicitly mentioned in the graphs. Water-soluble compounds were mixed with phosphate-buffered saline, deionized water, or DMSO. The sample volume added to whole cells was always less than 10% (0.5–25 L) to exclude DMSO toxicity [21].

Metal–Organic Framework Synthesis and Evaluation Metal–organic frameworks (MOFs) have recently gained attention as highly crystalline materials with permanent porosity and ultra-high internal surface areas. These frameworks usually have inorganic metal nodes and organic linkers with different topologies and chelation properties. MOFs find applications in various fields, such as gas storage/separation, catalysis, drug delivery, and therapeutic agents. In this study, the experiment aimed to construct a MOF motif composed of pyrene, a compound with strong fluorescence properties, as the functional group. Hence, the organic linker 4,4',4'',4'''-(pyrene-1,3,6,8-tetrayl)tetrabenzoic acid (H $_4$ TBAPy), containing pyrene as a backbone was chosen. Based on the charge density of hard-soft acid–base (HSAB) theory, zirconium (IV) with a high valence and closed-shell configuration could form a strong bond with carboxylate and produce solid fluorescence frameworks. Therefore, the solvothermal reactions between H $_4$ TBAPy and Zr (IV) resulted in a pale yellow crystalline MOF powder named Zr7Py under 120 °C, using DMSO as a solvent. Powder X-ray diffraction (PXRD) was employed to measure the crystallographic structure, indicating an isorecticular structure. The transmission electron microscopic image also showed that high crystalline compounds were produced.

5.3 Results

A kinetic repeated scan was conducted on human retinal pigment epithelium cells by utilizing fluorescence detection to exhibit that the Zr7Py compound, a zirconium metal–organic framework, can prompt the formation of single oxygen species. The successive additions of 5 μL of the compound are indicated by arrows in Fig. 5.1. The outcomes demonstrate that singlet oxygen was produced and quantified.

To demonstrate the toxicity of singlet oxygen and other oxidative agents in inducing apoptosis, a lactate dehydrogenase (LDH) assay was carried out, and Fig. 5.2 shows the results. The findings show that the zirconium metal–organic framework agent and hydrogen peroxide induce higher LDH activities, indicating cellular stress. In contrast, the addition of nitric oxide in the form of sodium nitroprusside or potassium ferrocyanide [$\text{K}_4[\text{Fe}(\text{CN})_6]$] was protective.

In order to understand the optimal incubation time for the zirconium metal–organic framework agent to function, the LDH percent change to unexposed whole cells was calculated and summarized in Fig. 5.3. The greatest stress was induced at 2–3 h, consistent with the premise that singlet oxygen-activated caspase activity is under transcriptional control and reaches a maximum between 2–5 h for most mammalian cell lines.

The LDH assay demonstrates that oxidative stress that leads to cell death is a summation of all oxidative species and is indirectly influenced by respiration. To investigate whether singlet oxygen is attributed to Zr7Py, superoxide, or hydrogen peroxide, or alterations in oxidative phosphorylation, the assay was performed with

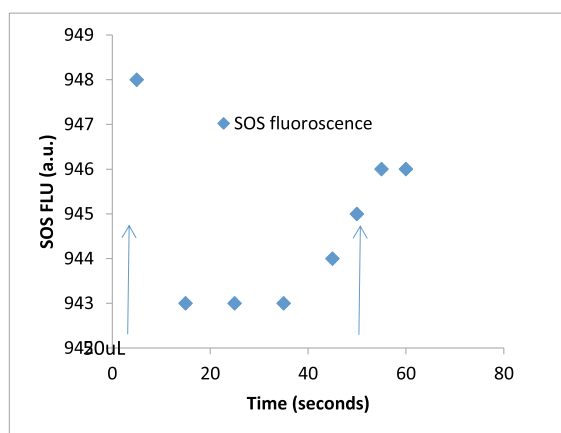


Fig. 5.1 Zirconium metal–organic framework (5 μL of 10 mg/mL in dimethyl sulfoxide, DMSO) was added (shown by the blue arrow) to approximately 50×10^3 cells per well and allowed to incubate for 30 s before measurement. The RPE cells were in phosphate-buffered saline (PBS) solution supplemented with 8 mM pyruvate. A control with methylene blue (100 μM in water) was also carried out. Both agents gave similar profiles, confirming singlet oxygen formation. The SOS dye was 1 μM (in DMSO)

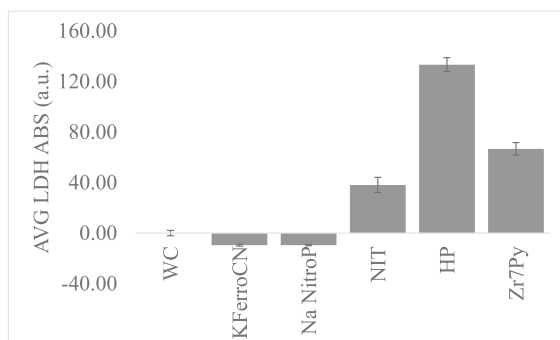


Fig. 5.2 A plot of percent change of absorbance of lactate hydrogenase (LDH relative to control) for RPE cells at 60 min with zirconium metal–organic framework agent (Zr7Pr). Zirconium metal–organic framework (5 μL of 10 mg/mL in dimethyl sulfoxide, DMSO) was added to approximately 50×10^3 cells per well and incubated for 60 min before measurement. The RPE cells were in phosphate-buffered saline (PBS) solution supplemented with 8 mM pyruvate. A control with potassium ferrocyanide (KFerroCN, $[\text{K}_4\text{Fe}(\text{CN})_6]$), 25 μL , 83 mM stock in H_2O); Sodium Nitroprusside (Na NitroP, 25 μL , 83 mM stock in H_2O), hydrogen peroxide (HP, 25 μL of 3% solution in H_2O by volume) was used for comparative analysis of the effectiveness of Zr7Pr as a cytotoxic agent

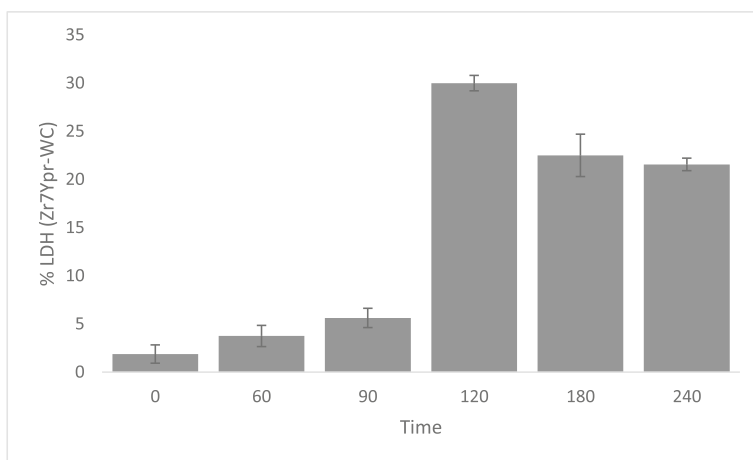


Fig. 5.3 A plot of percent change of absorbance of lactate hydrogenase (LDH relative to control) for RPE cells over 0–240 min with zirconium metal–organic framework agent (Zr7Pr). The Zr7Pr agent (5 μL of 10 mg/mL in dimethyl sulfoxide, DMSO) was added to approximately 50×10^3 cells per well. The RPE cells were in phosphate-buffered saline (PBS) solution supplemented with 8 mM pyruvate. The relative percent difference for LDH, estimated to be 30% for maximal activity, is shown

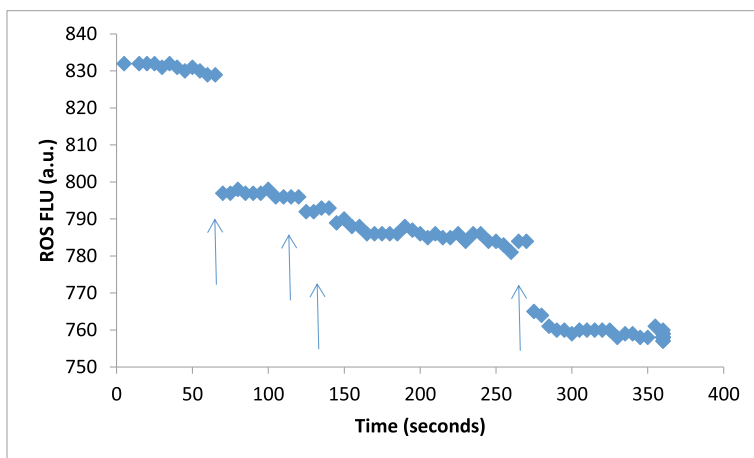


Fig. 5.4 A plot of change in ROS fluorescence versus time for RPE cells with Oxypurinol (5 μ L of a 0.21 mM stock in DMSO). The agent was injected into approximately 50×10^3 cells per well and allowed to incubate for 30 s before measurement. The RPE cells were in phosphate-buffered saline (PBS) solution supplemented with 8 mM pyruvate. A decrease in fluorescence was immediately detected. The ROS dye was 1 μ M (in DMSO)

known respiration inhibitors, including an inhibitor for xanthine oxidase. Xanthine oxidase is an enzyme that is known to generate superoxide.

A kinetic scan was run with oxypurinol to validate this assumption, showing a decreased ROS-attributed fluorescence (Fig. 5.4). Zoratti and Szabò have shown that singlet oxygen does not induce pore transitions in mitochondria, unlike other oxidants such as superoxide [22].

In order to understand the effects of Zr7Py on superoxide production, the experiment employed Zr7Ypr and allopurinol during cell incubation. The study also investigated the potential impact of uncoupling oxidative phosphorylation by utilizing an uncoupling agent FCCP and singlet oxygen control species such as oligomycin, rotenone, and methylene blue. ADP was not supplemented during cell incubation to promote stage 4 respiration. At the same time, oligomycin inhibited the proton pump of complex V of the respiratory chain without affecting electron transport (or stage IV respiration).

A small dose-dependent response was observed with oligomycin co-incubated with Zr7Py, from 57% increased LDH activity to almost 105% (Fig. 5.5). A slight decrease in LDH activity was observed upon adding rotenone, an inhibitor of mitochondrial respiratory chain complex I. The generation of reactive oxygen species, such as superoxide, by rotenone, is thought to be responsible for this effect. However, cellular superoxide dismutase (SOD) seems to counterbalance this effect. An experiment was conducted to understand the impact of methylene blue and Zr7Py on LDH activity in cultured RPE cells. The findings suggest that oxidative species were converted into hydrogen peroxide or superoxide and that the cellular SOD quenched them, resulting in decreased LDH activity. The mitochondria appear to be the site of

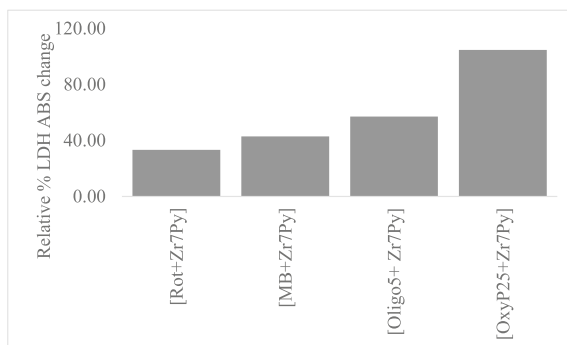


Fig. 5.5 Plot of relative percent change for lactate dehydrogenase (LDH) for RPE cells incubated with rotenone (Rot, 25 μL of a 100 μM stock in DMSO) was co-incubated with Zr7Py (0.5 μL of 10 mg/mL in DMSO); Methylene blue (MB, 25 μL of a 100 μM stock in H_2O with 0.5 μL of Zr7Py); oligomycin (Oligo, 5 or 25 μL of a 100 μM stock in DMSO with 0.5 μL of Zr7Py) were measured after 60 min using LDH assay and percent change relative to unexposed controls shown. The FCCP (17 μM in DMSO) alone was 24-fold higher than controls suggesting depolarization of the mitochondrial membrane potential

inhibition of Zr7Py, and oxidative stress at the mitochondria leads to apoptosis via the release of cytochrome c and activation of caspases. A plot of nitric oxide (NO), shown in Fig. 5.6, exhibited a relative increase upon adding NO-releasing agents such as sodium nitroprusside. However, Zr7Py itself did not lead to an increase in NO. Its activity may be directly oxidative via singlet oxygen, not nitric oxide, or the excess nitric oxide with hydroxyl radical might be converted to peroxynitrite, which lowers the measured NO.

The change in mitochondrial membrane potential using tetramethyl rhodamine methyl ester (83 μM) was also examined and shown to increase for FCCP (12.5%), HP (6.25%), and oligomycin 5 μL with Zr7Py, normalized to the relative change for control (set at 0%). The fluorescence of Zr7YPr was also measured and increased to 116% with [MB + Zr7Py] and decreased to 50% with [OxyP25 + Zr7Py], suggesting that some superoxide from Zr7Py was converted to superoxide and that superoxide was quenched using cellular SOD.

To evaluate whether the mitochondria was the stress site, the absorbance of cytochrome c oxidase, cytochrome b oxidase, and cytochrome a + a₃ oxidase was measured after 16 h with Zr7Py and other select agents. For example, adding sodium cyanide led to an overall absorbance increase of cytochrome a + a₃ of 2.5 fold, normalized to control. An increased absorbance of 17-fold was observed with Zr7Py alone or 18-fold in conjugation with methylene blue. The absorbance for cytochrome b increased 34-fold relative to increases for methylene blue with Zr7Py, strongly confirming that the site of action was the mitochondrial respiratory proteins.

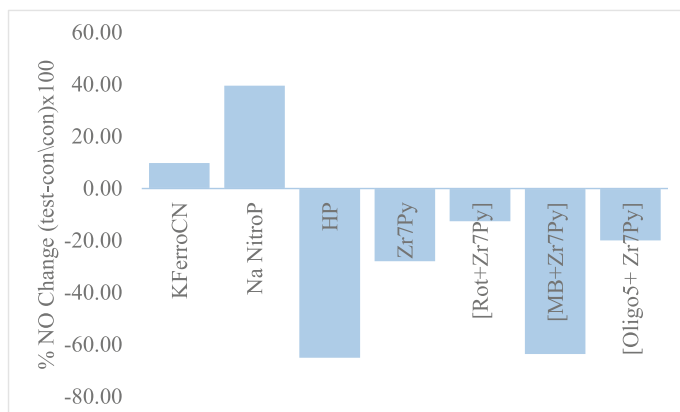


Fig. 5.6 A plot of relative percent change for nitric oxide fluorescence change (Control normalized to 0%) for RPE cells incubated potassium ferrocyanide (KFerroCN, $[K_4[Fe(CN)_6]]$), sodium nitroprusside (Na NitroP), hydrogen peroxide (HP, 3% v/v in H_2O), Zr7Py (5 μL , 10 mg/mL in DMSO), Rotenone (Rot, 25 μL of a 100 μM stock in DMSO) was co-incubated with Zr7Py (0.5 μL of 10 mg/mL in DMSO); Methylene blue (MB, 25 μL of a 100 μM stock in H_2O with 0.5 μL of Zr7Py); Oligomycin (Oligo, 5 μL of a 100 μM stock in DMSO with 0.5 μL of Zr7Py) were measured after 60 min

5.4 Discussion

The above data demonstrates that singlet oxygen stimulates apoptosis and that the degree of apoptosis can be controlled through the production of nitric oxide since cells incubated with sodium nitroprusside or potassium ferrocyanide exhibited higher NO fluorescence and lower mitochondrial membrane potential absorbance, where the membrane potential is a measure of the degree of apoptosis. Studies by Zhuang have shown that singlet oxygen in leukemia cells stimulates caspase-3 [23]. The cells incubated with Zr7Py exhibit caspase-mediated inhibition of oxidative phosphorylation as shown with rotenone and oligomycin, consistent with observations by Tao, who showed that the pan-caspase inhibitor benzyloxycarbonyl-Val-Ala-Asp-fluoromethyl ketone was able to block caspase-mediated inhibition and lower mitochondrial permeability transition and presumably membrane potential [24]. In a separate study by Vargas, they showed that oxypurinol could scavenge hydroxyl radicals but not singlet oxygen [25]. Both singlet oxygen and hydroxyl radical can facilitate lipid peroxidation. In the presence of either oxypurinol, vitamin C, or vitamin E, the degree of lipid peroxidation was lessened by 30, 65, and 70%, respectively. While vitamins A and E are anti-oxidants, allopurinol was thought to be a quencher of hydroxyl radicals, lowering the ROS pool for lipid peroxidation [26]. The result of lipid peroxidation is loss of membrane fluidity, the release of cytochrome c, and cell death. Therefore allopurinol may be able to redistribute the oxidative load. The results with oligomycin suggest that one possible site of interaction is ATP-synthase (complex V of the respiratory since the co-addition of

Zr7Py and oligomycin increases LDH activity, resulting in the inhibition of oxidative phosphorylation and cell death. The effect of singlet oxygen on mitochondrial respiration was also investigated by Atlante, who used FCCP, would, that singlet oxygen targeted the adenine nucleotide carrier, impairing oxidative phosphorylation [27]. Since the carrier is near complex V, this would suggest the likely mode of inhibition is the mitochondrial cytochrome $a + a_3$ (complex IV) and cytochrome b oxidase. It is suggested that the mode of inhibition is the mitochondrial cytochrome $a + a_3$ (complex IV) and cytochrome b oxidase because the carrier is located close to complex V. To understand the role of calcium release in/from the mitochondria, an experiment was conducted using DAF-FM DA to measure NO fluorescence with BAPTA. This cytosolic calcium chelator does not affect mitochondrial calcium levels [28]. Other cofactors used were supplemental CaCl_2 (to the cytoplasm), supplemental adenosine triphosphate (ATP) [29], and methyl ornithine, a competitive inhibitor of L-arginine [30]. The latter is a substrate for nitric oxide synthase for NO production [31]. The results relative to control (no treatment) showed an overall decrease in measured nitric oxide fluorescence of 18% (BAPTA), 9.5% (Ca^{2+}), 31% (ATP), and 67% (methyl ornithine). The results suggest the site of action is not inhibition of mitochondrial Ca^{2+} transport proteins [32] but pore-transition proteins or residues. Under conditions where the mitochondria cannot maintain a proton gradient, calcium ion leaves the matrix by reverse operation of the uniporter due to stress imposed by rotenone, which inhibits respiration [33]. The ratio of ATP/ADP determines cellular activity, where ATP levels are high, the addition of supplemental ATP is inhibitory in terms of NO production [34], while methyl ornithine supports the contention that nitric oxide synthase [35] synthesize NO. The experiment was conducted to understand the relationship between methyl ornithine and arginine in nitric oxide (NO) production. The results suggest that NO is initially produced by nitric oxide synthase (NOS) and is unaffected by singlet oxygen. However, as NO concentration increases, peroxynitrite generation occurs, decreasing measured NO levels. Pueyo et al. [36] confirmed this discovery by measuring the relative percent decrease of NO and the percent increase of peroxynitrite for both the Fe(III)_ascorbate system and Zr7YPr. The changes observed were $-47\% \text{ NO} / +219\% \text{ ONOO}$ (for Fe(III)-Asc) and $-34\% \text{ NO} / +34\% \text{ ONOO}$ (for Zr7Py), with changes in fluorescence (for NO) or absorbance for (ONOO^-) control cells normalized to 0%. The data indicate that in the initial stages (within 2 h), the respiratory capacity of the mitochondria is unaffected; the data with calcium also supports the contention that the steady-state Ca^{2+} accumulation maintained by the mitochondria was unaffected and that pore opening and closing to facilitate a membrane potential [37]. The results with the respiration inhibitors and monitoring of cytochrome absorbance suggest that the respiratory chain electron increased [38]. From the above considerations, superoxide and singlet oxygen interact in a distinct manner since the LDH, MMP, and NO measurements for hydrogen peroxide, Zr7YPr, are dissimilar. The site for Zr7YPr may be the inactivation of pore domains in the mitochondria due to the increased activity after adding FCCP [39]. Superoxide is believed to undergo conversion with NO to produce peroxynitrite, resulting in reduced NO fluorescence. Singlet oxygen chemistry suggests that protein cysteine and histidine residues, which control pore transition opening

and closing, are the prime targets. Oxidized cysteine may be produced, and oxidized glutathione to the corresponding dithiol. The experiment was conducted to gain a better understanding of these processes. The other accessible residue in mitochondrial pores is histidine, which may undergo ring opening and cycloaddition by singlet oxygen. The histidine would no longer be able to become deprotonated, and pore opening would be altered [40]. The adenine carrier is another likely candidate since oxidation of this carrier would inactivate mitochondrial pores and lead to inhibition of respiration. The work by Ricchelli has previously shown that singlet oxygen was capable of oxidizing proteins within the mitochondria [41] and that cysteines [42] and histidine [43] are critical to mitochondrial pore transition opening and closing.

Earlier research has shown that the co-administration of cells with rotenone [44] induces apoptosis by releasing cytochrome c and activating caspase 3, resulting in DNA fragmentation. Rotenone is known to decrease ATP production, and it has further been demonstrated that ATP/ADP ratio determines whether the cell undergoes apoptosis [45] or necrosis [46] or recovery [47]. Sweet and Singh also showed in HL-60 cells that co-administration of rotenone or oligomycin lowered ATP to approximately 20% of control [48]. In addition, in HT1080 cells, it was demonstrated that rotenone-induced cell death by increased reactive oxygen species [49]. Under a high ROS environment, superoxide can react with hydrogen peroxide to generate singlet oxygen and hydrogen radicals [50]. Cell lines which express Mn-SOD were more tolerant to rotenone-induced apoptosis due to the conversion of superoxide to hydrogen peroxide, since Mn-SOD is mitochondrial bound, the site of action of rotenone was confirmed to be within the mitochondria [51] and was consistent with our results. A plausible chemical mechanism and site of action are summarized in Figs. 5.7 and 5.8, respectively.

★ Oxygen+ e^- [from electron transport chain, (ETC)] $\rightarrow O_2^- + NO$ [from NOS] \rightarrow peroxynitrite A Set A reactions are centered on peroxynitrite. Examples include: $O_2^- + O_2^- + 2H^+ \rightarrow HOOH + {}^1O_2$; $ONOO^- + H^+ \rightarrow ONOOH$; $ONOOH \rightarrow NO_2^*$; $ONOO^- + HOOH \rightarrow NO_2^- + H_2O + {}^1O_2$; and $O_2^- + HOOH \rightarrow OH^* + OH^- + {}^1O_2$.

Zr7Py catalyzes singlet oxygen generation by accepting an electron from the electron transport chain (ETC). The ETC facilitates the transfer of electrons, which follows the redox potential gradient from complex I (NADH-ubiquinone oxidoreductase) and complex II (succinate-ubiquinone oxidoreductase). Subsequently, ubiquinone (coenzyme Q) participates in the redox reaction, producing ubisemiquinone and ubiquinol. The experiment aimed to understand that singlet oxygen production by Zr7Py was greater than known stressors. The electrons are then carried by ubiquinol to complex III (ubiquinol-cytochrome c oxidase reductase), which further passes them to cytochrome c. Then, cytochrome c transfers the electrons to complex IV (cytochrome a+a₃ oxidase) to donate an electron to oxygen, creating water. ATP is also produced by the enzyme apart from generating nitric oxide, especially when adenosine triphosphate (ATP) is required to be lessened.

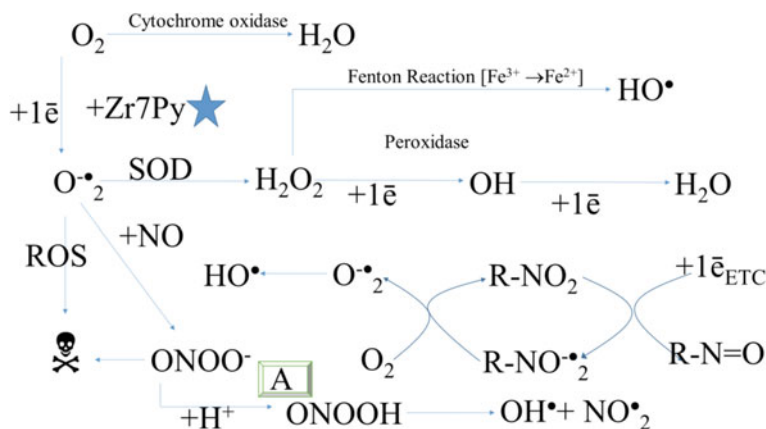


Fig. 5.7 Summary of the reactive oxygen species that can be generated. Molecular oxygen is the terminal electron acceptor in the mitochondrial electron transport chain (ETC). Electrons react with oxygen to form water catalyzed by cytochrome $a+a_3$. Electron (\bar{e}) can leak from the ETC and combine with molecular oxygen to form a superoxide radical anion. This radical's oxidative influence is minimized through the enzymatic action of Mn superoxide dismutase (Mn-SOD). The generated hydrogen peroxide is broken down by catalase or peroxidase enzymes to produce water. Electrons can also form singlet oxygen or other reactive oxygen species (ROS). When nitrogen is the heteroatom, peroxynitrite anion can be formed from hydroxyl radical and nitric oxide. The latter is formed from nitric oxide synthase using arginine as a substrate. The collective effect of ROS is lipid peroxidation and denaturation of proteins or nucleic acids resulting in apoptosis (☠).

Chemical energy in the form of ATP is produced by the transfer of electrons down a redo gradient from complexes I to V [52]. This drives protons (H^+) out of the mitochondrial inner membrane into the intermembrane space, resulting in a mitochondrial membrane potential that is coupled to ATP synthesis from adenosine diphosphate (ADP) and inorganic phosphate (P_i). In exchange for cytosolic ADP, ATP is released from the mitochondria using the carrier adenine nucleotide translocator (ANT). Mitochondrial permeability transition pores of voltage-dependent anion channel (VDAC), ANT, and cyclophilin D regulate ion mobility like calcium. Singlet oxygen is linked to covalent modification of critical amino acids within the MTP, like cysteine or histidine, leading to a loss of membrane potential, cytochrome c release, and apoptosis [53] (☠).

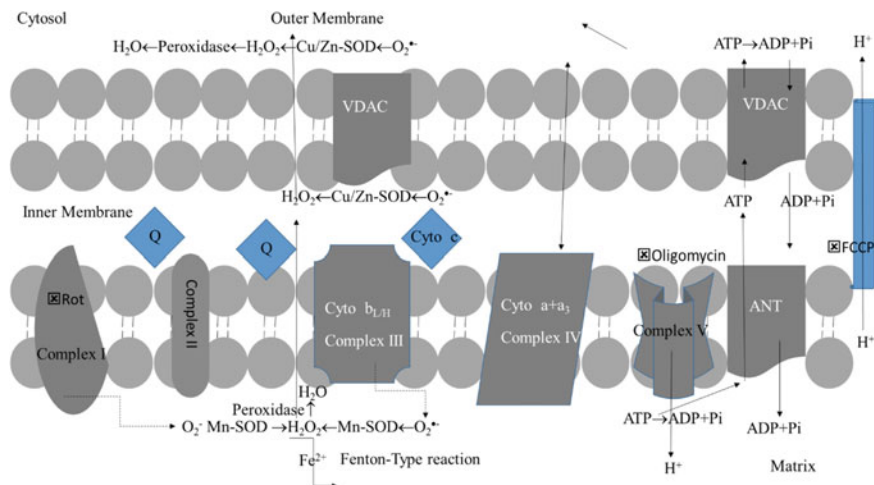


Fig. 5.8 The overview portrays the inhibition and induction of mitochondrial ROS. Complex I and III on the matrix side and both sides of the inner mitochondrial membrane produce superoxide. The study aimed to have a greater understanding of the oxidative singlet process. Complex I is inhibited by rotenone, while the conversion of superoxide to hydrogen peroxide is facilitated in the matrix enzyme by manganese superoxide dismutase (MnSOD) or the mitochondrial intermembrane space and cytosol enzyme, copper/zinc SOD (Cu/ZnSOD). Hydrogen peroxide can activate signaling such as caspase by diffusing outside the mitochondria. Glutathione peroxidase detoxifies hydrogen peroxide in water. In reduced iron hemes (such as Fe^{2+}), the Fenton reaction converts hydrogen peroxide to hydroxyl radical (OH^{\cdot}). These reactions also decouple nitric oxide synthase [NOS], and instead of generating nitric oxide (NO), superoxide gets produced, which, with hydroxyl radical, results in peroxynitrite [$ONOO^-$]

5.5 Conclusion

In conclusion, the data presented in this paper support the view that the singlet oxygen action of Zr7Pr results in an increase in lactate dehydrogenase (LDH) and mitochondrial membrane potential (MMP) activity of cultured controls relative to untreated control RPE cells. Further evaluation of nitric oxide and peroxynitrite and selective use of mitochondrial inhibitors places the site of Zr7Pr's catalyzed inhibition in the mitochondria. The results indicate that while singlet oxygen is a strong oxidant and can facilitate oxidative stress and apoptosis through the activation of caspases, the indirect action of singlet oxygen also generates superoxide. High levels of superoxide and nitric oxide generate peroxynitrite. Cells with a high absorbance for peroxynitrite had a low fluorescence of nitric oxide, suggesting the conversion of one oxidant to the other. Through analysis of similar studies in the literature, we hypothesize that the most likely site of action of Zr7Pr is through the inactivation of mitochondrial pore transitions (MPTs) rather than complete membrane peroxidation. The likely molecular targets are the exposed cysteines or histidine, which have been postulated in other molecular studies and appear to be consistent with our

trends in adenosine triphosphate levels, calcium homeostasis, and using a chelating agent. Upon modification of critical residues, the mitochondria are unable to regulate MPTs appropriately and undergo apoptosis through the well-documented pathway of caspase-cytochrome c. Our results show that cells tolerant to hydrogen peroxide poisoning may be susceptible to the actions of Zr7Pr, whose efficacy is most likely through impairment of mitochondrial function and covalent modification of the pore within the ANT domain of the MPT.

Acknowledgments and Author Contribution R. Welch Foundation (AC-0006) and Petroleum Research Funds are duly acknowledged. The technical support from the Department of Chemistry at Texas A&M University-Kingsville is also duly acknowledged. Dr. Hong-Cai Zhou and his team are also duly acknowledged for providing MOFs as photodynamic therapy agents, inducing nitric oxide as an apoptotic agent. SB conducted the in vitro experiments, and JL completed the nanoscience experiments; Dr. Wigle provided laboratory access, and the Zhou Group provided the MOF metal and ligands and laboratory access.

References

1. Cohen GM (1997) Caspases: the executioners of apoptosis. *Biochem J* 326(1):1–16
2. Jänicke RU, Sprengart ML, Wati MR, Porter AG (1998) Caspase-3 is required for DNA fragmentation and morphological changes associated with apoptosis. *J Biol Chem* 273(16):9357–9360
3. Reed JC (1997) Cytochrome c: can't live with it—can't live without it. *Cell* 91(5):559–562
4. Bonfoco E, Krainc D, Ankarcrona M, Nicotera P, Lipton SA (1995) Apoptosis and necrosis are two distinct events induced by mild and intense insults with N-methyl-D-aspartate or nitric oxide/superoxide in cortical cell cultures. *Proc Natl Acad Sci* 92(16):7162–7166
5. Lennon SV, Martin SJ, Cotter TG (1991) Dose-dependent induction of apoptosis in human tumor cell lines by widely diverging stimuli. *Cell Prolif* 24(2):203–214
6. Lin KT, Xue JY, Sun FF, Wong PY (1997) Reactive oxygen species participate in peroxynitrite-induced apoptosis in HL-60 cells. *Biochem Biophys Res Commun* 230(1):115–119
7. Goossens V, Grooten J, De Vos K, Fiers W (1995) Direct evidence for tumor necrosis factor-induced mitochondrial reactive oxygen intermediates and their involvement in cytotoxicity. *Proc Natl Acad Sci* 92(18):8115–8119
8. Staneloudi C, Smith KA, Hudson R, Malatesti N, Savoie H, Boyle RW, Greenman J (2007) Development and characterization of novel photosensitizer: scFv conjugates for use in photodynamic therapy of cancer. *Immunology* 120(4):512–517
9. Boobis AR, Fawthrop DJ, Davies DS (1989) Mechanisms of cell death. *Trends Pharmacol Sci* 10(7):275–280
10. Atabay C, Cagnoli CM, Kharlamov E, Ikonovic MD, Manev H (1996) Removal of serum from primary cultures of cerebellar granule neurons induces oxidative stress and DNA fragmentation: protection with anti-oxidants and glutamate receptor antagonists. *J Neurosci Res* 43(4):465–475
11. Greenlund LJ, Deckwerth TL, Johnson EM (1995) Superoxide dismutase delays neuronal apoptosis: a role for reactive oxygen species in programmed neuronal death. *Neuron* 14(2):303–315
12. Tamatani M, Ogawa S, Niitsu Y, Tohyama M (1998) Involvement of Bcl-2 family and caspase-3-like protease in NO-mediated neuronal apoptosis. *J Neurochem* 71(4):1588–1596
13. Epe B, Hegler J, Wild D (1989) Singlet oxygen is a reactive species in *Salmonella typhimurium* DNA damage induced by methylene blue/visible light. *Carcinogenesis* 10(11):2019–2024

14. Kristiansen KA, Jensen PE, Møller IM, Schulz A (2009) Monitoring reactive oxygen species formation and localization in living cells using the fluorescent probe CM-H₂DCFDA and confocal laser microscopy. *Physiol Plant* 136(4):369–383
15. Itoh Y, Ma FH, Hoshi H, Oka M, Noda K, Ukai Y, Toda N (2000) Determination and bioimaging method for nitric oxide in biological specimens by diaminofluorescein fluorometry. *Anal Biochem* 287(2):203–209
16. Lin H, Shen Y, Chen D, Lin L, Wilson BC, Li B, Xie S (2013) Feasibility study on quantitative measurements of singlet oxygen generation using singlet oxygen sensor green. *J Fluoresc* 23(1):41–47
17. Floryk D, Houek J (1999) Tetramethyl rhodamine methyl ester (TMRM) is suitable for cytofluorometric measurements of mitochondrial membrane potential in cells treated with digitonin. *Biosci Rep* 19(1):27–34
18. Wigle JC, Castellanos CC, Denton ML, Holwitt EA (2014) Nitric oxide measurements in hTERT-RPE cells and subcellular fractions exposed to low levels of red light. In: *SPIE BiOS*. International Society for Optics and Photonics, pp 89320D–89320D
19. Rieck P, Peters D, Hartmann C, Courtois Y (1993) A new, rapid colorimetric assay for quantitatively determining cellular proliferation, growth inhibition, and viability. *J Tissue Cult Methods* 15(1):37–41
20. Yang D, Elnor SG, Bian ZM, Till GO, Petty HR, Elnor VM (2007) Pro-inflammatory cytokines increase reactive oxygen species through mitochondria and NADPH oxidase in cultured RPE cells. *Exp Eye Res* 85(4):462–472
21. Öz ES, Aydemir E, Fışkın K (2012) DMSO exhibits similar cytotoxicity effects to thalidomide in mouse breast cancer cells. *Oncol Lett* 3(4):927
22. Zoratti M, Szabò I (1995) The mitochondrial permeability transition. *Biochim Biophys Acta (BBA) Rev Biomembr* 1241(2):139–176
23. Zhang S, Demirs JT, Kochevar IE (2001) Protein kinase C inhibits singlet oxygen-induced apoptosis by decreasing caspase-8 activation. *Oncogene* 20(46):6764–6776
24. Tao Z, Withers HG, Penefsky HS, Goodisman J, Souid AK (2006) Inhibition of cellular respiration by doxorubicin. *Chem Res Toxicol* 19(8):1051–1058
25. Vargas F, Rivas C, Zoltan T, Díaz Y, Alexander I, Padrón L, Cárdenas YM et al (2008) In vitro studies of the dual properties of allopurinol anti- and photo-oxidants Mechanisms. *Rev Colomb Cien Químico-Farm* 37(1):69–83
26. Vargas F, Rivas C, Canudas N (1994) It photosensitized lipid peroxidation by cinoxacin and its photoproducts—the involvement of a derived peroxide in its phototoxicity. *Pharmazie* 49(10):742–745
27. Atlante A, Passarella S, Quagliariello E, Moreno G, Salet C (1989) Haematoporphyrin derivative (Photofrin II) photosensitization of isolated mitochondria: inhibition of ADP/ATP translocator. *J Photochem Photobiol B Biol* 4(1):35–46
28. Boo YC, Sorescu GP, Bauer PM, Fulton D, Kemp BE, Harrison DG, Jo H et al (2003) Endothelial NO synthase phosphorylated at Ser 635 produces NO without requiring intracellular calcium increase. *Free Radical Biol Med* 35(7):729–741
29. Garvin JL, Herrera M, Ortiz PA (2011) Regulation of renal NaCl transport by nitric oxide, endothelin, and ATP: clinical implications. *Annu Rev Physiol* 73:359–376
30. Narayanan K, Griffith OW (1994) Synthesis of L-thiocitrulline, L-homothiocitrulline, and S-methyl-L-thiocitrulline: a new class of potent nitric oxide synthase inhibitors. *J Med Chem* 37(7):885–887
31. Cassina A, Radi R (1996) Differential inhibitory action of nitric oxide and peroxynitrite on mitochondrial electron transport. *Arch Biochem Biophys* 328(2):309–316
32. Kowaltowski AJ, Castilho RF, Vercesi AE (1995) Ca²⁺-induced mitochondrial membrane permeabilization: role of coenzyme Q redox state. *Am J Physiol Cell Physiol* 269(1):C141–C147
33. Casarejos MJ, Menendez J, Solano RM, Rodriguez-Navarro JA, de Yébenes JG, Mena MA (2006) Susceptibility to rotenone is increased in neurons from parkin null mice and is reduced by minocycline. *J Neurochem* 97(4):934–946

34. Passarella S, Ostuni A, Atlante A, Quagliariello E (1988) Increased ADP/ATP exchange in rat liver mitochondria irradiated *in vitro* by helium-neon laser. *Biochem Biophys Res Commun* 156(2):978–986
35. Babu BR, Griffith OW (1998) N 5-(1-Imino-3-butenyl)-1-ornithine a neuronal isoform selective mechanism-based inactivator of nitric oxide synthase. *J Biol Chem* 273(15):8882–8889
36. Pueyo ME, Arnal JF, Rami J, Michel JB (1998) Angiotensin II stimulates the production of NO and peroxynitrite in endothelial cells. *Am J Physiol Cell Physiol* 274(1):C214–C220
37. Bernardi P (1996) The permeability transition pore. Control points of a cyclosporin A-sensitive mitochondrial channel involved in cell death. *Biochimic Biophys Acta (BBA) Bioenerg* 1275(1):5–9
38. Salet C, Moreno G, Ricchelli F (1997) Effects of photofrin® photodynamic action on mitochondrial respiration and superoxide radical generation. *Free Radical Res* 26(3):201–208
39. Salet C, Moreno G, Atlante A, Passarella S (1991) Photosensitization of isolated mitochondria by hematoporphyrin derivative (Photofrin): effects on bioenergetics. *Photochem Photobiol* 53(3):391–393
40. Tomita M, Irie M, Ukita T (1969) Sensitized photooxidation of histidine and its derivatives. Products and mechanism of the reaction. *Biochemistry* 8(12):5149–5160
41. Ricchelli F, Gobbo S, Jori G, Salet C, Moreno G (1995) Temperature-induced changes in fluorescence properties as a probe of porphyrin microenvironment in lipid membranes. *Eur J Biochem* 233(1):165–170
42. Petronilli V, Costantini P, Scorrano L, Colonna R, Passamonti S, Bernardi P (1994) The oxidation-reduction state of vicinal thiols tunes the voltage sensor of the mitochondrial permeability transition pore. Increase of the gating potential by oxidants and its reversal by reducing agents. *J Biol Chem* 269(24):16638–16642
43. Nicolli A, Petronilli V, Bernardi P (1993) Modulation of the mitochondrial cyclosporin A-sensitive permeability transition pore by matrix pH. Evidence that the pore open-closed probability is regulated by reversible histidine protonation. *Biochemistry* 32(16):4461–4465
44. Barrientos A, Moraes CT (1999) Titrating the effects of mitochondrial complex I impairment in the cell physiology. *J Biol Chem* 274(23):16188–16197
45. Stefanelli C, Bonavita F, Farruggia G, Falcieri E, Robuffo I, Pignatti C, Caldarera CM et al (1997) ATP depletion inhibits glucocorticoid-induced thymocyte apoptosis. *Biochem J* 322(3):909–917
46. Eguchi Y, Shimizu S, Tsujimoto Y (1997) Intracellular ATP levels determine cell death fate by apoptosis or necrosis. *Can Res* 57(10):1835–1840
47. Leist M, Single B, Castoldi AF, Kühnle S, Nicotera P (1997) Intracellular adenosine triphosphate (ATP) concentration: a switch in the decision between apoptosis and necrosis. *J Exp Med* 185(8):1481–1486
48. Sweet S, Singh G (1995) Accumulation of human promyelocytic leukemia (HL-60) cells at two energetic cell cycle checkpoints. *Can Res* 55(22):5164–5167
49. Li N, Ragheb K, Lawler G, Sturgis J, Rajwa B, Melendez JA, Robinson JP (2003) Mitochondrial complex I inhibitor rotenone induces apoptosis by enhancing mitochondrial reactive oxygen species production. *J Biol Chem* 278(10):8516–8525
50. Freeman BA, Crapo JD (1982) Biology of disease: free radicals and tissue injury. *Lab Invest J Tech Methods Pathol* 47(5):412–426
51. Yasui K, Baba A (2006) Therapeutic potential of superoxide dismutase (SOD) for resolution of inflammation. *Inflamm Res* 55(9):359–363
52. Riss TL, Moravec RA (2004) Use multiple assay endpoints to investigate the effects of incubation time, a dose of toxin, and plating density in cell-based cytotoxicity assays. *Assay Drug Dev Technol* 2(1):51–62
53. Koresawa M, Okabe T (2004) High-throughput screening with quantitation of ATP consumption: a universal non-radioisotope, homogeneous assay for the protein kinase. *Assay Drug Dev Technol* 2(2):153–160

Part II
Energy and Fuels Applications

Chapter 6

Chemical Looping for CO₂ Conversion and Utilization—Recent Advances and Perspective



Zhuo Cheng, Pinak Mohapatra, Anuj Joshi, Rushikesh K. Joshi, and Liang-Shih Fan

Abstract A massive increase in the emissions of CO₂ is contributing to global warming and negatively impacting Earth's ecosystems. To achieve CO₂ removal or carbon neutrality, significant development of CO₂ conversion and utilization technologies is needed. Chemical looping is an emerging clean energy technology with inherent CO₂ separation. It involves the reaction and regeneration of solid materials termed as looping carriers. In recent years, the novel chemical looping processes and looping carriers were proposed, aiming at CO₂ utilization as a partial substitute for hydrocarbon feedstock or a soft oxidant for looping carrier regeneration. This article describes the advances on this subject with a focus on the fundamentals of CO₂ conversion during the redox reactions. It is expected that these new advances will accelerate the large-scale deployment of CO₂ utilization technologies.

Keywords Chemical looping · CO₂ conversion · Looping carrier · Redox reaction · Carbon neutrality

6.1 Introduction

Global carbon emissions have been increasing steadily for decades due to the continuous exploitation and use of fossil fuels [1]. Carbon dioxide (CO₂), a key greenhouse gas, accounted for about 76 percent of total emissions in 2019 [2]. To address this issue, a wide variety of CO₂ capture technologies have been developed to reduce its level in the atmosphere [3–5]. Once captured, CO₂ would be compressed and then sent to a suitable place for long-term storage in geological formations, or injected into the ocean [6, 7]. In comparison to CO₂ capture, CO₂ utilization is a more attractive

Z. Cheng · P. Mohapatra · A. Joshi · R. K. Joshi · L.-S. Fan (✉)

William G. Lowrie Department of Chemical and Biomolecular Engineering, The Ohio State University, Columbus, OH 43210, USA

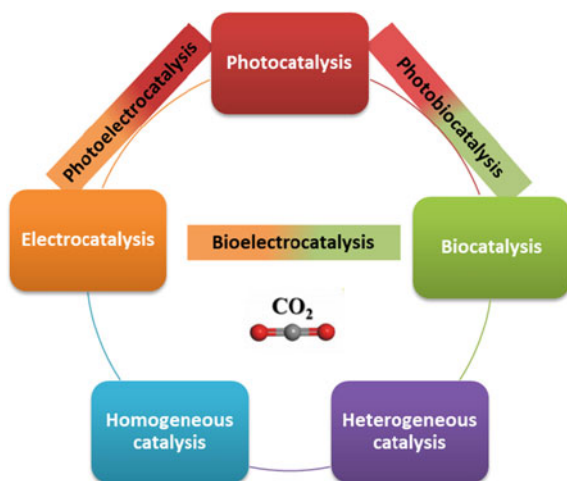
e-mail: fan.1@osu.edu

route towards carbon neutrality since it not only directly consumes the greenhouse gas but also produces fuels or valuable chemicals [8].

The main available approaches for CO₂ conversion are homogeneous catalysis [9], heterogeneous catalysis [10, 11], biocatalytic reduction [12], electrocatalytic reduction [13, 14], and photocatalytic reduction [15, 16], and combination approaches (Fig. 6.1). However, both homogeneous catalysis and heterogeneous catalytic hydrogenation require hydrogen, which is mainly produced via methane steam reforming, and thus produces a significant amount of CO₂. Biocatalytic CO₂ reduction reactions are cost-effective as they do not require high temperature and pressure, but the process is slow compared to other chemical reactions, and enzymes or bacteria, which are commonly used as biocatalysts, are only effective in an aqueous medium [17, 18]. Electrocatalytic reduction of CO₂ can generate CO, HCOOH, C₂H₄ and other valuable chemicals by using appropriate electrocatalysts. Nevertheless, it is difficult to achieve a high selectivity to target products. Additionally, the electrolysis process is energy-intensive and currently relies on conventional energy sources [19]. Photocatalytic reduction of CO₂, which can directly convert photon energy to chemical energy, has also been attracting considerable interest worldwide. However, the current light-to-fuel conversion efficiency of this approach is very low (<1%). As a result, there is still a significant amount of progress required to achieve commercial-level success [20, 21].

Chemical looping is an emerging clean energy technology with an intrinsic capability of highly efficient CO₂ capture and separation, which is being advanced towards commercialization [22, 23]. In a typical chemical looping process, a two-step redox reaction occurs where redox looping materials are first reduced by carbonaceous fuel in the fuel reactor, then oxidized in the regeneration reactor. During the reduction step, oxygen carriers supply lattice oxygen atoms to the fuel, resulting in the creation of oxygen vacancies in the bulk. Recent studies have shown that oxygen vacancies

Fig. 6.1 Approaches for CO₂ conversion into valuable chemicals and fuels



significantly impact the activity of oxygen carriers for hydrocarbon conversion reactions [24, 25]. When the formation energies of oxygen vacancies are too low, it becomes easy for the oxygen atoms to detach from the surface and bulk of oxygen carriers. This leads to the overoxidation of carbonaceous feedstocks, which in turn produces unwanted by-products. If their formation energies are too high, the surface activity would be unfavorable for the adsorption and oxidation of gaseous reactants [26]. Therefore, an ideal oxygen carrier should have appropriate formation energies of oxygen vacancies to ensure that the required amount of oxygen atoms can be transported to the surface to produce targeted chemicals. In addition, the oxygen carriers should possess properties like long-term stability, resistance to attrition, good recyclability, adequate heat capacity and tolerance to toxicity [27]. Several research efforts have been made towards developing highly active and robust oxygen carriers, which is critical for the success of chemical looping technology [28, 29]. For instance, Chung et al. recently designed an Fe-based oxygen carrier supported on Al-based skeleton and revealed that the skeleton support can drastically enhance its stability more than 3000 TGA redox cycles while maintaining low attrition rates and high physical strength [30]. Donat and Müller developed a perovskite type oxygen carrier ($\text{La}_{0.85}\text{Sr}_{0.15}\text{Fe}_{0.95}\text{Al}_{0.05}\text{O}_{3-\delta}$) which is structurally and compositionally flexible. The redox tests showed it can last ~ 4050 redox cycles and achieve complete conversion of CH₄ with a syngas selectivity of $> 99\%$ [31]. These advances demonstrate that chemical looping technologies are economically sustainable and commercially viable.

In recent years, the combination of chemical looping and CO₂ utilization has been attracting increasing attention. Generally, to ensure an efficient chemical looping technology for CO₂ utilization, the process should enable high conversion of CO₂ into fuel or valuable chemicals without incurring high costs or energy consumption. This article surveys the development of chemical looping technologies with CO₂ utilization and provides fundamental insights into the structure–activity relationships for CO₂ activation and conversion in various loop materials with views on the challenges and unique opportunities.

6.2 Chemical Looping Development and Process Schemes

In the nineteenth century, Arthur Brin developed a redox air separation process, which is regarded as the first chemical looping concept. The process involved using BaO–BaO₂ cycles in fixed bed retorts to capture and release oxygen via temperature and pressure swing [32]. In 1897, Franz Bergmann developed a Mn-based redox process for producing calcium carbide, using a blast furnace as the reducer, where manganese oxide reacts with coal and calcium oxide [33]. In the early 1900s, Messerschmitt and Lane developed an iron ore filled fixed bed for hydrogen production, which was referred to as the steam-iron process [34]. In the 1950s, Berg and Reed improved the efficiency of the steam-iron process by enhancing the interaction between solid and gas phases using fluidized beds [35]. In the 1970s, Institute of

Gas Technology (IGT) developed a FeO-Fe₃O₄ based looping process for syngas generation using two-stage countercurrent fluidized beds [36]. The term of chemical looping combustion (CLC) was first introduced by Richter and Knoche in 1983 based on the idea of improving the efficiency of irreversible combustion processes. Their theoretical study showed that avoiding immediate contact between oxygen molecules and fuels could reduce the irreversible entropy produced from combustion [37]. Since then, various CLC processes have been extensively investigated in laboratory scale experiments, and also quickly developed at bench and pilot scales [38]. In 2002, Chalmers University designed and built a 10 kWth CLC system containing a bubbling fluidized bed as the fuel reactor and a circulating fluidized bed as the regeneration reactor. This system allows long-term operation at combustion conditions with continuous natural gas feed [39], and provides a reliable database for CLC scale-up. In the 2010s, several large CLC systems were built and tested under the operation of > 250 kWth, including a 250 kWth coal direct CLC pilot plant between The Ohio State University and the Babcock & Wilcox research center [40], a 1 MWth coal-fueled CLC pilot at Technische Universität Darmstadt [41], and a 3 MWth limestone CLC pilot plant unit operated by Alstom [42]. These large pilot tests further demonstrate the feasibility of chemical looping processes under industrial conditions and provide important principles for the design of larger chemical looping units [43, 44]. The rapid advancement in CLC technology also facilitates the development of other chemical looping processes, including chemical looping partial oxidation (CLPO) [45–47], chemical looping selective oxidation (CLSO) [48, 49], and hybrid chemical looping [50, 51]. The continuous interest in the implementation of chemical looping technologies reflects their importance in the modern industrial society.

Figure 6.2 schematically shows chemical looping processes with different looping carriers and feedstocks. Despite major efforts made towards their development, the design and synthesis of highly active and selective looping carriers remain challenging. An efficient looping carrier should have three basic functions: generating metal ions and vacancies/defects, favoring their movement in the solid phase and possessing active sites for feedstock reactions [52, 53]. For metal oxide based looping carriers, the active components are mainly metal species and oxygen species, although dopants or supports can improve their functions [54]. Oxygen carriers can be used not only as redox materials for CLC, CLPO and CLSO, but also as catalytic materials for hybrid looping processes. With recent advancement in engineering, material science and catalysis, novel chemical looping systems with various high-performance oxygen carriers have been developed for efficient CO₂ conversion and utilization.

6.3 CO₂ as a Partial Substitute for CLPO

The significant increase in atmospheric CO₂ concentration and CH₄ production due to fracking has spurred interest in utilizing these greenhouse gases and converting them into valuable chemicals using catalysts. However, several drawbacks have limited the

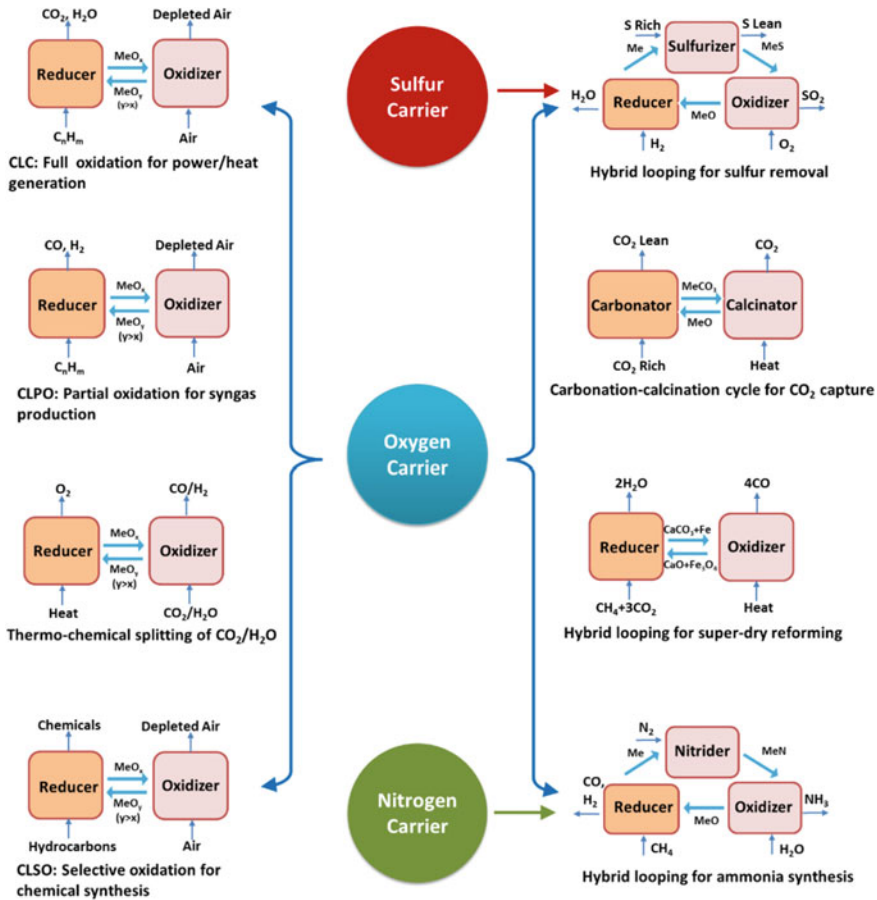


Fig. 6.2 Chemical looping processes using metal-based materials as looping carriers

commercial application of this approach. Conventional dry reforming, for example, is limited by a poor H₂:CO ratio and requires further down treatment. Additionally, carbon deposition issues have been reported, affecting the catalyst’s reactivity and resulting in a higher net heat requirement for catalyst regeneration. Furthermore, the endothermicity of the reaction necessitates the burning of CH₄, which generates CO₂ and increases the energy penalty. To address these challenges, a novel clean energy technology called CLPO coupled with CO₂ dry reforming (CLPOD) has been developed. This process combines methane partial oxidation and CO₂ reduction in the fuel reactor and has recently attracted increasing research interest because it uses low-cost looping carriers to simultaneously convert CH₄ and CO₂, while producing high-quality syngas [55, 56].

Cheng et al. conducted a study on CO₂ conversion over ilmenite-based oxygen carriers in a CLPOD system that utilized concurrent moving bed reactors as looping

reactors (Fig. 6.3a) [57]. The thermodynamic profile (Fig. 6.3b) shows that the gas-phase transforms to a high-purity syngas stream from CO_2 with the formation of $\text{FeTiO}_3\text{-Fe}$ at the bottom of the reducer, indicating a significant correlation between the reduction of CO_2 and the phase transition of oxygen carriers. In the co-feeding tests, the concentration of CO_2 as a partial substitute for CH_4 feedstock was reduced by adding N_2 while maintaining a constant total flow rate, resulting in a consistent gas residence time across all runs. Figure 6.3c depicts the equilibrium performance of the CLPOD system under steady state conditions (950 °C and 1 atm) for the different $\text{CH}_4\text{:CO}_2$ ratios. It demonstrates that the conversions of both CO_2 and CH_4 increase in a sigmoidal pattern with the rise in $\text{CH}_4\text{:CO}_2$ ratio. When the $\text{CH}_4\text{:CO}_2$ ratio increases to 8.75, 95% CO_2 conversion can be reached in the CLPOD system.

It is worth noting that the dry reforming of methane (DRM) on solid catalysts are fundamentally different from the CLPOD using solid oxygen carriers, where the morphological structure and active sites of oxygen carriers could change significantly due to oxygen vacancy formation and ionic diffusion both on the surface and in the bulk [58]. Thus, understanding the mechanism behind the evolution of CO_2 in CLPOD is critical for the development of oxygen carriers which can achieve highly efficient CO_2 utilization. Cheng et al. conducted a density functional theory (DFT) based Bader analysis and found that a net charge of 0.785|e| is transferred to CO_2 upon its adsorption onto the (0001) surface of FeTiO_3 . The calculated C-O distance between adsorbed CO_2 and the nearest surface O lattice atom is 2.229 Å, indicating

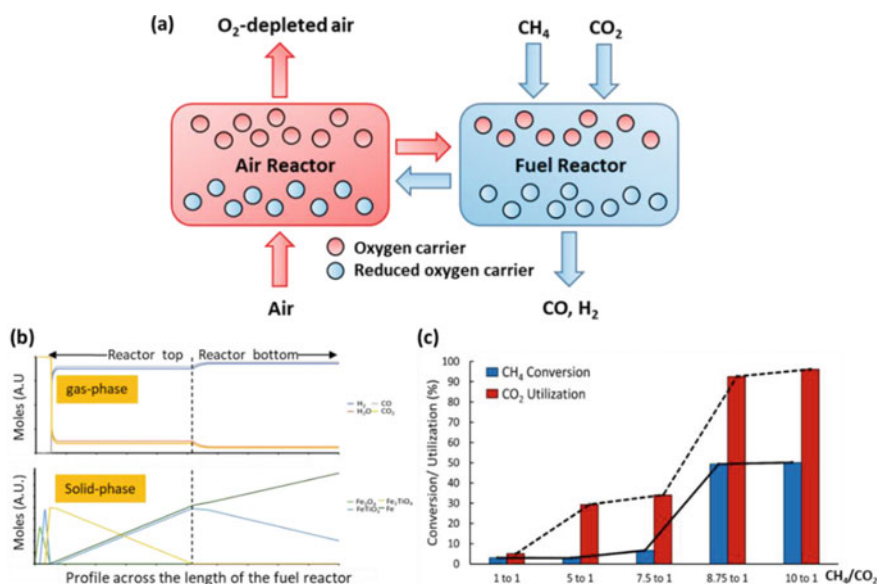


Fig. 6.3 a Schematic representation of the CLPOD system. b Thermodynamic profile across the length of the fuel reactor for the solid-phase and gas-phase. c CH_4 and CO_2 conversion over FeTiO_3 oxygen carriers under steady state condition with different $\text{CH}_4\text{:CO}_2$ ratios [57] (reproduced with permission from American Chemical Society)

weak interactions between CO₂ molecules and FeTiO₃ oxygen carriers. However, an increase in oxygen vacancy concentration will significantly enhance CO₂ adsorption on the surface of FeTiO₃. It is because excess electrons resulting from the introduction of oxygen vacancies on the surface redistribute around the adsorption sites. There are three possible reaction paths for CO₂ conversion over looping carriers in the CLPOD system: direct CO₂ decomposition, CO₂ hydrogenation via the COOH* (carboxylate) route, and CO₂ hydrogenation via the HCOO* (formate) route as shown in Fig. 6.4a. To map the energy profiles of these paths, climbing image-nudged elastic band (CI-NEB) calculations were carried out. It was found that breaking the C-O bond of CO₂ needs to overcome a high reaction barrier. Thus, CO formation from direct CO₂ dissociation on the oxygen carriers is kinetically inhibited. In contrast, the reaction barriers of the HCOO* and COOH* route are relatively low, as depicted in Fig. 6.4b [57]. It can therefore be asserted that both the oxygen vacancies and hydrogen atoms play critical roles in enhancing CO₂ activation and conversion in the CLPOD system.

Although the CLPOD process using ilmenite-based material as oxygen carriers is a promising alternative to conventional DRM, its efficiency for the simultaneous conversion of CH₄ and CO₂ to syngas is not high. This is because that adding CO₂ as a partial substitute for CH₄ inhibits the reduction of Fe [59]. The doping-induced surface modification is considered to be an efficient strategy for the enhancement of CLPO. Recently, Qin et al. modified iron oxide-based oxygen carriers using a low concentration isovalent dopant. Multiple redox tests showed that 1% Lanthanum dopant significantly enhanced the reactivity of Fe₂O₃ in each cycle [60]. The modification of oxygen carrier properties by means of aliovalent doping has also been widely investigated. Guo et al. conducted a DFT combined experimental study to analyze the effect of cobalt dopants on the activity of Fe₂O₃ oxygen carriers, and found that the addition of 2% cobalt increases the CH₄ conversion rate by 526% at 700°C [61]. Chen et al. designed a Ni-doped WO₃-based oxygen carrier Ni_{0.5}WO_x/Al₂O₃ for CLPO, and demonstrated that the Ni modification significantly promotes the production of CO [62]. Ni-based materials are also regarded to be the most effective dry reforming catalysts [63, 64]. Thus, it is anticipated that the addition of Ni into oxygen carriers will improve the CLPOD process. Kang et al. investigated the performance of 1 wt% Ni-doped Al₂O₃ supported Fe₂O₃ oxygen carrier during CLPOD processes. The materials were prepared through impregnation synthesis (C-Fe₂O₃/Al₂O₃) and sol-gel synthesis (CP-Fe₂O₃/Al₂O₃). The structural characterization revealed that the Ni aluminate forms in CP-Fe₂O₃/Al₂O₃, while NiFe₂O₄ forms in C-Fe₂O₃/Al₂O₃. The formation of the Ni aluminate phase indicates improved interaction between the metal and support of CP-Fe₂O₃/Al₂O₃, which could facilitate CO production and inhibit carbon deposition. Therefore, CP-Fe₂O₃/Al₂O₃ displays lower carbon deposition and H₂:CO ratios than C-Fe₂O₃/Al₂O₃ as shown in Fig. 6.5a. The schemes of CLPOD on C-Fe₂O₃/Al₂O₃ and CLPOD on CP-Fe₂O₃/Al₂O₃ are shown in Fig. 6.5b. It can be observed that Ni aluminates of CP-Fe₂O₃/Al₂O₃ promote DRM during CLPOD [65]. More recently, Sun et al. developed a NiO-modified ilmenite ore oxygen carrier. The evaluation of its performance in CLPOD revealed that the introduction of Ni species into the ilmenite oxygen carrier causes the formation of the metallic FeNi alloy which

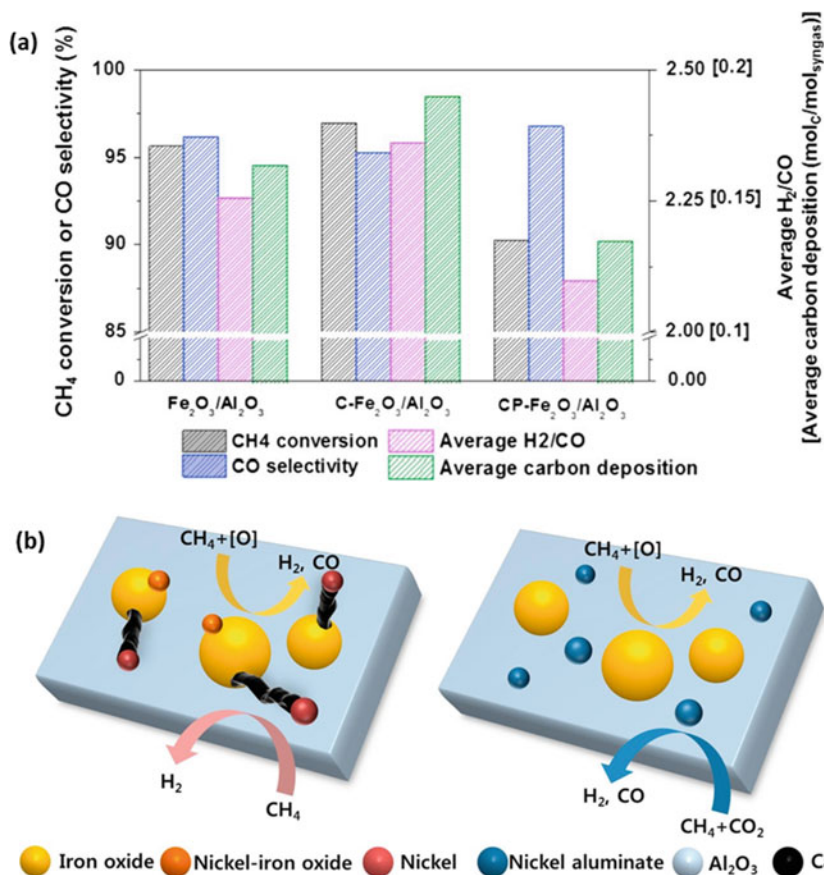


Fig. 6.5 **a** Comparison of CLPODs on Fe₂O₃/Al₂O₃ and Ni-enhanced Fe₂O₃/Al₂O₃ oxygen carriers (average O:CH₄ ratio is 0.24 and CO₂:CH₄ ratio is 0.38). **b** CLPO on C-Fe₂O₃/Al₂O₃ and CLPOD on CP-Fe₂O₃/Al₂O₃ [65] (reproduced with permission from Elsevier)

6.4 CO₂ Conversion via Chemical Looping Tri-Reforming

DRM for syngas production is an attractive CO₂ and CH₄ conversion process. However, its industrial implementation remains challenging due to high endothermicity of the reaction and severe coking formation tendency. Additionally, the low quality of syngas product (H₂: CO ratio ≤ 1) prohibits its direct use for some desirable downstream processes such as Fischer–Tropsch synthesis. Introducing steam as a cofeed has been studied advantageous resulting in an improvement in H₂:CO ratio alongside limiting carbon deposition. However, the endothermicity of reaction still requires burning CH₄ thereby affecting the process economics. Addition of O₂ can improve heat of reaction but it requires an additional air separation unit (ASU) which is extremely energy intensive. Kathe et al. proposed a novel chemical looping

tri-reforming (CLTR) process which combines methane partial oxidation, DRM and steam CH_4 reforming (SMR) in a chemical looping system as depicted in Fig. 6.6a [67]. The oxygen carrier employed in this process is a composite metal oxide-based material comprising of iron and titanium (ITCMO). The ITCMO particle consists of an inert support and a $\text{Fe}_2\text{O}_3\text{-TiO}_2$ mixture providing reaction sites and lattice oxygen atoms. This oxygen carrier circulates between the fuel reactor where CH_4 is partially oxidized by lattice oxygen atoms of ITCMO, CO_2 and H_2O , and the regenerator where the reduced ITCMO is replenished by air. The overall reactions in the fuel reactor and regenerator are endothermic and exothermic, respectively. Thus, the whole process benefits from friendly thermodynamics, leading to optimized energy efficiency. Figure 6.6b presents the change in the H_2 :CO ratio observed in systems utilizing molecular O_2 and ITCMO as oxidants, respectively. It can be seen that ITCMO-based CLTR system for CO_2 utilization in conjunction with a steam and CH_4 feedstock can yield hydrogen rich syngas with a maximum H_2 :CO ratio of ~ 3.25 . The uniqueness of the CLTR system is based the looping material and looping reactors. The looping material needs to possess not only high oxygen permeability during reduction and oxidation, but also high attrition resistance withholding its physical strength across multiple redox cycles. The fuel reactor used in CLTR is a co-current moving bed reactor. The moving bed gas–solid contact generated single oxidation state carrier after reduction which is an effective way to operate the reactor close to thermodynamic regime. Unlike fluidized bed, the particles in a moving bed are subjected to a single residence time that determines its reduced oxidation state at reducer outlet.

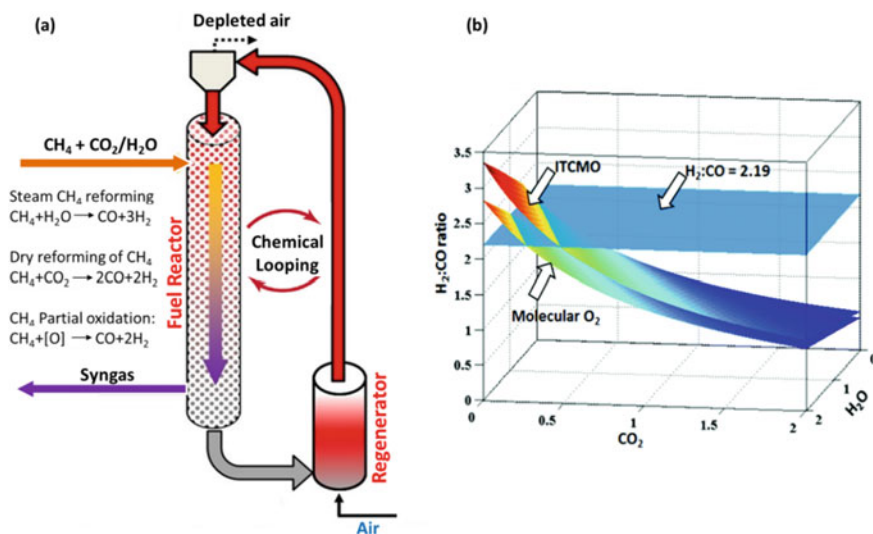


Fig. 6.6 a Schematic representation of the CLTR. b H_2 :CO ratio for the tri-reforming system using ITCMO at 1000°C and 5 atm [67] (reproduced with permission from Royal Society of Chemistry)

To expand on this concept, Park et al. conducted additional experiments in a 15 kW sub-pilot plant, which utilizes a co-current moving bed as the fuel reactor and a fluidized bed as the regenerator. CH₄ is introduced at the top of the fuel reactor and flows downward through the packed moving bed. The oxygen carrier is also introduced at the top of the reactor and uniformly moves in the same direction as the methane stream. This arrangement prevents gas bubble formation and thus minimizes channeling over the bed, favoring a higher methane conversion. The test results confirmed that the CLTR process can generate a high-quality syngas with a purity of over 91.97% and an H₂:CO ratio from 1.19 to 2.50 under all conditions, while overall consuming CO₂ [68]. Even though this process for CO₂ utilization presents an attractive alternative to conventional reforming processes, achieving higher process efficiency and syngas yield remains a challenge, which must be overcome before further scaling-up to industrial scale.

6.5 CO₂ as a Soft Oxidant for Oxygen Carrier Regeneration

In the CLPO process, methane is converted to syngas with oxygen carrier reduction in the fuel reactor and the reduced oxygen carriers then are oxidized by air in the regenerator. Instead of using air as the oxidant, CO₂ can be used as a soft oxidant for the regeneration of some oxygen carriers. Shah et al. investigated calcium ferrite-based oxygen carriers for syngas production with CO₂ splitting in a CLPO system as shown in Fig. 6.7a [69]. The Ca₂Fe₂O₅ oxygen carriers with different ratios on MgO support were tested for multiple redox cycles with CH₄ conversion of near 100% and CO₂ conversion of ~78%. Figure 6.7b displays the variation in solid conversion during the oxidation using CO₂ for 0, 10, 20 and 40% MgO supported Ca₂Fe₂O₅ samples over 10 redox cycles. The results indicate that all samples achieved consistent solid conversion rates exceeding 90%, demonstrating that CO₂, as a soft oxidant, can efficiently provide oxygen for the regeneration of reduced Ca₂Fe₂O₅. Ca₂Fe₂O₅ possesses a brownmillerite-type structure with surface layers alternating between corner-sharing tetrahedra and octahedral as illustrated in Fig. 6.7c. DFT calculations reveal that alternating octahedral and tetrahedral sites of Ca₂Fe₂O₅ play a critical role in the formation of oxygen vacancies serving as the active sites for CH₄ partial oxidation and CO₂ reduction. There are three chemically distinct lattice oxygen atoms in Ca₂Fe₂O₅: O_(t) in tetrahedral, O_(o) in corner-sharing octahedral, and O_(ot) between corner-sharing octahedra and tetrahedral. Their vacancy formation energies are 259.85, 205.81 and 311.72 kJ/mol, respectively. This suggests that the oxygen vacancy located at the octahedral site is primarily responsible for the activation of CO₂ [70]. Nevertheless, it is still difficult to modulate the concentration of surface oxygen vacancies and control their distribution. Thus, a deeper understanding of factors that can affect the oxygen vacancy formation and migration is needed.

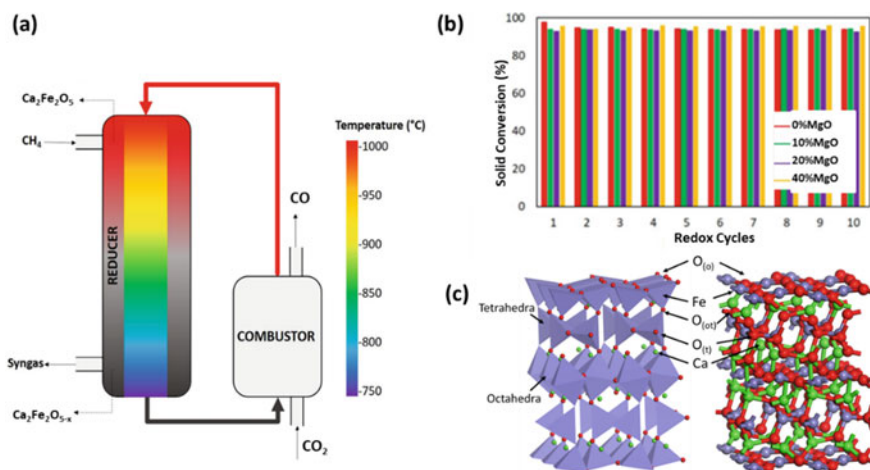


Fig. 6.7 **a** Schematic representation of the adiabatic CLPO process using calcium ferrite as oxygen carrier and CO_2 as soft oxidant, [69] (reproduced with permission from Royal Society of Chemistry) **b** solid conversion with CO_2 splitting across 10 isothermal redox cycles at 1000°C and 1 atm. **c** crystal structure of $\text{Ca}_2\text{Fe}_2\text{O}_5$ (001) surface [70] (reproduced with permission from Elsevier)

The incorporation of Ni dopants into Fe-based oxygen carriers has been found to enhance their reactivity during the chemical looping partial oxidation (CLPO) process, especially at lower temperatures. To investigate the effect of these dopants on the oxygen carriers' regeneration capability under CO_2 , the performance of Ni-doped and undoped $\text{Ca}_2\text{Fe}_2\text{O}_5$ was studied using extended redox cycles with CH_4 and CO_2 as the reducing and oxidizing agents, respectively. The results demonstrated that increasing the concentration of Ni in the sample resulted in improved oxidation performance during CO_2 oxidation at 750 and 900°C . Furthermore, the Ni-doped samples exhibited superior reduction performance over 15 redox cycles when using CO_2 compared to air. Figure 6.8d displays the energy profiles associated with CO_2 conversion to CO on reduced $\text{Ca}_2\text{Fe}_2\text{O}_5$ and reduced $\text{Ca}_2\text{Fe}_{1.95}\text{Ni}_{0.05}\text{O}_5$ slabs. The calculations reveal that $\text{Ca}_2\text{Fe}_2\text{O}_5$ has a higher energy barrier for C–O bond cleavage of CO_2 than $\text{Ca}_2\text{Fe}_{1.95}\text{Ni}_{0.05}\text{O}_5$. These findings suggest that Ni doping not only enhances methane partial oxidation but also improves CO_2 conversion during the regeneration process, which align with the results obtained through TGA tests.

To date, it remains unclear how incorporating Ni dopants into the oxygen carriers may impact their strength and attrition resistance. These are critical factors to consider given that the carriers will undergo high temperatures and repeated cycles of reduction and oxidation during the CLPO process. By gaining a deeper understanding of the relationship between reactivity and structure, it may be possible to determine the optimal concentration of dopants and preparation methods that can improve both the reactivity and mechanical properties of the oxygen carriers. Ultimately, this knowledge will be essential for developing next-generation technology that can more efficiently utilize CO_2 as a soft oxidant for oxygen carrier regeneration.

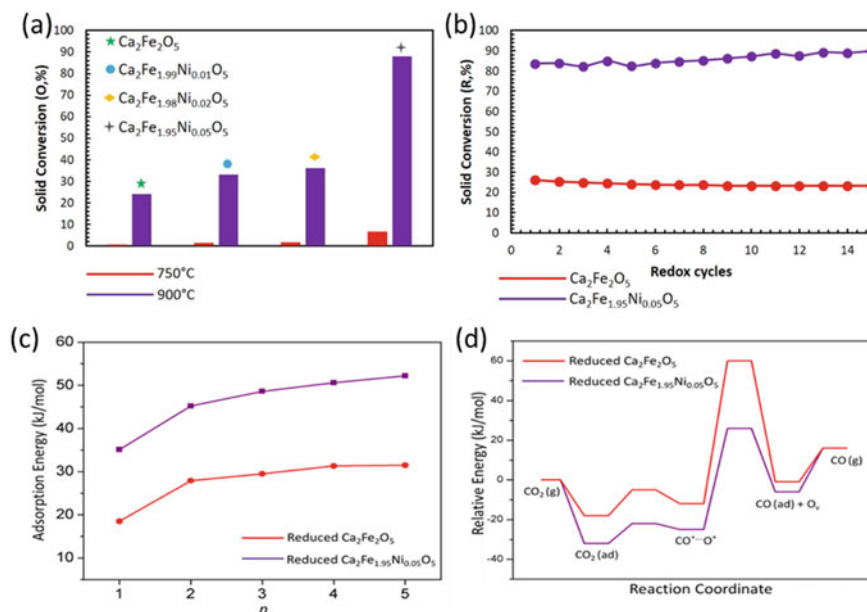


Fig. 6.8 **a** Solid conversion during oxidation with CO₂ **b** CH₄-CO₂ redox cycles at 900 °C and 1 atm. **c** The relationship between CO₂ adsorption energy and the number of oxygen vacancies, **d** the energy profile for CO₂ conversion to CO on Ca₂Fe₂O_{5-x}, and Ca₂Fe_{1.95}Ni_{0.05}O_{5-x} [69] (reproduced with permission from Royal Society of Chemistry)

6.6 CO₂ Utilization Through CaO-Assisted Carbonation-Calcination Route

The carbonation-calcination route in Fig. 6.2 represents the CaO-assisted calcium looping process, which has been demonstrated to be efficient for CO₂ capture and utilization [71]. Calcium looping involves selective CO₂ capture in the carbonator reactor where CO₂ reacts with CaO (used as a sorbent) to form CaCO₃. The CaCO₃ is then sent into the second reactor, calciner, where the calcination reaction proceeds for the sorbent regeneration. The overall calcination reaction occurs in two steps: the initial rapid carbonation controlled by the chemical reaction kinetics on the surface of the oxygen carrier, and the slow carbonation controlled by the diffusion kinetics in the bulk [72]. The slow step is attributed to the accumulation of CaCO₃ layer on the surface which prevents CO₂-CaO interactions [73]. However, an increase in temperature can enhance the solid conversion and calcination rate, thus improving the efficiency of the calcium looping [74].

Coupling calcium looping with CH₄ dry reforming is a novel technology which realizes CO₂ capture and conversion in an integrated process. During the CO₂ conversion and CH₄ reforming step, CaCO₃ dissociates to release CO₂, which is subsequently employed for reforming CH₄ on the Ni catalyst, resulting in the production

of syngas. Subsequently, the material reverts to its original state, ready for a new cycle. An important advantage of this process is its ability to use feedstocks with any CO_2 -containing gas composition, particularly flue gases containing up to 20 vol.% of CO_2 . The integration of CO_2 capture and conversion into a single process reduces energy consumption through improved process heat management and the elimination of CO_2 transport from the emission point to the utilization site [75]. Galvita et al. demonstrated the combined chemical looping coupling CO_2 sorption to oxygen storage reduction/oxidation in a lab-scale test [76]. Such chemical looping process can be described as a series of chemical charge and discharge cycles, as depicted in Fig. 6.9a. During the charge process, a feed containing CH_4 and CO_2 is introduced over a mixture of Fe_3O_4 and CaO . In this step, CH_4 reduces Fe_3O_4 to metallic iron. Simultaneously, CaO reacts with CO_2 to form CaCO_3 through carbonation. During the discharge process, CaCO_3 decomposes into CO_2 and CaO . Simultaneously, the released CO_2 will be reduced to CO by interacting with metallic iron. In their test, an equimolar mixture of CH_4 and CO_2 was sent to a fixed bed reactor containing $\text{NiO-Fe}_2\text{O}_3/\text{CeO}_2$ and $\text{CaO-Al}_2\text{O}_3$ mixture. Figure 6.9b shows the space-time yields of CO_2 , CO , CH_4 , and H_2 at 650°C . During the initial stage, CO_2 reaches a minimum as it is absorbed by CaO and also consumed during DRM. However, when the CaO sorbent is fully saturated, the CO_2 space-time yield will increase with the other products. Figure 6.9c shows the space-time yield for decarbonation of CaCO_3 and CO production. It can be seen that the both CO_2 and CO production increase in the initial stage then decrease toward to 0. This combined chemical looping process exhibits considerable flexibility in terms of both energy storage/release and fuel type.

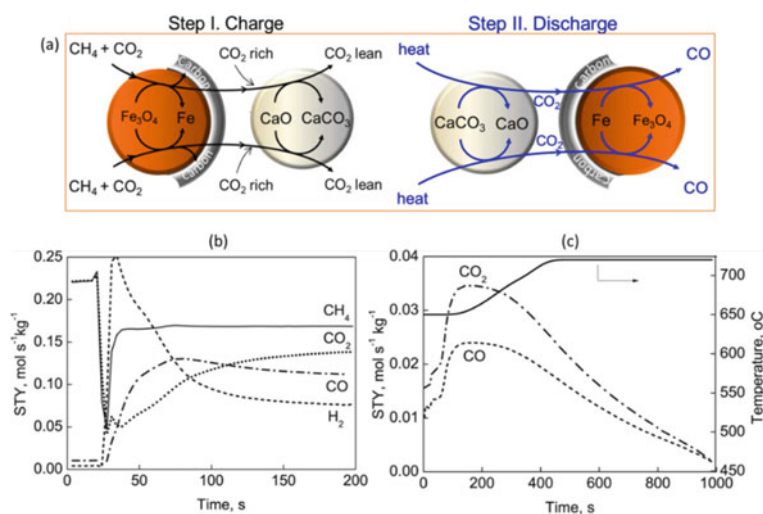


Fig. 6.9 **a** Schematic representation of combined chemical looping coupling CO_2 sorption to oxygen storage reduction/oxidation. **b** space-time yield against time for CaO carbonation and Fe_3O_4 reduction with $\text{CH}_4:\text{CO}_2$ of 1:1 at 650°C , and **c** space-time yield versus time on stream for decarbonation of CaCO_3 and CO production [76] (reproduced with permission from Elsevier)

6.7 Concluding Remarks

To reduce greenhouse gas emissions, a variety of CO₂ utilization strategies such as thermal catalysis, biocatalysis, electrocatalysis and photocatalysis, etc. have emerged in recent years. Among these technologies, chemical looping stands out as a promising approach for CO₂ utilization because of its potential for achieving high energy efficiency, scalability, flexibility, and low cost. The solid material, which serves as the looping carrier for multiple redox reactions, is the foundation for successful operation of a chemical looping system with CO₂ utilization as it significantly influences the desired product quality and reactant conversion. Extensive efforts have been made for decades to discover robust and efficient looping carriers for chemical looping processes, leading to a large number of materials being reported including single metal oxides, bimetallic oxides, mixed-metal oxides, perovskites, metal sulfides, metal nitrides and hybrid oxide nanoparticles. Transition metal-based oxygen carriers have been extensively synthesized and used, owing to their high oxygen capacity, ease of availability, good recyclability, and relatively low cost. Recent advancements have shown that these materials can efficiently convert CO₂ into CO through various reaction routes during chemical looping processes, such as tri-reforming of methane, dry reforming, direct reduction, and combined carbonation-calcination.

The redox reactions over oxygen carriers involve the formation and annihilation of oxygen vacancies in the bulk and surface phases, which could affect the electronic structures and chemical properties of the host system. An ideal carrier should allow for proper transportation of lattice oxygen atoms to sustain sufficient concentrations of surface oxygen vacancies, which plays a critical role in CO₂ adsorption and activation. In addition, the oxygen carriers need to have appropriate oxygen vacancy formation energies so that the surface can release a suitable amount of oxygen atoms for the production of targeted chemicals. Over the past decade, oxygen vacancies have been intensively investigated using a variety of techniques. Strategies such as doping, adding supports and utilizing electric field/solar energy have the potential to tune the oxygen vacancy population of oxygen carriers, and thus enhance the selective conversion of CO₂ into valuable products such as methane, formic acid and methanol, as illustrated in Fig. 6.10. Further research in these directions would be more attractive. In addition, it remains challenging to completely understand the relationship between the CO₂ reaction path and the morphological evolution of oxygen carriers. In-situ and operando studies which can characterize the surface oxygen vacancies and reaction intermediates coupled with advanced computational tools are highly recommended to advance the understanding of the mechanism and dynamics of oxygen vacancy-induced CO₂ conversion in chemical looping processes. These fundamentals are crucial for the development of superior chemical looping systems capable of selectively and economically converting large quantities of CO₂ to a vast array of value-added chemicals.

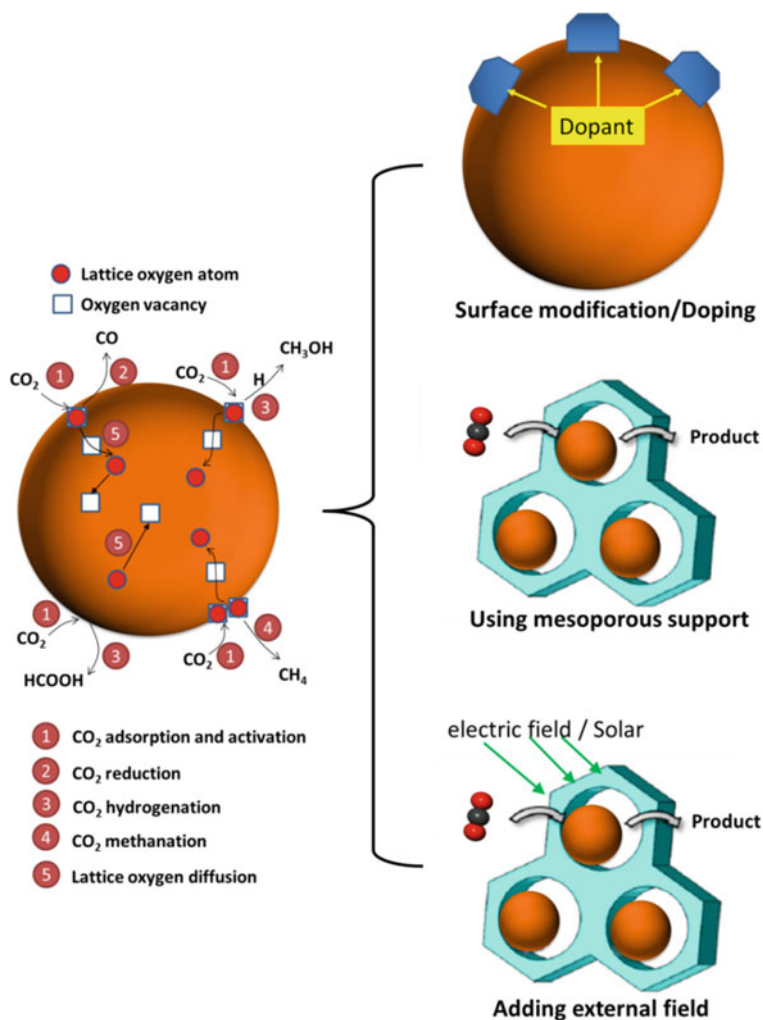


Fig. 6.10 Potential strategies for CO₂ conversion to value-added chemicals using novel oxygen carriers

References

1. Mardani A, Streimikiene D, Cavallaro F, Loganathan N, Khoshnoudi M (2019) *Sci Total Environ* 649:31–49
2. Energy/Emissions Data. Retrieved from <https://www.c2es.org/content/international-emissions/>
3. Fan L-S (2017) *Chemical looping partial oxidation: gasification, reforming, and chemical syntheses*. Cambridge University Press
4. Osman AI, Hefny M, Abdel Maksoud MIA, Elgarahy AM, Rooney D (2021) *W. Environ Chem Lett* 19:797–849

5. Bui M, Adjiman CS, Bardow A, Anthony EJ, Boston A, Brown S, Fennell PS, Fuss S, Galindo A, Hackett LA et al (2018) *Energy Environ Sci* 11(5):1062–1176
6. MacDowell N, Florin N, Buchard A, Hallett J, Galindo A, Jackson G, Adjiman CS, Williams CK, Shah N, Fennell P (2010) *Energy Environ Sci* 3(11):1645–1669
7. Doughty C, Freifeld BM, Trautz RC (2008) *Environ Geol* 54(8):1635–1656
8. Zheng Y, Zhang W, Li Y, Chen J, Yu B, Wang J, Zhang L, Zhang J (2017) *Nano Energy* 40:512–539
9. Pérez-Fortes M, Schöneberger JC, Boulamanti A, Harrison G, Tzimas E (2016) *Int J Hydrog Energy* 41:16444–16462
10. Maru MS, Ram S, Shukla RS, Noor-ul HK (2018) *Mol Catal* 446:23–30
11. Hariyanandam GG, Hyun D, Natarajan P, Jung K-D, Yoon S (2016) *Catal Today* 265:52–55
12. Molitor HR, Moore EJ, Schnoor JL (2019) *ACS Sustain Chem Eng* 7(10):9474–9479
13. Yang H, Kaczur JJ, Sajjad SD, Masel RI (2017) *J CO₂ Util* 20:208–217
14. Del Castillo A, Alvarez-Guerra M, Solla-Gullón J, Sáez A, Montiel V, Irabien A (2017) *J CO₂ Util* 18:222–228
15. Castro S, Albo J, Irabien A (2018) *ACS Sustain Chem Eng* 6(12):15877–15894
16. Suzuki TM, Takayama T, Sato S, Iwase A, Kudo A, Morikawa T (2018) *Appl Catal B Environ* 224:572–578
17. Kondaveeti S, Abu-Reesh IM, Mohanakrishna G, Bulut M, Pant D (2020) *Front Energy Res* 8:94
18. Arends JBA, Patil SA, Roume H, Rabaey KJ (2017) *CO₂ Util* 20:141–149
19. Gao F, Bao R, Gao M, Yu SJ (2020) *Mater Chem A* 8:15458–15478
20. Albero J, Peng Y, García H (2020) *ACS Catal* 10:5734–5749
21. Hurtado L, Natividad R, García H (2016) *Catal Commun* 84:30–35
22. Fan L-S (2011) *Chemical looping systems for fossil energy conversions*. Wiley
23. Joshi A, Shah V, Mohapatra P, Kumar S, Joshi RK, Kathe M, Qin L, Tong A, Fan L-S (2021) *Adv Appl Energy* 3:100044
24. Cheng Z, Qin L, Guo M, Fan JA, Xu D, Fan L-S (2016) *Phys Chem Chem Phys* 18:16423–16435
25. Mishra A, Li T, Li F, Santiso EE (2019) *Chem Mater* 31(3):689–698
26. Cheng Z, Qin L, Guo M, Xu M, Fan JA, Fan L-S (2016) *Phys Chem Chem Phys* 18:32418–32428
27. Zeng L, Cheng Z, Fan JA, Fan L-S, Gong J (2018) *Nat Rev Chem* 2(11):349–364
28. Cheng Z, Qin L, Fan JA, Fan L-S (2018) *Engineering* 4:343–351
29. Hu J, Galvita VV, Poelman H, Marin GB (2018) *Materials (Basel)* 11(7):1187
30. Chung C, Qin L, Shah V, Fan L-S (2017) *Energy Environ Sci* 10:2318–2323
31. Donat F, Müller CR (2020) *Appl Catal B* 278:119328
32. Hepworth TC (1892) *Oxygen for Limelight*. *Nature* 47:176–177
33. Bergmann FJ (1897) *Process for the production of calcium carbide in blast furnaces*. German Patent 29
34. Lane H (1913) *Process of producing hydrogen*. US Patent 1078686
35. Reed HC, Berg CH (1953) *Hydrogen*. US Patent 2635947
36. Institute of Gas Technology (1979) *Development of the steam-iron process for hydrogen production*. US Department Energy
37. Richter HJ, Knoche KF (1983) *ACS Symp Ser* 235:71–85
38. Zeng L, Kathe MV, Chung EY, Fan L-S (2012) *Curr Opin Chem Eng* 1:290–295
39. Berguerand N, Lyngfelt A (2008) *Fuel* 87:2713–2726
40. Zhang Y, Wang D, Pottimurthy Y, Kong F, Hsieh TL, Sakadjian B et al (2021) *Appl Energy* 282:116065
41. Ströhle J, Orth M, Epple B (2014) *Appl Energy* 113:1490–1495
42. Herberta A, Chui J, Thibeault P, Edberg C, Turek D, Kenney J, Abdullaly I, Chapman P, Kang S (2012) *Alstom's limestone-based (LCL™) chemical looping process*. In: 2nd International conference on chemical looping, TU Darmstadt, Germany
43. Fan L-S, Zeng L, Luo S (2015) *AIChE J* 61:2–22
44. Qin L, Cheng Z, Baser D, Goldenbaum T, Fan JA, Fan L-S (2020) *React Chem Eng* 5:2204–2220
45. Fan L-S, Zeng L, Wang W, Luo S (2012) *Energy Environ Sci* 5:7254–7280

46. Neal LM, Shafiefarhood A, Li F (2014) *ACS Catal* 4:3560–3569
47. Mihai O, Chen D, Holmen A (2012) *J Catal* 293:175–185
48. Chung EY, Wang WK, Nadgouda SG, Baser DS, Sofranko JA, Fan L-S (2016) *Ind Eng Chem Res* 55:12750–12764
49. Brady C, Murphy B, Xu B (2017) *ACS Catal* 7:3924–3928
50. Gao W, Guo J, Wang P, Wang Q, Chang F, Pei Q et al (2018) *Nat Energy* 3:1067–1075
51. Jangam K, Chen Y, Qin L, Fan L-S (2021) *ACS Sustain Chem Eng* 9(33):11204–11211
52. Qin L, Cheng Z, Guo M, Fan JA, Fan L-S (2017) *Acta Mater* 124:568–578
53. Li F, Kim HR, Sridhar D, Wang F, Zeng L, Chen J, Fan L-S (2009) *Energy Fuels* 23:4182–4189
54. Qin L, Cheng Z, Fan JA, Kopechek D, Xu D, Deshpande N, Fan L-SJ (2015) *Mater Chem A* 3:11302–11312
55. Kathe M, Sandvik P, Fryer C, Kong F, Zhang Y, Grigonis G, Fan L-S (2018) *Energy Fuels* 32(2):1139–1154
56. Najera M, Solunke R, Gardner T, Vesper G (2011) *Chem Eng Res Des* 89(9):1533–1543
57. Cheng Z, Baser DS, Shah V, Fan JA, Fan L-S (2020) *Energy Fuels* 34(12):15370–15378
58. Arora S, Prasad R (2016) *RSC Adv* 6:108668–108688
59. Abad A, Adanez J, Cuadrat A, Garcia-Labiano F, Gayan P, de Diego LF (2011) *Chem Eng Sci* 66:689–702
60. Qin L, Cheng Z, Guo M, Xu M, Fan JA, Fan L-S (2017) *ACS Energy Lett* 2:70–74
61. Guo M, Cheng Z, Liu Y, Qin L, Goetze J, Fan JA, Fan L-S (2020) *Catal Today* 350:156–164
62. Chen S, Zeng L, Tian H, Li X, Gong J (2017) *ACS Catal* 7:3548–3559
63. Dai X, Yu C, Li R, Wu Q, Hao Z (2008) *J Rare Earths* 26:76–80
64. Abdullah B, Abd Ghani NA, Vo DN (2017) *J Clean Prod* 162:170–185
65. Kang D, Lim HS, Lee M, Lee JW (2018) *Appl Energy* 211:174–186
66. Sun Z, Lu DY, Symonds RT, Hughes RW (2020) *Chem Eng J* 401:123481
67. Kathe M, Empfield A, Sandvik P, Fryer C, Zhang Y, Blair E, Fan L-S (2017) *Energy Environ Sci* 10:1345–1349
68. Park C, Hsieh T, Pottimurthy Y, Shah V, Xu D, Chen Y, Fan L-S, Tong A (2020) *Ind Eng Chem Res* 59(15):6886–6899
69. Shah V, Cheng Z, Mohapatra P, Fan L-S (2021) *Reaction Chemistry & Engineering* 6:1928–1939
70. Shah V, Cheng Z, Baser DS, Fan JA, Fan L-S (2021) *Appl Energy* 282:116111
71. Perejón A, Romeo LM, Lara Y, Lisbona P, Martínez A, Valverde JM (2016) *Appl Energy* 162:787–807
72. Bhatia SK, Perlmutter DD (1983) *AIChE J* 29:79–86
73. Barker RJ (1973) *Appl Chem Biotech* 23:733–742
74. Criado YA, Arias B, Abanades JC (2018) *Ind Eng Chem Res* 57:12595–12599
75. Tian S, Yan F, Zhang Z, Jiang J (2019) *Sci Adv* 5(4):eaav5077-1–eaav5077-9
76. Galvita VV, Poelman H, Marin GB (2015) *J Power Sources* 286:362–370

Chapter 7

Diversity Oriented Synthesis of Metal-Organic Frameworks



Yu-Chuan Hsu, Kun-Yu Wang, Kui Tan, Joshua A. Powell,
and Hong-Cai Zhou

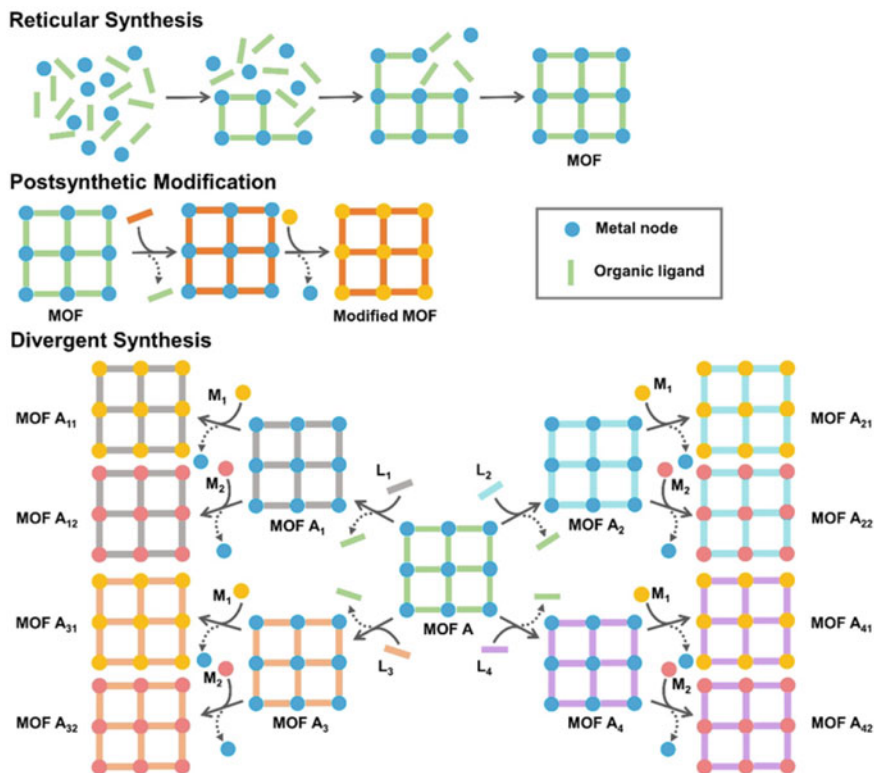
Abstract Metal–Organic Frameworks (MOFs) are an emerging class of novel porous materials bearing unique high surface area and structural tunability. Post-synthetic functionalization plays a pivotal role not only in facily diversifying MOF structures but also in meeting the requirement in practical applications. Herein, we explore the utility of diversity oriented synthesis (DOS) in the MOF field, summarizing the various post-synthetic modifications and pore engineering techniques and discussing how they regulate the pore environment and sizes of MOFs.

Keywords Metal–organic framework · Structural engineering · Post-synthetic modification

Metal–organic frameworks (MOFs) are advance porous materials constructed with organic linkers and metal nodes. Due to their high surface area and structural tunability, MOFs feature great application potential in various fields, including gas storage/separation, catalysis, and biomedicine. Driven by the practical applications and enthusiasm of MOF researchers, a library of ca. 99,000 MOF structures has been established to date. During the enrichment of the MOF library, researchers often autonomously capitalize a strategy named Diversity Oriented Synthesis (DOS), a methodology widely applied in organic chemistry, to achieve unprecedented MOF structures. In organic chemistry, DOS, or divergent synthesis, can prepare a library of molecules with an emphasis on skeletal diversity. For instance, starting from a compound A, a set of new compounds containing A1, A2, A3, etc. can be prepared as generation 1 through reacting with different reactants. On the basis of generation 1, a generation 2 of A11, A12, A13, etc. can be synthesized. As a result, the starting compound A diverges rapidly to a large number of compounds. Similarly, a MOF

Y.-C. Hsu · K.-Y. Wang · J. A. Powell · H.-C. Zhou (✉)
Department of Chemistry, Texas A&M University, College Station, TX 77843, USA
e-mail: zhou@chem.tamu.edu

K. Tan
Department of Materials Science and Engineering, University of Texas, Dallas, Richardson,
TX 75080, USA



Scheme 7.1 Different synthetic approaches to building MOFs. MOFs can be directly synthesized through reticular chemistry and post-synthetic modification. Diverse MOFs are proposed to be constructed through stepwise post-synthetic modifications

can also be manipulated to produce a large variety of structures. As a material with a tunable skeleton, a MOF can be readily functionalized, modified, or even disintegrated into other materials. This chapter will provide a retrospect and summary of methodologies for DOS of MOFs. Discussions are made on how these methodologies, such as linker functionalization and linker exchange, endow MOFs with structural complexity and functionality. The applicability and limitation of all these methodologies are evaluated. Besides, advanced tools, including automated synthesis and data mining, can be introduced into the DOS of MOFs. In summary, this chapter briefly introduces how various post-synthetic methodologies promote the discovery of diverse MOF structures, which will provide guidance and inspiration for future design and synthesis of MOFs (Scheme 7.1).

7.1 Functionalization of MOF Subunits

The ligand of MOFs can be functionalized post-synthetically, to introduce new functional groups, especially those that may be inaccessible by direct synthesis, into MOFs framework without the disruption of the MOF structure. One of the methods is called post-synthetic modification (PSM). Although PSM is a strong tool for the functionalization of MOFs, there are many criteria that need to be concerned. Most ligands used in this strategy should contain functional groups that do not interact with metal cluster but can be use as site for further functionalization. The candidate reaction for post-synthetic modification should also be chemically compatible with the MOF backbone. Pore size of the MOFs must be large enough for the reactant to diffuse sufficiently throughout the MOF crystal. Several methods have been successfully applied to create new covalent bond on the organic linker, including formation of amide, imine and ester, reduction of olefin, cyanation of aryl halides, ring-opening reaction, click reaction, and photochemical reactions. PSM has become more accessible with the development of much stable MOFs.

Another common post-synthetic modification technique is post-synthetic metalation, which can also refer as coordination modification, which incorporate another metal into the MOF structure. Many functional groups such as bipyridine [1], thiol [2], phosphine [3], porphyrin [4], and *N*-heterocyclic carbene have been implanted in MOF system as coordination site for a wide range of metal substrates [5]. The major challenge for this method is to avoid potential coordination of metal cluster with secondary coordination site on the ligand. One method is to utilize the hard-soft acid-base theory. In 2010, Yaghi and Long reported UiO-67-bipy, which utilize 2,2-bipyridine-5,5-dicarboxylate as linker which contain carboxylate group that can coordinate with hard metal ions for the construction of MOF structure with bipyridine stays free to coordinate with soft metal ions [1]. This system has become one of the most used strategy for post-synthetic metalation and has been used to coordinate a wide range of metal substrates to form the corresponding metalated frameworks. Another method is to perform a two steps PSM, the first step produces a new coordination site, follow by the introduction of metal at the second step. The advantage of this method is that the initial linker doesn't require a secondary coordination site, only a functional group need to be present for PSM.

A multi-step post-synthetic functionalization, or so-called "tandem PSM" introduced by Cohen in 2008, can be achieved with a modified sequence of reactions [6]. A notable example is the seven-step post-synthetic reaction sequence to install tripeptide on IRMOF-74-III reported by Yaghi [7]. With four thermal deprotection reactions in step 1,3,5,7 and three imine formation reactions in step 2,4,6 with amino acid, a specific tripeptide sequence can be installed in MOF. However, some limits of the sequential PSM also need to be concerned. Incomplete conversion of the functional groups produces MOF with multivariant set of linkers, which may interfere with following reaction sequences. With the functionalization sequence proceed, the number of functional sites for further modification may also decrease. The negative

impact of the structure integrity may also increase with each subsequent modification. With these limitations, the tandem PSM involving more than two types of reactions are mostly limited with very stable MOF. In 2011, a nitration–reduction–urea formation sequence on MIL-101(Cr) was reported by Stock [8]. In 2013, a nitration–reduction–azidation–click reaction sequences MIL-101(Cr) is reported by Zhao, which increased the CO₂ adsorption in MIL-101 [9]. In 2015, Li took a step further with introduction of terpyridyl moiety in the click reaction step and add an additional metalation step to generate heterogeneous Ru(III) catalyst with MIL-101 for oxidation of alcohols [10]. In 2020, a deprotection–azidation–click reaction sequences was performed on UiO-66-NH₃ for adsorption of palladium [11]. With less stable and water sensitive IRMOF-9 analogue, a epoxidation–ring opening azidation–ring closing aziridine formation PSM sequence was achieved by Richardson [12]. With tandem PSM, the final MOF shows higher surface area and crystallinity than the directly synthesized IRMOF-9 analogue using aziridine functionalized biphenydicarboxylate acid, demonstrating the advantage of tandem PSM.

Multi-functional MOF can also be achieved via post-synthetic functionalization. The first method is to perform PSM with a non-excess amount of reactant to preserve some of the functionable sites, and the second reagent can transform the remaining sites [6]. Another method is to install ligands with different functional sites that can perform different PSM reactions. The major challenge for these methods is to construct a well-defined, multi-functional environment in the MOF pore. In 2019, Gadzikwa introduce a method to create a bifunctional MOF KSU-1 by using two ligands with independent functional sites and coordination environments [13]. Using 2-amino-1,4-benzenedicarboxylic acid (BDC-NH₂) and *meso*- α,β -di(4-pyridyl)glycol (DPG), orthogonally coordinated to the Zn-paddlewheel. The two functional site amine and hydroxyl group can then individually go through PSM to add additional functionality. This method enables the generation of confined spaces that are uniformly decorated with multiple functional groups.

In addition to ligand functionalization, the inorganic SBUs of a MOF can also be modified to obtain new materials. This can be done either by performing a post-synthetic metal exchange or by functionalizing the existing metal node using processes such as atomic layer deposition (ALD) in MOFs (AIM).

Post-synthetic metal exchange is one technique by which inorganic SBUs can be further functionalized. In this process, the MOF is suspended in a solution of a metal precursor for several days, sometimes at elevated temperatures, to allow the exchange process to occur. The first example of complete metal metathesis was reported by Kim in 2009, in which a Cd-MOF with a tritopic linker was immersed in a lead(II) nitrate solution for a week, leading to complete substitution of the Cd ions in the framework for Pb [14]. Since this study, other studies have similarly shown complete metal metathesis, including works by Kim [15], Zhou [16–18], and Kaskel [19]. However, depending on the stability of the framework, post-synthetic metal exchange is more often incomplete [20], with the extent of the exchange able to be carefully controlled by adjusting the reaction time, temperature, and metal precursor identity and concentration to obtain mixed-metal MOFs. The ability of a given metal

ion to exchange with another metal ion is largely dictated by the relative thermodynamic stabilities of the metals in the framework, with labile metals being more easily replaced than more stable ones [19]. Furthermore, as metal exchange begins at the surface of the crystals, core-shell structures can be obtained via incomplete metathesis, as the process is diffusion-limited [21, 22].

MOF-5, comprised of basic zinc acetate clusters and BDC (benzene dicarboxylate) linkers, is a common platform for divergent synthesis using metal exchange, as the labile Zn^{2+} ions of the cluster can be readily replaced post-synthetically with other metals. One such example is work by Dincă, who studied the effects of solvent on the efficacy of the metal exchange reaction in this system. In their first study of this system, Ni^{2+} ions were substituted into the clusters in a 1:3 Ni/Zn ratio by soaking the Zn-based framework in a $\text{Ni}(\text{NO}_3)_2$ solution for one year [23]. In a later study, Dincă found that solvents with higher ligand field parameters for the solvated Ni^{2+} ions were more effective at replacing the Zn ions and demonstrated that partial replacement could be achieved in as little as one week [24]. Unexpectedly, Ni-incorporation into MOF-5 resulted in a distortion of the lattice to produce octahedrally coordinated Ni^{2+} , rather than the tetrahedral geometry that would be suggested by the topology of the framework [23]. However, upon heating under vacuum, the solvent (DMF) molecules were released, affording a tetrahedrally coordinated Ni^{2+} ion and minimal lattice distortion in the framework. Further treatment with sterically bulky ligands could afford a five-coordinate square pyramidal geometry around the Ni^{2+} ion [23], demonstrating that divergent synthesis can be used to obtain unusual coordination geometries that may otherwise be inaccessible. Examples of divergent synthesis via metal exchange are less common for highly stable frameworks such as UiO-66, comprised of highly stable $\text{Zr}_6\text{O}_4(\text{OH})_4$ clusters and BDC linkers, due to the stability of the metal-linker bonds, however a small number of studies do exist [25, 26].

While incomplete metal metathesis is often random [20, 27], in some cases, differences in the relative stability of metals in the clusters of the parent MOF can result in site selective metal exchange. An early example of this is a work by Volkmer, in which the four tetrahedral Zn ions in MFU-4l could be replaced with Co, but the central octahedral Zn atom of the cluster could not [28]. Other works by Dincă and Long have likewise shown that metal ions can be substituted in different sites within a cluster depending on the identity of the metal ion and their relative binding strength in the different sites [29, 30]. More recently, Yao and Liu have demonstrated that metal exchange can be selectively performed on a MOF containing two unique In sites, with only the In(II) paddlewheel being exchanged with Cu, leaving the mononuclear In(III) site unaffected (Fig. 7.1) [31]. This type of site specific metal exchange presents opportunities for controlled divergent synthesis in MOFs.

More recently, emphasis has been placed on techniques that graft additional metal species onto the periphery of the inorganic SBU instead of performing metal exchange, as this can further diversify the structures that can be obtained. One such technique is solvent-assisted metal incorporation, also known as solvothermal deposition in MOFs (SIM). This technique solvothermally deposits a secondary metal onto the surface of the inorganic SBU and is advantageous compared to post-synthetic

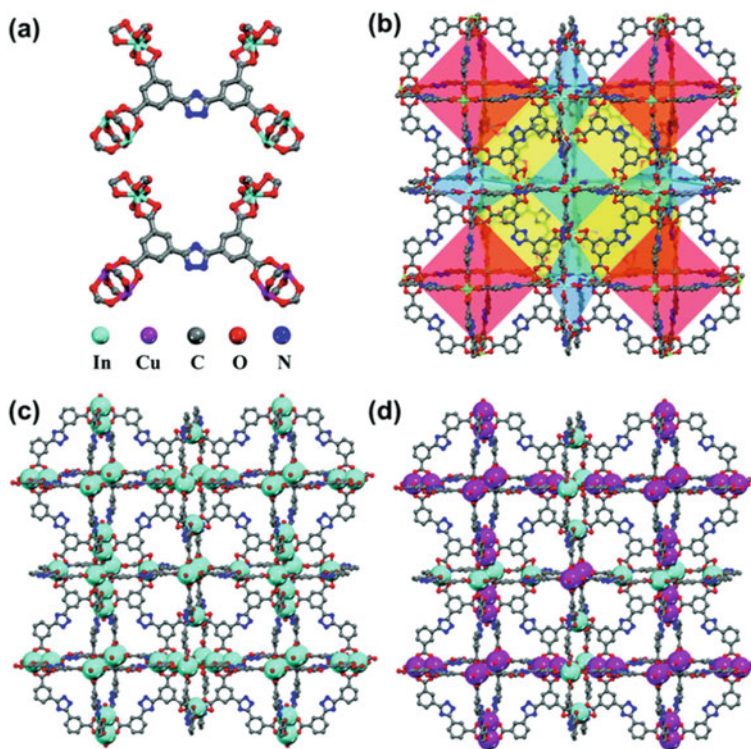


Fig. 7.1 Structural illustration of JLU-Liu40-In and JLU-Liu-40-In/Cu. **a** Inorganic and organic SBUs in JLU-Liu40-In and JLU-Liu40-In/Cu. **b** Three types of polyhedral cages in the MOFs. **c** Crystal structure of JLU-Liu40-In. **d** Crystal structure of JLU-Liu40-In/Cu. Reproduced with permission from Ref. [31]. Copyright 2020. RSC Publication

metal exchange due to the ability to incorporate metal species that are otherwise difficult to incorporate in an SBU, such as Ti. Due to the solvothermal conditions required for this type of metalation, Zr-MOFs such as UiO-66 (comprised of 12-connected $Zr_6(\mu_3-O)_4(\mu_3-OH)_4$ nodes and ditopic BDC linkers) and NU-1000 (comprised of 8-connected $Zr_6(\mu_3-O)_4(\mu_3-OH)_4$ nodes and 1,3,6,8-tetrakis(*p*-benzoic acid) pyrene linkers (see Fig. 7.1c) are particularly suited to this process, as they are highly stable even at elevated temperatures [32, 33]. Since Hupp and Farha's original report on SIM, they, along with others, have performed SIM with a wide range of metals [32–36].

In recent years, atomic layer deposition (ALD) has proven an effective tool for the metalation of MOFs materials [37, 39, 40]. ALD is a vapor phase technique based on sequential, self-limiting surface reaction between multiple precursors on substrates and thus enables the growth of nanomaterials with excellent controllability on composition and thickness, high conformity, and superior uniformity (Fig. 7.2a)

[41]. The surface chemistry of substrate is essential to activating the initial reaction and ensuring subsequent materials growth. The chemical tunability of MOFs surface makes it possible to graft various metals onto the parent metal oxide nodes with atomic precision (Fig. 7.2b) [39]. Implementation of ALD to functionalize MOF materials has been successfully demonstrated in numerous structures especially Zr_6 -based MOFs (Fig. 7.2c) [37, 40, 42–45]. The most notable example is ALD on NU-1000 pioneered by Hupp and co-workers [37, 38, 40, 43, 44, 46], NU-1000 features large hexagonal channels (~3 nm) constructed by 8-connected $Zr_6(\mu_3-O)_4(\mu_3-OH)_4$ octahedral node and 1,3,6,8-tetrakis(p-benzoic acid) pyrene linkers (see Fig. 7.1c) [37]. The mesoporous channels allow for accommodation of large-sized organometallic precursors and facile diffusion of the reaction products. Furthermore, the vacancies present on under-coordinated zirconium clusters are compensated by terminal-OH and H_2O , which serve as the active sites to initialize ALD growth. These merits, together with its high hydrothermal stability, make NU-1000 a promising ALD platform. The first metalation work on NU-1000 was done with trimethylaluminum (TMA) and diethylzinc (DEZ) precursors. Exposure of activated NU-1000 to TMA and DEZ between 110 and 140 °C results in their fast reaction with OH groups and therefore incorporation of Al and Zn to the Zr_6 -cluster [37]. Interestingly, TMA was found to react readily with all terminal OH species during a moderate precursor exposure, achieving a high metal loading up to 8 Al atoms for every Zr_6 -node in NU-1000. Large or prolonged TMA exposure induces the further reactions with extra-nodal oxygens and thus causes noticeable degradation of framework crystallinity and loss of internal surface area [46]. In contrast to TMA, DEZ preferentially reacts –OH group pointing into the small cavities that connect the large hexagonal channels (see Fig. 7.1c), leading to a regioselective deposition during the subsequent cycles as revealed by *in situ* synchrotron X-ray powder diffraction [43]. Such unusual selectivity for ALD reaction within NU-1000 is attributed to be driven by the local dispersion interactions that favor the binding of DEZ precursor prior to reaction. Different from TMA which reacts excessively beyond the hydroxylated node within NU-1000, another trivalent metal precursor trimethylindium (TMI) was found to exhibit the strict self-limiting behavior in reaction with only the node hydroxyls and ligated water [46]. DFT simulation predicted a highly symmetric structure having two In metals deposited on each of four faces of the Zr_6 -node, which was corroborated by experimental PDF analysis [46]. It is worth noting that, by a combined ALD and metal-exchange approach starting with Zn-NU-1000, various dispersed single atoms including Cu, Ni, and Co can be successfully installed into NU-1000 [47]. In such a two-step approach, the economical precursor DEZ was employed first to deposit Zn on Zr_6 -node; the resulting Zn-NU-1000 samples were soaked in methanolic solutions of metal salts $CuCl_2$, $NiCl_2$, $CoCl_2$ at various temperatures for exchanging Zn^{2+} with M^{2+} ions to obtain the porous materials with uniform target metal distribution [47]. In addition to grafting transition metal ions, noble metal platinum (Pt) has also been successfully deposited on the Zr_6 -nodes of NU-1000 in the form of single atoms and few-atom clusters using trimethyl(methylcyclopentadienyl)platinum(IV) precursor at moderate temperature (115 °C) [44]. Remarkably, these Pt clusters exhibit strong resistance to sintering

up even under harsh catalytic conditions, e.g., strongly exothermic hydrogenation reaction of ethylene, due to their site-isolation by organic linkers [44]. To establish a materials data base for ALD modification of NU-1000, Martinson and co-workers have screened and investigated the deposition of a large library of ALD precursors which span metals across group 6–13 of the periodic table [40]. With such a comprehensive study [40], the trends in the compatibility of metal precursor classes for ALD in NU-1000 has been established, which is of great importance to guide the future efforts in metalation of MOFs via ALD. Beside NU-1000, a number of other Zr_6 -MOFs such as UiO-66, UiO-66-NH₂, and MOF-808 have also been investigated for installing metal to the Z_6 -nodes by ALD [45, 48]. Compared with NU-1000, UiO-66 processes much smaller channel size and higher Z_6 -node connectivity (*12-linker coordinated*). Thus, it is not surprising to observe that reaction of bulky ALD precursors such as bis(N,N'-di-Butyl-acetamidinato)Ni(II) occurs predominantly in the near-surface region of the samples since diffusion into the bulk of crystallites is severely hindered [49]. For the smaller-sized precursor such as TMA, increasing temperature above 200 °C and modification of organic linker with amine moiety (–NH₂) [45], was found to facilitate the precursor diffusion and reaction at the Zr_6 -node of UiO-66 in that –NH₂ catalyzes ligand-exchange process by anchoring TMA molecule in close proximity to μ_3 –OH group [45].

In addition to these techniques, more traditional inorganic chemistry techniques have been employed to modify inorganic SBUs, exemplified by the work of Lin. Lin's work typically involves first deprotonating μ -OH sites in the inorganic SBU with *n*-BuLi or a Grignard-like species, before treating the deprotonated framework with a metal salt [50–54]. This technique has been especially successful in UiO-type structures, due to the presence of the aforementioned μ -OH sites decorating the cluster [53, 54]. Similarly, a study by Quadrelli demonstrated the post-synthetic grafting of a Au(I) species onto the μ -OH groups, however the reactivity was such that it was not necessary to deprotonate the cluster to bind the Au(I) species [55].

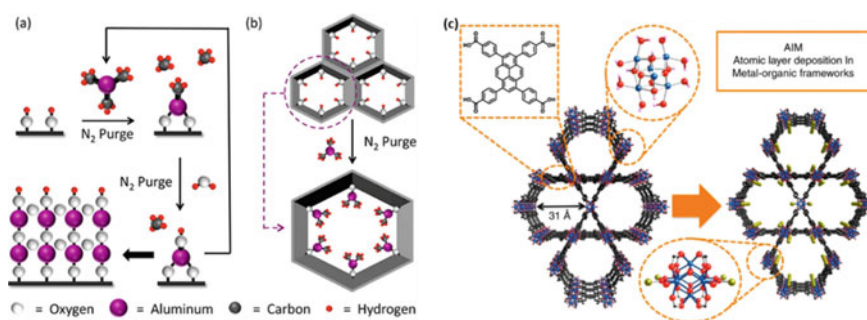


Fig. 7.2 **a** Scheme of ALD process on a flat surface; **b** Metalation by ALD In a MOF (AIM); **c** Structure of NU-1000 frameworks with the Zr_6 -node and organic linker, and modification by ALD. The blue, red and black spheres represent zirconium, oxygen and carbon, respectively. **a** and **b** are reproduced with permission from Ref. [37]. Copyright 2013. American Chemical Society; and **c** from Ref. [38]. Copyright 2015. Nature Publishing Group

7.2 Pore Engineering in MOFs

Linker exchange is a one effective approach to differentiate MOF structures. During a typical ligand exchange process, organic linkers of a substrate MOF will be replaced by other linkers, while integrity of the MOF is maintained. This interesting phenomenon was initially observed by Kitagawa and co-workers during the epitaxial growth of MOF-on-MOF architectures, when ligand exchange occurred only on MOF surface [56–58]. Through continuous efforts, the linker exchange was developed as a common and imperative method to modify MOF structures by Cohen, Hupp, Farha, Matzger, Choe, and other researchers. Linker exchange is driven by entropy changes and needs to overcome the energy barrier of coordination bonds' dissociation. Based upon the distribution of the linkers in substrate MOFs, linker exchange can be divided into two sorts, namely anisotropic and isotropic linker exchanges. During the isotropic linker exchange, organic linkers in the substrate MOF will be replaced gradually without preferred orientation or spatial selectivity. In contrast, the anisotropic linker exchange occurs in specific crystal faces of MOFs. Discussions are made here on how MOF types and reaction conditions affect the final MOF structures.

The anisotropic linker exchange usually occurred in mixed-linker MOFs. For instance, in 2011 Choe and co-workers synthesized a layered MOF PPF-20 (PPF = porphyrin paddlewheel framework), which contained a pillar ligand DPNI and 2D layer with TCPP ligand and $Zn_2(COO)_4$ paddlewheel cluster (DPNI = N,N'-di-4-pyridyl naphthalenetetracarboxydiimide, TCPP = tetrakis(4-carboxyphenyl)porphyrin) [60]. After immersed in solution with excess BPY, interestingly, the pillar ligand DPNI was replaced by the shorter BPY, resulting in a lattice with a contracted *c* parameter (BPY = 4,4'-bipyridine). Later, Farha, Hupp, and co-workers successfully utilized solvent-assisted linker exchange (SALE) to insert longer pillars into layered MOFs and continuously increase the *c* parameter and solvent accessible space of MOFs [59] (Fig. 7.3). These works indicate that anisotropic linker exchange can stretch or contract MOF lattices in specific directions. The versatility of this method has been confirmed in diverse layered MOFs, in which not only the topologies of MOF layers vary, but also the pillar ligands are diverse [61–64]. As a result, the combination of various MOF layers and pillar ligands dramatically increase the diversity of MOFs. Notably, through the SALE, the non-catenated nature of MOFs can be well-maintained, while the catenation control of MOFs is usually challenging through direct synthesis [65, 66]. Besides, after linker exchange, MOFs still feature high structural tunability and can be sequentially functionalized to afford MOFs inaccessible through direct synthesis. For instance, in 2013, Takaishi and coworker reported the construction of a porphyrin-based layered MOF through SALE, which can be further functionalized by linker metalation and metal exchange [67]. Furthermore, Hupp, Farha and coworkers combined the linker exchange, linker metalation, and layer-by-layer assembly to prepare thin-film MOFs with diverse structures [68]. Moreover, Cao and coworkers reported that the pillar ligand of an interpenetrated MOF could be sequentially exchanged, resulting in a fivefold length

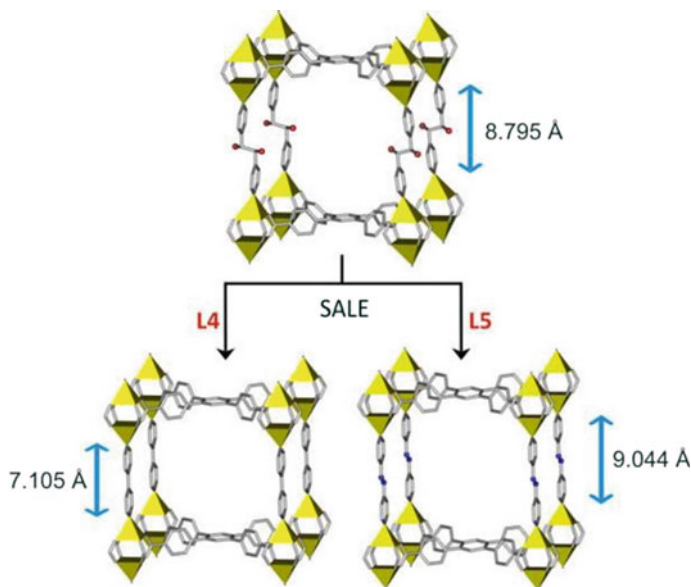


Fig. 7.3 Linker exchange to afford pillared MOFs with varied lattice parameters. Reproduced with permission from Ref. [59]. Copyright 2013. American Chemical Society

reduction [63]. In 2016, Hupp, Farha, and coworkers learnt from the thought experiment “Ship of Theseus” and fully uncovered the potential of SALE by converting a MOF into one with completely different components [69]. As a short summary, anisotropic linker exchange is one effective method to tune MOF lattice parameters, functionalize frameworks, and enhance structural diversity, without damaging the integrity and crystallinity of MOFs.

The isotropic linker exchange can take place in MOFs with various ligands, including imidazole, carboxylate acid, and even benzoquinone. During the linker exchange, there is usually no specific spatial selectivity for the ligand replacement, affording one isostructural MOF as a result. Besides, as a dynamic process, linker exchange is highly reversible and sensitive to the solution concentration, which contribute to the ligand free energy [70]. Dynamic studies confirm that linker exchange is usually rapid at the initial stage and then slows down by the interactions between ligands and frameworks [70, 71]. Dynamic control over exchange process will generate various products. In 2017, through the linker exchange of MOF-5 with deuterated linker, Matzger and coworkers uncovered the coupling between the diffusion and linker exchange, which would affect the linker distribution in the final MOF [71]. If the diffusion is more rapid than the linker exchange, the new linker will be distributed uniformly within the MOF [70, 72]. In contrast, if the linker exchange is more rapid, only linkers near the MOF edges will be replaced, arising a core-shell MOF architecture. In 2020, Matzger and coworkers further investigated the influence

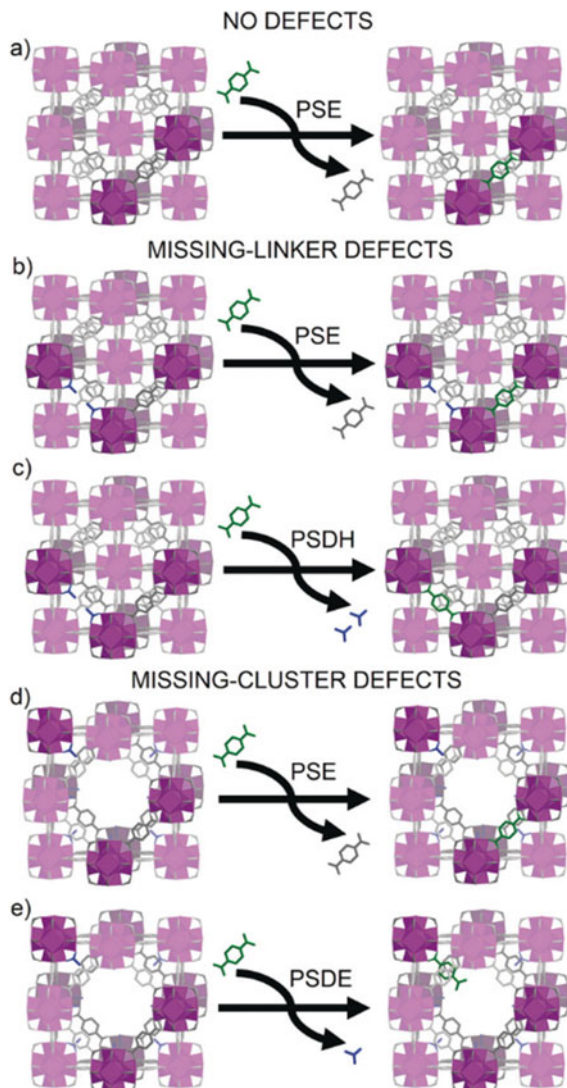
of solvents on the linker exchange, indicating that the solvent species can tune the shell thickness and exchange ratio in the core-shell product [73].

Linker exchange of UiO-type MOFs has been extensively studied (UiO = University of Oslo). As MOFs constructed with high-valence Zr clusters, UiO-type MOFs used to be described as an “intact” material difficult to functionalized. In 2012, however, Cohen and coworkers performed post-synthetic linker exchange of UiO-66 at the presence of solvent and successfully introduced functional linkers into the MOF [74]. Interestingly, the linker exchange can take place between solid/solid or solid/liquid. In 2015, Kaskel and coworkers introduced redox-active tetrazine linkers into UiO-66 by linker exchange, endowing the MOF with redox-active properties [75]. In 2019, Hecht and coworkers introduced an azo-containing photo-switchable linker into UiO-68 through linker exchange, generating a light-responsible core-shell MOF [76]. Upon irradiation of green or blue light, the azo-containing linker would experience photoisomerization between Z- and E-configurations, changing the gateway sizes for guest molecules’ diffusion. Notably, linker exchange is one effective approach to incorporate organometallic components into MOFs, producing catalytic MOFs difficult to obtain through direct synthesis. For instance, in 2013, Cohen, Ott, and coworkers incorporated a ligand $[\text{FeFe}](\text{bdt})(\text{CO})_6$ bearing the active site of $[\text{FeFe}]$ -hydrogenase into UiO-66 (bdt = benzenedithiolate) [77]. The as-formed UiO-66- $[\text{FeFe}](\text{bdt})(\text{CO})_6$ featured improved rates and production in photocatalytic hydrogen generation, compared to the molecular complex $[\text{FeFe}](\text{bdt})(\text{CO})_6$. In 2015, Fontecave and coworkers immobilized a Cp^*Rh -based ligand into UiO-67 and produced a MOF for photocatalytic CO_2 reduction (Cp^* = pentamethylcyclopentadiene) [78]. In 2015, Zou, Martin-Matute, and coworkers investigated different synthetic approaches of UiO-68 doped with an iridium N-heterocyclic carbene (NHC) linker [79]. It turned out that the MOFs prepared by linker exchange featured higher metal loading and better behavior in catalysis than the one from direct synthesis. In 2019, Fei, Wei, and coworkers also incorporated NHC linkers into UiO-68 through linker exchange [80]. Interestingly, the final MOF contained a metal-free NHC moiety, enabling transformation from CO_2 to methanol under ambient conditions. Moreover, in 2018, a series of chiral metallosalen linkers were immobilized onto UiO-68 by Cui and coworkers [81]. The presence of chiral catalytic sites endowed the MOF with superior performance in asymmetric catalysis. In 2018, Taddei and coworkers systematically studied the significance of defects in UiO-66 linker exchange [82] (Fig. 7.4). There are usually two types of defects within as-synthesized UiO-66, namely missing-linker and missing-cluster defects. During linker exchange of UiO-66 with missing-linker defects, the incoming linker will replace the two monocarboxylate modulators on the adjacent clusters. Subsequently, the missing-linker defects will be healed. In the case of UiO-66 featuring missing-cluster defects, the incoming linker will replace only one modulator on the defects. As a result, the dangling linker will decrease the UiO-66’s porosity. Therefore, this work confirmed the capability of linker exchange to engineer MOF defects. Later, Ameloot and coworkers further studied the linker exchange mechanism of UiO-66 and uncovered that the solvent, such as methanol, played an essential role in the linker exchange [83]. According to time-resolved characterization and simulation,

methanol molecules can cap on the $[\text{Zr}_6(\mu_3\text{-O})_4(\mu_3\text{-OH})_4]^{12+}$ clusters and stabilize the intermediate status with dangling linkers during the exchange. Once generated, the dangling linker can undergo fast exchange to immobilize the incoming linker. Notably, the presence of missing-cluster or missing-linker defects may not have significant effects on the MOF compositions after exchange.

Zeolitic imidazolate frameworks (ZIFs) are a large subclass of MOFs, which are generally comprised of single-metal nodes and deprotonated imidazole linkers [84, 85]. Due to the $\sim 145^\circ$ bridging metal-imidazolate-metal angle, ZIFs adopt

Fig. 7.4 Potential outcomes of linker exchange in UiO-66. **a** Defect-free UiO-66 can only exchange one terephthalate linker with the incoming linker. **b, c** UiO-66 containing missing-linker defects can either exchange one terephthalate linker or two modulator acids per incoming linker. **d, e** UiO-66 containing missing-cluster defects can either exchange one terephthalate linker or one modulator acid per incoming linker. Reproduced with permission from Ref. [82]. Copyright 2018. John Wiley and Sons



identical topologies with zeolites, indicating a diverse library of ZIFs. Through direct synthesis, however, only thermo-dynamically stable ZIF phases can be achieved, occupying a small amount of all the potential ZIFs [86]. Herein, linker exchange has been applied to synthesize novel ZIFs and enhance their structural diversity. For instance, in 2012, Farha, Hupp, and coworkers synthesized a cadmium-based ZIF CdIF-4 with eim linker (eim = 2-ethylimidazole) [87]. Through linker exchange with mim, the CdIF-4 can be converted into an unprecedented ZIF SALEM-1 (mim = 2-methylimidazole). The researchers then prepared another novel ZIF SALEM-2 Zn(im)₂ by SALE of ZIF-8 Zn(mim)₂ with im (im = imidazole) [88]. During the linker exchange, the SOD topology of ZIF-8 was retained. Notably, Zn(im)₂ with the SOD topology is elusive in direct synthesis and thermodynamically unstable according to calculation [89]. Furthermore, the researchers systematically studied the exchange in a series of mixed-linker ZIF, namely ZIF-69, ZIF-78, and ZIF-76, featuring both imidazolate and benzimidazolate linkers [90]. Interestingly, only the benzimidazolate linker was replaced, indicating the first example of selective linker exchange in ZIFs.

In 2017, Nair and coworkers reported that core-shell structures would arise during SALE of ZIF-8 and OHC-im linker (OHC-im = imidazole-2-carboxaldehyde) [91]. Similar to carboxylate-based MOFs, the generation of the core-shell morphology was attributed to the limited diffusion rates [71]. If the exchange was under harsher conditions, the initial ZIF-8 crystals would be partially etched to form hollow defects. Similar phenomena were also observed during SALE of MOF-5 and mim linkers [92]. According to the recent work from Wu, Xu, Ajayan, Cui, and coworkers, when MOF-5 crystals were placed in mim solution at room temperature, single-shell hollow ZIF-8 would be generated. If the temperature was slightly increased, the MOF-5 would be evolved into double-shell hollow ZIF-8. The formation of the diverse architectures should be attributed to the diffusion-controlled exchange process. The deprotonated mim ligand was prone to destruct the MOF-6 and react with the zinc node to produce ZIF-8 nuclei, while the diffusion of mim inward the crystal was not favored. As a result, the destruction of the MOF-6 was slower than the recrystallization of ZIF-8, yielding the void structures.

In 2019, Cohen and coworkers functionalized ZIF-8 nanoparticles with a surface capping imidazolium ligand, which could serve as initiator for atom transfer radical polymerization (ATRP) [93]. After polymerization reaction with methyl methacrylate (MMA), core-shell ZIF-8-PMMA particles were achieved, which can be self-assembled into layered superstructures. In addition, Rzayev and coworkers reported another linker exchange approach to prepare MOF-polymer hybrids [94]. A carboxylate linker with the polymer backbone can be exchanged with surface ligands of prototype MOFs, including ZIF-8, MOF-5, and UiO-66, producing a composite with a high MOF loading ratio.

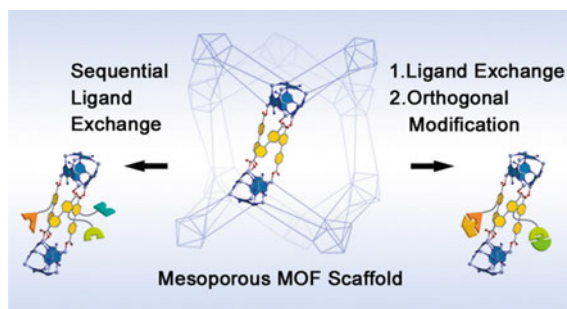
Although most examples of MOF linker exchange took place in solution, vapor-phase linker exchange (VPLE) on ZIFs has been discovered [95, 96]. In 2019, Ameloot and coworkers reported that the mim linker of ZIF-8 would be partially replaced when exposed to the vapor of another linker, including im, OHC-im,

bzim, NO₂-im, and 4,5-dCl-im (bzim = benzimidazole, NO₂-im = 2-nitro imidazole, 4,5-dCl-im = 4,5-dichloro imidazole) [45]. Interestingly, kinetic studies on the VPLe process demonstrated an independent relationship between crystal sizes and exchange ratios, in contrast to the solvent-based linker exchange of ZIF-8 limited by diffusion [91]. The VPLe also requires that the incoming linkers should be more acidic than the framework linker and both the linkers need to be volatile. In 2020, Li and coworkers incorporated a series of halogen-containing linkers into ZIF-8 via VPLe, producing materials with a high selectivity for gas separation [46].

Precise regulation of functional building units is a long-term challenge in materials science. In 2019, Zhou and coworkers reported a series of imprinted ZIFs (iZIF), in which the apportionment of function groups were manipulated by pre-locked linkers [97]. Initially, interlocked imidazolate linkers were incorporated into ZIF-8 through linker exchange and templating linkers were subsequently cleaved through hydrolysis. Structural simulation indicated that the length of the interlocked linker would determine the substitution locations, paving the way for predictable arrangement of function groups within multicomponent MOFs.

Linker exchange has been recognized as an efficient method to engineer MOFs with diverse linkage types [98, 99]. For instance, Rosi and coworkers performed stepwise linker exchange on bio-MOF-101 analogues to expand the pore sizes progressively [100]. Bio-MOF-101 featured Zn₈Ad₄O₂⁸⁺ clusters and NDC linkers, which can be exchanged with the longer linker BPDC to afford bio-MOF-100 (Ad = adeninate, NDC = 2,6-naphthalenedicarboxylate, BPDC = 4,4'-biphenyldicarboxylate). Through stepwise exchange, the BPDC linker can be replaced with ABTC and NH₂-TPDC, accompanied with volume expansion of crystals (ABTC = azobenzene-4,4'-dicarboxylate, NH₂-TPDC = 2'-amino-1,1':4,1''-terphenyl-4,4''-dicarboxylate). Furthermore, Rosi and coworkers performed sequential linker exchange on bio-MOF-100 and installed three different functional groups into the MOF scaffold [101]. Notably, the three functional groups can be modified orthogonally (Fig. 7.5). Besides, in 2020, Harris and coworkers successfully prepared a rare class of amidic MOFs through linker exchange [102]. Due to the strong metal-nitrogen bond, crystalline amidic MOFs are difficult to achieve through direct synthesis. Herein, this work represents a new approach to prepare MOFs with relatively irreversible bonds.

Fig. 7.5 Orthogonal functionalization in a mesoporous MOF bio-MOF-100. Reproduced with permission from Ref. [101]. Copyright 2015. ACS Publication



Sophisticated chemical processes in biological systems often require a precise sequence of binding moieties. To further regulate the apportionment of building units of MOFs to mimic the biochemical processes' conditions, the Zhou group raised a strategy to pre-incorporate interlocked linkers into MOFs [97]. ZIF-8 was adopted as the example MOF material due to its excellent tolerance toward post-synthetic modification. 2-imidazolecarboxaldehyde (Im-CHO) was chosen as the prototype and linked with diamines (CX, $X = 2, 3, 4, 6, 8$ and 12) to form pre-labile locked linker template (LX, $X = 2, 3, 4, 6, 8$ and 12). The pre-locked composite can be easily dissociated through hydrolysis, with the coordination bonds between Zn nodes and imidazole linkers robust enough to stand mild aqueous treatment. ZIF-8 with various exchange ratios were obtained, while N_2 adsorption isotherms suggest no mesopore formation due to MOF partial decomposition and total release of template molecules from the framework. Another strategy utilizing thermolabile cross-linkers for templating was developed by the Xiao group to address the limitation due to the imines' decomposition under MOF synthetic conditions [103]. A chemically stable cross-linker was successfully installed in $Mg_2dotpdc$, an expanded MOF-74 analog with carboxylic acid sites in pristine framework structure, after which the thermolysis of cross-linked MOF was showcased to yield the pristine MOF. Dramatic increases in both the BET and Langmuir surface areas were observed with infrared spectroscopy shift indicating a transformation from ester to free carboxylic acid.

The Zhou group provided a method to control the hierarchy of PCN-222@Zn-AzTPDC composites by simply tuning the ratios of the two MOF precursors [104, 105]. The concept of modular programming was developed, which isolates the functionality of a system into independent, interchangeable modules. Multivariate polymer/MOF hybrid composites are formed via the cross-linking of linkers and the removal of metal clusters. Through centrifugal precipitation, core PCN-222 powders stabilized at the bottom of the vials allow for the heterogeneous nucleation and anisotropic growth of Zn-AzTPDC. Increasing the concentration of Zn-AzTPDC precursors in the hierarchical MOF synthesis promotes the evolution of center-concentrated core-shell PCN-222@Zn-AzTPDC structures. The same strategy was extended to other representative MOFs, including PCN-224, MOF-801, UiO-66, UiO-67, PCN-160, and PCN-250 as the core MOFs, and stepwise installation of organic linkers and Zn_4O clusters outside the core MOFs, leading to the formation of MOF@Zn-AzTPDC. The complexity of the hierarchical systems was enhanced in three-module hierarchical MOFs. In addition, the modular programming can be further applied in other MOF@polymer composites containing polystyrene and polymethylmethacrylate [106]. Initially, a three-module MOF@MOF@polymer composite was prepared via stepwise synthesis, in which the two MOFs had distinct stability. Through modularly manipulating chemical compositions, the labile MOF portion could be selectively removed, generating a MOF@polymer composites inheriting the morphology and distribution of pristine MOFs. Such a transformation emulates the DNA transcription in nature, indicating a facile approach to passing MOFs' structural information to other materials. The functionalities in different modules of hierarchical MOFs and MOF-based composites may also sequence the substrates and promote tandem catalysis.

Acknowledgements H.-C. Z. acknowledges financial support from the Robert A. Welch Foundation through a Welch Endowed Chair to H.-C.Z. (A-0030) and the Qatar National Research Fund under Award No. NPRP9-377-1-080. K.T. acknowledges the U. S. Department of Energy, Office of Science, Basic Energy Sciences under Award No. DE-SC0019902.

References

1. Bloch ED, Britt D, Lee C, Doonan CJ, Uribe-Romo FJ, Furukawa H, Long JR, Yaghi OM (2010) Metal insertion in a microporous metal–organic framework lined with 2,2'-bipyridine. *J Am Chem Soc* 132(41):14382–14384
2. Yee K-K, Reimer N, Liu J, Cheng S-Y, Yiu S-M, Weber J, Stock N, Xu Z (2013) Effective mercury sorption by thiol-laced metal-organic frameworks: in strong acid and the vapor phase. *J Am Chem Soc* 135(21):7795–7798
3. Dunning SG, Nandra G, Conn AD, Chai W, Sikma RE, Lee JS, Kunal P, Reynolds JE III, Chang J-S, Steiner A, Henkelman G, Humphrey SM (2018) A metal-organic framework with cooperative phosphines that permit post-synthetic installation of open metal sites. *Angew Chem Int Ed* 57(30):9295–9299
4. Morris W, Voloskiy B, Demir S, Gándara F, McGrier PL, Furukawa H, Cascio D, Stoddart JF, Yaghi OM (2012) Synthesis, structure, and metalation of two new highly porous zirconium metal-organic frameworks. *Inorg Chem* 51(12):6443–6445
5. Kong G-Q, Ou S, Zou C, Wu C-D (2012) Assembly and post-modification of a metal-organic nanotube for highly efficient catalysis. *J Am Chem Soc* 134(48):19851–19857
6. Wang Z, Cohen SM (2008) Tandem modification of metal-organic frameworks by a postsynthetic approach. *Angew Chem Int Ed* 47(25):4699–4702
7. Fracaroli AM, Siman P, Nagib DA, Suzuki M, Furukawa H, Toste FD, Yaghi OM (2016) Seven post-synthetic covalent reactions in tandem leading to enzyme-like complexity within metal-organic framework crystals. *J Am Chem Soc* 138(27):8352–8355
8. Bernt S, Guillermin V, Serre C, Stock N (2011) Direct covalent post-synthetic chemical modification of Cr-MIL-101 using nitrating acid. *Chem Commun* 47(10):2838–2840
9. Li P-Z, Wang X-J, Tan RHD, Zhang Q, Zou R, Zhao Y (2013) Rationally “clicked” post-modification of a highly stable metal–organic framework and its high improvement on CO₂-selective capture. *RSC Adv* 3(36):15566–15570
10. Wu S, Chen L, Yin B, Li Y (2015) “Click” post-functionalization of a metal–organic framework for engineering active single-site heterogeneous Ru(III) catalysts. *Chem Commun* 51(48):9884–9887
11. Daliran S, Ghazagh-Miri M, Oveisi AR, Khajeh M, Navalón S, Álvaro M, Ghaffari-Moghaddam M, Samareh Delarami H, García H (2020) A pyridyltriazol functionalized zirconium metal-organic framework for selective and highly efficient adsorption of palladium. *ACS Appl Mater Interfaces* 12(22):25221–25232
12. Bryant MR, Cunyngame T, Hunter SO, Telfer SG, Richardson C (2021) Trisequential post-synthetic modification of a tagged IRMOF-9 framework. *Inorg Chem* 60(16):11711–11719
13. Samarakoon KP, Satterfield CS, McCoy MC, Pivaral-Urbina DA, Islamoglu T, Day VW, Gadzikwa T (2019) Uniform, binary functionalization of a metal-organic framework material. *Inorg Chem* 58(14):8906–8909
14. Das S, Kim H, Kim K (2009) Metathesis in single crystal: complete and reversible exchange of metal ions constituting the frameworks of metal–organic frameworks. *J Am Chem Soc* 131(11):3814–3815
15. Kim Y, Das S, Bhattacharya S, Hong S, Kim MG, Yoon M, Natarajan S, Kim K (2012) Metal-ion metathesis in metal-organic frameworks: a synthetic route to new metal-organic frameworks. *Chem Eur J* 18(52):16642–16648

16. Zou L, Feng D, Liu T-F, Chen Y-P, Yuan S, Wang K, Wang X, Fordham S, Zhou H-C (2016) A versatile synthetic route for the preparation of titanium metal-organic frameworks. *Chem Sci* 7(2):1063–1069
17. Park J, Feng D, Zhou H-C (2015) Dual exchange in PCN-333: a facile strategy to chemically robust mesoporous chromium metal-organic framework with functional groups. *J Am Chem Soc* 137(36):11801–11809
18. Liu T-F, Zou L, Feng D, Chen Y-P, Fordham S, Wang X, Liu Y, Zhou H-C (2014) Stepwise synthesis of robust metal-organic frameworks via postsynthetic metathesis and oxidation of metal nodes in a single-crystal to single-crystal transformation. *J Am Chem Soc* 136(22):7813–7816
19. Garai B, Bon V, Krause S, Schwotzer F, Gerlach M, Senkovska I, Kaskel S (2020) Tunable flexibility and porosity of the metal-organic framework DUT-49 through postsynthetic metal exchange. *Chem Mater* 32(2):889–896
20. Kim M, Cahill JF, Fei H, Prather KA, Cohen SM (2012) Postsynthetic ligand and cation exchange in robust metal-organic frameworks. *J Am Chem Soc* 134(43):18082–18088
21. Song X, Kim TK, Kim H, Kim D, Jeong S, Moon HR, Lah MS (2012) Post-synthetic modifications of framework metal ions in isostructural metal-organic frameworks: core-shell heterostructures via selective transmetalations. *Chem Mater* 24(15):3065–3073
22. Song X, Jeong S, Kim D, Lah MS (2012) Transmetalations in two metal-organic frameworks with different framework flexibilities: kinetics and core-shell heterostructure. *CrystrEngComm* 14(18):5753–5756
23. Brozek CK, Dincă M (2012) Lattice-imposed geometry in metal-organic frameworks: lacunary Zn₄O clusters in MOF-5 serve as tripodal chelating ligands for Ni²⁺. *Chem Sci* 3(6):2110–2113
24. Brozek CK, Bellarosa L, Soejima T, Clark TV, López N, Dincă M (2014) Solvent-dependent cation exchange in metal-organic frameworks. *Chem Eur J* 20(23):6871–6874
25. Smith SJD, Ladewig BP, Hill AJ, Lau CH, Hill MR (2015) Post-synthetic Ti Exchanged UiO-66 metal-organic frameworks that deliver exceptional gas permeability in mixed matrix membranes. *Sci Rep* 5(1):7823
26. Hon Lau C, Babarao R, Hill MR (2013) A route to drastic increase of CO₂ uptake in Zr metal organic framework UiO-66. *Chem Commun* 49(35):3634–3636
27. Sun D, Sun F, Deng X, Li Z (2015) Mixed-metal strategy on metal-organic frameworks (MOFs) for functionalities expansion: co substitution induces aerobic oxidation of cyclohexene over inactive Ni-MOF-74. *Inorg Chem* 54(17):8639–8643
28. Denysenko D, Werner T, Grzywa M, Puls A, Hagen V, Eickerling G, Jelic J, Reuter K, Volkmer D (2012) Reversible gas-phase redox processes catalyzed by Co-exchanged MFU-4l(arge). *Chem Commun* 48(9):1236–1238
29. Dincă M, Long JR (2007) High-enthalpy hydrogen adsorption in cation-exchanged variants of the microporous metal-organic framework Mn₃[(Mn₄Cl)₃(BTT)₈(CH₃OH)₁₀]₂. *J Am Chem Soc* 129(36):11172–11176
30. Brozek CK, Cozzolino AF, Teat SJ, Chen Y-S, Dincă M (2013) Quantification of site-specific cation exchange in metal-organic frameworks using multi-wavelength anomalous x-ray dispersion. *Chem Mater* 25(15):2998–3002
31. Liu S, Liu B, Yao S, Liu Y (2020) Post-synthetic metal-ion metathesis in a single-crystal-to-single-crystal process: improving the gas adsorption and separation capacity of an indium-based metal-organic framework. *Inorg Chem Front* 7(7):1591–1597
32. Kung C-W, Audu CO, Peters AW, Noh H, Farha OK, Hupp JT (2017) Copper nanoparticles installed in metal-organic framework thin films are electrocatalytically competent for CO₂ reduction. *ACS Energy Lett* 2(10):2394–2401
33. Geravand E, Farzaneh F, Ghiasi M (2019) Metalation and DFT studies of metal organic frameworks UiO-66(Zr) with vanadium chloride as allyl alcohol epoxidation catalyst. *J Mol Struct* 1198:126940
34. Noh H, Kung C-W, Otake K-I, Peters AW, Li Z, Liao Y, Gong X, Farha OK, Hupp JT (2018) Redox-mediator-assisted electrocatalytic hydrogen evolution from water by a molybdenum sulfide-functionalized metal-organic framework. *ACS Catal* 8(10):9848–9858

35. Noh H, Kung C-W, Islamoglu T, Peters AW, Liao Y, Li P, Garibay SJ, Zhang X, DeStefano MR, Hupp JT, Farha OK (2018) Room temperature synthesis of an 8-connected Zr-based metal-organic framework for top-down nanoparticle encapsulation. *Chem Mater* 30(7):2193–2197
36. Yuan S, Chen Y-P, Qin J, Lu W, Wang X, Zhang Q, Bosch M, Liu T-F, Lian X, Zhou H-C (2015) Cooperative cluster metalation and ligand migration in zirconium metal-organic frameworks. *Angew Chem Int Ed* 54(49):14696–14700
37. Mondloch JE, Bury W, Fairen-Jimenez D, Kwon S, DeMarco EJ, Weston MH, Sarjeant AA, Nguyen ST, Stair PC, Snurr RQ, Farha OK, Hupp JT (2013) Vapor-phase metalation by atomic layer deposition in a metal-organic framework. *J Am Chem Soc* 135(28):10294–10297
38. Wang TC, Vermeulen NA, Kim IS, Martinson ABF, Stoddart JF, Hupp JT, Farha OK (2016) Scalable synthesis and post-modification of a mesoporous metal-organic framework called NU-1000. *Nat Protoc* 11(1):149–162
39. Ren J, Jen T-C (2021) Atomic layer deposition (ALD) assisting the visibility of metal-organic frameworks (MOFs) technologies. *Coord Chem Rev* 430:213734
40. Kim IS, Ahn S, Vermeulen NA, Webber TE, Gallington LC, Chapman KW, Penn RL, Hupp JT, Farha OK, Notestein JM, Martinson ABF (2020) The synthesis science of targeted vapor-phase metal-organic framework postmodification. *J Am Chem Soc* 142(1):242–250
41. Johnson RW, Hultqvist A, Bent SF (2014) A brief review of atomic layer deposition: from fundamentals to applications. *Mater Today* 17(5):236–246
42. Zheng J, Ye J, Ortuño MA, Fulton JL, Gutiérrez OY, Camaioni DM, Motkuri RK, Li Z, Webber TE, Mehdi BL, Browning ND, Penn RL, Farha OK, Hupp JT, Truhlar DG, Cramer CJ, Lercher JA (2019) Selective methane oxidation to methanol on Cu-Oxo dimers stabilized by zirconia nodes of an NU-1000 metal-organic framework. *J Am Chem Soc* 141(23):9292–9304
43. Gallington LC, Kim IS, Liu W-G, Yakovenko AA, Platero-Prats AE, Li Z, Wang TC, Hupp JT, Farha OK, Truhlar DG, Martinson ABF, Chapman KW (2016) Regioselective atomic layer deposition in metal-organic frameworks directed by dispersion interactions. *J Am Chem Soc* 138(41):13513–13516
44. Kim IS, Li Z, Zheng J, Platero-Prats AE, Mavrandonakis A, Pellizzeri S, Ferrandon M, Vjunov A, Gallington LC, Webber TE, Vermeulen NA, Penn RL, Getman RB, Cramer CJ, Chapman KW, Camaioni DM, Fulton JL, Lercher JA, Farha OK, Hupp JT, Martinson ABF (2018) Sinter-resistant platinum catalyst supported by metal-organic framework. *Angew Chem Int Ed* 57(4):909–913
45. Tan K, Jensen S, Feng L, Wang H, Yuan S, Ferreri M, Klesko JP, Rahman R, Cure J, Li J, Zhou H-C, Thonhauser T, Chabal YJ (2019) Reactivity of atomic layer deposition precursors with OH/H₂O-containing metal organic framework materials. *Chem Mater* 31(7):2286–2295
46. Kim IS, Borycz J, Platero-Prats AE, Tussupbayev S, Wang TC, Farha OK, Hupp JT, Gagliardi L, Chapman KW, Cramer CJ, Martinson ABF (2015) Targeted single-site MOF node modification: trivalent metal loading via atomic layer deposition. *Chem Mater* 27(13):4772–4778
47. Klet RC, Wang TC, Fernandez LE, Truhlar DG, Hupp JT, Farha OK (2016) Synthetic access to atomically dispersed metals in metal-organic frameworks via a combined atomic-layer-deposition-in-MOF and metal-exchange approach. *Chem Mater* 28(4):1213–1219
48. Lemaire PC, Lee DT, Zhao J, Parsons GN (2017) Reversible low-temperature metal node distortion during atomic layer deposition of Al₂O₃ and TiO₂ on UiO-66-NH₂ metal-organic framework crystal surfaces. *ACS Appl Mater Interfaces* 9(26):22042–22054
49. Li Z, Peters AW, Liu J, Zhang X, Schweitzer NM, Hupp JT, Farha OK (2017) Size effect of the active sites in UiO-66-supported nickel catalysts synthesized via atomic layer deposition for ethylene hydrogenation. *Inorg Chem Front* 4(5):820–824
50. Ji P, Manna K, Lin Z, Feng X, Urban A, Song Y, Lin W (2017) Single-site cobalt catalysts at new Zr₁₂(μ₃-O)₈(μ₃-OH)₈(μ₂-OH)₆ metal-organic framework nodes for highly active hydrogenation of nitroarenes, nitriles, and isocyanides. *J Am Chem Soc* 139(20):7004–7011
51. Ji P, Manna K, Lin Z, Urban A, Greene FX, Lan G, Lin W (2016) Single-site cobalt catalysts at new Zr₈(μ₂-O)₈(μ₂-OH)₄ metal-organic framework nodes for highly active hydrogenation of alkenes, imines, carbonyls, and heterocycles. *J Am Chem Soc* 138(37):12234–12242

52. Ji P, Song Y, Drake T, Veroneau SS, Lin Z, Pan X, Lin W (2018) Titanium(III)-oxo clusters in a metal-organic framework support single-site co(II)-hydride catalysts for arene hydrogenation. *J Am Chem Soc* 140(1):433–440
53. Manna K, Ji P, Greene FX, Lin W (2016) Metal-organic framework nodes support single-site magnesium-alkyl catalysts for hydroboration and hydroamination reactions. *J Am Chem Soc* 138(24):7488–7491
54. Manna K, Ji P, Lin Z, Greene FX, Urban A, Thacker NC, Lin W (2016) Chemoselective single-site earth-abundant metal catalysts at metal-organic framework nodes. *Nat Commun* 7:12610
55. Larabi C, Quadrelli EA (2012) Titration of $Zr_3(\mu-OH)_4$ hydroxy groups at the cornerstones of bulk MOF UiO-67, $[Zr_6O_4(OH)_4(\text{biphenyldicarboxylate})_6]$, and their reaction with $[AuMe(PMe_3)]$. *Eur J Inorg Chem* 2012(18):3014–3022
56. Kondo M, Furukawa S, Hirai K, Kitagawa S (2010) Coordinatively immobilized monolayers on porous coordination polymer crystals. *Angew Chem Int Ed Engl* 49(31):5327–5330
57. Furukawa S, Hirai K, Nakagawa K, Takashima Y, Matsuda R, Tsuruoka T, Kondo M, Haruki R, Tanaka D, Sakamoto H, Shimomura S, Sakata O, Kitagawa S (2009) Heterogeneously hybridized porous coordination polymer crystals: fabrication of heterometallic core-shell single crystals with an in-plane rotational epitaxial relationship. *Angew Chem Int Ed Engl* 48(10):1766–1770
58. Furukawa S, Hirai K, Takashima Y, Nakagawa K, Kondo M, Tsuruoka T, Sakata O, Kitagawa S (2009) A block PCP crystal: anisotropic hybridization of porous coordination polymers by face-selective epitaxial growth. *Chem Commun (Camb)* 34:5097–5099
59. Karagiari O, Bury W, Tylisanakis E, Sarjeant AA, Hupp JT, Farha OK (2013) Opening metal-organic frameworks vol. 2: inserting longer pillars into pillared-paddlewheel structures through solvent-assisted linker exchange. *Chem Mater* 25(17):3499–3503
60. Burnett BJ, Barron PM, Hu CH, Choe W (2011) Stepwise synthesis of metal-organic frameworks: replacement of structural organic linkers. *J Am Chem Soc* 133(26):9984–9987
61. Pal TK, Neogi S, Bharadwaj PK (2015) Versatile tailoring of paddle-wheel Zn-II metal-organic frameworks through single-crystal-to-single-crystal transformations. *Chem-Eur J* 21(45):16083–16090
62. Vermeulen NA, Karagiari O, Sarjeant AA, Stern CL, Hupp JT, Farha OK, Stoddart JF (2013) Aromatizing olefin metathesis by ligand isolation inside a metal-organic framework. *J Am Chem Soc* 135(40):14916–14919
63. Cao L-H, Liu X, Tang X-H, Liu J, Xu X-Q, Zang S-Q, Ma Y-M (2019) A fivefold linker length reduction in an interpenetrated metal-organic framework via sequential solvent-assisted linker exchange. *Chem Commun* 55(84):12671–12674
64. Planes OM, Schouwink PA, Bila JL, Fadaei-Tirani F, Scopelliti R, Severin K (2020) Incorporation of clathrochelate-based metalloligands in metal-organic frameworks by solvent-assisted ligand exchange. *Cryst Growth Des* 20(3):1394–1399
65. Bury W, Fairen-Jimenez D, Lalonde MB, Snurr RQ, Farha OK, Hupp JT (2013) Control over catenation in pillared paddlewheel metal-organic framework materials via solvent-assisted linker exchange. *Chem Mater* 25(5):739–744
66. Xu Y, Howarth AJ, Islamoglu T, da Silva CT, Hupp JT, Farha OK (2016) Combining solvent-assisted linker exchange and transmetallation strategies to obtain a new non-catenated nickel (II) pillared-paddlewheel MOF. *Inorg Chem Commun* 67:60–63
67. Takaishi S, DeMarco EJ, Pellin MJ, Farha OK, Hupp JT (2013) Solvent-assisted linker exchange (SALE) and post-assembly metallation in porphyrinic metal-organic framework materials. *Chem Sci* 4(4):1509–1513
68. So MC, Beyzavi MH, Sawhney R, Shekhah O, Eddaoudi M, Al-Juaid SS, Hupp JT, Farha OK (2015) Post-assembly transformations of porphyrin-containing metal-organic framework (MOF) films fabricated via automated layer-by-layer coordination. *Chem Commun* 51(1):85–88
69. Xu Y, Vermeulen NA, Liu Y, Hupp JT, Farha OK (2016) SALE-Ing a MOF-based “ship of theseus”: sequential building-block replacement for complete reformulation of a pillared-paddlewheel metal-organic framework. *Eur J Inorg Chem* 2016(27):4345–4348

70. Gross AF, Sherman E, Mahoney SL, Vajo JJ (2013) Reversible ligand exchange in a metal-organic framework (MOF): toward MOF-based dynamic combinatorial chemical systems. *J Phys Chem A* 117(18):3771–3776
71. Boissonault JA, Wong-Foy AG, Matzger AJ (2017) Core-shell structures arise naturally during ligand exchange in metal-organic frameworks. *J Am Chem Soc* 139(42):14841–14844
72. Fluch U, Paneta V, Primetzhofer D, Ott S (2017) Uniform distribution of post-synthetic linker exchange in metal-organic frameworks revealed by Rutherford backscattering spectrometry. *Chem Commun* 53(48):6516–6519
73. Dodson RA, Kalenak AP, Matzger AJ (2020) Solvent choice in metal-organic framework linker exchange permits microstructural control. *J Am Chem Soc* 142(49):20806–20813
74. Kim M, Cahill JF, Su Y, Prather KA, Cohen SM (2012) Postsynthetic ligand exchange as a route to functionalization of ‘inert’ metal-organic frameworks. *Chem Sci* 3(1):126–130
75. Nickerl G, Senkowska I, Kaskel S (2015) Tetrazine functionalized zirconium MOF as an optical sensor for oxidizing gases. *Chem Commun* 51(12):2280–2282
76. Mutruc D, Goulet-Hanssens A, Fairman S, Wahl S, Zimathies A, Knie C, Hecht S (2019) Modulating guest uptake in core-shell MOFs with visible light. *Angew Chem Int Ed* 58(37):12862–12867
77. Pullen S, Fei H, Orthaber A, Cohen SM, Ott S (2013) Enhanced photochemical hydrogen production by a molecular diiron catalyst incorporated into a metal-organic framework. *J Am Chem Soc* 135(45):16997–17003
78. Chambers MB, Wang X, Elgrishi N, Hendon CH, Walsh A, Bonnefoy J, Canivet J, Quadrelli EA, Farrusseng D, Mellot-Draznieks C, Fontecave M (2015) Photocatalytic carbon dioxide reduction with rhodium-based catalysts in solution and heterogenized within metal-organic frameworks. *ChemSuschem* 8(4):603–608
79. Carson F, Martínez-Castro E, Marcos R, Miera GG, Jansson K, Zou X, Martín-Matute B (2015) Effect of the functionalisation route on a Zr-MOF with an Ir–NHC complex for catalysis. *Chem Commun* 51(54):10864–10867
80. Zhang X, Sun J, Wei G, Liu Z, Yang H, Wang K, Fei H (2019) In situ generation of an n-heterocyclic carbene functionalized metal-organic framework by postsynthetic ligand exchange: efficient and selective hydrosilylation of CO₂. *Angew Chem Int Ed* 58(9):2844–2849
81. Tan CX, Han X, Li ZJ, Liu Y, Cui Y (2018) Controlled exchange of achiral linkers with chiral linkers in Zr-based UiO-68 metal-organic framework. *J Am Chem Soc* 140(47):16229–16236
82. Taddei M, Wakeham RJ, Koutsianos A, Andreoli E, Barron AR (2018) Post-synthetic ligand exchange in zirconium-based metal-organic frameworks: beware of the defects! *Angew Chem Int Ed* 57(36):11706–11710
83. Marreiros J, Caratelli C, Hajek J, Krajnc A, Fleury G, Bueken B, De Vos DE, Mali G, Roeffaers MBJ, Van Speybroeck V, Ameloot R (2019) Active role of methanol in post-synthetic linker exchange in the metal-organic framework UiO-66. *Chem Mater* 31(4):1359–1369
84. Phan A, Doonan CJ, Uribe-Romo FJ, Knobler CB, O’Keeffe M, Yaghi OM (2010) Synthesis, structure, and carbon dioxide capture properties of zeolitic imidazolate frameworks. *Accounts Chem Res* 43(1):58–67
85. Zhang J-P, Zhang Y-B, Lin J-B, Chen X-M (2012) Metal azolate frameworks: from crystal engineering to functional materials. *Chem Rev* 112(2):1001–1033
86. Park KS, Ni Z, Cote AP, Choi JY, Huang RD, Uribe-Romo FJ, Chae HK, O’Keeffe M, Yaghi OM (2006) Exceptional chemical and thermal stability of zeolitic imidazolate frameworks. *P Natl Acad Sci USA* 103(27):10186–10191
87. Karagiari O, Bury W, Sarjeant AA, Stern CL, Farha OK, Hupp JT (2012) Synthesis and characterization of isostructural cadmium zeolitic imidazolate frameworks via solvent-assisted linker exchange. *Chem Sci* 3(11):3256–3260
88. Karagiari O, Lalonde MB, Bury W, Sarjeant AA, Farha OK, Hupp JT (2012) Opening ZIF-8: a catalytically active zeolitic imidazolate framework of sodalite topology with unsubstituted linkers. *J Am Chem Soc* 134(45):18790–18796

89. Lewis DW, Ruiz-Salvador AR, Gómez A, Rodriguez-Albelo LM, Coudert F-X, Slater B, Cheetham AK, Mellot-Draznieks C (2009) Zeolitic imidazole frameworks: structural and energetics trends compared with their zeolite analogues. *CrystEngComm* 11(11):2272–2276
90. Lalonde MB, Mondloch JE, Deria P, Sarjeant AA, Al-Juaid SS, Osman OI, Farha OK, Hupp JT (2015) Selective solvent-assisted linker exchange (SALE) in a series of zeolitic imidazolate frameworks. *Inorg Chem* 54(15):7142–7144
91. Jayachandrababu KC, Sholl DS, Nair S (2017) Structural and mechanistic differences in mixed-linker zeolitic imidazolate framework synthesis by solvent assisted linker exchange and de novo routes. *J Am Chem Soc* 139(16):5906–5915
92. Yu D, Shao Q, Song Q, Cui J, Zhang Y, Wu B, Ge L, Wang Y, Zhang Y, Qin Y, Vajtai R, Ajayan PM, Wang H, Xu T, Wu Y (2020) A solvent-assisted ligand exchange approach enables metal-organic frameworks with diverse and complex architectures. *Nat Commun* 11(1):927
93. Katayama Y, Kalaj M, Barcus KS, Cohen SM (2019) Self-assembly of metal-organic framework (MOF) nanoparticle monolayers and free-standing multilayers. *J Am Chem Soc* 141(51):20000–20003
94. Pastore VJ, Cook TR, Rzyayev J (2018) Polymer–MOF hybrid composites with high porosity and stability through surface-selective ligand exchange. *Chem Mater* 30(23):8639–8649
95. Marreiros J, Van Dommelen L, Fleury G, de Oliveira-Silva R, Stassin T, Iacomi P, Furukawa S, Sakellariou D, Llewellyn PL, Roeffaers M, Ameloot R (2019) Vapor-phase linker exchange of the metal-organic framework ZIF-8: a solvent-free approach to post-synthetic modification. *Angew Chem Int Ed Engl* 58(51):18471–18475
96. Wu W, Su J, Jia M, Li Z, Liu G, Li W (2020) Vapor-phase linker exchange of metal-organic frameworks. *Sci Adv* 6(18):eaax7270-1–eaax7270-7
97. Feng L, Wang KY, Lv XL, Powell JA, Yan TH, Willman J, Zhou HC (2019) Imprinted apportionment of functional groups in multivariate metal-organic frameworks. *J Am Chem Soc* 141(37):14524–14529
98. Han S-Y, Pan D-L, Chen H, Bu X-B, Gao Y-X, Gao H, Tian Y, Li G-S, Wang G, Cao S-L, Wan C-Q, Guo G-C (2018) A methylthio-functionalized-MOF photocatalyst with high performance for visible-light-driven H₂ evolution. *Angew Chem Int Ed* 57(31):9864–9869
99. Nguyen HTT, Tu TN, Nguyen MV, Lo THN, Furukawa H, Nguyen NN, Nguyen MD (2018) Combining linker design and linker-exchange strategies for the synthesis of a stable large-pore Zr-based metal-organic framework. *ACS Appl Mater Inter* 10(41):35462–35468
100. Li T, Kozłowski MT, Doud EA, Blakely MN, Rosi NL (2013) Stepwise ligand exchange for the preparation of a family of mesoporous MOFs. *J Am Chem Soc* 135(32):11688–11691
101. Liu C, Luo TY, Feura ES, Zhang C, Rosi NL (2015) Orthogonal ternary functionalization of a mesoporous metal-organic framework via sequential postsynthetic ligand exchange. *J Am Chem Soc* 137(33):10508–10511
102. Liu L, Li L, Ziebel ME, Harris TD (2020) Metal-diamidobenzoquinone frameworks via post-synthetic linker exchange. *J Am Chem Soc* 142(10):4705–4713
103. Geary J, Wong AH, Xiao DJ (2021) Thermolabile cross-linkers for templating precise multicomponent metal-organic framework pores. *J Am Chem Soc* 143(27):10317–10323
104. Feng L, Lv X-L, Yan T-H, Zhou H-C (2019) Modular programming of hierarchy and diversity in multivariate polymer/metal-organic framework hybrid composites. *J Am Chem Soc* 141(26):10342–10349
105. Feng L, Yuan S, Li J-L, Wang K-Y, Day GS, Zhang P, Wang Y, Zhou H-C (2018) Uncovering two principles of multivariate hierarchical metal-organic framework synthesis via retrosynthetic design. *ACS Cent Sci* 4(12):1719–1726
106. Wang K-Y, Feng L, Yan T-H, Qin J-S, Li C-X, Zhou H-C (2021) Morphology transcription in hierarchical MOF-on-MOF architectures. *ACS Mater Lett* 3(6):738–743

Chapter 8

The Promise and Reality of Sustainable Fuels



Robert Luckett and Jingbo Louise Liu

Abstract Challenges of world's energy supply and fuels consumption are highly dependent on the use of fossil fuels, coal, petroleum, and natural gases. The depletion of these resources is a major challenge as it leads to an increase in prices and a decrease in the availability of energy. Therefore, renewable energy sources, particularly sustainable fuels become critically demanding. Renewable sources of energy and fuels are abundant and do not emit greenhouse gases or contribute to climate change. The promotion of efficient energy use techniques promises to reduce energy consumption, thereby conserving fuel supplies. The diversity of sustainable fuel supplies is another driving force for the stakeholders to explore in this direction to fostering development and commercialization. The exploration and production of more diverse energy sources like natural gas, nuclear power, and biofuels help to sustain a diverse and secure energy supply. This chapter summarized the background of energy development, different families of fuel supplies, Geopolitical instability and grand challenges of sustainable aviation fuels.

Keywords Sustainable fuels · Diversity of fuel supply · Aviation fuels · Fuel consumption

8.1 Overview

Research has demonstrated that in the quest for zero emissions, there is no such thing as zero exploitation. However, many studies indicate that there are applications of green technology that will benefit not only the environment, but also stakeholders, who range from investors, to unskilled laborers. This is especially welcome news given the current pace of global warming, and the fast-approaching climate crisis.

R. Luckett (✉) · J. L. Liu
Texas A&M University-Kingsville, 700 University Blvd., MSC 123, Kingsville, TX 78363, US
e-mail: Robert.Luckett@tamuk.edu

J. L. Liu
Texas A&M Energy Institute, 1617 Research Pkwy, College Station, TX 77845, US

The chance to get it right this time was a missed opportunity 100 years ago when the American automobile industry established oil as the most reliable fuel source. In addition to failing to predict pollution, was a lack of true understanding of oil as a finite resource. To be fair, science at that time had little to offer in informing us of potential environmental damage from gasoline that could be permanent.

Now science can give us a solution to the climate crisis, and improve so many other problems at the same time, such as environmental damage, low employment, and complications of use of plants deemed unsuitable for consumption, or grown in quantities to meet both agricultural and energy needs. Different economies have different energy needs, and different cultures have different approaches to labor. Unfair working conditions in the U.S. are not the same as unfair working conditions in developing countries. Oil drilling in the U.S. is exploitative to the environment and to labor, but not to the same extent as oil drilling in the Middle East. Challenges to getting it right this time include being sure we obtain the most efficient feedstock, and refine and deliver it, in a clean way, so as not to offset gains expected to be achieved from a boom in green energy, as opposed to fossil fuels. There may not be another chance for a trifecta of cleaning the environment, creating jobs, and putting low demand plant life to work for providing long-term growth of energy for the billions of residents of the planet. Those with power, whether political or financial, are the lynchpin that gets it all started, if it ever is to take off.

Promises of clean energy solving all of society's ills have been made before. New advances in technology seem to be very close to delivering clean fuel, but we are still enduring old problems with outdated fuel sources, such as school children breathing air polluted by nearby coal mines. Sadly and predictably, levels deemed acceptable vary by location, with lower SES nations exposed to the most harmful levels, sometimes in violation of their own regulations [1]. Even prospects of using plants as feedstock for energy has unforeseen risks, from inedible plants harvested to the point of threatening green landscapes, to the potential of people losing food crops to biofuel refineries. People of Ghana endured more limits to access to land for growing their own food, as profiteers negotiated land deals with local leaders. On balance, there was general appreciation of biomass farming, because it brought jobs, and economic and food security [2]. Some have concerns that the promise of the benefits of biofuels are unrealistic. Considering that shifting from under-subsidized food production to support for biofuel from food crops risks displacing farmers, land encroachment, land exploitation in the form of farmers having their property taken by industry, to deforestation, and damage to soil. The need for 70–100% more food by 2050, by 2011 estimates, compounds the problem even further [3]. It might be helpful to review what has been attempted, and assess the best options for green energy, keeping in mind that not all solutions are viable for every population. As it is unlikely that one biofuel will be appropriate for all economies, it will be necessary to meet the challenges of integrating several biofuels to suit international needs.

While biofuel use has been indicated to be advantageous to most people, researchers in Brazil believe that there should be limits to participation in the biofuels industry, citing risks to rain forests, food agriculture, and social impact on working conditions. This should be taken into consideration along with respect to advantages

gained in air quality, global climate improvement, and economic advantages such as reaching the goal of energy independence [4]. This consideration comes after years of Brazil's establishment as a very successful ethanol producer and exporter as a solution to oil prices in the 1970s [5].

Perhaps the critical complications with the least margin for error exist in the quest for Sustainable Aviation Fuel (SAF), because air travel presents challenges that stationary users do not encounter. Even electric and hybrid cars can break down or run out of fuel, which is frustrating for drivers, but disastrous for fliers. While SAF is the focus of this chapter, it is worth reviewing related advancements in green energy, since a final application for SAF has not yet been made. On September 15, 22, and 29, 2022, the American Chemical Society (ACS) hosted a three-session event to promote SAF research and development, communication and analysis, deployment. The policy and sustainability and the commercial flight also play critical roles in the international SAF activities. The ACS-SAF event started with an overview of the SAF given by Dr. Valerie Sarisky-Reed, the director of the Bioenergy Technologies Office (BETO) in the Office of Energy Efficiency and Renewable Energy (EERE). Dr. Reed pointed out that "Biden Administration put the American economy on an irreversible pattern of net zero emissions" no later than 2050 as soon as taking to the office. The near-term target aims to reduce CO₂ emissions by over 50% as soon as 2030, compared to 2005 because energy is the heart of greenhouse gas emissions without affecting competitiveness. The DOE has been the leading agency to develop strategies to avoid carbon being released into the atmosphere while still providing the goods and services our country needs to function. Dr. Reed offered a few examples of creating new innovative building technologies across the continuum from production, storage, and transportation to utilization. The administration examined the US and "Renew Europe" standards to see how better the DOE can manage the conversion of waste feedstock to SAF and value-added molecules. The Aviation industry advocated SAF production from "wood and agricultural products, solid waste, landfill gas and biogas, and alcohol fuels." to lower CO₂ and meet current Jet Fuel A specifications. The SAF production, storage, mass balance and global distribution were shown in the Fig. 8.1.

According to the United Nations (UN), 24 million new green jobs could be created internationally, given enough support from stakeholders [6] but given past estimates of progress on green fuels, it is appropriate to maintain a healthy skepticism about its future, if it is not managed ethically, and responsibly. The goal to reach the 50% mark for all jet fuel is 2030, at 3 billion gallons per year, and one option is Fats, Oils, and Greases (FOG). By 2050, the goal is 100%, which is expected to be 35 billion gallons per year, accounting for growth [7]. Tax incentives might prompt industry where ethics have not, thus the Biden administration's encouragement of the use of SAF blending to reduce Greenhouse Gas (GHG) by incentivizing industry through tax credits. Known as the Inflation Reduction Act (2022), it includes the human element of raising tax credits when private industry locates their efforts in lower Socioeconomic Status (SES) areas, pays employees a living wage, and creates apprenticeships [8]. Green energy jobs from the Inflation Reduction Act estimate the need for over 200,000 jobs by 2030, with credentials ranging from high school

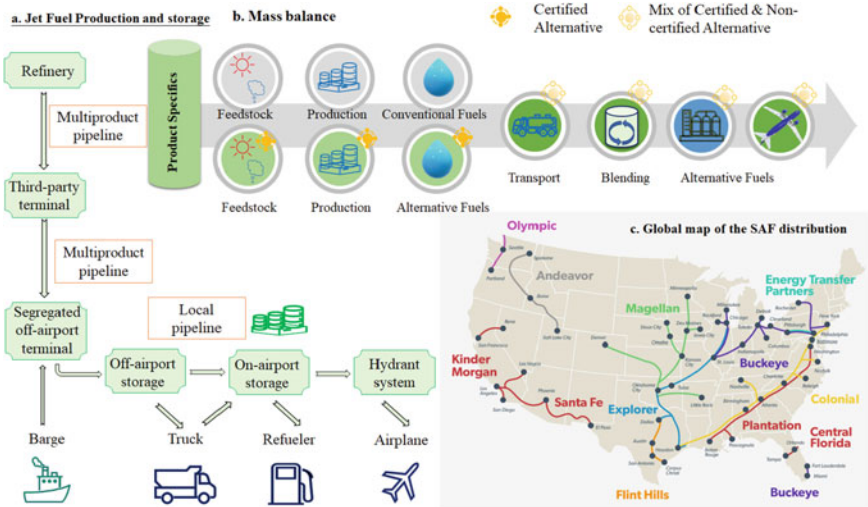


Fig. 8.1 Sustainable aviation fuels, a production and storage, b the mass balance and c map of SAF distribution

(or equivalent) to bachelor’s degree. The lowest pay is estimated at over \$47,000 per year. Not all of these jobs directly relate to jet fuel, but it would be difficult to claim that any are without connection at all, given the focus on use of electricity, often powered by refineries currently using fossil fuels. Thus, future refineries powered by wind, solar, and hydro, for example, could support refinement of blended and fully SAF in the future. This would be making use of renewable resources [8] to mitigate the GHG emission, which will take the effort from different sectors (Fig. 8.2).

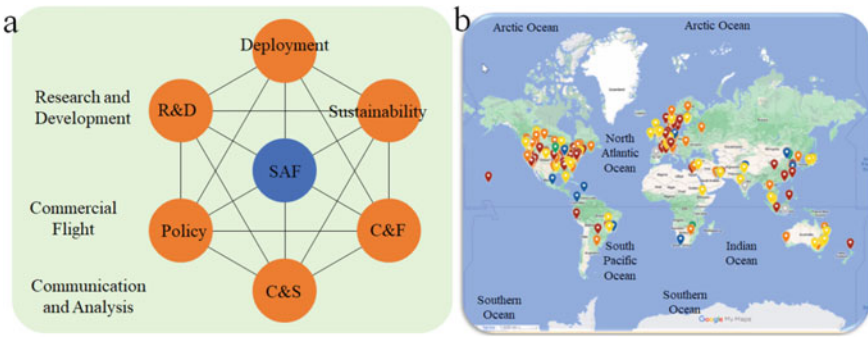


Fig. 8.2 Sustainable aviation fuels also defined as waste-derived aviation fuels, which involved in efforts from six sectors, a Coordination of plans in research, development, demonstration, and deployment through collaborations between different stakeholders and b The facility map, adapted from International Civil Aviation Organization (ICAO)

Since global warming is expensive to combat, solutions are necessary that meet current prices, or ideally are cheaper. Using carbon emissions trading is not a long-term solution, and at best moves the problem around the globe [9] which eventually spreads pollution farther. Carbon credits may be cost effective for big business in the U.S., but it only reduces environmental damage minimally, at best, arguably simply kicking the can down the road, which could be the most impactful procrastination of all, if it irreparably damages the planet.

Regarding industry's incremental advances, and the aviation industry's carbon footprint, reducing CO₂ emissions and other progress being accomplished by blending current fuels with new fuels, can also be a cost benefit to industry, and bring savings to end users [10]. Reduced use of fossilized fuels benefits industry by experimenting with manufacturing processes currently in use that offer flexibility leading to adaptation of established techniques, rather than those invented anew [11], and the process of phasing in new fuels gradually is already underway.

Distribution of biofuels is an important consideration regarding infrastructure's role in the transition away from fossil fuels, and into biofuels. Since specific equipment is needed to transport biofuels, investment could bring more jobs in designing and maintaining such equipment [12], but would this benefit people as well as industry? Drop-in biofuels, designed to be used with existing infrastructure, such as pipelines, and shipping containers used by trucks, trains, and ships [13], could be a preferable strategy, as opposed to all new equipment that may require significant changes, even to the point of creating new vehicles, especially if not suitable for use on interstate highways, train tracks, and ships requiring redesigns that might eliminate use of certain ports. The benefits of global interconnectedness in transitioning away from fossil fuels creates additional complications that must be addressed. Distribution planning in manufacturing SAF is an important step, but so is coordination of flight routes at the international level. To be most safe and efficient, jets that must be refueled using SAF must have as many airport stops available as currently exist for fossil fuels, and must also plan for anticipated growth. The Port of Seattle has been active in supporting SAF by leading in planning of flight routes and creation of infrastructure required of biofuels that differ from fossil fuel methods [14].

Policies to support all aspects of SAF, including technology and business applications in the aviation industry that is growing both in demand and committed to avoiding environmental damage, could bring interference from capitalist interests between global markets competing to control the technology, if stakeholders fail to work together to create workable policies to support the global effort, as identified by a study in the U.K. [15]. In 2022, research was conducted to explore the reason for the slow growth, given the rate of climate damage predicted by 2050, claiming that nothing short of total abandonment of fossil jet fuels would ultimately be effective. The authors cite the Paris Agreement is an example of essential collaboration among global stakeholders that is critical to the success of buy-in from government and industry, especially considering the improvement to the climate that SAF could bring [16]. These declarations, leading to the deadlines, prompt evaluation of what industry has discovered thus far, in the quest for SAF.

Since it is still undecided which new fuel will suit jet fuel applications, it might be helpful to review related advances in biofuel development, i.e., what has worked, and what has not. For example, research so far has discouraged use of kerosene as a sustainable source of CO₂ capture [17], which is important to note as all fossil fuels are targeted for elimination. Availability of feedstock must be addressed if renewable sources are to replace finite energy derived from fossil fuels, thus the relatively short-term phasing in of decarbonation by 2030, meant to be a benchmark for further planning to assess how to prepare for the 2050 deadline. Some areas of the world already impacted by decreases in fossil fuel production could benefit from upgrades to existing refineries to instead transition to promising renewables such as algae, potentially reducing GHG in the 68% range by one study's estimate [18], and 98% using a chemical process in another [19]. Conversion of existing refineries, specifically biorefineries, along with efficient management practices, is essential to the success of SAF [20]. In 2019, a study on the viability of biofuels predicted success if government funding continues, as costs associated with upgrading refineries are high, and if fossil fuels remain relatively low. Jet fuel being a more challenging undertaking, success in biofuels for other uses offer hope [21].

It is unclear what industry may learn from energy advances in personal transportation, as jet fuel is believed to be essential, with demand only growing during the entire phasing in period leading to 2050. Airplanes are not automobiles. Aviation adds complications of temperature limitations on fuel in flight that ground transport does not experience, which, for airplanes, has meant blending fossil fuel with options such as cooking oil waste, gradually increasing biomass and decreasing the fossil content. Current experiments are limited by undeveloped infrastructure needed to support the fuel blending process. Delays in making biofuels available bring reminders of early automobile limitations such as lack of refueling stations, as airlines must carefully plan their stops where blended fuels are available [22]. Coordination of upgrading airport infrastructure, with the added challenge of efficient placement of locations where SAF is available on different continents, is far more complicated than adding electric car recharging stations to convenience stores around the U.S. Further commitment to SAF would require a shift by the commercial airline industry, which is now less focused on sustainable fuels for environmental benefits, and more on cheaper fuel, with some studies estimating biomass fuels not reaching a cost benefit per liter until 2035 [23]. Where there is adequate support and resources, success has been achieved. New Zealand pioneered tests of a jet fuel blend that was half jet fuel, and half *Jatropha* plant, running a commercial aircraft successfully for two hours [24]. In the United Arab Emirates (UAE), Seawater Energy and Agricultural Systems (SEAS) sustainably grows seafood, and yields a biomass byproduct that can be processed as a fuel that contributes to SAF and green diesel. Tested on a commercial flight in 2019, it appeared to be efficient enough to be cost effective by 2020 [25].

In the early 2000s, solutions to environmental concerns were being explored somewhat in the U.S., motivated by combined concerns of pollution, energy independence and availability of fuels. Science and government began a collaboration on biomass options, with an eye on cost effectiveness, job creation, and inclusion of business interests [21]. This effort now extends far beyond the U.S. A 2002 article covered

two decades of efforts by Sweden to address biofuel introduction to their economy, calling on flexibility of stakeholders, especially those willing to go beyond limiting themselves to raw material production [26]. In the U.K. in 2014, the government required a decrease in the use of unsustainable biofuels in favor of biofuels designed to reduce harm to the environment, and address disputes over use of land for development of biofuel feedstock. Liquid fuels became a focus as biofuel technology was to be developed, and growth of that technology was to spur investment from other countries to help further establish the U.K. as an industrial and technological leader [27]. A study in 2009 outlined the risks associated with competition by industry's attempt to triumph in profiting from addressing global warming. Absence of international agreement and legal complications of international collaboration tends to motivate irresponsible practices, such as exploitation of workers, and access to water and food, as these resources are overtaken by economic interests at the expense of society [28].

Developing nations are also participating in green energy growth. Brazil, as the most prolific global producer of soybeans, has concentrated their efforts, and mostly for export, but deforestation has impacted hopeful results thus far. Still, plans to create a vertical supply chain could improve success of soybean production there [29]. Like Brazil, Indonesia has suffered political upheaval, leaving behind unemployment, high energy prices, and poverty, motivating them to develop energy technologies with the goal of addressing all of these social ills at once [30]. Industrial growth in Indonesia has led them to a significant increase in oil imports since 2004. In 2006, Indonesia increased palm oil biodiesel production to offset dependence on oil imports. By 2030, their goal is to save over \$4 billion in energy costs, and create over 10,000 new jobs [31]. Indonesia also has begun to address negative environmental complications associated with their use of palm oil, and dependence on it for export. This is a case of starting with fossil fuel replacement, then improving the quality of biomass options [32].

For developing nations with plenty of land to offer, challenges remain even if they possess natural crops that can be used for feedstock. Caution has been advised regarding microalgae that are genetically engineered for biofuels, because their ability to survive if left unchecked has not been established, which could create an environmental problem [33]. Energy is used in land preparation, such as clearing by use of heavy machinery. Some crop production pollutes air at levels that can exceed forest fires in Brazilian rain forests. At the time of this study, land preparation was responsible for the most GHG emissions in all of Indonesia. Neighboring Thailand, Malaysia, and Singapore complain that their air quality is affected. Indonesia's economy benefits too much from palm oil to phase it out completely, and losing the vast U.S. palm oil consumption market is a significant threat to their economy [32]. Recent concerns in the west regarding exploitative labor practices have had an impact on palm oil production in Kuala Lumpur, but a two-year import ban by U.S. Customs was recently lifted [34].

Success in producing biofuels has exceeded predictions around the world, so further investment in different feedstocks is justified, as it has the potential to improve quality of life, and not just for the wealthy. There are methods available to reduce

these heavily polluting methods, and unfair labor practices, but who will commit to this expense? There are limits to how green energy can be, especially depending on the application. To meet energy needs on the ground, options such as wind and solar can be factored in, but any type of jet fuel must be contained and flown, limiting solar and wind to benefit aviation only to processing fuel on the ground. Another reason palm oil as jet fuel does not appear to be competitive is because a glut in palm oil created by aviation's thirsty needs could drive the price down further, which could be a serious economic issue for farm owners. Without an appropriate and effective domestic use for palm oil rich countries, economists argue that increased dependence on palm oil is not a good investment [32].

A study in Thailand considered both social and economic factors related to biofuels production compared to petroleum production, finding that 10–20 times the number of workers can be employed in the creation of green energy, and even when labor costs were factored in, green energy was the cheaper option [35]. The European Union (E.U.) found similar results in 2018 [36].

Sub-Saharan Africa is the center of a significant struggle to afford fossil fuels, and as is the case all over the world, demand for energy there is increasing. Mozambique decided to make use of its ample land supply to address poverty, with some attention to gender and employment [37], but could still be targeted by capitalists interests in controlling land to grow biofuels where labor is cheap. While some of the most impoverished Sub-Saharan African countries do produce oil, even those local economies cannot balance demand for fuel, poverty, and diesel's cost, so wood remains the only affordable energy source there. Economies looking ahead to 2030 predict likely growth potential for green energy alternatives, but note that it would take collaboration from many countries to make production of biofuels viable, requiring reductions in taxes and other subsidies [38].

A study in Botswana claimed that most plant life available for biofuel production damages their environment at a level similar to that of invasive species [39]. Malawi studied poverty and their very common use of wood for energy, estimating that biofuels could overtake wood consumption, and continue to push fossil fuels out of the market, given their poverty, eliminating fossil fuels is an option, while also providing jobs in the production of biofuels [40]. Increased output of sugarcane on Brazilian plantations could improve their economy, but the requirement to expand irrigation for the crop could be an environmental problem in close proximity to rain forests [41]. Politics and limited technology hinder access to vast quantities of wood that could become biofuel in West African countries [42]. The forestry profession in China and India considered extracting feedstock from their forests, but found limitations due to lack of technology and lack of supportive policies [43]. The needs of some poor nations are more urgent than others. For example, biofuel production in the wake of war-torn and significantly impoverished Sierra Leon is projected to be an economic solution that can also serve pro poor development [44].

For wealthier nations, the more common obstacle to SAF is encouraging investment, and securing funding streams, despite indications that energy, environment, labor, and business could all benefit. Australia explored how to effectively wean themselves from fossil fuels in their quest for energy independence. A study concluded

that negative impact is offset by benefits to employment and the economy. Employment benefits would include more jobs for skilled labor, leading many to relocate domestically. If this step succeeds, the need for further economic development would follow, including improvements in infrastructure, creating even more jobs. A favorable Energy Return on Investment (EROI) is indicated, which is necessary to attract investors, and to justify government spending. Transportation of feedstock can be a financial issue in rural Australia, but these needs could be met by building new refineries, and locating them strategically, thus simultaneously potentially leading to a short-term boom in construction, and a long-term boost to local employment [45].

Efforts in Sweden to make the best use of biofuel resulted in careful planning in production by resisting limiting themselves to raw material production, and producers making use of the biofuels they produce for their own needs, in addition to marketing them [26]. A study in 2010 found that biofuel depends on supportive policies, a knowledge base on refineries, and government funding [46]. For example, although corn stover is the most abundant feedstock in the U.S., evaluation of its potential has yet to be completed. Support for this initiative has been expressed by Illinois, Indiana, Iowa, Minnesota, Nebraska and South Dakota [47]. Support for industry also tends to be clouded by perceptions of governmental and employment interests outweighing environmental impact [48], and it is difficult to determine the long-term effects of changing crops since ethanol from corn does not appear to be the most viable feedstock, and exploitation in land sales is a risk to struggling farm families. A 2017 study took into account what is needed to reach the 2030 goal for green energy, and indicated that over one million jobs could come from it, and profits would be significant [49]. A study in Poland found that refining biogas waste could significantly reduce carbon emissions, and called for government funding [50].

Developed nations have been experimenting with waste produced from their higher standard of living. A 2020 study in Spain argued that waste could be used from existing industry to create biofuels, such as from beer, dairy, bricks, and lime. The study claims that between 2018 and 2050, Small- and Medium-Sized Enterprises (SMEs) show promise using brick and lime waste. Beer and dairy show even more promise, and solid biofuels (SBFs) were predicted to create significant green jobs for all industrial waste tested [51]. Cheese whey, one of many feedstocks, is particularly useful in green energy because it is abundant in developed nations, yet currently disposed of in a manner that is environmentally harmful. Currently used in animal feed and food additives, it shows potential for use in biomass fuel [52].

Before the Biden administration's time, industry's attempts to dominate global energy were well underway. Kansas, Missouri, Oklahoma, and Texas all were exploring job creation possibilities in a 2015 study [53]. The Biden administration's continued support led to the discovery of indigenous crops that could benefit the farm industry in the U.S. A renewable option in development for SAF fuel is a bioenergy crop known as *carinata*, which is available in the southern U.S. This could invigorate production and economic opportunity for farmers in Georgia struggling with dependence on cotton and peanuts, as *carinata* could rotate in as an annual crop. Fixing the agreed contract price to reduce risk to growers could prompt commitment of 28–85% of farms there [54]. This support could come from government entities

seeking improvement of carbon footprint, production costs, profits, and job creation [55]. Given the estimate that carinata could reduce aviation's carbon footprint by up to 65% in the U.S. Alone, government support is of particular importance, up to and including the creation of reliable supply chains [56] if this high yield, low fertilizer crop is to be fully successful as an affordable and environmentally advantageous SAF and contributor to the farming industry [57].

Common crops could serve to ease complications of SAF availability for intercontinental flights. A 2016 study on feasibility of cellulosic biofuel production in Iowa, Georgia, and Mississippi, found that it could boost employment in the construction of new biorefineries alone, and that full biomass production would create more jobs than fuels blended with diesel. Once construction jobs conclude, employment would endure in agriculture, trade, and biorefinery operation [58]. The U.S. south could learn from Iran's experience with Okra, a plant common to both countries. Okra, an annual crop that is plentiful in Iran, was explored for use in biofuel production to address employment and increasing their technical job sector [59].

Many developing nations that are experimenting with biofuels are taking cues from developed nations. An article from Spain covering 2007–2013 discussed running a biodiesel plant, increasing employment, and raising their GDP nearly 10% [60]. A 2019 study in Uruguay predicted successful green job production, attributing the nation's satisfaction to taxes resulting from green energy, and contribution to energy security. Availability of sugarcane and sorghum were sources of their biodiesel production. This process was found to be more costly than the production of fossil fuel, but benefits to the economy more than balanced the equation in the end. There remain concerns about global market fluctuations that may impact that balance in the future, but job creation and climate improvement are assured [61].

Different countries have different indigenous plant life, and some of these could be on the cusp of becoming a more valuable resource than ever. Castor bean is a crop in plentiful supply in Mexico that shows potential as a biofuel source, as it is resilient, and resistant to pests. Mexico's biorefineries use less than 11% of turbine production, and produce 300 times what Mexican airports require, but the per gallon price for this biofuel is far from competitive at this time [62], a result shared by another lignocellulosic biomass study [63]. This is not necessarily completely unfortunate, as blended and other fuel options began as cost prohibitive, and became profitable as markets changed around the world.

Ironically, development of green applications can also create environmental problems themselves. For example, plant life making its way around the globe by SAF to generate more SAF could contain invasive species that could lead to biological invasion [64]. This could be a consequence of global trade that could create further tensions if not addressed appropriately. More support from different interests is an opportunity that can be gained by addressing numerous social needs along with energy needs.

There are more impoverished than wealthy nations, and profiteers are focused on them as green energy increases in viability, both commercially, and in addressing individual national interests. Thus, advantages from participation in biomass production by developing nations could be wiped out by international investors. A 2018 study

investigated legitimacy of energy policies in Latin American countries, critiquing whether there is true commitment to addressing global warming, or if instead mere appeasement is being offered by using fossil fuels to serve people. The interests of politics and business could determine whether social and societal impact are factored into addressing global warming. Brazil's president in 2007 declared that advances in fuel should be an energy revolution, with specific attention to social justice, protecting food crops, and jobs in the plan. The biofuel industry was to advance their economy, and benefit their people. Brazil had been exploited by policies made by past leaders with North American politicians at the expense of their people, by failing to fulfill promises of employment growth, and other social inequities. Wealth redistribution was promised, and progressivism was to reject use of family farms for foreign profit, in favor of becoming a vital link in their national economy that would prioritize their own people's needs instead. Issues related to Brazil's acceptance of the need to accomplish sustainable energy access, while simultaneously addressing complications of alleviating poverty, and improving the environment, resemble interests in other countries [65].

A common thread in all of these formulas is the need for capital that businesses are unwilling to shoulder on their own, and they seem to be waiting for government investment before committing their own capital. Few airline passengers are willing to pay extra for SAF. While attitude, social trust, and perceived risks have an effect, resistance remains. Campaigns by big business are underway to build awareness and acceptance of the importance of SAF [66], but they are unlikely to convince travelers that they should be the ones paying for improvements only to see profiteers become even richer. Most strategies around the world call for both taxes and private investment, but there is a higher likelihood in lower SES countries that profits, no matter how substantial, will not be used to alleviate poverty. Full energy independence is not considered realistic by economists, and dependence on only one crop carries risks that could devalue such a crop, along with the risk that one crop could suffer yield and other problems that could lead to a crisis, impacting trade with other countries. Regardless of the nature of a government's relationship with its people, no government can reliably address social needs of the general population without some control over individual private enterprises, such as family farms, i.e., the government should control what crops are grown to benefit the overall economy, and the individual [65].

8.2 Diversity of Fuel Supplies

The fuels are divided into two families, natural fuels and artificial (or prepared) fuels based on their occurrence. These fuels occur naturally in nature are considered primary fuels, whereas artificial fuels are defined as secondary fuels. The secondary fuels can be prepared by different processes by treating these primary fuels. Based on the DOE standard, the fuel supplies include biodiesel, electricity, ethanol, hydrogen, natural gases, renewable diesel, sustainable aviation fuel and emerging fuels. The

sustainable fuels can be broadly classified into three categories, biofuels, synthetic fuels and renewable electricity according to the origin and production process. Biofuels are normally derived from organic matters, which include these substances from the plants (for example algae) and animal waste (manure). These biofuels include ethanol, biodiesel, biogas, and other biofuels. They can be produced through fermentation, distillation, or other chemical processes (such as esterification). The SAF is one of the biofuels, which will be discussed in Sect. 8.3 (**Sustainable Aviation Fuels**). Synthetic fuels can be produced by synthesizing carbon dioxide (CO_2) and hydrogen (H_2) or carbon monoxide (CO) from renewable sources. They include synthetic gasoline, diesel and jet fuel as well as hydrogen and methane produced from renewable sources. Renewable electricity includes electricity generated from renewable sources such as wind, solar, geothermal and hydropower. It can be used to power electric vehicles, heat pumps and other electrical appliances. In the Table 8.1, the authors summarized the characteristics of selected fuels with an emphasis on renewable fuels.

8.3 Sustainable Aviation Fuels

As mentioned above, the ACS hosted a SAF discussion in September of 2022, starting with an overview of the ACS mission to support not only research and development, but also deployment and career training, given by Dr. Judith Gordian, the ACS president. She led a core group of professionals from different technical divisions of ACS (Fig. 8.3) in organizing the pre-president event series to provide solutions to climate change and explore new approaches to be independent of fossil fuels. Dr. Giordan is the co-founder of the Chemical Angels Network, Managing Director of ecosVC, Inc., and former Fortune 100 executive. Judy is a board member, co-founder, advisor, and investor in seed and early-stage start-ups and the 2023 ACS President. Dr. Jinxia Fu is an Assistant Researcher at Hawaii Natural Energy Institute, University of Hawaii at Manoa, Honolulu, Hawaii. She researched biomass resources, processing of biomass materials, thermochemical conversion of biomass, fuel characterization, and biofuel product development. Jinxia holds a Ph.D. degree in Chemistry from Brown University. Ms. Lisa Houston is Vice President at PAC, LP, an analytical instrumentation company, where she is responsible for the financial success of the Process Analytics instrumentation segment. Lisa is an experienced analytical and petroleum chemistry professional with over 30 years of increasing responsibility in business management, directing scientific personnel, product management, and project management. She received her bachelor's degree in biochemistry from the University of North Texas in 1986. Lisa has been an active American Chemical Society (ACS) volunteer at all levels including Local Section, Division, Regional Meeting and National since becoming a member in 1990. In 2013, she was named an ACS Fellow for her contributions to the profession and to ACS. She is currently serving on the ACS Board of Directors representing District IV. Dr. Matthew L Grandbois is a Strategic Partnership Manager for DuPont where he leads business development efforts focused on

Table 8.1 Summary of different fuels and their characteristics (data were collected from <https://afdc.energy.gov/fuels/properties>)

| Fuels | Gasoline/E10 | Biodiesel | Electricity | Ethanol/E100 | Hydrogen | Natural gas |
|---|---|---|--|--|---|---|
| Chemical structure | C ₈ H ₁₈ (C ₄ –C ₁₂) | Methyl esters of C ₁₂ to C ₂₂ fatty acids | N/A | CH ₃ CH ₂ OH | H ₂ | CH ₄ (75%), C ₂ H ₆ , C ₃ H ₈ , C ₄ H ₁₀ |
| Fuel material (feedstocks) | Crude oil | Fats and oils from soybeans, waste cooking oil, animal fats, and rapeseed | Natural gas, coal, nuclear, wind, hydro, solar, and small percentages of geothermal and biomass | Corn, grains, or agricultural waste (cellulose) | Natural gas reform, methanol, H ₂ O electrolysis | Underground reserves and renewable biogas |
| Gasoline or diesel gallon equivalent (GGE or DGE) | 1 gal = 1.00 GGE 1 gal = 0.80 DGE | B100 1 gal = 1.05 GGE 1 gal = 0.93 DGE | 1 kWh = 0.030 GGE 1 kWh = 0.027 DGE | 1 gal = 0.67 GGE 1 gal = 0.59 DGE | 1 kg = 1 GGE 1 kg = 0.9 DGE | 1 lb. = 0.18 GGE 1 lb. = 0.16 DGE |
| Energy comparison | 1 gallon of gasoline has 97 to 100% of energy in 1 GGE* | 1 gallon of B100 has 93% of the energy in 1 DGE | A typical battery with the same size as a gallon of gas (0.134 ft ³), for transportation, can store 15.3% of the energy in 1 GGE | 1 gallon of E85: 73–83% of the energy in 1 GGE 1 gallon of E100: 67% of the energy in 1 GGE | 1 kg of H ₂ : the same energy as 1 GGE | 5.66 lb. of CNG: the same energy as 1 GGE 6.37 lb. of CNG: the same energy as 1 DGE |
| Energy content (lower heating value) | 12,114 to 116,090 Btu gal ⁻¹ | 126,700 Btu gal ⁻¹ for B100 | 3,414 Btu kWh ⁻¹ | 76,330 Btu gal ⁻¹ for E100 | 51,585 Btu lb ⁻¹ (33.3 kWh kg ⁻¹) | 20,160 Btu lb ⁻¹ |
| Energy Content (higher heating value) | 120,388–124,340 Btu gal ⁻¹ | 127,960 Btu gal ⁻¹ for B100 | 3,414 Btu kWh ⁻¹ | 84,530 Btu gal ⁻¹ for E100 | 61,013 Btu lb ⁻¹ | 22,453 Btu lb ⁻¹ |
| Physical state | Liquid | Liquid | N/A | Liquid | Compressed gas or liquid | Compressed gas |

(continued)

Table 8.1 (continued)

| Fuels | Gasoline/E10 | Biodiesel | Electricity | Ethanol/E100 | Hydrogen | Natural gas |
|--------------------------|--------------|--|-------------|------------------------------------|--|---|
| Pump octane number | 84–93 | 48–65 | N/A | 110 | 130+ | 120+ |
| Flash point | – 45°F | 212–338°F | N/A | 55°F | N/A | – 300°F |
| Autoignition temperature | 495°F | ~ 300°F | N/A | 793°F | 1,050 to 1,080°F | 1004°F |
| Maintenance Issues | | Lubricity is improved over that of conventional low sulfur diesel fuel | N/A | Special lubricants may be required | High-pressure tanks require periodic inspection and certification H ₂ requires minimal maintenance when used in fuel cells | High-pressure tanks require periodic inspection and certification |

* Standard fuel: 90% gasoline, 10% ethanol

the automotive electronics and telecommunications industries. Prior to this role, Matt held positions within R&D and Marketing for Dow Chemical. He received his Ph.D. in Chemistry from the University of Minnesota and his B.A. in Chemistry (ACS Approved) from Augustana College (Sioux Falls, SD). Matt is a long-time member and active volunteer leader within the American Chemical Society at every level of governance. He is currently the Chair of the Central Massachusetts Local Section (CMSACS), General Co-Chair of the 2023 Northeast Regional Meeting (NERM), Councilor for the ACS Division of Professional Relations (PROF), Programming Chair for the ACS Division of Business Development and Management (BMGT), and elected Member of the ACS Committee on Council Policy (CPC). Matt is a Six Sigma Black Belt, former Fulbright Scholar to Norway, author of 10 peer-reviewed publications, holds 14 granted U.S. patents, and has been a featured ACS Webinar presenter on topics related to the professional development of scientists. Jennifer Maclachlan is the co-owner and Managing Director of PID Analyzers, LLC, founder and organizer of the Cape Cod Science Cafe and STEM Journey. Jennifer is the co-Chair of the American Chemical Society's (ACS) Committee on Chemical Safety's (CCS) Partnership Subcommittee and the 2022 recipient of the ACS Grady-Stack Award for Interpreting Chemistry to the Public. Dr. James Skinner is the Chairman of the Board of three companies—one public, two private. He is the member of the Board of Directors of several public and private firms including Chairman of the Compensation and Stock Option Committee and Member of the Finance Committee. He is responsible for or involved with raising more than \$200 million in public and private transactions. Dr. Jarrod Cohen is a Scientist II at Secant Group in the Translational Product Development Group. His current work focuses on building sustained long-acting implantable platforms for the delivery of small molecules in multipurpose prevention technologies and ocular therapies. He has been responsible for Analytical method development for all drug delivery applications as well as the formulation and characterization of implant devices. Dr. J. Louise Liu is a Full Professor of Chemistry and the Director of the Center for Teaching Effectiveness at Texas A&M University-Kingsville. She is affiliated with the Texas A&M Energy Institute due to her contributions to the field of engineered nanomaterials in alternative energy. Dr. Liu has co-authored patents, books, book chapters, and peer-reviewed journal articles (>150). Currently, she serves as the elected Councilor of Energy and Fuels technical division, certified Career Consultant, and DEIR Experts Panel, American Chemical Society (ACS).

The keynote speaker, Dr. Valerie Sarisky-Reed, has been the director of the Bioenergy Technologies Office (BETO) in the Office of Energy Efficiency and Renewable Energy (EERE). She manages efforts to improve performance, lower costs, accelerate market entry of bioenergy technologies, and oversees strategic planning and development budget (annual: \$250 M). Dr. Reed summarized what the administrators are trying to do and what the DOE supports. She pointed out that Biden Administration put the American economy on an irreversible pattern of net zero emissions no later than 2050 as soon as taking to the office. The near-term target has been created to reduce CO₂ emissions by over 50% as soon as 2030, compared to 2005



Fig. 8.3 The organizing team was fostering sustainable aviation fuels to reduce greenhouse gas emissions

because energy is the heart of greenhouse gas emissions without affecting competitiveness. The DOE has been the leading agency to develop strategies to avoid carbon being released into the atmosphere while still providing the goods and services our country needs to function. Dr. Reed offered a few examples of creating new innovative building technologies across the continuum from production, storage, and transportation to utilization. The administration examined the US and “Renew Europe” standards to see how better the DOE can manage the conversion of waste feedstock to SAF and value-added molecules. The Aviation industry advocated SAF production from “wood and agricultural products, solid waste, landfill gas and biogas, and alcohol fuels” to lower CO₂ and meet current Jet Fuel A specifications.

Dr. Reed has decades of experience working with these feedstocks to convert them into final fuels. Due to the higher production costs, incentives are needed for SAFs, including promoting emerging industries. These are necessary to reduce prices and manage risk in the emerging industry. The DOE can leverage its expertise in scale-up and infrastructure build-up to test and evaluate catalyst development and synergy between carbon utilization and processes to generate liquid fuels, including SAFs, to lower the overall cost by using diverse sources such as bio-crude, solid wastes, fats, greases using gasification, syngas to hydrocarbons. She also shared that the political will in Washington, DC led to the passage of the inflation reduction act with incentive programs and packages to help support the production of SAF and renewable diesel to meet many markets, which will be critical in the next 5–10 years. Beyond near-term options, Dr. Reed mentioned that we would need 300 million metric tons (MMT) of renewable carbon if we can meet aviation’s needs, the chemical sector, and other places where biomass is an important commodity. The DOE is working hard to support technology development for the next generation. By increasing the number of feedstock and pathways to produce SAF, we will ultimately be able to reduce the cost of the fuels. Due to the regional nature of the feedstocks, people all over the

country can benefit from this emerging industry since the conversion processes would be decentralized. These feedstocks in a different region may be slightly different. We will have the technology to meet those needs and help to produce the fuels where they can be utilized.

The Sustainable Aviation Fuel Grand Challenge will be announced in September 2022. This grant challenge gives us a series of goals as we move toward government and industry partnerships. The grand challenge looks at 3 billion gallons by 2030, which will be about a 20% reduction in greenhouse gas in the aviation sector (current production is 5–7 million gallons). By getting there, we need to show that this industry is possible and will lead us to the future growth of 35 billion gallons by 2050. The road as we get together as a government, the work being done in DOE, coupled with our partners with USDA, FAA, and CAFFI. We created a roadmap examining the technical, feedstock, and political and policy barriers we must overcome if this industry becomes a reality. We already established that life-cycle assessment working group that comes together to take the models to evaluate the greenhouse emissions coming to us from international spaces and US space. We come together to look at these models and determine the commonalities and differences and how it ultimately impacts our ability to certify aviation fuels and provide incentive programs based on the amount of CO₂ we were able to reduce. DOE is very active in trying to scale up the technologies. We must go to the demonstration scale for the research to become a commercial product. DOE's funding helps provide the cost-sharing necessary for the industry to take the risk in using these technologies, build large-scale facilities, and demonstrate that they can produce the fuels they expect.

Beyond biomass, we are also looking towards increasing our consideration of the use of CO₂ emissions. Over the last year, carbon capture and carbon capture sequestration to value molecules has focused on utilizing CO₂ for sustainable aviation fuel effectively, liquid fuels, and liquids to heat and power. Capturing CO₂ from existing biorefineries or generally from industry (steel industry) will enable us to exceed 300 MMT of carbon needed to meet anticipated demand. However, this comes to a huge amount of technology and R&D that we still need to continue to meet the aviation and energy demands over the next three decades. You will see our programs not only funding demonstration as near-term possibilities but also research that reaches back and gives us options to take us to 2050, the ultimate.

Mr. Steve Csonka (CAAFI) shared the ideas of “drop-in fuels”, commonly known as renewable hydrocarbon biofuels. Aviation has an entity that is the first industry sector to commit to decarbonization. Dr. Fenwick provided three key points on focus on low carbon fuel solutions, (1) to maintain the airworthiness of the existing fleet, which is certified to operate with a certified fuel; (2) to require the fleet to upgrade or complete replacement of the existing fleet with the same chemical and physical properties; and (3) bio-jet fuel or blended fuel at the producer level meeting the jet fuel specification without infrastructure or airport redesign. As long as the synthetic fuel meets the ASTM specification D1655 standard and must be pure (normal, iso, cyclo) hydrocarbons from C₇–C₁₇ with a defined aromatic content without oxygen that meets the current physical and chemical characteristics of Jet Fuel A (flash point, viscosity, autoignition temperature, freezing point, density, specific energy, defined

in specification ASTM D4054) is the molecular toolbox which can be derived from lignins, sugars, greases, oils, diesel, and other hydrocarbon sources.

Jieun Kirtley pointed out that to support the aviation industry's goal of reaching net-zero CO₂ emissions by 2050, GE will develop regulations and technologies to keep alternative fuels that meet D1655 specifications and operational improvements through a mix of revolutionary aircraft and propulsion technologies. The biggest lever to pull is SAF, which is the compatibility of aromatic content, storage stability, and stability with the injection, transmission, engine, and exhaust, as well as meeting the ASTM standard. GE Aviation has been actively assessing and qualifying SAF since 2007 and works closely with producers, regulators, and operators to help ensure SAF can be widely adopted for use. Seven approved pathways to allow 50% blending have overcome the technical barriers of mixing with Jet Fuel A. Steve: airline barriers and limitations from the aromatic content may come from other aspects of the specification; seven approved pathways require blending with jet fuel. Since the ASTM requires a specific composition of aromatics, research has shown that certain C7 cyclic kinds of paraffin can be excluded without degrading physical or chemical fuel performance. The advantage is that such processes would not need blending with current Jet Fuel A and enhance SAF production and availability as a drop-in fuel without blending.

Mr. Joseph Ran, VP of Business Development at World Energy, LLC, discussed his spots, scaling, impact, and necessity and came to this point of the energy bases of sustainable aviation fuels. He talked about the challenges that the world is confronted with today. World Energy addressed the climate changes due to carbon emissions and developed and scaled up the technology on how SAF can manage the energy challenge to achieve zero emissions and improve air quality. The goal is to produce 35 million gallons of SAF at Jet Fuel A pricing, which is currently feasible from a chemistry standpoint but not a price point. The price can be lowered by examining different chemistries to convert bio or low-cost wastes to liquid fuels using cost-effective conversion technologies in terms of CAPAX infrastructure costs which guide the selection of feedstocks.

Aviation alone contributes to 2% of global anthropogenic carbon emissions today. In the future, that sector aims to reduce CO₂ emissions by 25% by 2050. To meet the expected reduction in CO₂ means replacing the hydrocarbon fossil fuel technologies developed over 100 years within the next 30 years to utilize multiple feedstocks, unlike fossil fuel technologies which only use petroleum hydrocarbons. When other sectors continue to electrify, the aviation field to power aircraft still uses liquid fuel, primarily fossil fuel. Meeting anticipated CO₂ reduction targets also means an emerging technology deployment cycle of 3 years instead of the traditional 20 years to meet the stated goals. Without doing anything, the field will create a carbon footprint introduced by the sector. CO₂ emission reduction is not a choice anymore but an obligation, particularly in aviation. World Energy focuses on a new form of energy to reduce aviation's net carbon emissions and aims to push decarbonizing and scale up the advanced low-carbon fuels network. Hydrogen is a hot topic. By illustration, we are not only sacrificing by focusing on carbon reduction and will bring green hydrogen into the market by 2025 and 2050. By 2027, we will be producing green

hydrogen. Another company in Germany, the wind energy consortium. World energy will be a part of the consortium to bring green hydrogen to Europe by the earliest date of 2025. Ultimately the green liquid hydrogen will be obtained by 2030 by capturing CO₂ and producing aviation energy fuels: world energy, the world's leading company committed to zero-emission technology. World Energy took actions to get green energy to commercial scale by 2026; working with other partners, and value chain partners, the company will bring 500 million annual gallons of SAF. By 2030, the 1-billion-gallon goal will be achieved. To completely replace jet fuel consumption today, 21-billion-gallon domestic and commercial jet fuel will be needed.

8.4 Conclusion

There are no reasonable arguments in conflict with the existence of global warming and its associated risks. It is also universally understood that current energy sources widely used are not only threatening the earth, but also finite. This creates an obvious and critical need to accomplish more than one goal simultaneously. We must have a plan if we are to have reliable energy long term, and the new source of energy must be safe to the planet, in development, production, implementation, and use. Though the problem is older than are efforts to address it, universal acceptance of the situation as a crisis is growing. Those who have thought ahead of others have been predicting different methods to resolve it, and estimating intentional and unintentional outcomes.

With the future of the planet hanging in the balance, a global effort is the only option. This will require international agreements, and flexible collaboration between diverse nations. Taxes will be an essential resource if pollution, employment, and energy needs are to be met simultaneously. Capitalists are unlikely to move forward without government funding, which is far more likely to be able to secure control of private investment to include addressing social needs.

Consideration of the needs and wellbeing of all economies (not just the west) are more assured if supply chains include as many nations as possible. This enormous shift in energy production is a once in a lifetime opportunity for developing nations to secure their futures, if they are not shut out by wealthy investors. Information is updated frequently on the progress of green energy with a few clicks on the internet. If the West is to lead in this initiative, then other nations could look to the U.S. Bureau of Labor Statistics' assertion in 2022 that there will be more significant growth in green jobs (24 million of them), and that labor will not be excluded, as so many of these jobs do not require a college degree [8]. This is especially important in countries rich in land and feedstocks, but lacking in higher education. Imagine if advances in green energy ushered in further development of everything related to it (construction, shipping, etc.), using the very fuels to build that are designed to serve long-term. Even failing that, it would be of benefit for fossil fuel to die on the vine as it contributed its own demise on its way to obsolescence.

References

1. Olufemi AC, Mji A, Mukhola MS (2019) Health risks of exposure to air pollutants among students in the vicinity of coal mines. *Energy Explor Exploit* 37(6):1638–1656. <https://doi.org/10.1177/0144598718765489>
2. Schoneveld GC, German LA, Nutakor E (2011) Land-based investments for rural development? A grounded analysis of the local impacts of biofuel feedstock plantations in Ghana. *Ecol Soc* 16(4):1–16. <https://doi.org/10.5751/ES-04424-160410>
3. Gomiero T, Pimentel D, Paoletti MG (2011) Is there a need for a more sustainable agriculture? *Crit Rev Plant Sci* 30(1–2):6–23. <https://doi.org/10.1080/07352689.2011.553515>
4. Trindade SC (2009) The sustainability of biofuels depends on international trade. *Energy Sources Part A Recovery, Utilization Environ Eff* 31(18):1680–1686. <https://doi.org/10.1080/15567030903022010>
5. Clancy JS (2008) Are biofuels pro-poor? Assessing the evidence. *Eur J Dev Res* 20(3):416–431. <https://doi.org/10.1080/09578810802245618>
6. United Nations (n.d.) Green jobs: the only way to go. Retrieved from <https://www.un.org/en/climatechange/climate-solutions/green-jobs>
7. U.S. Department of Energy (2022) Sustainable aviation fuel grand challenge roadmap: flight plan for sustainable aviation fuel report. Retrieved from <https://www.energy.gov/eere/bioenergy/articles/sustainable-aviation-fuel-grand-challenge-roadmap-flight-plan-sustainable>
8. U.S. Bureau of Labor Statistics (2022) Green growth: employment projections in environmentally focused occupations. Retrieved from <https://www.bls.gov/careeroutlook/2022/data-on-display/green-growth.htm>
9. Yusaf T, Kadirgama K, Hall S, Fernandes L (2022) The future of sustainable aviation fuels, challenges and solutions. *Energies* 15(21):8151. <https://doi.org/10.3390/en15218151>
10. Bwapwa JK, Anandraj A, Trois C (2017) Possibilities for conversion of microalgae oil into aviation fuel: a review. *Renew Sustain Energy Rev* 80:1345–1354. <https://doi.org/10.1016/j.rser.2017.05.224>
11. Meurer A, Kern J (2021) Fischer–tröpsch synthesis as the key for decentralized sustainable kerosene production. *Energies* 14(7):1836. <https://doi.org/10.3390/en14071836>
12. Illukpitiya P, Yuldashev F, Nasiru K (2022) Designing harvesting and hauling cost models for energy cane production for biorefineries. *Energies* 15(15):5403. <https://doi.org/10.3390/en15155403>
13. Birch K, Calvert K (2015) Rethinking “drop-in” biofuels: on the political materialities of bioenergy. *Sci Technol Stud* 28(1):52–72
14. Leavitt E, Meyn S, Purcell A, Stanton L (2018) Moving toward sustainable aviation fuel at Seattle-Tacoma international airport. *J Airport Manage* 12(4):391–398
15. Gössling S, Lyle C (2021) Transition policies for climatically sustainable aviation. *Transp Rev* 41(5):643–658. <https://doi.org/10.1080/01441647.2021.1938284>
16. Baledón MS, Trudel M, Kosoy N (2022) Alternative jet fuels and climate geopolitics: *what, why* does it and *who* matters in the environmental policy-making process. *Int J Sustain Transp* 16(6):541–557. <https://doi.org/10.1080/15568318.2021.1912225>
17. Drünert S, Neuling U, Zitscher T, Kaltschmitt M (2020) Power-to-liquid fuels for aviation—processes, resources and supply potential under German conditions. *Appl Energy* 277:115578. <https://doi.org/10.1016/j.apenergy.2020.115578>
18. Prussi M, Weindorf W, Buffi M, López JS, Scarlat N (2021) Are algae ready to take off? GHG emission savings of algae-to-kerosene production. *Appl Energy* 304:117817. <https://doi.org/10.1016/j.apenergy.2021.117817>
19. Rony ZI, Mofijur M, Hasan MM, Ahmed SF, Almomani F, Rasul MG, Jahurul MI, Show PL, Kalam MA, Mahlia TMI (2023) Unanswered issues on decarbonizing the aviation industry through the development of sustainable aviation fuel from microalgae. *Fuel* 334(Part 1):126553. <https://doi.org/10.1016/j.fuel.2022.126553>

20. Batten R, Galant O, Karanjikar M, Spatari S (2023) Meeting sustainable aviation fuel policy targets through first generation corn biorefineries. *Fuel* 333(Part 1):126294. <https://doi.org/10.1016/j.fuel.2022.126294>
21. Guo M, Song W (2019) The growing U.S. bioeconomy: drivers, development and constraints. *New Biotech* 49:48–57. <https://doi.org/10.1016/j.nbt.2018.08.005>
22. Higher Profile for Biofuels (2018) *Mech Eng* 140(4):27
23. Hayward JA, O’Connell DA, Raison RJ, Warden AC, O’Connor MH, Murphy HT, Booth TH, Braid AL, Crawford DF, Herr A, Jovanovic T, Poole ML, Di Prestwidge, Raisbeck-Brown N, Rye L (2015) The economics of producing sustainable aviation fuel: a regional case study in Queensland, Australia. *GCB Bioenergy* 7(3):497–511. <https://doi.org/10.1111/gcbb.12159>
24. Wassener B (2008) Airline flies a 747 on fuel from a plant. In: *The New York Times*. Retrieved from <https://www.nytimes.com/2008/12/31/business/31air.html>
25. Laveille P, Uratani J, Barron JGG, Brodeur-Campbell M, Chandak NR, George A, Morin S, Galvan AR, Berthod M (2022) Sustainable pilot-scale production of a *Salicornia* oil, its conversion to certified aviation fuel, and techno-economic analysis of the related biorefinery. *Biofuels Bioprod Biorefin* 16(1):27–42. <https://doi.org/10.1002/bbb.2260>
26. Hillring B (2002) Rural development and bioenergy—experiences from 20 years of development in Sweden. *Biomass Bioenergy* 23(6):443–451. [https://doi.org/10.1016/S0961-9534\(02\)00084-3](https://doi.org/10.1016/S0961-9534(02)00084-3)
27. Levidow L, Papaioannou T (2014) UK biofuel policy: envisaging sustainable biofuels, shaping institutions and futures. *Environ Planning A Econ Space* 46(2):280–298. <https://doi.org/10.1068/a45711>
28. Lima MGB (2009) Biofuel governance and international legal principles: is it equitable and sustainable? *Melbourne J Int Law* 10(2):470–492
29. Guarengi MM, Walter A, Seabra JEA, Rocha JV, Vieira N, Damame D, Santos JL (2022) Areas available for the potential sustainable expansion of soy in Brazil: a geospatial assessment using the SAFmaps database. *Remote Sens* 14(7):1628. <https://doi.org/10.3390/rs14071628>
30. Yuliar S, Nurlaila I, Amir S (2008) Cultivating energy, reducing poverty: biofuel development in an Indonesian village. *Perspect Glob Dev Technol* 7(2):113–132
31. Farobie O, Hartulistiyoso E (2022) Palm oil biodiesel as a renewable energy resource in Indonesia: current status and challenges. *BioEnergy Res* 15(1):93–111. <https://doi.org/10.1007/s12155-021-10344-7>
32. Prananta W, Kubiszewski I (2021) Assessment of Indonesia’s future renewable energy plan: a meta-analysis of biofuel energy return on investment (EROI). *Energies* 14(10):2803. <https://doi.org/10.3390/en14102803>
33. Snow AA, Smith VH (2012) Genetically engineered algae for biofuels: a key role for ecologists. *BioScience* 62(8):765–768. <https://doi.org/10.1525/bio.2012.62.8.9>
34. Ananthalakshmi A, Latiff R (2023) U.S. lifts import ban on some darby plantation products. In: *Reuters*. Retrieved from <https://www.reuters.com/business/sustainable-business/us-says-sime-darby-plantation-products-no-longer-produced-with-forced-labour-2023-02-03/>
35. Silalertruksa T, Gheewala SH, Hünecke K, Fritsche UR (2012) Biofuels and employment effects: implications for socio-economic development in Thailand. *Biomass Bioenergy* 46:409–418. <https://doi.org/10.1016/j.biombioe.2012.07.019>
36. Fragkos P, Paroussos L (2018) Employment creation in EU related to renewables expansion. *Appl Energy* 230:935–945. <https://doi.org/10.1016/j.apenergy.2018.09.032>
37. Arndt C, Benfica R, Thurlow J (2011) Gender implications of biofuels expansion in Africa: the case of Mozambique. *World Dev* 39(9):1649–1662. <https://doi.org/10.1016/j.worlddev.2011.02.012>
38. Ianda TF, Sales EA, Nascimento AN, Padula AD (2020) Optimizing the cooperated “multi-countries” biodiesel production and consumption in Sub-Saharan Africa. *Energies* 13(18):4717. <https://doi.org/10.3390/en13184717>
39. Kashe K, Kgathi DL, Teketay D (2021) Invasiveness of biofuel crops: implications for energy research and policy in Botswana. *S Afr Geogr J* 103(2):259–281. <https://doi.org/10.1080/03736245.2020.1768583>

40. Openshaw K (2010) Biomass energy: employment generation and its contribution to poverty alleviation. *Biomass Bioenergy* 34(3):365–378. <https://doi.org/10.1016/j.biombioe.2009.11.008>
41. de Oliveira JT, de Oliveira RA, Brito OA, da Cunha FF, Gava R (2021) Increase in the irrigated area of sugarcane and its potential in the bioenergetic generation of Brazil. *Colloquium Agrariae* 17(3):33–38. <https://doi.org/10.5747/ca.2021.v17.n3.a437>
42. Fletcher E, Adeboye PT, Duedu KO (2017) Toward a sustainable bioeconomy in West Africa: a focus on biorefining. *Biofuels Bioprod Biorefin* 11(5):775–783. <https://doi.org/10.1002/bbb.1793>
43. Halder P (2014) Forest biomass for energy production: perceptions of state forestry professionals from China and India. *Challenges* 5(2):338–350. <https://doi.org/10.3390/challe5020338>
44. Maconachie R, Fortin E (2013) ‘New agriculture’ for sustainable development? Biofuels and agrarian change in post-war Sierra Leone. *J Mod Afr Stud* 51(2):249–277. <https://doi.org/10.1017/S0022278X13000189>
45. Malik A, Lenzen M, Geschke A (2016) Triple bottom line study of a lignocellulosic biofuel industry. *GCB Bioenergy* 8(1):96–110. <https://doi.org/10.1111/gcbb.12240>
46. Cascone R, Burke B (2010) Biorenewables update: what is beyond ethanol and biodiesel? *Hydrocarb Process* 89(9):51–55
47. Alavijeh MK, Karimi K (2019) Biobutanol production from corn stover in the US. *Ind Crops Prod* 129:641–653. <https://doi.org/10.1016/j.indcrop.2018.12.054>
48. Selfa T (2010) Global benefits, local burdens? The paradox of governing biofuels in Kansas and Iowa. *Renew Agric Food Syst* 25(2):129–142. <https://doi.org/10.1017/S1742170510000153>
49. Rogers JN, Stokes B, Dunn J, Cai H, Wu M, Haq Z, Baumes H (2017) An assessment of the potential products and economic and environmental impacts resulting from a billion ton bioeconomy. *Biofuels Bioprod Biorefin* 11(1):110–128. <https://doi.org/10.1002/bbb.1728>
50. Wicki L, Naglis-Liepa K, Filipiak T, Parzonko A, Wicka A (2022) Is the production of agricultural biogas environmentally friendly? Does the structure of consumption of first- and second-generation raw materials in Latvia and Poland matter? *Energies* 15(15):5623. <https://doi.org/10.3390/en15155623>
51. Valdivia M, Galan JL, Laffarga J, Ramos JL (2016) Biofuels 2020: biorefineries based on lignocellulosic materials. *Microb Biotechnol* 9(5):585–594. <https://doi.org/10.1111/1751-7915.12387>
52. Osorio-González CS, Gómez-Falcon N, Brar SK, Ramírez AA (2022) Cheese whey as a potential feedstock for producing renewable biofuels: a review. *Energies* 15(18):6828. <https://doi.org/10.3390/en15186828>
53. Kim S, Dale BE (2015) Potential job creation in the cellulosic biofuel industry: the effect of feedstock price. *Biofuels Bioprod Biorefin* 9(6):639–647. <https://doi.org/10.1002/bbb.1616>
54. Ullah KM, Dwivedi P (2022) Ascertaining land allocation decisions of farmers about the adoption of carinata as a potential crop for sustainable aviation fuel production in the Southern United States. *GCB Bioenergy* 14(7):824–839. <https://doi.org/10.1111/gcbb.12945>
55. Cabrera E, de Sousa JMM (2022) Use of sustainable fuels in aviation—a review. *Energies* 15(7):2440. <https://doi.org/10.3390/en15072440>
56. Dwivedi P (2021) Sustainable aviation fuel production from Brassica carinata in the Southern United States. *GCB Bioenergy* 13(12):1854–1858. <https://doi.org/10.1111/gcbb.12900>
57. Alam A, Masum MFH, Dwivedi P (2021) Break-even price and carbon emissions of carinata-based sustainable aviation fuel production in the Southeastern United States. *GCB Bioenergy* 13(11):1800–1813. <https://doi.org/10.1111/gcbb.12888>
58. Zhang Z, Wei K, Li J, Wang Z (2022) Life-cycle assessment of bio-jet fuel production from waste cooking oil via hydroconversion. *Energies* 15(18):6612. <https://doi.org/10.3390/en15186612>
59. Moosavi SA, Aghaalikhani M, Ghobadian B, Fayyazi E (2018) Okra: a potential future bioenergy crop in Iran. *Renew Sustain Energy Rev* 93:517–524. <https://doi.org/10.1016/j.rser.2018.04.057>

60. Cansino JM, Cardenete MA, González-Limón JM, Román R (2013) Economic impacts of biofuels deployment in Andalusia. *Renew Sustain Energy Rev* 27:274–282. <https://doi.org/10.1016/j.rser.2013.06.006>
61. Lechón Y, de la Rúa C, Rodríguez I, Caldés N (2019) Socioeconomic implications of biofuels deployment through an Input-Output approach. A case study in Uruguay. *Renew Sustain Energy Rev* 104:178–191. <https://doi.org/10.1016/j.rser.2019.01.029>
62. Romero-Izquierdo AG, Gómez-Castro FI, Hernández S, Gutiérrez-Antonio C (2022) Computer aided-design of castor bean fruit-based biorefinery scheme to produce sustainable aviation fuel. *Chem Eng Res Des* 188:746–763. <https://doi.org/10.1016/j.cherd.2022.10.025>
63. Rivas-Interian RM, Sanchez-Ramirez E, Quiroz-Ramirez JJ, Segovia-Hernandez JG (2023) Feedstock planning and optimization of a sustainable distributed configuration biorefinery for biojet fuel production via ATJ process. *Biofuels Bioprod Biorefin* 17(1):71–96. <https://doi.org/10.1002/bbb.2425>
64. Smith AL, Klenk N, Wood S, Hewitt N, Henriques I, Yan N, Bazely DR (2013) Second generation biofuels and bioinvasions: an evaluation of invasive risks and policy responses in the United States and Canada. *Renew Sustain Energy Rev* 27:30–42. <https://doi.org/10.1016/j.rser.2013.06.013>
65. Córdoba D, Chiappe M, Abrams J, Selfa T (2018) Fuelling social inclusion? neo-extractivism, state–society relations and biofuel policies in Latin America’s southern cone. *Dev Change* 49(1):63–88. <https://doi.org/10.1111/dech.12362>
66. Xu B, Ahmad S, Charles V, Xuan J (2022) Sustainable commercial aviation: what determines air travellers’ willingness to pay more for sustainable aviation fuel? *J Cleaner Prod* 374:133990. <https://doi.org/10.1016/j.jclepro.2022.133990>
67. Ghasemikafroudi E, Amini M, Habibi MR, Hassankiadeh QD (2017) Environmental effects and economic study on flare gas recovery for using as fuel gas or feedstock. *Pet Coal* 59(1):18–28

Chapter 9

Thermal Analysis During Metallic Additive Manufacturing



Gaoqiang Yang, Zheng Chen, Yaji Huang, Jingke Mo, Zhenye Kang, and Feng-Yuan Zhang

Abstract Due to its ability to produce 3D parts with anfractuous and complex structures with limited post-processing and minimal wastage of raw materials, additive manufacturing (AM) technology opens a new route for manufacturing without tooling and/or machining limits. Therefore, it is constantly used in industrial and research sectors all over the world with expanding prospects. However, the temperature distribution and heat transfer during AM processes directly affect the properties and structures of the printed parts, especially for metallic components. Herein, a comprehensive summary of thermal analysis and heat transfer during metallic AM processes is presented. Metallic AM methods are divided into several categories, including powder bed fusion (PBF), direct energy deposition (DED), and other metallic AM processes. The challenges of heat transfer in each metallic AM process are fully discussed, and the energy insertion and material thermal properties are also discussed for better fundamental understanding. Finally, the experimental and computational studies of thermal analysis in different metallic AM methods are summarized, and a view of the future research is provided.

G. Yang (✉) · Z. Chen

College of Mechanical and Vehicle Engineering, Hunan University, Changsha 410082, China
e-mail: gyang@hnu.edu.cn

Y. Huang

Key Laboratory of Energy Thermal Conversion and Control of Ministry of Education, School of Energy and Environment, Southeast University, Nanjing 210096, China

J. Mo

Department of Aeronautics and Astronautics, Fudan University, Shanghai 200433, China

Z. Kang

State Key Laboratory of Marine Resource Utilization in South China Sea, School of Chemical Engineering and Technology, Hainan University, Haikou 570228, China

F.-Y. Zhang (✉)

Department of Mechanical, Aerospace and Biomedical Engineering, University of Tennessee, Knoxville (UTK), Knoxville, TN 37966, USA
e-mail: fzhang@utk.edu

Keywords Thermal analysis · Heat transfer · Temperature profile · Additive manufacturing · Metal material · Modelling

9.1 Introduction

Additive manufacturing (AM) technology, also called 3-dimensional (3D) printing, is a process developed in the late 1980s to produce 3D parts in a layer-by-layer manner with freeform fabrication [1, 2]. AM can be used to fabricate anfractuons components with complex inner features and almost zero raw material wastage from 3D digital models. It is an economical and rapid manufacturing method that is used in several industries now, including aerospace, energy conversion devices [3–6], automotive [7], medical [8] and other industries [9]. Due to its advantages and applications, AM technology is constantly spreading all over the world, and this booming is expected to continue for the next few decades. According to a recent report [10], the sales of metal AM machines had a dramatic growth in 2017, as shown in Fig. 9.1, and this increasing trend is likely to continue over the next several decades.

The metallic AM processes involve complex physical changes and transformations, such as melting, solidification, and heat/mass transfer. Thus, it is challenging to achieve good quality and reproducibility of fabricated items. Moreover, the process parameters could have significant impact on the morphology, microstructure, mechanical and chemical properties of AM parts, such as the percentage of different grain phases and mechanical strength. To overcome these challenges, it is necessary to have an accurate control of parameters, such as input power location, power density, scanning speed, melt pool size, etc., to achieve higher quality of

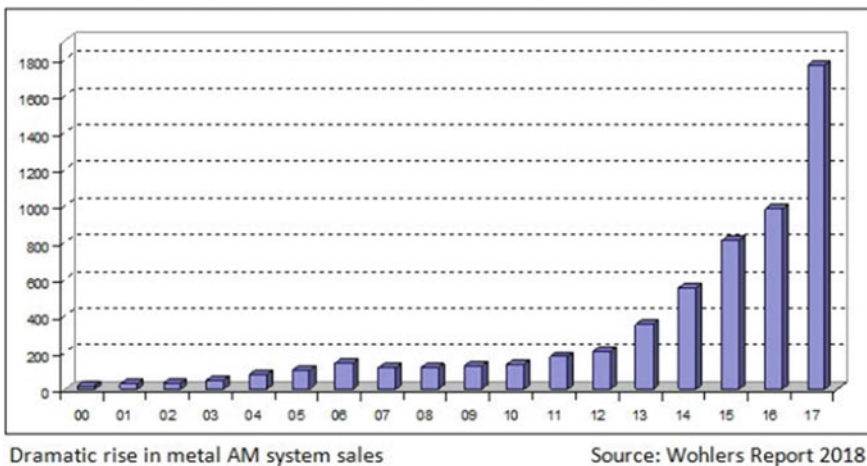


Fig. 9.1 Metal AM machine annual sales [10]

products. In fact, the manufacturing process parameters determine the thermal energy distribution, as well as the fusing or melting regions of materials during fabrication. This is because the temperature fields can directly impact the properties and structures of the parts, and a homogeneous temperature field during manufacturing could improve the quality of parts. For example, during the powder bed fusion method, a laser or electron beam is used to heat the materials to melting point. Then, rapid cycles of heating and cooling lead to convective and radiative heat transfer between the molten pool and the surroundings. If the density of molten powder exceeds the threshold point, deep cavities would appear as a result of localized overheating and evaporation of the powder without an accurate control of temperature distribution on the powder bed. If the relevant thermal analysis is identified and modeled, it can be used to decide the process parameters, and to improve the quality of AM parts. Thus, a clear understanding of the thermal transport and analysis is essential for the further investigation and optimization of AM processes.

Numerous studies about thermal analysis have been published to improve the thermal analysis during metallic AM processes. However, the literature and past efforts have not yet been compiled to provide a clear summary and categorization of metallic AM systems. This chapter provides an introduction of metallic AM systems, discusses the challenges of heat transfer, and presents the energy insertion and material thermal properties during metallic AM. Then, a summary of thermal analysis is presented with regard to three categories of metallic AM: powder bed fusion (PBF) process, direct energy deposition (DED) process, and other manufacturing processes, such as electron beam freedom fabrication (EBF) and sheet lamination. This comprehensive summary on the thermal analysis is expected to be helpful for the further development of metallic AM systems.

9.2 Metallic Additive Manufacturing Systems

Different kinds of categorizations of AMs exist in literature, which are based on raw materials, energy resources, building methods, etc. In this chapter, the material feed system is employed to categorize the AM processes. There are three broad categories: PBF process, DED process, and other processes. Figure 9.2 shows the different categories of metallic AM processes which will be discussed in detail in the following sections.

9.2.1 Powder Bed Fusion

The PBF process is illustrated in Fig. 9.3. A roller or rake creates a layer of powder bed of different thicknesses across the substrate or component. Then, focused energy sources (laser or electron beam) selectively irradiate the surface of the powder and heat it to melting or sintering temperature. The melted metal powders form the

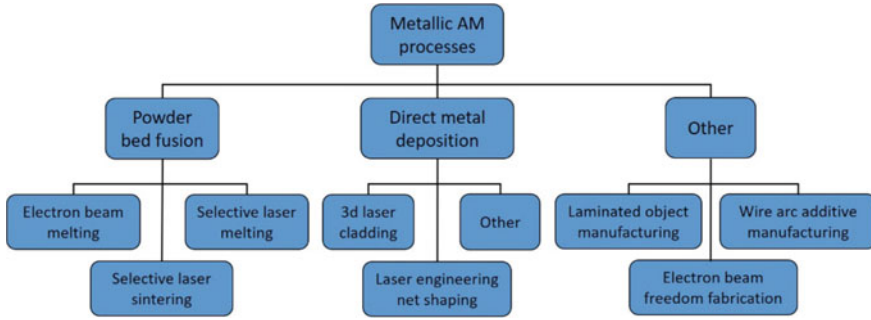
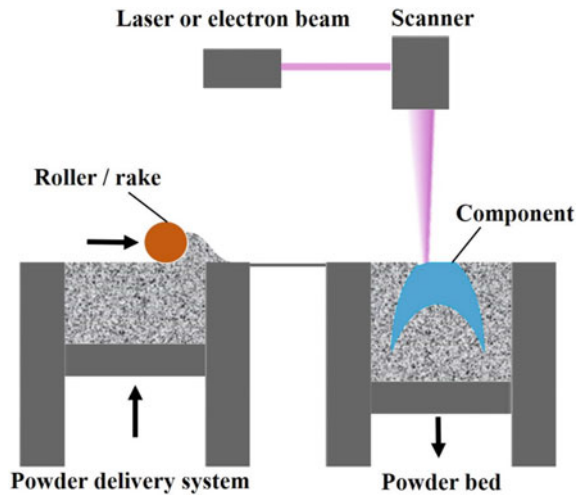


Fig. 9.2 Overview of the different metallic AM processes

Fig. 9.3 General schematic of the PBF system



components, while the unmelted powders remain behind to support the upper structures. This process is repeated until the 3D part is completely manufactured. It should be pointed out that vacuum or inert gases are used in the building chamber in order to avoid oxidation of metal powders. This method could provide parts with high resolution features, internal patterns, etc. Commercial PBF-based systems mainly include selective laser sintering (SLS), selective laser melting (SLM), and electron beam melting (EBM).

9.2.1.1 Selective Laser Sintering

The SLS technology is a type of powder bed laser melting process dealing with materials such as metals, plastics, and ceramics. It is also called direct metal laser sintering (DMLS) when it is applied to alloys. Before sintering, the entire powder

bed is preheated to a temperature slightly below the melting temperature of the materials, which can reduce the thermal distortions and improve the fusion of the previously printed layer. SLS has high accuracy and can provide parts with better surface structure, higher porosity, and thinner layer. However, this process is relatively slow compared with other processes, such as EBM.

9.2.1.2 Selective Laser Melting

Similar to SLS, the SLM method is another kind of powder bed laser melting process. During the SLM process, the powder is melted completely instead of being sintered to increase the density of the part. The laser beam power (typically 400 W) in this method is much higher than that in SLS. Other PBF processes, like laser curing, are very similar to the typical laser-based PBF processes that have been introduced. For laser curing, the laser beam is reflected by drive motors and mirrors to control the direction and the irradiation area.

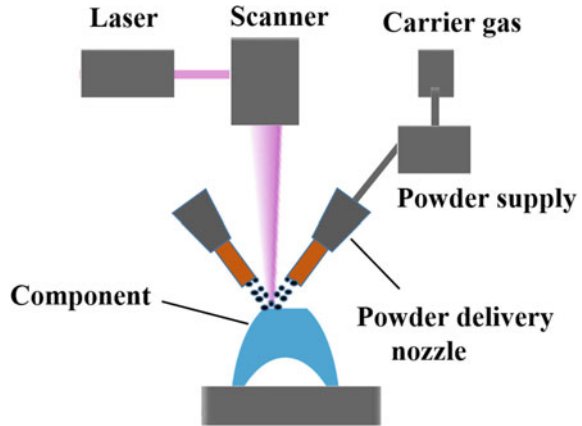
9.2.1.3 Electron Beam Melting

EBM technology was first proposed at MIT in 1995. Since then, ARCAM, a Swedish company, has manufactured several products based on EBM [11]. EBM is a powder-bed based AM process, in which an electron beam generated by a high voltage range from 30 to 60 kV is used as the energy source to melt metal powder. The EBM process is conducted in a near-vacuum chamber to reduce the oxidation of metal materials, and the convective heat transfer during EBM is also significantly reduced. A variety of materials have been used for producing raw powders, such as Ti-6Al-3 V, aluminum, copper, stainless steel, etc. During EBM process, the vacuum chamber is kept at a relatively high temperature of 700–1000 °C, which could reduce the induced stresses and offer uniform temperature distribution during the heating and cooling cycles. Besides, the EBM process also has a faster build rate. However, it yields products with lower accuracy and a rougher surface.

9.2.2 Direct Energy Deposition

The DED process, also called the metal deposition technology, uses the same energy source for irradiation as the PBF process, but this process employs a different metal powder feed mechanism. In PBF, the powders are pre-laid on the substrate or powder bed before melting or fusing. On the other hand, during the DED process, a deposition head or powder nozzle is used to jet powders with the carrier gas onto the work area, as shown in Fig. 9.4. The energy source, the laser or electron beam, comes out from the guidance system and melts the added materials. There are two types of moving parts in the DED system: the moving deposition head and the moving aim part. DED

Fig. 9.4 General schematic of DED process



usually provides a larger build volume, and the surface of the substrate could be any shape. It could be used for rapid prototyping, cladding or refurbishing damaged parts.

Commercial DED processes include laser engineered net shaping (LENS), 3D laser cladding, 3D laser welding, directed light fabrication (DLF), direct metal deposition (DMD), etc. These processes follow the general approaches, while different powers, materials, powder delivery approaches, and different types of moving platforms are utilized to meet the different requirements.

9.2.2.1 3D Laser Cladding

The 3D laser cladding process takes advantage of laser powder injection technology and is also known as direct metal deposition (DMD) or laser welding. It has been widely used for complex coating, repairing damaged parts, and rapid prototyping. In this process, the metal powder is jetted into the laser beam and melt pool through a coaxial nozzle. Typical physical changes of metal powders include laser-powder interactions, heat transfer to powders, melting, fluid flowing and cooling. 3D laser cladding can provide a much thicker additive layer compared with conventional techniques, and provide better binding between the coating material and surface. Moreover, various materials can be used for laser cladding, such as copper, stainless steel, aluminum, magnesium, titanium alloys, etc.

9.2.2.2 Laser Engineering Net Shaping

The LENS technology is another kind of laser powder injection process, which was first proposed by Sandia National Lab. LENS can be used to manufacture fully dense,

near-net-shaped and complex metal implants with interface between different materials. Therefore, it can be used for rapid prototyping and joining of dissimilar metal materials. Many metal materials, such as stainless steels, nickel-based alloys, titanium, and intermetallic compounds, can be used as raw feedstock. The difference between LENS and other laser AM processes is the lower laser power, which could provide a smaller heat-affected area. Other DED processes include laser consolidation, directed light fabrication (DLF), etc. However, these processes are very similar to the DED processes introduced previously, and they have been developed by different institutes or companies for different applications, such as medicine and aerospace.

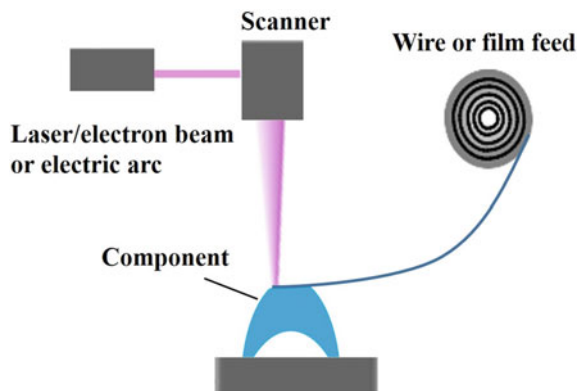
9.2.3 Other Metallic AM Processes

In addition to PBF and DED processes, other metallic AM processes have been developed by using other types of heating sources, materials, and/or different material feed systems. Some examples include electron beam freedom fabrication (EBF), laminated object manufacturing (LOM) or sheet lamination, binder jetting (BJ), and wire arc additive manufacturing (WAAM). For these processes, the typical difference is that metal wire and film are fed instead of powders, as shown in Fig. 9.5, which will lead to different thermal properties and heat transfer processes.

9.2.3.1 Electron Beam Freedom Fabrication

EBF technology is another kind of electron beam-based AM, but the raw material is metal wire instead of metal powder. NASA Langley Research Center first developed the EBF process to manufacture unitized structures with high-reflectance aerospace

Fig. 9.5 Schematic of electron beam freeform fabrication system



alloys, such as Al or Ti. In EBF, the metal wire is fed into a melt pool, which is continually irradiated by an electron beam, and then parts are produced layer by layer. EBF is a suitable method for manufacturing parts with protruding structures. However, traditional manufacturing methods need to cut a large volume of raw material away to form protruding structures, which leads to a large wastage of raw material. It is a fast method which can be used for on-orbit repairing of parts on space ships or space stations.

9.2.3.2 Laminated Object Manufacturing

LOM technology involves a layer-by-layer lamination of foils. In LOM, each material foil is a cross-sectional layer of the component. The foils are cut by energy source and bonded with each other using gluing, adhesive bonding, or thermal bonding. For thermal bonding, the cut foils are bonded together in an inactive atmosphere, and heated slightly above the melting point of the materials. But thermal-based defect is one of big issues of WAAM processes, so the thermal analysis is urgent for the quality improvement of WAAM.

9.2.3.3 Wire Arc Additive Manufacturing

Other than using laser or an electron beam as energy source, WAAM use electric arc as an energy source and welding wire as feedstock, and this technology is nowadays gaining much attention from both academic and industrial sectors because of its high deposition rate, low costs of production, and low costs of equipment investment. The heating sources mainly include gas metal arc, gas tungsten arc, and plasma arc [12]. The commonly commercially available wires are titanium alloys, aluminum alloys, steel, and nickel-based superalloys [13].

9.3 Challenges of Heat Transfer During Metallic AM

The AM processes involve a large variety of parameters, including power type (laser or electron), beam diameter, the spatial energy distribution of laser or electron beams, shielding gas flow rate, gas flow rate for powder delivery, beam scanning speed, powder or wire feeding rate, material property changes (absorptivity, melting point, thermal conductivity, etc.), material characteristics (size distribution and structure of powder/wire), raw material feeding method (powder bed, side injection, and concentric injection), toolpath patterns, etc. These variables significantly affect the complicated physical processes, such as melting and cooling (solidification) cycles, and fluid flow phenomena. All these physical processes entail comprehensive heat transfers, so there are great challenges involved in heat transfer during metallic AM.

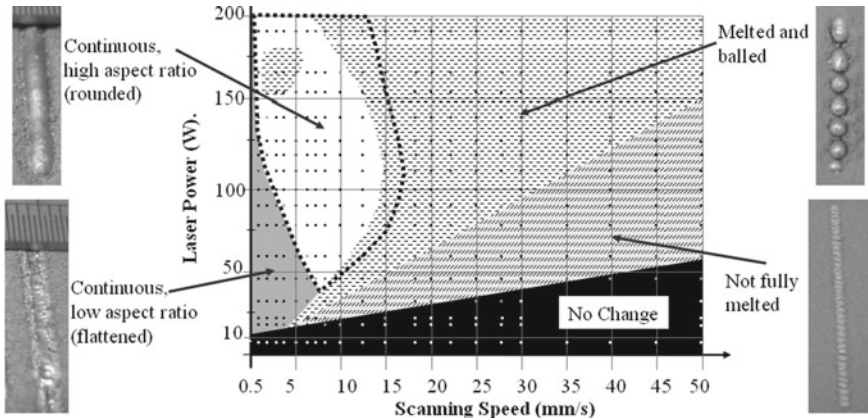


Fig. 9.6 314S single track process map produced using a laser spot size of 1.1 mm [14, 15]

SLS and SLM processes using metallic powders usually have a “balling” phenomenon. When parameters are not appropriate or the process of heat transfer is too radical, the powders are not melted fully and fuse into a large drop instead of forming a flat layer. A single track process map was developed for SLM with different laser powers and scanning speeds, which shows the effect of different parameters on the balling and round surface, as shown in Fig. 9.6 [14].

Large thermal stresses caused by non-uniform cooling and thermal distortion can lead to volume shrinkage and thermal gradients, which in turn would result in errors in the manufactured parts. A drawback of AM process is delamination, as shown in Fig. 9.7a. In PBF process, the top powder layer is selectively fused and solidified. If the heat source inserted into the powder bed is highly non-uniform, the temperature gradients will cause residual stresses. When the residual stresses are greater than the binding force between two layers, the two layers detach from each other and delamination occurs [16]. Cavities and pores are also challenging during the AM process, as shown in Fig. 9.7b. When localized over-heating and evaporation of metal materials occurs, the material density is higher than the threshold point, and a deep vapor cavity forms in the melt pool [17]. Such a cavity could reduce the mechanical strength of the part, and even lead to breakage.

Cracks frequently occur on metal grain boundaries during typical ‘low energy’ fabrication, as shown in Fig. 9.7c [20]. Warping defects usually occur during the rapid solidification in melt pools where the thermal stress is extremely large, as shown in Fig. 9.7d. When the thermal stress overcomes the material strength, warping occurs. Therefore, analyses of heat transfer and temperature profile during AM processes are essential for improving the overall properties of printed parts.

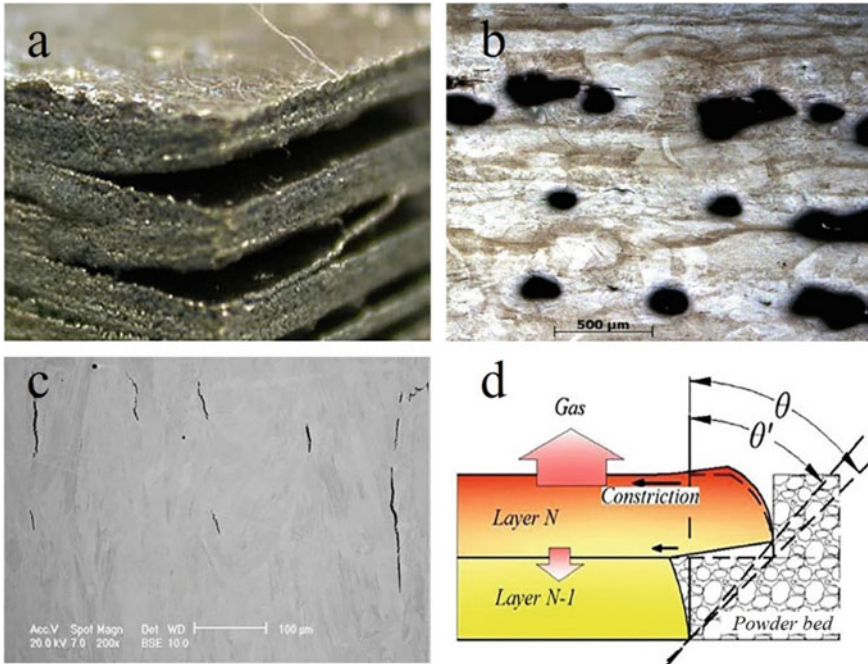


Fig. 9.7 Defects produced in metallic AM. **a** Delamination [18, 19], **b** Holes and voids [17], **c** Cracking [20], **d** Warping [21]

9.4 Energy Insertion and Material Thermal Properties

9.4.1 Energy Distribution of Heat Sources

During AM processes, the energy distribution of heat source has a great impact on the temperature distribution, deposition geometry, and solidification of the heat-affected zone (HAZ). For different heat sources, the energy distribution and absorptivity of the beam vary significantly with different temperatures, diameters, and powers. During thermal analysis of the AM process, different models used for energy sources would result in different temperature profiles for the substrates and materials.

Laser is a kind of electromagnetic radiation, and the incident photons provide high energy density and better focusing characteristics. In the AM application, the most widely used lasers include Nd:YAG laser, CO₂ slab laser, and disc lasers. The CO₂ laser has a wavelength of about 10 μm in the infrared range, which has a reliable power distribution and better efficiency. Nd:YAG lasers provide two pulse modes; the long pulsed mode is suitable for machining thicker materials, while the short pulse mode provides a shorter wavelength which is suitable for highly reflective metals. The electron beam is another kind of fine beam manipulated by electric and magnetic fields, which can convert into heat when irradiated on solid-state surface.

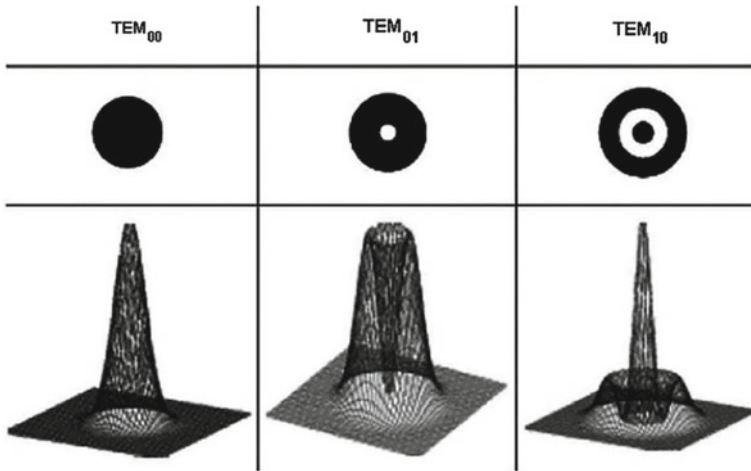


Fig. 9.8 Gaussian beam mode profiles [22, 27]

The accuracy of the energy insertion model is important for thermal analysis, and various laser and electron beam models have been proposed for simulation during AM processes. Gaussian model and double ellipsoidal model are commonly used methods for simulating beam energy insertion, as shown in Fig. 9.8 [22]. The Gaussian model provides symmetrical distribution of laser irradiance. The double ellipsoidal model is certified to be used in the welding process [23].

Yan et al. developed a new model based on Monte Carlo simulation to obtain the energy distribution of an electron beam with the kinetic energy of 60 keV irradiated on a Ti-based substrate [24]. Thermal simulation was conducted for comparison with conventional surface and volumetric energy flux models. Their results showed a different peak temperature, and the model could explain the eruption and explosion phenomena observed during EBM AM process. Tong et al. showed that parabolic model and Gaussian model of thermal sources resulted in two different heat distributions on the material surface [25]. Fachinotti et al. provided exact analytical solutions for double-ellipsoidal heat source, and compared double-ellipsoidal and double elliptical models [26]. Their results showed that this heat source model provided an analytical solution for the double-ellipsoidal case with higher accuracy and less computational cost.

9.4.2 Feedstock Properties

The absorption of heat by feedstock affects the temperature distribution during AM processes. Thus, a quantitative evaluation of the feedstock properties is needed. The metal materials used for the AM include a wide range of pure metals and alloys,

such as Ti-based, Ni-based, Fe-based, Al-based, Co-based and Cu-based materials. Due to their limited mechanical properties and corrosion resistance, pure metals are not commonly used. Alloys are considered as the most promising materials for the AM process. During AM, metallic materials go through intense temperature cycles and physical changes. The material properties, including absorption, thermal conductivity, viscosity, porosity, density, and enthalpy, will change with the temperature and phase. Thus, the heat transfer processes affected by these property changes will in turn have a significant influence on the manufactured parts. For example, the absorptivity values of carbon steel for CO₂ laser are 4, 30 and 90% at room temperature, melting temperature and vaporizing temperature, respectively [28]. Figure 9.9 shows the changes in specific heat, density, and thermal conductivity of Ti-alloy (TiAl6V4) with temperature [29]. It can be seen that the thermal conductivity of TiAl6V4 above the melting temperature is several times greater than that at low temperatures. The increase in thermal conductivity with temperature can be used to model the heat convection process in the melt pool [30].

Numerous models have been developed to investigate the interrelation between raw materials and solid thermal conductivities. Field properties are dependent on the porosity and pore geometries, as given by Eq. (9.1):

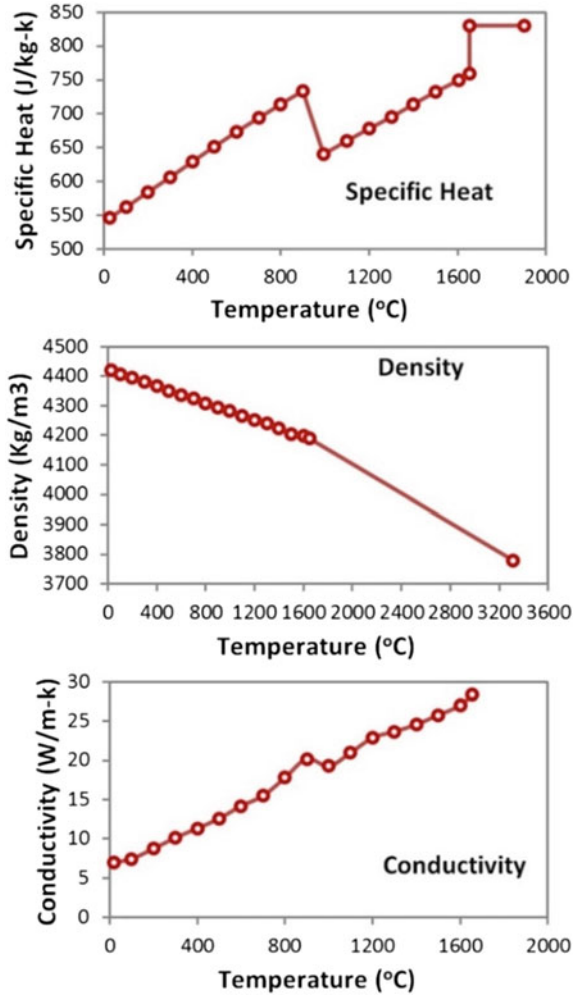
$$\lambda_p = \lambda(1 - \phi) \quad (9.1)$$

where λ_p , λ , and ϕ are effective thermal conductivities of the powder bed and solid metal, and the porosity, respectively. The effective thermal conductivity of porous raw powders is determined by the porosity of powder bed. Roberts et al. studied the light extinction phenomenon in loose powders, and discovered the independence of powder effective thermal conductivity with material properties [22]. More importantly, they found that the conductivity was highly dependent on the particle size, morphology, void fraction, and gas thermal conductivity.

9.5 Theoretical and Experimental Studies of Thermal Analysis in Different Metallic AM Methods

There are many challenges during metallic AM processes, as discussed in Sect. 9.3. Thus, overall thermal analysis is required for overcoming these problems and optimizing metallic AM processes. The process parameters, such as heat source geometry, speed, power, and melt pool geometry, will determine the solidification kinetics and thermal energy transfer. Thermal analysis can be achieved by either experimental analysis or modelling simulation. A large number of research groups have published their efforts on thermal analysis of metallic AM processes.

Fig. 9.9 Variation of thermophysical properties for Ti-alloy (TiAl6V4) with temperature [29, 31]



9.5.1 PBF Processes

Due to the nature of PBF processes, solid powders remain in the powder bed, and the working atmosphere is a vacuum or inert gas. The gas movement is driven by the temperature difference during manufacturing, so the convection heat transfer is relatively small compared to other kinds of heat transfer. Thus, convection heat transfer is seldom considered in the literature.

9.5.1.1 SLM Process

Early studies focused on measuring the temperature distribution in the melt pool by using infrared sensors during the laser-based PBF process. A dichroic mirror was employed to combine the beam path of laser and camera light, in order to determine the temperature [32]. Childs et al. [14] reported an experimental study on the effects of CO₂ laser beam powers and scan speeds on the printing track. Subsequently, they developed a 314S single track process map, which showed 5 regions: continuous and flat topped, continuous and rounded, occasionally broken, balled and only partially melted, as shown in Fig. 9.6. The results indicated that good performance was obtained if materials were melted over wide temperature ranges. Later, Kruth et al. [33] set up coaxial cameras with illumination sources to record the temperature distribution coaxially with laser beams, and then established the relationship between temperature distributions and scanning patterns. Islam et al. [34] used a setup with camera and pyrometer to measure temperature distribution on EOS PH1 stainless steel powder layer for analyzing the balling phenomenon during PBF process. This study helped to define the process characteristics of balling phenomenon. Other researchers also tried to study the thermal phenomena on the powder bed by using thermocouples and two-wavelength pyrometers [35, 36]. For those thermal measurement systems, thermal results are influenced by the distance of the infrared imaging devices and powder bed, which bring errors for thermal analysis. In addition, thermal cameras are unable to capture the temporarily higher skin temperature at specific conditions, and the temperature below threshold will present in the camera data, which will need to be solved in the future.

Modeling and simulation methods provide many benefits for thermal analysis during SLM processes. Figure 9.10 shows the schematic of heat transfer during SLM processes. The general energy balance equation in the printing system can be written as [22, 38]:

$$\vec{Q}_H = \vec{Q}_{IS} - \vec{Q}_{CD} - \vec{Q}_{CV} - \vec{Q}_R \quad (9.2)$$

where \vec{Q}_H , \vec{Q}_{IS} , \vec{Q}_{CD} , \vec{Q}_{CV} , and \vec{Q}_R are the heat accumulation and vector heat energy insertion due to laser or electron beams, conductive, convective, and radiative heat transfers, respectively.

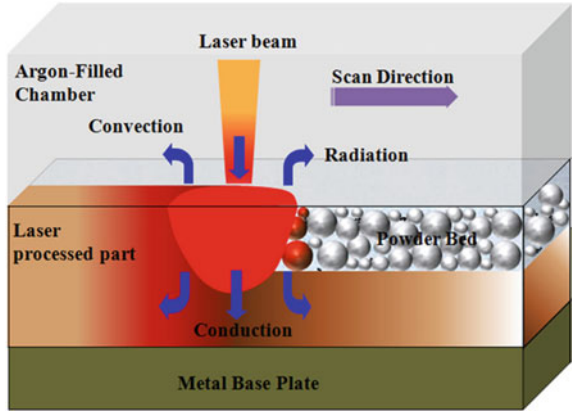
The commonly used governing equations can be written as:

$$\lambda \left(\frac{\partial^2 T}{\partial^2 x} + \frac{\partial^2 T}{\partial^2 y} + \frac{\partial^2 T}{\partial^2 z} \right) + \vec{Q}_H = \rho c \frac{\partial T}{\partial t} \quad (9.3)$$

Initial condition:

$$T(x, y, z, t = 0) = T_0 \quad (9.4)$$

Fig. 9.10 Schematic representation of heat transfer during SLM process [37]



where T is the material temperature, λ is the material conductivity coefficient, ρ is the material coefficient density, c is the material heat capacity.

The boundary conditions are chose based on the assumption for specific case, which include the conduction/convection/radiation heat transfer with the gas atmosphere, heat conduction to the powder bed and bottom, and heat convection in the liquid melting pool.

Williams and Deckard [39] proposed a 1D finite element (FE) model for predicting the heat transfer during SLS processes, and the solution was derived by using a basic feed forward finite difference (FD) method. But 1D model is always insufficient to investigate the details of the thermal properties and heat transfer due to the oversimplified assumption. Employing the Galerkin method with the backward difference scheme, Matsumoto et al. [40] further established an elastic 2D FE model for simulating the temperature and stress profiles of a single layer of nickel based alloy during SLM process. The 2D model is not as time-consuming and expensive compared to 3D, and can provide a more precise result compared to 3D. But it is not able to fully deliver the complex SLM process and the thermal field in heat affected zone. For better understanding, Kolossov et al. [41] proposed a 3D finite element thermal model, which considered non-linear thermal conductivity and specific heat due to temperature and phase changes. This method helped to simulate temperature fields on a single layer of titanium powder bed during SLS processes. The simulation showed that the thermal model using temperature-dependent properties of materials accurately predicted temperature profiles of manufactured parts, which had a good agreement with experimental results. This publication verified the 3D model can provide a precise results, which can reflect the thermal process during PBF process. Furthermore, Zeng et al. [42] modified a dynamic meshing framework called fine and coarse mesh method with ANSYS and Matlab based 3DSIM algorithms. This method predicted thermal distributions during SLMs and improved the computational speed and model size. Yang et al. [43] proposed a 3D transient finite element model with a moving Gaussian laser beam to simulate temperature profiles of Ti6Al4V during PBF process. The simulated results were compared with the depth and width of the

heat affected zone from experiments. They found that the depth and width increased with the increase in laser power, and decreased with the increase in laser spot size and scan rate.

However, 3D model has limitations due to its time-consuming and expensive nature. Li et al. [44] presented a computational fluid dynamics (CFD) method under the framework of the volume of fluid (VOF), which could predict rapid temperature changes and the solidification process. This study also provided cross-section shape changes of metallic powder beds, which were induced by rapid temperature change. Yuan and Gu [37], Gu et al. [45] found that Marangoni convection was of great importance for heat transferring and altering the melt pool geometry. They also demonstrated that the applied laser power had a greater influence on the maximum temperature gradient within the melt pool than the laser scan speed. Their work provided a guideline on how to control the temperature gradient and to reduce the defect during PBF process. Panwisawas et al. [46] performed mesoscale modelling of thermal fluid dynamics during SLM, and proposed a particle dropping model to predict the thermal fluid and powder-laser interaction, as illustrated in Fig. 9.11. They found that particle size distribution was important for SLM modelling, and they developed the relationship between thermal fluid flow and microstructure evolution. Other PBF processes, such as laser curing, are very similar to typical PBF processes. Thus, their thermal analysis processes are almost identical and not discussed in this paper. Overall, 2D model is not as time-consuming and expensive compared to 3D, however, it is not able to fully deliver the complex SLM process and the thermal field in heat affected zone. For 3D model, it remains absolutely necessary to fully understand the thermal process during SLM, regardless its time-consuming and expensive nature. So far, the relative error between the experiment and simulation results can be less than 5%, which still have limitations for its application to predict the thermal field for fabricating precision type instrument due to the simplification of thermal analysis.

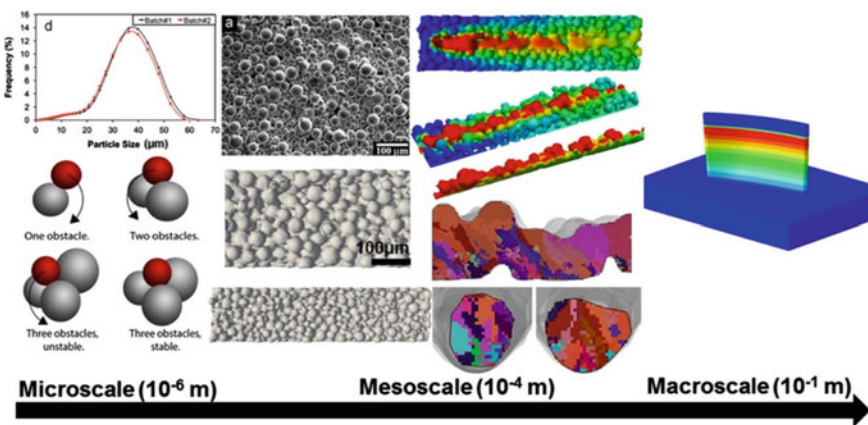


Fig. 9.11 A multi-scale model for selective laser melting [47]

9.5.1.2 EBM Process

Previous reports have demonstrated that the operating parameters of EBM process have great impact on the thermal distribution of manufactured parts. Kobryn and Semiatin [48] investigated powder microstructures with the changing part geometry and processing conditions, and proposed a solidification map for Ti-based materials which showed the relationship between process parameters and thermal distribution and solidification. The map could be used to estimate prior-beta grain morphology and estimate grain size, which helps researches on predicting the printing results during EBM processes. Mireles et al. [49] used an infrared camera to investigate the temperature distribution of a part in an Arcam A2 EBM system. They showed that temperature stabilization during the AM process could result in a more uniform microstructure and better mechanical properties. Furthermore, complete spatial and temporal control of thermal distribution would benefit the production of controlled microstructural architectures. But the relationships between instantaneous temperature changes and the final grain size are still remained unexplored. Raplee et al. [50] established a method to calibrate temperature profiles gathered from thermographic data. This method could monitor the emittance change between the manufactured surface and the powder bed, and the produced thermographic data is shown in Fig. 9.12. By employing this approach, the thermal gradient and solid-liquid interface velocity were predicted, and the influence of thermal conditions on the microstructure of parts was monitored. To expand the application of this method, inferred thermography also can help to measure the repeatability of printing parts, and its feasibility for detecting defects can also be explored, even for other AM processes.

Numerical modeling is an effective tool for thermal analysis during the EBM process. Körner et al. [51] developed a 2D lattice Boltzmann model to investigate the melting and solidifying processes of a powder bed irradiated by a Gaussian electron beam. However, 2D simulation cannot accurately reflect the actual printing process. Mahale [52] further proposed a 3D model with FD method and finite difference method for the EBM process with Al alloy. The electron beam was simulated as a point heat source, and the moving pattern was defined by MATLAB. The properties of temperature-dependent materials were considered, and radiation and metal powder densification were neglected. However, the neglect on radiation and metal powder densification will lead to the error to simulate the temperature distribution and material properties during EMB process, which will result in the defects, such as holes and voids as a result of overheating. Shen and Chou [30], Sahoo and Chou [53] also provided a 3D FD model for investigating the transient heat transfer in 3D printed parts, which irradiated by a moving heat source with a Gaussian volumetric distribution. The effects of powder porosity and beam size on the melt pool geometry and temperature distribution were evaluated. Nevertheless, a constant preheat temperature was assumed for the entire powder bed, while the preheat temperature would be nonuniform due to the insufficient time. Moreover, the heat convection as a result of flow in molten pool was not considered in this paper. In order to investigate the flow effect, Jamshidinia et al. [54] developed a 3D thermal-fluid flow model to study the flow and temperature distribution in the melt pool. The effect of flow convection was

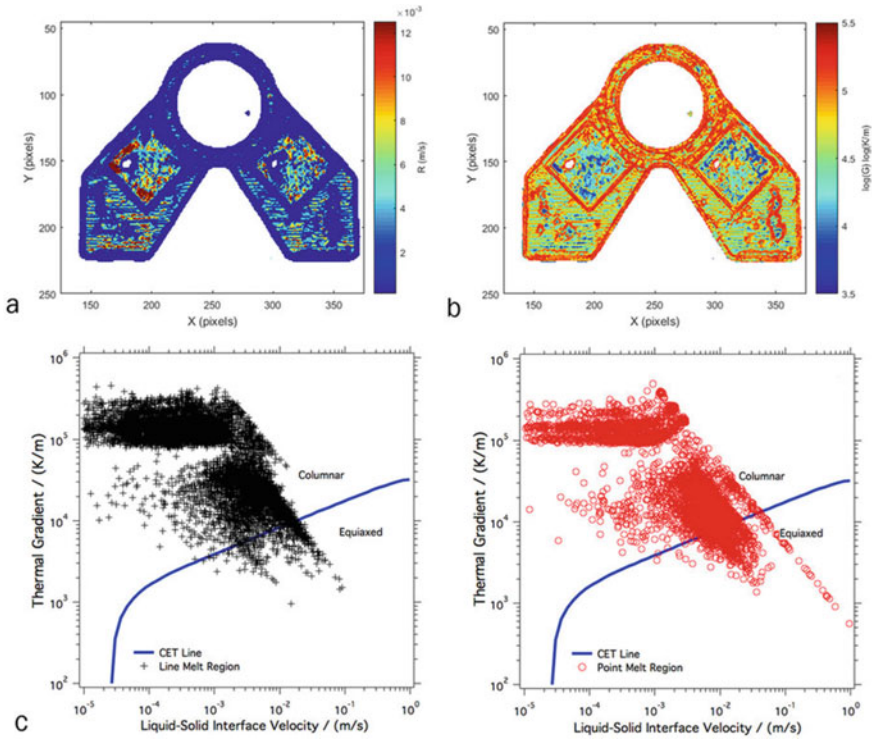


Fig. 9.12 Thermal gradients of layers **a**, interface velocity **b**, and CET curve **c** [50]

also investigated. The results showed that neglecting the convection inside the melt pool led to an error in predicting the melt pool geometry. However, a better understanding of fluid convection and temperature distribution will be gained if a CFD model can be employed and coupled with finite element method. Liu et al. [55] incorporated the linear six-node “Tri-Prism” element during transient nonlinear thermal analyses of EBM with Ti-6Al-4 V alloy. They employed the Goldak double-ellipsoid volumetric heat source and a backward difference technique, which facilitated the simulation of beam and feedstock interactions. Besides, they used the accelerated Newton–Raphson method (ANRM) to overcome the challenges in material nonlinear properties and radiation. This development discretized the geometry complexity by extruding as-obtained 2D triangle meshes, and provided a more efficient way than the isoperimetric hexahedron element method.

Furthermore, the influence of material properties was also investigated. Sahoo and Chou [53] investigated the influence of powder porosity of Ti-6Al-4 V on its thermal characteristics in the EBM. The results showed that larger powder porosity would increase the peak temperature and melt pool size, and brought a new insight into the thermal analysis for EMB process. Romano et al. [56] proposed a model including both powder melting and solidification processes to predict the geometry of melt

pool and temperature profile. This model can be used for different materials, such as titanium, steel, and aluminum powders. Comparison of the results demonstrated that titanium experienced higher local temperature and larger melt pool than steel and aluminum. This work provide a guideline for selecting parameters, which can bring the optimal local temperature with different materials.

9.5.2 Directed Energy Deposition (DED) Processes

During the DED processes, the materials are jetted into the beam and melt pool through a coaxial nozzle and then deposited onto the surface of the previous layer. The interaction between materials and beams would change the thermal properties of materials and further influence the thermal distribution of the parts. Thus, the thermal analysis of DED processes is different from that of PBF processes.

9.5.2.1 3D Laser Cladding and Welding

Several experimental studies have been conducted on the thermal analysis for 3D laser cladding and welding. Akbari et al. [57] used thermocouples to measure the temperature change due to welding speed. They also examined how welding speed affect the temperature profile and weld depth/width. Courtois et al. [58] proposed a series of dedicated experiments using thermocouple, pyrometry, and high-speed camera for validating the change of temperature distribution and fluid flow in a keyhole during laser welding. The direct thermal visualization can provide a complete validation for the numerical simulation.

Numerical simulation provides an effective way for exploring the heat transfer and thermal profile during 3D cladding process. Michaleris [59] employed both quiet and inactive element methods for minimizing calculation errors in 1D and 3D models of heat transfer analyses, and developed a hybrid quiet inactive metal deposition technique. Results showed that these methods provided similar temperature profiles, and both surface convection and radiation heat transfers were non-negligible. This method shortened the running time, and reduced the computation cost. Gouge et al. [60] simulated the heat transfer during DED cladding and investigated different convection boundary condition effects, including no convection, natural convection alone, forced convection measured by lumped capacitance experiments, forced convection data extracted from literature, and forced convection data from hot-film anemometry experiments. Quantified error analyses indicated that the three forced convection boundary conditions led to more accurate results, and that surface-dependent hot-film anemometry was the best method. This work provided a guideline on choosing suitable convection boundary condition for different cases during DED process. Rai et al. [61] reported a comprehensive model for 3D transient heat transfer and fluid flow, which considered the interaction between laser beam and flying powder particles. They also studied the keyhole mode laser welding,

and developed a quasi-steady state model for welding systems with different Peclet numbers.

Bannour et al. [62] implemented the heat source model from Goldak's method into finite volume thermal (FVM) simulations. This method was able to simulate the temperature distribution in melt pools, and study the influence of shielding gas and temperature-dependent material properties, such as absorption coefficient and thermophysical properties, on the temperature profiles and dimensions of melt pools. The melt pool geometry and temperature profile were greatly influenced by the absorption coefficient and effective thermal conductivity of powders. The shielding gas strongly affected the solidification of melt pools. Devesse et al. [63] also reported a numerical simulation method to study the interaction between powder flow and laser beam during laser cladding by generating a set of powder particle trajectories using the Monte Carlo method. This work provided an approach for investigating the effects of powder flow-laser beam interaction on thermal distribution.

9.5.2.2 LENS

LENS is different from other laser processing techniques, which uses laser beams with low power, and the low laser power reduced the size of heat-affected zone [64, 65]. Unocic and DuPont [66] studied the effect of different process parameters on the laser beam absorption by substrate material during LENS process, in which H-13 tool steel and copper powders were deposited on steel substrates. They introduced dimensionless parameters, Ry and Ch , to build a relationship between the weld size and the fabricating parameters, and the observed Γ parameter, $\dot{V} / (\eta_a \eta_m P / S)$, was correlated reciprocally with the deposition efficiency. The measured process efficiencies in this study helps to develop accurate heat flow and solidification models for LENS in the future. Hofmeister and Griffith [67], Griffith et al. [68] tried other experimental thermal analyses including *in-situ* thermal imaging of the melt pool and temperature monitoring with thermocouple. These analyses were conducted for understanding the solidification process, residual stress of the melt pool and deposition process. The study provide a guideline on how to control the laser power real time for achieving an optimal molten pool size, cooling rate, and microstructure. To provide a more accurate control during the LENS process, Marshall et al. [69, 70] employed an in-chamber infrared camera and a dual wavelength pyrometer to monitor the thermal history of manufactured parts and temperature distribution in melt pool.

The thermal inspection system and thermal images are shown in Fig. 9.13. The cooling rate and temperature gradients were measured, which helped to understand the process-property relationships during LENS. Based on this research, in the future, the IR data of previously deposited layers, and current melt pool data (superheat, average temperature, shape, etc.), would be mathematically 'extrapolated' to upcoming geometrical features so as to predict and compensate for thermal disturbances. Furthermore, due to the disadvantage that finite element incorporation

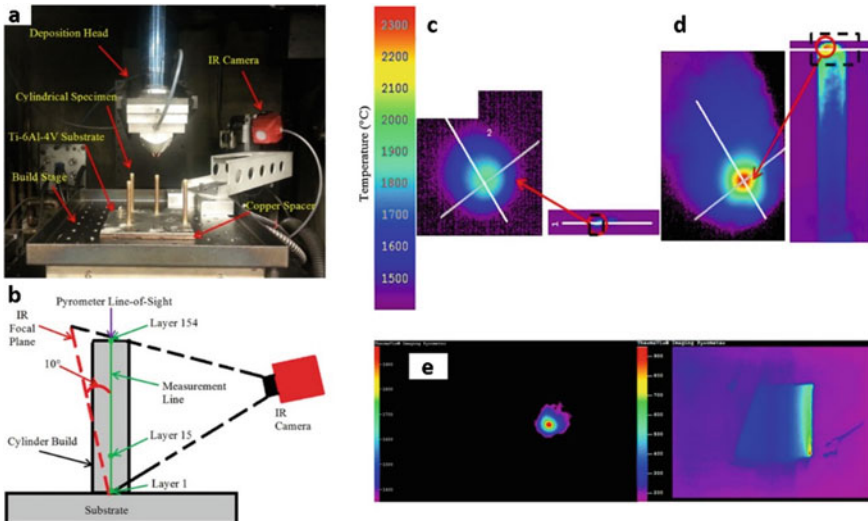


Fig. 9.13 **a** Image of the LENS printing system with IR camera. **b** Side view of the IR camera focal plane from vertical direction. Melt pool image was captured by pyrometer (left) and IR (right) simultaneously during deposition of layer 1 **c** and layer 85 **d**. **e** Pyrometer (left) and IR (right) data gathered at the end of manufacturing Ti-6Al-4 V thin wall [69, 70]

is not probable for the inherently small time scales of DED processes, the predictions would be of low fidelity, which need to be improved in the future.

Zheng et al. [71] employed an alternate-direction explicit (ADE) FD model to numerically simulate the thermal behavior during LENS process, which involved numerous reheating cycles. The thermal history of printed parts was assumed as discrete pulses in the study. They found that a rapid quenching effect appeared with a low temperature substrate, which weakened or disappeared when the deposited layer was thick enough. Manvatkar et al. [72] developed a 3D FE method to investigate the layer-wise changes in thermal cycles and melt pool geometry in a multilayer wall steel part. The prediction of temperature distributions showed good agreement with the actual deposition process. However, further investigation is required to get more reliable data on how to control heat transfer parameters for the more accurate prediction of layerwise hardness distribution.

9.5.3 Other Metallic AM Processes

9.5.3.1 WAAM

During WAAM, evaporation of low melting point elements and adsorption of atmospheric gases as a result of heat accumulation or overheating, will lead to the composition change and oxidation of printed parts, so the thermal analysis is important for the development of WAAM [13]. Wang et al. [73] studied the temperature cycles to calculate the cooling rates of different deposition layers. To protect thermoelectrode from fusing at high temperature, a Type-K thermocouple with shielding was buried through a hole and below the bottom of different deposition layers to record the temperature history, which provide a guideline for the visualization of thermal process during WAAM. It is also found that the peak temperature on the deposition layer increase with increasing deposited height as a result of greater cooling rates. Wu et al. [74] employed an infrared pyrometer to monitor the in-situ interpass temperature during gas tungsten WAAM. Couple with a high speed camera, the heat accumulation and other optical phenomena on deposition layer were evaluated to improve the bead formation, arc stability and metal transfer behavior. They found the impact of heat accumulation of manufacturing stability is significant, indicating that proper interpass temperature is crucial for the quality control of WAAM parts.

Chen et al. [75] studied the influence of weave frequency and weave amplitude on temperature distribution in butt-welded plates using 3D symmetric finite element simulation with ABAQUS. Higher weave frequency and weave amplitude decreased the peak temperature and the average temperature, due to the changed energy density and welding speed. This work can bring an insight on improving the weld bead and increasing weld efficiency. But the influence of temperature change as a result of changing weave frequency and amplitude on the welding quality is still unknown. Recently, Hejripour et al. [76] developed 3D transient thermal models to simulate simulated thermal cycles on the wall and tube during WAAM. Compared with experimental results, they found the complex thermal cycles and cooling rates greatly impact the microstructure, due to the changed maximum temperature and size of molten pool at different conditions. However, the accuracy of the simulation results is still high enough, which need to be further improved.

9.5.3.2 LOM, UAM and Other Processes

Tang et al. optimized a 3D transient heat source model by incorporating free surface evolutions of weld pool with the Level Set method during single track EBF of Ti6Al4V [77]. They found that the regular impact of molten droplet affected the heat transfer in the melt pool, and the high-frequency irradiation of the electron beam reduced its temperature gradient, while the recoil pressure has a weak impact on the fluid flow during EBF process. For LOM technology, it can produce 3D parts through the metallurgical bonding of successive layers of metal foils or films at a

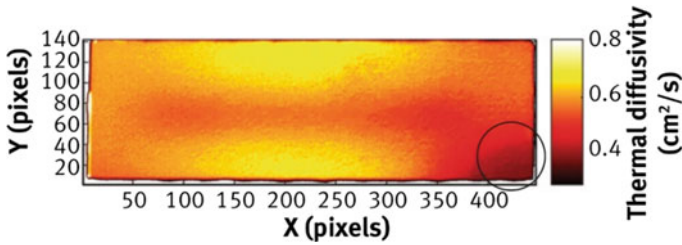


Fig. 9.14 Delamination location examined with low values in spatial thermal diffusivity mapping; the circled darker part indicates the delamination [78]

low temperature [78]. Schick et al. [79] used a FE method to predict thermal diffusion rates and derived the effective thermal diffusivity during ultrasonic additive manufacturing (UAM) process. Embedded thermocouples were used to reveal the thermal history throughout all interfaces of the UAM build, and the simultaneous heating phenomenon was initially documented, which will enable other researchers to develop more accurate models of UAM process.

Plotkowski et al. [78] also studied the spatial distribution of thermal characteristics of hybrid AA6061 + water parts during the UAM process by using infrared flash diffusivity testing. It was found that flash thermography could effectively measure the spatial dependence of thermal performance of hybrid materials, as well as estimate the local effect of manufacturing characteristics. For example, the delamination location, confirmed by stitched optical micrographs, was examined by identifying the low values in the image of spatial thermal diffusivity mapping, and the circled darker part indicated the delamination, as shown in Fig. 9.14. However, in this research UAM processing parameters was not used to tune the thermal performance of components by affecting the interlayer bonding characteristics, which need to be studied in the future. Kelly et al. [80] developed another FE method to predict the weld energy during the UAM process. They also used infrared thermography to record the welding process and to establish a relationship between input energy and mechanical properties of the manufactured aluminum part. But this work mainly focused on the thermal analysis in the steady-state weld regions, future research may include the transient temperature region and exploring the potential of employing an IR camera for monitoring and for real-time feedback control of bond strength.

9.6 Summary

AM technology is constantly growing all over the world. This expansion is expected to continue due to its ability to produce parts with anfractuious and complex internal structures with limited post-processing and no wastage of raw materials. The temperature fields during AM processes directly affect the properties and structure of the

printed parts, and determine the quality and detect. This chapter provides a comprehensive summary of thermal analysis during metallic additive manufacturing. Various metallic AM systems, including SLM, EBM, 3D laser cladding, LENS, EBF, WAAM, etc. were introduced and categorized. The commonly used energy insertions, material thermal properties, and defects of these methods were compared and the heat transfer challenges during metallic AM processes were presented. Most importantly, the computational and experimental studies of thermal analysis in different metallic AM methods were categorized and discussed, and the influence of parameters, modelling methods and thermal visualization methods were provided in the paper.

Although many efforts have been made on thermal analysis in AM processes, further studies and investigations are needed for improving the AM processes and microstructures. Some aspects to be considered for future work include the following: (1) Raw materials go through complex thermal cycles during AM. Thus, it is necessary to develop further correlations between microstructure, processing, and material properties for printed parts, and to establish a database for different AM materials. Considerable efforts have been focused on Ti-based materials, while only limited studies have considered other metals. (2) Further studies could explore the use of element birth and death in the study of thermal and residual stresses in multi-layer LM parts. (3) More effective simulation models capable of processing a large data stream are in high demand for accurate thermal analysis of AM processes. Due to the nonlinear nature of the physics-based FEA, a heavy computational burden will be presented. Therefore, adapted meshing technology should be employed for thermal analysis models. Despite the efforts made on thermal analysis models, other challenges in the AM process are still unsolved. For example, a better understanding is required regarding input energy model including laser power distribution, diffusivity of material, and energy penetration ratio. (4) More well-developed temperature monitoring systems are desired to validate the numerical modelling results, which will help to optimize the process parameters of metallic AM processes. Hence, advanced infrared cameras, thermocouples, or other sensing systems should be *in-situ* investigated in the future.

Acknowledgements The authors greatly appreciate the support from Hunan University under Research start-up fund (Grant NO. 521118010179), and ‘100 Talents Project’ of Hunan Province, U.S. Department of Energy’s Office of Energy Efficiency and Renewable Energy (EERE) under the Fuel Cell Technologies Office Award Number DE-EE0008426, National Renewable Energy Laboratory under Award DE-AC36-08GO28308, and National Energy Technology Laboratory under Award DE-FE0011585.

References

1. Levy GN, Schindel R, Kruth J-P (2003) Rapid manufacturing and rapid tooling with layer manufacturing (LM) technologies, state of the art and future perspectives. *CIRP Ann Manuf Technol* 52(2):589–609
2. Lin K, Gu D, Xi L, Yuan L, Niu S, Lv P, Ge Q (2019) Selective laser melting processing of 316L stainless steel: effect of microstructural differences along building direction on corrosion behavior. *Int J Adv Manuf Technol* 104:2669–2679
3. Yang G, Mo J, Kang Z, Dohrmann Y, List FA, Green JB, Babu SS, Zhang F-Y (2018) Fully printed and integrated electrolyzer cells with additive manufacturing for high-efficiency water splitting. *Appl Energy* 215:202–210
4. Yang G, Mo J, Kang Z, List FA, Green JB, Babu SS, Zhang F-Y (2017) Additive manufactured bipolar plate for high-efficiency hydrogen production in proton exchange membrane electrolyzer cells. *Int J Hydrogen Energy* 42(21):14734–14740
5. Yang G, Yu S, Mo J, Kang Z, Dohrmann Y, List FA, Green JB, Babu SS, Zhang F-Y (2018) Bipolar plate development with additive manufacturing and protective coating for durable and high-efficiency hydrogen production. *J Power Sources* 396:590–598
6. Mo J, Dehoff RR, Peter WH, Toops TJ, Green Jr. JB, Zhang F-Y (2016) Additive manufacturing of liquid/gas diffusion layers for low-cost and high-efficiency hydrogen production. *Int J Hydrogen Energy* 41(4):3128–3135
7. Love LJ (2015) Utility of big area additive manufacturing (BAAM) for the rapid manufacture of customized electric vehicles. Oak Ridge National Laboratory (ORNL), Manufacturing Demonstration Facility (MDF)
8. Mueller B (2012) Additive manufacturing technologies—rapid prototyping to direct digital manufacturing. *Assembly Autom* vol 32(2):385–390
9. Yang Q, Andrew JY, Simonton J, Yang G, Dohrmann Y, Kang Z, Li Y, Mo J, Zhang F-Y (2017) An inkjet-printed capacitive sensor for water level or quality monitoring: investigated theoretically and experimentally. *J Mater Chem A* 5(34):17841–17847
10. Wohlers T (2018) Wohlers report 2018: 3D printing and additive manufacturing state of the industry: annual worldwide progress report. Wohlers Associates
11. Kirchner A, Klöden B, Luft J, Weißgärber T, Kieback B (2015) Process window for electron beam melting of Ti-6Al-4V. *Powder Metall* 58(4):246–249
12. Lin J, Lv Y, Liu Y, Xu B, Sun Z, Li Z, Wu Y (2016) Microstructural evolution and mechanical properties of Ti-6Al-4V wall deposited by pulsed plasma arc additive manufacturing. *Mater Des* 102:30–40
13. Wu B, Pan Z, Ding D, Cuiuri D, Li H, Xu J, Norrish J (2018) A review of the wire arc additive manufacturing of metals: properties, defects and quality improvement. *J Manuf Process* 35:127–139
14. Childs T, Hauser C, Badrossamay M (2004) Mapping and modelling single scan track formation in direct metal selective laser melting. *CIRP Ann Manuf Technol* 53(1):191–194
15. Hauser C, Childs T, Dalgarno K, Eane R (1999) Atmospheric control during direct selective laser sintering of stainless steel 314S powder. In: *Proceedings of solid freeform fabrication symposium*, pp 265–272
16. Zäh MF, Lutzmann S (2010) Modelling and simulation of electron beam melting. *Prod Eng Res Devel* 4(1):15–23
17. Thijs L, Verhaeghe F, Craeghs T, Van Humbeeck J, Kruth J-P (2010) A study of the microstructural evolution during selective laser melting of Ti-6Al-4V. *Acta Mater* 58(9):3303–3312
18. Kahnert M, Lutzmann S, Zaeh M (2007) Layer formations in electron beam sintering. In: *Proceedings of the 2007 international solid freeform fabrication symposium*, pp 88–99
19. Sames WJ, List F, Pannala S, Dehoff RR, Babu SS (2016) The metallurgy and processing science of metal additive manufacturing. *Int Mater Rev* 61(5):315–360
20. Carter LN, Attallah MM, Reed RC (2012) Laser powder bed fabrication of nickel-base superalloys: influence of parameters; characterisation, quantification and mitigation of cracking. *Superalloys* 2012:577–586

21. Wang D, Yang Y, Yi Z, Su X (2013) Research on the fabricating quality optimization of the overhanging surface in SLM process. *Int J Adv Manuf Technol* 65(9–12):1471–1484
22. Roberts I, Wang C, Esterlein R, Stanford M, Mynors D (2009) A three-dimensional finite element analysis of the temperature field during laser melting of metal powders in additive layer manufacturing. *Int J Mach Tools Manuf* 49(12):916–923
23. Fu G, Gu J, Lourenco MI, Duan M, Estefen SF (2015) Parameter determination of double-ellipsoidal heat source model and its application in the multi-pass welding process. *Ships Offshore Struct* 10(2):204–217
24. Yan W, Smith J, Ge W, Lin F, Liu WK (2015) Multiscale modeling of electron beam and substrate interaction: a new heat source model. *Comput Mech* 56(2):265–276
25. Tong Z, Zhentai Z, Rui Z (2013) A dynamic welding heat source model in pulsed current gas tungsten arc welding. *J Mater Process Technol* 213(12):2329–2338
26. Fachinotti VD, Anca AA, Cardona A (2011) Analytical solutions of the thermal field induced by moving double-ellipsoidal and double-elliptical heat sources in a semi-infinite body. *Int J Numer Meth Biomed Eng* 27(4):595–607
27. Ready J (1971) *Effects of high-power laser radiation*. Academic Press Inc., New York
28. Schuöcker D (1998) *Handbook of the eurolaser academy, vol 2*. Springer Science & Business Media
29. Cheng B, Price S, Lydon J, Cooper K, Chou K (2014) On process temperature in powder-bed electron beam additive manufacturing: model development and validation. *J Manuf Sci Eng* 136(6):061018
30. Shen N, Chou K (2012) Thermal modeling of electron beam additive manufacturing process: powder sintering effects. In: *International manufacturing science and engineering conference collocated with the 40th North American manufacturing research conference and in participation with the international conference on tribology materials and processing*. American Society of Mechanical Engineers 2012 (ASME 2012), pp 287–295
31. Gusarov A, Yadroitsev I, Bertrand P, Smurov I (2007) Heat transfer modelling and stability analysis of selective laser melting. *Appl Surf Sci* 254(4):975–979
32. Benda J (1994) Temperature controlled selective laser sintering. In: *Proceedings of the solid freeform fabrication symposium, DTIC Document*, pp 277–284
33. Kruth J-P, Mercelis P, Van Vaerenbergh J, Craeghs T (2007) Feedback control of selective laser melting. In: *Proceedings of the 3rd international conference on advanced research in virtual and rapid prototyping*, pp 521–527
34. Islam M, Purtonen T, Piili H, Salminen A, Nyrrhilä O (2013) Temperature profile and imaging analysis of laser additive manufacturing of stainless steel. *Phys Procedia* 41:835–842
35. Shishkovsky I, Scherbakov V, Morozov Y, Kuznetsov M, Parkin I (2007) Surface laser sintering of exothermic powder compositions: a thermal and SEM/EDX study. *J Therm Anal Calorim* 91(2):427–436
36. Doubenskaia M, Pavlov M, Chivel Y (2010) Optical system for on-line monitoring and temperature control in selective laser melting technology. *Key Eng Mater* 437:458–461. *Trans Tech Publ*
37. Yuan P, Gu D (2015) Molten pool behaviour and its physical mechanism during selective laser melting of TiC/AlSi10Mg nanocomposites: simulation and experiments. *J Phys D Appl Phys* 48(3):035303
38. Zeng K, Pal D, Stucker B (2012) A review of thermal analysis methods in Laser Sintering and Selective Laser Melting. In: *Proceedings of solid freeform fabrication symposium, Austin, TX*
39. Williams JD, Deckard CR (1998) Advances in modeling the effects of selected parameters on the SLS process. *Rapid Prototyping J* 4(2):90–100
40. Matsumoto M, Shiomi M, Osakada K, Abe F (2002) Finite element analysis of single layer forming on metallic powder bed in rapid prototyping by selective laser processing. *Int J Mach Tools Manuf* 42(1):61–67
41. Kolossov S, Boillat E, Glardon R, Fischer P, Locher M (2004) 3D FE simulation for temperature evolution in the selective laser sintering process. *Int J Mach Tools Manuf* 44(2):117–123

42. Zeng K, Pal D, Gong H, Patil N, Stucker B (2015) Comparison of 3DSIM thermal modelling of selective laser melting using new dynamic meshing method to ANSYS. *Mater Sci Technol* 31(8):945–956
43. Yang J, Sun S, Brandt M, Yan W (2010) Experimental investigation and 3D finite element prediction of the heat affected zone during laser assisted machining of Ti6Al4V alloy. *J Mater Process Technol* 210(15):2215–2222
44. Li C-J, Tsai T-W, Tseng C-C (2016) Numerical simulation for heat and mass transfer during selective laser melting of titanium alloys powder. *Phys Procedia* 83:1444–1449
45. Gu D, Rao X, Dai D, Ma C, Xi L, Lin K (2019) Laser additive manufacturing of carbon nanotubes (CNTs) reinforced aluminum matrix nanocomposites: processing optimization, microstructure evolution and mechanical properties. *Addit Manuf* 29:100801
46. Panwisawas C, Perumal B, Ward RM, Turner N, Turner RP, Brooks JW, Basoalto HC (2017) Keyhole formation and thermal fluid flow-induced porosity during laser fusion welding in titanium alloys: experimental and modelling. *Acta Mater* 126:251–263
47. Panwisawas C, Qiu C, Anderson MJ, Sovani Y, Turner RP, Attallah MM, Brooks JW, Basoalto HC (2017) Mesoscale modelling of selective laser melting: thermal fluid dynamics and microstructural evolution. *Comput Mater Sci* 126:479–490
48. Kobryn P, Semiatin S (2003) Microstructure and texture evolution during solidification processing of Ti–6Al–4V. *J Mater Process Technol* 135(2):330–339
49. Mireles J, Terrazas C, Medina F, Wicker R, Paso E (2013) Automatic feedback control in electron beam melting using infrared thermography. In: *Proceedings of the solid freeform fabrication symposium*
50. Raplee J, Plotkowski A, Kirka MM, Dinwiddie R, Okello A, Dehoff RR, Babu SS (2017) Thermographic microstructure monitoring in electron beam additive manufacturing. *Sci Rep* 7:43554
51. Körner C, Attar E, Heinel P (2011) Mesoscopic simulation of selective beam melting processes. *J Mater Process Technol* 211(6):978–987
52. Mahale TR (2009) Electron beam melting of advanced materials and structures
53. Sahoo S, Chou K (2016) Phase-field simulation of microstructure evolution of Ti–6Al–4V in electron beam additive manufacturing process. *Addit Manuf* 9:14–24
54. Jamshidinia M, Kong F, Kovacevic R (2013) Numerical modeling of heat distribution in the electron beam melting of Ti-6Al-4V. *J Manuf Sci Eng* 135(6):061010
55. Liu P, Cui X, Deng J, Li S, Li Z, Chen L (2019) Investigation of thermal responses during metallic additive manufacturing using a “Tri-Prism” finite element method. *Int J Therm Sci* 136:217–229
56. Romano J, Ladani L, Razmi J, Sadowski M (2015) Temperature distribution and melt geometry in laser and electron-beam melting processes—a comparison among common materials. *Addit Manuf* 8:1–11
57. Akbari M, Saedodin S, Toghraie D, Shoja-Razavi R, Kowsari F (2014) Experimental and numerical investigation of temperature distribution and melt pool geometry during pulsed laser welding of Ti6Al4V alloy. *Opt Laser Technol* 59:52–59
58. Courtois M, Carin M, Le Masson P, Gaied S, Balabane M (2016) Guidelines in the experimental validation of a 3D heat and fluid flow model of keyhole laser welding. *J Phys D Appl Phys* 49(15):155503
59. Michaleris P (2014) Modeling metal deposition in heat transfer analyses of additive manufacturing processes. *Finite Elem Anal Des* 86:51–60
60. Gouge MF, Heigel JC, Michaleris P, Palmer TA (2015) Modeling forced convection in the thermal simulation of laser cladding processes. *Int J Adv Manuf Technol* 79(1–4):307–320
61. Rai R, Kelly S, Martukanitz R, DebRoy T (2008) A convective heat-transfer model for partial and full penetration keyhole mode laser welding of a structural steel. *Metall Mater Trans A* 39(1):98–112
62. Bannour S, Abderrazak K, Mhiri H, Le Palec G (2012) Effects of temperature-dependent material properties and shielding gas on molten pool formation during continuous laser welding of AZ91 magnesium alloy. *Opt Laser Technol* 44(8):2459–2468

63. Devesse W, De Baere D, Guillaume P (2015) Modeling of laser beam and powder flow interaction in laser cladding using ray-tracing. *J Laser Appl* 27(S2):S29208
64. Palčić I, Balazić M, Milfelner M, Buchmeister B (2009) Potential of laser engineered net shaping (LENS) technology. *Mater Manuf Processes* 24(7–8):750–753
65. Neela V, De A (2009) Three-dimensional heat transfer analysis of LENS TM process using finite element method. *Int J Adv Manuf Technol* 45(9–10):935
66. Unocic R, DuPont J (2004) Process efficiency measurements in the laser engineered net shaping process. *Metall Mater Trans B* 35(1):143–152
67. Hofmeister W, Griffith M (2001) Solidification in direct metal deposition by LENS processing. *JOM* 53(9):30–34
68. Griffith M, Schlienger M, Harwell L, Oliver M, Baldwin M, Ensz M, Essien M, Brooks J, Robino C, Smugeresky J et al (1999) Understanding thermal behavior in the LENS process. *Mater Des* 20(2):107–113
69. Marshall GJ, Young WJ, Thompson SM, Shamsaei N, Daniewicz SR, Shao S (2016) Understanding the microstructure formation of Ti-6Al-4V during direct laser deposition via in-situ thermal monitoring. *JOM* 68(3):778–790
70. Marshall GJ, Thompson SM, Shamsaei N (2016) Data indicating temperature response of Ti-6Al-4V thin-walled structure during its additive manufacture via Laser Engineered Net Shaping. *Data Brief* 7:697–703
71. Zheng B, Zhou Y, Smugeresky J, Schoenung J, Lavernia E (2008) Thermal behavior and microstructural evolution during laser deposition with laser-engineered net shaping: Part I. Numerical calculations. *Metall Mater Trans A* 39(9):2228–2236
72. Manvatkar V, Gokhale A, Reddy GJ, Venkataramana A, De A (2011) Estimation of melt pool dimensions, thermal cycle, and hardness distribution in the laser-engineered net shaping process of austenitic stainless steel. *Metall Mater Trans A* 42(13):4080–4087
73. Wang J, Sun Q, Wang H, Liu J, Feng J (2016) Effect of location on microstructure and mechanical properties of additive layer manufactured Inconel 625 using gas tungsten arc welding. *Mater Sci Eng A* 676:395–405
74. Wu B, Ding D, Pan Z, Cuiuri D, Li H, Han J, Fei Z (2017) Effects of heat accumulation on the arc characteristics and metal transfer behavior in Wire Arc Additive Manufacturing of Ti6Al4V. *J Mater Process Technol* 250:304–312
75. Chen Y, He Y, Chen H, Zhang H, Chen S (2014) Effect of weave frequency and amplitude on temperature field in weaving welding process. *Int J Adv Manuf Technol* 75(5–8):803–813
76. Hejrípour F, Binesh F, Hebel M, Aidun DK (2019) Thermal modeling and characterization of wire arc additive manufactured duplex stainless steel. *J Mater Process Technol* 272:58–71
77. Tang Q, Pang S, Chen B, Suo H, Zhou J (2014) A three dimensional transient model for heat transfer and fluid flow of weld pool during electron beam freeform fabrication of Ti-6-Al-4-V alloy. *Int J Heat Mass Transf* 78:203–215
78. Plotkowski A, Dinwiddie R, Babu S (2018) Thermal Design of Hybrid Materials Produced via Ultrasonic Additive Manufacturing. *Mater Eval* 76(4):503–513
79. Schick D, Babu SS, Foster DR, Dapino M, Short M, Lippold JC (2011) Transient thermal response in ultrasonic additive manufacturing of aluminum 3003. *Rapid Prototyping J* 17(5):369–379
80. Kelly GS, Just MS, Advani SG, Gillespie JW (2014) Energy and bond strength development during ultrasonic consolidation. *J Mater Process Technol* 214(8):1665–1672

Part III
Environmental and Spectroscopic
Application

Chapter 10

Single Atom Catalysts for Environmental Remediation



Jieming Yuan and Xingmao Ma

Abstract Single-atom catalysts (SACs) represent an advanced class of catalysts that contain well-dispersed metal atoms on a support material. Recent studies have demonstrated the enormous potential of SACs in environmental applications. In addition to the metal atoms, the supporting material also plays an important role in the catalytic properties of SACs. The most commonly employed support material for SACs in environmental applications is the nitrogen-doped carbon due to its active chemo-electrical property, adjustable surface functional groups, porous structure, and eco-friendly nature. In environmental applications, SACs are mostly used as an activator of hydrogen peroxide, peroxymonosulfate and peroxydisulfate, extending the reaction pH limitation from less than 4.0 to a wider range of 4.0–10.0 and generating highly reactive radicals. This chapter briefly discussed the common characterization techniques of SACs, the role of supporting materials and focused primarily on the activation mechanisms of common oxidants by SACs. At the end, research gaps and future needs are discussed. Overall, the unique properties and exceptional catalytic performance of SACs offer great potential for addressing the persistent environmental challenges that threaten our planet.

Keywords Single-atom catalyst · Organic contaminants · Environmental remediation · Carbon support

10.1 Introduction

The rapid progress in nanotechnology has spurred extensive applications of metal-based nanomaterials in diverse fields such as battery technology [57], sensing [2], biomedicine [12], and catalysis [14]. However, the tendency of metal nanoparticles to aggregate owing to the increased surface energy at the nano-scale [55] has impeded their broad uses and increased their cost, particularly for precious metals

J. Yuan · X. Ma (✉)

Zachry Department of Civil and Environmental Engineering, Texas A&M University, College Station, TX 77843, USA

e-mail: xma@civil.tamu.edu

such as platinum, gold, silver, palladium, and ruthenium utilized in catalysts [59]. Consequently, considerable endeavors have been made over the last two decades to decrease the size of metal particles in catalysts from nanoparticles to single atoms [54]. The first thorough investigation of single-atom catalysts (SAC) can be traced back to 2011, when an atomically dispersed Pt/FeOx catalyst was synthesized to oxidize CO and showed a 300% higher efficiency than the bulk Pt [48]. SACs are catalysts that contain well-dispersed, catalytically active single-atom sites that are stabilized by a solid material. The catalytic process of SAC involves each metal atom in the catalyst, leading to 100% metal utilization in theory. Thus, the success of SAC can lower the cost of metal-based nanocatalysts by improving the usage of incorporated metal while reducing the risk of metal ion leakage that can negatively affect human and ecological health [12]. Most studies on SACs focus on CO oxidation, hydrogenation, and CO₂ reduction [7, 33, 50]. For instance, a FeOx-supported platinum single-atom catalyst was shown to be 20 times more efficient in hydrogenation than the best reported platinum-based catalyst [72]. A manganese dioxide-supported silver single-atom catalyst achieved 95.7% Faradic efficiency at -0.85 V vs. RHE, resulting in stable electrochemical CO₂ reduction [85]. Recent studies have demonstrated that SACs have great potential in removing contaminants from water [4, 36, 87]. For example, a carbon nanotube-supported Fe SAC was reported to achieve 100% bisphenol A degradation via the activation of peroxymonosulfate (PMS) in one minute [47], while a nitrogen-rich carbon-supported Fe SAC achieved over five times faster phenol degradation than the Fe nano-catalyst via the activation of PMS [87].

While SACs have attracted a lot of attentions and many solid reviews have been available, they mostly focus on oxygen reduction reaction, hydrogenation and CO₂ reduction [7, 33, 50]. This book chapter aims to fill the gap by summarizing the opportunities and potential challenges of applying SACs in environmental applications. Because reviews discussing the synthesis and characterization of SAC [24, 34] have been available [7, 16, 53], this chapter will focus on the applications of SACs in water treatment. A brief introduction of characterization technology will be given, followed by a discussion on the importance of supporting materials, and the applications and mechanisms of SAC in different contaminant degradation processes. The challenges and further research need of SAC will be discussed toward the end of this work.

10.2 Single Atom Catalyst Characterization

10.2.1 *High-Angle Annular Dark-Field Scanning Transmission Electron Microscope (HAADF-STEM)*

Transmission electron microscopy (TEM) is a common technique for material characterization [56]. However, the conventional TEM is not capable of visually detecting the morphology of the single-atom sites in the catalyst due to the resolution limitation. With the rapid advancement of TEM technology in the last decades, high-angle annular dark-field scanning transmission electron microscope (HAADF-STEM) was developed based on the atomic number contrast between metals and the support materials [34]. Recently [70], a carbon black based single-atom cobalt catalyst (CoN₄-CB) was synthesized and characterized with HAADF-STEM. As shown in Fig. 10.1a, the bright spots representing metal atoms can be clearly identified in the image. Energy dispersive spectroscopy (EDS) affiliated with TEM is typically used for element mapping. Figure 10.1b shows the ultra-fine distribution of N, C, and Co atoms in the catalyst [70]. Similar images were obtained by many recent single atom studies via HAADF-STEM [51, 84, 85]. However, the development of a higher resolution HAADF-STEM is still an urgent need in this field to identify every single atom active site.

10.2.2 *X-ray Adsorption Spectroscopy (XAS)*

XAS provides more direct information on the chemical structure and coordination environment of SACs. XAS collects the information of transmitted X-ray and the signal of scattered electrons to generate a XAS spectrum [53]. Based on the spectral region, XAS can be divided into X-ray adsorption near-edge structure spectroscopy (XANES) within the range of 30–50 eV and extended X-ray adsorption fine structure spectroscopy (EXAFS) in the range of 50–1000 eV [80]. XANES contains the information of chemical state of the targeted metal element as shown in Fig. 10.2a, indicating that Fe in the SAC has a valance state close to Fe₂O₃. EXAFS is capable of providing information on the coordination conditions of metal atoms in SAC, which includes the number of different coordinating species, binding energy, bond length, bond angle and so on [6, 80]. XAS can accurately capture the signal of the backscattered atoms based on the path-length criterion [6]. However, it is difficult to distinguish the backscattered atoms with the same path-length. The assistance of wavelet transform (WT) is essential to identify the specific backscattered atoms based on the information of the k position [54]. Therefore, with the help of WT, FT (Fourier transformed) EXAFS can reveal the metal coordination environment, and a further fitting can reveal the coordination structure of the targeted element as shown in Fig. 10.2b, c.

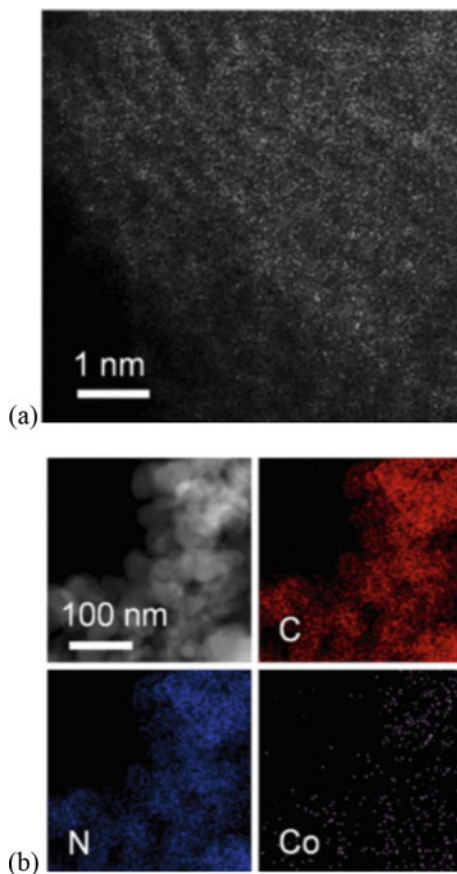


Fig. 10.1 a HAADF-STEM image of CoN₄-CB, b elemental mapping of CoN₄-CB [70]

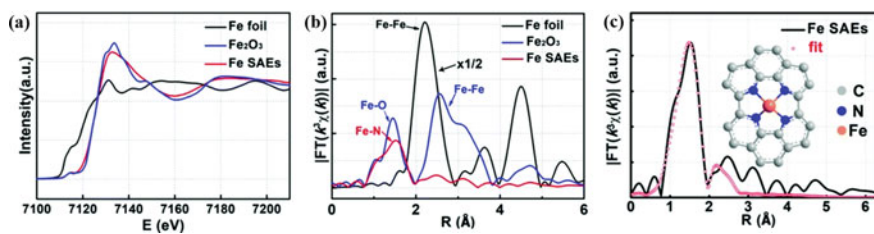


Fig. 10.2 a Normalized Fe K-edge XANES spectrum of Fe foil, Fe₂O₃, and Fe SAC b Fourier transformed EXAFS of Fe foil, Fe₂O₃, and Fe SAC c EXAFS fitting results of Fe SAC data [86]

10.2.3 X-ray Photoelectron Spectroscopy (XPS)

XPS is a widely used characterization technique to determine the elemental composition of SAC as well as their surface electron structure [8, 71]. XPS cannot provide direct evidence on the formation of single-atom metal active sites. However, it can measure the elemental composition of metal single atom catalysts in the parts per thousand range, revealing information on the chemical state and electronic state of metals in the catalyst that can be used to gain insight into the electronic and coordination environment [34].

10.2.4 Other Techniques

In addition to the above-mentioned three techniques, new characterization techniques are also emerging. For example, the *in-situ* Fourier transform infrared spectroscopy (FTIR) has been used to verify the existence of single-atom sites in carbon-based catalyst. The unchanged band position of adsorbed CO on the catalyst by *in-situ* FTIR analysis after the CO pressure increase indicates the weak interaction between CO molecules and isolated single-atom sites [48]. Therefore, the band position of CO is used as an indicator of the presence of single metal atoms. Due to the importance of metal loading rate, which affects the active metal sites on SACs, inductively coupled plasma (ICP) is a powerful tool to measure the total content of metals in the single atom metal catalyst [64]. Other more traditional methods such as X-ray diffraction (XRD), Raman spectroscopy, scanning electron microscope (SEM) have also been used in the literature for SAC characterization, however, outputs from these techniques are often used as supporting evidence of the formation of SACs [54].

10.3 Supporting Materials of SACs

The composition of SAC support is essential for the performance of SACs. Various materials such as TiO₂, FeO_x, ZnO, carbon nanotubes, graphitic nitrogen, biochar, and polymer have been used as supporting materials, and they can be mainly divided into metal-based and carbon-based [23, 25, 48]. Metal-based support materials for SACs offer several advantages such as the high thermal stability, mechanical strength, and catalytic activity [28]. However, the controlled dispersion of metal atoms on metal-based support materials can be a significant challenge, leading to the formation of metal clusters which reduce the catalytic activity and selectivity of SACs. Furthermore, metal-based support materials can be relatively expensive and the metal ion leaching problem could add new pollution to a water system, which limits their application in environmental processes. On the other hand, carbon-based materials have

high specific surface area, porosity and tunable surface, excellent electrical conductivity, and low cost [16]. Carbon-based SAC supports are highly tunable and other elements can be easily doped into the carbon structure to greatly enhance the activity of the metal single atom sites as a result of the increased impact of coordination environment on the behavior of the metal atom [66, 67]. Among all carbon-based support materials, nitrogen-doped carbon (N-doped carbon) was very popular because of the highly stable metal-nitrogen-carbon bond and the active chemoelectrical nature of N-doped carbon [7, 13]. The N-doped carbon have higher metal loading and stability than pure carbon materials because the valance shell of N atom has one more electron than C atom and it provides higher binding energy between N and metal atoms [29]. Additionally, N-doped carbon has an excellent chemoelectrical property comparable to the expensive platinum (Pt) based electrode in oxygen reduction reaction [17]. N-doping could also alter the local coordination environment of the metal single-atom sites, and greatly enhance the oxidization efficiency of carbon-based SACs [45, 46]. Thus, the incorporation of SAC into N-doped carbon becomes the most popular combination for carbon-based SACs. Additional modification of N-doped carbon support can further enhance the catalytic performance of produced SACs. For example, the extra doping of oxygen into N-doped carbon support boosted the catalytic efficiency of Fe SAC on nitrogen-rich carbon by 5.13 times [87]. In addition, fluorine doping on the N-doped carbon was reported to increase the charge density of the nearby pyridinic N, and an outstanding CO evolution rate of $1,146 \text{ mmol g}^{-1} \text{ h}^{-1}$ was achieved by the produced nickel (Ni) SAC [18]. Metal organic framework (MOF) as a special category of N-doped carbon has been extensively applied in environmental applications, and the combination of SACs and MOFs can better exert their catalytic effects [30, 74]. The well-organized structure of MOF makes it an excellent support material for the ultrafine distribution of single atoms, and the highly designable structure can further provide a precise control of the binding location for the single-atom sties [83]. However, the cost of MOF is higher than traditional carbon-based materials, making it less cost-effective. Silica (SiO_2) is also employed as a support material for SACs because of its remarkable thermal stability, enabling SACs to perform well in harsh environments [44]. However, the research on silica-based SACs is still limited. A better understanding of the fundamental interaction between single-atom sites and the silica support is needed.

10.4 Application and Mechanisms

10.4.1 Photocatalysis

Recent efforts in photocatalysis primarily focused on exploring advanced materials that can enhance the efficiency of photocatalysis by higher light harvesting and greater charge separation. SACs provide a promising solution to the future development in this field and the photocatalytic degradation of organic contaminants by

SAC is gaining increased attention in recent years [35, 52, 67]. To be photocatalytic, SACs usually require a semiconductor support with the semiconductor functioning as a light harvesting unit and single-atom sites providing unique electronic structures to boost the photocatalytic process [13]. The natural sunlight consists of 52% infrared light, 43% visible light, and 5% UV light. Great efforts have been made to design catalysts that can utilize visible light or even infrared light to achieve a better light utilization [60]. The incorporation of SAC into a light-harvesting support can modify the energy band structure that shifts the catalyst from UV-responsive to visible light-responsive [68]. For example, the coordination of single-atom Pt into $g\text{-C}_3\text{N}_4$ resulted in a visible-light active photocatalyst, and the light absorption range was expanded from $\lambda < 460$ nm for bare $g\text{-C}_3\text{N}_4$ to the range of 460–900 nm for Pt SAC on $g\text{-C}_3\text{N}_4$ [30]. Similar result was reported for an Ag SAC on $g\text{-C}_3\text{N}_4$ support, and a 100% bisphenol A degradation was obtained under visible light irradiation within 60 min [65]. The metal single-atom site can enhance the separation of photo-generated electrons and holes at the interface of the semiconductor. Metal single-atom sites that are very chemoelectrical active can induce a much faster transfer of the photogenerated electrons to the targeted contaminants to reduce the electron/hole recombination [68, 77]. Photoluminescence spectroscopy was used to monitor the separation of photogenerated electrons and holes in a Pd SAC on $g\text{-C}_3\text{N}_4$, and a much lower charge recombination rate was found with Pd SAC/ $g\text{-C}_3\text{N}_4$ than the $g\text{-C}_3\text{N}_4$ only [5]. Furthermore, the introduction of single-atom sites into semiconductor can also modify the structure of the catalyst to achieve a faster electron transfer. The local light-harvesting units in $g\text{-C}_3\text{N}_4$ was found to be enhanced by the incorporation of single atom Cu into the catalyst, leading to the decrease of the charge transfer distance between light-harvesting units and thus enhanced photocatalytic activity [27]. The mechanisms of SAC enhanced photocatalysis were summarized as Fig. 10.3.

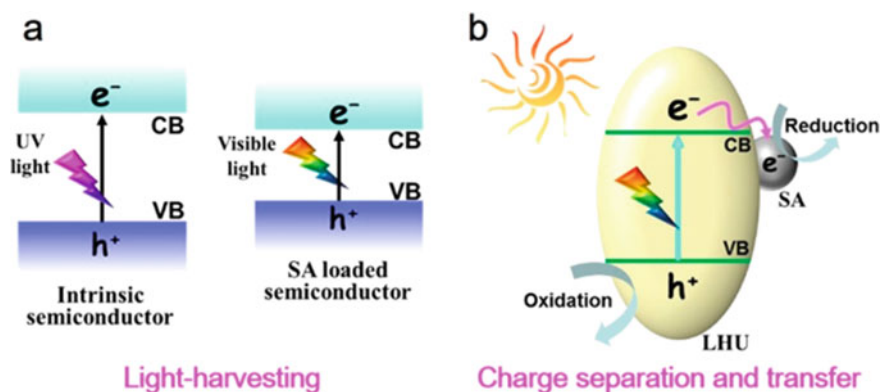


Fig. 10.3 Schematic illustration for the roles of single-atoms in enhancing the **a** light-harvesting, **b** charge separation and transfer [13]

10.4.2 Activation of H_2O_2

Hydrogen peroxide (H_2O_2) is a powerful oxidizing agent which is commonly used in environmental remediation [15, 41]. For example, H_2O_2 could be activated by the Fenton and Fenton-like reaction to produce highly reactive $\cdot OH$ with a redox potential of +2.8 V (vs NHE) [40] to react rapidly and non-selectively with organic contaminants [76]. Unfortunately, the classic activation of H_2O_2 via Fenton reaction still suffers from many drawbacks including the requirement of low pH < 4 [61], and the leaching of iron ions into the water system [42].

SACs outperform traditional metal-loaded catalysts in the activation of H_2O_2 because of the abundant active single-atom sites, relative stable structure with less metal leaching, and a wider pH window for the activation [79]. Due to the aggregation of traditional metal nanoparticles, only a small amount of active metal sites is exposed to H_2O_2 [76]. In contrast, SACs can greatly enhance the activation of H_2O_2 to generate $\cdot OH$ thanks to the utmost utilization of ultrafine single-atom metal sites [21]. For example, a Copper (Cu) SAC on g- C_3N_4 was applied to active H_2O_2 , leading to a 99.97% degradation of rhodamine B (RhB) in 5 min while less than 40% of RhB was removed by nano Cu-containing catalysts. [76]. The SAC could also result in an enhanced H_2O_2 activation via stronger absorption of H_2O_2 onto the single-atom sites. The M-N_x sites was reported to have a strong free binding energy with H_2O_2 for a rapid adsorption [79] And similar result was reported by another study that synthesized Fe, Co, Ni, Cu SAC on N-doped carbon, and found that Fe-N₄ has the fastest $\cdot OH$ generation from H_2O_2 activation because of the highest d-band center value [11]. Furthermore, the introduction of SAC into H_2O_2 activation also extend pH limitation of the Fenton/Fenton-like reaction to a boarder pH range [61]. The SAC Cu synthesized on mesoporous silica support was reported to have an efficient activation of H_2O_2 to generate $\cdot OH$ in a wider pH range of 4.0–7.0. Additionally, the immobilization of single-atom Fe on the combination of graphitized carbon and g- C_3N_4 was found to have an excellent H_2O_2 activation in a wide pH range of 4.0–10.0 [37]. However, the field of SACs catalyzing H_2O_2 has been relatively under-studied, and it is crucial to further elucidate the catalytic mechanisms of H_2O_2 activation by SACs.

10.4.3 Activation of Peroxymonosulfate (PMS)

Peroxymonosulfate (PMS) has been extensively researched for its ability to generate free radicals, specifically $SO_4^{\cdot -}$, which is effective in breaking down organic contaminants [38, 43]. The $SO_4^{\cdot -}$ has a higher redox potential (+2.5–3.1 V vs NHE) and a longer half-life (~40 μs) than $\cdot OH$ with a potential of +1.8–2.7 V (vs NHE) and half-life of 1–100 ns [10, 69]. In addition, the activation of PMS is less pH sensitive and can proceed in a wider pH range of 2.0–8.0

[54]. Thus, the application of $\text{SO}_4^{\bullet-}$ -based reaction is more suitable in various environmental conditions. The recent introduction of SACs into the activation of PMS has garnered significant attention in the field of environmental remediation [39, 78]. SAC showed a greatly enhanced PMS activation than metal nano-particle catalysts. For instance, 33 times higher phenol degradation was observed via the PMS activation by Fe-SAC than Fe_3O_4 nanoparticles [32]. Similar conclusion was drawn in another study that 100% removal of Orange II was achieved in 60 min via PMS activation by Fe-SAC while only 29.5% removal was obtained by Fe_3O_4 nanoparticle and PMS [82]. The activation of PMS by SAC can be mainly divided into two pathways: radical-based and non-radical based pathways. Firstly, the PMS can be activated by SACs to generate radicals, predominantly $\text{SO}_4^{\bullet-}$ and $\cdot\text{OH}$ [19, 63, 75, 84]. The generation of these radicals was via the activation of PMS by a carbon supported cobalt SAC for the fast degradation of atrazine, nitrobenzene, bisphenol A, phenol and 4-chlorophenol [63]. A Cu-SAC on reduced graphene oxide system was also found to be highly effective in degrading various antibiotics including sulfafurazole, sulfamethoxazole, and meropenem in a wide range of pH, and $\text{SO}_4^{\bullet-}$ was found as the dominant reactive species [6]. It also exhibited a remarkable mineralization capacity, with a removal efficiency of up to 99% of total organic carbon after 120 min of reaction [6]. The generation of singlet oxygen ($^1\text{O}_2$) and the direct electron transfer are important non-radical pathways of PMS activation [45, 49, 78]. $^1\text{O}_2$ is highly reactive with a redox potential of +2.2 V vs NHE [88]. A graphitic carbon nitride (g- C_3N_4) supported Fe single-atom catalyst with 11.2 wt% Fe loading was reported to have a highly selective generation of 100% $^1\text{O}_2$ by activating PMS and achieved a first order rate constant of 1.43 min^{-1} in p-chlorophenol degradation [84].

The direct electron transfer is another main degradation mechanism that a PMS-SAC complex forms upon the adsorption of PMS on SAC, and the further contact between this complex and targeted contaminant induces the direct electron transfer between them [45, 73, 78]. Direct electron transfer was identified as the dominant mechanism for the degradation of naproxen by a SA Co on N-doped carbon, while the generation of reactive oxygen species was confirmed as a minor pathway as Fig. 10.4 shows. Similar result was found in the chloroquine phosphate degradation by PMS activated by a biomass carbon-based cobalt single-atom catalyst, and 98% chloroquine phosphate was degraded in 30 min [46].

10.4.4 Activation of Perdisulfate (PDS) and Sulphite

Peroxydisulphate (PDS) is another persulfate compound with a structure that includes a peroxide O–O bond length of 1.322 Å, providing higher stability compared to the asymmetric PMS. The distinctive structures of PDS and PMS contribute to differences in their activation mechanisms leading to a more active PMS activation by a wide range of carbonaceous materials and transition metal catalysts [62]. However, PDS has a lower bond dissociation energy of 92 kJ mol^{-1} compared with 377 kJ mol^{-1}

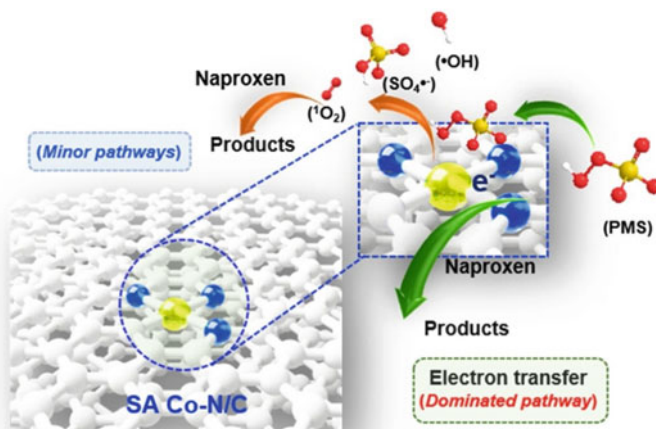


Fig. 10.4 The activation mechanism of PMS by SA Co on N-doped carbon [49]

of PMS [3], resulting in an easier activation of PDS by energy transfer [54]. Recent advancements in catalysts have aimed to enhance PDS activation, with SACs outperforming conventional catalysts due to their highly dense and reactive single atom metal sites [20]. The activation of PDS is similar to PMS in terms of the reactive radical species. A cobalt SAC stabilized on N-doped carbon effectively activated PDS to generate $\text{SO}_4^{\bullet-}$ to achieve a high specific activity of $0.067 \text{ Lmin}^{-1} \text{ m}^{-2}$ for the degradation of bisphenol A [26]. Notably, instead of the activation of PDS by SAC to oxidize contaminants directly, PDS can oxidize the metals in SAC to generate high valence metals to react with pollutants. One study found the generation of Fe (V) in PDS activation by Fe (III) SAC on N-doped carbon [22]. The Fe (III) site was oxidized by the PDS via a two-electron abstraction to Fe (V) as a metastable oxidant (Fig. 10.5), which enables selective 97% degradation of 2,4-dichlorophenol in 90 min [22].

Sulphite has gained recognition as a more environmentally friendly alternative to PMS and PDS in the production of oxysulphur radicals such as $\text{SO}_3^{\bullet-}$, $\text{SO}_4^{\bullet-}$,

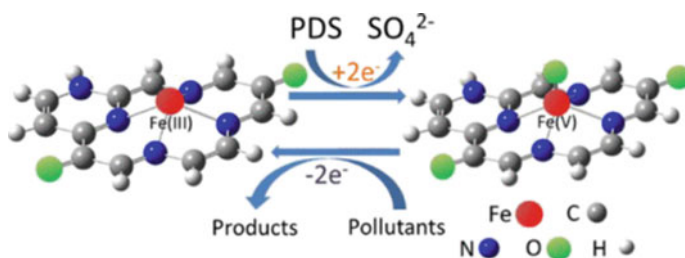


Fig. 10.5 The generation of Fe (V) via the activation of PDS by SAlFe on N-doped carbon [22]

and $\text{SO}_5^{\bullet-}$ to break down refractory organic compounds [9, 81]. Unlike PMS and PDS, sulphite has lower chronic biotoxicity and cost, leading to a more sustainable and environmentally friendly treatment process. However, the traditional transition metal-based catalyst is not able to achieve an efficient sulphite activation [54]. The introduction of SACs into sulphite activation greatly enhances this process. A Co-SAC on MOF resulted in a 2.6 times higher oxidation rate than other Co-based nanoparticles, and $\text{SO}_4^{\bullet-}$ radical was detected as the dominant reactive species [31]. $\text{SO}_5^{\bullet-}$ radical was reported as the dominating reactive species generated by a Fe SAC supported on molybdenum disulfide, and a 90% degradation of propranolol was obtained in 30 min.

PDS and sulphite represent promising oxidizing agents in environmental remediation due to their low cost, widespread availability, and high oxidation capacity [1, 22, 31]. While PMS and H_2O_2 have been extensively studied in advanced oxidation processes (AOPs), the catalytic potential of SAC in PDS and sulphite-based systems remains relatively unexplored. Therefore, the development of cost-effective and efficient SACs for PDS and sulphite activation is highly desirable.

10.5 Future Research Needs

The development of single atom catalysts encounters multiple challenges that must be tackled to further improve their stability and performance. The first challenge is the precise control of the uniform dispersion of single atoms on the support, which necessitates precise control over the synthesis process. The utilization of MOF as support material for SACs could be a potential solution because the highly organized structure of MOF can be easily designed to load desired single-atom sites [83]. The atomic layer deposition method can have the precise control of the distribution of the single-atom sites in the produced catalyst, however, efforts are needed to cut down the cost of this method [58]. Furthermore, optimizing interactions between single atoms and the support is necessary to ensure efficient charge transfer and catalytic activity. Doping of two or more elements simultaneously into the catalyst could be a promising method to further enhance the catalytic activity of SACs. The doping of oxygen and nitrogen into carbon support was found to result in an improved catalytic performance [87], while the double-doping of fluorine and nitrogen on carbon support was reported to increase the charge density of the produced SAC [18]. However, the scalability and cost-effectiveness of the SAC synthesis process are still at a low end. The synthesis of the SAC is still limited to lab scale due to the strict reaction conditions and the complicated synthesis method. Addressing these challenges would unlock the potential of carbon-based single atom catalysts for a boarder application in the environmental field.

10.6 Conclusions

In summary, SACs have shown great potential in environmental applications, particularly in water treatment. Their unique properties of high efficiency, selectivity, and 100% atom utilization have made them a promising alternative to conventional metal-based catalysts. Various studies have demonstrated the successful application of SACs in the degradation of environmental contaminants via photocatalysis or the activation of H₂O₂, PMS, PDS and sulphite, showing their excellent stability and outstanding catalytic performance. However, there are still many challenges to overcome, such as the low control of the distribution of the single-atom sites, low scalability and cost-effectiveness of the SAC synthesis process. Overall, the potential of SACs in environmental applications is enormous, and the development of SACs holds great promise for the future of sustainable and green technology in the environmental field.

References

1. Abdelhaleem A, Chu W, Farzana S (2020) Diphenamid photodegradation using Fe (III) impregnated N-doped TiO₂/sulfite/visible LED process: influence of wastewater matrix, kinetic modeling, and toxicity evaluation. *Chemosphere* 256:127094
2. Bai J, Zhou B (2014) Titanium dioxide nanomaterials for sensor applications. *Chem Rev* 114(19):10131–10176
3. Benson SW (1978) Thermochemistry and kinetics of sulfur-containing molecules and radicals. *Chem Rev* 78(1):23–35
4. Cai S, Zuo X, Zhao H, Yang S, Chen R, Chen L, Zhang R, Ding D, Cai T (2022) Evaluation of N-doped carbon for the peroxymonosulfate activation and removal of organic contaminants from livestock wastewater and groundwater. *J Mat Chem A* 10(16):9171–9183
5. Cao S, Li H, Tong T, Chen H, Yu A, Yu J, Chen HM (2018) Single-atom engineering of directional charge transfer channels and active sites for photocatalytic hydrogen evolution. *Adv Func Mater* 28(32):1802169
6. Chen F, Wu X-L, Yang L, Chen C, Lin H, Chen J (2020) Efficient degradation and mineralization of antibiotics via heterogeneous activation of peroxymonosulfate by using graphene supported single-atom Cu catalyst. *Chem Eng J* 394:124904
7. Cheng N, Zhang L, Doyle-Davis K, Sun X (2019) Single-atom catalysts: from design to application. *Electrochem Ene Rev* 2(4):539–573
8. Ding K, Gulec A, Johnson AM, Schweitzer NM, Stucky GD, Marks LD, Stair PC (2015) Identification of active sites in CO oxidation and water-gas shift over supported Pt catalysts. *Science* 350(6257):189–192
9. Ding W, Xiao W, Huang W, Sun Q, Zheng H (2020) Sulfite activation on a silica-supported well-dispersed cobalt catalyst via an electron transfer complex path. *J Clean Prod* 257:120457
10. Duan X, Sun H, Wang S (2018) Metal-free carbocatalysis in advanced oxidation reactions. *Acc Chem Res* 51(3):678–687
11. Duan J, Zhou Y, Ren Y, Liu F, Deng P, Yang M, Ge H, Gao J, Yang J, Qin Y (2023) Effect of electronic structure over late transition-metal M1–N4 single-atom sites on hydroxyl radical-induced oxidations. *ACS Catal* 13:3308–3316
12. Fan Y, Liu S, Yi Y, Rong H, Zhang J (2021) Catalytic nanomaterials toward atomic levels for biomedical applications: from metal clusters to single-atom catalysts. *ACS Nano* 15(2):2005–2037

13. Gao C, Low J, Long R, Kong T, Zhu J, Xiong Y (2020) Heterogeneous single-atom photocatalysts: fundamentals and applications. *Chem Rev* 120(21):12175–12216
14. Gao C, Lyu F, Yin Y (2020) Encapsulated metal nanoparticles for catalysis. *Chem Rev* 121(2):834–881
15. Gao J, Yang H, Huang X, Hung S-F, Cai W, Jia C, Miao S, Chen HM, Yang X, Huang Y, Zhang T, Liu B (2020). Enabling direct H₂O₂ production in acidic media through rational design of transition metal single atom catalyst. *Chem* 6(3):658–674. <https://doi.org/10.1016/j.chempr.2019.12.008>
16. Gawande MB, Fornasiero P, Zbořil R (2020) Carbon-based single-atom catalysts for advanced applications. *ACS Catal* 10(3):2231–2259
17. Gong K, Du F, Xia Z, Durstock M, Dai L (2009) Nitrogen-doped carbon nanotube arrays with high electrocatalytic activity for oxygen reduction. *Science* 323(5915):760–764
18. Han S-G, Ma D-D, Zhou S-H, Zhang K, Wei W-B, Du Y, Wu X-T, Xu Q, Zou R, Zhu Q-L (2021) Fluorine-tuned single-atom catalysts with dense surface Ni-N₄ sites on ultrathin carbon nanosheets for efficient CO₂ electroreduction. *Appl Catal B* 283:119591
19. Hu L, Zhang G, Liu M, Wang Q, Wang P (2018) Enhanced degradation of Bisphenol A (BPA) by peroxymonosulfate with Co₃O₄-Bi₂O₃ catalyst activation: effects of pH, inorganic anions, and water matrix. *Chem Eng J* 338:300–310
20. Huang B, Wu Z, Zhou H, Li J, Zhou C, Xiong Z, Pan Z, Yao G, Lai B (2021) Recent advances in single-atom catalysts for advanced oxidation processes in water purification. *J Hazard Mater* 412:125253
21. Ji S, Jiang B, Hao H, Chen Y, Dong J, Mao Y, Zhang Z, Gao R, Chen W, Zhang R (2021) Matching the kinetics of natural enzymes with a single-atom iron nanozyme. *Nat Catal* 4(5):407–417
22. Jiang N, Xu H, Wang L, Jiang J, Zhang T (2020) Nonradical oxidation of pollutants with single-atom-Fe (III)-activated persulfate: Fe (V) being the possible intermediate oxidant. *Environ Sci Technol* 54(21):14057–14065
23. Jiao L, Wu J, Zhong H, Zhang Y, Xu W, Wu Y, Chen Y, Yan H, Zhang Q, Gu W (2020) Densely isolated FeN₄ sites for peroxidase mimicking. *ACS Catal* 10(11):6422–6429
24. Kottwitz M, Li Y, Wang H, Frenkel AI, Nuzzo RG (2021) Single atom catalysts: a review of characterization methods. *Chem-Method* 1(6):278–294
25. Lai W, Zhang L, Hua W, Indris S, Yan Z, Hu Z, Zhang B, Liu Y, Wang L, Liu M (2019) General π -electron-assisted strategy for Ir, Pt, Ru, Pd, Fe, Ni single-atom electrocatalysts with bifunctional active sites for highly efficient water splitting. *Angew Chem Int Ed* 58(34):11868–11873
26. Liang X, Wang D, Zhao Z, Li T, Chen Z, Gao Y, Hu C (2022) Engineering the low-coordinated single cobalt atom to boost persulfate activation for enhanced organic pollutant oxidation. *Appl Catal B* 303:120877
27. Li Y, Wang Z, Xia T, Ju H, Zhang K, Long R, Xu Q, Wang C, Song L, Zhu J (2016) Implementing metal-to-ligand charge transfer in organic semiconductor for improved visible-near-infrared photocatalysis. *Adv Mater* 28(32):6959–6965
28. Li X, Bi W, Zhang L, Tao S, Chu W, Zhang Q, Luo Y, Wu C, Xie Y (2016) Single-atom Pt as co-catalyst for enhanced photocatalytic H₂ evolution. *Adv Mater* 28(12):2427–2431
29. Li X, Rong H, Zhang J, Wang D, Li Y (2020) Modulating the local coordination environment of single-atom catalysts for enhanced catalytic performance. *Nano Res* 13(7):1842–1855
30. Li Y, Yang T, Qiu S, Lin W, Yan J, Fan S, Zhou Q (2020) Uniform N-coordinated single-atomic iron sites dispersed in porous carbon framework to activate PMS for efficient BPA degradation via high-valent iron-oxo species. *Chem Eng J* 389:124382
31. Li M, Guo Q, Xing L, Yang L, Qi T, Xu P, Zhang S, Wang L (2020) Cobalt-based metal-organic frameworks promoting magnesium sulfite oxidation with ultrahigh catalytic activity and stability. *J Colloid Interface Sci* 559:88–95
32. Li Z, Li K, Ma S, Dang B, Li Y, Fu H, Du J, Meng Q (2021) Activation of peroxymonosulfate by iron-biochar composites: Comparison of nanoscale Fe with single-atom Fe. *J Colloid Interface Sci* 582:598–609

33. Liu L, Corma A (2018) Metal catalysts for heterogeneous catalysis: from single atoms to nanoclusters and nanoparticles. *Chem Rev* 118(10):4981–5079
34. Liu Q, Zhang Z (2019) Platinum single-atom catalysts: a comparative review towards effective characterization. *Catal Sci Technol* 9(18):4821–4834
35. Liu J, Zou Y, Cruz D, Savateev A, Antonietti M, Vilé G (2021) Ligand–metal charge transfer induced via adjustment of textural properties controls the performance of single-atom catalysts during photocatalytic degradation. *ACS Appl Mater Interfaces* 13(22):25858–25867
36. Liu X, Pei Y, Cao M, Yang H, Li Y (2022) Highly dispersed copper single-atom catalysts activated peroxymonosulfate for oxytetracycline removal from water: mechanism and degradation pathway. *Chem Eng J* 450:138194
37. Ma J, Yang Q, Wen Y, Liu W (2017) Fe-g-C₃N₄/graphitized mesoporous carbon composite as an effective Fenton-like catalyst in a wide pH range. *Appl Catal B* 201:232–240
38. Matafonova G, Batoev V (2018) Recent advances in application of UV light-emitting diodes for degrading organic pollutants in water through advanced oxidation processes: a review. *Water Res* 132:177–189
39. Miao W, Liu Y, Wang D, Du N, Ye Z, Hou Y, Mao S, Ostrikov KK (2021) The role of Fe-N_x single-atom catalytic sites in peroxymonosulfate activation: formation of surface-activated complex and non-radical pathways. *Chem Eng J* 423:130250
40. Miklos DB, Remy C, Jekel M, Linden KG, Drewes JE, Hübner U (2018) Evaluation of advanced oxidation processes for water and wastewater treatment—a critical review. *Water Res* 139:118–131
41. Myers RL (2007) The 100 most important chemical compounds: a reference guide. ABC-CLIO
42. Neyens E, Baeyens J (2003) A review of classic Fenton's peroxidation as an advanced oxidation technique. *J Hazard Mater* 98(1–3):33–50
43. Oh W-D, Dong Z, Lim T-T (2016) Generation of sulfate radical through heterogeneous catalysis for organic contaminants removal: current development, challenges and prospects. *Appl Catal B* 194:169–201
44. Ohyama J, Abe D, Hirayama A, Iwai H, Tsuchimura Y, Sakamoto K, Irikura M, Nakamura Y, Yoshida H, Machida M (2022) Selective oxidation of methane to formaldehyde over a silica-supported cobalt single-atom catalyst. *J Phys Chem C* 126(4):1785–1792
45. Peng X, Wu J, Zhao Z, Wang X, Dai H, Wei Y, Xu G, Hu F (2022) Activation of peroxymonosulfate by single atom Co-NC catalysts for high-efficient removal of chloroquine phosphate via non-radical pathways: electron-transfer mechanism. *Chem Eng J* 429:132245
46. Peng X, Wu J, Zhao Z, Wang X, Dai H, Xu L, Xu G, Jian Y, Hu F (2022) Activation of peroxymonosulfate by single-atom Fe-g-C₃N₄ catalysts for high efficiency degradation of tetracycline via nonradical pathways: Role of high-valent iron-oxo species and Fe–N_x sites. *Chem Eng J* 427:130803
47. Qian K, Chen H, Li W, Ao Z, Wu Y, Guan X (2021) Single-atom Fe catalyst outperforms its homogeneous counterpart for activating peroxymonosulfate to achieve effective degradation of organic contaminants. *Environ Sci Technol* 55(10):7034–7043
48. Qiao B, Wang A, Yang X, Allard LF, Jiang Z, Cui Y, Liu J, Li J, Zhang T (2011) Single-atom catalysis of CO oxidation using Pt 1/FeO_x. *Nat Chem* 3(8):634–641
49. Qi Y, Li J, Zhang Y, Cao Q, Si Y, Wu Z, Akram M, Xu X (2021) Novel lignin-based single atom catalysts as peroxymonosulfate activator for pollutants degradation: Role of single cobalt and electron transfer pathway. *Appl Catal B* 286:119910
50. Rivera-Cárcamo C, Serp P (2018) Single atom catalysts on carbon-based materials. *Chem-CatChem* 10(22):5058–5091
51. Rong X, Wang H, Lu X, Si R, Lu T (2020) Controlled synthesis of a vacancy-defect single-atom catalyst for boosting CO₂ electroreduction. *Angew Chem* 132(5):1977–1981
52. Ruta V, Sivo A, Bonetti L, Bajada MA, Vilé G (2022) Structural effects of metal single-atom catalysts for enhanced photocatalytic degradation of gemfibrozil. *ACS Appl Nano Mat* 5(10):14520–14528
53. Shang Y, Duan X, Wang S, Yue Q, Gao B, Xu X (2021) Carbon-based single atom catalyst: synthesis, characterization. DFT calculations. *Chinese Chem Lett*

54. Shang Y, Xu X, Gao B, Wang S, Duan X (2021) Single-atom catalysis in advanced oxidation processes for environmental remediation. *Chem Soc Rev*
55. Shrestha S, Wang B, Dutta P (2020) Nanoparticle processing: understanding and controlling aggregation. *Adv Coll Interface Sci* 279:102162
56. Sohlberg K, Pennycook TJ, Zhou W, Pennycook SJ (2015) Insights into the physical chemistry of materials from advances in HAADF-STEM. *Phys Chem Chem Phys* 17(6):3982–4006
57. Song J, Bazant MZ (2012) Effects of nanoparticle geometry and size distribution on diffusion impedance of battery electrodes. *J Electrochem Soc* 160(1):A15
58. Stambula S, Gauquelin N, Bugnet M, Gorantla S, Turner S, Sun S, Liu J, Zhang G, Sun X, Botton GA (2014) Chemical structure of nitrogen-doped graphene with single platinum atoms and atomic clusters as a platform for the PEMFC electrode. *J Phys Chem C* 118(8):3890–3900
59. Tang J, Tang D (2015) Non-enzymatic electrochemical immunoassay using noble metal nanoparticles: a review. *Microchim Acta* 182(13):2077–2089
60. Tong T, Zhu B, Jiang C, Cheng B, Yu J (2018) Mechanistic insight into the enhanced photocatalytic activity of single-atom Pt, Pd or Au-embedded g-C₃N₄. *Appl Surf Sci* 433:1175–1183
61. Vasquez-Medrano R, Prato-Garcia D, Vedrenne M (2018) Chapter 4—Ferrioxalate-mediated processes. In: Ameta SC, Ameta R (eds) *Advanced oxidation processes for waste water treatment*. Academic Press, pp 89–113. <https://doi.org/10.1016/B978-0-12-810499-6.00004-8>
62. Wang J, Wang S (2018) Activation of persulfate (PS) and peroxymonosulfate (PMS) and application for the degradation of emerging contaminants. *Chem Eng J* 334:1502–1517
63. Wang S, Wang J (2023) Single atom cobalt catalyst derived from co-pyrolysis of vitamin B12 and graphitic carbon nitride for PMS activation to degrade emerging pollutants. *Appl Catal B* 321:122051
64. Wang L, Zhang W, Wang S, Gao Z, Luo Z, Wang X, Zeng R, Li A, Li H, Wang M (2016) Atomic-level insights in optimizing reaction paths for hydroformylation reaction over Rh/CoO single-atom catalyst. *Nat Commun* 7(1):1–8
65. Wang Y, Zhao X, Cao D, Wang Y, Zhu Y (2017) Peroxymonosulfate enhanced visible light photocatalytic degradation bisphenol A by single-atom dispersed Ag mesoporous g-C₃N₄ hybrid. *Appl Catal B* 211:79–88
66. Wang A, Li J, Zhang T (2018) Heterogeneous single-atom catalysis. *Nat Rev Chem* 2(6):65–81
67. Wang F, Wang Y, Feng Y, Zeng Y, Xie Z, Zhang Q, Su Y, Chen P, Liu Y, Yao K (2018) Novel ternary photocatalyst of single atom-dispersed silver and carbon quantum dots co-loaded with ultrathin g-C₃N₄ for broad spectrum photocatalytic degradation of naproxen. *Appl Catal B* 221:510–520
68. Wang Q, Zhang D, Chen Y, Fu W-F, Lv X-J (2019) Single-atom catalysts for photocatalytic reactions. *ACS Sustain Chem Eng* 7(7):6430–6443
69. Wang C, Kim J, Malgras V, Na J, Lin J, You J, Zhang M, Li J, Yamauchi Y (2019) Metal-organic frameworks and their derived materials: emerging catalysts for a sulfate radicals-based advanced oxidation process in water purification. *Small* 15(16):1900744
70. Wang C, Ren H, Wang Z, Guan Q, Liu Y, Li W (2022) A promising single-atom Co-NC catalyst for efficient CO₂ electroreduction and high-current solar conversion of CO₂ to CO. *Appl Catal B* 304:120958
71. Wang P, Huang C, Gao J, Shi Y, Li H, Yan H, Yan S, Zhang Z (2020) Resveratrol induces SIRT1-Dependent autophagy to prevent H₂O₂-Induced oxidative stress and apoptosis in HTR8/SVneo cells. *Placenta* 91:11–18
72. Wei H, Liu X, Wang A, Zhang L, Qiao B, Yang X, Huang Y, Miao S, Liu J, Zhang T (2014) FeOx-supported platinum single-atom and pseudo-single-atom catalysts for chemoselective hydrogenation of functionalized nitroarenes. *Nat Commun* 5(1):1–8
73. Wu X, Kim J-H (2022) Outlook on single atom catalysts for persulfate-based advanced oxidation. *ACS ES&T Engineering* 2(10):1776–1796
74. Xiong Z, Jiang Y, Wu Z, Yao G, Lai B (2021) Synthesis strategies and emerging mechanisms of metal-organic frameworks for sulfate radical-based advanced oxidation process: a review. *Chem Eng J* 421:127863

75. Xu L, Fu B, Sun Y, Jin P, Bai X, Jin X, Shi X, Wang Y, Nie S (2020) Degradation of organic pollutants by Fe/N co-doped biochar via peroxymonosulfate activation: Synthesis, performance, mechanism and its potential for practical application. *Chem Eng J* 400:125870
76. Xu J, Zheng X, Feng Z, Lu Z, Zhang Z, Huang W, Li Y, Vuckovic D, Li Y, Dai S (2021) Organic wastewater treatment by a single-atom catalyst and electrolytically produced H₂O₂. *Nat Sustain* 4(3):233–241
77. Xue Z-H, Luan D, Zhang H, Lou XWD (2022) Single-atom catalysts for photocatalytic energy conversion. *Joule*
78. Yang T, Fan S, Li Y, Zhou Q (2021) Fe-N/C single-atom catalysts with high density of Fe-N_x sites toward peroxymonosulfate activation for high-efficient oxidation of bisphenol A: electron-transfer mechanism. *Chem Eng J* 419:129590
79. Yang W, Hong P, Yang D, Yang Y, Wu Z, Xie C, He J, Zhang K, Kong L, Liu J (2021) Enhanced Fenton-like degradation of sulfadiazine by single atom iron materials fixed on nitrogen-doped porous carbon. *J Colloid Interf Sci* 597:56–65. <https://doi.org/10.1016/j.jcis.2021.03.168>
80. Yano J, Yachandra VK (2009) X-ray absorption spectroscopy. *Photosynth Res* 102(2):241–254
81. Yuan Y, Zhao D, Li J, Wu F, Brigante M, Mailhot G (2018) Rapid oxidation of paracetamol by Cobalt (II) catalyzed sulfite at alkaline pH. *Catal Today* 313:155–160
82. Zeng T, Li S, Hua J, He Z, Zhang X, Feng H, Song S (2018) Synergistically enhancing Fenton-like degradation of organics by in situ transformation from Fe₃O₄ microspheres to mesoporous Fe, N-dual doped carbon. *Sci Total Environ* 645:550–559
83. Zhang Q, Zhang X, Wang J, Wang C (2020) Graphene-supported single-atom catalysts and applications in electrocatalysis. *Nanotech* 32(3):032001
84. Zhang L, Jiang X, Zhong Z, Tian L, Sun Q, Cui Y, Lu X, Zou J, Luo S (2021) Carbon nitride supported high-loading Fe single-atom catalyst for activation of peroxymonosulfate to generate 1O₂ with 100% selectivity. *Angew Chem Int Ed* 60(40):21751–21755
85. Zhang N, Zhang X, Tao L, Jiang P, Ye C, Lin R, Huang Z, Li A, Pang D, Yan H (2021) Silver single-atom catalyst for efficient electrochemical CO₂ reduction synthesized from thermal transformation and surface reconstruction. *Angew Chem Int Ed* 60(11):6170–6176
86. Zhao C, Xiong C, Liu X, Qiao M, Li Z, Yuan T, Wang J, Qu Y, Wang X, Zhou F (2019) Unraveling the enzyme-like activity of heterogeneous single atom catalyst. *Chem Commun* 55(16):2285–2288
87. Zhou Z, Li M, Kuai C, Zhang Y, Smith VF, Lin F, Aiello A, Durkin DP, Chen H, Shuai D (2021) Fe-based single-atom catalysis for oxidizing contaminants of emerging concern by activating peroxides. *J Hazard Mater* 418:126294
88. Zhu S, Li X, Kang J, Duan X, Wang S (2018) Persulfate activation on crystallographic manganese oxides: mechanism of singlet oxygen evolution for nonradical selective degradation of aqueous contaminants. *Environ Sci Technol* 53(1):307–315

Chapter 11

Topological Interpenetrative Covalent Anchored Network (TIP CAN) for H₂S Detection, Storage, and Remediation Relevance to Shipboard Wastewater



Sajid Bashir Liu and Jingbo Louise Liu

Abstract Hydrogen Sulfide (H₂S) can be generated on ships from seawater with sulfates storage or oil-bilge tanks containing hydrocarbons with sulfur and sulfur-containing detergents or gray- and blackwater storage tanks, where H₂S is generated microbiologically. This workplace hazard requires carefully venting these tanks before inspection and maintenance. Here we report the synthesis and evaluation of iron peroxide (FeOOH), silver reduced with ascorbate [Ag(ASC)], copper tricarboxylate metal–organic framework (CuMOF), chromium terephthalate metal–organic framework doped with silver [MIL101(Cr)Ag] or silver and magnesium [MIL101(Cr)AgMg] demonstrated excellent removal of H₂S from an offline slurry reactor, eliminating 100% of 100 ppm H₂S under 35 min, at 90 °F. The adsorbents were evaluated for different concentrations of H₂S using pulsed injections. The time was taken to reach 0 ppm, including regeneration using hydrogen peroxide to oxidize the surfaces of this catalyst. Regeneration after 5 cycles showed H₂S effectiveness of around 75% relative to the new catalyst averaged over the top five adsorbents. The sulfur binding capacity of at least 78 mg/g was shown, and a catalyst mass of even less than 100 mg was effective at removing 100 ppm of H₂S. The slurry reactor workflow has the advantages of speed of operation, simplicity of design, and ease of use. It would suit a ship with a general crew who would not require a specialist degree to operate the offline slurry reactor to remove H₂S. The kinetics of the reaction were modeled on a shrinking model, and the lowering of the effectiveness of H₂S was attributed to the formation of elemental sulfur and sulfate indirectly confirmed using x-ray photon electron spectroscopy which could block active hydroxyl sites that are avenues for attracting the H₂S molecule. The surface adsorption of H₂S by the exchange with oxygen is suggested as the main mechanism whereby H₂S is removed, followed by surface area and catalyst porosity. This study also suggests

S. B. Liu (✉) · J. L. Liu

The Department of Chemistry, Texas A&M University-Kingsville, 700 University Blvd.,
Kingsville, TX 78363, USA
e-mail: br9@tamuk.edu

J. L. Liu

Texas A&M Energy Institute, 1617 Research Pkwy, College Station, TX 77845, USA

guidelines for developing filter-based ceramics that could be deployed on ships to remove H₂S from tanks without venting or exposing the crew to possible exposure.

Keywords Hydrogen sulfide · Abatement · Capture · Conversion · Catalyst

11.1 Introduction

Hydrogen sulfide (H₂S) [1] is a modulator that serves in several biological [2] and pathological [3] processes, including neuronal activity [4] and tissue homeostasis [5] in low doses [6]. In moderate to high doses (5–100 ppm), H₂S acts as a poison and disrupts normal biological functions, and causes disorientation [7], vomiting, diarrhea, and nonconsciousness including death [8]. The gas is also corrosive, flammable, and has a strong odor [9], co-mixed with flammable gases, such as natural gas and liquid propane, to detect leaks through the sense of smell [10]. Hydrogen sulfide can be generated using anaerobic processes and industrial processes such as the generation of biogas, natural gas reforming, and flue gas treatment [11]. On ships, H₂S is generated in ballast (holding sea water), greywater, blackwater, and bilgewater tanks. This results from sulfate-reducing bacteria (SRB) metabolizing organics and SO₄ without oxygen. As a result, linings of wastewater holding tanks can be damaged through microbial-influenced corrosion mechanisms, and the production of H₂S poses a potentially serious risk to sailors. The MARPOL international guidelines stipulate the removal of organics and hydrogen sulfide from gray water before discharge to control the emissions of H₂S [12]. To control H₂S in ballast, bilge, gray, and dark water storage tanks, different desulfurization chemistries to remove H₂S are utilized [13]. These strategies rely on irreversible sulfide conversion [14], displacement of metal ions by the sulfide ion [15], or coordination of H₂S to the metal center [16]. These chemistries are applied to systems that promote photocatalytic oxidation [17], anaerobic digestion [18], and adsorption [19].

Materials for adsorption for H₂S include first-row transition metal and their oxides, of which ZnO is the most common approach [20]. One drawback of using ZnO is its low adsorption capacity at room temperature, high enthalpies at higher temperatures [21], and reduction to the zero-valent metal [22]. A substitute metal candidate was selected in terms of silver, which has been used in medical applications as an H₂S selective probe [23]; magnesium peroxide (MgOOH) has been used in the elimination of mercaptan compounds [24], and iron peroxide (FeOOH) as a catalyst in water purification [25]. The catalyst has a high equilibrium constant for sulfidation at low temperatures [26]. It has previously been demonstrated in H₂S adsorption, which breakthrough curves within operational parameters (<100 ppm) [27] and would be effective at H₂S removal from neutral to alkaline pH conditions [28], with an adsorption capacity of 36.9 g H₂S/g absorbent at pH = 8 due to phase change to the alpha form of γ -FeOOH, due to the large surface area of the alpha phase in a fixed-bed reactor system [29]. A comparison using a fixed-bed reactor system showed that the binding capacity was lower than that of ZnO.

An alternate approach is to utilize a slurry reactor, routinely used to process exhaust gas in a gas–liquid and liquid–solid interface, which would be amenable to shipboard holding tanks [30]. The slurry reactor can also be operated continuously at low pressure and temperature or in limited operations. It can utilize smaller particle sizes, larger areas, and lower catalyst loadings, promoting particle diffusion and improving the mass transfer coefficient by considering the system as a three-phase homogeneous reaction under standard temperature and pressure.

Here we demonstrate a small-scale laboratory slurry offline reactor design for gamma γ -FeOOH and compare this with three different systems: silver, copper, and chromium with pulsed H₂S injection to simulate duty shifts for generation of oil/water bilge, greywater from the washing of galley pots, and pans, crew showers, ballast and black water from the flushing of toilets, all of which can generate and store H₂S. The operational parameter was to reduce 100 ppm H₂S to 0 ppm within 30 min, limiting exposure to maintenance crews that must service these holding or ballast tanks. The iron catalyst was synthesized, characterized, and evaluated for removing H₂S. The catalyst was also subjected to recycling using hydrogen peroxide. The H₂S removal efficiency as a function of operating temperature, H₂S input load, catalyst load, and speed of H₂S removal in an offline slurry reactor might be utilized on a ship was evaluated. The catalyst was evaluated using Fourier transform infrared spectroscopy (FTIR), thermogravimetric analysis, and (TGA) Differential scanning calorimetry (DSC). The synthesized catalyst developed high kinetics and adsorption capacity and would be useful for offline H₂S removal in ships' ballast with minimal redesign and cost.

11.2 Method

All chemicals, unless otherwise specified, were obtained from VWR International (Houston, TX) and in-house ultrapure water (18 MW). The chemicals were iron sulfate (FeSO₃·7H₂O), sodium carbonate (Na₂CO₃), sodium sulfide (Na₂S·9H₂O), zinc sulfide (ZnS), hydrogen peroxide (H₂O₂, 30 wt. %), magnesium (Mg) turnings, silver nitrate (AgNO₃), Chromium(III) nitrate (Cr(NO₃)₃·9H₂O), copper nitrate (Cu(NO₃)₂·3H₂O), terephthalic acid (C₆H₄-1,4-(CO₂H)₂), chloroacetic acid (ClCH₂COOH), glacial hydrochloric acid (HCl), concentrated sulfuric acid (H₂SO₄), dimethylformamide (DMF, HCON(CH₃)₂), tetrahydrofuran (THF, C₄H₈O), ethanol (CH₃CH₂OH), dry methanol (CH₃OH), and acetonitrile (CH₃CN).

Preparation of γ -FeOOH. The iron peroxide was synthesized using 0.02 mol of iron sulfate in 20 mL of deionized water and mechanically stirred at 70 °C for 35 min in a three-necked flask with aluminum foil wrapped to limit light. During the moving processes and 0.035 mol (~3.7 g) of sodium carbonate was added slowly. The sample was stirred for 25 min with a pH of 7.5 by adding sulfuric acid or sodium hydroxide solution. The sample was allowed to cool to room temperature and washed thrice with ice-cold ethanol and distilled water. The filtered samples were oven dried at 70 °C

overnight. This sample was designated γ -FeOOH. An illustration of the synthesis scheme is shown in Fig. 11.1a.

Preparation of MIL101(Cr). 2 g of chromium(III) nitrate and 0.82 g of terephthalic acid were dissolved in deionized water. The sample was mechanically stirred for 30 min at room temperature. The sample was refluxed at 85 °C for 6 h, transferred to a Teflon-sealed tube, and heated in a vacuum oven at 125 °C overnight. The sample was allowed to cool to room temperature and washed with ice-cold water, methanol, and THF three times and then with ice-cold water twice more. The sample was then redissolved in DMF, refluxed for 6 h at 70 °C, filtered and washed with ice-cold water twice, and used as the base catalyst MIL101(Cr). An illustration of the synthesis scheme is shown in Fig. 11.1b.

Preparation of MIL 101(Cr)-COOH. The 0.5 g of sample was vacuum oven dried at 110 °C for 4 h, allowed to cool to room temperature in a sealed three-neck flash on ice, and dissolved with 5 mL of THF injected using a hypodermic needle syringe and stirred for 15 min. This solution added approximately 0.5 g of chloroacetic acid, which was also dissolved in 15 mL of THF using a second hypodermic syringe dropwise with continuous stirring. The sample was stirred for an additional 20 min, filtered, and washed with ice-cold deionized water and room-temperature methanol. The sample was redissolved in ethanol for 6 h and dried at 70 °C for 6 h.

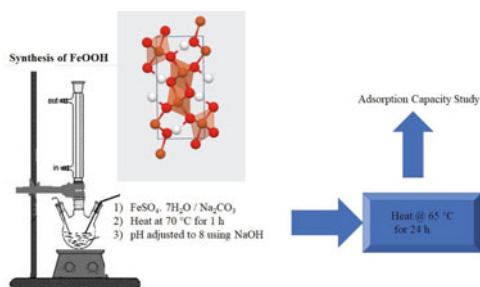
MIL 101(Cr)COOAg. The sample (0.42 g) that was modified with chloroacetic acid was dissolved in ethanol to which 0.12 g of silver nitrate was previously dissolved in 3 mL water/acetonitrile (1:1 v/v) and mechanically stirred for 30 min at room temperature for 6 h and washed and filtered with ice-cold water.

Preparation of MIL 101(Cr)COOAg...Mg. In a three-necked round bottom flask, 0.1 M Mg(OMe)₂ was prepared by adding 0.24 g of magnesium turnings and 100 mL of dried methanol and stirred at room temperature for 20 min, with 1 mL of 30% hydrogen peroxide in methanol (1:2 v/v), and 1 mL of water–methanol (1:1 v/v) was added to convert the Mg(OMe)₂ to MgOOH. To this, 0.35 g of MIL 101(Cr)COOAg⁺ was added, and the sample was filtered and washed with ice-cold methanol and dried at 120 °C for 6 h. This final product was tested for the removal of H₂S.

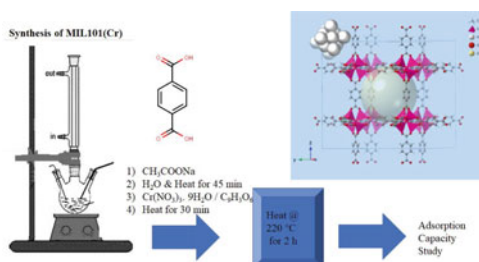
Preparation of Ag(ASC) Nanoparticles (NPs). In a three-necked round bottom flask, 2 mL of 10 mM silver nitrate was injected using a hypodermic syringe, and 1 mL of 100 mM ascorbic acid was injected mechanically, stirring at 40 °C for 3 h. The sample was filtered and washed with ice-cold water, methanol, and water and oven dried at 120 °C for 6 h. This sample was designated as Ag(ASC) NPs. An illustration of the synthesis scheme is shown in Fig. 11.1c.

Preparation of Ag(Al) Nanoparticles (NPs). In a three-necked round bottom flask, 2 mL of 10 mM silver nitrate was injected using a hypodermic syringe and 10 mg of aluminum (Al) foil. The sample was refluxed at 70 °C for 3 h with mechanical stirring. The sample was filtered and washed with ice-cold water, methanol, and water and oven dried at 120 °C for 6 h. This sample was designated as Ag(Al) NPs.

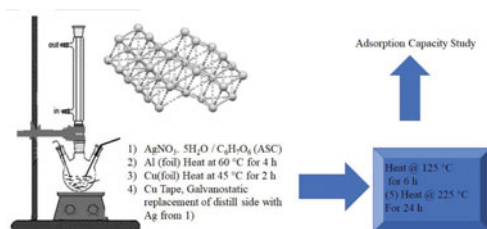
Fig. 11.1 a Synthesis schematic of the adsorbent γ -FeOOH with the 3D structure of crystal lattice. **b** Synthesis schematic of the adsorbent MIL101(Cr) with the 3D structure of crystal lattice. The lattice on the upper left is representative of silver doping. **c** Synthesis schematic of the adsorbent silver nanoparticles with the 3D structure of crystal lattice unit cell for silver metal. **d** Synthesis schematic of the adsorbent Cu BTC MOF with the 3D structure of crystal lattice upper middle and void volume (upper right)



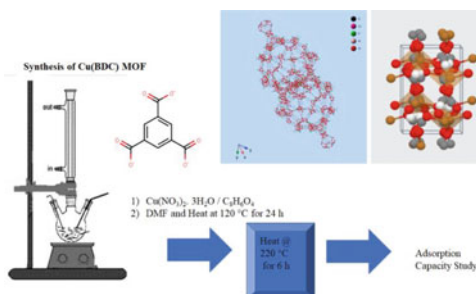
a: Synthesis schematic of the adsorbent γ -FeOOH with the 3D structure of crystal lattice.



b: Synthesis schematic of the adsorbent MIL101(Cr) with the 3D structure of crystal lattice. The lattice on the upper left is representative of silver doping.



c: Synthesis schematic of the adsorbent silver nanoparticles with the 3D structure of crystal lattice unit cell for silver metal.



d: Synthesis schematic of the adsorbent Cu BTC MOF with the 3D structure of crystal lattice upper middle and void volume (upper right).

Preparation of Ag(Cu) Nanoparticles (NPs). In a three-necked round bottom flask, 2 mL of 10 mM silver nitrate was injected using a hypodermic syringe and 10 mg of Cu-Tape, and the sample was refluxed at 75 °C for 3 h with mechanical stirring. The sample was filtered and washed with ice-cold water, methanol, and water and oven dried at 120 °C for 6 h. This sample was designated as Ag(Cu) NPs.

Preparation of Ag(Cu Δ) Nanoparticles (NPs). In a three-necked round bottom flask, 2 mL of 10 mM silver nitrate was injected using a hypodermic syringe and 10 mg of Cu-Tape, and the sample was refluxed at 75 °C for 3 h with mechanical stirring. The sample was filtered and washed with ice-cold water, methanol, and water and oven dried at 120 °C for 6 h and reheated in a vacuum oven at 300 °C for 6 h. This sample was designated as Ag(Cu Δ) NPs.

Preparation of Cu/Ag Tape. In a 50 mL breaker with 10 mL of 0.1 mM silver nitrate solution, one graphite electrode and one copper tape of 4 cm were immersed, and the tape and electrode were connected to an external power source. Approximately 0.4 A of current passed for 2 h. During this time, the copper was displaced with silver on one face of the face, and once the entire face was gray in coloration, the current was discontinued. The tape was washed with room temperature deionized water and oven dried at 65 °C for 3 h. This sample was designated as Ag/Cu tape.

Preparation of Cu(BDC) MOF. 2 mmol of terephthalic acid was injected into a three-neck round bottom flask with 18 mL DMF and mechanically stirred for 5 min at room temperature. Separately 2 mmol of copper nitrate was injected with 12 mL of DMF, and the co-mixture was heated to 25 °C and stirred for 15 min; then, the filtered cake was immersed in ethanol for 12 h and heated to 70 °C for 6 h. This was repeated four times, and on the fourth occasion, the sample was heated to 100 °C for 18 h. This sample was designated Cu MOF. An illustration of the synthesis scheme is shown in Fig. 11.1d.

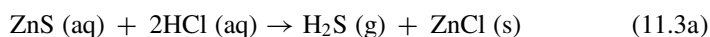
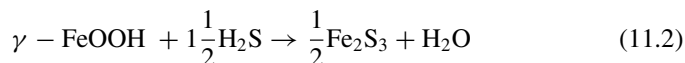
Slurry Reactor Design: An offline slurry reactor design was utilized due to its simplicity. A borosilicate glass vial of 40 mL with polyurethane inserts and a polypropylene cap was used on a hotplate with fixed heating. All experiments were conducted at room temperature unless specified. The air from the interior was removed using a 15 mL hypodermic needle. This sample added 0.2 mL of zinc sulfide and 2.8 mL of 0.2 M HCl. The sample was equilibrated for 3 min at room temperature of a specific temperature. The outlet H₂S concentration was measured using an electrochemical H₂S detector previously calibrated and certified with gaseous H₂S from 0 to 100 ppm in increments of 4 ppm, with an overshoot of 118 pm. The H₂S also had an alarm circuit, activated at 105 ppm, and a LED light lit at 118 ppm. While the detector readout was set to 0–118 ppm, samples of H₂S at concentrations greater than 100 ppm would activate the alarm sooner than when 118 ppm were injected. The concentration of H₂S was calculated using the ZnS mole ratio and confirmed using a calibration from 0 to 118 ppm. The hypodermic needle diameter was 0.1 mm and was used to release any potential overpressure within the offline reactor.

In the initial investigation, the gaseous formation of H₂S was generated by adding zinc chloride (1.29 mmol/mL, 126 ppm) and 0.2 M HCl into an evacuated 40 mL

vial. After 90 s, the gas was evacuated using a hypodermic syringe and injected into a separate vial with the γ -FeOOH catalyst, where the air was partially evacuated. The increase in mass of the γ -FeOOH after a specified duration was measured, and the percent conversion was estimated using the relationship (Eq. 11.1) from (Eq. 11.2), knowing the quantity of initial ZnS shown in Eq. (11.3a–c):

$$\text{H}_2\text{S removal efficiency} = [1 - M_f/M_i] \times 100 \quad (11.1)$$

where C_i was the initial H_2S gas injected using the relationship.



$$1.29 \text{ mmol/mL} \rightarrow 1.29 \text{ mmol/mL} \quad (11.3b)$$

$$126 \text{ ppm (in)} \rightarrow 44 \text{ ppm (out)} \quad (11.3c)$$

The mass conversion and increase from the γ -FeOOH to the Fe_2S_3 can be estimated using the relationship (Eq. 11.4), where 0.200 is a weighted factor experimentally determined to account for the greater hydrogen density sulfide and mass increase due to potential humidity.

$$\% \text{ conversion} = \frac{\text{Mass}_{\text{final}} - \text{Mass}_{\text{initial}}}{0.200 \times M_{\text{initial}}} \quad (11.4)$$

The sample mass was measured, and the experiment was repeated using a 3 mL total volume of ZnS and HCl to determine of adsorption capacities of the other silver and metal–organic catalysts.

11.3 Results

Desulfurization Study: The stock concentration of ZnS and HCl was kept constant at 1.29 mmol/mL for ZnS and 0.2 mmol/mL for HCl. The volume of ZnS was fixed at 0.1 mL, and the volume of HCl varied from 0.1 to 1.0 mL. The H_2S was electrochemically measured and compared with theoretical yield as predicted by Eq. (11.3a) and shown by the parabolic curve (in Fig. 11.2, black-filled squares) with excellent agreement between measured and calculated H_2S concentration. The concentration of HCl was then fixed at 1.0 mL, and the concentration of ZnS was increased from 0.1 to 1.0 mL to inject up to 500 ppm of H_2S , and the time for the alarm to trigger was measured as the detector was saturated above 118 ppm. Due to

detector saturation, this power relationship (red-filled squares) would plateau after 118 ppm. However, the responsiveness to the triggering of the alarm was related to the injected concentration of H_2S . For example, an injection of 118 ppm would trigger the alarm in approximately 70 s [H_2S injector \rightarrow detection \rightarrow alarm], but would take less than 1 s if 500 ppm (calc) were injected.

Adsorption kinetics: The adsorption mass and the breakthrough concentration, approximately $\frac{1}{3}$ th of the initial load was measured. The $FeOOH$ catalyst was approximately 68 mg/g $\gamma-FeOOH$ using gas-phase injection (Fig. 11.3). This is similar to an earlier reported value of 57 mg/g reported for $FeOOH$ [29].

In the gas-phase study, the adsorptive capacity was similar to that published was determined. The test was conducted for an offline slurry (0.1 mL ZnS + 2.9 mL HCl , calibrated using 0–100 ppm Na_2S + HCl) for 90 s. The calculated value was slightly higher (78 mg/g), reflecting the additional solution-solid interactions. To investigate the type of kinetics involved in H_2S removal, the mass increase, and adsorbent conversion were plotted in an offline slurry reactor design and are shown in Fig. 11.4a. A 153 mg/g adsorbent of the adsorption capacity was obtained at adsorption equilibrium, which corresponds to approximately 69% conversion of the $\gamma-FeOOH$ adsorbent, which is consistent with other reported capacities for iron oxide and

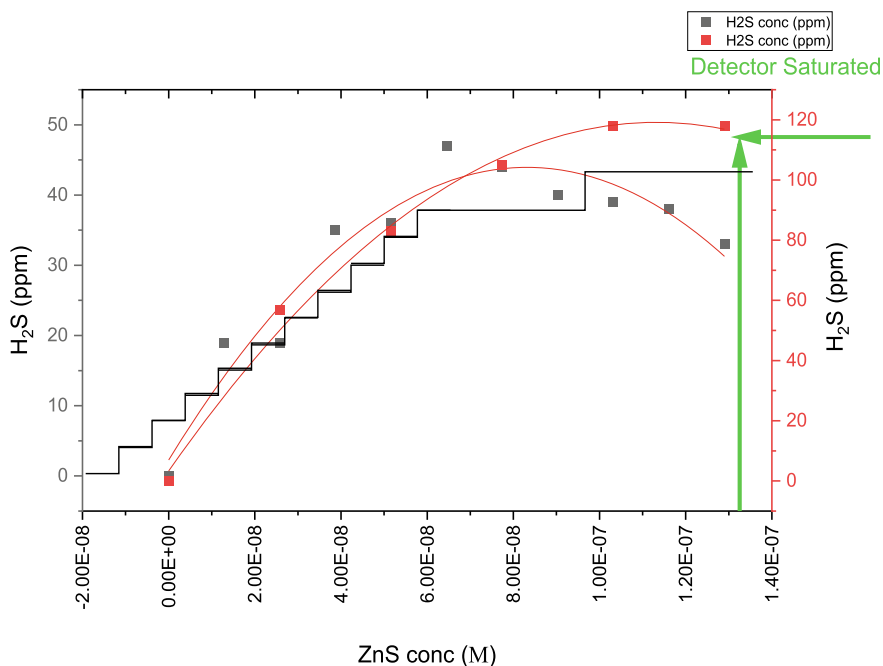
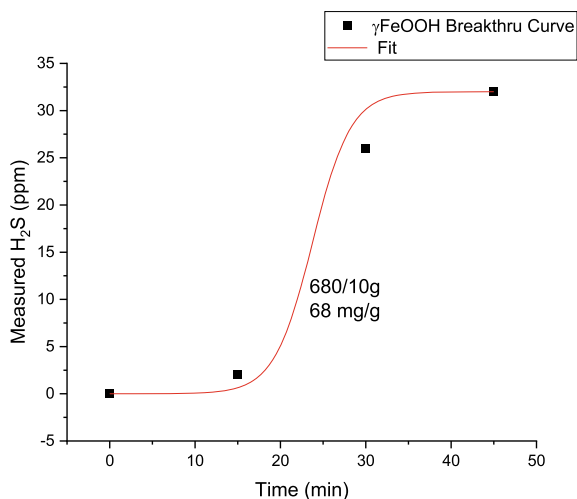


Fig. 11.2 Summary of calibration plot between measured (vertical axes) and calculated axes (horizontal). For injection of H_2S over 118 ppm, the time until detector saturation (alarm, LED lit time) was also recorded. The top black square wave is the H_2S pulsed profile

Fig. 11.3 H₂S adsorption breakthrough curve at 300 K, γ -FeOOH 7.0 wt.%, reaction incubation time 180 s, initial (C₀) H₂S concentration was 100 ppm



hydroxides (168 mg/g for iron(III)hydroxide [30]). Desulfurization of γ -FeOOH in the offline slurry bed exhibited sulfur capacities consistent with published literature. However, at room temperature and the curves were linearized using a log mass difference percent loss against a long time, it was observed that the linearized plot had a 'hockey-stick' profile with an early stage linear relationship related to reaction kinetics and a flat late stage profile related to particle diffusion.

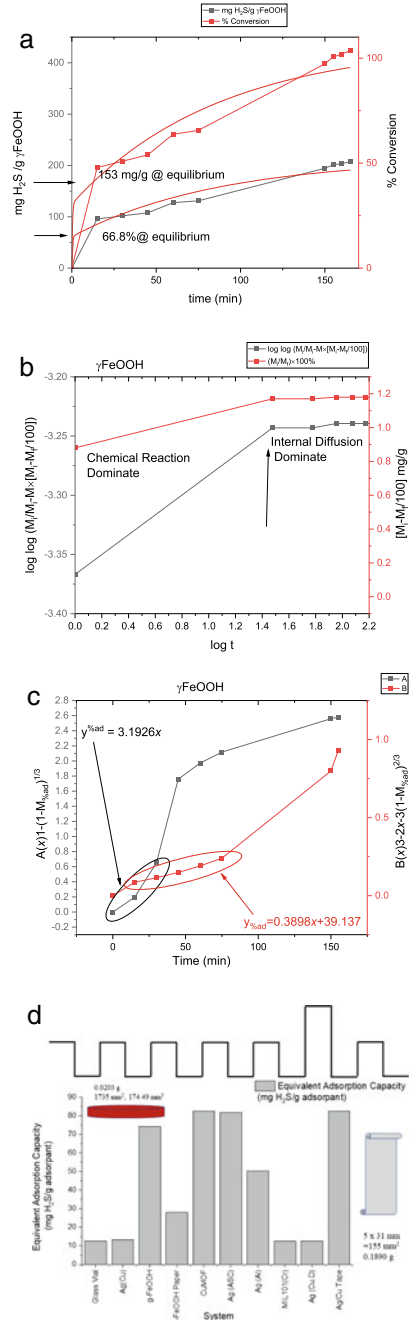
The two curves could be deconvoluted by fitting to a shrinking core model, where $t = A(x) = A[1-x]^{1/3}$, $T = B(x) = B[3-2x-3(1-x)^{2/3}]$, where t is the reaction time (min), x is the degree of conversion of the adsorbent (dimensionless), M_i is the sulfur capacity at initial equilibrium, and M_f is the sulfur capacity at the final redpoint (mg/g), with A and B as fitting coefficients. The linearised relationship is shown in Fig. 11.4b, and the deconvoluted spectra in Fig. 11.4c with the fitting parameters.

The offline slurry reaction system was evaluated for different adsorbents after the initial values for γ -FeOOH were similar to those published for iron oxide and oxyhydroxides [31]. The system was applied to a cylinder reactor of 40 mL volume with borosilicate constructions to allow for visible inspection of the reaction, silver nanoparticles reduced with copper tape [Ag(Cu)], iron peroxide filtered onto a glass fiber membrane of area 174 mm² [γ -FeOOH Paper], Copper metal organic-framework with terephthalic organic liners [CuMOF], silver reduced with ascorbate [Ag(ASC)], silver nanoparticles reduced with aluminum foil [Ag(Al)], chromium metal-organic framework with benzene tricarboxylate linkers [MIL101(Cr)], silver nanoparticles reduced with copper tape and heated calcinated [Ag(Cu, Δ)] and copper tape with one face with silver nano-electrodeposited of area 155 mm² [Ag/Cu Tape].

Compared with the physisorption of the borosilicate glass, poor sulfur adsorption was observed for silver reduced with copper, or copper and calcinated, and MIL101(Cr). Greater surface area using filtered γ -FeOOH [γ -FeOOH_{filter_paper}]

Fig. 11.4 a Summary of adsorption equilibrium capacity for γ -FeOOH adsorbent at equilibrium using the Shrinking core model to categorize the interactions involved to account for the reduction in observed H_2S .


b Linearization of the Shrinking core model for γ -FeOOH adsorbent at equilibrium to distinguish between H_2S related to chemical reactions at the gas–liquid and liquid–solid interfaces and between ion and species transport at the surface into the interior and void spaces **c**: Deconvolution of the Shrinking core model with parameterization of A and B to show a degree of fitness for γ -FeOOH adsorbent at equilibrium to show that the A and B parameters fit with high regression for the reaction kinetics component and internal diffusion/migration component, respectively which define the intrinsic sulfur binding capacity of the adsorbent. **d** The offline slurry reactor binding capacity of silver-based, copper, chromium, and γ -FeOOH-based adsorbent, including filter and tape topologies, to assess chemistries and bulk material topography binding to H_2S in an offline slurry reactor. The H_2S pulsed injection square wave profile is also shown on top



exhibited a higher H₂S adsorption. However, not as high as powered γ -FeOOH [γ -FeOOH_{powdered}], which was not the highest adsorbent in the series of adsorbents (Fig. 11.4d). The CuMOF and silver were reduced with ascorbate. The electrochemically generated silver copper tape formed at approximately 70 mg/g ratio in 30 min. This suggests that surface area and pore volume are important but may not be dominant as the MIL101 has one of the largest surface areas per gram. Surface charges attract and bind to H₂S or redox chemistries in generating zero-valent sulfur or sulfides more likely to influence H₂S removal than adsorbent pore volume.

Effect of reaction temperature: Three adsorbents were evaluated at three different temperatures (90 °F, 135 °F, 190 °F, and 260 °F), as shown in Fig. 11.5a. The slurry reactor was injected with 118 ppm H₂S, and the free H₂S was measured after 300 s. The Ag/Cu Tape, CuMOF, and Ag(ASC) all had 0 ppm values within 300 s and were not evaluated. Only systems that displayed non-zero values were used. The graphs suggest that sulfur adsorption drops as the temperature increases. While higher temperatures assist with chemical reaction rates and mass transport, higher temperatures also decrease H₂S solubility in water, limiting gas–liquid distribution and lower adsorption.

In the offline slurry reactor, lower temperatures gave the best adsorption capacities, as shown in Fig. 11.5b. The trend is related to the type of interactions that dominate H₂S binding. Higher temperatures assisted with H₂S binding on the glass surface, while the reverse was true for MIL101(Cr), where lower temperatures w Higher temperatures also resulted in less adsorption of H₂S for the Ag(Al) system. This is due to the different surface chemistries between the three systems reflecting general trends. For the other systems, the values were zero over the entire temperature range within the 300 s delay. To further explore the type of kinetics, the system H₂S after injection was measured .

[Injection ] or after a wait of 30 min. In most adsorbents, however, for CuMOF and tape, the binding and removal are almost instantaneous, and surface interactions are optimized without particle diffusion.

Effect of adsorbent catalyst solid mass: To investigate whether the mass of the adsorbent is related to the speed of removal of H₂S, three adsorbents were tested at three masses with repeated injections of H₂S into a slurry offline reactor. The relationship between the draw-down of H₂S after repeated injections of H₂S is shown in Fig. 11.5c. The results show that for a 10 ppm injection of H₂S, all systems except the glass vial can reduce the output to 0 ppm within 300 s. A second injection of 50 ppm shows the non-zero output for silver nanoparticles reduced with copper [Ag(Cu)]. The most effective removal was with 103 mg of adsorbent, with higher amounts being less effective. This may be due to the availability of active sites distributed more effectively at the lower mass relative to the higher masses, where adsorbent sites are less accessible due to aggregation or clustering of the adsorbent. For the copper MOF, masses of 122 mg or higher result in complete removal of H₂S, which was also observed for γ -FeOOH, where 111 mg or higher resulted in

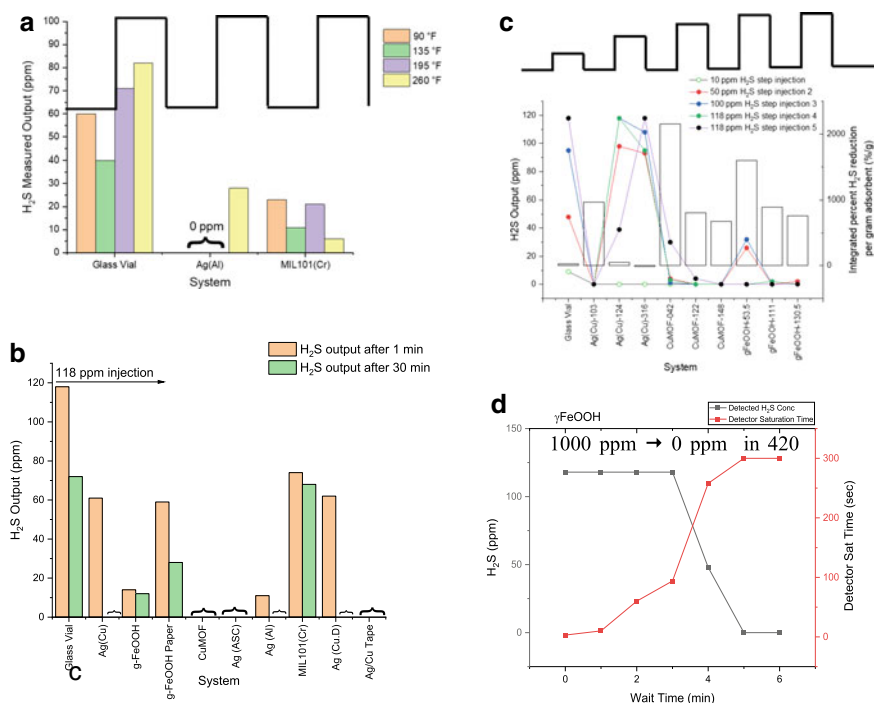


Fig. 11.5 **a** The effect of slurry temperature on the draw-down of H₂S after injection of 60 ppm of H₂S at 90 °F and 135 °F and a second injection of 100 ppm at 195 °F and 260 °F for reactor vessel with borosilicate glass lining, silver nanoparticles reduced with aluminum foil [Ag(Al)], and MIL101(Cr). A complex relationship is down. H₂S reduction occurs at lower temperatures for the glass vial but higher temperatures for MIL101(Cr), reflecting different surface chemistries. The H₂S pulsed injection square wave profile is also shown on top. **b** the draw-down of H₂S after an initial injection of 118 ppm for several adsorbents, showing that for the borosilicate glass, greater reaction time lowers final H₂S, which is also seen for the other systems reflecting that surface adsorption requires binding and diffusion, however for CuMOF, Ag(ASC), and the Ag/Cu Tape greater H₂S residency time does not affect the final H₂S concentration suggesting that the elimination of H₂S at the surface is almost instantaneous **c**: The reduction of 10, 50, 100, and 118 ppm of H₂S for three adsorbents of increasing mass (left-hand axis) and the normalized unit effectiveness of H₂S removal (percent removal per unit mass, right-hand axis). The H₂S pulsed injection square wave profile is also shown on top. **d**: The rate of H₂S removal after a single pulsed injection of 1000 ppm using the time taken to saturate the detector and the total elapsed time for the value to reach zero for the γ -FeOOH adsorbent

near complete removal of H₂S. These trends were observed when higher amounts of H₂S were injected where the lower mass of Ag(Cu) was the most effective and intermediate masses of CuMOF, and γ -FeOOH resulted in near-removal of H₂S. The delay time was 300 s between pulsed injections. The total integrated amount was the sum of the concentrations, and the percent reduction of H₂S to this amount was divided by the mass of the adsorbent to determine the unit value. Since the glass vial had no adsorbent, the surface area was used and plotted as a bar graph in Fig. 11.5c.

For copper, the lowest mass was the most effective. It was distributed uniformly, with every adsorbent being effective at H₂S removal up to a calculated injection of 500 ppm (Fig. 11.5d). The CuMOF and γ -FeOOH higher masses resulted in greater removal of H₂S, with the most optimal mass being the lowest evaluated, suggesting that most of the adsorbent is being used at lower masses. In contrast, although more adsorbent is available for interactions at higher masses, the effectiveness per unit mass is less.

The decrease of H₂S to near zero at higher adsorbent solid mass is due to increased catalytic sites, which are accessible for sulfur binding, thereby increasing the total sulfur capacity per unit volume. However, a greater solid mass of adsorbents would also increase the viscosity of the slurry and generate bubble cavitation, leading to lower gas–liquid mass transfer and decreased gas holdup, especially if the adsorbent resin/powders obscured the lower layers or aggregated, thereby limiting free sites for binding. This would result in lower binding per unit mass. Lastly, the higher concentrations resulted in faster removal except for Ag(Cu), related to the availability of free sites for binding. Higher concentrations will result in greater proportional gas dissolving in the liquid phase due to the higher partial pressure of H₂S, improving H₂S solution solubility and mass transfer between the gas and liquid interface. However, greater concentrations will also utilize more sites, leaving fewer sites for binding, and adsorbents, where particle diffusion is important, will have less time due to the greater abundance of H₂S, indicating lower initial concentrations of H₂S enhance the adsorption efficiency of the adsorbents.

Effect of initial H₂S injection concentration on adsorbent removal effectiveness:

This was further evaluated with γ -FeOOH by injecting a calculated concentration of 1000 ppm H₂S. As the detector is calibrated to 100 ppm with an overshoot of 118 ppm, the output reading is leveled at 118 ppm. However, the time taken for detector saturation was determined. The H₂S test was injected with a residency time of 300 s, followed by a measurement of H₂S output by either reading the value in ppm [up to 118 ppm] or the time taken for the detector LED to be activated (seconds). The output was measured every 60 s for 360 s until the final readout was zero. It can be seen that at 1000 ppm input, the time taken to reach 118 ppm was approximately 200 s. This corresponds to an approximate removal efficiency of 764%/g @ 1000 ppm, lower than the corresponding value at 100 ppm of 1595%/g @ an integrated total of 396 ppm of H₂S.

Regeneration of the Catalytic System by Hydrogen peroxide Treatment:

The samples were subjected to a 60 ppm injection of H₂S, 300-s residency, and measurement of H₂S output. Then the samples were washed with 3 mL hydrogen peroxide for 30 s, filtration, heating at 110 °C for 1 h, and utilization within the offline slurry reactor, followed by a second injection of 118 ppm H₂S and measurement with the 60 ppm. This was repeated until the cycle when 100 ppm was injected. The measurement of H₂S output was ratio to the initial input, and the adsorption capacity (mg/g) was calculated and is summarised in Fig. 11.6.

There was a slight increase after the first cycle of regenerative wash, but a much greater increase after the second cycle was maintained until the last cycle when

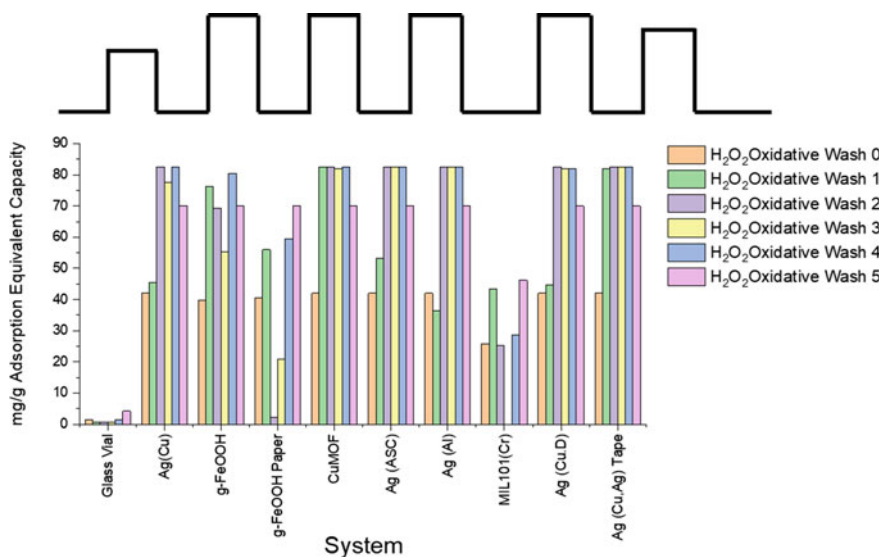
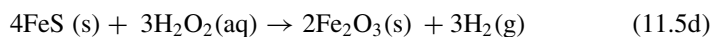
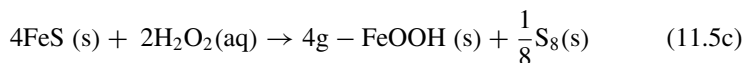
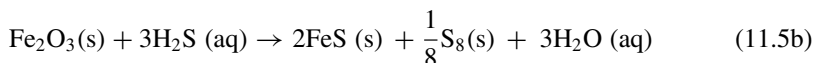
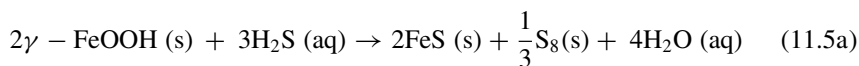
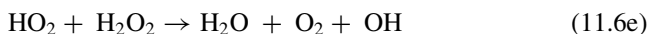
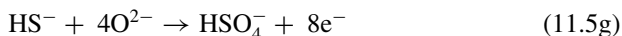
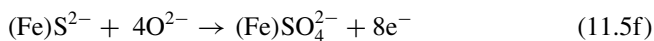
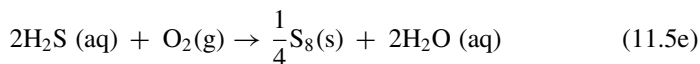


Fig. 11.6 The effect of hydrogen peroxide-assisted regeneration of different adsorbents evaluated using pulsed H_2S from 60–118 to 100 ppm. The pulsed profile is shown on top, and the initial increase, plateau, and decrease in sulfur capacity are observed for most systems

there was a drop. This decrease in sulfur capacity was attributed to a partial loss of adsorbent in the oxidation process and the potential formation of OH radical, which promotes the formation of sulfate (SO_4^{2-}) instead of sulfur (S), summarized in (Eq. 11.5), lowering the desulfurization capacity. The iron catalyst species is regenerated after hydrogen peroxide treatment in this reaction. Water moisture was visible inside the reaction vessel when the glass vial was used, supporting (Eq. 11.5a, b, e) and bubbles. These bubbles could either be hydrogen from the decomposition by-product (Eqs. 11.5d and 11.6e) due to one electron redox from the H_2O_2 , where the electron is either from the metal or donated to the metal, which in the air with oxides can form sulfate (Eq. 11.5f) instead of sulfur (Eq. 11.5c) and various hydroxide or hydroperoxyl radicals shown in (Eq. 11.6a–f).





Upon chemisorption of the H_2S species with surface OH^- , the species SH^- is likely generated [$\text{H}_2\text{S}_{\text{ads}} + \text{OH}^- \rightarrow \text{H}_2\text{O} + \text{SH}^-$ and $\text{H}_2\text{S} + \text{O}^{2-} \rightarrow \text{OH}^- + \text{HS}^-$] and conversion of Fe in $\gamma\text{-FeOOH}$ to Fe^{3+} , as well as oxidation of S^{2-} to S^0 . The electrons can be supplied by hydrogen peroxide or oxygen and are incorporated into the catalytic structure [$\text{O}_2 + 2\text{e}^- \rightarrow \text{O}^{2-}$]. Further exposure can generate sulfate species [SO_4^{2-} and HSO_4^-], lowering the catalytic efficiency of the adsorbent. The surface can be loosely considered a weak Bronsted acid, promoting the dissociation of H_2S , with iron peroxides showing higher OH catalytic sites. Fourier adds this interpretation to transform infrared spectra (Fig. 11.7a–i) that show features diagnostic of sulfur species. The FTIR spectra can be categorized into two broad groups and are illustrated by the copper/silver tape (Fig. 11.7d, and also observed in Fig. 11.7b–e, h (black curve), and Fig. 11.7i) with a weak bond stretch at 1620 cm^{-1} ($\delta(\text{HOH})$) and a much stronger absorption peak at 3600 cm^{-1} ($\nu(\text{OH})$) [31].

Another peak around 3400 cm^{-1} is related to surface hydroxyl groups ($\nu(\text{OH})$) [32]. Some samples also show a region between 2500 and 1800 cm^{-1} , which is also observed for sulfuric acid ($\nu(\text{OH})$) [33]. Smaller peaks at 1280 cm^{-1} and 1150 cm^{-1} are attributed to asymmetric vibrations of bidentate sulfate species [34]. The second class illustrated by silver nanoparticles filtered and heated into a thick disc with added H_2S and reheated to $300\text{ }^\circ\text{C}$ to remove physisorbed species (Fig. 11.7a, but also observed in Fig. 11.7f–h (red curve)) shows a series of discrete peaks from 3900 cm^{-1} to 3400 cm^{-1} , 2200 cm^{-1} to 1300 cm^{-1} , and 1040 cm^{-1} to 860 cm^{-1} sulfate stretching vibrations, and metal-sulfur vibrations (S–O). Other peaks correspond to physisorbed

Fig. 11.7 **a** FTIR of silver nanoparticles reduced and filtered, with the filtrate on the fiber paper heated to 100 °C and then 1 mL of 100 ppm H₂S added and heated to 50 °C. **b** FTIR of γ -FeOOH + H₂S heated to 500 °C (black) and γ -FeOOH + H₂S heated to 50 °C (red). **c** FTIR of MIL101(Cr) (blue), MIL101(Cr) doped with silver (red), MIL101(Cr) co-doped with silver and magnesium (green), and MIL101(Cr) co-doped with Ag and Mg after 30–500 °C TGA ramp (black). **d**: FTIR of silver reduced with copper and oven heated to 300 °C (Cu Δ). **e** FTIR of silver reduced with copper foil (red) and with 100 ppm of H₂S added and heated to 100 °C (green) and further heated to 300 °C (black). **f** Silver reduced with copper foil with the addition of 10 ppm H₂S dried at room temperature. **g** FTIR of silver reduced with ascorbate (red) and 100 ppm of H₂S added and heated to 100 °C (red). **h** FTIR of Copper metal–organic framework (CuMOF) heated at 100 °C

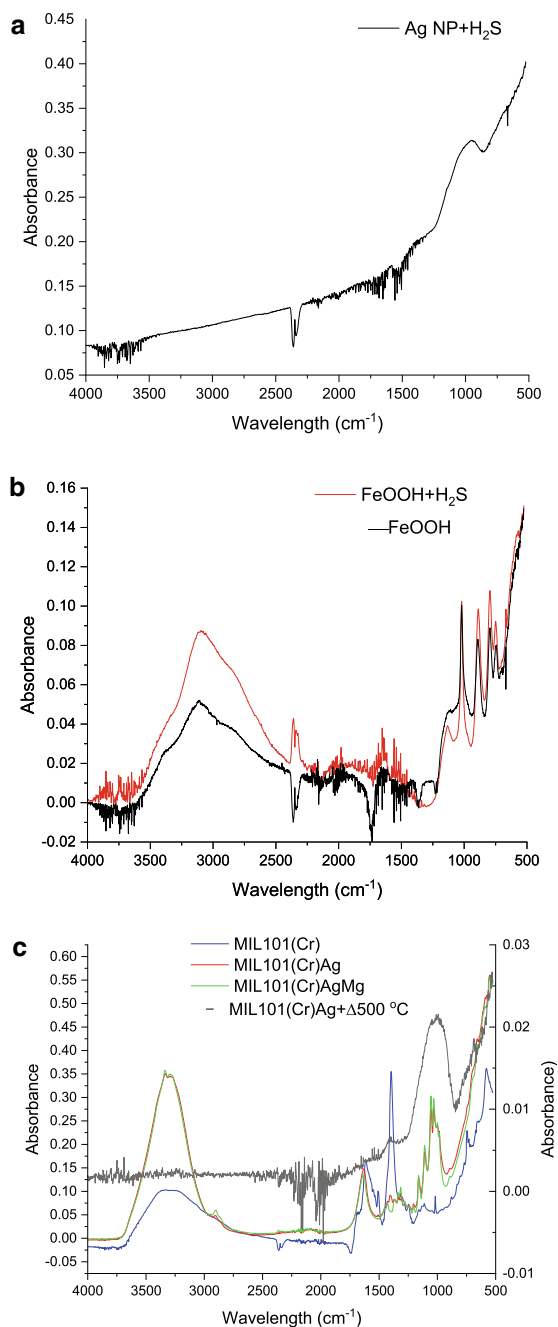


Fig. 11.7 (continued)

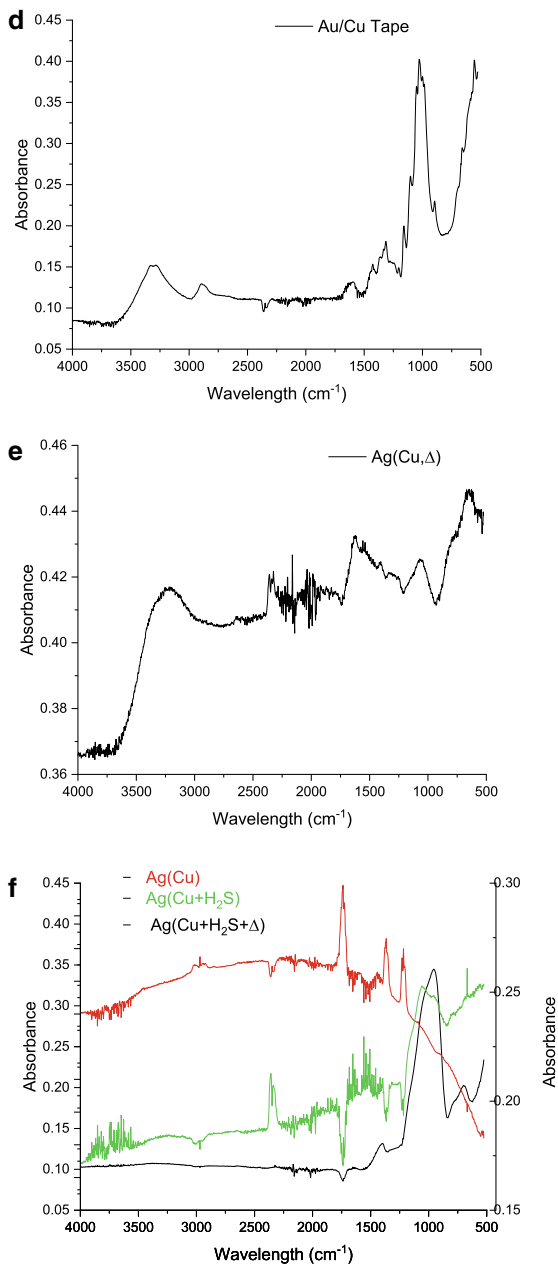
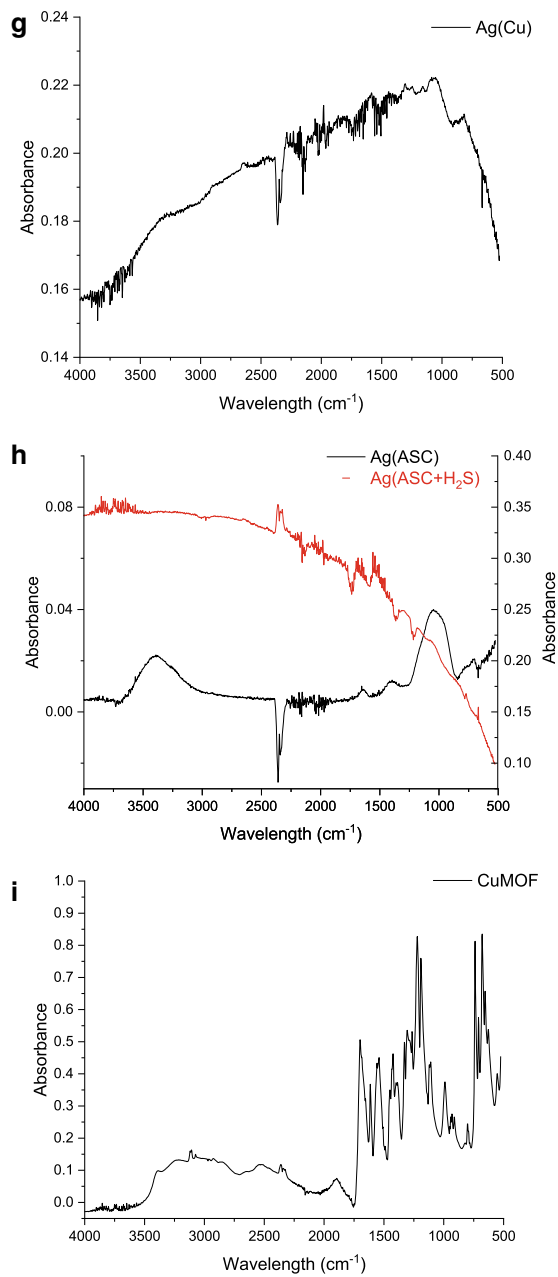


Fig. 11.7 (continued)



hydrogen sulfide at 2560 cm^{-1} (Fig. 11.7a). However, these peaks are shifted to lower wavenumbers reflecting different surface interactions. The degree of surface bonding is related to the particle geometry and degree of the surface dipole, hydrophilicity, and extent of Bronstead acidity [35].

Other peaks are specific to the adsorbent. For example, for MIL101(Cr) (Fig. 11.7c), the peaks at approximately 1600 cm^{-1} and 1400 cm^{-1} correspond to symmetric and asymmetric vibrational stretching modes of COO^- groups [36]. The peaks at 1155 cm^{-1} , 1013 cm^{-1} , and 743 cm^{-1} are related to the benzene ring vibrations of the linker [37]. The broad peaks around 3400 cm^{-1} are consistent with the OH vibration of water that is bound inside the framework or generated by binding to H_2S [$\text{M}_x\text{O}_y + y\text{H}_2\text{S} \rightarrow \text{M}_x\text{S}_y + y\text{H}_2\text{O}$] [38]. The CuMOF (Fig. 11.7i) also displays a broad peak around 3400 cm^{-1} attributed to vibrations of physically adsorbed water molecules, and 3000 cm^{-1} to 2900 cm^{-1} are the C–H vibrations of the benzene linker. Additional peaks from 1200 to 1000 cm^{-1} are the benzene linker's in-plane and out-of-plane C–H bending modes. The peaks at 1710 cm^{-1} , 1636 cm^{-1} , and 1386 cm^{-1} are attributed to the C = C and C = O groups within the BTC framework [39]. For the FeOOH (Fig. 11.7b) catalyst, the peak at 892 cm^{-1} is caused by d(O–H) deformation vibrations [40]. The broad peaks around 3000 cm^{-1} to OH stretching frequency. The frequency at 3300 cm^{-1} and 893 cm^{-1} are due to O–H and O–Fe stretching vibrations [41]. Peaks between 1350 and 1300 cm^{-1} are due to OH deformations [42], while the region between 1670 to 1500 cm^{-1} is related to the Fe–O vibrations from the crystal lattice [43]. For silver (Fig. 11.7h), the peaks are related to the organic coatings and binding agents, not silver directly, as silver interactions are observed using ultraviolet spectroscopy. The peaks around 2900 cm^{-1} are C–H stretch vibrations.

These FTIR observations were also correlated with thermogravimetric analyses of the samples exposed to 10 ppm H_2S and then heated to $100\text{ }^\circ\text{C}$ to drive off physisorbed H_2S and are all very similar and share three general features in common (Fig. 11.8a–f). Mass loss between 20 and $100\text{ }^\circ\text{C}$ (Fig. 11.8a, d) corresponds to surface-bound water from the environment or is generated by in-situ binding with H_2S . The second phase is approximately 100 – $250\text{ }^\circ\text{C}$ (Fig. 11.8b, c, e). It is related to molecular water bound using hydrogen bonding within the catalyst surface to yield the semi-anhydrous state [44]. The last stage is the complete removal of water or a phase transition to the thermodynamically more stable phase (Fig. 11.8a, d, e) or decomposition of the crystal structure for MIL101 and CuMOF (Fig. 11.8b, f), suggesting that the adsorbents are stable up to a bulk temperature of $250\text{ }^\circ\text{C}$, which is not the inlet gas temperature, as hotter gases have low residency times with the adsorbent and would not lead to disruption of the catalytic sites. The TGA is the equilibrium temperature of the adsorbent catalyst system, demonstrating that the systems are thermally stable, especially the silver-based nanoparticles [45].

One novel observation was that the MIL101(Cr) removal effectiveness was low. However, its surface area and porosity are high due to chromium incorporation as metal redox centers. This observation supports the hypothesis that material porosity and surface area influence H_2S removal. However, the impact is greater for materials with surface-exposed hydroxyl groups that can act as Bronstead acid sites. This was

Fig. 11.8 **a** TGA/DSC of γ -FeOOH + 10 ppm H₂S heated to 100 °C before TGA analysis **b** TGA/DSC of MIL101(Cr) + 10 ppm H₂S heated to 100 °C prior to TGA Analysis (black) and silver doped (blue) and silver-magnesium co-doped (green). Note that silver and silver magnesium yield near identical profiles, suggesting that magnesium has not distributed the structure or bonding of silver. **c** TGA/DSC of silver reduced with copper (Ag, Cu) + 10 ppm H₂S heated to 100 °C prior to TGA Analysis (blue) and silver reduced with copper and heated to 300 °C [Ag(Cu, $\Delta\Delta$)] before the addition of H₂S and then heated to 100 °C prior to TGA analysis. **d** TGA/DSC of silver reduced with ascorbate (Ag, ASC) + 10 ppm H₂S heated to 100 °C before TGA Analysis. **e** TGA/DSC of silver reduced with aluminum (Ag, Al) + 10 ppm H₂S heated to 100 °C before TGA Analysis. **f** TGA/DSC of copper MOF + 10 ppm H₂S heated to 100 °C before TGA analysis

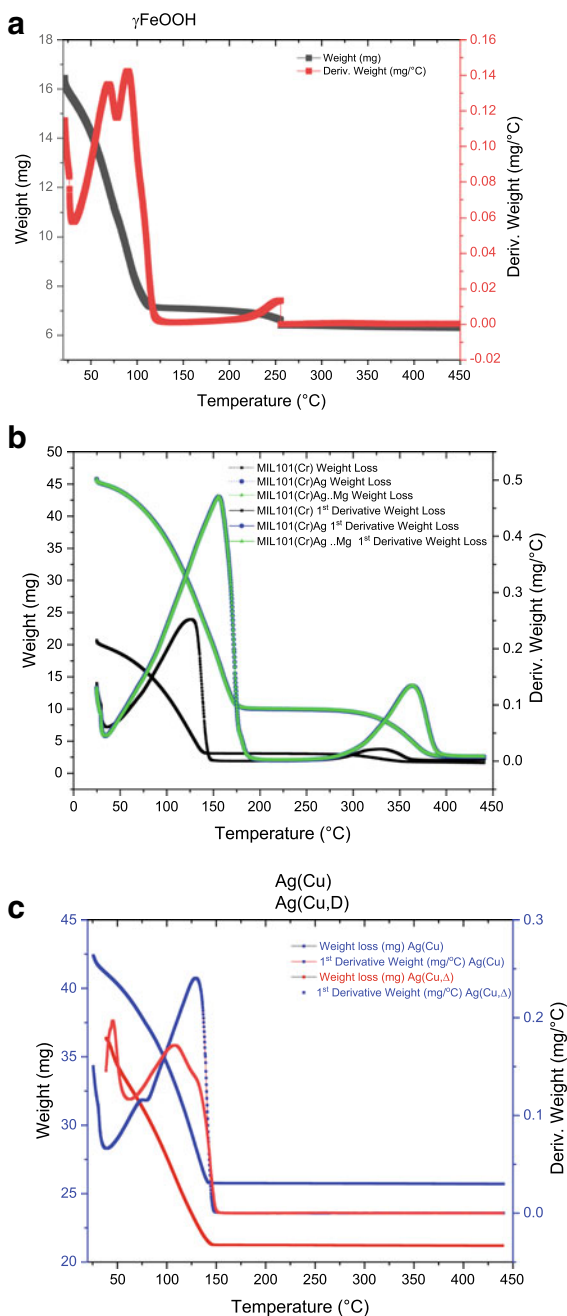
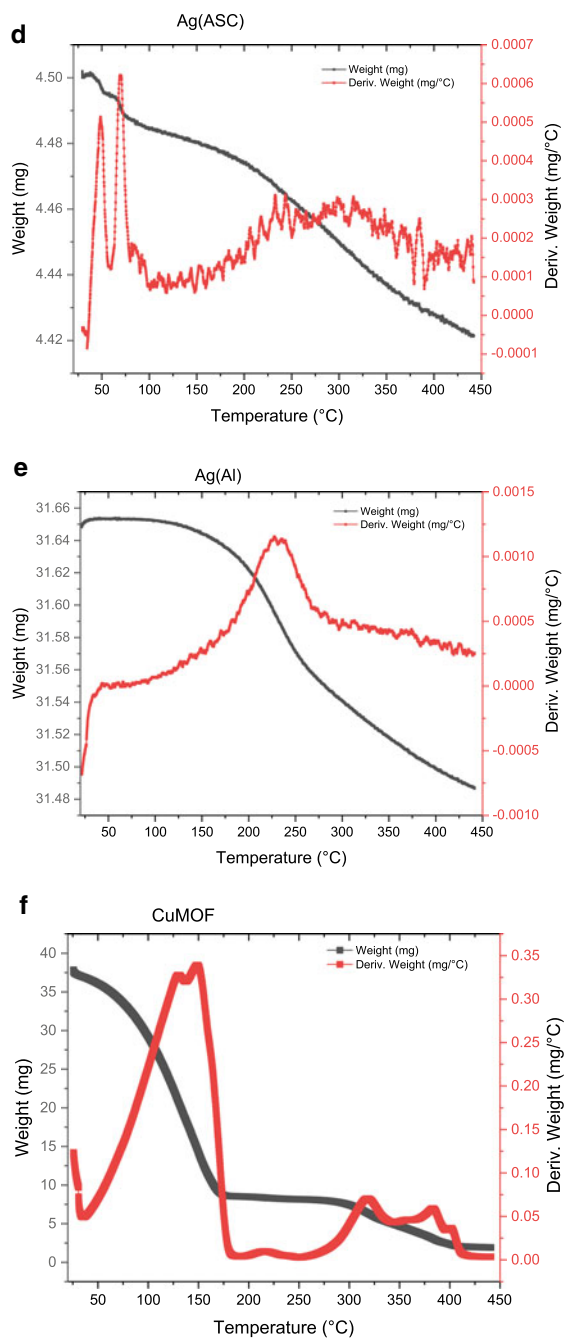


Fig. 11.8 (continued)



demonstrated through doping and cooping of the parent MIL101(Cr) with silver only [MIL101(Cr).Ag] and silver and magnesium [MIL101(Cr)..Ag.Mg] is shown in Fig. 11.9, along with a schematic of the three-dimensional MOF structure. The calculated sulfur binding capacities were 12.6 mg/g for MIL101(Cr) and 71.4 mg/g for MIL101(Cr).Ag, and 75.6 mg/g for MIL101(Cr).Ag.Mg is statistically significant at the 0.05 level of sophistication for the t-test ($n = 3$, $p < 0.05$). Since the surface area is similar to the pore volume, the differences are the incorporation of silver and magnesium that can form ion–dipole. M-OH sites attract the H_2S or H_2O . H_2S towards the catalytic surface.

After H_2S and heating, the catalytic samples were subjected to X-ray photon spectroscopy (Fig. 11.10a–e) for sulfur. The survey scans for MIL101(Cr) did not detect sulfur (Fig. 11.10d). At the same time, those doped with silver (Fig. 11.10c) and silver/magnesium (Fig. 11.10d) showed a trace amount of less than 1 atomic percent, suggesting that silver and magnesium can interact with the sulfur through their orbitals with lone pair of electrons and potential M-OH interactions. The γ -FeOOH, the first catalyst evaluated, also demonstrated trace binding (Fig. 11.10a), as did silver reduced with ascorbate (one of the top candidates in removing H_2S , Fig. 11.10b).

Lastly, copper MOF has one of the highest sulfur capacities and exhibited the lowest atomic sulfur suggesting that more binding occurred at the surface of the sulfur, was loosely coordinated with the organic framework, and could be desorbed up to 100 °C (Fig. 11.10e). These compounds had a solution sulfur capacity of around 75 mg/g or greater. However, they had bound S peaks from 0.21 to 0.91 atomic %,

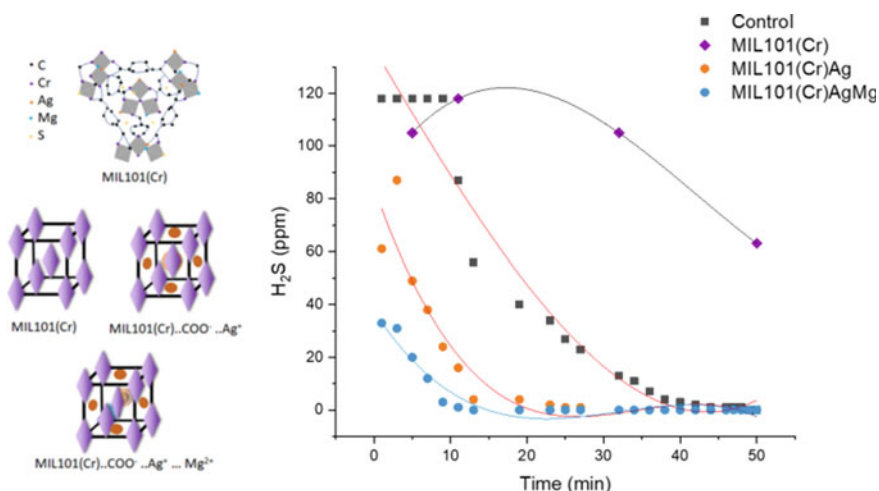
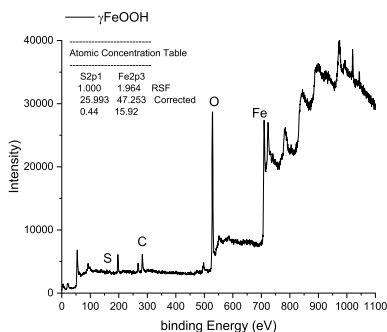
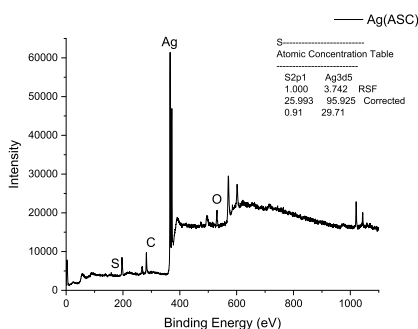


Fig. 11.9 The binding capacity of borosilicate glass (black), MIL101(Cr) (purple), MIL101(Cr)Ag (orange), and MIL101(Cr) Ag.Mg (blue) in the speed of binding with 118 ppm H_2S . The time taken to reach an output concentration of 0 ppm was measured and is shown to be statistically significant between the undoped [MIL 101(Cr)] and the single doped [MIL 101(Cr) ... Ag⁺] and co-doped [MIL 101(Cr) ... Ag⁺ ... Mg²⁺] derivatives

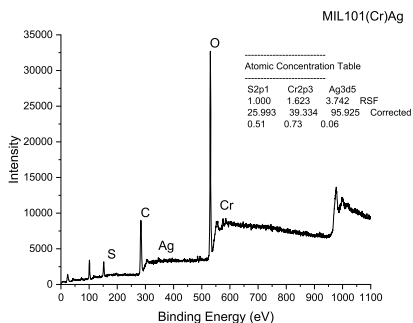
Fig. 11.10 **a** Survey Scan of γ -FeOOH + 10 ppm H₂S heated to 100 °C prior to XPS Analysis with more sensitive composition for S and Fe listed using multiplex scan calibrated to core peak for carbon and oxygen. **b** survey Scan of silver reduced with ascorbate + 10 ppm H₂S heated to 100 °C prior to XPS Analysis with more sensitive composition for S and Ag listed using multiplex scan calibrated to core peak for carbon and oxygen. **c** survey Scan of MIL101(Cr) doped with silver + 10 ppm H₂S heated to 100 °C prior to XPS Analysis with more sensitive composition for S and Cr, and Ag listed using multiplex scan calibrated to core peak for carbon and oxygen. No S was observed for the parent MIL101(Cr) compound. **d** survey Scan of MIL101(Cr) doped with silver and magnesium + 10 ppm H₂S heated to 100 °C prior to XPS Analysis with more sensitive composition for S and Cr, Mg, and Ag listed using multiplex scan calibrated to core peak for carbon and oxygen. No S was observed for the parent MIL101(Cr) compound. **e** survey Scan of CuMOF + 10 ppm H₂S heated to 100 °C prior to XPS Analysis with more sensitive composition for S and Cu listed using multiplex scan calibrated to core peak for carbon and oxygen.



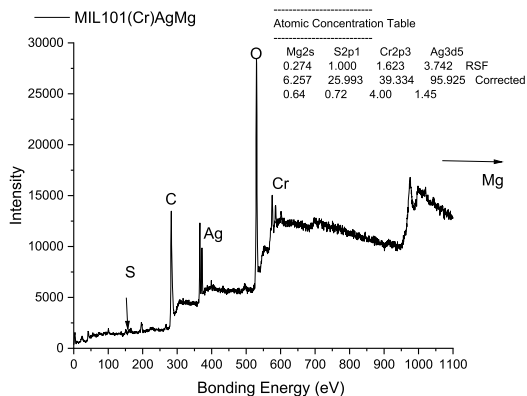
a: Survey Scan of γ -FeOOH + 10 ppm H₂S heated to 100 °C prior to XPS Analysis with more sensitive composition for S and Fe listed using multiplex scan calibrated to core peak for carbon and oxygen.



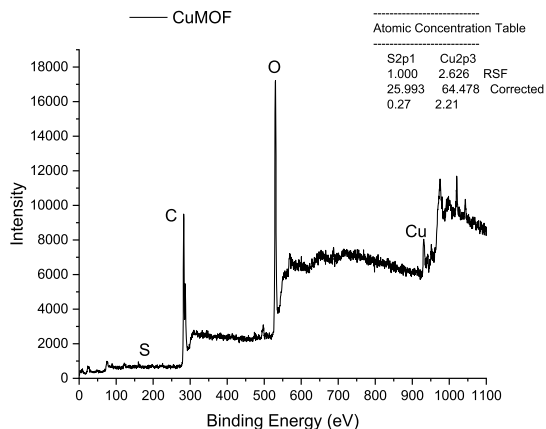
b: Survey Scan of silver reduced with ascorbate + 10 ppm H₂S heated to 100 °C prior to XPS Analysis with more sensitive composition for S and Ag listed using multiplex scan calibrated to core peak for carbon and oxygen.



c: Survey Scan of MIL101(Cr) doped with silver + 10 ppm H₂S heated to 100 °C prior to XPS Analysis with more sensitive composition for S and Cr, and Ag listed using multiplex scan calibrated to core peak for carbon and oxygen. No S was observed for the parent MIL101(Cr) compound.



d: Survey Scan of MIL101(Cr) doped with silver and magnesium + 10 ppm H₂S heated to 100 °C prior to XPS Analysis with more sensitive composition for S and Cr, Mg, and Ag listed using multiplex scan calibrated to core peak for carbon and oxygen. No S was observed for the parent MIL101(Cr) compound.



e: Survey Scan of CuMOF + 10 ppm H₂S heated to 100 °C prior to XPS Analysis with more sensitive composition for S and Cu listed using multiplex scan calibrated to core peak for carbon and oxygen.

Fig. 11.10 (continued)

suggesting that strong binding to the surface is not a prerequisite for efficiently removing H₂S from the air or the liquid–air interface.

These catalysts were synthesized without sulfur-containing compounds, but after exposure to H₂S and heating to remove surface-bound species, trace materials were found at around 164 eV. Although the peak intensities were low, these peaks were broad and indicative of sulfur species, not zero-valent ones [46]. The metal sulfide formation, such as FeS₂, sulfate at higher oxygen content, and zero-valent sulfur at low oxygen levels, are thermodynamically plausible and have been reported in

the literature [47]. For γ -FeOOH, two peaks around 714 eV and 725 eV are visible even in the lower-resolution survey scan. Examination of the peak areas is consistent with the iron reduction from the Fe^{3+} to the Fe^{2+} species, which stoichiometrically is consistent with FeS_2 and not FeSO_4^{2-} , which potentially terminates with the formation of S^0 [48]. The higher oxidation of S would also generate sulfuric acid, lowering H_2S solution solubilities [$\text{FeS}_2 + 3\frac{1}{2}\text{O}_2 \rightarrow \text{FeSO}_4 + \text{H}_2\text{SO}_4$] suggests that $\text{Fe(III)} \rightarrow \text{Fe(II)S}$ is the desulfurization step where H_2S is removed, H_2O is generated, and a regeneration cycle where Fe(II)S_x is converted to Fe(III) and the surface or bound sulfur converted to zero-valent sulfur or sulfate with hydrogen peroxide or molecular oxygen as the oxidizer and source of oxygen atoms. The catalytic surface can be regenerated for five cycles with over 75% efficiency retained relative to the new catalyst.

The lower H_2S adsorption of $\text{Ag(Cu } \Delta)$ relative to Ag(Cu) suggests that calcination to metallic silver is less efficient than AgO and Ag_2O as sorbent sites with the S interacting with the M and the H interacting with the O (M), where M is the metal on the outer surface and M within the crystal lattice. This would explain why most of the H_2S desorbed after 100 °C heating but not all and why different S species were observed instead of coordinated H_2S . A copper Engelhard Titanosilicate-2 complex has a sulfur capacity of 30 mg/g [49], while a copper metal–organic framework has a 20%Cu/MSU-1 sulfur capacity of 19 mg/g [50]. Liu et al. prepared a Fe–Al co-doped CuO with the largest reported sulfur capacity of 114 mg/g in 2015 [51]. Wang et al. fabricated ZnO nanoparticles incorporated into Santa Barbara amorphous material-15 zeolites sorbent with the highest reported sulfur capacity published of ~ 436 mg/g with 3.04 wt% Zn [52]. Liu et al. synthesized ZnO/SiO₂ gel composites with 30 wt% ZnO, demonstrating a maximal sulfur capacity of 96 mg/g [53]. A different ZnO–Al₂O₃ composite exhibited a sulfur capacity of 52 mg/g [54]. ZnO/SiO₂ composites achieved a sulfur capture capacity of 161 mg/g at 30 °C [55]. A Zn-25%Bi mixed blend oxide demonstrated a sulfur binding capacity of 80 mg/g [56], and a copper metal–organic framework heated at 80 °C exhibited a sulfur binding capacity of 57 mg/g [57].

Recently Liu et al. reviewed approximately 119 publications using metal-based sorbents for hydrogen sulfide at lower temperatures and found a modal sulfur binding capacity of 41 mg/g, indicating that our average sulfur binding capacity of 78.05 mg/g places these materials in the top percentile in terms of binding effectiveness at room temperature. If bulk catalyst mass is taken, as Liu et al. reviewed, indicating the adsorbent was 1–8 g range, the present percent reduction of H_2S per unit mass is even more compelling in terms of their effectiveness compared to a benchmark of varying metal/metal catalysts published in the literature and reviewed by Liu et al. [57].

11.4 Conclusions

We have demonstrated that gamma FeOOH is an effective adsorbent for the catalytic removal of H₂S from water in an offline slurry reactor model test. The γ -FeOOH sites have OH⁻ sites that attract H₂S through its weak dipole and are converted to elemental sulfur and other oxidized species depending on oxygen availability. As the resident time is increased, the conversion of H₂S to FeS and S⁰ or S₈ increases, accompanied by the formation of water and a decrease in available Bronsted acid sites, which is less sensitive to intrinsic surface area and pore volume, as the degree of Bronsted acid sites determines the likely H₂S adsorption. Hydrogen peroxide treatment for γ -FeOOH will likely generate Fe²⁺ and O²⁻/OH⁻ species, which can also be generated from water that can behave as a co-catalyst from the previously chemisorbed H₂S on the surface. This regeneration is related to structural changes within the crystal phase, which is unlikely in Fe₂O₃. The generation of elemental sulfur reduces OH⁻ sites and likely H₂S and, to a lesser degree, O₂ uptake, limiting sulfur binding capacity, and was visualized through successive H₂O₂ regeneration cycles of the Fe adsorbent. In addition, silver ascorbate, galvanostatic silver/copper tape, copper metal-organic framework, and MIL101(Cr) co-doped with silver and magnesium were equally effective in removing up to 100 ppm of H₂S in approximately 30 min. This was confirmed by direct measurement of H₂S output and indirectly from FTIR/TGA spectra and confirmed with trace amounts of S (around 164 eV) detected in the surface scan by XPS. These materials offer low-cost adsorbents to be evaluated in ships where storage, bilge, or ballast tanks must vent H₂S before inspection and the associated health risks.

Several generalizations regarding catalyst design and understanding the processes whereby H₂S is removed can be offered. The model to fit the physical binding can be based on the shrinking model; although not explicitly modeled, the double log plot is consistent with a pseudo-first-order reaction rate concerning temperature in the fixed H₂S injection model but may be pseudo-second-order for temperature and hydrogen sulfide up to a maximum sulfide concentration, for our study was 118 ppm. The kinetics and temperature study also indicates that the activation of hydrogen sulfide on the metal oxide surface is between 70 and 100 kJ/mol, depending on the metal. Upon binding, hydrogen sulfide is decomposed with the reduction of the metals to lower oxidation states and the formation of metal sulfides. With weak Bronsted acids, at low temperatures, H₂S sulfide can be decomposed to HS⁻ and S²⁻ and ultimately to sulfuric acid if moist lowering overall binding capacity. At higher temperatures, H₂S can be composed of elemental sulfur and hydrogen. The FTIR spectra are consistent with the hypothesis that two types of interactions occur. The first is the metal oxygen on the outer surface, the metal sulfur in the interior, and grain boundaries if calcinated at high temperatures. These side reactions ultimately limit overall binding capacity and catalyst efficiency.

Acknowledgements The Naval Surface Warfare Center, Carderock Division, Drs J. Church, J. Price, J. Barkyoumb, and S. Verosto, for their technical assistance. The Oil Pollution and Abatement

Group members include Dr. Miae Ha, Mr. Madara Jayatilake, Mr. Alex Mack, Mr. Tim Kelly, Ms. Christine Park, and Mr. Lee Sang.

Author Contribution Sajid Bashir conducted all the H₂S experiments, and Jingbo L Liu assisted him in the synthesis design and partial synthesis of the catalysts used for H₂S detection and absorption. Drs Church, Verosto supervised the experimental design and overview of remediation problem. Drs Price and Barkyoub with logistics and Oil Pollution and Abatement Group members for assistance with lab access, safety, and access to or ordering chemicals and general assistance.

References

1. Łowicka E, Beltowski J (2007) Hydrogen sulfide (H₂S)-is pharmacologists' third gas of interest. *Pharma Rep*: PR 59(1):4–24
2. Beltowski J, Jamroz-Wiśniewska A (2016) Hydrogen sulfide in the adipose tissue—physiology, pathology and a target for pharmacotherapy. *Molecules* 22(1):63
3. Kimura Y, Kimura H (2004) Hydrogen sulfide protects neurons from oxidative stress. *FASEB J* 18(10):1165–1167
4. Olas B (2015) Gasomediators (·NO, CO, and H₂S) and their role in hemostasis and thrombosis. *Clin Chim Acta* 445:115–121
5. Olas B (2014) Hydrogen sulfide in hemostasis: friend or foe? *Chem Biol Interact* 217:49–56
6. Hua MS, Ku YW, Huang CC (1992) Neuropsychological deficits in a case of H₂S anoxic encephalopathy. *Arch Clin Neuropsychol* 7(1):63–76
7. Spassov SG, Faller S, Goeft A, Von Itter MNA, Birkigt A, Meyerhoefer P, Hoetzel A et al (2022) Profiling distinctive inflammatory and redox responses to hydrogen sulfide in stretched and stimulated lung cells. *Antioxidants* 11(5):1001
8. Tvedt B, Edland A, Skyberg K, Forberg O (1991) Delayed neuropsychiatric sequelae after acute hydrogen sulfide poisoning: affection of motor function, memory, vision, and hearing. *Acta Neurol Scand* 84(4):348–351
9. Hirsch AR, Zavala G (1999) Long-term effects on the olfactory system of exposure to hydrogen sulphide. *Occup Environ Med* 56(4):284–287
10. Eapi GR, Sabnis MS, Sattler ML (2014) Mobile measurement of methane and hydrogen sulfide at natural gas production site fence lines in the Texas Barnett Shale. *J Air Waste Manag Assoc* 64(8):927–944
11. Morimoto T, Wu S, Uddin MA, Sasaoka E (2005) Characteristics of the mercury vapor removal from coal combustion flue gas by activated carbon using H₂S. *Fuel* 84(14–15):1968–1974
12. Midson D (2010) The lessons learned from hydrogen sulphide incidents in the Royal Australian Navy. *Headmark* 135:45–47
13. Jung H, Kim D, Choi H, Lee C (2022) A review of technologies for in-situ sulfide control in anaerobic digestion. *Renew Sustain Energy Rev* 157:112068
14. Dumont E (2015) H₂S removal from biogas using bioreactors: a review. *Int J Energy Environ* 6(5):479–498
15. Kaushik R, Ghosh A, Jose DA (2017) Recent progress in hydrogen sulphide (H₂S) sensors by metal displacement approach. *Coord Chem Rev* 347:141–157
16. Mirra S, Milione S, Strianese M, Pellicchia C (2015) A copper porphyrin for sensing H₂S in aqueous solution via a “coordinative-based” approach. *Eur J Inorg Chem* 2015(13):2272–2276
17. Alonso-Tellez A, Robert D, Keller N, Keller V (2012) A parametric study of the UV-A photocatalytic oxidation of H₂S over TiO₂. *Appl Catal B* 115:209–218
18. Tian G, Xi J, Yeung M, Ren G (2020) Characteristics and mechanisms of H₂S production in anaerobic digestion of food waste. *Sci Total Environ* 724:137977
19. Truong LA, Abatzoglou N (2005) An H₂S reactive adsorption process for biogas purification prior to its use as a bioenergy vector. *Biomass Bioenerg* 29(2):142–151

20. Wang C, Chu X, Wu M (2006) Detection of H₂S down to ppb levels at room temperature using sensors based on ZnO nanorods. *Sens Actuators, B Chem* 113(1):320–323
21. Babé C, Tayakout-Fayolle M, Geantet C, Vrinat M, Bergeret G, Huard T, Bazer-Bachi D (2012) Crystallite size effect in the sulfidation of ZnO by H₂S: geometric and kinetic modeling of the transformation. *Chem Eng Sci* 82:73–83
22. Al Mamun MR, Torii S (2015) Removal of hydrogen sulfide (H₂S) from biogas using zero-valent iron. *J Clean Energy Tech* 3(6):428–432
23. Tokuda H, Kuchar D, Mihara N, Kubota M, Matsuda H, Fukuta T (2008) Study reaction kinetics and selective precipitation of Cu, Zn, Ni, and Sn with H₂S in single-metal and multi-metal systems. *Chemosphere* 73(9):1448–1452
24. Gardner FT, Higgins EC (1932) Magnesium hydroxide in the petroleum industry. *Ind Eng Chem* 24(10):1141–1146
25. Peng F, Luo T, Qiu L, Yuan Y (2013) An easy method to synthesize graphene oxide–FeOOH composites and their potential application in water purification. *Mater Res Bull* 48(6):2180–2185
26. Chen Z, Xie J, Liu Q, Wang H, Gao S, Shi L, Liu Z (2019) Characterization of direct coal liquefaction catalysts by their sulfidation behavior and tetralin dehydrogenation activity. *J Energy Inst* 92(4):1213–1222
27. Raabe T, Mehne M, Rasser H, Krause H, Kureti S (2019) Study on iron-based adsorbents for alternating removal of H₂S and O₂ from natural gas and biogas. *Chem Eng J* 371:738–749
28. Wang T, Hu B, Li JW, Nie LH, Tan JJ (2020) Hydrogen sulfide removal by hydroxyl-ferric oxide in a slurry reactor at low temperature. *Ind Eng Chem Res* 59(4):1402–1412
29. Liu D, Li B, Wu J, Liu Y (2020) Sorbents for hydrogen sulfide capture from biogas at low temperature: a review. *Environ Chem Lett* 18(1):113–128
30. Sheinson RS, Williams BA (2007) Preventing hydrogen sulfide formation in shipboard AFFF fire protection systems. Naval Research Lab, Washington DC. <https://apps.dtic.mil/sti/citations/ADA573086>
31. Davydov A, Chuang KT, Sanger AR (1998) Mechanism of H₂S oxidation by ferric oxide and hydroxide surfaces. *J Phys Chem B* 102(24):4745–4752
32. Badri A, Binet C, Lavalley JC (1996) An FTIR study of surface ceria hydroxy groups during a redox process with H₂. *J Chem Soc, Faraday Trans* 92(23):4669–4673
33. Stopperka K (1966) Infrarotspektroskopische Untersuchungen an den flüssigen Systemen SO₃–H₂O und SO₃–D₂O. II. Die Infrarot- und Protonenresonanzspektren von Oleum. *Zeitschrift für anorganische und allgemeine Chemie* 345(5–6):264–276
34. Pradier CM, Dubot P (1998) Adsorption and reactivity of sulfur dioxide on Cu (110). influence of oxidation and hydroxylation of the surface. *J Phys Chem B* 102(26):5135–5144
35. Reshetenko TV, Khairulin SR, Ismagilov ZR, Kuznetsov VV (2002) Study the reaction of high-temperature H₂S decomposition on metal oxides (γ-Al₂O₃, α-Fe₂O₃, V₂O₅). *Int J Hydrogen Energy* 27(4):387–394
36. Askari S, Lotfi R, Rashidi AM, Koolivand H, Koolivand-Salooki M (2016) The rheological and thermophysical properties of ultra-stable kerosene-based Fe₃O₄/Graphene nanofluids are for energy conservation. *Energy Convers Manage* 128:134–144
37. Maksimchuk NV, Timofeeva MN, Melgunov MS, Shmakov AN, Chesalov YA, Dybtsev DN, Kholdeeva OA et al (2008) Heterogeneous selective oxidation catalysts based on coordination polymer MIL-101 and transition metal-substituted polyoxometalates. *J Catal* 257(2):315–323
38. Chavan S, Bonino F, Valenzano L, Civalieri B, Lamberti C, Acerbi N, Bordiga S et al (2013) Fundamental aspects of H₂S adsorption on CPO-27-Ni. *J Phys Chem C* 117(30):15615–15622
39. Gupta NK, Kim S, Bae J, Kim KS (2021) Chemisorption of hydrogen sulfide over copper-based metal-organic frameworks: methanol and UV-assisted regeneration. *RSC Adv* 11(9):4890–4900
40. Frost R, Zhu HY, Wu P, Bostrom T (2005) Synthesis of acicular goethite with surfactants. *Mater Lett* 59(17):2238–2241
41. Parikh SJ, Chorover J (2006) ATR-FTIR spectroscopy reveals bond formation during bacterial adhesion to iron oxide. *Langmuir* 22(20):8492–8500

42. Kaghazchi L, Naderi R, Ramezanzadeh B (2020) Construction of a high-performance anti-corrosion film based on the green tannic acid molecules and zinc cations on steel: electrochemical/Surface investigations. *Constr Build Mater* 262:120861
43. Edwards DC, Nielsen SB, Jarzęcki AA, Spiro TG, Myneni SC (2005) Experimental and theoretical vibrational spectroscopy studies of acetohydroxamic acid and desferrioxamine B in aqueous solution: pH and iron complexation effects. *Geochim Cosmochim Acta* 69(13):3237–3248
44. Garces HF, Galindo HM, Garces LJ, Hunt J, Morey A, Suib SL (2010) Low-temperature H₂S dry-desulfurization with zinc oxide. *Micropor Mesopor Mater* 127(3):190–197
45. Ke D, Feng JF, Wu D, Hou JB, Zhang XQ, Li BJ, Zhang S (2019) Facile stabilization of a cyclodextrin metal-organic framework under a humid environment via hydrogen sulfide treatment. *RSC Adv* 9(32):18271–18276
46. Yang C, de Falco G, Florent M, Fan H, Bandosz TJ (2020) Support features govern the properties of the active phase and the performance of bifunctional ZnFe₂O₄-based H₂S adsorbents. *Carbon* 169:327–337
47. Costa C, Cornacchia M, Pagliero M, Fabiano B, Vocciante M, Reverberi AP (2020) Hydrogen sulfide adsorption by iron oxides and their polymer composites: a case-study application to biogas purification. *Materials* 13(21):4725
48. Chen S, Guo Y, Zhang J, Guo Y, Liang X (2022) CuFe₂O₄/activated carbon adsorbents enhance H₂S adsorption and catalytic oxidation from humidified air at room temperature. *Chem Eng J* 431:134097
49. Rezaei S, Jarligo MOD, Wu L, Kuznicki SM (2015) Breakthrough performances of metal-exchanged nano titanate ETS-2 adsorbents for room temperature desulfurization. *Chem Eng Sci* 123:444–449
50. Montes D, Tocuyo E, González E, Rodríguez D, Solano R, Atencio R, Moronta A et al (2013) Reactive H₂S chemisorption on mesoporous silica molecular sieve-supported CuO or ZnO. *Micropor Mesopor Mater* 168:111–120
51. Liu D, Chen S, Fei X, Huang C, Zhang Y (2015) Regenerable CuO-based adsorbents for low-temperature desulfurization application. *Ind Eng Chem Res* 54(14):3556–3562
52. Wang X, Sun T, Yang J, Zhao L, Jia J (2008) Low-temperature H₂S removal from gas streams with SBA-15-supported ZnO nanoparticles. *Chem Eng J* 142(1):48–55
53. Liu G, Huang ZH, Kang F (2012) Preparation of ZnO/SiO₂ gel composites and their performance of H₂S removal at room temperature. *J Hazard Mater* 215:166–172
54. Tajizadegan H, Rashidzadeh M, Jafari M, Ebrahimi-Kahrizangi R (2013) Novel ZnO–Al₂O₃ composite particles as sorbent for low-temperature H₂S removal. *Chin Chem Lett* 24(2):167–169
55. Yang C, Wang J, Fan H, Hu Y, Shen J, Shangguan J, Wang B (2018) Activated carbon-assisted fabrication of cost-efficient ZnO/SiO₂ desulfurized with high loadings and dispersion characteristics. *Energy Fuels* 32(5):6064–6072
56. Sandra F, Schade E, Leistner M, Grothe J, Kaskel S (2017) Solvothermal synthesis of a bismuth/zinc mixed oxide material for H₂S removal at room temperature: synthesis, performance, characterization, and regeneration ability. *Mater Chem Phys* 199:329–339
57. Li Y, Wang LJ, Fan HL, Shangguan J, Wang H, Mi J (2015) Removal of sulfur compounds by a copper-based metal-organic framework under ambient conditions. *Energy Fuels* 29(1):298–304

Chapter 12

Matrix-Assisted Laser Desorption/ Ionization Mass Spectrometry with Re-Engineered 2, a 5-Dihydroxypheny Acid Derivative



Sajid Bashir, M. Gomez, K. A. Beran, J. L. Liu, and P. J. Derrick

Abstract Matrix-assisted laser desorption ionization (MALDI) has been a mainstay in protein mass spectrometry, imaging, and proteomics. The common approach to matrix design and selection has been empirical. The most common matrices used are 2,5-dihydroxybenzoic (2,5-DHB) and alpha-cyano-4-hydroxycinnamic acid (aCCa). Using the known relationship between 2,5-phenyl carboxylic acid and tyrosine amino

It is with profound sadness that SB writes this acknowledgment. There is a word in the Old Testament, *salah*, meaning to pause, reflect and think. As I reflect on what Peter did for me, it is almost impossible to believe our previous submission of similar work was [Analyst, 2003, 128, 1452–1457] twenty years ago! It feels like a few months. Peter was my academic father, and his loss is painful now. He will be missed, and I hope that the series of papers we will submit this year will act as a posthumous remembrance because individuals like Peter have to be remembered. J. Liu writes that the day Dr. Derrick passed away [Feb 06, 2017], I stepped into Dr. Bashir's office; he looked at me with deep sorrow and silence, "Peter di.. di... di.... died.....". The atmosphere was frozen, the clock stopped clicking, tears booming, heart pounding...My only feeling at that moment was that my blood pressure could be 240, and I asked: "Are you sure?" "Yes, I just received an email from Alex." In a simple, slow, and affirmatively sad manner, Dr. Bashir replied. From his eyes, I saw a warrior who suddenly lost his colonel on the battlefield, solemnly dignified his academic father, and believed Dr. Derrick's spirit would continuously lead his way. Dr. Derrick was our role model; he was humble and completely devoted himself to the science, technology, and chemistry community. Led by his example, we knew our responsibility was to build a strong, harmonic society where our young generation could grow. There are three very painful experiences in my life: the death of my grandparents, who raised me and taught me to be a nice person; the death of my parents, who gave me a life of me and encouraged me to be a strong person; the death of Dr. Derrick who I never met, but has been a chemistry hero, guiding me through the righteous academic journey. Dr. Peter Derrick will always linger in my future prayer the sweet, courageous, and ever-lasting name.

S. Bashir (✉) · P. J. Derrick
Institute of Mass Spectrometry, University of Warwick, Coventry CV4 7AL, UK
e-mail: br9@tamuk.edu

P. J. Derrick
e-mail: p.j.derrick@auckland.ac.nz

S. Bashir · M. Gomez · J. L. Liu
Department of Chemistry, Texas A&M University-Kingsville, 700 University Blvd, Kingsville,
TX, USA

© The Author(s), under exclusive license to Springer Nature Switzerland AG 2024
M. Wu et al. (eds.), *Advanced Materials for Multidisciplinary Applications*,
https://doi.org/10.1007/978-3-031-39404-1_12

A 2,5-dihydroxyphenylcarboxylic acid molecule based on the hydroquinone core of 2,5-DHB was designed and synthesized (M10) by using the known relationship between 2,5-phenyl carboxylic acid and tyrosine amino acids. The two matrices (aCCa and M10) were compared and contrasted using neuronal peptide mixtures, tryptic digests from two-dimensional gel spots from culture *Escherichia coli*, and mature green tomato fruit. The peptide mixtures or mass fingerprints were analyzed similarly, except only a 30 s analysis time window per sample was allocated for M10, whereas 3 min per sample were allocated for aCCa. The results are that M10 generated greater ion yield, sequence coverage, and probable Mascot identification scores over aCCa, or the scores were comparable with less sample acquisition time for M10. The *n*-decanoic acid side chain promotes matrix-to-analyte interactions and proton transfer during crystallization. Our findings support the hypothesis of pseudo proton transfer from the excited matrix species during crystallization as a dominant mechanism for generating protonated and deprotonated analyte ions due to the lower proton affinity of M10 that is computed using density functional theory and the 6-311G** basis set for the protonated matrix species. The enhanced performance of matrix M10 will positively impact MALDI research and will extend the lifetime and operability of older instruments at hospitals, laboratories, and teaching-intensive universities where instrument budgets are stretched. By using M10 as a matrix, the sampled runtime is reduced, ion yield is increased, and potential instrument usage lifetime is increased.

12.1 Introduction

Matrix-assisted laser desorption ionization (MALDI) is a technique with co-crystallization of organic ultraviolet absorbing matrix [1] and analyte as a binary drop ('dried-drop method') [2] or two successive later matrices followed by analyte ('sandwich method'). Upon absorption of a UV pulse ($\lambda = 337$ nm), ablation, desorption, and gas-phase ionization occur without extensive fragmentation of the analyte [3]. Although the technique has become dominant, progress towards the rational discovery of newer matrices has been hindered due to a lack of understanding of the

M. Gomez

Department of Chemistry, Texas A&M University, 580 Ross St, Ste 3255, College Station, TX 77843, USA

K. A. Beran

Department of Chemistry and Biochemistry, Texas A&M University, 2601 W. Avenue N, San Angelo, TX 76909, USA

J. L. Liu

Texas A&M Energy Institute, 1617 Research Pkwy, College Station, TX 77845, USA

P. J. Derrick

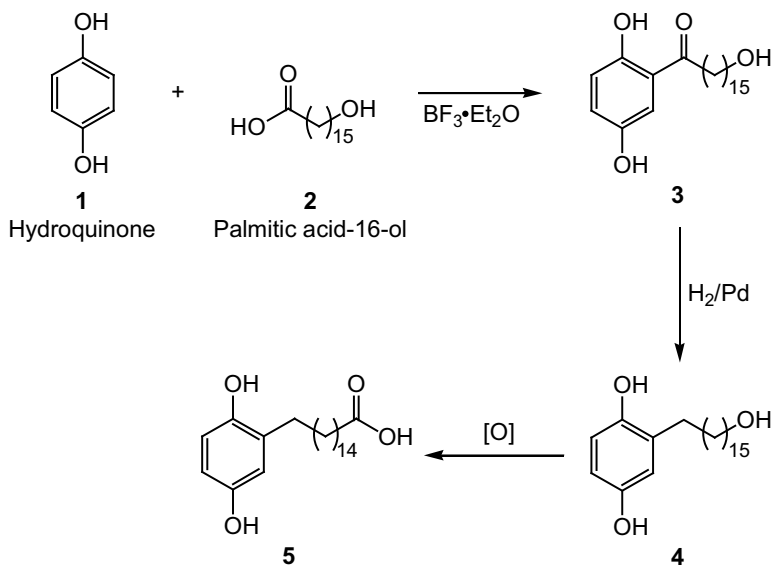
Department of Physics, The University of Auckland, 7 Symonds Street, Auckland 1061, New Zealand

mechanisms related to desorption and ionization [4]. Two of the most heavily used matrices in protein identification are 2, 5-dihydroxybenzoic acid and alpha-cyano-4-hydroxycinnamic acid (aCCa) in positive-ion mode; yield the pseudo-molecular ion as a protonated species [5]. The ease of this technique and the ability to couple peptide mass fingerprint [6] to a database has enabled these techniques to be applied to whole cells [7] instead of isolated mixtures [8] and extended its outreach into system biology [10], chemical biologies [11], and metabolite profiling [12] as well as imaging [13]. In the classic approach, the pseudo molecular ions (e.g., in positive-ion mode) are generated after the protein(s) is/are subjected to proteolytic digestion [14]. Alternatively, specific proteins are subject to enzymatic digestion and analyzed as a set of mass-to-charge ratios isolated and subjected to further fragmentation as a form of two-dimensional (MS2) mass spectrometry [15]. The fragmented peptide mass fingerprint or MS2 generated is compared to stored protein or deoxyribonucleic acid (DNA) sequences from which algorithmic matches and putative identities are determined [16].

The digested peptides are often isolated from spots on a one- or two-dimensional sodium dodecyl sulfate–polyacrylamide gel electrophoresis (SDS-PAGE) without the traditional isolation and crystallization of single proteins [17]. To achieve higher throughputs, the gel excitation, digestion, and MALDI sample preparation can be automated, in addition to the generation of the peptide mass fingerprint and putative search and identification of proteins at 50 fmol levels [18]. The MALDI technique has several drawbacks, such as high yield from low mass matrix species [19] or matrix clusters [20]. Other technical hurdles from low analyte signal intensities from peptide mixtures ('analyte suppression effect') for certain peptide components [21]. This is due to arginine-rich systems that are ionized more easily than small acidic peptides, which are less well ionized, lowering surface coverage and sample identification [22]. Other factors are a spot-to-spot signal variation of the analyte [23]. This is due to non-uniform crystallization and variations in the matrix-to-analyte ratio across the spot area profiled by the laser pulse, which in turn may be due to the non-uniform drying of the matrix on a metal surface [24].

12.2 Experimental

All chemicals were purchased from Sigma-Aldrich (Dorset, UK) and were an analytical grade, except when otherwise noted. 2,5-dihydroxybenzoic acid, bovine serum albumin, and pep mix were obtained from Bruker Daltonics (Coventry, UK). Doubly distilled deionized water was used, and hydrochloric acid, trifluoroacetic acid, acetonitrile, methanol, chloroform, and 16-(2,5-dihydroxy phenyl)-ol and hexadecanoic acid from VWR (Lutterworth, UK). The rationale for designing the hydroxyphenyl carboxylic acid derivative was its interactions with tyrosine and select phenols in skin tissue [25]. It was hypothesized that this known interaction in cells might also occur in the gas phase and increase the ion yield of acidic peptides, which are usually poorly ionized under MALDI-TOF conditions. The synthesis



Scheme 12.1 Synthesis of 16-(2,5-dihydroxy phenyl)hexadecanoic acid (M10) from hydroquinone

(Scheme 12.1) was performed using Friedel–Crafts acylation [26] upon hydroquinone (**1**) using boron trifluoride and saturated fatty acid (**2**) to generate the 1-(2,5-dihydroxy phenyl)-15-hydroxyalkyl-1-one via Fries rearrangement first step [27] followed by a Curtius rearrangement [28] reaction between the 4-methoxy phenol and vinyl bromide to generate (**3**), that is reduced to the 2-(15-hydroxyalkyl)benzene-1,4-diol (**4**) due to the proximity of the carbonyl group alpha to the aromatic ring, using hydrogen and palladium (H_2/Pd) [29]. The primary alcohol functionality in **4** is oxidized to produce the target compound (**5**) by oxidation using treatment with BBR_3 and an excess of periodic acid (H_5IO_6) in the presence of about 1.2 mol % of chromium trioxide (CrO_3) [30].

The crude product was washed with distilled water and purified by recrystallization from the crude mixture that was recrystallized from a mixture of ethyl acetate and heptane (50:50), yielding white crystals. The crystallization process was repeated twice more. The final product was purified using silica gel columns followed by additional recrystallization from acetonitrile/water and 1% isooctane. Overall yields were between 65 and 88%. The MALDI determined that the molecular mass was 365.534 Da for the protonated species and 387.516 Da for the sodiated species.

Computational methodology: The main objective of this computational study was to determine the structural properties of M10 and its ionic derivatives corresponding to the global minimum on the potential energy surface. The conformation distribution of the molecular species was analyzed at the semi-empirical level using the PM3 model [31]. This analysis selected the three conformers with the lowest energy for further optimization. Geometric optimization of these conformers was then carried

out using density functional theory without any symmetry constraints. The B3LYP was functional with the 6-31G* basis set used for this purpose [32–34]. Subsequently, thermodynamic data such as zero-point vibrational energy (ZPVE) [35], vibrational energy, and the entropic degrees of freedom were obtained at the same level of theory for the subsequent proton affinity (PA) and gas-phase basicity (GB) calculations.

In order to verify the stability of the optimized molecular structures, vibrational analysis was carried out, which confirmed that the geometries of M10 and its derivatives occupy a stationary point with no imaginary frequencies. Theoretical values of the zero-point vibrational energy, vibrational energy, and vibrational entropy were then scaled accordingly. The single-point energy for each optimized structure was determined using the B3LYP/6-311 + G**//B3LYP/6-31G* level of theory. Finally, the matrix's proton affinity (PA) and gas-phase basicity (GB) were calculated using the single-point energies. A qualitative assessment of the absorption coefficient for derivatives of 2,5-dihydroxybenzoic acid (2,5-DHB) via substitution of the 2-OH was conducted by employing DFT-B3LYP/6-31G* housed in the Spartan'08 software package [36].

Bacterial cell culture: Each experiment was performed in two biological replicates. *Escherichia coli* (*E. coli*) cells (soluble fraction [37] with Ampicillin plasmid and a separate variant with a Rifampicin plasmid) were grown in a 1 L flask containing 250 mL of minimal M9 media supplemented with L-Lysine [38]. Once an optical density (OD) of 0.4 at 600 nm was reached (OD₆₀₀), the cells were harvested. Tomatoes that broke color from green to red were also harvested, and proteins were isolated [39].

Protein extraction and mixing: The process of harvesting cells involved a centrifugation step at 4000 g for 10 min. Next, the media was removed and the resulting pellets were resuspended in BPER bacterial protein extraction reagent (Thermo Scientific) along with lysozyme (50 µg/mL) [40]. The lysing of cells was done on ice for 20 min to eliminate DNA and other impurities, which were removed by a second centrifugation step at 8000 g for 30 min. A crude protein extract was then obtained and precipitated with the methanol/chloroform approach. The collected proteins were re-suspended in a denaturation buffer that contained 6 M urea/2 M thiourea in 10 mM Tris. The concentration of protein was evaluated using the Bradford assay (Bio-Rad, Munich, Germany) [41].

Isoelectric focusing: The peptides were subjected to separation using the Biorad protein isoelectric focusing (IEF) protocol, after passive rehydration of 200 µg protein reconstituted in 200 µL rehydration buffer for 12 h. 11 cm immobiline dry strip gel (IPG) Strips possessing a pH separation gradient of 4–7 were used for separation, with a maximum of 50 µA at 20 kV, with a 6 h focusing time [42]. The strips were reduced with dithiothreitol (DTT) and alkylated at room temperature, after which the second dimension was run using a Bio-Rad Criterion electrophoresis cell system with Bis–Tris 4–12% gradient gels and 800 mL running buffer at 200 V for 1 h [43]. Subsequently, the gel was washed with deionized water thrice, stained using Coomassie Blue (G250) stain for 1 h, and destained in deionized water for 1.5 h

[44]. The gel was examined using Bio-Rad Molecular Imager, followed by washing with 10 mM ammonium bicarbonate and acetonitrile (ACN) (1:1, v/v) for every gel spot, with the protein spots in the Eppendorf tube being reduced with 10 mM DTT in 20 mM (ABC) for 45 min at 56 °C and alkylated with 55 mM iodoacetamide (IAA) in 20 mM ammonium bicarbonate for 30 min in the dark (Al-foil) at room temperature [45]. The gel spots were washed twice with 5 mM ammonium bicarbonate, followed by a dehydration step by incubating with 100% ACN at room temperature.

Standard in-solution digestion with 25 mM ammonium bicarbonate buffer solution was used to perform tryptic digestion of β -casein from bovine milk as the control, as well as the excised gel spots [46]. A 10- μ L sample of each peptide solution (100 μ M) was mixed with 9 μ L of aqueous ammonium hydrogen carbonate (50 mM) and 1 μ L of trypsin solution (1 μ g/ μ l) and left to digest overnight at 37 °C. The resulting stock solution was diluted with acetonitrile (30%) and water (70%) supplemented with 0.5% trifluoroacetic acid (TFA) to a final concentration of 0.1 μ M [47]. The sample was zip-tipped with the same elution solvent directly onto a stainless steel surface that had either 2,5-dihydroxybenzoic acid (DHB) or 16-(2,5-dihydroxy phenyl)hexadecanoic acid (M10) and allowed to dry [48]. Subsequently, 1 μ L of Ammonium dihydrogen phosphate ($\text{NH}_4\text{H}_2\text{PO}_4$) was deposited onto the dried spots for 2 s and removed, after which the sample was allowed to dry for 5 min at room temperature. The samples were analyzed using matrix-assisted laser desorption/ionization time-of-flight mass spectrometry (MALDI-TOF MS) in positive ion mode [49].

Mass spectrometry: The Bruker Biflex (Bruker, Coventry, U.K.) was used to perform all MS measurements. A nitrogen laser at 337 nm was employed for positive mode spectra in the linear mode. Twenty-shot spectra were sampled unless stated otherwise. The laser power was adjusted to achieve a signal-to-noise ratio of three or greater. The lowest power was restrained between diverse signal-to-noise ratios that were three or greater. To obtain high accuracy, a spectrum of twenty shots was saved using a calibration of pepmix, dextran, or insulin, depending on the expected mass-to-charge ratio of the sample. In some cases, an extraction delay time of 50–150 ns was utilized to improve resolution and prevent detection saturation. Spectra containing 20–200 shots were obtained.

Data processing: The MS data obtained were processed using Bruker software and analyzed with the Mascot search engine. Enzyme specificity was fully enforced, allowing for two missed cleavages, and trypsin was employed as the protease [50]. The peptide mass fingerprint spectra underwent a search using two algorithms, the MOWSE scoring algorithm and Mascot. The search was conducted against a database of NCBI, TIGR, and dbEST, using organisms such as *Escherichia coli*, *Solanum*, and related species. Peptide mass tolerance was kept up to 50 ppm, and variable modifications included methionine oxidation and protein N-terminal acetylation [51]. Cysteine carbamidomethylation was a fixed modification. Additionally, MS scan mass tolerance was maintained at 6 ppm. Confident protein identification was scored by Mascot Score and percent sequence coverage, which were calculated for each tissue using matrix species analysis [52].

12.3 Results and Discussion

12.3.1 Laser Power Adjustment to Obtain Optimal Fluence

The rationale of the approach was to synthesize M10 matrix candidates by Perkin condensation of the benzene-1,4-diol unit. The long alkyl increased the molecular hydrophobicity to interact with more hydrophobic residues while maintaining flexibility. The terminal carboxylic was retained as a source of pseudo-proton transfer to the analyte during the crystallization process and proton transfer between analyte molecules as a disproportionation process. Here, an excited matrix transfers energy to the analyte dimer (carboxylic acid of (1) matrix and (2) analyte with (3) amino groups of the analyte) to produce a cation and an anion simultaneously. The matrix-to-analyte crystal interactions generate ion-pairs and (1 & 2 \rightarrow 3) protonation/deprotonation from the excited matrix species. The 2- and 5-position hydroxyl groups were kept to keep the molecules' optical properties in the ultraviolet range and enable the generation of the hydroxylate anion to act as a coordination source for sodium to promote cationization where protonation was not possible. By separating the alkyl chain from the aromatic, it was anticipated that the matrices' proton affinity might decrease, increasing the likelihood of chemical ionization of neutrals in the gas phase if they were not protonated during crystallization. For any gas-phase proton transfer, the matrix species is expected to have a lower proton affinity than the parent DHB moiety. The results were compared and contrasted with α -cyano cinnamic acid (aCCa), the primary matrix for peptide analysis and peptide mass fingerprinting-based surveys.

The relationship between laser power setting and fluence is summarized in Fig. 12.1, and the power was kept below 60 since the relationship is approximately linear here.

To improve the solubilization of hydrophobic peptides in the matrix and reduce spot-to-spot variations in ion signal, a long chain of M10 was designed. The benefit of this design is that the laser power can remain constant across multiple digest-type samples, eliminating the need to determine the sweet spot with optimal signal intensity empirically. Figure 12.2 illustrates the total protonated and cationized ion signal for substance P [53] (2NH- RPKPQQFFGLM-COOH, pI of 11.00, and GRAVY score of -0.700 [54]) using commonly used matrices for peptide analysis, including 2,5-dihydroxybenzoic acid (DHB), Sinapinic acid (SA), M10, and aCCa.

It can be seen that the highest aggregate ion signal was from SA < DHB < aCCa < M10, with the laser power variations, to obtain a signal-to-noise ratio of at least three, being the least for M10 < DHB > aCCa > SA.

In order to investigate the correlation between ion yield and laser power, the laser power was gradually increased. The point at which the signal-to-noise ratio fell below three was identified, and the resulting data was summarized in Fig. 12.3 for model peptide SP. For matrix M10, it was observed that the ion yield was highest at around 25 units of laser power, with detectable levels of cationized species. Conversely, aCCa exhibited high ion yields at lower laser power (around 20 units) but failed to produce significant ion yields at higher laser powers.

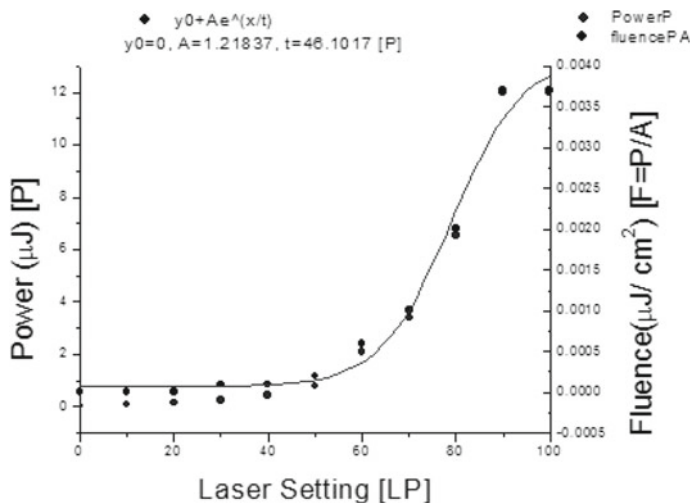


Fig. 12.1 Relationship between actual fluence and laser power setting on software instrument 'panel'

Adrenocorticotrophic hormone (ACTH) [55] clip 18–29 (2NH-RPVKVYPNGAEDESAAEAFPLEF-COOH, pI 4.25 and GRAVY score of -0.614) was evaluated. The peptide clip has a similar hydrophobicity to SP; however, its isoelectric values are lower, with five residues capable of retaining a negative charge in contrast to SP, which has zero residues capable of retaining a negative charge. A comparison of peptides with varying isoelectric is given in Table 12.1. In every instance, the spread of percent error [(percent deviation/average ion yield value) (100%)] to obtain a signal-to-noise ratio of at least three was greater with aCCa than M10. However, the medium laser power of M10 was higher than for aCCa (25 units versus 21.7 units).

For the proteomic component, 28 spots were identified using *E-coli*- Amp plasmid, and 72 spots were identified with *E-coli*- Rif plasmid. The spots were excised and digested with trypsin, and the peptide mass fingerprint was acquired and searched against the national center for biotechnology information division genbank expressed nucleotide sequence tag (NCBI db EST) database [56].

When conducting proteomics experiments with numerous spots, samples that could not acquire an optimal spectrum within the given time limit were either not processed or given a spectrum with low signal-to-noise. The acquired peptide mass fingerprint was then searched against the NCBI protein database for better database match scores, as opposed to searching against the dbEST [57]. Based on the results summarized in Table 12.2, aCCa and M10 had higher identification scores and sequence match percentages.

A functional break of the proteins identified from the two-dimensional sodium dodecyl sulfate polyacrylamide gel electrophoresis (2D-SDS PAGE) gel spots is summarized in Figs. 12.4 and 12.5 as analyzed using aCCa and M10 as matrices

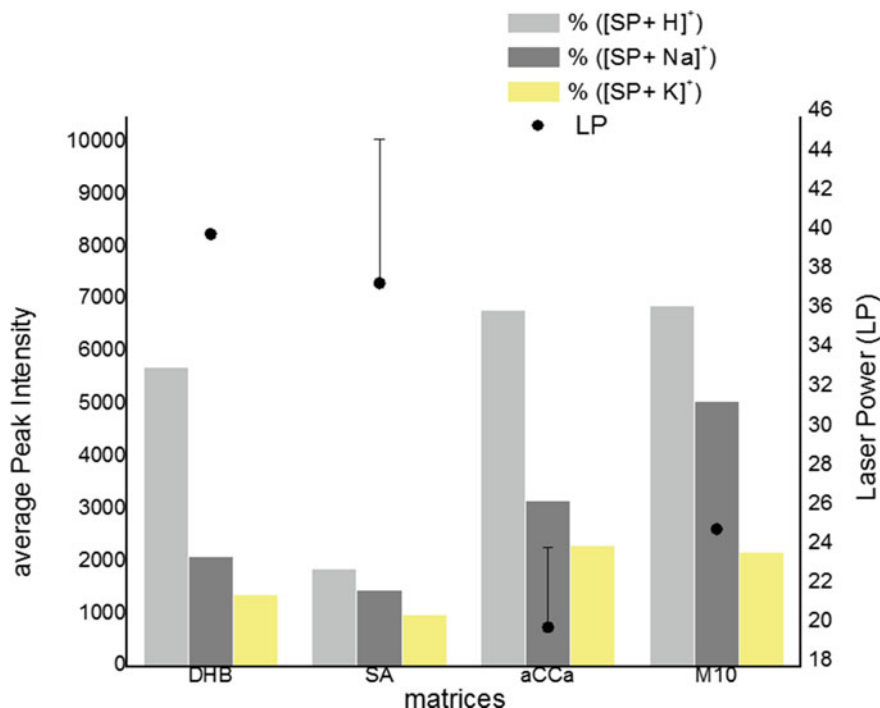


Fig. 12.2 Relationship between laser power and ion yield for substance P (SP, 1) nmol/ μ L) and 0.1 M of common peptide matrices. Approximately 1 μ L of the matrix was deposited onto the slide and allowed to dry. For 2,5-dihydroxybenzoic acid (DHB was dissolved in CH₃OH) and substance P (SP in 1:1 H₂O/C₂H₃N with 0.05% C₂HF₃O₂ at a DHB: SP ratio of 2000:1). The other matrices were prepared analogously, except sinapinic acid (SA was dissolved in H₂O/C₂H₃N with 0.05% C₂HF₃O₂) and M10 was dissolved in 2:1:1 ratio of H₂O: C₂H₃N: C₃H₇NO. The laser power was adjusted to obtain a signal-to-noise ratio of at least three and at least twenty spots per spectra. For each analysis, ten individual spectra were acquired over three spots. The laser power was adjusted for each region, and the standard deviation was obtained. Where the standard deviation was < 5% of the average ion yield, the error bar was omitted for clarity

under similar conditions. The bulk of the identified hits were related to the proteome, or plasmids or proteins that could be categorized as having a molecular or biological function. Using the gene ontology (GO) annotation [58] (depicted in the central pie-chart), the biggest difference (set at 5% or greater) between the two matrices was that the matrix M10 enabled greater identification of proteins classified as having a biological (21% vs. 14%), ligand (12% vs. 7%) and nucleotide (29% vs. 38%) role between M10 and aCCa respectively (Fig. 12.6).

The percent sequence similarity was analyzed by comparing the peptide mass fingerprint obtained from both matrices to compare the ion yield of tryptic digests generated by different matrices. Figure 12.7 displays the scatter plot, indicating approximately four distinct populations. The major population exhibits similar percent sequence scores for both matrices, but matrix M10 shifts it to the right. The

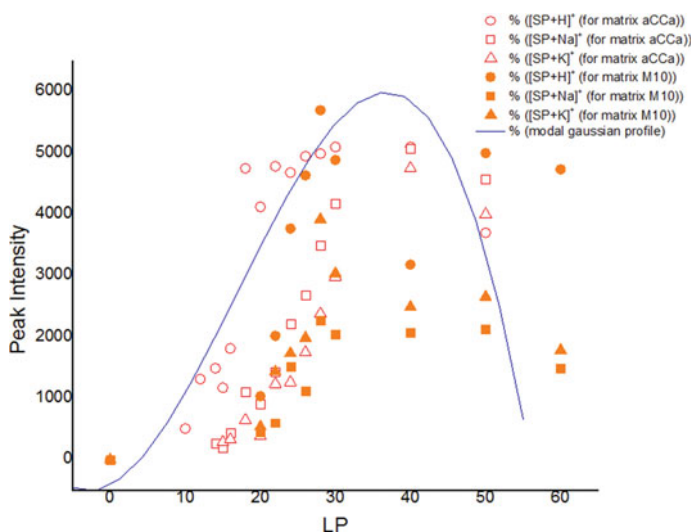


Fig. 12.3 The relationship between laser power and ion yield for substance P (SP, 1 nmol/ μ L) and 0.1 M of aCCa and M10

Table 12.1 Summary of common peptides and ion yield error using matrices aCCa and M10

| Matrix | LP | % LP error | ACTH (18-39) CLIP [A + H] + ion yield | % Peptide Error | Somatostatin [A + H] + ion yield | % Peptide error |
|------------------|-------------|------------|--|------------------|----------------------------------|-----------------|
| aCCa | 21.7 | 11.9 | 3,528.8 | 122.3 | 1,830.0 | 122.5 |
| M10 | 25.0 | 0.0 | 4,359.8 | 65.0 | 1,073.0 | 60.9 |
| Peptide property | Substance P | | % Peptide error | Angiotensin I | | % Peptide error |
| aCCa | pI | GRAVY | 78.6 | pI | GRAVY | 82.3 |
| M10 | 11 | -0.700 | 53.3 | 6.92 | -0.200 | 51.4 |
| Peptide property | Bombesin | | % Peptide error | ACTH (1-17) CLIP | | % Peptide error |
| aCCa | pI | GRAVY | 93.5 | pI | GRAVY | 84.4 |
| M10 | 10.84 | -0.738 | 56.6 | 10.45 | -1.453 | 0 |

smaller cluster in the lower left-hand quadrant prefers aCCa. In contrast, the upper left-hand quadrant favors aCCa, and another satellite cluster near the main clusters favors neither matrix. The protein database at NCBI generated higher sequence similarities than the expressed sequence tags also hosted at NCBI.

A plot can be constructed that is analogous to peptide mass fingerprints generated from mature green tomato (*Lycopersicon esculentum*) fruit (Fig. 12.8).

Table 12.2 Peptide Mass Fingerprint acquired using aCCa or M10 as matrices and searched against nucleotide or protein database. The identified protein score and percent coverage for each matrix and standard deviation error is listed

| Average score | Score std | Percent coverage | Coverage std | Database/matrix |
|---------------|-----------|------------------|--------------|-----------------|
| 15.53 | 4.45 | 9.75 | 4.46 | DB EST/aCCa |
| 28.58 | 10.87 | 19.10 | 18.51 | DB EST/M10 |
| 36.96 | 6.87 | 22.26 | 20.26 | NCBI/aCCa |
| 34.16 | 8.77 | 23.50 | 25.74 | NCBI/M10 |

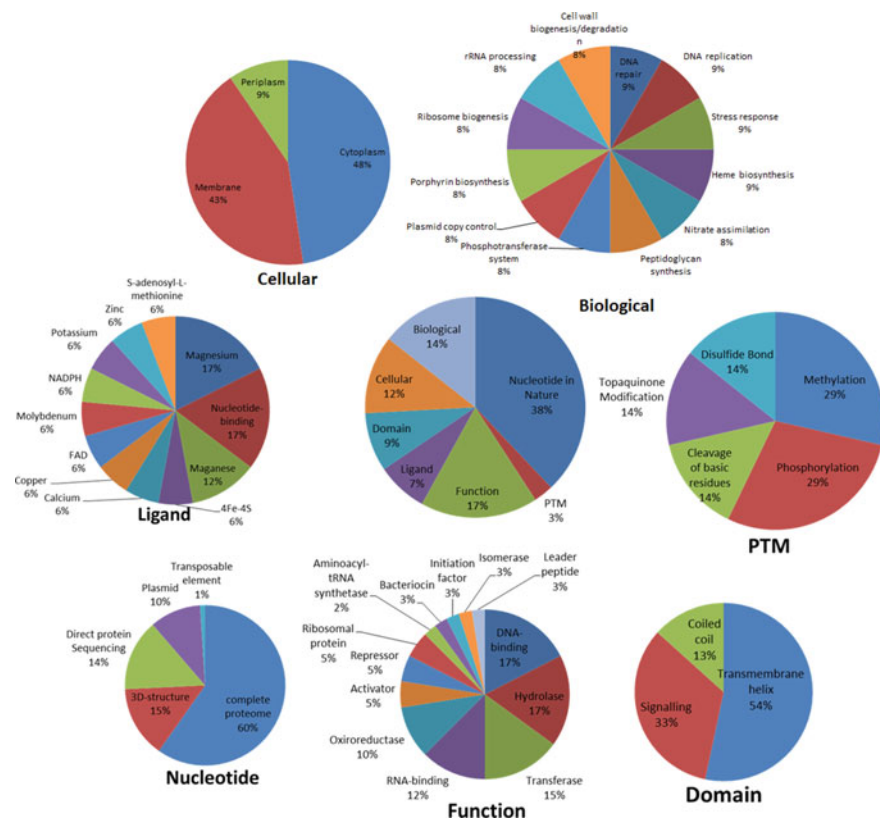


Fig. 12.4 Gene ontology (GO) annotation of *E. coli* from the UniProt-GOA database acquired using a maximum acquisition run time of three minutes per sample using aCCa as a matrix

The plot line for that for *Escherichia coli* has three general trends. The left upper quadrant favors the matrix aCCa. In contrast, the right upper quadrant favors the matrix M10, and the central cluster appears to favor neither matrix to any great extent; however, the results scores as higher when searched against the database at

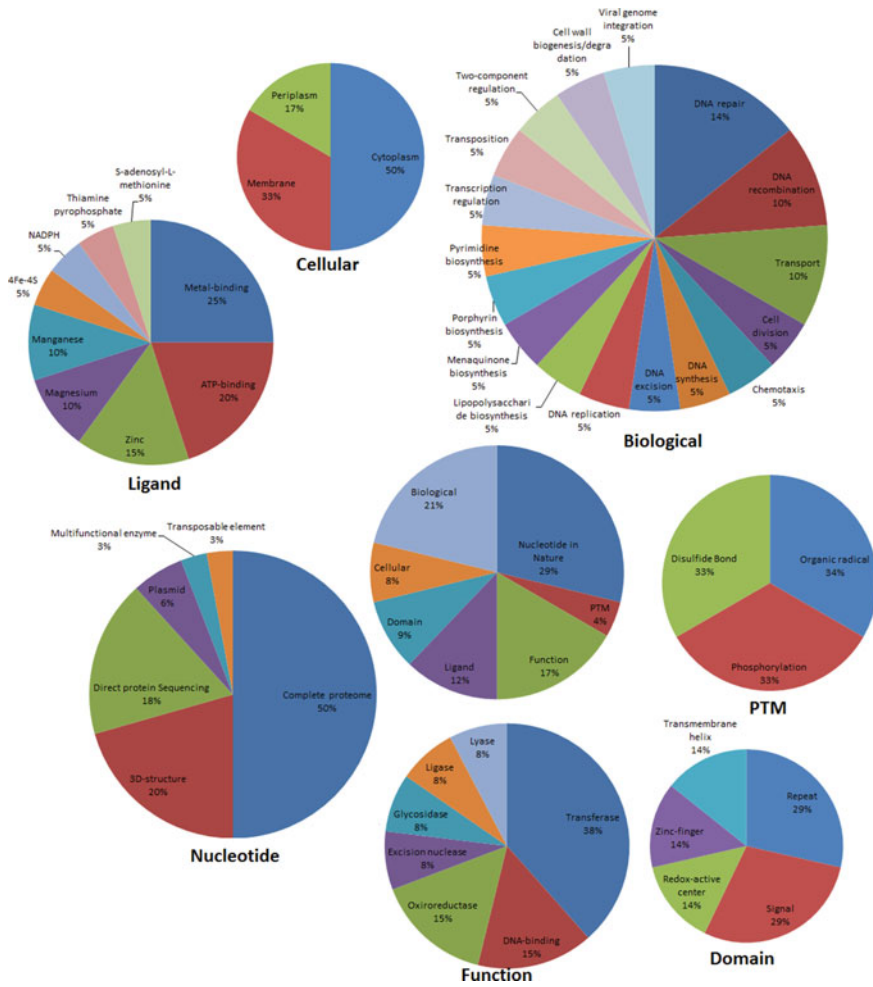


Fig. 12.5 Gene ontology (GO) annotation of *E. coli* from the UniProt-GOA database acquired using a maximum acquisition run time of thirty seconds per sample using M10 as a matrix

TIGR, which may have higher curated protein and nucleotide sequences specific to *Solanum* over the more general database at NCBI.

To examine if the similarity sequences from the peptide mass fingerprints were similar across an annotated class, such as ligands, or membrane proteins, a plot percent sequence score versus hit from the nucleotide or protein sequences database for each matrix was compared. The larger the area of the circle, the greater the standard deviation for the specific functional class, as illustrated in Figs. 12.9 and 12.10 using the TIGR database. The plot shows tighter circles than the corresponding plot with aCCa (Fig. 12.10), indicating that the matrix M10 transfers more energy to

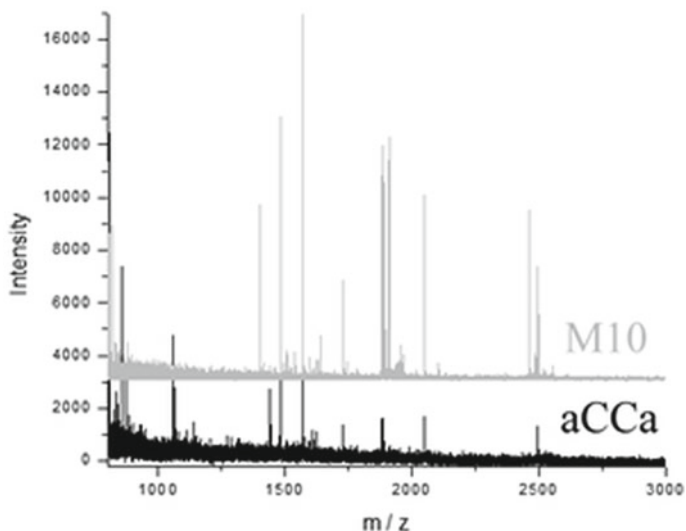


Fig. 12.6 MALDI-TOF PMF of tomato digests using matrices aCCa and M10 and searched using Mascot on the TIGR database

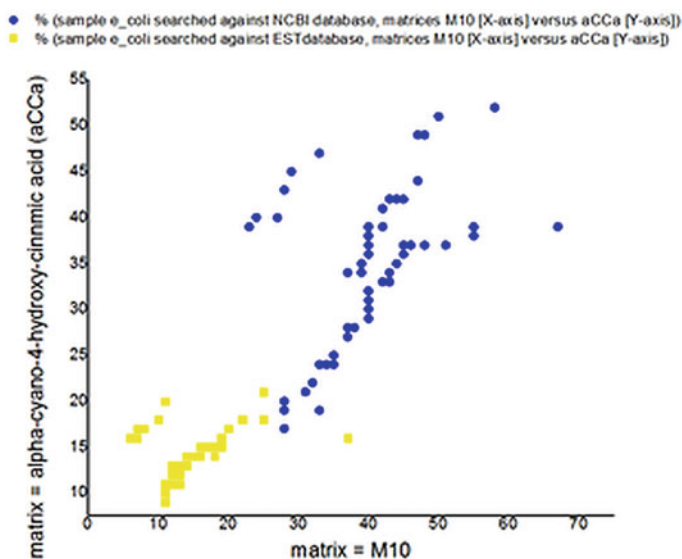


Fig. 12.7 Summary of predicted percent sequence similarity to peptide mass fingerprinted from 2D gel spots of cultured *Escherichia coli* obtained using matrices aCCa and M10 when searched against expressed sequence tag (EST) nucleotide or protein sequence databases at the National Center for Biotechnology Information (NCBI)

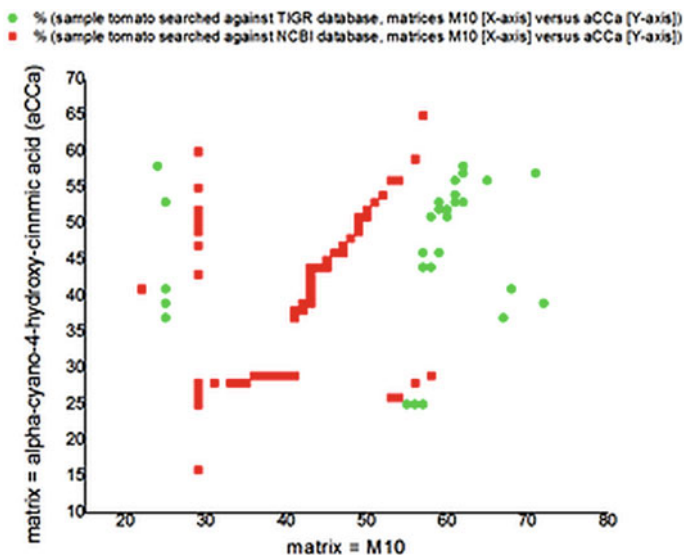


Fig. 12.8 Summary of predicted percent sequence similarity to peptide mass fingerprinted from 2D gel spots of mature green tomato (*Lycopersicon esculentum*) fruit obtained using matrices aCCa and M10 when searched against expressed sequence tag (EST) nucleotide database at the Institute for Genomic Research (TIGR) or the protein sequence database at the National Center for Biotechnology Information (NCBI)

the analyte causing more fragmentation, which translates to higher percent sequence coverage and match scores.

12.3.2 Design Criteria and Possible Mechanism of Action of Matrix 10

The enhanced ion intensities across different types of analytes from plants, microorganisms, or peptide mixtures are rationalized through improved M10-to-analyte interactions during crystallization. It is hypothesized that the analyte is incorporated into matrix crystals during this phase [59], promoting excited matrix proton transfer during this phase [60], in addition to chemical ionization after laser desorption in the gas plume [61]. Any neutral analyte would become charged through proton transfer from the protonated matrix species [62] in the plume. The charging site would be near the carboxylic acid (RCOO^-) moiety, where the proton can produce polar or hydrogen interaction and charge stabilization. The charge can then partition across the aromatic ring promoted by the electron-donating power of the 5-OH group for M10. Our density functional theory electron-density calculations with the 6-311G** basis set for the protonated M10 species indicate a loss of net positive

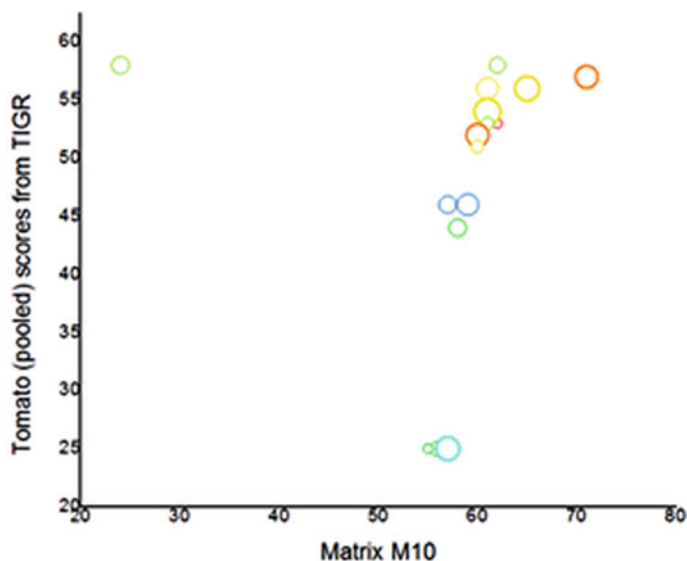


Fig. 12.9 Space diagram of the effect of percent similarity score of mature green tomato (*Lycopersicon esculentum*) fruit obtained using matrix M10 when searched against expressed sequence tag (EST) nucleotide database at the Institute for Genomic Research (TIGR)

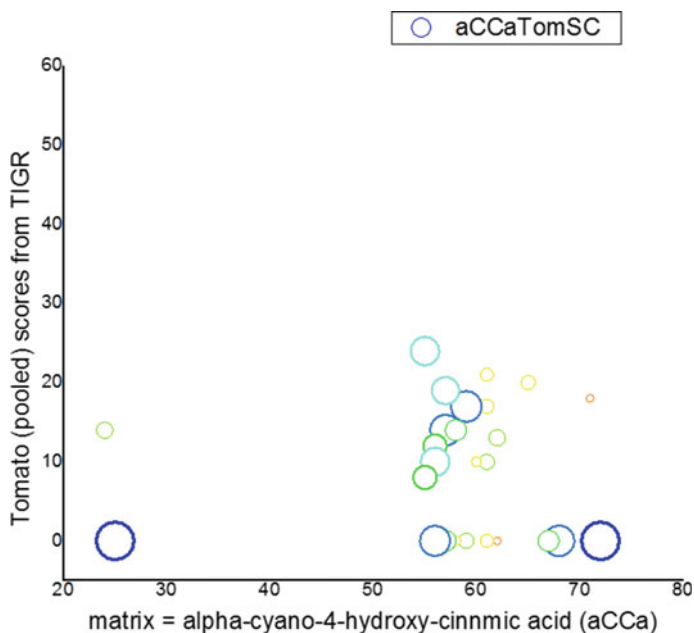


Fig. 12.10 By searching the expressed sequence tag (EST) nucleotide database at the Institute for Genomic Research (TIGR) using matrix aCCa, the effect of the percent similarity score of mature green tomato (*Lycopersicon esculentum*) fruit was depicted in a space diagram

charge around the 2-OH and RCOO^- position due to strong electron-withdrawing -5-OH group. Thus, while 2,5-dihydroxybenzoic acid (2,5-DHB) can be protonated with the charge distribution across the entire delocalized π -system [63], stabilized by the proximity between the 2-OH hydroxyl and carboxylic acid, this tendency is lessened in M10. The stabilization is weakened due to the long aliphatic chain terminating with the carboxylic acid, resulting in M10 exhibiting a lower proton affinity (PA) than 2,5-DHB or aCCa [64]. In the case of aCCa, like in the case of 2,5-DHB, the charge is delocalized across the entire π system promoted by the 4-OH group. Suppose PA is a dominant parameter in the generation of quality spectra. In that case, it is expected that M10 will undergo more efficient proton transfer than DHB or aCCa in the gas phase, with low basicity analytes in the tryptic digests [65]. The propensity to form cation dimers $[\text{A}^+]_x[\text{B}^-]_y$, where $x > y$ was not observed. Therefore, the survival of performed clusters as the main mechanism of ion formation was not observed within the 100 ns timeframe with matrix M10 [61]. The study by Moon et al. would suggest other factors, such as PA, have a greater influence on the quality of the generated spectra [62]. In this instance, smaller proton affinities between aCCa and M10 can lead to significant differences in analyte ion yields due to the tendency to undergo gas-phase proton transfer [9], and proton transfer during the crystallization process [67]. During the crystallization process, peptide (analyte) incorporation into the matrix crystal may favor analyte protonation at the most basic residues [68], whereas, in the gas phase, other sites are favored, such as the amide bonds, due to the lower interaction time [69]. During plume formation, collisions between neutral matrices can facilitate matrix protonation [70] or a back reaction favoring re-neutralization [71], which diminishes the charge analyte pool and proton transfer between analytes [72]. The enhanced lipophilicity of M10 with the alkyl chain terminating with a carboxylic acid enables M10 to exhibit greater degrees of freedom than aCCa and a greater probability of proton transfer [73], as opposed to ionization from ejection of photoelectrons from the metal or the metal-matrix interface [74]. This is due to the more efficient coating of the stainless steel metal surface, limiting electron ejection and ion formation [75]. The higher ion yields are thus either due to preformed ions during crystallization or the net difference between processes promoting matrix recombination and separation of charges in the plume generating charged analyte species and higher ion yields [76]. These interactions may also lead to greater energy transfer, resulting in greater peptide fragmentation [77], as shown in Fig. 12.6. Other design criteria were considered: absorption coefficients, or absorbance intensity, at the laser wavelength, used [78] as a function of the type of ring substitution at the second position. For example, we theoretically considered derivatives of 2,5-DHB in which substitution of the 2-OH by a methyl, phosphate, halide, nitrite, or amine group was considered. Theoretically generated UV/VIS spectra, utilizing the Spartan'08 software package, were analyzed to assess the absorption characteristics of derivatives of 2,5-DHB. Regardless of the substituent group, whether an electron donating group (halides) or electron withdrawing group (nitrite), there was a decrease in the absorption characteristics of the derivative relative to 2,5-DHB at 337 nm. Consequently, there would be predicted to be a corresponding decrease in the propensity of the derivative molecule to utilize

the total fluence [79]. The higher fragmentation allows a lower laser threshold to be employed, lowering potential detector saturation [80].

The fragmentation data support proton transfer via crystallization as a primary mode of charge transfer rather than gas phase processes [81], due to the lower time the analyte and matrix are nearby in the gas phase [80]. During the crystallization process, approximately 30 min are required to produce discrete crystals or satellites of polydisperse crystals. The comparative interaction time in the gas phase would be 100 ns, assuming an extraction voltage of 2500 V and a 10 mm distance between the sample and the first extraction plate, using laser fluence that promotes desorption without fragmentation and space charge effects [82]. Under these conditions, the neutral analyte is separated by 1 μm with a velocity of 1.5×10^5 m/s in a conical trajectory with the plume density decreasing. Assuming a plume pressure of 1.5 mbar, a molecular cross-section of 1×10^{-14} cm^2 (σ), a flight time of 60 ns (t), and bulk ionization efficiency of 0.01% and 1000 fmol (6×10^{11} analyte molecules) would be in the order of 5.4×10^{-7} for protonated $[\text{A} + \text{H}]^+$ or deprotonated $[\text{A}-\text{H}]^-$ species from the protonated matrix dimer [$6 \times 10^{11} \times 1 \times 10^{-14} \times 0.01\% \times 60 \times 10^{-9} \times 1.5 \times 10^5$]. With an upwards revision of 5000, the value increases to 1.6×10^{-3} which defines the likely lower and upper boundary conditions [83]. Although an oversimplification, the values indicate the analyte dimer ion formation should be negligible if photochemical ionization processes are the dominant method to generate charged ions in the gas phase. Observing such ions would diminish the likelihood of this mechanism as the primary mechanism for ionization [84]. Since the cluster model is a gas phase phenomenon, the cluster ionization model cannot rationalize the occurrence of charged analytes of differing polarities or matrix-analyte 'sweet spots.' However, charge transfer during crystallization is consistent with the generation of sweet spots and higher order analyte aggregates, as well as generate similar levels of protonated and deprotonated species, due to excited state matrix proton transfer during crystallization to analytes with an equal probability that analytes in equal proximity would be protonated and deprotonated by equal measure. The matrix-to-analyte ratio is known to affect the quality of the MALDI spectra [85]. It can be rationalized as competition between neutralization of the ion-pair by the counterions arising from the analyte or matrix, as the concentrations of the analyte (and analyte ion-pairs) become similar to matrix ion-pairs, resulting in analyte and matrix suppression. For example, when the concentration of $[\text{M}10][\text{H}^-] > [\text{SP}-\text{Cl}]^-$ ion-pairs H^- are more likely as counter ions for $[\text{SP}^+]$ and $[\text{M}10^+]$. When $[\text{M}10][\text{H}^-] \sim [\text{SP}-\text{Cl}]^-$, the counter ions from SP increase and can neutralize a significant pool of $\text{M}10^+$ species resulting in matrix suppression [24]. *Chang's* group was able to desorb a single *Escherichia coli* K-12 using MALDI, showing clusters as large as micrometers can occur during MALD as mono-charged ions [86]. It is statistically unlikely that singly-charged ions would predominate during the desolvation process within a 1 μs flight time of such a large cluster [66]. On the other hand, proton transfer predominantly occurred during the crystallization phase $[\text{A}^+-\text{X}^-] + [\text{M}-\text{H}]^+ \rightarrow [\text{A}]^+ + \text{M} + \text{HX}$, where A is the analyte species, M the matrix species, or fragment, such as hydroquinone and HX the neutralized anion derived from the analyte. Using the collision probability at 10 bar for sodium chloride results in neutral species in the

form of ion pairs, some of which are dielectrically screened and are released as readily formed ions in the gas phase, reliant upon the analyte ion-to-neutral matrix ratio [77]. Thus, preformed ion-pairs are amenable to the often observed optimal matrix-to-analyte ratio ('sweet-spot') phenomena, with excited state proton transfer to the nearest analyte neighbor producing more mono-charged rather than multiply charged species. Since the ratio of neutrals to charged is approximately 10 million to 1 for small organic matrices (< 500 Da), the total number of collisions within the 100 ns time frame is in the 1×10^{-3} , since the bulk of the collisions, are over within the first 10 ns [87]. Desolvation of these clusters in the micrometer size range ought to produce analytes with multiple charges, which is not the dominant species in the MALDI spectra. The singly charged species is the dominant species, supporting our contention that preformed ions are generated as ion pairs separated from anions, or facile charge transfer occurs in the gas phase between the prior generated ion pairs as neutrals facilitated by matrix-derived cations [88].

12.3.3 Theoretical Considerations

See Tables 12.3 and 12.4.

Proton affinity is determined by the energy change from adding a proton to a molecule. The ability of a molecule to accept protons or its basicity can be characterized by its proton affinity. The highest proton affinity was observed

Table 12.3 Proton affinities (PA) and Sodium affinities (NaA) for matrix M10 and comparable MALDI matrices

| Matrix | $M + H^+ \rightarrow [M + H]^+$ | | | $[M-H]^- + H^+ \rightarrow M$ | $M + Na^+ \rightarrow [M + Na]^+$ | $[M-H]^- + Na^+ \rightarrow MNa$ |
|---------|---------------------------------|-----------------------|---------------------|-------------------------------|-----------------------------------|----------------------------------|
| | PA (kJ/mol) | | | | NaA (kJ/mol) | |
| | Present work | Literature values | | Present work | | |
| 2,5-DHB | 852.9 | 846 ^{a=88} | 857 ^{b=89} | 1363.3 | 138.7 | 536.4 |
| aCCa | 845.7 | 841 ^{c=90} | N/A | 1314.7 | 184.2 | 441.6 |
| CICCa | 821.6 | 831.7 ^{d=91} | N/A | 1463.4 | 170.5 | 635.4 |
| M10 | 889.5 | N/A | N/A | 1333.3 | 200.2 | 539.2 |

Table 12.4 Vertical ionization energies (VIE) and vertical electron affinities (VEA) for matrix M10 and comparable MALDI matrices

| Matrix | VIE (eV) | VEA (eV) |
|---------|----------|----------|
| 2,5-DHB | 8.18 | 0.22 |
| aCCa | 8.47 | 1.23 |
| CICCa | 8.85 | 1.59 |
| M10 | 7.45 | 0.57 |

in 2,5-dihydroxyphenylcarboxylic acid (M10) at 889.5 kJ/mol, followed by 2,5-dihydroxybenzoic acid (2,5-DHB) at 852.9 kJ/mol, alpha-cyano-4-hydroxycinnamic acid (aCCa) at 845.7 kJ/mol, and 4-chloro-alpha-cyanocinnamic acid (ClCCa) at 821.6 kJ/mol. The proton affinity trend observed can be attributed to various factors, such as functional groups, aromaticity, and electron density distribution in the molecule. The carboxylic acid functional group in 2,5-dihydroxyphenylcarboxylic acid contributes to its high proton affinity by acting as a strong proton acceptor via the lone electron pair. However, this functional group is absent in the other three compounds, explaining their lower proton affinities compared to M10. 2,5-dihydroxybenzoic acid and aCCa have phenolic hydroxyl groups, contributing to their proton-accepting ability [89].

Moreover, their aromatic rings increase electron density for greater stability of protonated forms of the molecules. However, chlorine attachment to the aromatic ring of 4-chloro-alpha-cyanocinnamic acid reduces electron density, increasing the instability of its protonated form, which explains its lower proton affinity. In conclusion, functional groups, aromaticity, and electron density distribution of molecules affect proton affinity and explain the trend observed among the four compounds.

In this chemical reaction $[M-H]^- + H^+ \rightarrow M$, the energy difference between the initial and final states measures the strength of the interaction between the deprotonated matrix and the proton. Proton affinities for different compounds ranged from 1314 kJ/mol to 1463 kJ/mol for aCCa and ClCCa, respectively. Proton affinity values were similar for 2,5-DHB and M10, ranging from 1333 to 1363 kJ/mol. The presence of the carboxylic acid group in M10 did not significantly alter its proton interacting ability compared to 2,5-DHB. The variance in proton affinities may be due to variations in electronic and steric properties. In ClCCa, the cyano group may act as an electron-withdrawing group, enhancing the anion stabilization and increasing basicity or proton affinity. The hydroxyl groups in 2,5-DHB and aCCa can function as electron donors, lowering the interaction strength between the deprotonated matrix and proton [90].

The sodium ion affinity (or basicity) of the four compounds is in the order of $M10 > aCCa > ClCCa > 2,5-DHB$. This trend can be explained by considering the electronic and steric properties of the compounds. M10 has the highest sodium ion affinity due to the presence of two hydroxyl groups and a carboxylic acid group, capable of donating electron density to the carbonyl oxygen upon interaction with the sodium ion. In addition, the steric hindrance around the carbonyl group is relatively low, allowing for efficient coordination with the sodium ion. On the other hand, 2,5-DHB has the lowest sodium ion affinity as it lacks any functional group capable of donating electron density to the carbonyl oxygen. Additionally, the steric hindrance around the carbonyl group is relatively high due to the ortho-dihydroxy substitution pattern on the benzene ring, making it difficult for the sodium ion to approach the carbonyl oxygen. aCCa and ClCCa have intermediate sodium ion affinities due to the presence of an electron-withdrawing cyano group and a chlorine atom, respectively, which can partially counteract the electron-donating ability of the hydroxyl groups in these molecules. The exact order of affinities between these two compounds can be attributed to the steric effects introduced by the substitution pattern around the

benzene ring. The sodium ion acts as a counter-ion, neutralizing the charge and forming a heterodimer. The affinity or basicity of the deprotonated matrix for the sodium ion is a measure of the tendency of the matrix to form the heterodimer. The sodium ion affinity or basicity depends on the structure and chemical properties of the deprotonated matrix. In general, the basicity increases with the matrix's electron-withdrawing ability or the hydrogen atom's acidity that is lost during deprotonation. The higher the basicity, the greater the tendency of the matrix to form a heterodimer with a sodium ion.

The sodium ion affinity of the studied compounds reveals that 2,5-DHB has the lowest affinity at 536 kJ/mol compared to the other three compounds. One explanation for this could be the presence of hydroxyl groups in the 2,5-DHB molecule, which acts as electron donors, eventually decreasing the electron-withdrawing ability of the carboxylic acid group. As a consequence, the acidity of the hydrogen atom undergoing deprotonation decreases, thereby leading to a reduction in sodium ion affinity. Conversely, alpha-cyano-4-hydroxycinnamic acid has a higher sodium ion affinity of 441 kJ/mol. A cyano group, an electron-withdrawing group, enhances the hydrogen atom's acidity lost during deprotonation, increasing sodium ion affinity. 4-Chloro-alpha-cyanocinnamic acid has the highest sodium ion affinity among the studied compounds at 635 kJ/mol. The chloro group's electronegativity, greater than hydrogen, enhances the hydrogen atom's acidity lost during deprotonation, much like the cyano group in aCCa.

Additionally, the chloro group may also reinforce the electron-withdrawing effect of the cyano group, further enhancing the electron-withdrawing ability and acidity. 2,5-Dihydroxyphenylcarboxylic acid (M10) also has a high sodium ion affinity of 539 kJ/mol, comparable to 2,5-DHB. The presence of the carboxylic acid group in M10 enhances the acidity of the hydrogen atom that is lost during deprotonation, resulting in a high sodium ion affinity. However, the presence of the hydroxyl groups in the phenyl ring also reduces the electron-withdrawing ability of the carboxylic acid group, as in the case of 2,5-DHB, resulting in a sodium ion affinity comparable to that of 2,5-DHB.

The stronger the basicity of a molecule, the lower its ionization energy. In the case of 2,5-DHB, it has two hydroxyl groups that can act as hydrogen bond donors, making it more basic and easier to ionize than the other matrices. However, it is not a strong proton acceptor, which explains its relatively high VIE of 8.18 eV. Alpha-cyano-4-hydroxycinnamic acid (aCCa) is a stronger proton acceptor than 2,5-DHB due to its cyano group, which can stabilize the positive charge of the conjugate acid by resonance. The presence of a hydroxyl group in aCCa increases its basicity as it donates a hydrogen bond. As a result, aCCa is easier to ionize than 2,5-DHB, leading to a VIE of 8.47 eV. ClCCa, on the other hand, has a higher VIE of 8.85 eV owing to the electron-withdrawing effect of chlorine, which reduces the molecule's basicity and makes it more difficult to ionize than aCCa. M10, devoid of chlorine or cyano group, displays the lowest VIE at 7.45 eV. This can be detailed by its two hydroxyl groups, which intensify its hydrogen bond donation and reduce its proton acceptor capability. The VEA can be related to a molecule's electron-attracting ability, which

may depend on its proton affinity and basicities. 2,5-dihydroxybenzoic acid has a low VEA value, indicating a low electron affinity, and does not easily attract electrons.

The matrix contains two hydroxyl groups that can act as proton donors, reducing its proton affinity and basicities. Alpha-cyano-4-hydroxycinnamic acid has a higher VEA value than 2,5-DHB, indicating a stronger electron-attracting ability. The matrix contains a cyano group which acts as an electron-withdrawing group, leading to its high VEA value. The cyano group increases the molecule's proton affinity and basicities, contributing to its electron-attracting ability. 4-chloro-alpha-cyanocinnamic acid has the highest VEA value among the four matrices, implying it has the strongest electron-attracting ability. The matrix contains a cyano and a chloro group, contributing to its high electron affinity. The chlorine atom is electronegative and can pull electron density towards itself, increasing the molecule's electron-attracting ability. The presence of a cyano group enhances the molecule's proton affinity and basicities, contributing to its electron-attracting ability as well. 2,5-dihydroxyphenylcarboxylic acid has a moderate VEA value but is higher than 2,5-DHB, indicating its moderate electron-attracting ability. The molecule possesses one hydroxy group, which can act as a proton donor. However, it lacks other functional groups capable of enhancing its proton affinity or basicities, thereby limiting its electron-attracting ability.

The trend shows an increase in both VIE and VEA values as we move from 2,5-DHB to CICC*a*, indicating that the matrices' electron affinity and ionization energy is more favorable for protonation and deprotonation reactions. This trend suggests that CICC*a* is the best matrix for protonation and deprotonation reactions compared to the other matrices. The interaction of these matrices with sodium ions or the formation of the sodium-matrix neutral dimer depends on the specific conditions and the experimental setup. However, one can predict that the matrices with higher electron affinity and ionization energy values, such as CICC*a*, will interact more strongly with sodium ions and form more stable complexes.

In summary, In this study, we investigated four matrices for their proton affinity, deprotonation enthalpy, sodiation enthalpy, and electron ionization. We aimed to identify the most effective matrix for generating protonation, deprotonation, and sodiation species. Based on the proton affinity values, we found that the 2,5-dihydroxyphenylcarboxylic acid (M10) matrix exhibited the highest proton affinity at 889 kJ/mol. The 4-chloro-alpha-cyanocinnamic acid (CICC*a*) matrix exhibited the lowest proton affinity at 821 kJ/mol. The dissociation enthalpy values for the deprotonated dimer suggest that the M10 matrix performs best for deprotonation at 1333 kJ/mol, while the CICC*a* matrix has the highest dissociation enthalpy for the deprotonated dimer at 1463 kJ/mol.

Regarding sodiation, we observed that the 2,5-DHB matrix had the lowest sodiation enthalpy value of 536 kJ/mol, while the CICC*a* matrix exhibited the highest sodiation enthalpy at 635 kJ/mol. The dissociation enthalpy followed by sodium ion attachment values suggests that the CICC*a* matrix would form the most stable sodium-matrix neutral dimer. Finally, we analyzed the data for each matrix's vertical ionization energies (VIE) and vertical electron affinities (VEA). We found that the CICC*a* matrix exhibited the highest VEA value at 1.59 eV, while the aCC*a* matrix

had the highest VIE value at 8.47 eV. The M10 matrix had the lowest VIE value of 7.45 eV, while the 2,5-DHB matrix had the lowest VEA value of 0.22 eV.

Our analysis concludes that the M10 matrix is the best candidate for protonation and deprotonation species generation, while the ClCCa matrix is the most effective for generating sodiation species. Additionally, the ClCCa matrix can form a doubly charged species, making it a promising candidate for applications that require high charge density.

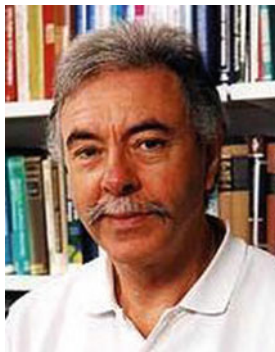
12.4 Conclusion

A matrix based on a hydroquinone core of 2,5-DHB terminating with an n-decanoic acid (M10) was evaluated across three analyte types. In each case, the MALDI optimization time was restricted to 30 s for M10 and 3 min for aCCa. Peptide mass fingerprinting using the MOWSE scoring algorithm (12) and Mascot as a search engine yielded confident protein identification using Mascot Scoring parameters and sequence coverage for M10 comparable or superior to that obtained with aCCa, with one-sixth the optimization time. Using proton affinity (PA) calculations from density functional theory 6-311G** basis set for the protonated matrix M10 species, it was shown that the PA of M10 was lower than that of 2,5-DHB and aCCa and contributed to pseudo proton transfer during the crystallization phase, where analyte molecules are incorporated into the matrix and can be protonated or deprotonated or cationized (or $[A + Na - 2H +]^-$). The enhanced ion yield was attributed to the more efficient matrix-to-analyte interaction under the n-decanoic acid functional group. The longer alkyl chain extended the degree of freedom of M10 relative to aCCa, enabling proton transfer to occur at a greater degree or similar to aCCa but with much less MALDI preparation time. The model for proton transfer is unlikely to be photochemical ionization due to ns flight times in the source, thereby limiting molecular collisions in the gas plume, except for short acidic peptides that can be desorbed without organic matrices. The matrix cluster ionization mechanism is also favored for certain types of analytes, where analyte molecules are charged by desolvation of the matrix from cluster ions that have been documented to occur under MALDI conditions. However, multiply charged species are anticipated under such conditions since completed desolvation within the source chamber is not expected under microsecond flight times.

Regarding analyte ion yield, peptide mass fingerprint percent coverage, and protein identification scores, M10 demonstrated greater efficiency than aCCa. These results were comparable to or greater than those obtained with aCCa, with a six-fold reduction in acquisition and optimization time. The higher ion yield was related to the energy transfer from the excited matrix during the crystallization process as a primary mechanism for obtaining altered analytes. Furthermore, M10 as a matrix can extend the operational lifetime of older mass spectrometers, benefiting undergraduate-intensive universities, colleges, hospitals, or clinical laboratories with

limited instrument budgets; using the M10 matrix results in sensitivity and ion yield gains through more efficient proton transfer.

Acknowledgements SB would like to thank Drs. Roger Mutter and Martin Wills (University of Warwick) for initial assistance with synthesizing M10 and Drs. Ian Herbert and John Horsler (Accordis, U.K) for access to the Bruker Biflex. SB would also like to thank Dr. Jocelyn Rose for access to his laboratory (Cornell University) to complete some proteomics components started at the University of Warwick and completed at Cornell University when SB joined Dr. Rose's group as a postdoctoral associate. In addition, SB would extend his appreciation to the entire Rose Group and Staff.



SB would like to thank the Engineering and Physical Sciences Research Council (EPSRC), Akzo Noble, and the Robert A. Welch Foundation Departmental Grant (AC006) for financial support. KAB would like to express gratitude for financial support from the Robert A. Welch Foundation (AW-0013) and funds from the Opportunities for Student Achievement and Transfer (OSAT) grant (P031C080116-09). JL would like to thank the American Chemical Society Petroleum Research Fund (53827-UR10) and Welch Foundation (AC-0006) for assistance.

Author Contribution PJD conceived the project and allowed access to the laboratory. MG undertook the synthesis clean-up previously attempted by M10 by RM KAB and carried out the entire DFT component of the project. JL carried out the data analysis and proteomic figure generation. SB carried out the entire mass spectrometry component. All authors reviewed and re-edited the manuscript by SB, JL, and KAB. Please note that PJD passed away during the preparation of this research.

References

1. Karas M, Bachmann D, Hillenkamp F (1985) *Anal Chem* 57:2935
2. Karas M, Hillenkamp F (1988) *Anal Chem* 60:2999
3. Vorm O, Roepstorff P, Mann M (1994) *Anal Chem* 66:3281
4. Zenobi R, Knochenmuss R (1998) *Mass Spectrom Rev* 17:337
5. Hillenkamp F, Karas M (1990) *Met Enzymol* 193:280
6. Rose JK, Bashir S, Giovannoni JJ, John MM, Saravanan RS (2004) *Plant J* 39:715
7. Shevchenko A, Loboda A, Shevchenko A, Ens W, Standing KG (2000) *Anal Chem* 72:2132

8. Ryzhov V, Fenselau C (2001) *Anal Chem* 73:746
9. Cohen SL, Chait BT (1996) *Anal Chem* 68:31
10. Cornett DS, Reyzer ML, Chaurand P, Caprioli RM, Nat Met 4:828
11. Jespersen S, Chaurand P, van Strien FJ, Spengler B, van der Greef J (1999) *Anal Chem* 71:660
12. Dupont CL, Nelson RK, Bashir S, Moffett J, Ahner BA (2004) *Limnol Oceanogr* 49:1754
13. Jurchen JC, Rubakhin SS, Sweedler JV (2005) *J Am Soc Mass Spectrom* 16:1654
14. Mallick P, Kuster B (2010) *Nat Biotech* 28:695
15. Domon B, Aebersold R (2006) *Science* 312:212
16. Aebersold R, Mann M (2003) *Nature* 422:198
17. Shevchenko A, Wilm M, Vorm O, Mann M (1996) *Anal Chem* 68:850
18. Henzel WJ, Watanabe C, Stults JT (2003) *J Am Soc Mass Spectrom* 14:931
19. Knochenmuss R, Dubois F, Dale MJ, Zenobi R (1996) *R. Rapid Commun Mass Spectrom* 10:871
20. Dreisewerd K (2003) *Chem Rev* 103:395
21. Karas M, Krüger R (2003) *Chem Rev* 103:427
22. Karas M, Glückmann M, Schäfer J (2000) *J Mass Spectrom* 35:1
23. Tholey A, Heinze E (2006) *Anal BioAnal Chem* 386:24
24. Knochenmuss R, Zenobi R (2003) *Chem Rev* 103:441
25. Wilson DP, Wan ZK, Xu WX, Kirincich SJ, Follows BC, Joseph-McCarthy D, Foreman K, Moretto A, Wu J, Zhu M, Binnun E, Zhang Y-L, Tam M, Erbe DV, Tobin J, Xu X, Leung L, Shiling A, Tam SY, Mansour TS, Lee J (2007) *J Med Chem* 50:4681
26. Cui W, Zhang J, Wang Q, Gao K, Zhang W, Yang J (2014) *J Chem Res* 38:686
27. Yakubovskaya AY, Pokhilo ND, Mishchenkoand NP, Anufriev VF (2007) *Russ Chem Bull* 56:819
28. Yoshida M, Higuchi, Shishido K (2009) *Org Lett* 11:4752
29. Nelb RG, Stille JK (1976) *J Am Chem Soc* 98:2834
30. Song ZJ, Zhao M, Desmond R, Devine P, Tschaeen DM, Tillyer R, Frey L, Heid R, Xu F, Foster B, Li J, Reamer R, Volante R, Grabowski EJ, Dolling UH, Reider PJ, Okada S, Kato Y, Mano E (1999) *Org Chem* 64:9658
31. Stewart JJP (1989) *J Comput Chem* 10:209
32. Lee C, Yang W, Parr RG (1988) *Phys Rev B* 37:785
33. Becke AD (1993) *J Chem Phys* 98:1372
34. Becke AD (1993) *J Chem Phys* 98:5648
35. Scott AP, Radom L (1996) *J Phys Chem* 100:16502
36. Spartan'08, Wavefunction, Inc., Irvine, CA
37. Shiloach J, Fass R (2005) *Biotech Adv* 23:345
38. Korz DJ, Rinas U, Hellmuth K, Sanders EA, Deckwer W-D (1995) *J Biotech* 39:59
39. Rose JKC, Bashir S, Giovannoni JJ, Jahn MM, Saravanan RS (2004) *Plant J* 5:715
40. Rosenbusch JP (1974) *J Biol Chem* 249:8019
41. Zor T, Selinger Z (1996) *Anal Biochem* 236:302
42. Rabilloud T, Adessi C, Giraudel A, Lunardi J (1997) *Electrophoresis* 18:307
43. Hochstrasser DF, Harrington MG, Hochstrasser A-C, Miller MJ, Merrill CR (1988) *Anal Biochem* 173:424
44. Candiano G, Bruschi M, Musante L, Santucci L, Ghiggeri GM, Carnemolla B, Orecchia P, Zardi L, Righetti PG (2004) *Electrophoresis* 25:1327
45. Shevchenko A, Tomas H, Havli J, Olsen V, Mann M, Nat Protoc 1:2856
46. Jiménez CR, Huang L, Qiu Y, Burlingame AL (2001) *Curr Proc Prot Sci* 14:16.4.1
47. Katayama H, Nagasu T, Oda Y (2001) *Rapid Commun Mass Spectrom* 15:1416
48. Baczek T (2004) *J Pharmaceut Biomed Anal* 5:851–860
49. Bashir S, Mutter R, Derrick PJ (2003) *Analyst* 128:1452
50. Cottrell JS, London U (1999) *Electrophoresis* 20:3551
51. Thiede B, Höhenwarter W, Krah A, Mattow J, Schmid M, Schmidt F, Jungblut PR (2005) *Methods* 35:237
52. Chamrad DC, Körting G, Stühler K, Meyer HE, Klose J, Blüggel M (2004) *Proteomics* 4:619

53. Datar P, Srivastava S, Coutinho E, Govil G (2004) *Cur Top Med Chem* 4:75
54. Kyte J, Doolittle RF (1982) *J Mol Biol* 157:105
55. Li CH, Evans HM, Simpson ME (1943) *J Biol Chem* 149:413
56. Choudhary J, Blackstock WP, Creasy DM, Cottrell JS (2001) *Trends Biotech* 19:17
57. Benson DA, Cavanaugh M, Clark K, Karsch-Mizrachi I, Lipman DJ, Ostell J, Sayers EW (2012) *Nucleic Acid Res* 41:D36
58. Ashburner M, Ball CA, Blake JA, Botstein D, Butler H, Cherry JM, Davis AP, Dolinski K, Dwight SS, Eppig JT, Harris MA, Hill DP, Issel-Tarver L, Kasarskis A, Lewis S, Matese JC, Richardson JE, Ringwald M, Rubin GM, Sherlock G (2000) *Nat Gen* 25:25
59. Jaskolla TW, Karas M (2011) *J Am Soc Mass Spectrom* 22:976
60. Glückmann M, Pfenninger A, Krüger R, Thierolf M, Karas M, Homeffer V, Hillenkamp F, Strupat K (2001) *Int J Mass Spectrom* 210:121
61. Liang CW, Lee CH, Lin YJ, Lee YT, Ni C-K (2013) *J Phy Chem* 117:5058
62. Moon JH, Shin YS, Bae YJ, Kim MS (2012) *J Am Soc Mass Spectrom* 23:162
63. Rebber BL, Halfacre JA, Beran KA, Beller NR, Gomez M, Bashir S (2006) Giannakopoulos and P. J. Derrick. *Eur J Mass Spectrom* 12:385
64. Yamazaki T, Takeuchi M, Watanabe T, Sugahara K, Takeuchi T (2016) *Rapid Commun Mass Spectrom* 30:2650
65. Chu KY, Lee S, Tsai M-T, Lu I-C, Dyakov YA, Lai YH, Lee Y-T, Ni C-K (2014) *J Am Soc Mass Spectrom* 25:310
66. Knochenmuss R (2015) *J Am Soc Mass Spectrom* 26:1645
67. Trimpin S, Wang B, Inutan ED, Li J, Lietz CB, Harron A, Pagnotti VS, McEwen CN (2012) *J Am Soc Mass Spectrom* 23:1644
68. Wei J, Buriak JM, Siuzdak G (1999) *Nature* 399:243
69. Frankevich V, Knochenmuss R, Zenobi R (2002) *Int J Mass Spectrom* 220:11
70. Knochenmuss R (2004) *Anal Chem* 76:3179
71. McCombie G, Knochenmuss R (2006) *J Am Soc Mass Spectrom* 17:737
72. Knochenmuss R, Zhigilei LV (2012) *Anal BioAnal Chem* 402:2511
73. Lu I-C, Chu KY, Lin C-Y, Wu S-Y, Dyakov YA, Chen JL, Gray-Weale A, Lee Y-T, Ni C-K (2015) *J Am Soc Mass Spectrom* 26:1242
74. Lee C, Lu I-C, Hsu HC, Lin H-Y, Liang SP, Lee YT, Ni C-K (2016) *J Am Soc Mass Spectrom* 27:1491
75. Knochenmuss R (2006) *Analyst* 131:966
76. Karbach V, Knochenmuss R (1998) *Rapid Commun Mass Spectrom* 12:968
77. Hsu HC, Lu I, Lin PH, Dyakov YA, Bagchi A, Lin CY, Hung S-W, Lee YT, Ni CK (2014) *Rapid Commun Mass Spectrom* 28:1082
78. Allwood DA, Dreyfus RW, Perera IK, Dyer PE (1996) *Rapid Commun Mass Spectrom* 10:1575
79. Yoon SH, Moon JH, Kim MS (1876) *J Am Soc Mass Spectrom* 2010:21
80. Spengler B (1997) *Mass Spectrom*, 32:1019
81. Bae YJ, Moo JH, Kim MS (2011) *J Am Soc Mass Spectrom* 22:1070
82. Lin H-Y, Hsu HC, Lu I-C, Hsu K-T, Liao C-Y, Lee Y-Y, Tseng C-M, Lee Y-T, Ni C-K (2014) *J Chem Phys* 141:164307
83. Alonso E, Zenobi R (2016) *Phys Chem Chem Phys* 18:19574
84. Bae YJ, Choe JC, Moon JH, Kim MS (1807) *J Am Soc Mass Spectrom* 2013:24
85. Lu I-C, Lee C, Lee YT, Ni C-K (2015) *Ann Rev Anal Chem* 8:21
86. Peng WP, Yang YC, Kang MW, Lee YT, Chang HC (2004) *J Am Soc Mass Spectrom* 126:11766
87. Bourcier S et al (2001) *Int J Mass Spectrom* 210(211):59–69
88. Mormann M et al (2000) *J Am Soc Mass Spectrom* 11:544–552
89. Jorgensen TJD et al (1998) *Eur J Mass Spectrom* 4:39–45
90. Jaskolka TW et al (2008) *Proc Natl Acad Sci. USA* 105:12200–12205

Chapter 13

Hydrophilic/Phobic Tailored Multi-laned/Layer Matrix-Assisted Laser Desorption/Ionization (HTML-MALDI)



Sajid Bashir, Jingbo Liu, and Peter J. Derrick

Abstract This study aimed to enhance ion yield from a protein mixture using hydrophobic and hydrophilic structured surfaces to enhance analyte solubilization and the spatial separation of matrices to enable multi-matrix desorption and ionization of the peptide mixtures. The use of solid-stated anchored compounds can aid in sample cleanup and digestion, further improving the signal intensity of digests. However, this research suggested that the results were partly dependent upon the protein's basicity. The more basic lysozyme was found to generate the highest sum peptide intensities under the dried drop methods. On the other hand, the less basic myoglobin produced the highest sum intensities with anchor support. It was critical to use the matrix species in the middle lane for optimizing analyte peak intensities, although using matrices in peripheral lanes did lead to signal enhancements.

It is with profound sadness that SB writes this acknowledgment. There is a word in the Old Testament, *salah*, meaning to pause and reflect. I deeply miss Peter, but I will never forget the important lessons he taught me about being a scientist, teacher, and human. JL Liu writes I never met Dr. Derrick, but his knowledge to advance science and responsibility to educate the young generation has inspired me. There are three very painful experiences in my life: the death of my grandparents, who raised me and taught me to be a nice person; the death of my parents, who gave me life and encouraged me to be a strong person; and the death of Dr. Derrick who greatly affected Dr. Bashir. I have known and worked with Dr. Bashir for over a decade. I know the type of man he is and know this is largely due to Peter Derrick. I shall never forget the sweet, courageous, and dedicated man whose name will always linger in my thoughts. Thank you, Dr. Peter Derrick, and God Speed.

S. Bashir (✉) · P. J. Derrick (Deceased)
Institute of Mass Spectrometry, University of Warwick, Coventry CV4 7AL, UK
e-mail: br9@tamuk.edu

P. J. Derrick (Deceased)
e-mail: p.j.derrick@auckland.ac.nz

S. Bashir · J. Liu
Department of Chemistry, Texas A&M University-Kingsville, 700 University Blvd., Kingsville,
TX, USA

P. J. Derrick (Deceased)
Department of Physics, The University of Auckland, 7 Symonds Street, Auckland 1061, New
Zealand

Keywords MALDI-TOF MS hydrophobic-tailored surfaces · Hydrophilic-tailored surfaces · Enhanced ion yield · Enhanced desorption

13.1 Introduction

Matrix-assisted laser desorption ionization time-of-flight (MALDI-TOF) mass spectrometry is a technique in which an organic aromatic molecule (known as the matrix) is deposited independently or co-mixed with an analyte onto a metal surface. Once the mixture is dry, the sample is analyzed by irradiance with an ultraviolet (UV) laser pulse, in which the analyte ions are desorbed and observed either in the protonated or cationized ($[M + H]^+$ or $[M + X]^+$) forms. The primary advantage of MALDI-TOF mass spectrometry is the desorption and ionization of macromolecules with the minimal fragmentation of several different classes of compounds such as synthetic polymers [1, 2], proteins [3], glycoproteins [4], oligosaccharides [5, 6] and nucleotides [7] of masses up to 500 kDa [8]. The analytes' desorbed and ionized mechanisms are not fully understood. However, an oversimplification of the MALDI process can occur in two discrete steps, the physical process of sublimation/desorption and the photochemical/physical process leading to ionization. Ionization can be conceptualized as occurring in two steps, where primary ions, once generated during crystallization, interact with the gas plume neutrals or ion pairs leading to secondary ion formation. Although a quantitative model has been developed to take account of the observed MALDI phenomena [9–12], no single matrix species can be used to analyze a wide variety of compounds [13].

The advantage mentioned above of high mass detection with low fragmentation is off-set with lack of a 'universal' MALDI matrix compound and, in some instances, large precision in the average ion yield (measured as $[M + H]^+$ or $[M + X]^+$, where X represents either a singly charged cation (of a formerly double charge cation that has been reduced) for the analyte. Therefore, techniques have been attempted to utilize more 'efficient' matrices or 'sample preparation techniques to minimize signal variations. The early studies by Tanaka et al. demonstrated that MALDI was a viable technique using cobalt powder (as the matrix species) finely dispersed in glycerol analyzed at 337 nm [14]. Karas and Hillenkamp, at the same time frame, obtained the first MALDI spectra of proteins using 3-pyridine carboxylic acid (nicotinic acid as the matrix species) with a 266 nm laser and later introduced 2, 5-dihydroxybenzoic acid (DHB) [15], and 2-hydroxybenzoic acid [16] as matrices in the analysis of a wide variety of compounds such as proteins, lipids, and carbohydrates [17]. Over the years, many other compounds [12, 18, 19] have been used as potential matrices in the analysis of specific compounds, such as glycolipids [20] or porphyrins [21], or polymers [22–24]. Aside from 2, 5-DHB, carboxylic or cinnamic acid derivatives are the most commonly used matrix [25]. The 'correct' selection of the matrix is empirical and time-consuming. Due to the unpredictability of the optimal analyte-to-matrix composition, 2-5-DHB [26], α -cyano-4-hydroxycinnamic acid (aCCa) [27]

or 3, 4-dimethoxy-4-hydroxycinnamic acid [28] is the primary matrices of choice [29].

Inconsistency in the MALDI spectra arises due to matrix and analyte inhomogeneity [30]. This can be minimized by several methods, such as using detergent to promote micelle formation of matrix and aid interaction with the analyte [31]. Other approaches to minimize analyte signal intensity include synthetic modification of the surface, where matrix-to-analyte interaction may be promoted, enhancing the signal intensity. The use of pre-structured support surfaces [32] or membranes [33] to aid sample retention and desorption has been attempted before with the use of Nafion, nitrocellulose [34], self-assembled monolayers [35], silicon-coated surfaces [36], nanoscale Fe(III) support [37], carbon nanotubes [38], titanium surface [39] investigated the effect of protein growth, protein adhesion as opposed to protein signal enhancement and gold surfaces [40] have all been employed to minimize signal variance and enhance the average signal intensity of the analyte under investigation. This chapter uses spatial geometry to allow for increased analyte sensitivity. This is accomplished by the selective use of hydrophobic and hydrophilic tailored anchors (HTML) on the metal surface of the MALDI target plate and the deposition of different matrices on each type of anchor, thereby examining any synergic interaction between the matrices and matrix-to-analyte to aid:

(a) analyte sensitive by way of identification of unique peptide from a peptide mixture of seven peptides (sample coverage), (b) enhancement of the average protonated peak intensity for the peptides or sum of the protonated peak intensities, and (c) lowering of the standard deviation of the protonated peak intensity in comparison to the standard dried drop approach (CLASSIC). Furthermore, our approach uses a simple setup with no optimization, pre-sample cleanup, or sample preparation expertise to simulate the typical conditions encountered in a standard laboratory setup. On the slide, protein digestion was also attempted (ON) and compared to off-slide solution digestion (OFF) to determine whether the system could be used for sample digestion and analysis in one setup. The parameters to determine whether the layering anchors are more efficient than the use of the dried drop approach were statistically compared through post hoc ANOVA analysis to determine significance at the 95 confidence level ($P < 0.05$) was also evaluated [41].

13.2 Material and Methods

13.2.1 Chemical and Reagents

2,5-dihydroxybenzoic acid, alpha-cyano-4-hydroxycinnamic acid (aCCa), nor Harman, Sinapinic acid (SA) were all obtained from Sigma-Aldrich and were used without purification (Dorset, UK). Trypsin, myoglobin (Myo), ammonium carbonate (ABC) and, egg-white lysozyme (EWL), substance P (SubP) were also purchased from Sigma-Aldrich. A peptide mixture was obtained from Mr. Phil Green (PGmix)

and used without modification or pre-treatment. The solvents, such as methanol were HPLC grade and used without further filtration; distilled water was used where appropriate. The hydrophobic (lauryl methacrylate, LMA, CW $\sim 10^{-4}$ mM) [42] and hydrophilic (glycerol mono-methacrylate, GMA, CW $\sim 10^{-1}$ mM) [43] polymers were donated by Professor Haddleton (Warwick University, Department of Chemistry) [44].

13.2.2 *Sample Preparation*

1 mg/ml of support polymer (LMA or GMA) was dissolved in the appropriate solvent. The stainless steel MALDI slide was heated to 50 °C, then anchored, layered horizontally along the slide, and oven-dried. This was repeated with the other polymer to give a three-lane system, described as LMA-GMA-LMA or no treatment [NT] of the entire surface or one specific lane. Each lane occupied about a third of the slide (3 mm, width-wise). Once dry, the matrices were layered on top of the polymer support. This second layer can be described as the matrix alone that is dried and upon which the analyte is separately deposited [Matrix 1–Analyte] or the matrix and analyte are premixed and deposited [Matrix 1 + Analyte], or the matrix is deposited without the addition of analyte [matrix]. In the adjacent lanes, the same matrix, no matrix [NT], or a different matrix was deposited and would be indicated as [Matrix 2][Matrix 3] if different matrices were applied. The classical setup would be [NT]-[Matrix 1–Analyte]-[NT]. The typical arrangement was DHB-aCCa-(SA or nor-harmane), where aCCa always occupied the middle track. The tryptic digest was finally sprayed using an internally mixing dual-action airbrush (Hansa 451, Hansa-Technik GmbH, Norderstedt, Germany) and air-dried. For comparison with the dried drop approach, no polymer support was used, and this system was annotated as [NT]-[aCCa-EWL]-[NT]. This annotation would denote that the middle lane contained alpha-cyano-4-hydroxycinnamic acid deposited with the egg while the adjacent lines were empty. No polymeric support was used on any lane.

13.2.3 *Enzyme Digestion*

The enzyme digestion was done in an Eppendorf at 40 °C for 5 min in a buffer (NH_4CO_3 , at pH 7.0). The reaction was terminated by freezing the system at -30 °C. An equal digest volume was diluted with 1:1 methanol/water with a 0.2% trifluoroacetic (TFA) acid solvent system. These digest products were co-mixed with matrix (1:1 v/v), and the mixture was sprayed onto the slide (OFF) and air-dried. The concentration of the matrix was 0.1 M, and that of the digest was 100 μM . Where the digest was performed on the slide, the enzyme was placed in the middle track, and the system incubated at 40 °C for 5 min in a high humidity environment. The reaction

was terminated after 5 min by spraying 1:1 methanol/water with 0.2% trifluoroacetic acid solvent (ON) and air-dried.

13.2.4 Maldi TOF MS

A Kratos Kompact IV was used in positive linear mode (25 kV accelerating potential) with a 5 ns pulse width nitrogen laser. The data was collected and analyzed using a SunSPARC workstation (Sun Microsystems, CA).

13.2.5 MALDI Sample Preparation

The peptide mixture (each peptide was 1 mg/ml stock in 1:1 water/methanol + 0.2% trifluoroacetic acid) was deposited either by the dried drop procedure (CLASSIC). In this procedure, the matrix was deposited onto the stainless steel (SS) surface with a pipette, and once dried, the peptide standard mixture (PGmix) or protein digest (EWL or MYO) was deposited. Where the polymer support was used, the above procedure was used; the matrix and or analyte were spray coated onto the polymer supports. The analyte was only applied to the middle lane (HTML). Generally, 0.5 μL of matrix or analytes was deposited on the stainless slide and allowed to dry using the dried drop approach. For the spray, 100 μL of the stock solutions was sprayed onto the surface over 1–3 s. Approximately 0.5 μL of tryptic digest that had previously been diluted by 50% with 1:1 water/methanol + 0.2% trifluoroacetic acid was deposited (HTML_OFF). Where the digest was carried out on the polymer support surface (HTML_ON), the reaction was terminated by adding a matrix either by the dried drop procedure or by air spraying. Once dry, the system was analyzed using MALDI-TOF (Kratos) mass spectrometer.

13.2.6 MALDI-TOF Calibration

The spectra were initially calibrated using the mass peaks for Na (22.99 Da), [DHB + Na]⁺, (177.11 Da), and [SubP + Na]⁺ substance P (1370.59 Da) or the protonated peptides in PGmix. A minimum of ten experiments were carried out for the peptide standard mixture and digests.

13.2.7 *Statistical Analysis*

To assess the relative merits of each system, the number of unique peptides identified from the standard peptide mixture, the sum of the protonated peptide intensities, and the corresponding standard deviation from each set of experiments ($n = 10$). Where the different formulations were compared, their significance was evaluated using the analysis of variance between groups (ANOVA), Student *t* (assuming unequal variances) and Scheffe's test at the 0.05 (95% confidence) level. The statistical results are summarized as either significant ($P < 0.05$) or not significant ($P > 0.05$).

13.3 Results and Discussion

13.3.1 *Improvement in Ion Yield Using Peptide Mixture*

The threshold for improvement was set at either greater peptide coverage (from the standard peptide mixture, PGmix), greater summed peak intensities for the protonated peptides, or greater sequence coverage of the model proteins, egg-white lysozyme (EWL), or horse heart myoglobin (MYO). In order to evaluate the efficacy of the anchor system, we compared and contrasted the polymer-coated slide (known as HTML) with the equivalent system utilizing the dried drop method (CLASSIC). We employed alpha-cyano-4-hydroxycinnamic acid (aCCa) as the matrix and PGmix as the standard mixture for the first investigation. Figure 13.1 illustrates a schematic of the HTML slide. The candidate element in focus here is the HTML slide.

The MALDI mass spectrum of PG Mix under CLASSIC and HTML conditions is shown in Figs. 13.2 and 13.3, respectively. The peak intensities of the three matrices used in the HTML design were detected and are shown in Fig. 13.4. The mass accuracy and peak intensity (in millivolts) are summarized in Table 13.1.

It can be seen that the layered approach was able to resolve and detect all seven peptides from the standard peptide mixture PGmix, whereas with the classic approach, only five out of seven peptides were detected, some of the very high signal-to-noise ratios. The applicability to peptide digests was also evaluated using two standard proteins. Egg white lysozyme and myoglobin were used, and the order of the anchor and the matrix were varied to determine if there was a difference in the sequence coverage and intensity. This was evaluated using a one-way ANOVA comparison and two-way student *t*-test at the 95% confidence limit and by post hoc means comparison using Scheffe's Test ($0.05 > p < 0.05$). A mass spectrum of EWL with alpha-cyano cinnamic acid as the matrix by the dried drop approach is shown in Fig. 13.5. The corresponding spectrum with the polymer support and [GMA-DHB][[LMA-aCCa-EWL]-[GMA-DHB]] is shown in Fig. 13.6, and the polymer

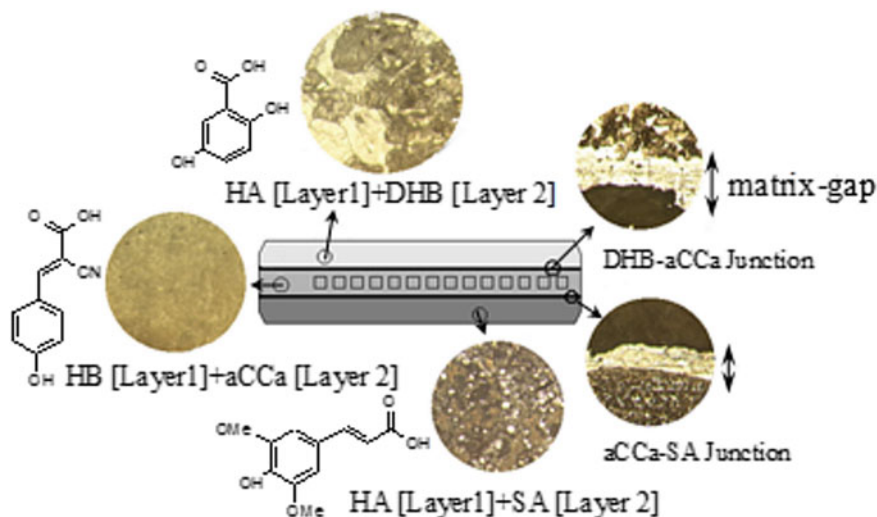


Fig. 13.1 Schematic of layering of hydrophobic (GMA) and hydrophilic (LMA) polymers with three different matrices (SA, DHB, and aCCa) and optical micrographs of cross sections of individual layers

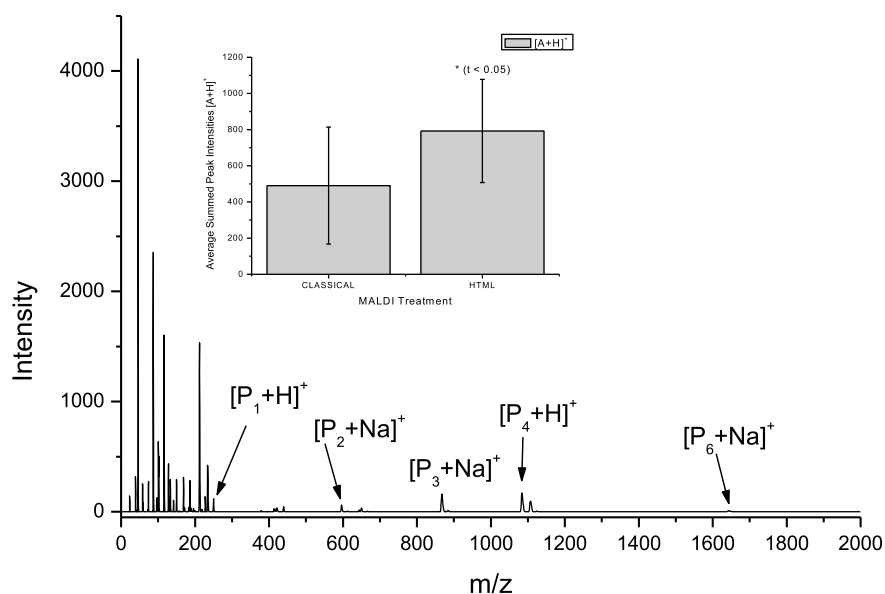


Fig. 13.2 MALDI-TOF MS in a positive-ion model using the peptide mixture's dried-drop (classical) sample preparation method. The specific peptides detected are labeled from the lowest molecular mass to the highest molecular mass. The summed ion intensities of all detected peptides are compared and contrasted with an almost identical setup but with LMA-aCCa-GMA hydrophilic/hydrophobic surfaces to promote analyte solubilization. A post hoc statistical analysis indicates that the higher summed ion yield under HTML preparation conditions was statistically significant

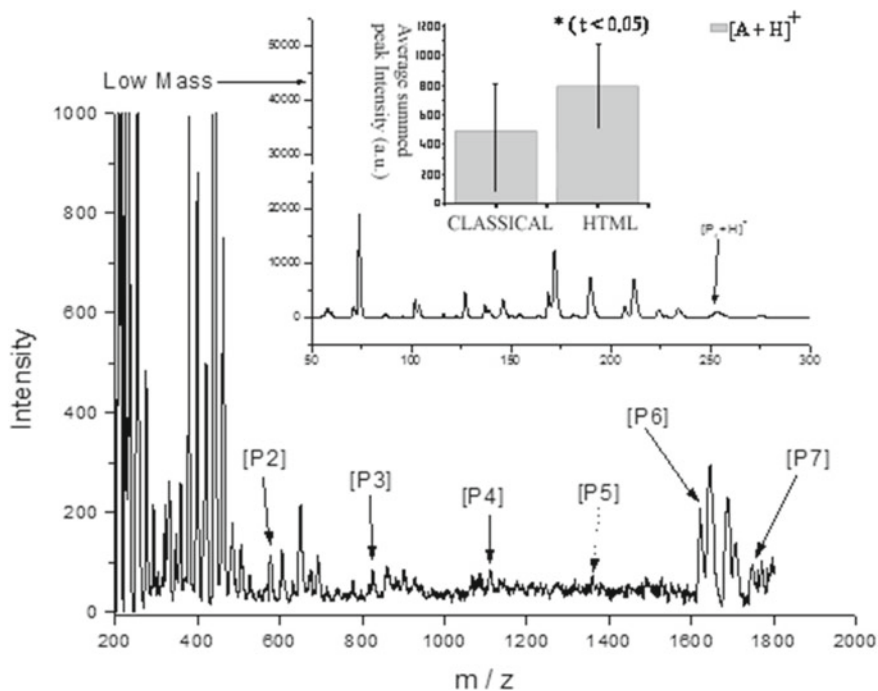


Fig. 13.3 MALDI-TOF MS in a positive-ion model using surface tailoring multi-matrix sample preparation method. The specific peptides detected are labeled from the lowest molecular mass to the highest molecular mass. The summed ion intensities of all detected peptides are compared and contrasted with an almost identical setup but without LMA-aCCa-GMA hydrophilic/hydrophobic surfaces to promote analyte solubilization. A post hoc statistical analysis indicates that the higher summed ion yield under HTML preparation conditions was statistically significant

system with matrix only in the central lane ([GMA]-[LMA-aCCa-EWL]-[GMA]) in Fig. 13.7.

A summary of the anchor versus dried drop results is summarized in Table 13.2.

It can be seen that with basic proteins such as lysozyme (pI 9.32), the use of polymer surface leads to a decrease in the sum of the peptide intensities with alpha-cyano cinnamic acid as the matrix species (Group 1 versus Groups 2 and 3), where sinapinic acid as the matrix, there is a two-fold decrease in the peptide summed intensities (Group 2 versus Group 1). On-slide digestion with sinapinic acid as the matrix was also ineffective (Group 5 versus Group 2), indicating that the protein-surface interaction may interfere with the protein-enzyme interaction leading to incomplete digestion and lower fragments that were subsequently detected or the on-slide digestion procedure was not optimal for the specific polymer anchors employed. With a less basic protein, such as horse heart myoglobin (pI 7.36), the use of the anchor added the summed peptide intensities (Group 6 versus Groups 7, 8, and 9), and

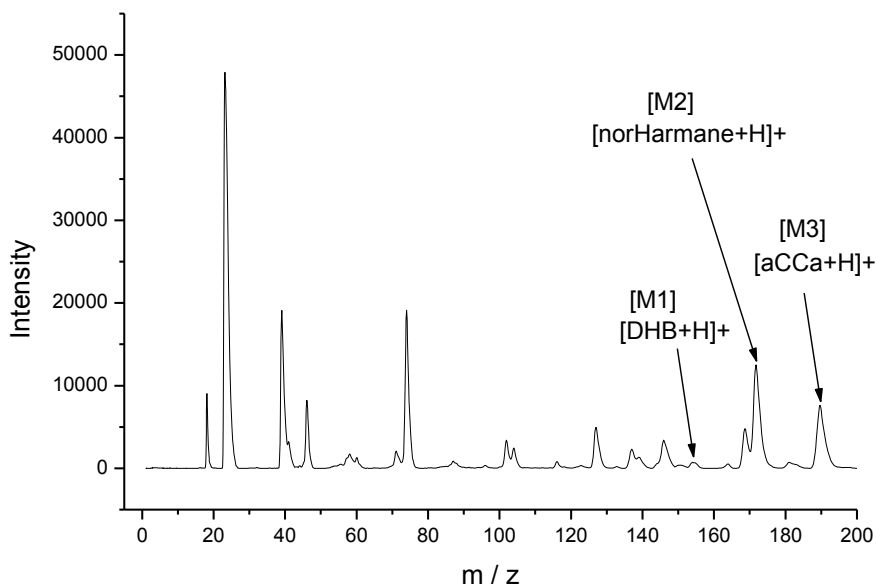


Fig. 13.4 MALDI-TOF MS in a positive-ion model using surface tailoring multi-matrix sample preparation method. The protonated molecular ion for the matrices is shown

Table 13.1 Summary of peptide ion intensities, percent error as a function of surface treatment

| Theoretical [T] | Actual [E] | Δm [T-E] | % error [$\Delta m/E \times 100\%$] | Pk. Intensity (mV) | Species |
|-----------------|------------|------------------|--|-----------------------|---|
| 155.4 | 153.4 | 2.0 | 1.3 | 3.34 | [DHB + H] ⁺ [M1] |
| 169.2 | 168.0 | 1.2 | 0.7 | 39.25 | [norharmaine + H] ⁺ [M1] |
| 190.0 | 190.0 | 0.0 | 0.0 | 49.42 | [aCCa + H] ⁺ [M3] |
| 271.7 | 275.0 | -3.3 | -1.2 | 14.89 | [Gly-Gly hydrochloride + Na] ⁺ [P1] |
| 574.0 | 576.0 | -2.0 | -0.3 | 3.49 | [Methionine Enkephalin + H] ⁺ [P2] |
| 867.7 | 860.0 | 7.7 | 0.9 | 2.79 | [[Ser(Ac)7]Demorphin + Na] ⁺ [P3] |
| 110.7 | 1110.0 | -3.0 | -0.3 | 2.60 | [Vasopressin + Na] ⁺ [P4] |
| 1358.9 | 1359.5 | -0.6 | 0.0 | 2.21 | [Angiotensin + Cu] ⁺ [P5] |
| 1620.0 | 1620.0 | 0.0 | 0.0 | 6.40 | [Bombesin + H] ⁺ [P6] |
| 1798.0 | 1798.0 | 0.0 | 0.0 | 3.31 | [Renin Substrate tetrapeptide + K] ⁺ [P7] |

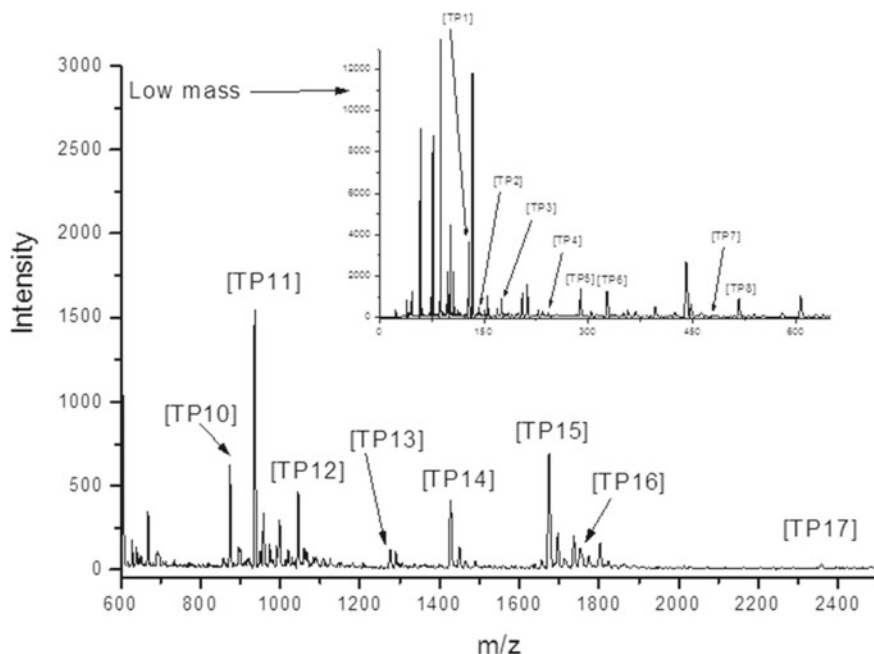


Fig. 13.5 MALDI-TOF MS in a positive-ion model using surface tailoring multi-matrix sample preparation method. The specific peptides detected are labeled from the lowest molecular mass to the highest molecular mass. The summed ion intensities of all detected peptides are compared and contrasted with an almost identical setup but without LMA-aCCa-GMA hydrophilic/hydrophobic surfaces to promote analyte solubilization. A post hoc statistical analysis indicates that the higher summed ion yield under HTML preparation conditions was statistically significant

the use of sinapinic acid as the middle lane matrix with alpha-cyano cinnamic acid as the end lane matrices also lead to a two-fold improvement in the summed peak intensities (Group 7 versus group 9). It can be seen that the summed intensities can be enhanced/degraded by the choice of matrix and choice of polymer support. To determine whether the anchor placement affected the average peak intensity of the (EWL/MYO) protein digests, additional formulations were used and are summarized in Table 13.3.

Comparison of the system with alpha-cyano cinnamic acid as the control (Group 10 versus Groups 11, 12, 13, and 14, Table 13.3) indicated that Group the choice of the matrix was critical in the sum and average peak intensities from the digest (Group 12 versus group 13, $p < 0.01$) and that use of anchor with matrices at the peripheral lanes was also statistically significant (Group 10 versus group 12, $p < 0.01$). There was no statistical significance between the other sets (Group 10 versus Group 11 and 14), indicating that including the matrix in the middle lane was essential for the high sensitivity of peptide detection. However, the signal was observed,

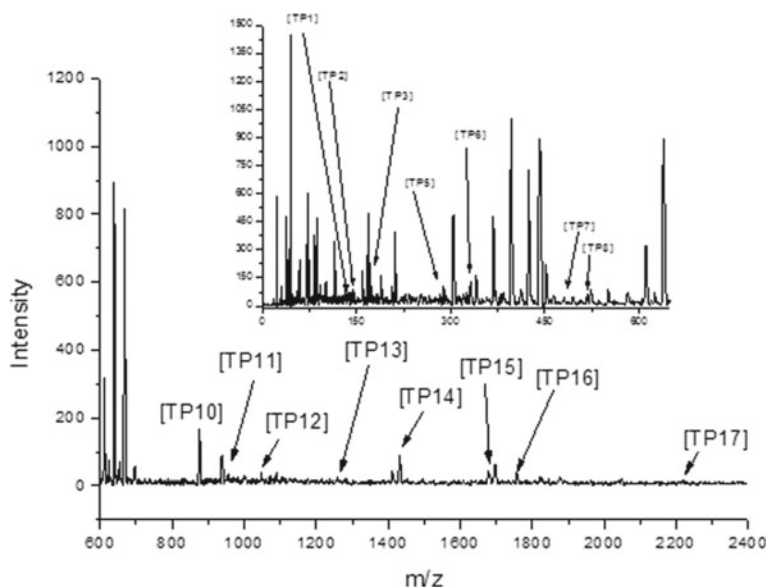


Fig. 13.6 MALDI-TOF MS in a positive-ion model using surface tailoring multi-matrix sample preparation method. The specific peptides detected are labeled from the lowest molecular mass to the highest molecular mass. The summed ion intensities of all detected peptides are compared and contrasted with an almost identical setup but without LMA-aCCa-GMA hydrophilic/hydrophobic surfaces to promote analyte solubilization. A post hoc statistical analysis indicates that the higher summed ion yield under HTML preparation conditions was statistically significant

indicating that matrices from adjacent lanes assisted them in desorption instead of laser desorption. The effect on the analyte's average peptide intensity and placement was also investigated and found to be statistically insignificant (Group 15 versus Group 16), as was the anchor placement (Group 17 versus Group 18). The effect on the analyte peak intensity of the premixing enzyme with polymer support (Group 19 and 22) or enzyme and protein (Group 21) was not statistically significant to where the layers were added separately (Group 20). Although the average peak intensities were greater with additional matrices in the peripheral lanes, this was not statistically significant (Group 20 versus Group 23) or premixing of protein and matrix (Group 24). In the latter case, the matrix may reduce the efficiency of the trypsin.

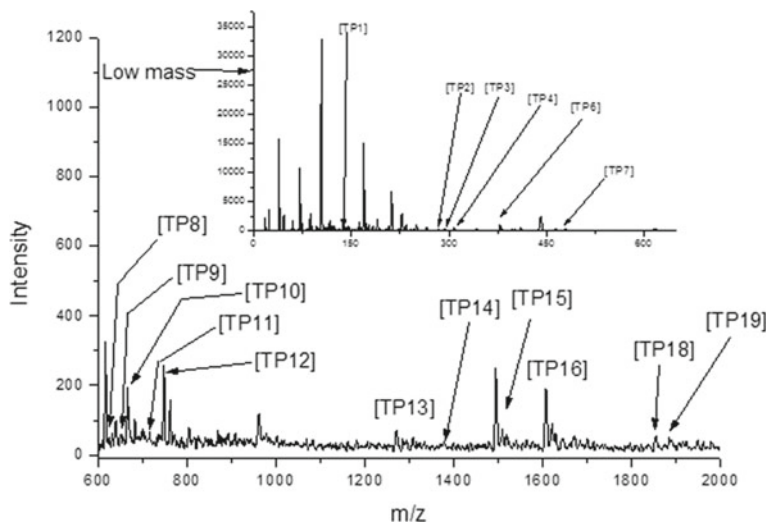


Fig. 13.7 MALDI-TOF MS in a positive-ion model using surface tailoring multi-matrix sample preparation method. The specific peptides detected are labeled from the lowest molecular mass to the highest molecular mass. The summed ion intensities of all detected peptides are compared and contrasted with an almost identical setup but without LMA-aCCa-GMA hydrophilic/hydrophobic surfaces to promote analyte solubilization. A post hoc statistical analysis indicates that the higher summed ion yield under HTML preparation conditions was statistically significant

Table 13.2 Summed ion intensities for MYO/EWL as a function of surface functionalization and use of one or multiple matrices. The protein digest was conducted on the slide or in a glass vial and oven

| Group | System | AVG | SD |
|-------|--|------|-------|
| 1 | [GMA-DHB]-[LMA-EWL]-[GMA-aCCa]-OFF | 1.63 | 1.15 |
| 2 | [GMA-aCCa]-[SS-aCCa-EWL]-[GMA-SA]-OFF | 0.63 | 0.33 |
| 3 | [GMA-aCCa]-[SS-SA-EWL]-[GMA-SA]-OFF | 0.87 | 0.92 |
| 4 | [GMA-aCCa]-[SS-EWL]-[GMA-DHB]-OFF | 2.26 | 2.34 |
| 7 | [SS]-[SS-SA-EWL]-[SS]-OFF | 1.37 | 0.99 |
| 8 | [SS-MYO]-[SS-aCCa-MYO]-[SS-MYO]-OFF | 2.81 | 2.86 |
| 9 | [SS]-[SS-aCCa-MYO]-[SS]-OFF | 4.98 | 4.87 |
| 10 | [GMA-DHB]-[LMA-aCCa-MYO]-[GMA-SA]-OFF | 5.15 | 8.59 |
| 11 | [LMA-DHB]-[SS-aCCa-MYO]-[GMA-SA]-OFF | 2.26 | 1.8 |
| 12 | [SS]-[GMA + TRYPSIN-MYO-aCCa]-[SS]-ON | 2.36 | 2.55 |
| 13 | [SS]-[GMA-TRYPSIN-MYO-aCCa]-[SS]-ON | 3.21 | 2.36 |
| 14 | [SS]-[GMA-TRYPSIN + MYO-aCCa]-[SS]-ON | 4.35 | 2.67 |
| 15 | [SS-SA]-[GMA + TRYPSIN-MYO-aCCa]-[SS-DHB]-ON | 3.24 | 2.67 |
| 16 | [SS-SA]-[GMA-TRYPSIN-MYO-aCCa]-[SS-DHB]-ON | 8.25 | 14.20 |

Table 13.3 Summed ion intensities for EWL or MYO as a function of surface functionalization and use of one or multiple matrices. The protein digest was conducted on the slide or in a glass vial and oven

| Group | Sm Pk. Int (mv) | STDEV (mv) | System (where no polymer support is used, the exposed surface was stainless steel [SS]) | | | On/Off slide digestion |
|-------|----------------------|---------------|---|-----------------------------|------------|------------------------------|
| | [P + H] ⁺ | | Left Lane | Middle Lane | Right Land | |
| 10 | 13.83 | 27.42 | [SS] | [SS-aCCa-EWL] | [SS] | OFF |
| 11 | 1.63 | 1.15 | [GMA-DHB] | [LMA-EWL] | [GMA-aCCa] | OFF |
| 12 | 0.63 | 0.33 | [GMA-aCCa] | [SS-aCCa-EWL] | [GMA-SA] | OFF |
| 13 | 0.87 | 0.92 | [GMA-aCCa] | [SS-SA-EWL] | [GMA-SA] | OFF |
| 14 | 2.26 | 2.34 | [GMA-aCCa] | [SS-EWL] | [GMA-DHB] | ON |
| 15 | 2.81 | 2.86 | [SS-MYO] | [SS-aCCa-MYO] | [SS-MYO] | OFF |
| 16 | 4.98 | 4.87 | [SS] | [SS-aCCa-MYO] | [SS] | OFF |
| 17 | 5.15 | 8.59 | [GMA-DHB] | [LMA-aCCa-MYO] | [GMA-SA] | OFF |
| 18 | 2.36 | 1.8 | [LMA-DHB] | [SS-aCCa-MYO] | [LMA-SA] | OFF |
| 19 | 2.36 | 2.55 | [SS] | [GMA + TRYPSIN-MYO-aCCa] | [SS] | ON |
| 20 | 3.21 | 2.36 | [SS] | [GMA-TRYPSIN-MYO-aCCa] | [SS] | ON |
| 21 | 4.35 | 4.26 | [SS] | [GMA-TRYPSIN + MYO-aCCa] | [SS] | ON |
| 22 | 3.24 | 2.67 | [SS-SA] | [GMA + TRYPSIN-MYO-aCCa] | [SS-DHB] | ON |
| 23 | 8.25 | 14.2 | [SS-SA] | [GMA-TRYPSIN-MYO-aCCa] | [SS-DHB] | ON |
| 24 | 2.49 | 2.47 | [SS-SA] | [GMA-TRYPSIN-MYO + aCCa] | [SS-DHB] | ON |

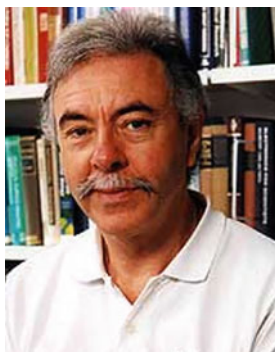
13.4 Conclusion

The use of solid anchors to aid in sample cleanup and digestion has been shown to improve the signal intensity of digests. In our study, this was also confirmed. However, the results were partly dependent upon the protein's basicity. The more basic lysozyme gave the highest sum peptide intensities under the dried drop methods, whereas the less basic myoglobin gave the highest sum intensities with anchor support. Using the matrix species in the middle lane was critical to optimizing analyte peak intensities, although using matrices in peripheral lanes did lead to signal enhancements. However, these enhancements were not statistically significant ($P < 0.05$). The use of on-slide digestion versus off-slide digestion, order of addition of enzyme (with polymer support, with the analyte, or separately) was also investigated. Similar results indicated that the order was not critical to high peptide intensities. However, the addition of the enzyme to the polymer support or co-addition with matrices led to lower signal intensities for the protein digests, indicating that the efficiency of the enzyme digests was compromised due to these additives. Therefore the optimal procedure is the addition of the components individually to the central lane

with alpha-cyano cinnamic acid as the main matrix species. No polymer peaks were observed, indicating that the layer was stable and did not cause interference with the matrix species. Also, matrices from the adjacent lanes were observed, indicating that the laser pulse could be used to desorb matrices without allowing them to mix in solution.

Abbreviations: 2,5-DHB, 2–5-Dihydroxybenzoic acid; ABC, Ammonium bicarbonate; aCCa, α -cyano-4-hydroxycinnamic acid; CLASSIC, Dried-drop sample deposition method; EWL, Egg white lysozyme; GMA, glycerol mono-methacrylate; HTML, hydrophobic and hydrophilic tailored anchors; LMA, lauryl methacrylate; MALDI, matrix-assisted laser desorption/ionization; MS, Mass Spectrometry; MYO, myoglobin protein; NT, No treatment; OFF, Off-slide protein digestion; ON, On-slide protein digestion; PGmix, “Phil Green” peptide mixture; SA, sinapinic acid; TFA, trifluoroacetic acid; TOF, time-of-flight.

Acknowledgments SB would like to thank Drs. I. Herbert and J. Horsler (Accordis, U.K) for access to the Bruker Biflex. The Department of Physics for access to the scanning electron microscope (Warwick University), and Dr. A.E. Giannakopoulos (Warwick University) for their helpful suggestions concerning the manuscript. SB would also like to acknowledge financial support from the Engineering and Physical Sciences Research Council (EPSRC), Akzo Noble, and the Robert A. Welch Foundation Departmental Grant (AC006). LL would like to thank the Petroleum Research Fund of the American Chemical Society (53,827-UR10).



Author Contribution Dr. Peter Derrick conceived the research idea and access to the laboratory and supplies. SB undertook all the experimental research, JL verified the data and suggested the ‘temperature at surface’ desorption mechanism.

Conflict of Interest The authors have no conflict of interest with the editorial staff, publishers, or funding agencies supporting this research.

References

1. McEwen CN, Simonsick WJ, Larsen BS, Ute K, Hatada K (1995) The fundamentals of applying electrospray ionization mass spectrometry to low-mass poly (methyl methacrylate) polymers. *J Am Soc Mass Spectrom* 6(10):906–911
2. Nielen MW (1999) MALDI time-of-flight mass spectrometry of synthetic polymers. *Mass Spectrom Rev* 18(5):309–344
3. Beavis RC, Chait BT (1990) High-accuracy molecular mass determination of proteins using matrix-assisted laser desorption mass spectrometry. *Anal Chem* 62(17):1836–1840
4. Hillenkamp F, Karas M (1990) Mass spectrometry of peptides and proteins by matrix-assisted ultraviolet laser desorption/ionization. *Methods Enzymol* 193:280–295
5. Huberty MC, Vath JE, Yu W, Martin SA (1993) Site-specific carbohydrate identification in recombinant proteins using MALD-TOF MS. *Anal Chem* 65(20):2791–2800
6. Harvey DJ (1999) Matrix-assisted laser desorption/ionization mass spectrometry of carbohydrates. *Mass Spectrom Rev* 18(6):349–450
7. Tang K, Allman SL, Chen CH (1992) Mass spectrometry of laser-desorbed oligonucleotides. *Rapid Commun Mass Spectrom* 6(6):365–368
8. Karas M, Hillenkamp F (1988) Laser desorption ionization of proteins with molecular masses exceeding 10,000 daltons. *Anal Chem* 60(20):2299–2301
9. Zenobi R, Knochenmuss R (1998) Ion formation in MALDI mass spectrometry. *Mass Spectrom Rev* 17(5):337–366
10. Ehring H, Karas M, Hillenkamp F (1992) Role of photoionization and photochemistry in ionization processes of organic molecules and relevance for matrix-assisted laser desorption ionization mass spectrometry. *J Mass Spectrom* 27(4):472–480
11. Beavis RC, Chaudhary T, Chait BT (1992) α -Cyano-4-hydroxycinnamic acid as a matrix for matrix-assisted laser desorption mass spectrometry. *J Mass Spectrom* 27(2):156–158
12. Gimon ME, Preston LM, Solouki T, White MA, Russell DH (1992) Are proton transfer reactions of excited states involved in UV laser desorption ionization?. *J Mass Spectrom* 27(7):827–830
13. Knochenmuss R (2006) Ion formation mechanisms in UV-MALDI. *Analyst* 131(9):966–986
14. Tanaka K, Waki H, Ido Y, Akita S, Yoshida Y, Yoshida T, Matsuo T (1988) Protein and polymer analyses up to m/z 100 000 by laser ionization time-of-flight mass spectrometry. *Rapid Commun Mass Spectrom* 2(8):151–153
15. Strupat K, Karas M, Hillenkamp F (1991) 2, 5-Dihydroxybenzoic acid: a new matrix for laser desorption—ionization mass spectrometry. *Int J Mass Spect Ion Proces* 111:89–102
16. Karas M, Ehring H, Nordhoff E, Stahl B, Strupat K, Hillenkamp F, Krebs B et al (1993) Matrix-assisted laser desorption/ionization mass spectrometry with additives to 2, 5-dihydroxybenzoic acid. *J Mass Spectrom* 28(12):1476–1481
17. Karas M, Krüger R (2003) Ion formation in MALDI: the cluster ionization mechanism. *Chem Rev* 103(2):427–440
18. Xu N, Huang ZH, Watson JT, Gage DA (1997) Mercaptobenzothiazoles: a new class of matrices for laser desorption ionization mass spectrometry. *J Am Soc Mass Spectrom* 8(2):116–124
19. Nonami H, Tanaka K, Fukuyama Y, Erra-Balsells R (1998) β -Carboline alkaloids as matrices for UV-matrix-assisted laser desorption/ionization time-of-flight mass spectrometry in positive and negative ion modes. analysis of proteins of high molecular mass and of cyclic and acyclic oligosaccharides. *Rapid Comm Mass Spect* 12(6):285–296
20. Juhasz P, Costello CE (1992) Matrix-assisted laser desorption ionization time-of-flight mass spectrometry of underivatized and permethylated gangliosides. *J Am Soc Mass Spectrom* 3(8):785–796
21. Bartlett MG, Busch KL, Wells CA, Schey KL (1996) Use of 2-hydroxy-1-naphthoic acid as a matrix for matrix-assisted laser desorption/ionization mass spectrometry of low molecular weight porphyrins and peptides. *J Mass Spectrom* 31(3):275–279
22. Tang X, Vertes A, Dreifuss PA (1995) New matrices and accelerating voltage effects in matrix-assisted laser desorption/ionization of synthetic polymers. *Rapid Commun Mass Spectrom* 9(12):1141–1147

23. Montaudo G, Montaudo MS, Puglisi C, Samperi F, Daolio S (1994) 2-(4-hydroxyphenylazo)-benzoic acid: A solid matrix for matrix-assisted laser desorption/ionization of polystyrene. *Rapid Commun Mass Spectrom* 8(12):1011–1015
24. Donny Liu HM, Schlunegger UP (1996) Matrix-assisted laser desorption/ionization of synthetic polymers with Azo compound matrices. *Rapid Commun Mass Spectrom* 10(5):483–489
25. Jaskolla TW, Lehmann WD, Karas M (2008) 4-Chloro- α -cyano cinnamic acid is an advanced, rationally designed MALDI matrix. *Proc Natl Acad Sci* 105(34):12200–12205
26. Glückmann M, Pfenninger A, Krüger R, Thierolf M, Karasa M, Horneffer V, Strupat K et al (2001) Mechanisms in MALDI analysis: surface interaction or incorporation of analytes? *Int J Mass Spectrom* 210:121–132
27. Fournier I, Brunot A, Tabet JC, Bolbach G (2005) Delayed extraction experiments using a repulsing potential before ion extraction: evidence of non-covalent clusters as ion precursor in UV matrix-assisted laser desorption/ionization. Part II—Dynamic effects with α -cyano-4-hydroxycinnamic acid matrix. *J Mass Spect* 40(1):50–59
28. Bashir S, Derrick PJ, Mutter R (2004) Parameterizing matrix-assisted laser desorption/ionization (MALDI): effect of solvents and co-additives on analyte peak intensities. *Eur J Mass Spectrom* 10(4):487–493
29. Jaskolla TW, Karas M (2011) Compelling evidence for a lucky survivor and gas phase protonation: the unified MALDI analyte protonation mechanism. *J Am Soc Mass Spectrom* 22(6):976–988
30. Giannakopoulos AE, Bashir S, Derrick PJ (1998) Comment: Reproducibility of spectra and threshold fluence in matrix-assisted laser desorption/ionization (MALDI) of polymers. *Eur Mass Spectrom* 4(2):127–131
31. Breaux GA, Green-Church KB, France A, Limbach PA (2000) Surfactant-aided, matrix-assisted laser desorption/ionization mass spectrometry of hydrophobic and hydrophilic peptides. *Anal Chem* 72(6):1169–1174
32. Schuereberg M, Luebbert C, Eickhoff H, Kalkum M, Lehrach H, Nordhoff E (2000) Prestructured MALDI-MS sample supports. *Anal Chem* 72(15):3436–3442
33. Redeby T, Roeraade JE (2004) A simple fabrication of a structured matrix-assisted laser desorption/ionization target coating for increased sensitivity in mass spectrometric analysis of membrane proteins. *Rapid Commun Mass Spectrom* 18(10):1161–1166
34. Preston LM, Murray KK, Russell DH (1993) Reproducibility and quantization of matrix-assisted laser desorption ionization mass spectrometry: effects of nitrocellulose on peptide ion yields. *Biol Mass Spectrom* 22(9):544–550
35. Brockman AH, Dodd BS, Orlando RA (1997) desalting approach for MALDI-MS using on-probe hydrophobic self-assembled monolayers. *Anal Chem* 69(22):4716–4720
36. Miliotis T, Marko-Varga G, Nilsson J, Laurell T (2001) Development of silicon microstructures and thin-film MALDI target plates for automated proteomics sample identifications. *J Neurosci Methods* 109(1):41–46
37. Stensballe A, Andersen S, Jensen ON (2001) Characterization of phosphoproteins from electrophoretic gels by nanoscale Fe(III) affinity chromatography with off-line mass spectrometry analysis. *Proteomics* 1(2):207–222
38. Xu S, Li Y, Zou H, Qiu J, Guo Z, Guo B (2003) Carbon nanotubes as an assisted matrix for laser desorption/ionization time-of-flight mass spectrometry. *Anal Chem* 75(22):6191–6195
39. Leize EM, Leize EJ, Leize MC, Voegel JC, Dorsselaer A (1999) Matrix-assisted laser desorption ionization mass spectrometry: a new tool for probing interactions between proteins and metal surfaces. Use in dental implantology. *Anal Biochem* 272(1):19–25
40. Teng CH, Ho KC, Lin YS, Chen YC (2004) Gold nanoparticles as selective and concentrating probes for samples in MALDI MS analysis. *Anal Chem* 76(15):4337–4342
41. Hilton A, Armstrong RA (2006) Statnote 6: *post-hoc* ANOVA tests. *Microbiol*, 34–36. <https://publications.aston.ac.uk/id/eprint/39919/>
42. Tauer K, Ali AI, Yildiz U, Sedlak M (2005) On the role of hydrophilicity and hydrophobicity in aqueous heterophase polymerization. *Polymer* 46(4):1003–1015

43. Save M, Weaver JVM, Armes SP, McKenna P (2002) Atom transfer radical polymerization of hydroxy-functional methacrylates at ambient temperature: comparison of glycerol monomethacrylate with 2-hydroxypropyl methacrylate. *Macromolecules* 35(4):1152–1159
44. Haddleton DM, Waterson C, Derrick PJ, Jasieczek CB, Shooter AJ (1997) Monohydroxy terminally functionalized poly (methyl methacrylate) from atom transfer radical polymerization. *Chem Commun* 7:683–684
45. Jacobs A, Dahlman O (2001) Enhancement of the quality of MALDI mass spectra of highly acidic oligosaccharides by using a Nafion-coated probe. *Anal Chem* 73(3):405–410
46. Landry F, Lombardo CR, Smith JW (2000) A method for application of samples to matrix-assisted laser desorption ionization time-of-flight targets that enhances peptide detection. *Anal Biochem* 279(1):1–8

Chapter 14

Achievements Made by Professionals with Diversified Backgrounds



Marinda Li Wu, Wei Gao, Chu-An Chang, Lei Li, Yingchun Lu,
and Jingbo Louise Liu

14.1 Introduction

The Chinese American Chemical Society (CACS) was founded in 1981 as a nonprofit, professional organization with no political affiliation. The CACS aims to bridge chemistry & chemical engineering communities in Asia and America. The membership is open to professionals and students in chemistry, chemical engineering, and related fields, individuals and corporations supporting the objectives of the society. In 2023, the CACS renewed the ACS-CACS partnership for 2023–2028 since established in 2016.

Currently, the society is composed of 4 major local chapters in North America (East, Great Lakes, Southwest, and Northern California Chapter). The new executive committee reflects the inclusion, dynamics, and accessibility, including retirees, well-established professionals, and junior rising stars (Fig. 14.1). The leadership has been

M. L. Wu · C.-A. Chang

Chinese American Chemical Society and American Chemical Society, 18427 Clifton Way, Castro Valley, CA 94546, USA

W. Gao

Corporate Research and Development, Dow Inc, Collegetown, PA 19034, USA

L. Li

Chemical/Petroleum Engineering, University of Pittsburgh, 3700 O'Hara Street, Pittsburgh, PA 15261, USA

Y. Lu

Atomwise, 717 Market Street, Suite 800, San Francisco, CA 94103, USA

J. L. Liu (✉)

Chinese American Chemical Society, South Brunswick, New Jersey 08824, USA

e-mail: jingbo.liu@tamuk.edu

The Texas A&M Energy Institute, Frederick E. Giesecke Engineering Research Bldg., 3372 TAMU, College Station, TX 77843, USA

overseen by Dr. Marinda Li Wu (Board Chair and President of Northern California Chapter local chapter), Past President ACS, Dow Chemical (retired) and Dr. Chu-An Chang (Treasurer), ThermoFisher Scientific (retired). The well-established scientist, engineer and professors are Dr. Yingchun Lu, a senior researcher (Immediate Past President); Dr. Wei Gao, R&D/TS&D Fellow, Analytical Sciences, Core R&D, Dow Inc., Dr. Lin Zhou (First Vice President), the FCC Technology Leader at Honeywell UOP; and Dr. J. Louise Liu (Standing President of CACS), Professor of Chemistry at Texas A&M University-Kingsville and Energy Institute. Drs. Gao, Liu, and Wu have been certified Career Consultants of the American Chemical Society to provide guidance and suggestions for students and young professionals during their career development. The junior team members include Dr. Yunlong Zhang (Second Vice President), staff scientist at ExxonMobil; Xiaozhou (John) Zhang (President of East chapter), Scientist at ExxonMobil; Mengmeng Li (President of Southwest Chapter), R&D Manager, at Dow Inc.; Shuai Tan (President of Great Lakes Chapter) Lead R&D Engineer/Scientist in Honeywell UOP; and Huping Luo (President-Elect of Northern California Chapter), senior research engineer at Chevron.



Fig. 14.1 The 2023 Leadership team, **a** The standing presidents and president-elect of four local chapters (from left to right: Xiaozhou Zhang, Mengmeng Li, Shuai Tan and Huping Luo, President-elect), **b** The senior officers (from left to right: Marinda Li Wu, Chu-An Chang, and Wei Gao), and **c**. The CACS national officers (from left to right: Yingchun Jasmine Lu (2022 President), Ling Zhou (1st VP), Yunlong Zhang (2nd VP) and Jingbo Louise Liu (2023 President))

The CACS hosted a series of invited talks, given by distinguished professors from tier 1 institutions in concurrence with ACS and AIChE National meetings (Fig. 14.2). The speakers addressed the leading-edge research activities to showcase their expertise and empower the future generations to remain in the STEM fields.

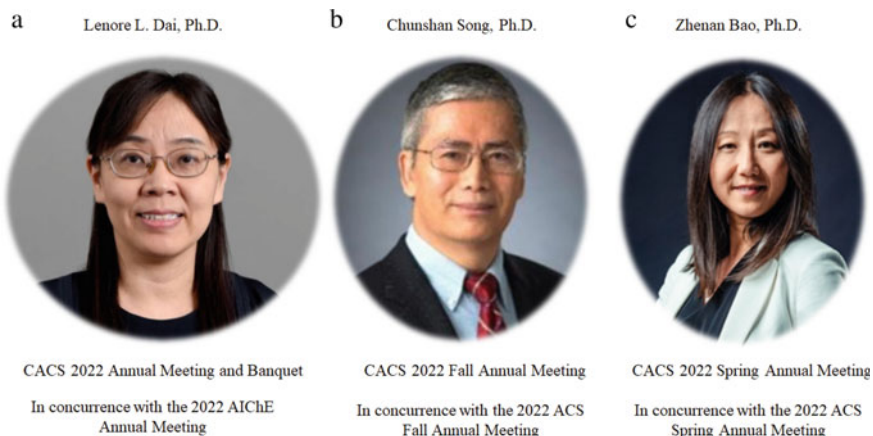


Fig. 14.2 The CACS keynote speeches, **a** Dr. Lenore Dai, the keynote speaker at the AIChE National Meeting, **b** Dr. Chunshan Song, the keynote speaker at the American Chemical Society (Spring 2022), and **c** Dr. Zhenan Bao, the keynote speaker at the American Chemical Society (Spring 2021)



Fig. 14.3 The Women panel discussion, **a**. Seven panelists who shared their experience and future plans during discussion based on the above questions and **b**. CACS officers to facilitate the event, give opening and closing remarks

Dr. Lenore Dai is a professor of chemical engineering and the director of the School for Engineering of Matter, Transport and Energy at Arizona State University (ASU). She presented “Soft Materials: from Fundamentals to Applications” (Fig. 14.2a). She pointed out that “the Soft materials are ubiquitous in natural and industrial processes”. In the presentation, she elaborated on three groups of less explored soft materials: Pickering emulsions, mechanophore incorporated polymers, and ionic liquid-based electrolytes.

Dr. Chunshan Song is Wei Lun Professor of Chemistry and Dean of Science at the Chinese University of Hong Kong, and Distinguished Professor Emeritus in Fuel Science and Chemical Engineering at the Pennsylvania State University since July 2020. He presented a talk on “CO₂ Capture and Conversion to Carbon-Neutral Chemicals and Fuels (Fig. 14.2b).” He indicated that the capturing of CO₂ from flue gases and converting CO₂ using H₂ produced from H₂O with renewable energy into carbon-neutral chemicals, materials, and fuels, is an important path for sustainable development. He also provided new design approaches to CO₂ capture/separation and catalytic CO₂ conversion to chemicals and fuels.

Dr. Zhenan Bao is Department Chair and K.K. Lee Professor of Chemical Engineering, and by courtesy, a Professor of Chemistry and a Professor of Material Science and Engineering at Stanford University. She presented her achievements on “Skin-inspired organic electronics (Fig. 14.2c).” She emphasized that the team has developed “materials design concepts to add skin-like functions to organic electronic materials without compromising their electronic properties. These new materials and new devices enable a range of new applications in medical devices, robotics and wearable electronics.”

On March 30, 2023, the CACS hosted a Women Panel Discussion to celebrate the Month of Women History. Seven professionals from senior to mid-career and to junior levels were invited to serve as the panelists (Fig. 14.3a). The panelists shared their insights on the nine topics. Three CACS officers also actively participated in this discussion (Fig. 14.3b). Dr. Lu facilitated the discussion where Dr. Wu gave the opening remarks and Dr. Zhou closed this event, pointing out that “Women hold up half of the sky”.

The following topics were addressed by the panelists:

1. What are the sweet spots for you to pursue during your career within chemical sciences and beyond?
2. What are the key skill development areas for you to advance your career?
3. What are your future priorities as a chemical science professional (researcher, scientists, professor and other professionals)?
4. What are your achievements which encourage you to move forward?
5. When you encounter barriers (difficult time periods), what are your responses, and how do you overcome these difficulties?
6. What are your strategies to balance career and life as female professionals?
7. What are your experiences in the DEIR (Diversity, Equity, Inclusivity, Respect) perspectives?

8. Who are the people who protect you the most (close your eyes for 1 min and think about)?
9. Do you have any other thoughts on enhancing women advancement?

Dr. Jasmine (Yingchun) Lu holds a BS degree in Chemistry from Peking University, an MS from Southern Methodist University, and a Ph.D. in Organic Chemistry from Dartmouth College. She is currently a Senior Director at WuXi Biologics and has been the Senior Alliance Manager at Atomwise, a preclinical pharma company revolutionizing how drugs are discovered with AI. Prior to joining Atomwise in 2021, she worked for the US Innovation Center of Shimadzu, a top-five global instrumentation company, and AcceleDev, a US-Sino CDMO company, as the Director of Project Management. Her earlier careers included as a Senior Medicinal Chemist in Morphochem and Pharmacopeia Drug Discovery, focusing on drug discovery for oncology and immune suppressants projects. Jasmine is a life member of the Chinese American Chemical Society (CACCS). She has served on the Board of its Tri-State Chapter since 2012 and was the Chair of 2019. She joined the American Chemical Society (ACS) in 1994 and has served as an Alternate-Councilor in ACS North Jersey Chapter. She has also served on the Board of NJACS Mass Spectrometry Discussion Group and was the Chair of 2017.



Dr. Qiong Yuan received a B.S degree from Wuhan University on Organic Chemistry and a Ph.D. from Shanghai Institute of Organic Chemistry (SIOC), Chinese Academic of Sciences. She actively promotes Asian culture and heritage and lead several organizations including Alliance of Chinese Alumni (ACA, Vice President), Chinese American Chemical Society (CACCS, Board Director) and Columbus Asian Festival Corporation (AFC, Board Director). Currently, she serves as the director of CAS Innovation (CAS is a division of ACS). Dr. Yuan currently works in its Innovation Division and focuses on developing transformative scientific information solutions to help customers accelerate breakthroughs. Since joined CAS in 1999, she served the organization through variety roles in Product Management, Sales,

Research and SciFinder Product Development. She has been working collaboratively with ACS other Divisions (Publications, Membership, etc.) to promote ACS Core Values and execute ACS globalization initiative in Asia.



Dr. Wang received her Ph.D. from Peking Union Medical College & Chinese Academy of Medical Sciences, and B.S. from Peking University, Beijing, China (B.S). She worked as a Postdoctoral Fellow at Emory University, Atlanta, GA, 1998.2–2000.10. She served as the VP and CSO of BeiGene Startup Factory, BeiGene Innovation Center, Guangzhou, since 2021. She acted as the Senior Vice President & Co-founder, Acerand Therapeutics, in Indianapolis & Shanghai from 2020.4 to 2021.11. She also served as the Program Team Leader, Project Management, Business Transformation Advisor; Director, Eli Lilly & Company from 2000.10 to 2020.4. Dr. Wang has enriched experiences in industry as the Founder & Head of Chemistry and Director, China Chemistry, Lilly China R&D Center, Shanghai, China 2009.5–2015.6. She is the Progress from Research Scientist, Principal Scientist, and Research Advisor to head of chemistry, in Lilly Corporate Center, Indianapolis, IN from 2000.10 to 2009.5.



Prof. Dongling Ma (FRSC, FIAAM), holder of the Canada Research Chair (Tier 1) in Advanced Functional Nanocomposites, has been a professor at Institut national de la recherche scientifique (INRS) since 2006. Her main research interest consists in the development of various nanomaterials (e.g., semiconductor quantum dots, transition metal catalytic nanoparticles, plasmonic nanostructures) and different types of nanohybrids for applications in energy, environment, catalysis and biomedical sectors. She has co-authored > 170 articles in a broad range of areas, centered on materials science, in selective, high-impact journals such as *J. Am. Chem. Soc.*, *Nat. Commun.*, *Adv. Mater.*, *Adv. Energy Mater.*, *ACS Nano*, *Adv. Funct. Mater.*, *Energy Environ. Sci.*, *Chem. Mater.* and *Chem. Soc. Rev.* with a H-index of 61 (Google Scholar). She has co-authored 4 granted patents and 4 book chapters. She has delivered > 120 invited speeches at international conferences and prestigious universities/government laboratories. She is an associate editor of *ACS Applied Nano Materials* and also serves/served on multiple journal editorial advisory boards, including the prestigious *ACS Energy Lett.*, *Scientific Reports* (Springer-Nature), *Frontiers (Energy)*, *PhotonX* (Springer), etc. She also acted as the section Editor-in-Chief for the section “Solar Energy and Solar Cells” of *Nanomaterials*, and acts in Section Editor Group of National Science Review (NSR, Materials Science). Her recent awards include the 2022 Clara Benson Award from the Chemical Institute of Canada.



Dr. Lu obtained her PhD in analytical chemistry from the University of Pittsburgh and BS in chemistry from Nanjing University. She has authored over 15 high-impact journal publications with more than 300 citations. She is serving as an expert reviewer for over 10 prestigious journals in the field of analytical chemistry and pharmaceutical science. Dr. Dujuan Lu is the Manager/Global Leader-E&L, SGS. Dr. Lu serves as the manager for the extractables and leachables (E&L) team at the SGS Health Science Fairfield New Jersey facility as well as the global leader amongst the global E&L centers of excellence. Before joining SGS, she worked at Fresenius Kabi as a research scientist, leading E&L projects to support transfusion and infusion medical device and parenteral products. She has extensive CRO and pharmaceutical/medical device industry experience with more than 700 E&L projects on a broad range of

packaging systems, including process materials, pharmaceutical finished packaging, and medical devices. As a subject matter expert in the E&L field, she is frequently presenting at various conferences as invited speakers and technical session chairs. She was named one of the top 60 most influential people working in the pharmaceutical industry in the Medicine Maker's 2020 power list.



Dr. Mi Shen received her Ph.D. in Chemistry, The University of Texas at Austin. She is an Assistant Professor, Department of Chemistry, Neuroscience Program, Department of Bioengineering, Center for Biophysics and Quantitative Biology, Beckman Institute for Advanced Science and Technology, University of Illinois at Urbana-Champaign. Her research covers a wide spectrum, Impact of environmental pollutants on the gut-brain-axis and on the brain activities, Harnessing the microbiome to combat the neurotoxicity of organic mercury, Synaptic neurotransmitter release dynamics in real time, In vivo monitoring of chemical transmission activities of behaving rodents, Alzheimer's diseases and Parkinson's diseases. She received dozens of award and honors, such as, 2019–2024 NSF CAREER Award, 2021 ACS Arthur F. Fondeis Award for Achievements by a Young Analytical Scientist, 2021–2022 Scialog: Microbiome, Neurobiology and Disease Collaborative Award and Rising Star Award from CACS.



Dr. Mengmeng Li received her Ph.D. in Chemical & Biomolecular Engineering, University of Houston in 2017. She is the R&D Manager, Freeport, Texas. She has rich experiences in industry, Associate Research Scientist, Dow Inc, Lake Jackson, Texas; Project and platform lead for ACCLAIM™ K-100, UCAT™ B and UCAT™ G technologies. Expertise in heterogenous catalyst discovery, scale up and implementation. She has been managing a pilot scale lab including talent development, lab capability expansion and safety. She also in charge of implementing data visualization and digitalization tools for catalyst batch reactors. Dr. Li worked as an Engineer in Volvo Group Truck Technology, Hagerstown, Maryland. She took different responsibilities, including “Developed multi-scaled global kinetic and reactor models of heavy-duty EATS, integrated EATS model into virtual powertrain simulation application developed a user-friendly graphic user interface (GUI) for EATS model, and studied heterogenous catalyst deactivation process and mitigating field degradation issues”.



Professor Xuan Wang is an instructional associate professor at Texas A&M Higher Education at McAllen, where she holds appointments in the College of Science at Texas A&M University. Her academic training includes undergraduate study at Oklahoma Christian University (B.S., 2011) and graduate study under the direction of Professor Hong-Cai Zhou at Texas A&M University (Ph.D., 2016). Her research interests include synthesizing and developing metal–organic frameworks and porous coordination polymers for chemical sensing and their application in the environmental science field. After graduation, she began an academic career as a visiting assistant professor at Colorado State University–Pueblo.



Dr. Ling Zhou is currently a Principal Engineer and FCC Technology Leader at Honeywell UOP in Des Plaines, Illinois. He is responsible for the strategic development of FCC technology roadmap, innovation in refinery process/catalyst, new product introduction, and breakthrough initiatives. Prior to taking this role, Ling was a Principal Engineer in the Manufacturing & Product Technology group responsible for catalyst development and scale-up. Before joining Honeywell UOP in 2014, Ling worked as a core technology team leader in a startup company KiOR in Houston, Texas, which has been developing and commercializing a catalytic pyrolysis process to convert biomass to biofuel in a proprietary fluidized-bed reactor system since 2009.

Ling received his master's degree in chemical engineering from the University of Petroleum in Beijing in 2001, and his PhD degree in Physical Chemistry and Electrochemistry from the University of Hannover, in Germany in 2005. He also had a four-year research and development experience at Harvard University, School of Engineering and Applied Sciences (2005–2009). In 2014, Ling joined the executive committee of the Great Lake Chinese American Chemical Society (GLCACS) and has actively served for the society since then. In 2021, Ling was appointed as the GLCACS President. He rebuilt the executive committee and reactivated the social activities which were forced to stop in 2020 due to COVID-19 pandemic. After a successful Annual Conference held in 2022, Ling and the executive committee reinstalled the new student committee, established an extended industrial sponsorship, in order to set a good foundation for strengthening the society influence in the future.



The CACS organized a symposium, Crossroads of polymer, composite and sustainable energy in collaboration with POLY and ENFL to promote Energy materials in the 2023 Spring National Meeting. During this national meeting, there are 82 recipients of awards administered by the American Chemical Society for 2023. Among these awardees, seven Chinese-originated professionals received the national recognition from ACS. With the exception of the Arthur C. Cope Scholars, recipients will be honored at the awards ceremony on Tuesday, March 28, 2023, in conjunction with the ACS Spring 2023 meeting in Indianapolis. The CACS leaders, members and friends received recognitions due to their leadership roles, innovation and contribution to fields and communities.

A retired scientist from Dow Chemical Company and former President of the American Chemical Society, Dr. Marinda Li Wu was named one of the 2023 Distinguished Women in Chemistry or Chemical Engineering by the International Union of Pure and Applied Chemistry (IUPAC). A ceremony will be held to recognize the honorees for their leadership and community service in August during the IUPAC World Chemistry Congress in Hague, Netherlands. Dr. Wu was one of 12 women to receive this honor, including two in the United States and three Chinese-originated female professionals. These distinguished women are Lidia Armelao, National Research Council and University of Padova, Italy; Annette G. Beck-Sickinger, Leipzig University, Germany; Chunying Chen, National Center for Nanoscience and Technology of China; Bin Liu, National University of Singapore, Singapore; Laura McConnell, Bayer U.S., Crop Science Division, USA; Marcia Foster Mesko, Federal University of Pelotas, Brazil; Jyotirmayee Mohanty, Bhabha Atomic Research Centre, Mumbai, India; Tatjana Parac-Vogt, Katholieke Universiteit Leuven, Belgium; Gill Reid, University of Southampton, UK; Mikiko Sodeoka, RIKEN, Japan; Nguyễn Thị Kim Thanh, University College London, UK; and Marinda Wu, Dow, USA. Awardees will be honored at the 2023 IUPAC World Chemistry Congress in The Hague, The Netherlands. Dr. Wu was recently elected as one of three 2023 Fellows for the Federation of Asian Chemical Societies (FACS).



Dr. Huainan (H.N.) Cheng received two distinguished awards (1) Spencer Award, ACS Divisions AGRO, AGFD plus the local ACS KC Section and (2) Charles H. Herty 2022, Georgia Section. Dr. Cheng received his Ph.D. degree, Department of Chemistry, University of Illinois, Urbana-Champaign, Illinois. Over 300 publications, 26 patent publications and edited 23 books. As he stated, “over the years I have enjoyed working with colleagues, friends, teachers, and students in the global chemistry enterprise. I am proud of being a chemist, and proud to be an ACS member. Despite the pandemic in the past three years, I have been working hard, together with ACS colleagues and staff, to enhance our profession and benefit our members.” His Presidential platform has been “Growth, Collaboration, and Advocacy” (C&EN Comment, 12/7/2020). In a highly competitive world, growth is desirable and necessary. Some of the ways we can help grow the chemistry enterprise include: (1) Innovation and disciplinary growth, (2) Industrial engagement and entrepreneurship, (3) International collaborations, and (4) Advocacy for public and government support of scientific research.”



Liang-Shih Fan received the Warren K. Lewis Award for Chemical Engineering Education and he will be honored at the 2023 AIChE Annual meeting in Orlando on November 5–10, 2023. **L.-S. Fan** is Distinguished University Professor and C. John Easton Professor in Engineering in the Department of Chemical and Biomolecular Engineering at The Ohio State University. His research fields are in particle technology and multiphase reaction engineering. He is an inventor of eight clean fossil energy conversion processes including OSCAR, CARBONOX, pH Swing, Calcium Looping, Hydrogen Looping, Syngas Looping, Coal-Direct Chemical Looping and SULGEN Processes for CO₂, SO₂, and NO_x emission control and electricity, syngas, hydrogen, chemicals or liquid fuels production. He has also invented the commercially used electrical capacitance volume tomography for three-dimensional multiphase flow imaging. Professor Fan is the Editor-in-Chief of Powder Technology and has authored or co-authored 460 journal papers, 60 patents, and six books including the most recent textbook (2021) “Dynamics of Multiphase Flows” by Cambridge University Press. He was named as one of the “One Hundred Engineers in the Modern Era” by the AIChE in its centennial celebration in 2008. Dr. Fan is a member of the U. S. National Academy of Engineering, Academician of the Academia Sinica, National Academy of Inventors, and a Foreign Member of the Chinese Academy of Engineering, the Australia Academy of Technology and Engineering (ASTE), the Indian National Academy of Engineering, & the Mexican Academy of Sciences.



Elsevier and the Board of Executive Editors of Elsevier’s Tetrahedron journal series are pleased to announce that the 2022 Tetrahedron Prize for Creativity in Organic Synthesis has been awarded to Professor Chi-Huey Wong, Scripps Family Chair Professor of Chemistry at Scripps Research and Distinguished Professor at Genomics Research Center, Academia Sinica. Wong is well-known for Chemoenzymatic and programmable synthesis of oligosaccharides and glycoproteins, elucidation of glycosylation effect on protein folding and function, and development of glycan microarrays, universal vaccines and homogeneous antibodies against influenza, SARS-CoV-2, and cancer. Chi-Huey Wong is the Scripps Family Chair Professor, Department of Chemistry, The Scripps Research Institute. He received his

B.S. (1970) and M.S. (1977) degrees (with KT Wang) from National Taiwan University, and Ph.D. (1982) in Chemistry (with George M. Whitesides) from Massachusetts Institute of Technology. He then worked at Harvard University as a postdoctoral fellow (with George M. Whitesides) for another year, and became a faculty member at Texas A&M University (1983) where he was promoted to full professor in 1987. He then moved to the Scripps Research Institute in 1989 as Professor and Ernest W. Hahn Chair in Chemistry. From 2006 to 2016, he served as President of Academia Sinica in Taiwan. He is currently the Scripps Family Chair Professor in the Department of Chemistry at The Scripps Research Institute and holds a joint appointment as Distinguished Professor at the Genomics Research Center, Academia Sinica.



Professor Wong received numerous honors for recognition of his accomplishments, including, for example, the Searle Scholar Award in Biomedical Sciences (1985), the Presidential Young Investigator Award in Chemistry, USA (1986), the Roy Whistler Award of the International Carbohydrate Organization (1994), the ACS Harrison Howe Award in Chemistry (1998), the ACS Claude S. Hudson Award in Carbohydrate Chemistry (1999), the International Enzyme Engineering Award (1999), the US Presidential Green Chemistry Challenge Award (2000), The ACS Award for Creative Work in Synthetic Organic Chemistry (2005), Humboldt Research Award for Senior Scientists (2006), the FA Cotton Medal (2008), the Nikkei Asia Prize for Science, Technology and Innovation (2012), the ACS Arthur C. Cope Medal (2012), the Wolf Prize in Chemistry (2014), and the Robert Robinson Award of the Royal Society of Chemistry, UK (2015). Dr. Wong is a member of Academia Sinica (1994), the American Academy of Arts and Sciences (1996), the US National Academy of Sciences (2002) and the US National Academy of Inventors (2014). He served as an Editorial Advisory Board member for the Journal of American Chemical Society and *Angewandte Chemie*, Chairman of the Executive Board of Editors of the Tetrahedron Publications (2006–2008), Head of the Frontier Research Program on Glycotechnology at RIKEN in Japan (1991–1999), and a board member of the US National Research Council on Chemical Sciences and Technology (2000–2003). In

addition, he has received many hon-orary doctor degrees (including one from Technion), given numerous plenary and named lectures, and served as a science advisor to many organizations, including a scientific advisor to the Max-Planck Institute (2000–2008), a member of RIKEN Advisory Council (2010–2016), and the Chief Science Advisor to the Taiwan. Government (2006–2015). His research interests are in the field of chemical biology and synthetic chemistry, with particular focus on the development of new methods and tools for the synthesis and study of complex carbohydrates and glycoproteins associated with disease progression related to aberrant biological glycosylation. He has published over 750 papers and more than 120 patents, and is a highly cited scientist with an h-index of 148.

Reuben Jih-Ru Hwu was invited to attend The First Gulf Chemistry Association International Conference and Exhibition. Accordingly, he had a chance to visit Kingdom of Bahrain November, 2022. The guests were key persons from Kuwait, Oman, and Saudi Arabia. Reuben Jih-Ru Hwu received his PhD from Stanford University in 1982. He serves in different positions, Associate Professor, The Johns Hopkins Univ. (1986–1990); Director of Preparatory Office for College of Biomedical Science and Engineering (2010–2012), Dean of College of Science (2007–2010), Chair Professor (2008–2012), National Central University; Distinguished Chair Professor, National Tsing Hua University (2015–present); Founder, Well-being Biochemical Corp. (2000–); Curriculum Director (1996–1999), International Foundation for Sciences; President of Chinese American Chemical Society, U.S.A. (1991–1993); President of Asian Federation for Medicinal Chemistry (2012–2013); President of the Federation of Asian Chemical Societies (2019–2022).



Dr. Hwu is the Fellow of The Academy of Sciences for the Developing World (1999–); Fellow of IUPAC (2000–); Fellow of The Royal Society of Chemistry (2005–); Fellow of The Federation of Asian Medicinal Chemistry (2013–); Member of the European Academy of Sciences and Arts (2019–). Representative Awards: Excellent Senior Teacher with 30 Years of Service (2020); National Chair Professorship (2015–2018); National Academic Research Innovation Award (2017); Nano Industrial Technology Excellence Award (2013); Outstanding Scholar Award

(2007–2012); Award for an Outstanding Achievement (2008), Senior Distinguished Research Fellow (2005–2007); The 1997 Third World Academy of Sciences Award (in Chemistry), The Third World Academy of Sciences; The Outstanding Young Persons of the World for 1994, Junior Chamber International; Federation of Asian Chemical Societies 1992 and 1993 Distinguished Young Chemist Award; Distinguished Research Award (3 times, 1992–2001); Alfred P. Sloan Research Fellow (twice 1988–1990), U.S.A.; Stuart Pharmaceuticals Achievement Award (1986), ICI Americas Inc.; Ming-Yu-Wen-Hwa Award (1976), Japan. Research fields include nano-biomaterials, new drug development, organic synthesis, and organosilicon chemistry; published > 228 scientific articles and obtained 50 patents. Invented > 14 new biochemical products as merchandize being sold on the market.



Jiali Gao received the national award in the ACS 2023 Computers in Chemical and Pharmaceutical Research, sponsored by the ACS Division of Computers in Chemistry. Dr. Jiali Gao is a Professor of Chemistry, University of Minnesota. He is a theoretical and computational biochemist, whose work focuses on the structure and properties of macromolecular systems. This includes the understanding of protein dynamics and enzyme catalysis, biomolecular interactions and assembly, and biophysical systems biology, as well as the development of quantum and classical mechanical methodologies. The major focus of his research in the past few years has been the understanding of enzyme catalysis based on analyses of the structure and energetics from dynamics simulations in which quantum mechanics is used both to represent the potential energy surface and to treat the nuclear tunneling. He is currently pioneering an effort to develop a fully quantal force field for simulation and modeling of materials, fluids, and biomacromolecules. He recently introduced the concept of analytical coarse-graining of macromolecular particles for the study of diffusion and assembly of proteins and nucleic acids in cells.



Younan Xia received the ACS Award for Creative Invention, sponsored by ACS Corporation Associates. Younan Xia, Brock Family Chair and Georgia Research Alliance Eminent Scholar in Nanomedicine, Georgia Institute of Technology. Dr. Xia received his Ph.D. from Harvard University in 1996. The current research centers on the design and synthesis of novel nanomaterials for a broad range of applications, including nanomedicine, regenerative medicine, cancer theranostics, tissue engineering, controlled release, catalysis, and fuel cell technology. He published > 850 papers and received dozens of honors and awards: Outstanding Achievement in Research Innovation Award, Georgia Institute of Technology, 2023; Best Scientist 2022 (ranked #48 in the world and #33 in the United States), Research.com; Frontier Materials Scientists Award, International Union of Materials Research Society (IUMRS), 2022; World's Top Materials Scientists (ranked #5), Highly Cited Researchers in Chemistry, Clarivate Analytics, 2022.



Qinghuang Lin received the E. V. Murphree Award in Industrial and Engineering Chemistry, sponsored by ExxonMobil Research & Engineering. Dr. Lin received his B.E. and M.S. degrees from Tsinghua University, Beijing, China and his Ph.D. degree from the University of Michigan, Ann Arbor, Michigan, USA. He was a post-doctoral fellow at the University of Texas at Austin prior to joining IBM. He also completed a MicroMBA Program taught by faculty members from the Stern School of Business at New York University and Columbia University Business School at IBM Watson Research Center. Dr. Qinghuang Lin is Director of Lam Research, USA. Before that, he was Director of Technology Development Center at ASML, a global leader in semiconductor lithography equipment, in San Jose, California, USA. Before joined ASML, Dr. Lin was a Research Staff Member, a Senior Manager and an IBM Master Inventor at the IBM Thomas J. Watson Research Center in Yorktown Heights, New York, USA. He has more than 15 years of experience in the semiconductor industry, all with IBM. He has held a variety of positions in semiconductor research, development, engineering, management and technology strategy for IBM's 0.25 μm to 5 nm CMOS technologies, IBM's 512 Mbit & 1 Gbit DRAM, novel memory technologies and other exploratory research. Dr. Lin has more than 90 issued US patents with more than 70 pending US patents. He is a recipient of 25 IBM Invention Plateau Achievement Awards. A frequent organizer and speaker of professional conferences, he is the editor or co-editor of 6 books and 9 conference proceedings volumes and author and co-author of more than 70 technical papers. Dr. Lin is an Associate Editor of *Journal of Micro/Nanolithography, MEMS, and MOEMS* and a Guest Editor of *Journal of Materials Research* focus issue on self-assembly and directed assembly of advanced materials. He has delivered more than 50 keynote or invited lectures worldwide. In 2002, Dr. Lin received an IBM Research Achievement Award for "invention, development and implementation of 248 nm bilayer resist technology in manufacturing." This IBM bilayer resist technology was also part of the 40 years of innovations in semiconductor technology that won IBM 2004 US National Medal of Technology—the highest honor awarded by the President of the United States to America's leading innovators.



In 2015, Dr. Lin, along with colleagues, received an IBM Research Division Outstanding Achievement Award for “Spin Torque Magnetic Random Access Memory (MRAM)” and an IBM Research Division Achievement Award for “193 nm Negative-Tone Development Process for Advanced Memory and Logic Fabrication.” In 2016, Dr. Lin, along with colleagues, received an IBM Research Division Achievement Award for “Contributions to Fundamental Understanding of Line Edge Roughness in Semiconductor Technology.” In 2014, Dr. Lin was named a Fellow of the American Chemical Society (ACS Fellow). In 2015, he was named a Fellow of the Division of Polymeric Materials Science and Engineering (PMSE), American Chemical Society (PMSE Fellow). He was elected to a Fellow of the International Society for Optical Engineering (SPIE Fellow) in 2017. In 2018, he received the Industrial Polymer Scientist Award from the American Chemical Society Polymer Chemistry Division. A member of AAAS, ACS, MRS, SPIE and New York Academy of Sciences, Dr. Lin currently serves as Chair of the American Chemical Society: Polymeric Materials Science and Engineering (PMSE) division and a member of the PMSE Executive Committee. He was Chairman of SPIE Advanced Etch Technology Conference in 2015 and 2016, a member of the Executive Committee of the SPIE Advanced Lithography Symposium and a past chairman of the SPIE Resist Conference. Dr. Lin also served on the Electorate Nominating Committee, Industrial Science and Technology Section of the American Association for the Advancement of Science (AAAS), the Materials Secretariat of American Chemical Society and Co-chair of PMSE Fellows Selection Committee. Dr. Lin has been active in serving the scientific communities, having served as conference chair, co-chair, vice chair, organizers and organizing committees of more than 60 international conferences. He is a member of two engineering honor societies: Tau Beta Pi and Alpha Sigma Mu.

Drs. Ruizhi “Richard” Li, Qi “Tony” Yan, Ming Zeng, Pfizer along with other members Sean O. Bowser, Adam R. Brown, Nga Do, Shane Eisenbeis, Aran K. Hubbell, Matthew M. Marchewka, Ryan S. O’Neill, Giselle P. Reyes, Frank Riley, Philipp Roosen, John F. Sagal, Omar A. Salman, Karen Sutherland received the ACS Award for Team Innovation, sponsored by ACS Corporation Associates. Three professionals expressed their gratitude to their family, friends and colleagues, and shared their future visions (quotation was listed below).

Ruizhi “Richard” Li

Current position: Senior manager, Bristol Myers Squibb

Education: BS, chemical engineering, Columbia University; MS and PhD, chemical and biomolecular engineering, University of Pennsylvania

Li on winning this award: “This award is dedicated to my late mother, for without her love, guidance, and unwavering belief in me this would have never been possible. To the mom who sacrificed much to raise me into a young and responsible scientist that was able to make an impact in this world.”

Qi “Tony” Yan

Current position: Senior principal scientist, Pfizer

Education: BSc, chemistry, Shanghai University of Science and Technology; PhD, analytical chemistry, University of Missouri

Yan on what he hopes to accomplish in the next decade: “I hope our team’s mRNA technology will be used as a cancer vaccine.”

“This will save lives and help people live longer.”

Ming Zeng

Current position: Senior principal scientist, Pfizer

Education: MS, analytical chemistry, Governors State University

Zeng on a memorable project: “The COVID-19 vaccine/lipid project is one of the most memorable projects I have worked on. What makes this project stand out from others is the level of the teamwork demonstrated. Everyone, with their own specialties, cooperated with each other to produce our highly efficient processes, which were transferred successfully to the manufacturing sites.”

Dr. Tianning Diao received Arthur C. Cope Scholar Awards, sponsored by the Arthur C. Cope Fund. Other recipients for this award include Javier Read De Alaniz, University of California, Santa Barbara; Thorsten Bach, Technical University of Munich; Suzanne A. Blum, University of California, Irvine; Kevin Burgess, Texas A&M University; Steven P. Nolan, Ghent University; Jennifer A. Prescher, University of California, Irvine; Hans Renata, Rice University; Vincent M. Rotello, University of Massachusetts; Dean J. Tantillo, University of California, Davis.



Dr. Diao is an Associate Professor and Director of Graduate Studies, New York University. She received her Ph.D. in Chemistry, University of Wisconsin-Madison. Her research expertise spans from Organic, Organometallic, Inorganic, to Catalysis. She received a dozen of honors and fellowships, such as Camille-Dreyfus Teacher-Scholar Award (2019), Thieme Chemistry Journal Award (2019), Organometallics-Editorial Advisory Board (2019), ACS Organometallics Distinguished Author Award (2018), Sloan Research Fellowship (2018), NSF-CAREER Award (2016), and Charles and Martha Casey Excellence Award in Organic Chemistry Research (2012).

Dr. Shuai Tan received 2023 RINENG Young Investigator Award, Results in Engineering. Dr. Tan is currently Lead R&D Engineer/Scientist in Honeywell UOP in Des Plaines IL, USA. He holds a B.S. in Chemistry from Nankai University (2008), a B. Eng. in Chemical Engineering from Tianjin University (2008), and a Ph.D. in Chemical Engineering from University of South Carolina (2013, Prof. Chris Williams & Prof. John Monnier). He performed post-doctoral research at Georgia Institute of Technology (2013–2016, Prof. Chris Jones), and was appointed as research associate in Oak Ridge National Laboratory (2016–2018, Dr. Zili Wu), before joined Honeywell UOP. Shuai owns 21 peer-reviewed publications, with 830+ citations. He has served on the editorial boards of Trends in Renewable Energy since 2015. Shuai's career progresses through various areas of R&D topics. His research interests include development of new catalytic materials for various energy and petrochemical applications, including propane dehydrogenation, acetylene hydrogenation, and alcohol conversion.



Yunlong Zhang was appointed as The Delegate as a Young Observer, IUPAC and Associate Member of ACS Committees on International Activities. Dr. Yunlong Zhang received his BS and MS in China before he came to the US in 2005 and received his PhD in Chemistry from The Ohio State University in 2010. He did his postdoc research at Massachusetts Institute Technology before joining the corporate research labs of ExxonMobil in New Jersey in 2014. Yunlong is currently a staff scientist who leads the advanced characterization of petroleum mixtures and carbon materials. Yunlong's research interests include studying the structure–reactivity of hydrocarbons to find sustainable solutions for energy transition. He has published about 60 publications and has delivered 50 invited lectures and keynote speeches. Yunlong holds several patents and has contributed several book chapters (and books), and numerous company reports. His work has been recognized by winning several awards, including 2021 Rising Star Award by ACS Energy Fuels, 2020 R&D Excellence Award by ExxonMobil, and the 2019 Glenn Award by ACS ENFL Division. Yunlong is the 2022 President of Tri-State chapter of CACS, after serving as a board member for over 8 years. He led the executive committee on revising bylaws and restructuring the governance to improve organizational efficiency. He has been actively involved in the National CACS by serving on the executive committee since 2020. Yunlong is also actively involved in ACS ENFL and I&EC technical divisions, including serving on executive and programming committees, chairing the C&T subcommittee, and founding and chairing the industry subcommittee for ENFL. He is the main organizer of the PetroPhase International Conference in 2020–2021. Yunlong is currently an Associate Editor for ACS Energy & Fuels.



Dr. Wei Gao was elected as the R&D/TS&D Fellow, Analytical Sciences, Core R&D, Dow Inc. and Certified ACS Career Consultant. Wei Gao is a Principal Research Scientist in Analytical Science, Corporate Research and Development, at Dow Inc. She received her BS degree from Fudan University and PhD in Polymer Chemistry and Physics from Peking University. She then worked as a postdoctoral fellow and an Associate Professor in the Institute of Chemistry, Chinese Academy of Sciences. Employment at the NSF-I/UCRC center for Biocatalysis and Bioprocessing of Macromolecules at Polytechnic University (Now NYU Tandon School of Engineering) followed in 2000, and in 2005, she became a Research Assistant Professor.



In 2006, Wei joined Rohm and Haas/Dow. She intensively works on polymer and particle characterization, the synthesis—structure—property relationship of polymeric and colloidal systems, and sustainable polymers. She has published over 30 peer reviewed journal articles and book chapters, edited one book, and has more than 20 patents and patent applications. She has organized American Chemical Society (ACS) symposia in the areas of separation and characterization of macromolecules and particles, polymer sciences for everyday things, and polymer colloids. She a

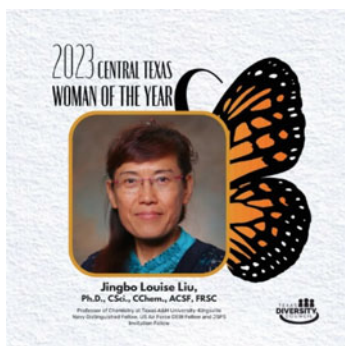
lifetime member of Chinese American Chemical Society (CACS). She also served on the scientific program committee for the GPC2015 conference and the Steering board member for international symposium on Field- and Flow-Based Separations (FFF2018 and FFF2022). She was the recipient of the NOVA Innovation Award from Rohm and Haas Company (2008), US EPA Presidential Green Chemistry Challenge Awards (2003 and 2013), Vernon A. Strenger Scientists' Award from Dow (2019), and ACS Polymer Chemistry Division (POLY) fellow (2021).

Jinxia Fu was elected as The ENFL Treasurer & Program Chair-elect and Associate Member of Committee on Divisional Activities, ACS. On September 15, 22, and 29, 2022, the American Chemical Society (ACS) hosted a series of inaugural presidential Virtual Value Chain (VVC) events focused on SAF. The topics are Opportunities and Challenges for Building Market-Aligned Sustainable Aviation Fuels, led by Dr. Fu. Due to her extraordinary leadership, she was mentioned by Dr. Judith Giordan at the Councilor meeting at the ACS National Meeting, March 29, 2023. Dr. Fu is a research faculty with research interests in biomass and waste processing, biofuel and fuel additive development, and bioenergy conversion technologies. Dr. Fu's recent research is on biomass resources, processing of biomass materials, thermochemical conversion of biomass, sustainable aviation fuel, and development of "green" biofuel additives. Dr. Fu also serves in leadership and steering committee/council roles at University of Hawaii to create and implement policies to foster a teaching, research, and work environment that is characterized by shared values of diversity, equity, and inclusion. Dr. Fu is also as an associate editor of Fuel- Elsevier since 2021.

Dr. Fu's group is actively working with the U.S. Navy Fuels Cross-Functional Team at Naval Air Station Patuxent River (Pax River) and the Fuel Laboratory at Naval Supply System Command Fleet Logistic Center Pearl Harbor (NAVSUP FLC Pearl Harbor) on developing novel analytical methods for advanced fuel characterization, including identification and quantification of trace amount heteroatomic organic species (HOS) in aviation, maritime, and diesel fuels, and determination of the primary precursor compounds that contribute to reduced storage and oxidation stability of fuels. The new analytical methods can reliably and rapidly determine the composition of fuels currently in use and those stored as strategic reserves and investigate the impacts of crucial nitrogen and sulfur containing compounds and additives on fuel properties. Comprehensive fuel composition information is further employed to replace costly experimental measurements by calculating various physicochemical properties of fuels. The knowledge gained in this project improves the understanding of the influences of HOS and fuel additive deterioration on fuel stability and physicochemical properties, guides efforts to preserve fuel quality, and reduces the cost of fuel characterization. To date, the methods for identifying and quantifying nitrogen compounds have been developed and passed round-robin tests performed by multiple fuel labs and used for Navy operational fuel analysis.



Dr. Jingbo Louise Liu was named Women of the Year, TX Diversity Council and certified Career Consultant & appointed as the Associate Member of Committee on Budget and Finance, ACS. Dr. Liu was appointed as the Director of the Center of Teaching Effectiveness in 2021 and previously promoted to the rank of Full Professor in 2016 at Texas A&M University-Kingsville (TAMUK). She is also affiliated with the Texas A&M Energy Institute. Dr. Liu received her Ph.D. in Materials Science and Engineering from the University of Science and Technology Beijing in 2001. Her research expertise focuses on nanostructured inorganic materials preparation, characterization, fundamental physical and chemical properties, and applications of engineered nanomaterials in alternative energy and biological science. She established the highest power density to advance the performance of proton exchange membrane fuel cells and directed a new paradigm to apply metal–organic frameworks in disinfection science. During 16-year services in TAMUK, she taught about 12,000 students; trained more than 200 undergraduate students. She supervised ca. 50 graduate (master & Ph.D.) students. She has hosted and co-hosted 15 visiting scholars to conduct leading-edge research on biomedicine, hydrogen fuel cells, photocatalysis, and nanotechnology. She served as NSF panelist and chaired the proposal review panel. She also served as journal editor and reviewer.



Dr. Liu was a Woman of the Year Award winner, Texas Diversity Council's 2023, and named as the Fellow of 2022 by the American Chemical Society and awarded as the Distinguished Fellow at NSWC—Carderock Division ONR Summer Faculty Program in 2022. She was named Distinguished Women in Chemistry or Chemical Engineering by the International Union of Pure and Applied Chemistry in 2021. She serves as the ACS Certified Career Consultant, elected Councilor of the Energy and Fuels Division, Chair of the South Texas Chapter of the American Chemical Society. She has been elected as an Honorary member of the Golden Key International Society, a Fellow of the Linnean Society of London, a Fellow of the Royal Society of Chemistry, DEBI faculty fellow at the US Air Force Research Laboratory. She was awarded the Chartered Scientist and Chartered Chemist. She was awarded Japan Society for the Promotion of Science Invitation Fellow and worked at the Department of Materials Science, University of Tokyo (2010–2011). She has served as a “Faculty and Student Team” fellow, collectively funded by the National Science Foundation and US Dept. of Energy, Office of Science, and worked at the Argonne National Laboratory (2009). She also received Faculty Fellowship Summer Institute in Israel (2008) and outstanding research and teaching awards at the university level. She directed and participated in projects (> 40) supported by the NSF (USA, CHINA), NSERC (CANADA), ACS Petroleum Research Funds (PRF), R. Welch Foundation (departmental), Dept. of Education, industrial and TAMUK.